

UNCLASSIFIED

AD NUMBER

AD317697

CLASSIFICATION CHANGES

TO: UNCLASSIFIED

FROM: CONFIDENTIAL

LIMITATION CHANGES

TO:
Approved for public release; distribution is unlimited. Document partially illegible.

FROM:
Distribution authorized to U.S. Gov't. agencies and their contractors;
Administrative/Operational Use; MAY 1960. Other requests shall be referred to Air Force Air Proving Ground Center, Eglin AFB, FL. Document partially illegible.

AUTHORITY

31 MAY 1972, DoDD 52000.10; 31 MAY 1972, apgc

THIS PAGE IS UNCLASSIFIED

UNCLASSIFIED

AD NUMBER

AD317697

CLASSIFICATION CHANGES

TO:

CONFIDENTIAL

FROM:

SECRET

AUTHORITY

31 jan 1963, DoDD 52000.10

THIS PAGE IS UNCLASSIFIED

UNCLASSIFIED

AD _____

DEFENSE DOCUMENTATION CENTER

FOR

SCIENTIFIC AND TECHNICAL INFORMATION

CAMERON STATION ALEXANDRIA, VIRGINIA

DOWNGRADED AT 3 YEAR INTERVALS
DECLASSIFIED AFTER 12 YEARS
DOD DIR 5200.10



UNCLASSIFIED



AD

317 697

Reproduced by
Armed Services Technical Information Agency

ARLINGTON HALL STATION; ARLINGTON 12 VIRGINIA

NOTICE: WHEN GOVERNMENT OR OTHER DRAWINGS, SPECIFICATIONS OR OTHER DATA ARE USED FOR ANY PURPOSE OTHER THAN IN CONNECTION WITH A DEFINITELY RELATED GOVERNMENT PROCUREMENT OPERATION, THE U. S. GOVERNMENT THEREBY INCURS NO RESPONSIBILITY, NOR ANY OBLIGATION WHATSOEVER; AND THE FACT THAT THE GOVERNMENT MAY HAVE FORMULATED, FURNISHED, OR IN ANY WAY SUPPLIED THE SAID DRAWINGS, SPECIFICATIONS, OR OTHER DATA IS NOT TO BE REGARDED BY IMPLICATION OR OTHERWISE AS IN ANY MANNER LICENSING THE HOLDER OR ANY OTHER PERSON OR CORPORATION, OR CONVEYING ANY RIGHTS OR PERMISSION TO MANUFACTURE, USE OR SELL ANY PATENTED INVENTION THAT MAY IN ANY WAY BE RELATED THERETO.



317 697

APGC-TR-60-25

ASTIA
DOCUMENT

MAY 1960

CR 341376001

AF 08(635)-542

Copy No. 71

7
~~SECRET~~

FILE COPY
Return to
ASTIA
ARLINGTON HALL STATION
ARLINGTON 12, VIRGINIA
NOX

AD No. 317 697

ASTIA FILE COPY

Pye Wacket

Lenticular Rocket Feasibility Study

(TITLE UNCLASSIFIED)

Prepared by

Convair / Pomona
Convair Division of
General Dynamics Corporation
Pomona, California

ASTIA
RECEIVED
JUL 1 1960
RECEIVED
TIPDR A

for

AIR PROVING GROUND CENTER

EGLIN AIR FORCE BASE, FLORIDA

SPECIAL HANDLING REQUIRED
NOT RELEASABLE TO FOREIGN NATIONALS
The information contained in this document will not be disclosed to Foreign Nationals or their representatives.

~~SECRET~~

Qualified Requestors

MAY OBTAIN COPIES OF THIS REPORT FROM

Armed Services Technical Information Agency

Document Service Center

Arlington Hall Station

Arlington 12, Virginia

Department of Defense contracts must be established for ASTIA services, or have their "need-to-know" certified by the cognizant military agency of their project or contract.

This document contains information affecting the national defense of the United States within the meaning of the Espionage Laws, Title 18, U. S. C., Section 793 and 794. Its transmission or the revelation of its contents in any manner to an unauthorized person is prohibited by law.

SPECIAL HANDLING REQUIRED
NOT RELEASABLE TO FOREIGN NATIONALS

The information contained in this document will not be disclosed to Foreign Nationals or their representatives.

When Government drawings, specifications, or other data are used for any purpose other than in connection with a definitely related Government procurement operation, the United States Government thereby incurs no responsibility nor any obligation whatsoever; and the fact that the Government may have formulated, furnished, or in any way supplied the said drawings, specifications, or other data, is not to be regarded by implication or otherwise as in any manner licensing the holder or any other person or corporation, or conveying any rights or permission to manufacture, use, or sell any patented invention that may in any way be related thereto.

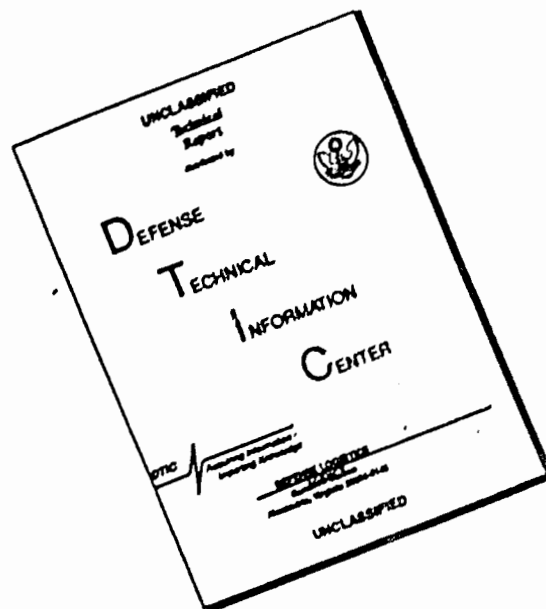
GOVERNMENT AGENCIES

Retain or destroy in accordance with AR 205-1. Do not return.

DEPARTMENT OF DEFENSE CONTRACTORS

Retain this document until contract is completed, then destroy under the provisions of the Information Security Manual for safeguarding classified information.

DISCLAIMER NOTICE



THIS DOCUMENT IS BEST QUALITY AVAILABLE. THE COPY FURNISHED TO DTIC CONTAINED A SIGNIFICANT NUMBER OF PAGES WHICH DO NOT REPRODUCE LEGIBLY.

~~SECRET~~
APGC-TR-60-25

AD

May 1960

PYE WACKET

LENTICULAR ROCKET FEASIBILITY STUDY

CR 341 376 001
ARDC Project 3811
Contract AF 08(635)-542

14 January 1960

CONVAIR/POMONA
Convair Division of General Dynamics Corporation
Pomona, California

Prepared for

AIR PROVING GROUND CENTER
Air Research and Development Command
United States Air Force
Eglin Air Force Base, Florida

~~SECRET~~

SECRET

FOREWORD

This report was prepared under Air Force Contract No. AF 08(635)542, Project 3811, (U) "Lenticular Rocket." The work was administered under the direction of Weapons Laboratory, Air Proving Ground Center, Eglin Air Force Base, Florida.

This document, except the title, is classified SECRET in accordance with AFR 205-1, paragraph 30b, because of the nature and potential military application of the research work and data described herein.

SECRET

SECRET

ABSTRACT

A series of studies was conducted to determine design feasibility of lenticular rockets as airborne weapons. Detailed studies were conducted in the areas of aerodynamics (including wind tunnel tests), aerodynamic heating, propulsion, control systems, structures, and missile performance. Limited guidance and launch studies were conducted. Results of this program showed significant advantages for the lenticular configuration, compared to conventional missiles, particularly as related to omnidirectional launch and high maneuver capability.

Nominal vehicle configurations were determined, based on the parametric data generated, and design feasibility layouts with supporting data are shown for these configurations. Design scaling information was determined for preliminary weight and performance estimates of various-size PYE WACKET missiles. Recommendations are made with regard to the direction future programs should take to: (1) prove out stability, control, and omnidirectional launch capability with flight test vehicles, (2) evaluate overall system problems including launch platform, and (3) initiate prototype engineering work.

SECRET

SECRET

CONTENTS

Section

1. Introduction	
1.1 List of References	1.1
2. Configuration Evaluation	
2.1 Selection of Cross-Section	2.1.1
2.2 Planform Evaluation	2.2.1
2.3 Comparison with Conventional Shapes	2.3.1
2.4 Advantages and Problem Areas	2.4.1
2.5 Manned-Aircraft Defense	2.5.1
2.6 Other Applications	2.6.1
2.7 List of References	2.7.1
3. Design Feasibility Studies	
3.1 Background	3.1.1
3.2 Aerodynamics	3.2.1
3.2.1 Basic Studies	3.2.2
3.2.2 Experimental	3.2.13
3.2.3 Aerodynamic Characteristics	3.2.36
3.2.4 Areas Requiring Investigation	3.2.46
3.2.5 Summary of Aerodynamic Investigations	3.2.46
3.2.6 Symbols and Definitions	3.2.48
3.2.7 List of References	3.2.50
3.3 Launch System	3.3.1
3.3.1 Problem Areas	3.3.1
3.3.2 Method of Approach	3.3.5
3.3.3 Conclusions	3.3.10
3.3.4 List of References	3.3.11
3.4 Propulsion	3.4.1
3.4.1 General Description of Systems Requirements	3.4.1
3.4.2 Air-Breathing Engines	3.4.3
3.4.3 Rocket Engines	3.4.11
3.4.4 Vehicle Performance Studies	3.4.40
3.4.5 Conclusions	3.4.46
3.4.6 Symbols and Definitions	3.4.48
3.4.7 List of References	3.4.50

SECRET

3.5	Aerodynamic Heating	
3.5.1	Thermal Environment	3.5.1
3.5.2	Structural Protection	3.5.8
3.5.3	Summary	3.5.30
3.5.4	Symbols and Definitions	3.5.32
3.5.5	List of References	3.5.33
3.6	Structures	
3.6.1	Types of Materials Considered	3.6.1
3.6.2	Static Considerations	3.6.2
3.6.3	Aeroelastic Considerations	3.6.29
3.6.4	Summary of Structures Study	3.6.40
3.6.5	Symbols and Definitions	3.6.41
3.6.6	List of References	3.6.44
3.7	Control Systems	
3.7.1	Aerodynamic Controls	3.7.1
3.7.2	Reaction-Jet Control	3.7.28
3.7.3	Autopilot	3.7.47
3.7.4	Maneuver Capabilities	3.7.94
3.7.5	Summary	3.7.98
3.7.6	Symbols and Definitions	3.7.98
3.7.7	List of References	3.7.100
3.8	Guidance	
3.8.1	Inertial	3.8.1
3.8.2	Beamriding	3.8.1
3.8.3	Semiactive Homing	3.8.2
3.8.4	Command	3.8.4
3.8.5	Infrared	3.8.4
3.8.6	Conceptual Systems	3.8.12
3.8.7	Summary	3.8.15
3.8.8	List of References	3.8.15
3.9	Performance Studies	
3.9.1	Normal Maneuvers	3.9.1
3.9.2	Omnidirectional Launch Trajectories	3.9.7
3.9.3	Summary	3.9.20
3.10	Feasible Designs	
3.10.1	Feasibility Design of Nominal Missiles	3.10.1
3.10.2	Design Scaling	3.10.21
3.10.3	Performance Scaling	3.10.48
3.10.4	Small Missile Design	3.10.52
3.10.5	Summary	3.10.61
3.10.6	Symbols and Definitions	3.10.62

SECRET

4. Recommendations

- 4.1 Review of Results 4.1
- 4.2 Work to be Done 4.1
- 4.3 Test Vehicle Program 4.2
- 4.4 Prototype Missiles 4.4
- 4.5 Other Applications 4.5

Appendix A – Research and Development Exhibit A.1

Figure

- 2.1.1 Lenticular Configurations for Cross Section Evaluation. 2.1.2
- 2.1.2 Comparison of Lift Coefficient Slope 2.1.2
- 2.1.3 Comparison of Zero-Lift Drag 2.1.2
- 2.1.4 Variation of Center of Pressure Location 2.1.2
- 2.2.1 Comparison of Lift Coefficient of Different Planforms 2.2.2
- 2.2.2 Comparison of Drag Coefficient of Different Planforms 2.2.2
- 2.2.3 Comparison of Lift-to-Drag Ratios for Different Planforms 2.2.2
- 2.2.4 Comparison of Lift Curve Slope of Different Planforms 2.2.2
- 2.2.5 Comparison of Airframe Efficiency of Different Planforms 2.2.3
- 2.3.1 Comparison of PYE WACKET Lift Capability With
Present Airframe Capabilities 2.3.2
- 2.3.2 Comparison of PYE WACKET Airframe Efficiency With
Present Airframe Capabilities 2.3.2
- 2.3.3 Comparison of Maneuver Capabilities 2.3.2
- 2.3.4 Comparison of Turning Radius Capabilities 2.3.2
- 2.5.1 PYE WACKET Unidirectional Launch Capabilities 2.5.2
- 2.5.2 PYE WACKET Rear Intercept Capability Using Unidirectional
Launch 2.5.2
- 2.5.3 Omnidirectional Launch Thrust Phase Performance
Envelope 2.5.4
- 2.5.4 Omnidirectional Launch Performance Envelope 2.5.4
- 2.5.5 Omnidirectional Launch Thrust Phase Performance
Envelope 2.5.4
- 2.5.6 Omnidirectional Launch Thrust and Glide Phase
Performance Envelope 2.5.4
- 3.1.1 Planetary Flight Corridor 3.1.3
- 3.1.2 Total Integrated Volume Versus Thickness-to-Chord Ratio 3.1.4
- 3.1.3 Variation of Zero-Lift Drag Coefficient With Thickness-to-
Chord Ratio 3.1.4
- 3.1.4 Pressure Vessel Required Skin Thickness Versus Thickness-
to-Chord Ratio 3.1.4

3.1.5	Down Range Versus Thickness-to-Chord Ratio	3.1.4
3.2.1	Comparison of Two-Dimensional Theory With Three-Dimensional Test Data	3.2.6
3.2.2	Comparison of Two-Dimensional Theory With Three-Dimensional Test Data	3.2.6
3.2.3	Comparison of Two-Dimensional Theory With Three-Dimensional Test Data	3.2.6
3.2.4	Circular Planform Regions of Influence	3.2.6
3.2.5	Cross Sections Considered	3.2.10
3.2.6	Estimated Variation of Lift-to-Drag Ratio With Volume Parameter	3.2.12
3.2.7	Estimated Variation of Lift-to-Drag Ratio With Volume Parameter	3.2.12
3.2.8	Estimated Variation of Lift-to-Drag Ratio With Volume Parameter	3.2.12
3.2.9	Estimated Variation of Drag Coefficient With Volume Parameter	3.2.12
3.2.10	Estimated Variation of Drag Coefficient With Volume Parameter	3.2.13
3.2.11	Estimated Variation of Drag Coefficient With Volume Parameter	3.2.13
3.2.12	Cross Section Shapes	3.2.14
3.2.13	Model III	3.2.15
3.2.14	Model III, Partially Fabricated	3.2.15
3.2.15	Model III, Top View	3.2.16
3.2.16	Model III, Side View	3.2.16
3.2.17	Model II	3.2.17
3.2.18	Model II, Partially Fabricated	3.2.17
3.2.19	Model II, Side View	3.2.18
3.2.20	Model I	3.2.18
3.2.21	Model I, Side View	3.2.19
3.2.22	Test Article Arrangement	3.2.19
3.2.23	Model I, Mach Number 3	3.2.22
3.2.24	Model III, Mach Number 3	3.2.23
3.2.25	Model I, Mach Number 6	3.2.24
3.2.26	Model III, Mach Number 6	3.2.25
3.2.27	Model I, Mach Number 2	3.2.26
3.2.28	Model IV, Mach Number 2	3.2.27
3.2.29	Model I, Mach Number 2	3.2.28
3.2.30	Model IV, Mach Number 2	3.2.29
3.2.31	Comparisons of Lift and Drag Coefficients	3.2.31

SECRET

3.2.32	Comparisons of Lift and Drag Coefficients	3.2.31
3.2.33	Comparisons of Lift and Drag Coefficients	3.2.31
3.2.34	Comparisons of Lift and Drag Coefficients	3.2.31
3.2.35	Comparisons of Lift and Drag Coefficients	3.2.32
3.2.36	Comparison of Lift-to-Drag Ratio	3.2.32
3.2.37	Comparison of Lift-to-Drag Ratio	3.2.32
3.2.38	Comparison of Lift-to-Drag Ratio	3.2.32
3.2.39	Comparison of Lift-to-Drag Ratio	3.2.33
3.2.40	Comparison of Lift-to-Drag Ratio	3.2.33
3.2.41	Comparison of Lift Coefficient Slope	3.2.35
3.2.42	Comparison of Zero-Lift Drag	3.2.35
3.2.43	Comparison of Pitching Moment Coefficient Slope	3.2.35
3.2.44	Variation of Center of Pressure Location	3.2.35
3.2.45	Comparison of Predicted and Experimental Lift Coefficient . .	3.2.37
3.2.46	Comparison of Predicted and Experimental Zero-Lift Drag Coefficient	3.2.37
3.2.47	Variation of Skin Friction, Base, Wave, and Zero-Lift Drag Coefficients	3.2.37
3.2.48	Variation of Skin Friction, Base, Wave, and Zero-Lift Drag Coefficients	3.2.37
3.2.49	Variation of Zero-Lift Drag Coefficient With Thickness-to- Chord Ratio	3.2.38
3.2.50	Drag Increment Due to Blunting Leading Edge	3.2.40
3.2.51	Variation of Normal Force Derivative With Mach Number . . .	3.2.40
3.2.52	Variation of Normal Force Coefficient With Angle of Attack . .	3.2.40
3.2.53	Variation of Normal Force Coefficient With Angle of Attack . .	3.2.40
3.2.54	Variation of Pitching Moment Derivative - Thickness/ Chord = 0.14	3.2.41
3.2.55	Variation of Pitching Moment Derivative - Thickness/ Chord = 0.21	3.2.41
3.2.56	Body Yaw Moment Per Degree Yaw Angle	3.2.42
3.2.57	Estimated Variation of Yawing Moment Coefficient	3.2.43
3.2.58	Typical Seeker Locations	3.2.44
3.2.59	Effect of Seekers on Zero-Lift Drag	3.2.44
3.2.60	Effect of Seekers on Pitching Moment Derivative	3.2.45
3.2.61	Variation of Drag Due to Protuberances	3.2.45
3.2.62	Variation of Drag Due to Protuberances	3.2.45
3.2.63	Variation of Drag Due to Protuberances	3.2.45
3.3.1	Longitudinal Angularity Field	3.3.2
3.3.2	Dynamic Pressure Field	3.3.2
3.3.3	Shock Wave Loading	3.3.3

3.3.4	Rocket Jet Expanding to Ambient Pressure (Constant Mach Number Diagram)	3.3.4
3.3.5	Rocket Jet Expanding to Ambient Pressure (Static Pressure Diagram)	3.3.4
3.3.6	Rocket Jet Expanding to Ambient Pressure (Temperature Diagram)	3.3.4
3.3.7	Rocket Jet Envelopes for Expansion to Ambient Pressure	3.3.4
3.3.8	Flow Field About XF3D Wing Section	3.3.6
3.3.9	Pitching Deviation	3.3.6
3.3.10	Displacement Versus Time for Various Initial Ejection Velocities During Launch	3.3.7
3.3.11	Accelerating Force Required as a Function of Action Distance and Ejection Velocity	3.3.8
3.3.12	Impulse Requirements for Velocity and Distance at the End of Separation	3.3.8
3.3.13	Typical Pitch Angle - Time Histories, Mach No. 2, Altitude = 50,000 Feet, B-58 Airplane	3.3.9
3.3.14	Typical Altitude - Time Histories, Mach No. 2, Altitude = 50,000 Feet, B-58 Airplane	3.3.9
3.3.15	Vertical Displacement Between Airplane and Controlled Pod Mach No. 2, Altitude = 50,000 Feet, B-58 Airplane	3.3.10
3.4.1	Dimensionless Shape Contours	3.4.2
3.4.2	Dimensionless Shape Contours	3.4.2
3.4.3	Dimensionless Shape Contours	3.4.2
3.4.4	Integrated Volume Versus Chord Station	3.4.2
3.4.5	Inlet Compression Systems	3.4.5
3.4.6	Inlet Efficiency Versus Mach Number	3.4.5
3.4.7	Contraction Ratio Versus Mach Number	3.4.7
3.4.8	Pitching Moment Coefficient Versus Angle of Attack for Super Talos	3.4.7
3.4.9	Turbojet, Matching Drag Penalties	3.4.8
3.4.10	Relative Sizes for Ramjets With Equal Net Thrust	3.4.9
3.4.11	Body Drag Versus Mach Number	3.4.9
3.4.12	Net Jet Thrust Coefficient for Fixed Geometry Engines	3.4.11
3.4.13	Effect of Angle of Attack on Inlet Performance	3.4.11
3.4.14	Specific Impulse Versus Chamber Pressure	3.4.13
3.4.15	Specific Impulse Versus Altitude	3.4.14
3.4.16	Lenticular Solid Propellant Rocket Motor Configuration	3.4.16
3.4.17	Solid Propellant Motor Configuration	3.4.16
3.4.18	Right Circular Cylinder Motor Configuration	3.4.18
3.4.19	Available Volume With Three Cylinder Motor	3.4.19

SECRET

3.4.20	Specific Impulse Versus Chamber Pressure	3.4.19
3.4.21	Predicted Delivered Specific Impulse Growth Trends	3.4.21
3.4.22	Configuration and Nomenclature	3.4.23
3.4.23	Tapered Cylinder Motor Configuration	3.4.23
3.4.24	Thrust Versus Burning Time	3.4.27
3.4.25	Configuration and Nomenclature for Tapered Cylinder	3.4.27
3.4.26	Configuration and Nomenclature for Sandwich Material and Stay-Bars of Solid Propellant Pancake Motor	3.4.31
3.4.27	Comparison of Theoretical and Experimental Performance for Storable Liquid Propellants	3.4.36
3.4.28	Predicted Delivered Specific Impulse Growth Trends	3.4.37
3.4.29	Delivered Specific Impulse Versus Chamber Pressure	3.4.38
3.4.30	Delivered Specific Impulse Versus Chamber Pressure	3.4.38
3.4.31	Burnout Velocity Versus Thickness to Chord Ratio	3.4.42
3.4.32	Range to Mach 2.5 Versus Thickness to Chord Ratio	3.4.43
3.4.33	Time to 10,000 Feet Range Versus Thickness to Chord Ratio	3.4.43
3.4.34	Velocity Versus Time	3.4.45
3.4.35	Range Versus Time	3.4.45
3.4.36	Velocity Versus Time	3.4.45
3.4.37	Range Versus Time	3.4.45
3.4.48	Time to 10,000 Feet Range Versus Thickness to Chord Ratio	3.4.46
3.4.39	Range Versus Time	3.4.46
3.5.1	Radiation Equilibrium Temperature	3.5.2
3.5.2	Radiation Equilibrium Temperature for Re-Entry Trajectories	3.5.2
3.5.3	Mach Number Versus Time	3.5.2
3.5.4	Mach Number Versus Time	3.5.2
3.5.5	Normalized Heat Input Versus Altitude	3.5.4
3.5.6	Normalized Maximum Recovery Temperature Versus Altitude	3.5.4
3.5.7	Total Heat Input Versus Dimensionless Distance	3.5.4
3.5.8	Aerodynamic Heating Rate Versus Time	3.5.4
3.5.9	Flat Plate Recovery Temperature	3.5.6
3.5.10	Turbulent Recovery Temperature Versus Dimensionless Distance	3.5.6
3.5.11	Heat Transfer Coefficient for Blunt Leading Edge	3.5.8
3.5.12	Heat Transfer Coefficient Versus Dimensionless Distance	3.5.8
3.5.13	Ablating Wall Example Used to Check Numerical Com- putation Against Analytical Solution	3.5.15
3.5.14	Total Ablation Mass Loss Versus Altitude	3.5.16
3.5.15	Ablation Mass Versus Dimensionless Distance	3.5.16

3.5.16	Ablation Mass Versus Dimensionless Distance	3.5.16
3.5.17	Ablation Weight Versus Flight Time	3.5.16
3.5.18	Ablation Weight Versus Flight Time	3.5.17
3.5.19	Temperature Distribution Versus Time	3.5.17
3.5.20	Temperature Distribution Versus Time	3.5.17
3.5.21	Temperature Distribution Versus Time	3.5.17
3.5.22	Temperature Distribution Versus Time	3.5.18
3.5.23	Temperature Distribution Versus Time	3.5.18
3.5.24	Temperature Distribution Versus Time	3.5.19
3.5.25	Mass Injection Effect on Stanton Number	3.5.22
3.5.26	Mass Rates of Transpiration and Ablation Versus Time	3.5.23
3.5.27	Mass Rates of Transpiration and Ablation Versus Time	3.5.23
3.5.28	Leading Edge Geometry	3.5.26
3.5.29	Stagnation Temperature History	3.5.26
3.5.30	Simplified Leading Edge	3.5.28
3.5.31	Thermal Model	3.5.28
3.5.32	Normalized Leading Edge Temperature	3.5.30
3.5.33	Leading Edge Surface Temperature Versus Time	3.5.30
3.5.34	Temperature Gradient Through Leading Edge	3.5.31
3.6.1	Basic Structure Configuration	3.6.3
3.6.2	Corrugated Stiffener	3.6.4
3.6.3	Panel Stability Stress Versus Ratio of Panel Length-to-Skin Thickness	3.6.5
3.6.4	Leading Edge Corrugations	3.6.5
3.6.5	Optimization of Corrugation Stiffness	3.6.6
3.6.6	Corrugation Depth Versus Ratio Of Panel Length-to-Skin Thickness	3.6.6
3.6.7	Corrugation Depth to Corrugation Thickness Ratio Versus Panel Length-to-Skin Thickness Ratio	3.6.7
3.6.8	Skin Load Capacity Versus Ratio Of Panel Length-to-Skin Thickness	3.6.8
3.6.9	Skin Load Capacity Versus Skin and Corrugation Weight	3.6.8
3.6.10	Determination of Skin Loading	3.6.9
3.6.11	Leading Edge, Solid Skin	3.6.11
3.6.12	Thickness-to-Chord Ratio Versus Forward Section Solid Skin Weight	3.6.13
3.6.13	Leading Edge, Sandwich Skin	3.6.13
3.6.14	Weight Comparison of Forward Section Structure Designs	3.6.15
3.6.15	Half Cylinder Closure	3.6.15
3.6.16	Elliptical Closure	3.6.16
3.6.17	Edge Closure Nomenclature	3.6.16

SECRET

3.6.18	Tank Edge	3.6.17
3.6.19	Optimization of Rocket Motor End Closure Ellipse Ratio	3.6.19
3.6.20	Thickness-to-Chord Ratio versus Rocket Motor End Closure Weight	3.6.20
3.6.21	Tank Plate Cover	3.6.20
3.6.22	Plate Tank Cover, Solid Skin	3.6.21
3.6.23	Tank Plate Cover, Grid Skin	3.6.22
3.6.24	Planform Rocket Motor Honeycomb Skin	3.6.25
3.6.25	Weight Comparison of Fuel Tank Skin Structures	3.6.26
3.6.26	Thickness-to-Chord Ratio Versus Weight of Posts and Post Fittings	3.6.27
3.6.27	Thickness-to-Chord Ratio Versus Total Structural Weight	3.6.28
3.6.28	Thickness-to-Chord Ratio Versus Total Structural Weight	3.6.28
3.6.29	Thickness-to-Chord Ratio Versus Total Structural Weight	3.6.28
3.6.30	Planform of Solid Propellant Rocket Motor	3.6.28
3.6.31	Stability Derivatives	3.6.31
3.6.32	Sketch of Configuration	3.6.34
3.6.33	Altitude Versus Critical Panel Flutter Mach Number	3.6.35
3.6.34	Skin Thickness Versus Critical Panel Flutter Mach Number	3.6.35
3.6.35	Effect of Internal Stiffening on Critical Panel Flutter Mach Number	3.6.36
3.6.36	Physical Properties of Reference Vehicle	3.6.37
3.6.37	Deflection Shapes and Frequencies for Reference Configuration	3.6.37
3.6.38	Variation of Frequency With Dimension Changes	3.6.38
3.6.39	PYE WACKET Vibration Tests	3.6.39
3.6.40	Static Aeroelastic Effect on Center of Pressure as a Function of Mach Number and Vehicle Stiffness	3.6.40
3.7.1	Configuration and Nomenclature for Aerodynamic Controls	3.7.3
3.7.2	Aerodynamic Force, Moment, and Angle Notation	3.7.4
3.7.3	Side View of Model III With Aft P_1 Pitchvator at -25° Incidence, Mach No. = 4	3.7.7
3.7.4	Side View of Model III With Aft P_1 Pitchvator at -25° , Mach No. = 5	3.7.8
3.7.5	Side View of Model III With Aft P_1 Pitchvator at -20° Incidence, Mach No. = 6	3.7.9
3.7.6	Variation of Pitchvator Effectiveness Due to Aspect Ratio and Area	3.7.10
3.7.7	Effect of Pitchvator Aspect Ratio and Area on Control Capability	3.7.11
3.7.8	Effect of Pitchvator Aspect Ratio and Area on Normal Force Coefficient	3.7.11

3.7.9	Effect of Pitchvator Aspect Ratio and Area on Axial Force . .	3.7.13
3.7.10	Effect of Pitchvator Aspect Ratio and Area on Control Capability	3.7.13
3.7.11	Comparison of Effectiveness of Fore and Aft Pitchvators With Aft Pitchvator Only	3.7.13
3.7.12	Comparison of Effectiveness of Fore and Aft Pitchvators With Aft Pitchvator Only	3.7.13
3.7.13	Comparison of Effectiveness of Fore and Aft Pitchvators With Aft Pitchvator Only	3.7.14
3.7.14	Variation of Pitchvator Effectiveness Due to Incidence	3.7.14
3.7.15	Variation of Pitchvator Effectiveness Due to Incidence	3.7.14
3.7.16	Variation of Trim Angle of Attack With Pitchvator Angle of Incidence	3.7.14
3.7.17	Variation of Trim Angle of Attack with Pitchvator Angles of Incidence	3.7.15
3.7.18	Comparison of Pitching Moment Effects Due to Pitchvators and Leading Edge Deflection	3.7.16
3.7.19	Top View of Model III With Aft P ₁ Pitchvator at 20° Incidence and Conevators at Zero Deflection, Mach No. = 2	3.7.17
3.7.20	Top View of Model III With Conevators at 20° Differential Deflection, Mach No. = 5	3.7.18
3.7.21	Rolling Moment Derivative Due to Conevators	3.7.19
3.7.22	Comparison of Zero-Lift Drag Coefficient for Body With and Without Conevators	3.7.19
3.7.23	Comparison of Pitching Moment Derivative for Body With and Without Conevators	3.7.20
3.7.24	Increase in Normal Force Coefficient Per Degree Angle of Attack Due to Conevators	3.7.21
3.7.25	Roll Control Induced Yawing Moment Per Degree Differential Deflection per Degree Angle of Attack	3.7.21
3.7.26	Top View of Model III With Wedgevators at 20° Differential Deflection, Mach No. = 2	3.7.22
3.7.27	Top View of Model III With Wedgevators at 15° Differential Deflection, Mach No. = 5	3.7.23
3.7.28	Side View of Model III Rolled 20° With Wedgevators at 15° Differential Deflection, Mach No. = 4	3.7.24
3.7.29	Rolling Moment Derivative Due to Wedgevators	3.7.25
3.7.30	Comparison of Rolling Moment Coefficient for Conevators, Wedgevators, and Side Elevons	3.7.26
3.7.31	Variation of Yawing Moment With Mach Number for Different Yaw Control Angles of the Wedgevators	3.7.26

SECRET

3.7.32 Comparison of Zero-Lift Drag Coefficient for Body With and Without Wedgevators 3.7.26

3.7.33 Yaw Control Induced Rolling Moment Coefficient per Degree Difference in Wedgevator Yaw Control Angle per Degree Angle of Attack 3.7.26

3.7.34 Schematic of Jet Paddles Relative to Rocket Nozzle 3.7.29

3.7.35 Extendable Nozzle Deflectors 3.7.29

3.7.36 Lateral Forces Developed From the Introduction of a Secondary Jet of Gas 3.7.31

3.7.37 Variation of Nozzle Side Force With Secondary Flow. 3.7.31

3.7.38 Variation of Side Force With Secondary Flow 3.7.31

3.7.39 Methods of Thrust-Vector Control 3.7.31

3.7.40 Typical Jetevator and Nozzle Assembly With Blowback Seal 3.7.33

3.7.41 Jet Deflection Versus Jetevator Deflection 3.7.33

3.7.42 Flexible Seal Nozzle Design 3.7.34

3.7.43 Comparison of Performance of Various Methods of Jet Deflection 3.7.35

3.7.44 Diagram for Reaction Controls 3.7.38

3.7.45 Nozzle Flow Rates for Secondary Control System 3.7.38

3.7.46 Duration for Secondary Control System 3.7.39

3.7.47 Duration for Modulated Secondary Control System 3.7.40

3.7.48 Duration for Modulated Secondary Control System 3.7.40

3.7.49 Optimization of Nozzle Angle Based on Minimum Flow for 3 Seconds Yaw Plus 40 Seconds Pitch 3.7.41

3.7.50 Transient Response Characteristics for Lenticular Control Nozzles 3.7.43

3.7.51 Jet Interference Produced by Side-Exhausting Jet Issuing From Cylindrical Body 3.7.44

3.7.52 Jet Interference Correlation of Experimental Data 3.7.44

3.7.53 Normal Force Magnification Factor versus Jet Stagnation Pressure Ratio 3.7.46

3.7.54 Normal Force Magnification Factor versus Jet Stagnation Pressure Ratio 3.7.46

3.7.55 Roll Moment Derivative Due to Roll Deflection Versus Mach Number 3.7.50

3.7.56 Roll Moment Derivative Due to Roll Angle Rate Versus Mach Number 3.7.50

3.7.57 Simplified Block Diagram of a Linear Roll System 3.7.52

3.7.58 Transient Responses Mach 2 Altitude 60K $\phi_c \pm 90^\circ$ 3.7.53

3.7.59 Transient Responses Mach 5 Altitude 60K $\phi_c \pm 90^\circ$ 3.7.54

3.7.60	Transient Responses Mach 2 Altitude 30K $\phi_c \pm 90^\circ$	3.7.55
3.7.61	Transient Responses Mach 5 Altitude 30K $\phi_c \pm 90^\circ$	3.7.56
3.7.62	Linear Autopilot Gain Variations	3.7.57
3.7.63	Simplified Block Diagram of a Two-State Non-Linear Roll System	3.7.59
3.7.64	Simplified Block Diagram of a Four-State Non-Linear Roll System	3.7.59
3.7.65	Transient Responses Mach 5 Altitude 30K $\phi_c \pm 90^\circ$	3.7.60
3.7.66	Transient Responses Mach 5 Altitude 60K $\phi_c \pm 90^\circ$	3.7.61
3.7.67	Transient Responses Mach 5 Altitude 60K $\phi_c \pm 15^\circ$	3.7.62
3.7.68	Reaction Control Autopilot Gain Variation	3.7.63
3.7.69	Phase Plane Plot of a 15 Degree Step Input	3.7.63
3.7.70	Stability Analysis of Roll System Utilizing the Describing Function	3.7.64
3.7.71	Yaw Reaction Control System Geometry and Force Sign Convention	3.7.67
3.7.72	Yaw Autopilot Block Diagram	3.7.69
3.7.73	Transient Response Mach 5 Altitude 30K $\beta_c \pm 10^\circ$	3.7.71
3.7.74	Transient Response Mach 5 Altitude 30K $\beta_I + 10^\circ, \beta_I + 100^\circ/\text{SEC}$	3.7.72
3.7.75	Transient Response Mach 5 Altitude 60K $\beta_c + 10^\circ$	3.7.73
3.7.76	Transient Response Mach 5 Altitude 60K $\beta_I + 10^\circ, \beta_I + 50^\circ/\text{SEC}$	3.7.74
3.7.77	Yaw Autopilot Gain Variation	3.7.75
3.7.78	Yaw Autopilot Time Constant Variation	3.7.75
3.7.79	Pitch Geometry	3.7.76
3.7.80	Linear Pitch Autopilot Block Diagram	3.7.78
3.7.81	Transient Responses Mach 5 Altitude 60K $\eta_c + 30g's$	3.7.79
3.7.82	Transient Responses Mach 2 Altitude 30K $\eta_c + 30g's$	3.7.80
3.7.83	Transient Responses Mach 2 Altitude 60K $\eta_c + 30g's$	3.7.81
3.7.84	Linear Pitch Autopilot Gain Variation K	3.7.82
3.7.85	Linear Pitch Autopilot Gain Variation K_1	3.7.82
3.7.86	Linear Pitch Autopilot Pitchlevator Deflection Versus Pitching Moment	3.7.84
3.7.87	Nonlinear Reaction Control Pitch Autopilot Block Diagram	3.7.86
3.7.88	Transient Responses Mach 5 Altitude 30K $\eta_c + 10g's$	3.7.87
3.7.89	Transient Responses Mach 5 Altitude 30K $\eta_c + 30g's$	3.7.88
3.7.90	Transient Responses Mach 5 Altitude 60K $\eta_c + 30g's$	3.7.89
3.7.91	Transient Responses Mach 2 Altitude 30K $\eta_c + 30g's$	3.7.90
3.7.92	Transient Responses Mach 2 Altitude 60K $\eta_c + 30g's$	3.7.91
3.7.93	Reaction Control Pitch Autopilot Gain Variation K_1	3.7.93

SECRET

3.7.94	Reaction Control Pitch Autopilot Gain Variation K_2	3.7.93
3.7.95	Pitch Autopilot Response Times	3.7.94
3.7.96	Available Normal Acceleration, Mach 2	3.7.97
3.7.97	Available Normal Acceleration, Mach 5	3.7.97
3.8.1	IR Window	3.8.6
3.8.2	Two-Color Photocell	3.8.11
3.8.3	Target Test and Background Reduction	3.8.12
3.8.4	Guidance and Control Schematic	3.8.13
3.9.1	Missile Vertical Plane Geometry and Nomenclature	3.9.2
3.9.2	Analog Patchboard Mounted in Computer Console	3.9.4
3.9.3	Maximum Maneuver Trajectories	3.9.6
3.9.4	Maximum Maneuver Trajectories	3.9.6
3.9.5	Maximum Maneuver Trajectories	3.9.6
3.9.6	Maximum Maneuver Trajectories	3.9.6
3.9.7	Missile Planform Plane Geometry and Nomenclature	3.9.8
3.9.8	Omnidirectional Launch Thrust and Glide Phase Performance Envelopes	3.9.13
3.9.9	Omnidirectional Launch Thrust Phase Performance Envelope	3.9.13
3.9.10	Omnidirectional Launch Thrust and Glide Phase Performance Envelopes	3.9.13
3.9.11	Omnidirectional Launch Thrust Phase Performance Envelope	3.9.13
3.9.12	Omnidirectional Launch Performance Envelope	3.9.14
3.9.13	Omnidirectional Launch Thrust Phase Performance Envelope	3.9.14
3.9.14	Omnidirectional Launch Thrust and Glide Phase Performance Envelope	3.9.14
3.9.15	Omnidirectional Launch Thrust Phase Performance Envelope	3.9.14
3.9.16	Omnidirectional Launch Thrust and Glide Phase Performance Envelopes for Various Burning Times	3.9.15
3.9.17	Omnidirectional Launch Thrust and Glide Phase Performance Envelopes for Various Burning Times	3.9.15
3.9.18	Omnidirectional Launch Thrust and Glide Phase Performance Envelopes for Various Burning Times	3.9.15
3.9.19	Omnidirectional Launch Thrust and Glide Phase Performance Envelopes for Various Burning Times	3.9.15
3.9.20	Omnidirectional Launch Thrust and Glide Phase Performance Envelopes for Various Burning Times	3.9.16
3.9.21	Omnidirectional Launch Thrust and Glide Phase Performance Envelopes for Various Burning Times	3.9.16

3. 9. 22 Omnidirectional Launch Thrust and Glide Phase Performance
Envelopes for Different Thickness-to-Chord Ratios 3. 9. 16

3. 9. 23 Omnidirectional Launch Thrust and Glide Phase Performance
Envelopes for Different Thickness-to-Chord Ratios 3. 9. 16

3. 9. 24 Omnidirectional Launch Performance Enevelope 3. 9. 17

3. 9. 25 Omnidirectional Launch Performance Envelope 3. 9. 17

3. 9. 26 Omnidirectional Launch Performance Envelope 3. 9. 18

3. 10. 1 Feasibility Layout of 60-Inch Diameter 21 Percent PYE
WACKET Missile 3. 10. 3

3. 10. 2 Feasibility Layout of 60-Inch Diameter 14 Percent PYE
WACKET Missile 3. 10. 5

3. 10. 3 Scaled Launch Weights 3. 10. 7

3. 10. 4 Scaled Range Performance 3. 10. 7

3. 10. 5 Integrated Missile Volume 3. 10. 9

3. 10. 6 Leading Edge 3. 10. 9

3. 10. 7 Layout of Reaction Control System 3. 10. 11

3. 10. 8 Variation of Maneuverability With Reaction Jet Thrust 3. 10. 16

3. 10. 9 Effect of Altitude on Downrange 3. 10. 16

3. 10. 10 Required and Available Yawing Moment at Launch 3. 10. 16

3. 10. 11 Variation of Roll Acceleration With Reaction Jet Thrust 3. 10. 16

3. 10. 12 Variation of Maneuverability With Reaction Jet Thrust 3. 10. 21

3. 10. 13 Effect of Altitude on Downrange 3. 10. 21

3. 10. 14 Required and Available Yawing Moment at Launch 3. 10. 22

3. 10. 15 Scaled Total Volume 3. 10. 23

3. 10. 16 Beam Loading 3. 10. 25

3. 10. 17 Resultant Forces Diagram 3. 10. 25

3. 10. 18 Spanwise Section 3. 10. 26

3. 10. 19 Scaled Structural Weights 3. 10. 29

3. 10. 20 Scaled Rocket Weights 3. 10. 33

3. 10. 21 Scaled Control System Weights 3. 10. 36

3. 10. 22 Typical IR Homing System 3. 10. 37

3. 10. 23 Typical Semiactive CW Doppler Guidance System 3. 10. 37

3. 10. 24 Typical Command Guidance 3. 10. 37

3. 10. 25 Evolution of Electronic Packaging 3. 10. 37

3. 10. 26 Standard and Improved Standard Packaging 3. 10. 39

3. 10. 27 Transistorized Guidance Package 3. 10. 39

3. 10. 28 Transistorized Video Amplifier 3. 10. 40

3. 10. 29 Evolution in Packaging Diode Assembly 3. 10. 40

3. 10. 30 PYE WACKET Electronic Package Mockup 3. 10. 42

3. 10. 31 Scaled Electronic Section Weights 3. 10. 42

3. 10. 32 Scaled Fuze Weights 3. 10. 44

SECRET

3.10.33 Scaled Battery Power Supply Weights	3.10.46
3.10.34 Scaled Battery Power Supply Weights	3.10.46
3.10.35 Scaled Flight Times	3.10.47
3.10.36 Scaled Ablation Material Weights	3.10.49
3.10.37 Scaled Miscellaneous Weights	3.10.49
2.10.38 Scaled Warhead Weights	3.10.51
3.10.39 Scaled Standoff Distances	3.10.51
3.10.40 Feasibility Layout of 36-Inch Diameter 21 Percent PYE WACKET Missile	3.10.55
3.10.41 PYE WACKET 36-Inch Mockup	3.10.58
3.10.42 PYE WACKET 36-Inch Mockup	3.10.58
3.10.43 PYE WACKET 36-Inch Mockup	3.10.59
3.10.44 Variation of Maneuverability With Reaction Jet Thrust	3.10.59
3.10.45 Effect of Altitude on Downrange	3.10.60
3.10.46 Required and Available Yawing Moment at Launch	3.10.60
3.10.47 Variation of Roll Acceleration With Reaction Jet Thrust	3.10.61

Table

3.1.1 Vehicle Characteristics	3.1.1
3.1.2 Hypothetical Aircraft Characteristics	3.1.2
3.2.1 Pitchvator Geometrical Characteristics	3.2.20
3.4.1 Propellant Properties	3.4.20
3.4.2 Advanced Propellant	3.4.22
3.4.3 Cylindrical Motor Comparison	3.4.25
3.4.4 Tapered Cylinder Sizes	3.4.27
3.4.5 Tapered Cylinder Motors	3.4.28
3.4.6 Titanium Characteristics	3.4.30
3.4.7 Case Weights and Dimensions	3.4.32
3.4.8 Solid Propellant Pancake Motor	3.4.33
3.4.9 Storable Liquid Propellant Performance	3.4.35
3.4.10 Performance Trends (Storable Liquid Propellant)	3.4.36
3.4.11 Storable Liquid Propellant Pancake Motors	3.4.39
3.6.1 Tensile Yields In Welded Condition	3.6.1
3.6.2 Effect of Thickness-to-Chord Ratio on Maximum Weight	3.6.10
3.6.3 Effect of Thickness-to-Chord Ratio on Weight/Square Inch	3.6.10
3.6.4 End Closure Weights	3.6.18
3.7.1 Pitchvator Geometric Characteristics	3.7.3
3.7.2 Comparison of Reaction-Jet Controls	3.7.4
3.7.3 Correlation Between Computed And Empirical Results	3.7.45

3.7.4	Summary of Transient Response Times And Control	
	Torques	3.7.52
3.9.1	PYE WACKET Configuration Investigation	3.9.10
3.9.2	Study Conditions	3.9.10
3.9.3	Omnidirectional Launch Study	3.9.11
3.10.1	PYE WACKET 21 Percent 60-Inch Diameter	3.10.13
3.10.2	Weight and Balance Statement for 60-Inch Diameter 21	
	Percent PYE WACKET Missile	3.10.14
3.10.3	PYE WACKET 14 Percent 60-Inch Diameter	3.10.18
3.10.4	Weight and Balance Statement for 60-Inch Diameter 14	
	Percent PYE WACKET Missile	3.10.19
3.10.5	Weight and Balance Statement for 36-Inch Diameter 21	
	Percent PYE WACKET Missile	3.10.53
3.10.6	PYE WACKET 21 Percent 36-Inch Diameter	3.10.57

CONFIDENTIAL



PYE WACKET

CONFIDENTIAL

SECRET

**Section 1
INTRODUCTION**

A general aerodynamic evaluation and a vehicle feasibility design study was conducted to determine the overall technical feasibility of the lenticular cross section, circular planform configuration as a potentially significant advance in airborne weaponry.

The lenticular cross section, circular planform concept originated with the Technical Planning Group of the Air Proving Ground Center, Air Research and Development Command, Eglin Air Force Base, Florida. This group conducted a preliminary in-house study on the feasibility of lenticular rockets. Parameters for a lenticular cross section, circular planform configuration were chosen and feasibility calculations were made. Data obtained from these theoretical analyses indicated a possibility for advanced missile applications for both offensive and defensive roles.

The efforts of the Technical Planning Group were furthered by an experimental program conducted in Tunnel E-1 of the Gas Dynamics Facility, Arnold Engineering Development Center. Two configurations of a proposed lenticular munition were considered. The results of this experimental program, contained in Reference 1.1, indicated that a circular planform configuration can offer an efficient airframe of low drag and high maneuver capability.

As a result of this effort a request for proposal (Reference 1.2) was issued by the Directorate of Procurement of the Air Proving Ground Center. This request concerned a study program whose purpose was to evaluate the technical feasibility of the lenticular configuration as a potentially significant advance in airborne weaponry. Particular emphasis was placed on the determination of the characteristics of the circular planform as pertains to flight characteristics, stability, control, and maneuverability. A further objective of the study was to establish the design feasibility of the configuration as a potential airborne weapon. The unclassified code name "PYE WACKET" was assigned to the study.

A technical proposal was submitted by Convair-Pomona, among others, in answer to the APGC request (Reference 1.3); a contract entitled, "Lenticular Rocket," AF08(635)-542, was awarded to Convair-Pomona in June of 1959.

This report summarizes the results of a 6-month study conducted under the direction of the Weapons Laboratory to: (1) evaluate the configuration, aerodynamically, and (2) establish design feasibility for airborne weapon applications. The report-submitted as a requirement of the contract-is divided into three primary sections, namely, Configuration Evaluation, Design Feasibility Studies, and Recommendations.

SECRET

1.1

SECRET

The Configuration Evaluation is contained in Section 2. Here the cross-section is established and the planform is evaluated; comparisons of the PYE WACKET configuration are then made with conventional bodies with respect to maneuver capability, drag, and airframe efficiency. Advantages and problem areas are evaluated. In addition, potential applications of the configuration to airborne weapons are outlined.

The Design Feasibility Studies are contained in Section 3. These studies include investigation of the major design areas necessary for feasibility evaluation, i.e., propulsion, structure, aerodynamic heating, guidance, etc. In addition, the most promising aerodynamic configuration and the required control system were determined. This section also includes "design feasibility" layouts of nominal PYE WACKET configurations.

Recommendations are presented in Section 4. This section considers the effort required to design and fly feasibility test vehicles as well as the scope of the work required to produce the prototype flight vehicles of a high performance air-to-air missile.

1.1 LIST OF REFERENCES

- 1.1. Technical Planning Group, Directorate of Development, Air Proving Ground Center, Eglin Air Force Base, Florida, "Experimental and Theoretical Investigations on Lenticular Rocket Shapes."
- 1.2. Directorate of Procurement, Air Proving Ground Center, United States Air Force, Eglin Air Force Base, Florida, "Request for Proposal, Purchase Request PGEM 59-116; Lenticular Rocket (U)," 23 March 1959.
- 1.3. Convair-Pomona, CPC-1393, "Proposal for Lenticular Rocket Feasibility Study," April 1959.

SECRET

SECRET

Section 2 CONFIGURATION EVALUATION

As discussed in Section 1, the first of the two major objectives of this study was to establish the aerodynamic feasibility of circular planform, lenticular cross section configurations. In particular, the advantages and shortcomings of the PYE WACKET concept were to be examined with reference to conventional configurations.

In making the evaluation, aerodynamic fundamentals have been emphasized. Where design-type information must be brought into the discussion for clarity, reference is made to Section 3:

2.1 SELECTION OF CROSS SECTION

The first step in the aerodynamic evaluation of circular planform bodies was to determine which of the lenticular cross sections had the best combination of characteristics, particularly lift effectiveness, aerodynamic efficiency, and longitudinal stability. A detailed treatment of this selection process is presented in subsection 3.2. Briefly, the initial evaluation of configurations utilized theoretical techniques and available wind tunnel information. This initial effort resulted in three configurations that were further investigated experimentally. Sketches of these configurations showing planform and side views are shown in Figure 2.1.1.

The three configurations shown are:

1. Model I - symmetrical lenticular cross section
2. Model II - intermediate cross section with the planform contour circles tangent to the aft edge
3. Model III - modified tangent contours

Model III (frequently called "blunted lenticular" configuration in the text) was predicted to have the best aerodynamic characteristics as well as the most desirable volume distribution for the packaging of a propulsion system.

Some of the results of wind tunnel testing are summarized in Figures 2.1.2, 2.1.3, and 2.1.4. Figure 2.1.2 presents plots of lift curve slope, $C_{L\alpha}$, versus Mach number for the three cross sections considered. Model III is shown to

SECRET

2.1.1

2.1.2

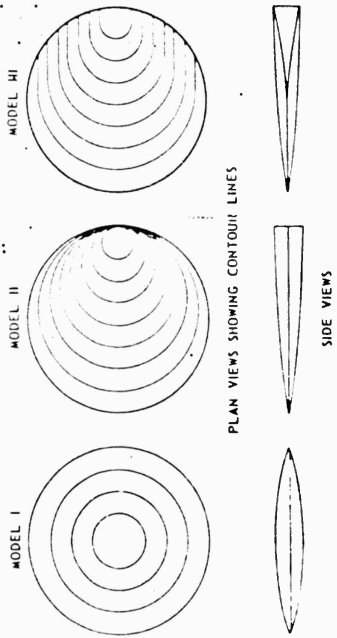


Figure 2.1.1. Lenticular Configurations for Cross Section Evaluation.

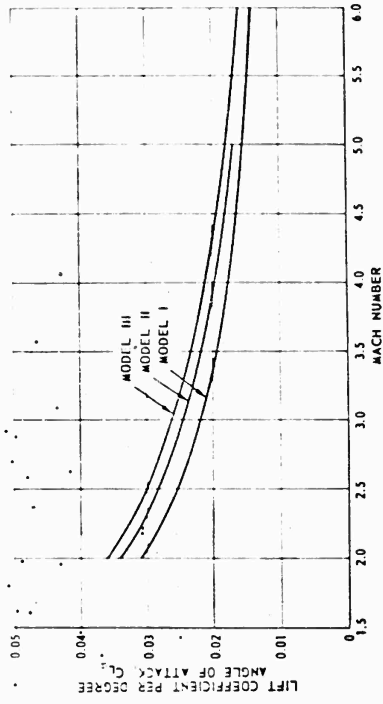


Figure 2.1.2. Comparison of Lift Coefficient Slope.

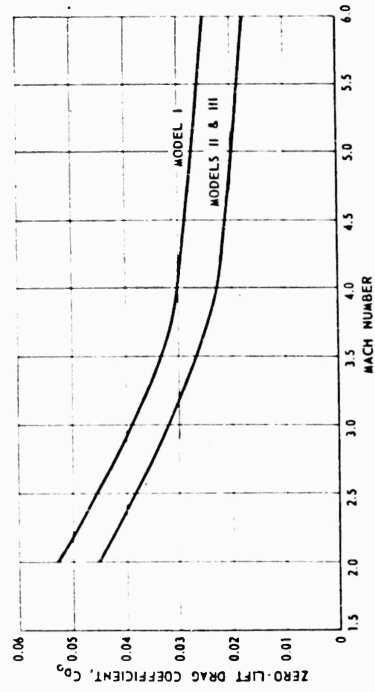


Figure 2.1.3. Comparison of Zero-Lift Drag.

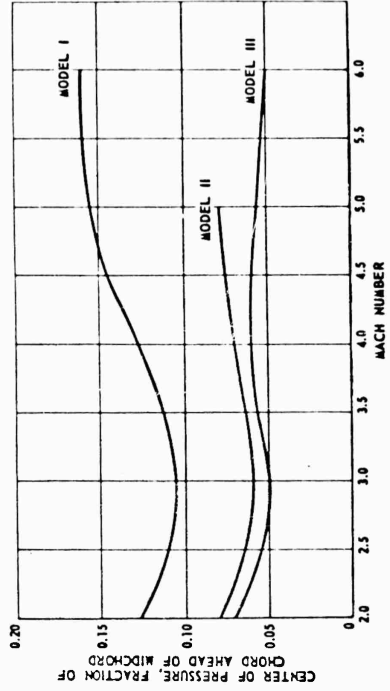


Figure 2.1.4. Variation of Center Pressure Location.

SECRET

provide the greatest lift effectiveness over the entire test Mach number range. Figure 2.1.3 presents plots of zero-lift drag, C_{D_0} , versus Mach number and indicates that Models II and III have identical drag curves that are considerably below the drag curve of Model I. Figure 2.1.4 presents plots of center of pressure location with reference to the midchord of the circular planform as a function of Mach number. Model III is shown to have the farthest aft center of pressure location at all Mach numbers.

Prior to proceeding further, some qualifying comments are required concerning the relative stability of Models I and III. Purely on an aerodynamic basis, Model III is more stable than either Models I or II because the center of pressure and center of gravity location. For example, the centroids (equivalent to uniform density in an actual vehicle) of Model I and Model III are at the midchord and 9 percent aft of the midchord, respectively. If the centroids were representative of center of gravity locations, Models I and III would have similar longitudinal stability characteristics. Since center of gravity position is dependent on the design layout of internal components, further discussion of stability margins is deferred until Section 3. It should be mentioned, however, that design feasibility layouts of the blunted lenticular PYE WACKET configuration for missile applications demonstrate acceptable center of gravity locations.

SECRET

2.1.3

SECRET

2.2 PLANFORM EVALUATION

In attempting to aerodynamically optimize the PYE WACKET configuration, it was considered desirable to check the relative effectiveness of the circular planform with those of other geometries. Adhering to fundamental aerodynamic concepts, the effects of planform geometry can be compared in terms of thin flat plates. Experimental data obtained from Reference 2.2.1 provide bases for the comparison of three elementary geometries - circle, square, and triangle.

Figures 2.2.1, 2.2.2, and 2.2.3 were plotted from these data (for Mach No. 6.8) and indicate the variation of lift and drag coefficients, and the lift-to-drag ratio as functions of angle of attack. Although these plots lack data for the circular planform below an angle of 45° the trends indicate that, in the hypersonic region, planform aerodynamics are little affected by geometry.

A more sophisticated evaluation can be made of planform aerodynamics by considering bodies of finite volume. Taking the simple planforms, comparisons were established for bodies of approximately equal volume and planform area. The bodies had the following characteristics:

1. The circular planform configuration had the blunted lenticular cross section of Model III. The wind tunnel data used in the comparison were corrected to a sharp leading edge.
2. The triangular planform had equilateral sides and was elliptical in spanwise cross section. This particular cross section was used because of the availability of information for computing lift and wave drag. (Reference 2.2.2).
3. The square planform employed a wedge (chordwise) cross section. Lift and wave drag calculations were made using the two-dimensional approach of Reference 2.2.3, corrected for a finite planform.

For all three bodies, Van Driest's method (Reference 2.2.4) was used to obtain the skin-friction drag. The techniques of Reference 2.2.5 were used in estimating base drag.

The results of these calculations should provide reasonable estimates of the aerodynamic characteristics of the planforms to be compared. A completely qualitative comparison would require consistent experimental data and greater correspondence in cross section geometry.

Lift curve slope as a function of Mach Number is shown in Figure 2.2.4. Lift-to-drag ratio is presented in Figure 2.2.5. In both comparisons, the circular planform characteristics generally fall between those of the square and the triangles. As the hypersonic flow regime is entered, the lift-to-drag ratio of the square planform rises above the other two, which converge.

Although these finite body comparisons cannot be considered completely quantitative, they and the flat plate comparisons, discussed earlier, indicate that the circular planform is acceptable aerodynamically.

SECRET

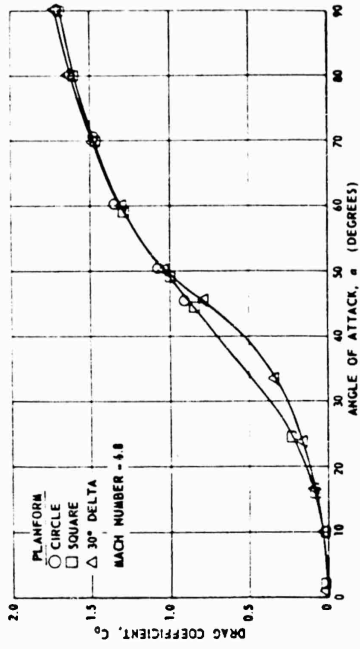


Figure 2.2.2. Comparison of Drag Coefficient of Different Planforms.

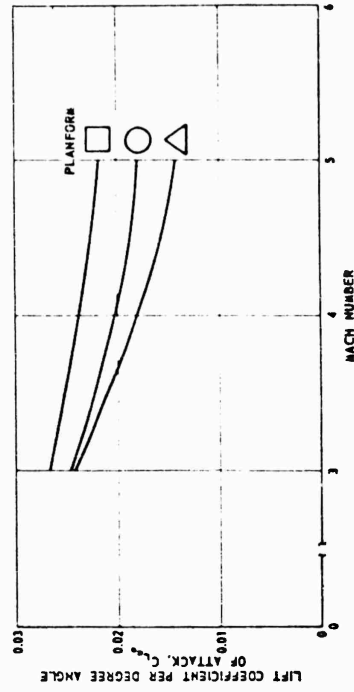


Figure 2.2.4. Comparison of Lift Curve Slope of Different Planforms.

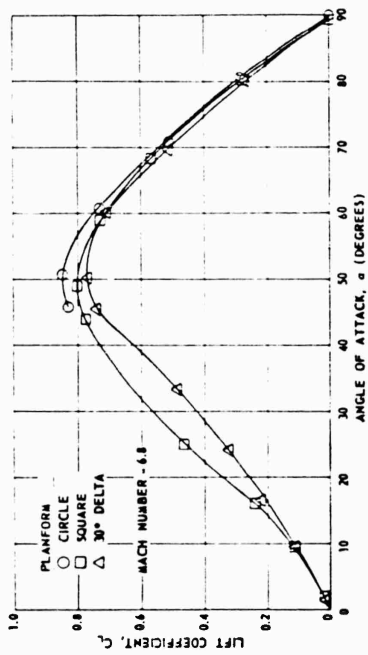


Figure 2.2.1. Comparison of Lift Coefficient of Different Planforms.

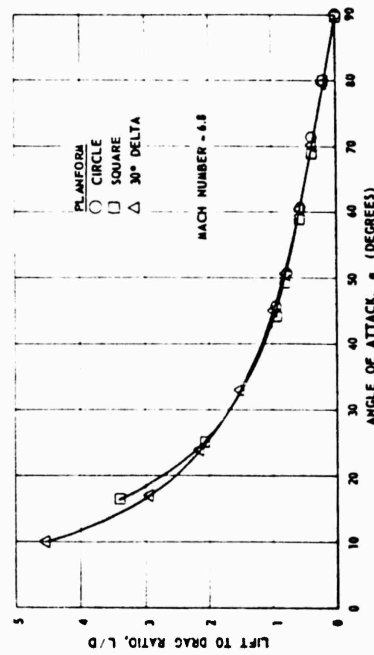


Figure 2.2.3. Comparison of Lift-to-Drag Ratios for Different Planforms.

SECRET

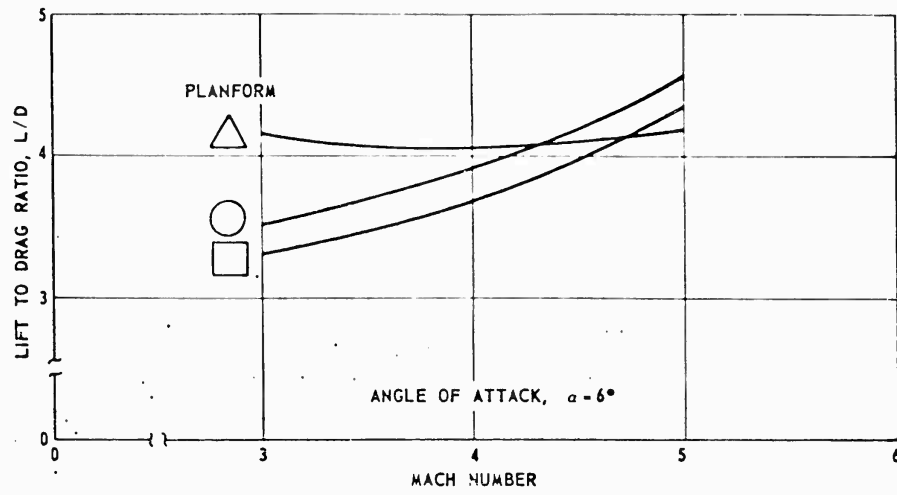


Figure 2.2.5. Comparison of Airframe Efficiency of Different Planforms.

SECRET

2.2.3

SECRET

2.3 COMPARISON WITH CONVENTIONAL SHAPES

Having completed the selection of the blunted lenticular cross section and the comparison of the circular planform with other lifting planforms, a comparison of the aerodynamic characteristics of the PYE WACKET configuration with those of conventional missile bodies was made. Five anti-aircraft missiles were selected for this comparison. These included Falcon (Model D), Talos, Tartar, Nike (Model 47), and Sparrow III. A hypersonic, manned, research vehicle, the X-15, was also included in the comparison.

Figures 2.3.1, 2.3.2, 2.3.3, and 2.3.4 present normalized comparisons of the aerodynamic capabilities of the PYE WACKET and these conventional configurations.

Figure 2.3.1 presents a comparison of lift capabilities. To put the data for each of the missiles on a common basis, the lift curve slopes were determined at an angle of attack of $\alpha = 4$ degrees, and were converted to coefficient form per unit of the planform area of each vehicle. It should be noted that, except for portions indicated by dashed lines, the curves represent wind tunnel data. Data for the X-15, Falcon, Talos, Nike, Sparrow, and Tartar were taken from References 2.3.1, 2.3.2, 2.3.3, 2.3.4, 2.3.5, and 2.3.6, respectively.

Examination of these data reveal that the PYE WACKET configuration (Model III) has a considerable advantage in lift curve slope over conventional missiles. For example, at Mach number $M = 5$, PYE WACKET has a 67 percent larger value of lift curve slope than the Falcon. Similarly, at $M = 2.5$, the PYE WACKET lift curve slope is 80 percent larger than the value for the Talos RTV-N-26a configuration. In all cases, the lift curve slope exhibited by the circular planform with the blunted lenticular profile is superior to the conventional body-lifting surface configurations.

Figure 2.3.2 presents a comparison of aerodynamic coefficients in terms of the lift-to-drag ratio. As in Figure 2.3.1, the curves of Figure 2.3.2 - except for the dashed portions - represent wind tunnel test results. Examination of these data indicates that the aerodynamic efficiency of PYE WACKET is significantly greater than that of three of the conventional body-lifting surface configurations. It should be noted that, due to the fact that fabricating and assembly protuberances were not accounted for in the PYE WACKET wind tunnel tests, the PYE WACKET curve is probably high by approximately 5 percent. In general, this figure illustrates that the characteristics of PYE WACKET represent an upper limit. That is, as a configuration approaches an all lifting surface, such as PYE WACKET, the lift-to-drag ratio will approach the maximum value. (See also the discussion of planforms in subsection 2.2.)

The Talos RTV-N-6a4 configuration exhibits exceptionally high lift-to-drag ratios for a body-lifting surface combination. However, with an open nose configuration it is possible that some of the inlet drag may have been included with the internal drag.

SECRET

2.3.2

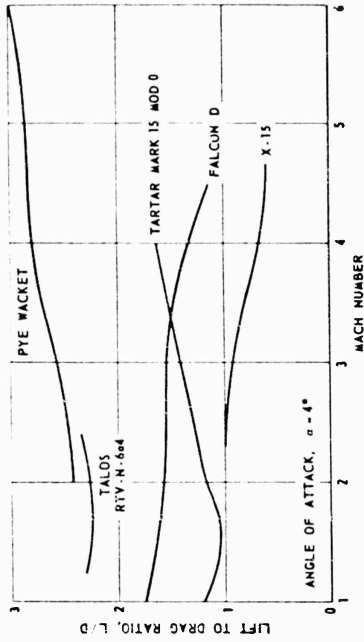


Figure 2.3.1. Comparison of PYE WACKET Lift Capability With Present Airframe Capabilities.

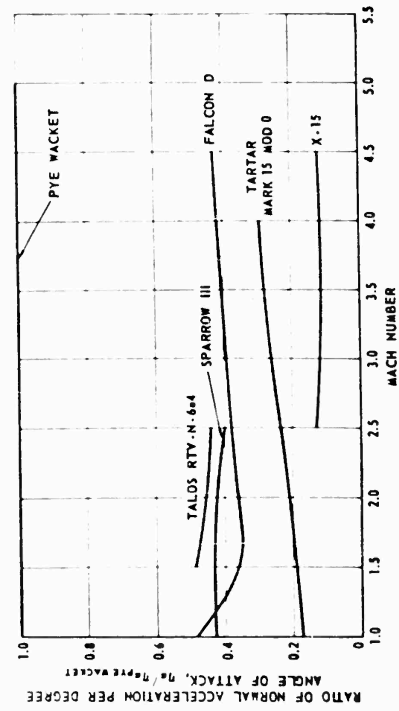


Figure 2.3.2. Comparison of PYE WACKET Airframe Efficiency With Present Airframe Capabilities.

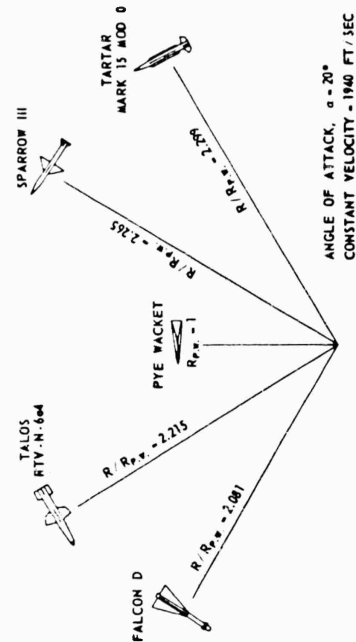


Figure 2.3.3. Comparison of Maneuver Capabilities.

Figure 2.3.4. Comparison of PYE WACKET Airframe Efficiency With Present Airframe Capabilities.

SECRET

Figure 2.3.3 presents a comparison of maneuver capabilities in terms of normal acceleration. In this figure, the maneuver capabilities of the conventional configurations are normalized with respect to PYE WACKET. Equal volume and weight were assumed for all configurations in making this comparison. The curves of Figure 2.3.3 indicate that PYE WACKET has a significant advantage over the other configurations in normal force capability. The information presented in Figure 2.3.3 has been replotted in a slightly different form in Figure 2.3.4. Here, maneuver capability is given in terms of turning radius, at constant velocity, normalized to PYE WACKET. This figure demonstrates that PYE WACKET would turn in half the radius of the conventional missiles used in the comparisons.

The results of these comparisons with conventional cylindrical bodies show that PYE WACKET has significantly better aerodynamic characteristics. Because it is a lifting body, it can generate much larger normal forces to obtain a very short radius of turn. This advantage is possible while maintaining a superior aerodynamic efficiency (L/D).

SECRET

2.3.3

SECRET

2.4 ADVANTAGES AND PROBLEM AREAS

The previous discussion has demonstrated several aerodynamic advantages of the PYE WACKET configuration. Aerodynamically, it is an efficient configuration, particularly at hypersonic velocities. It has the high lift slope of a lifting body that allows it to turn easily on shorter radii than conventional configurations and provides good maneuverability margins at altitude. In the practical vein, its geometry is compact as compared to other configurations, such as dart bodies, allowing easy stowage as a missile. Each of these points adds to its attraction as an airborne weapon.

Returning again to aerodynamic fundamentals, it should be noted that the circular planform is insensitive to wind vector orientation in the plane of its planform. Thus, unlike conventional finned configurations, which develop large yawing moments tending to align the body axis of rotation with the relative wind, the circular planform offers the potential of orienting the thrust vector in the plane of the planform without regard to the relative wind. This would be of advantage when the body is launched from a moving aircraft.

In examining the possibilities for the exploitation of the blunted lenticular, circular planform, certain problems are immediately evident. Due to the inherent compactness of the circular planform, as opposed to conventional bodies of high fineness ratio, the available control moment arm is limited. Because of this, and the fact that rapid control response will be necessary for the high lift PYE WACKET configuration, unusual control techniques must be investigated.

The unconventional, blunted lenticular geometry indicates structural inefficiency and possible aeroelastic effects. These include the problems of packaging an integral propulsion system which, in large part, would probably be a pressure vessel. Furthermore, the structure will need protection from a high speed thermal environment and in this geometry the wetted area to volume ratio is comparatively large.

These are the problem areas immediately apparent when considering the design of a vehicle for airborne applications. Since these are design problems deserving of a thorough treatment, they are discussed extensively in Section 3.

SECRET

2.4.1

SECRET

2.5 MANNED AIRCRAFT DEFENSE

Earlier in this section, it was determined that the PYE WACKET configuration has several highly desirable aerodynamic characteristics. The next step, before examining the design feasibility, is to look at possible airborne weapon applications that require the unique features of this configuration.

Probably the most promising application of PYE WACKET is for manned-aircraft defense. An urgent need exists for a missile possessing omnidirectional launch capabilities. This need stems from the inability of forward launched (unidirectional) missiles to afford manned-aircraft defense from all approaches of attack. This is particularly true for those cases where the attack is made from the two aft quadrants as observed from the aircraft. Figures 2.5.1 and 2.5.2 illustrate the limitations imposed on the inner boundary of the defense envelope by the forward launching of a defensive missile to intercept an attacker approaching in one of the aft quadrants. The calculations for the trajectories of the hypothetical PYE WACKET missiles were constrained to a maximum maneuver of 50 g's, or angle of attack of 30 degrees, whichever occurred first. The effects of two thrust levels, (same total impulse), on the maneuver trajectory are also shown.

Figure 2.5.1 is illustrative of the larger "no-defense" zone that would result in attempting to protect a high performance aircraft with a forward launched PYE WACKET. There would be no intercept capability for several miles laterally, in either direction, and none for many more miles aft. The defense boundaries are further degraded when considering a conventional missile, as may be noted from the Tartar trajectory.

Figure 2.5.2 is indicative of an operational bomber's defense zone limits. The minimum stand-off is greatly improved over that of the high performance aircraft of Figure 2.5.1, but, as can be noted for the lower thrust trajectory, the long turning maneuver can severely deteriorate missile Mach number and thus maneuver capability.

Having examined the defensive capabilities of unidirectional launched missiles, an investigation of the defensive envelopes with an omnidirectional launched missile is in order. Prior to attempting this, a definition of "omnidirectional launch capability" is necessary.

A broad definition of omnidirectional launch capability, as it pertains to an air-launched missile, is as follows: the ability to perform satisfactorily - that is, to achieve or maintain a prescribed or commanded heading or course - when launched at any selected heading with respect to the velocity vector of the launching aircraft.

In a strict sense, therefore, omnidirectional launch, requires spherical launch heading capability about the launching aircraft. However, for the purposes of this investigation, omnidirectional launch is interpreted to imply circular launch heading capability about the launching aircraft, in the plane formed by the

SECRET

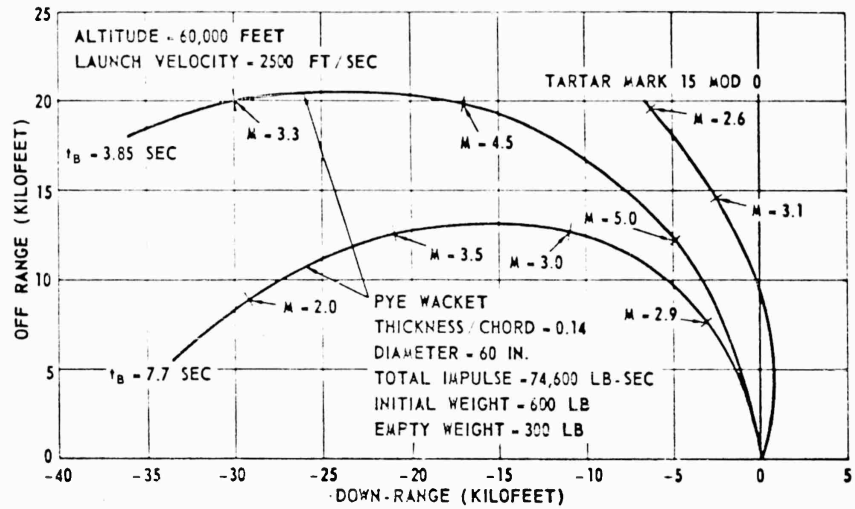


Figure 2.5.1. PYE WACKET Unidirectional Launch Capabilities.

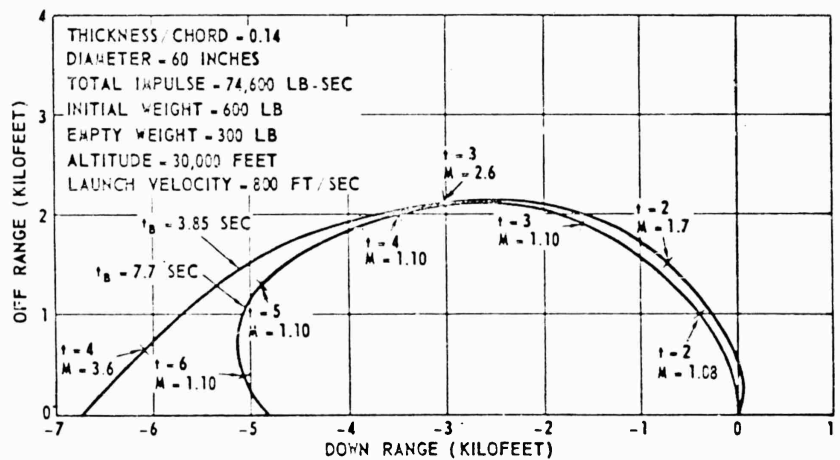


Figure 2.5.2. PYE WACKET Rear Intercept Capability Using Unidirectional Launch.

longitudinal and lateral axes of the launching aircraft. As will be demonstrated, a missile which satisfies this restricted definition offers significant advantages that will allow for adequate manned-aircraft defense.

The principal gain achieved by employing omnidirectional launch is the negation of the requirement that the initial heading of the missile be identical to the velocity vector of the launching aircraft. This allows for the missile to travel to

SECRET

any point in the plane of the launching aircraft without requiring large accelerations normal to its flight path. Conversely, in a unidirectional launch, the thrust force is initially applied in the direction of the launch velocity vector and a second, control or auxiliary, force is used to change the direction of motion to a desired heading. An appreciable time interval may be necessary to change the heading of the unidirectional-launch missile from the direction of the initial velocity vector to the desired direction. Therefore, kinetic energy and time are wasted during the turn-to-target maneuver of the unidirectional-launched missile. Herein lies the distinctive feature of the omnidirectional trajectory. During the entire time the unidirectional missile is turning, the omnidirectional missile is accelerating toward the predicted target intercept point.

Results of simplified omnidirectional launch trajectory analyses for the high performance aircraft and the subsonic bomber with the "lower thrust" hypothetical PYE WACKET vehicle are shown in Figures 2.5.3 through 2.5.6. Striking performance improvements are evident in Figures 2.5.3 and 2.5.6 for the two launching aircraft. Furthermore, even when the missile is at low velocities, i. e., close to the origin, it is oriented for target intercept and has some maneuver capability. This is not so in the unidirectional launch trajectories of Figures 2.5.1 and 2.5.2 where the zones inside the trajectories are not attainable. Figures 2.5.4 and 2.5.6 show the interesting long range stand-offs possible with omnidirectional-launch missiles.

Because of the unique possibilities in using the PYE WACKET configuration for airborne defense, the emphasis of the technical studies in Section 3 is in this area. The feasible designs presented in subsection 3.10, in particular, were with reference to manned-aircraft defense.

SECRET

2.5.4

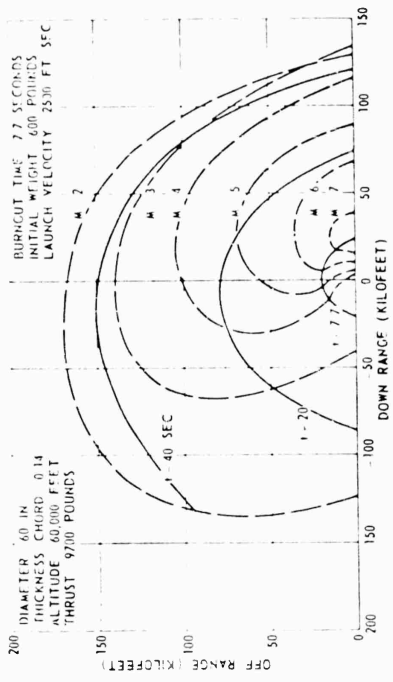


Figure 2.5.4. Omnidirectional Launch Performance Envelope.

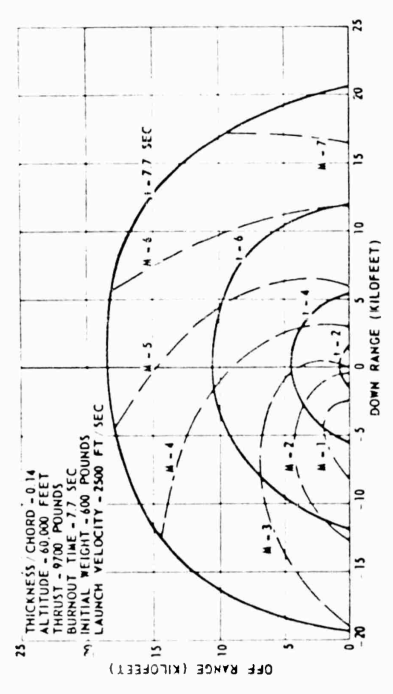


Figure 2.5.3. Omnidirectional Launch Thrust Phase Performance Envelope.

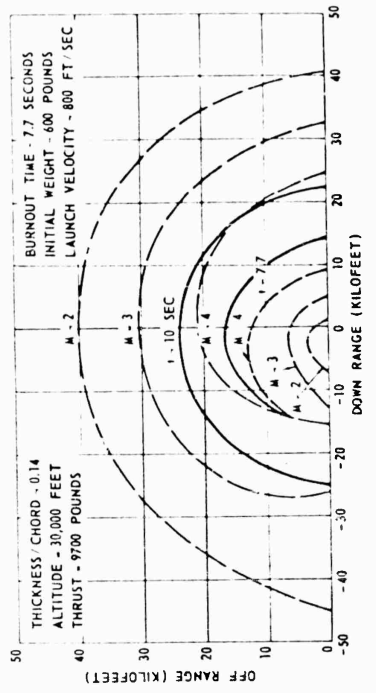


Figure 2.5.6. Omnidirectional Launch Thrust and Glide Phase Performance Envelope.

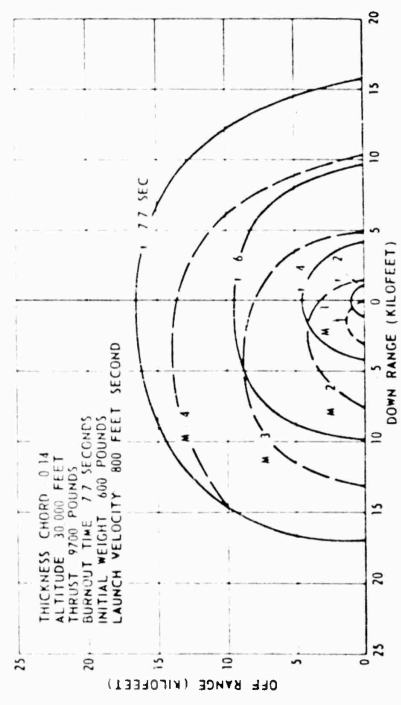


Figure 2.5.5. Omnidirectional Launch Thrust Phase Performance Envelope.

SECRET

2.6 OTHER APPLICATIONS

Because of the possibilities for omnidirectional launch, as well as the other excellent performance characteristics, the most promising application for PYE WACKET is as a missile for manned-aircraft defense. Other airborne weapon applications of the configuration also appear to have advantages. For example, an offensive weapon possessing omnidirectional launch capability frees the interceptor aircraft from the necessity of flying a line-of-sight course with the target during the launching of the offensive weapon. Obviously, for certain headings of the interceptor aircraft relative to the target aircraft heading, this advantage allows the interceptor to remain in the vicinity of the target for a greater time interval. If multiple targets are involved, this advantage could allow simultaneous firings at widely separated targets, e.g., an attacking, but dispersed squadron of bombers. As indicated by Figures 2.5.4 and 2.5.6, typical spherical stand-off capabilities of the order of 45,000 feet and 120,000 feet can be obtained at 30,000 feet altitude and 60,000 feet altitude, respectively. At higher altitudes, this stand-off capability would increase up to the limits of the airframe capability (i.e., the altitude at which the induced drag begins to be a dominant factor).

Use of PYE WACKET as an air-to-surface tactical weapon in special cases where "off-set" is desirable offers attractive possibilities. In this case, an offensive weapon possessing omnidirectional launch capability frees the launching aircraft from the necessity of passing too near the target. Extremely large off-set ranges would be available in such an application. Referring again to Figures 2.5.4 and 2.5.6 shows that large off-set ranges are possible before the missile Mach number drops below 2. Since these are constant altitude trajectories, it is, therefore, logical to assume that supersonic ground impact points well in excess of these distances from the line of flight of the launching aircraft are possible with PYE WACKET. With proper flight programming it should be possible to appreciably extend these distances for air-to-surface applications.

Another possibility is the use of a circular planform, blunted lenticular vehicle as an atmosphere re-entry vehicle - particularly for manned re-entry. Current thinking on re-entry vehicles includes two approaches:

1. Blunt body decelerated by aerodynamic drag (Reference 2.6.1)
2. "High lift" body that utilizes lift for deceleration (Reference 2.6.2)

Since the PYE WACKET configuration satisfies (1) when at an angle of attack of 90° and (2) when at small angles, it offers intriguing possibilities as a re-entry vehicle. It is conceivable that, by proper altitude programming, maximum utilization of both forms of aerodynamic forces might widen the possibilities and the flexibility of trajectories in the "re-entry corridor."

SECRET

SECRET

2.7 LIST OF REFERENCES

- 2.2.1 NASA TM X-65, "Static Longitudinal Aerodynamic Characteristics of Several Wing and Blunt-Body Shapes Applicable for Use as Reentry Configurations at a Mach Number of 6.8 and Angles of Attack up to 90°," by Jim A. Penland and William O. Armstrong, October 1959
- 2.2.2 "Elliptic Cones Alone and With Wings at Supersonic Speeds," by Leland H. Jorgensen, NACA TN 4045, October 1957
- 2.2.3 "Two-Dimensional Airfoils at Moderate Hypersonic Velocities," by W. H. Dorrance, J.A.S., Volume 19, No. 9, September 1952
- 2.2.4 North American Aviation, Inc., Report No. AL-958, "Turbulent Boundary Layer for Compressible Fluids on an Insulated Flat Plate," by E. R. Van Driest, 15 September 1959.
- 2.2.5 Convair-Pomona, TM-334-337, "Compilation of Power-Off Base Drag Data and Empirical Methods for Predicting Power-Off Base Drag," by E. E. Honeywell, 23 June 1959.
- 2.3.1 NASA Memo 4-27-59L, "Investigations of the Aerodynamic Characteristics of a 0.067-Scale Model of the X-15 Airplane (Configuration 2) at Mach Numbers of 2.29, 2.98, 3.96, and 4.65," by Arthur E. Franklin and H. Normal Silvers. National Aeronautics and Space Administration, Washington, May 1959.
- 2.3.2 Report No. 40-28-P, "Falcon Seeker Missile, Project MX-904 Fourth Quarter 1952," Hughes Aircraft Company, Culver City, California.
- 2.3.3 Bumblebee Series Report No. 158, "Aerodynamic Report of the RTV-N-6a Guided Missile," by J. E. Hege. The Johns Hopkins University, Applied Physics Laboratory, Silver Spring, Maryland, June 1951.
- 2.3.4 Report No. SM-13554. "Report on Supersonic Wind Tunnel Tests of a 0.075-Scale Model of the Nike 47 Missile," by H. S. Fischer, Douglas Aircraft Company, Inc., Santa Monica, California, May 1950.
- 2.3. Semi-Annual Progress Report, "July 1 to 31 December 1954, Report No. 10, SPARROW III," Raytheon Manufacturing Company, Missile and Radar Division, Bedford, Massachusetts.
- 2.3.6 Report CR-334-502-004, "TARTAR Complete Missile Round Mark 15 MOD 0, Aerodynamic Parameters Report," Convair, A Division of General Dynamics, Pomona, California, July 1958.
- 2.6.1 JAS Volume 25, No. 4, "Hypersonic Flight and Re-Entry Problem (Twenty-First Wright Brothers Lecture) by H. Julian Allen, April 1958.
- 2.6.2 JARS Volume 29, No. 9, "Use of Aerodynamic Lift During Entry into the Earth's Atmosphere," by Lester Lees, Federic W. Hartwig and Clarence B. Cohen, September 1959.

SECRET

2.7.1

SECRET

Section 3
DESIGN FEASIBILITY STUDIES

3.1 BACKGROUND

The performance of design investigations for the purpose of establishing the characteristics of the missile portion of a weapon system is normally guided by a specific set of mission requirements. In the case of the PYE WACKET concept, this was not possible in the Phase I effort being reported in this document, since an operational requirement could not be established until the characteristics and utility of the circular planform were determined. General guidance for the design feasibility studies was obtained from R and D Exhibit PGEM 58-1 2 (reproduced as Appendix A). This exhibit described two vehicle configurations whose characteristics are summarized in Table 3.1.1

Table 3.1.1
VEHICLE CHARACTERISTICS

	Vehicle	
	<u>No. 1</u>	<u>No. 2</u>
Diameter, IN.	60	60
Maximum thickness, IN.	7.5	10
Thickness-to-chord ratio	12.5%	16.7%
Approximate weight, LB	350	800
Stand-off		
Minimum, FT (60,000 FT altitude)	2000 - 7000	_____
Maximum, NMI	_____	15-25
Operational altitudes, 1000's FT	0	100
Velocity		up To M = 10

From this information, a nominal vehicle configuration was established with a diameter of 60 inches and a maximum thickness of 8.4 inches (thickness-to-chord ratio of 14 percent). The wind tunnel models and most of the earlier parametric studies in the various technical specialties were based on this configuration.

As shown in Section 2 of this report, one of the major attractions of the PYE WACKET configuration is its capability for omnidirectional launch. This characteristic could provide the basis for the design of a PYE WACKET missile for the active defense of manned vehicles, such as bombers, or provide an attack weapon for interceptors which would allow a considerable increase in the variety

SECRET

3.1.1

of interception tactics. To provide a reasonable simulation of aircraft launch for the technical studies, the hypothetical aircraft characteristics given in Table 3.1.2 were used.

Table 3.1.2
HYPOTHETICAL AIRCRAFT CHARACTERISTICS

Aircraft	Velocity	Altitude	
		Operational	Cruise
No. 1	800 FPS	0 - 60 K FT	30 K FT
No. 2	2,500 FPS	0 - 90 K FT	60 K FT
No. 3	10,000 FPS		150 K FT

Hypothetical aircraft Nos. 1 and 2 provide simulations of current and near-operational manned aircraft. No. 3 has been inserted merely as an indication of a high performance craft further up the planetary flight corridor shown in Figure 3.1.1. Performance based on No. 3 conditions was not investigated in detail and, therefore, is not presented in this report, however, for the cases analyzed, ranges were extremely great.

As noted previously, parts of the design feasibility study were initially based on a nominal 14 percent thickness-to-chord ratio vehicle to permit the work to proceed. Simultaneously with this effort, parametric studies were made to obtain an understanding of the trends that would develop with configuration variation. The establishment of parametric trends was of unique importance to this feasibility study, since, unlike the conventional cylinder designs, the PYE WACKET configuration has no significant accumulation of technical information to be used as a starting point.

Throughout the study of design feasibility, there was a continuous process of re-cycling of the investigations in each of the technical areas as data and information were refined and as new concepts developed. This process generated large quantities of data. Much of this interim study information will not be reported since its main significance now is only historical.

The reader should be cautioned that, since this study was directed toward determining design feasibility, the amount of re-cycling given to any particular technical investigation was limited to this determination and was taken no further in many instances. The result of terminating the effort once a particular point has been established caused some lack of uniformity in the "models" analyzed, and in some cases, numerical deviations. However, the information generated is sufficiently consistent to provide a sound basis for feasibility evaluation.

The study of the effect of thickness-to-chord ratio on several variables was the most important of all the parametric studies, since it essentially established the configuration. A brief discussion of the information generated in this area provides an example of the procedures used to establish data for feasible design.

SECRET

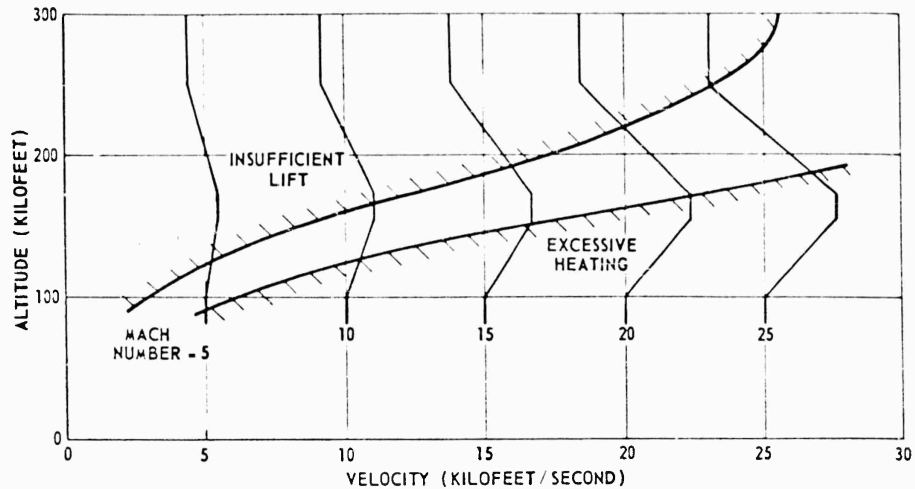


Figure 3.1.1. Planetary Flight Corridor.

Having accepted a particular cross section configuration (blunted-lenticular), which is briefly discussed in Section 2 and developed in greater detail in subsection 3.2, it is apparent that the next major determination is the thickness-to-chord ratio, t/C . Qualitatively, it is obvious that there are conflicting requirements from the several technical aspects. Stated in a simple fashion, packaging and structure dictate a large t/C , while the vehicle aerodynamics demand the reverse. The problem is then one of determining an acceptable range of t/C values for the configuration and general category of missions already described.

Looking at the problem more quantitatively, Figure 3.1.2 shows that internal volume increases almost linearly with t/C , but, as plotted in Figure 3.1.3, the drag increases approximately as a squared function. Conversely, as the thickness/chord ratio is decreased, skin thickness (structural weight--based on simple membrane theory) rises at a rapid rate (Figure 3.1.4).

To obtain a resolution of these conflicting demands, a parameter that includes the factors just discussed (Figures 3.1.2, 3.1.3, and 3.1.4), and others, must be examined. Probably the best basis for the determination is range, on the basis of "all other things being equal." As shown in Figure 3.1.5, range does peak at a given t/C . Note, however, that the maximum will vary with flight altitude and flight cutoff Mach no. (as shown in Figure 3.1.5) as well as many other variables. Figure 3.1.5 (and other data) does provide an indication of practical thickness-to-chord ratios which appear to be between 10 percent and 30 percent. Additional practical determinants, such as practical packaging limitations on the low side and the range degradation on the high side will further limit the t/C values to be considered.

SECRET

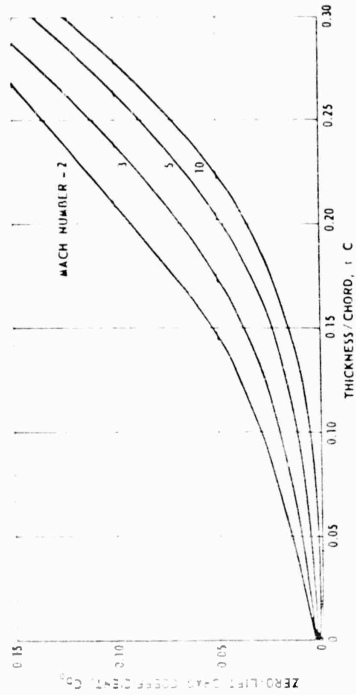


Figure 3.1.3. Variation of Zero-Lift Drag Coefficient With Thickness-to-Chord Ratio.

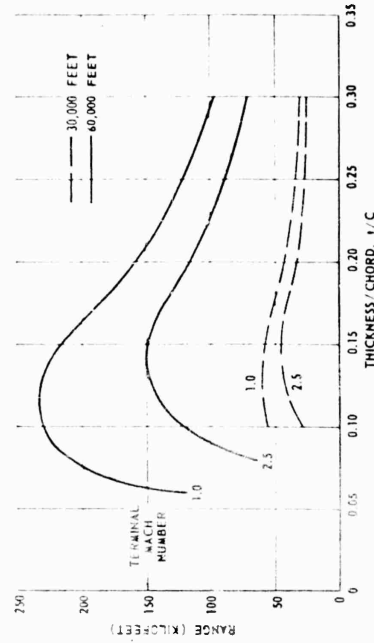


Figure 3.1.5. Down Range Versus Thickness-to-Chord Ratio.

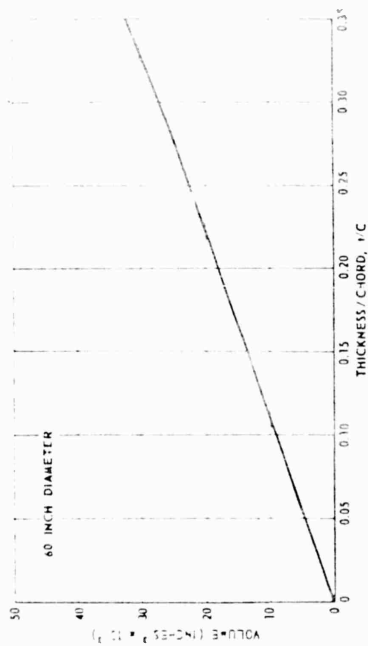


Figure 3.1.2. Total Integrated Volume Versus Thickness-to-Ratio.

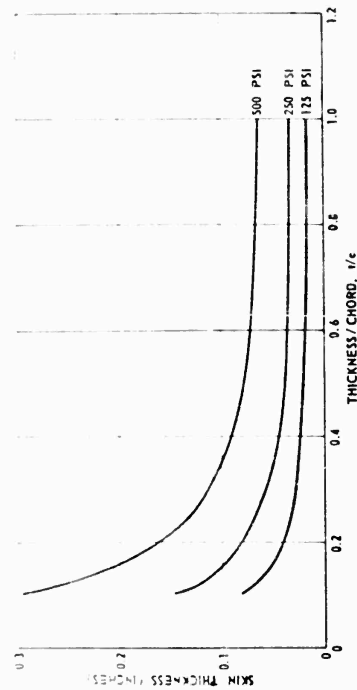


Figure 3.1.4. Pressure Vessel Required Skin Thickness Versus Thickness-to-Chord Ratio.

SECRET

In this feasibility study, t/C limits were finally set at 14 percent to 21 percent for investigation of the omnidirectional launch missile airborne weapon application.

In the technical subsections that follow, the major problem areas are explored. Emphasis is directed towards obtaining a solution or, in some instances, several solutions that provide feasible design approaches to make PYE WACKET a practical vehicle. In developing these approaches, the technical studies have shown trends and the relative importance of various missile parameters associated with obtaining feasibility design information. With the establishment of these parameters in a practical, quantitative range, layouts of feasible designs have been made in subsection 3.10. The performance possibilities of these designs are discussed and directions are determined for proceeding with actual hardware designs. So, in essence, the technical studies and the feasibility designs discussed in this section provide the first iteration in the process of establishing the composite design of a vehicle or family of vehicles based on the PYE WACKET concept. Much work remains to be done.

SECRET

3.1.5

SECRET

3.2 AERODYNAMICS

One of the primary objectives in this study program was the determination of the overall aerodynamics of technically feasible forms of the circular planform configuration. The main objective of this program was the selection of the most promising circular planform cross-sectional shape. Emphasis in this selection was given to drag, stability, and lift characteristics.

The Aerodynamics portion of this report provides a comprehensive examination of the effects of cross-sectional shape on the aerodynamic characteristics of the circular planform. The method followed in selecting the most promising circular planform cross sections for guided missile use is presented below:

A thorough examination was first made of the results of the Air Proving Ground Center (APGC) investigations of the lenticular-cross section, circular planform concept (Reference 3.2.1) to acquire some understanding of the aerodynamic problems that might be encountered in a technical study of the configuration. This examination indicated that high lift effectiveness ($C_{L\alpha}$) and airframe efficiency (L/D) could be obtained from a circular planform configuration. However, the symmetrical lenticular configuration investigated in Reference 3.2.1 exhibited unsatisfactory moment characteristics. In general, the aerodynamic center of pressure of the symmetrical configuration showed excessive movement with both Mach number and angle of attack. In addition, the most rearward location of the center of pressure was 35 percent of the missile diameter aft of the leading edge. It was felt that this would result in excessive moments from a control standpoint.

It appeared that considerable improvement could be made in the stability characteristics of the circular planform, while achieving even better lift and drag characteristics, by altering the cross-sectional shape of the vehicle. Therefore, a major effort was made, within the time and funds allocated to this study, to select the most promising cross section from a feasibility standpoint as well as a performance standpoint.

A detailed study was made of applicable reference material to determine methods of improving the aerodynamic characteristics of the circular planform. The findings from these references are presented in detail further in the text. In general, these findings were that drag reduction and lift increases would result if the maximum thickness were shifted to the aft end of the planform. In addition, these references indicated that an aft movement of the aerodynamic center of pressure would accompany a rearward shift of the maximum thickness.

Conferences were held with Mr. W. Dorrance, of the Convair Scientific Research Laboratory, and Mr. A. J. Eggers Jr., of the National Aeronautics and Space Administration, on improving the aerodynamic characteristics of the

SECRET

SECRET

circular planform. The results of these conferences, reported in References 3.2.2 and 3.2.3, substantiated the findings of the reference material mentioned above.

A theoretical study of the variation of the aerodynamic characteristics of circular planform with cross-sectional shape was made. In this study, volume was used as the parameter for comparing the aerodynamic characteristics to determine the most favorable body cross-sectional shape. For a particular volume (required for payload, guidance equipment, propellant, control system, etc.) the body cross section having the lowest drag would have the most favorable velocity-time history and the body cross section having the highest lift-to-drag ratio would have the most favorable range capabilities.

A detailed presentation of this theoretical investigation is made further in the text. As expected, this investigation indicated that a blunt trailing edge cross section, with the maximum thickness moved to the aft end, provided the most promising aerodynamic configuration for the circular planform.

It should be noted that these results are compatible with the packaging and propulsion requirements for the circular planform missile. A considerable volume is required in the aft end of the missile for the rocket nozzle, propellant, and control system equipment, as shown in subsection 3.10. The results of this investigation was therefore, very encouraging from a design feasibility standpoint.

Based on the results of the above mentioned analyses, a wind tunnel program was conducted to obtain aerodynamic design data and to confirm the conclusion reached above.

Tests were conducted in the Arnold Engineering Development Center (AEDC), Wind Tunnel "A", for a Mach number range of 2 to 6 to determine the drag and longitudinal and lateral stability characteristics of several lenticular configurations. Longitudinal, lateral, and roll control devices were also investigated as well as the effects of blunting the leading edges.

A complete treatment of the results of this test program is presented later in this discussion. Briefly, these results indicate, as predicted by Reference 3.2.4 and the theoretical investigation of this study, that a blunt trailing edge configuration possesses superior aerodynamic performance in lift, drag, and stability. This superiority increases as Mach number increases.

It should be noted that this discussion deals only with the aerodynamic characteristics of the body alone. A treatment of the aerodynamic control surfaces is presented in subsection 3.5 along with a treatment of reaction controls.

3.2.1 BASIC STUDIES

Prior to discussing specific problem areas, it is advisable to first consider the application of theory to the circular planform.

3.2.2

SECRET

SECRET

Several flow regimes deserve attention. The initial regime to be discussed is subsonic where compressibility is a negligible effect. Theoretical solutions for flows in this regime have been obtained by several people. One such solution is documented in Reference 3.2.5. The transonic regime has not been explored analytically or experimentally for the three-dimensional case. A great deal of data is available for two-dimensional profiles but none with a circular planform. A similar situation exists in the supersonic and hypersonic regimes. The only three-dimensional test data available are from the present study program and the conceptual study program of Reference 3.2.1. In general, the dividing line between supersonic and hypersonic flow requires definition. In supersonic flow, as Mach number increases, the equations describing the flow variation in passing a slender object require non-linear expressions. The degree of non-linearity of the flow equations is dependent on the speed the flow has attained. Supersonic flow merges into hypersonic flow when the non-linearity becomes a dominant characteristic of the flow. Some of the essential features of hypersonic flow are strong curved shock waves and large entropy gradients. As a result, supersonic linear theory becomes inadequate for describing the flow parameters.

One parameter commonly used for differentiating supersonic from hypersonic flow is $\beta(t/C)$. Where β is the supersonic similarity parameter $\sqrt{M^2 - 1}$ and t/C is the thickness-to-chord ratio. When $\beta(t/C)$ begins to approach unity, the flow becomes predominantly non-linear and is hypersonic. More simply, when $M\delta$ is the order of one (where M is the Mach number and δ is the flow deflection in radians) the flow becomes hypersonic. The similarity parameter, $M\delta$, was originally introduced by Tsien. Subsequently, it was used in a small disturbance theory by Van Dyke.

It might be pointed out that the flow deflection, δ , is composed of the local slope of the body and the angle of attack. Hence, it is possible to enter the hypersonic flow regime at a moderate Mach number by going to a high angle of attack.

Many two-dimensional methods are available for computing theoretical aerodynamic coefficients in supersonic and hypersonic flow. Only one method, the method of characteristics, is available for computation of theoretical aerodynamic coefficients for a three-dimensional body. A short discussion of these methods and their relative merits is given below.

Supersonically, Ackeret's first order theory, second order theory, and Busemann's third order theory are available for estimates on a two-dimensional profile. These methods and their limitations are very well covered in the literature and so will not be dwelt upon here. Another method, an extension of the technique used in Reference 3.2.6 by Allen and Perkins for slender bodies, was used by Flax and Lawrence in Reference 3.2.7 for low aspect ratio wings. This method can be extended for use in this configuration. In this theory, the linear term is determined by the longitudinal flow and is identical to that given by the

SECRET

Ackeret first order theory. The second order term is dependent on the square of the angle of attack and is caused by the normal component of the flow. In particular, it is the effect of the viscous cross flow about the body. The form of the resulting equation is

$$C_N = \frac{C_{N\alpha}}{(57.3)} \alpha + \frac{C_{D\alpha}}{(57.3)^2} \frac{A_P}{S_P} \alpha^2 \quad (3.2.1)$$

The C_{DC} term is the cross flow drag, A_P is the planform area and S_P is the reference area.

All of the preceding theoretical methods are for supersonic flow and begin to have limitations in their accuracy in the hypersonic flow regime. Again, each of these methods is two dimensional except the method of Reference 3.2.7 (cross flow drag) and must be corrected to three-dimensional flow.

In the hypersonic flow regime, some of the available theories for computing aerodynamic coefficients are; shock expansion, Dorrance's work of Reference 3.2.8, and Newtonian flow theory.

The generalized shock expansion method uses the relations through a shock wave (oblique or conical), along with the Prandtl-Meyer relations for expansive flow, to establish flow relations in the vicinity of the body. This method is essentially a computational method and is a long involved procedure.

The method developed by Dorrance in Reference 3.2.8 is essentially a modification of the generalized shock expansion method. This modification uses the hypersonic similarity parameter $M\delta$ in the oblique shock equations and in the Prandtl-Meyer equations for expansion. The resulting expressions for compression and expansion are identical for $M\delta$ the order of unity. This allows a closed solution for the pressure coefficients over a two-dimensional profile. The pressure coefficients are integrated to obtain aerodynamic coefficients on various profiles.

In general, this method is good for low angles of attack and small thickness ratios for Mach numbers $M = 3$ to 12. A note of caution must be inserted in regard to this method. In making the analysis, isentropic compression (i. e., change in entropy across the shock is small) was assumed at the body leading edge. When the leading-edge shock wave becomes sufficiently non-isentropic to negate this assumption, large errors may result.

The Newtonian flow theory gives excellent results at the higher ranges of hypersonic flow. This theory uses the principle that the normal component of the flow momentum is given up to the body on impact. This theory, in general, will give good accuracy on the magnitude of the forces, but not upon their distribution.

The three aforementioned methods are for two-dimensional profiles and must be corrected for three-dimensional flow.

In order to evaluate the relative merits for each of the theories or methods which have thus far been covered, some preliminary computations were made

SECRET

and the results were compared with three-dimensional experimental data from Reference 3.2.1. The model used had a sharp leading edge. These computations were made for the basic lenticular configuration at Mach numbers $M = 3, 4$ and 5 . The results are contained in Figures 3.2.1, 3.2.2, and 3.2.3. The similarity parameter $M\delta$ ($\delta =$ slope at the leading edge) is $0.732, 0.977,$ and 1.22 , which indicates that at zero angle of attack, hypersonic flow is rapidly being approached. At angle of attack, the similarity parameter $M\delta$ approaches one even more rapidly since δ is the sum of $\alpha + \delta$. Figures 3.2.1, 3.2.2, and 3.2.3 show that:

1. The linear theory rapidly deteriorates as Mach number increases.
2. The Newtonian or impact theory becomes increasingly better as Mach number increases.
3. Busemann's third order theory overestimates at all cases considered.
4. Dorrance's work gives a good approximation in all cases.

Therefore, the best agreement is achieved by using the experimental normal slope linear data and incorporating a cross flow drag term.

In general, the trends indicated by the various methods used were as expected. An indication of the magnitude of the correction of the two-dimensional data is indicated. In normal force, indications are that a reduction of 15 percent in two-dimensional normal force (Dorrance) will give data identical to the experimental data.

Another method, the only one which can give three-dimensional solutions, is the method of characteristics. The necessity of three-dimensional solutions for a circular planform can be readily illustrated by regions of influence. For a circular planform the regions of influence for two points on the leading edge are shown in Figure 3.2.4.

In Figure 3.2.4, point (3) falls within the regions of influence of points (1) and (2). That is, the conditions at points (1) and (2) can affect the flow conditions resulting at point (3). For example, if the leading edge angle is changed at point (1), the pressure and density at point (3) will be changed. Since point (2) is displaced aft of point (1), its influence on the flow at point (3) is not the same as the influence of point (1). Therefore, the flow on a circular planform is three dimensional over the entire planform.

The only way currently available to compute three-dimensional aerodynamic coefficients is with the method of characteristics. The general equation for potential flow for a three-dimensional body without axial symmetry in cylindrical coordinates is

$$\begin{aligned} & \left(1 - \frac{u^2}{a^2}\right) \frac{\partial^2 \phi}{\partial x^2} + \left(1 - \frac{v^2}{a^2}\right) \frac{\partial^2 \phi}{\partial y^2} + \left(1 - \frac{w^2}{a^2}\right) \frac{1}{y^2} \frac{\partial^2 \phi}{\partial \varphi^2} - \frac{2uv}{a^2} \frac{\partial^2 \phi}{\partial x \partial y} - \frac{2uw}{a^2} \frac{1}{y} \frac{\partial^2 \phi}{\partial \varphi \partial x} \\ & - \frac{2vw}{a^2} \frac{1}{y} \frac{\partial^2 \phi}{\partial \varphi \partial y} + \frac{v}{y} \left(1 + \frac{w^2}{a^2}\right) = 0 \end{aligned} \quad (3.2.2)$$

SECRET

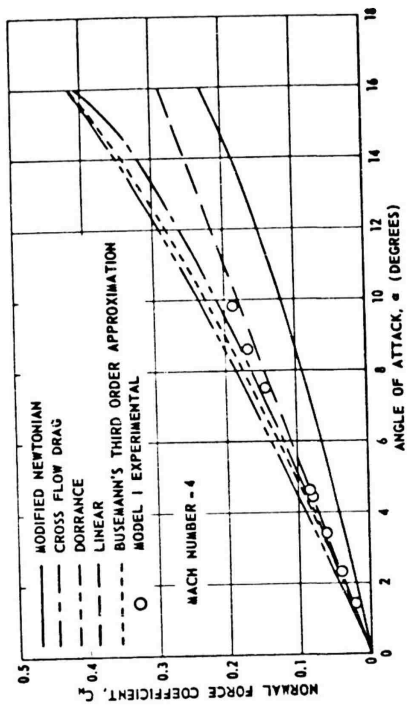


Figure 3.2.2. Comparison of Two-Dimensional Theory with Three-Dimensional Test Data.

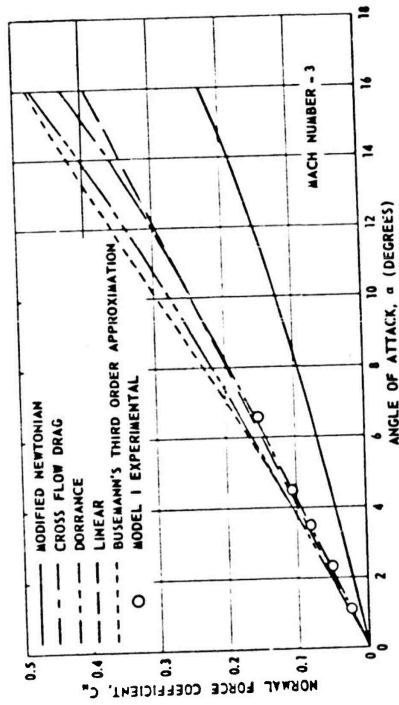


Figure 3.2.1. Comparison of Two-Dimensional Theory with Three-Dimensional Test Data.

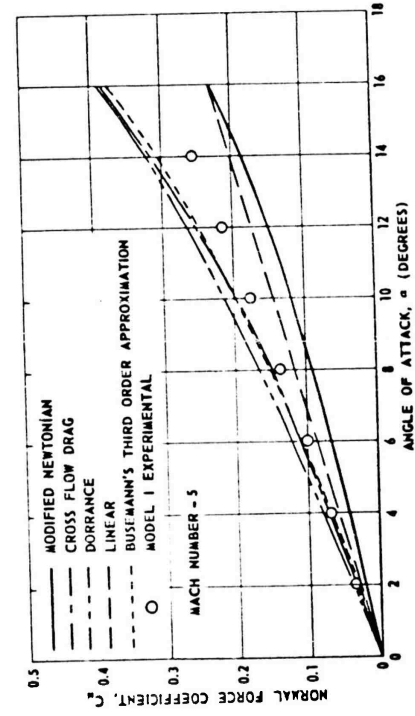


Figure 3.2.3. Comparison of Two-Dimensional Theory with Three-Dimensional Test Data.

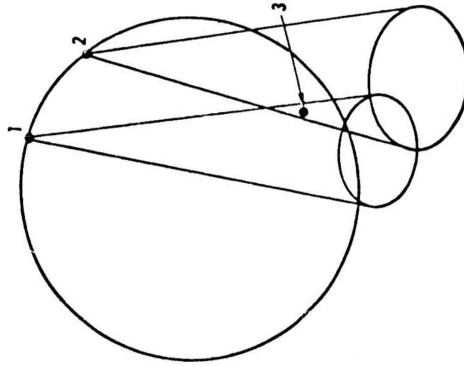


Figure 3.2.4. Circular Platform Regions of Influence.

SECRET

in which u , v , and w are the respective velocity components along the axes, ϕ is velocity potential, a is the speed of sound, and ψ is the angular coordinate of the meridian plane. The characteristic surfaces of this equation can be shown to be the envelope surfaces of Mach cones which have their vertices at points from which the disturbance in the flow begins. These surfaces define the regions of influence of the disturbance. Every plane normal to the longitudinal axis contains two families of characteristic surfaces. By appropriate manipulation of the characteristics lines and the parallel and meridian planes, the flow properties along intersection lines may be determined.

The initial conditions assumed include a sharp leading edge. The process determines the location of a characteristic surface and the flow property variation along parallel and meridian planes. Then the variation of properties along intersections and the variation of flow properties in the field can be determined. The process is extremely complex. However, no other exact method is available for computing three-dimensional aerodynamic coefficients in the supersonic and hypersonic regime.

In evaluating the technical feasibility of the circular planform configuration a critical examination was made of the cross section from a drag, lift, and stability standpoint. This was done to see if the drag and lift characteristics could be improved while achieving a more neutrally stable configuration compatible with reasonable control forces.

The first step of this study dealt with the consideration of symmetrical as opposed to cambered lenticular shapes - that is, should the vehicle be symmetrical or unsymmetrical about the projected planform area of the missile? The following method was employed in arriving at a symmetrical shape about the horizontal center plane:

1. With any type guidance system, the vehicle must be capable of performing maneuvers of equal magnitude and response in either direction along the normal to the projected planform area of the missile. A cambered surface would increase the maneuverability of the vehicle in one direction at the expense of the maneuverability in the opposite direction. Hence, for equal pitch maneuverability in either direction, a shape which is symmetrical about the horizontal center plane was indicated.
2. The wind tunnel data of Reference 3.2.1 indicated adequate available maneuverability with angle of attack control for symmetrical shapes.
3. No advantage could be seen for a cambered lenticular shape from a drag standpoint. Therefore, due to the necessity of maneuvering in all directions and the high lift available through angle of attack, a vehicle which is symmetrical about the horizontal center plane is considered the most promising.

SECRET

Once the above decision had been made, the longitudinal cross-sectional shape of the vehicle was considered. For conventional double-wedge and biconvex airfoils, References 3.2.9 through 3.2.16 show that by shifting the maximum thickness point rearward from the midchord, lift will be augmented and drag reductions can be obtained. In particular, Reference 3.2.9 states that at Mach numbers between 7 and infinity, a 5 percent thick airfoil with a blunt trailing edge would yield between 15 and 25 percent greater lift than a corresponding 5 percent thick airfoil with a sharp trailing edge. Reference 3.2.13 shows that the blunt trailing edge modification would yield a drag reduction of up to 20 percent in the Mach number range of 2.7 to 5. Theory indicated, References 3.2.8 and 3.2.11, that the blunt trailing edge airfoil will always have less drag at the high Mach numbers which are of interest for the vehicle being considered. At high Mach numbers, because of the entropy rise at the front shock, the pressure on the base of the body can be higher than free stream, thereby producing thrust instead of drag, Reference 3.2.17.

References 3.2.11 and 3.2.16 also show that the lift increase and drag reduction, resulting from blunting the trailing edge of airfoils, improves with increasing Mach number. The above references also indicate an increase in lift with an increase in airfoil thickness ratio. This fact is quite important, especially in the design of a longer range vehicle due to propulsion system packaging requirements.

Data on the effects of moving the maximum thickness to the trailing edge on the pitching moment are very scarce. However, References 3.2.15 and 3.2.16 show a small rearward shift of the center of pressure. This rearward shift of the center of pressure provides a stabilizing effect which is very desirable.

Having determined from the above mentioned reference material that definite advantages were possible by shifting the maximum thickness to the aft end of the circular planform, an analytical investigation was made to verify the above indications and serve as a guide for selection of the most attractive cross-sectional shapes for the wind tunnel models to be fabricated.

It was shown above that no theoretical method is available for computing three-dimensional aerodynamic coefficients for a circular planform other than the method of characteristics. Since the use of this method was impossible in the time scale of this study, a two-dimensional method of estimating (Dorrance) was used. Therefore, the results of this analytical study should be considered in a qualitative sense only. However, as verified by later test data, the analytical results, although qualitative in nature were indicative of the most desirable cross section shape.

This investigation was limited to the calculation of the lift, drag, and lift-to-drag ratio variation with the thickness ratio, angle of attack, and volume for four cross section shapes at three Mach numbers. The cross section shapes considered

SECRET

in this study are illustrated in Figure 3.2.5. The thickness ratio for these sections was varied from zero to 0.20. The angle of attack range was from zero to 10 degrees and the Mach numbers considered were 3, 4, and 5. The effects of blunting the leading edges were not considered in this analysis, as all leading edges are sharp (i. e., all leading edges formed by the intersection of the continuous sloping upper and lower surfaces).

The lift characteristics discussed below were calculated by employing the methods of Dorrance (Reference 3.2.8) for two-dimensional flow and adjusting for three-dimensional effects. The three-dimensional adjustment was obtained by comparing the two-dimensional values calculated for the biconvex section with experimental data (Reference 3.2.1) obtained for a circular planform body similar to a 14 percent thick biconvex airfoil. It was found that the experimental C_N data were approximately 85 percent of the calculated two-dimensional values. Therefore, two-dimensional C_N values calculated by the following equations for the four airfoil sections considered were reduced by 15 percent to obtain three-dimensional C_N values.

$$\text{Symmetrical Double Wedge } C_N = \frac{4\alpha}{M} + 2.4M\alpha\delta^2 + 0.8M\alpha^3 \quad (3.2.3)$$

$$\text{Blunt Trailing Edge Double Wedge } C_N = \frac{4\alpha}{M} + 2.4\alpha\delta + 0.6M\alpha\delta^2 + 0.8M\alpha^3 \quad (3.2.4)$$

$$\text{Blunt Trailing Edge Parabolic } C_N = \frac{4\alpha}{M} + 2.4\alpha\delta + 0.8M\alpha^3 + 0.8M\alpha\delta^2 \quad (3.2.5)$$

$$\text{Flat Plate } C_N = \frac{4\alpha}{M} + 0.8M\alpha^3 \quad (3.2.6)$$

$$\text{Symmetrical Biconvex } C_N = \frac{4\alpha}{M} + 0.8M\alpha^3 + 3.2M\alpha\delta^2 + 1.28M\alpha\delta^4 \quad (3.2.7)$$

Where

$$\delta = \frac{t}{c} \text{ and } \alpha \text{ is in radians}$$

Two-dimensional wave drag was calculated for the four airfoil sections by the methods of Reference 3.2.8. The equations of Reference 3.2.8 reduce to the following for the four cross sections considered:

SECRET

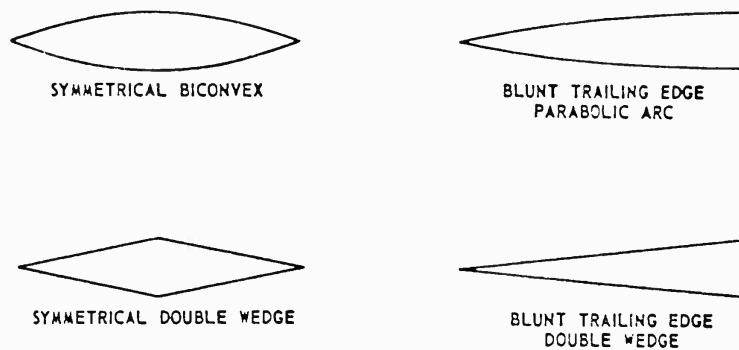


Figure 3.2.5. Cross Sections Considered

Biconvex

$$C_{D_W} = \frac{5.333\delta^2}{M} + \frac{4\alpha^2}{M} + \frac{2.13\delta^4}{M} + 6.4M\alpha^2(\delta^2) + 2.56M(\delta^4) + 0.8M\alpha^4 + 2.56M\alpha^2(\delta^4) + 4.38M\delta^6 \quad (3.2.8)$$

Symmetrical Double Wedge

$$C_{D_W} = \frac{4\alpha^2}{M} + \frac{4\delta^2}{M} + 0.8M\alpha^4 + 4.8M\alpha^2(\delta^2) + 0.8M\delta^4 \quad (3.2.9)$$

Blunt Trailing Edge Double Parabolic

$$C_{D_W} = \frac{4\alpha^2}{M} + 0.8M\alpha^4 + \frac{1.333\delta^2}{M} + 3.6\alpha^2\delta + 1.6M\alpha^2\delta^2 + 0.6\delta^3 + 0.16M\delta^4 \quad (3.2.10)$$

Blunt Trailing Edge Double Wedge

$$C_{D_W} = \frac{\delta^2}{M} + 4\alpha^2 + 0.3\delta^3 + 3.6\alpha^2\delta + 0.05M\delta^4 + 1.2M\alpha^2\delta^2 + 0.8M\alpha^4 \quad (3.2.11)$$

Where

 $\delta = t/C$ and α is in radians

The two-dimensional drag values calculated by the above equations at $M = 3$, 4, and 5 for the biconvex section were compared with the data of Reference 3.2.1 for a symmetrical lenticular body having a t/C of 0.14. The experimental data were approximately 54 percent of the calculated two-dimensional values over an α range of 0 to 12 degrees. Therefore, three-dimensional wave drag was obtained by using a factor of 0.54 with the above two-dimensional equations.

In addition to the wave drag, calculated as explained above, the blunt trailing edge double wedge section and the blunt trailing edge double parabolic section incur a base drag. Three-dimensional base drag was calculated by the following equation from Reference 3.2.18.

3.2.10

SECRET

$$\text{FOR } 1.1 \leq M \leq 5.0; C_{D_B} = 0.255 - 0.135 \ln M \quad (3.2.12)$$

$$\text{FOR } 5.0 \leq M \leq 8.0; C_{D_B} = 0.019 - 0.012(M-5) + \frac{0.1}{M} \quad (3.2.13)$$

The above coefficients of base drag are referenced to base area. To change the reference area to that of the circular planform and to make C_{D_B} a function of t/C the following factor, K , was applied to the above equations:

$$K = \frac{8t}{3\pi c} \quad (3.2.14)$$

Skin friction drag coefficients were calculated by the methods of Van Driest (Reference 3.2.19) for a sea level flight condition. The total drag coefficient values were then obtained by the summation of wave drag, base drag (where applicable) and skin friction drag.

Presented in Figure 3.2.6 through 3.2.8 are plots of L/D versus a volume parameter, V/C^3 (volume/chord³), for the four cross sections at an angle of attack of 6 degrees and for Mach numbers 3, 4, and 5, respectively. For Mach numbers 3 and 4 the blunt trailing edge parabolic arc section is shown to be considerably more favorable than the other three sections. At Mach number 5 the L/D values for the parabolic arc and the blunt trailing edge wedge section are essentially identical and considerably above the other two sections.

Volume, rather than t/C , is used as the parameter for comparing the aerodynamic characteristics to determine the most favorable body cross section shape. This is because, for a particular volume (i. e., fixed payload, guidance and motor envelope) the body cross section having the lowest drag will therefore have the most favorable velocity-time history and the section having the highest lift-to-drag ratio will have the most favorable performance capabilities.

Comparison plots of C_D versus V/C^3 for all four sections at an angle of attack of 6° are presented in Figures 3.2.9 through 3.2.11 for $M = 3, 4,$ and $5,$ respectively. The parabolic arc section is the section having the lowest C_D .

The conclusions of this analytical investigation are, as summarized in Figures 3.2.6 through 3.2.11, that of the four cross section shapes considered for a body having a circular planform, the blunt trailing edge parabolic arc cross section is most favorable, having the lowest drag and highest lift-to-drag ratio for a specified body volume. The parabolic arc cross section with a blunt trailing edge was therefore selected with first priority for the wind tunnel test program.

The results of this study substantiated the views expressed in Reference 3.2.4. Figure 3.2.12 shows the four cross section shapes proposed for study at that time. Model III closely approximates the parabolic arc configuration with a blunt trailing edge that was selected above as a first priority for testing.

SECRET

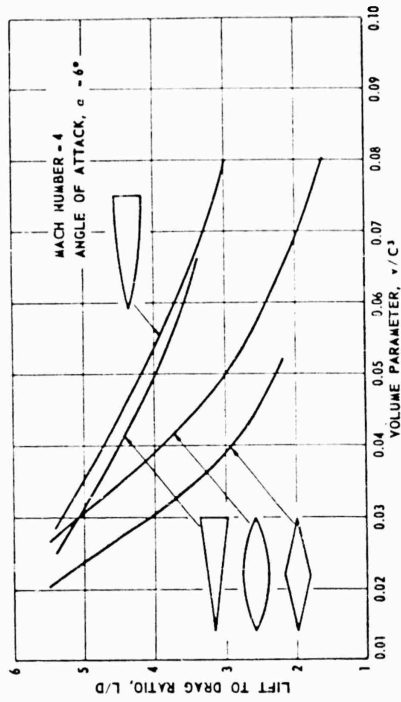


Figure 3.2.7. Estimated Variation of Lift-to-Drag Ratio With Volume Parameter.

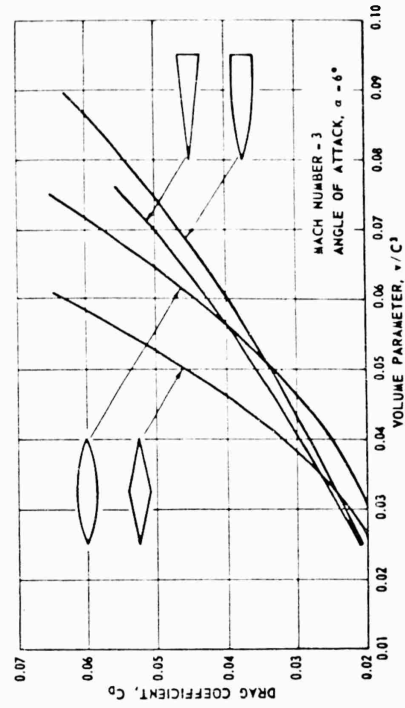


Figure 3.2.9. Estimated Variation of Drag Coefficient With Volume Parameter.

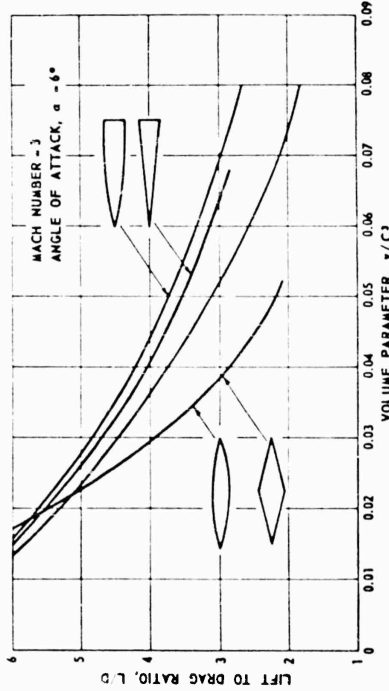


Figure 3.2.6. Estimated Variation of Lift-to-Drag Ratio With Volume Parameter.

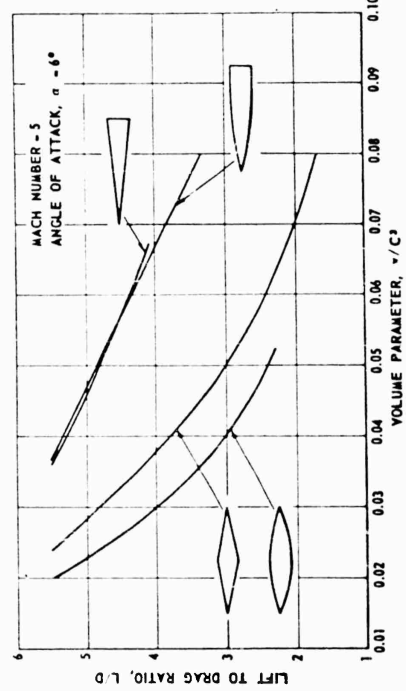


Figure 3.2.8. Estimated Variation of Lift-to-Drag Ratio With Volume Parameter.

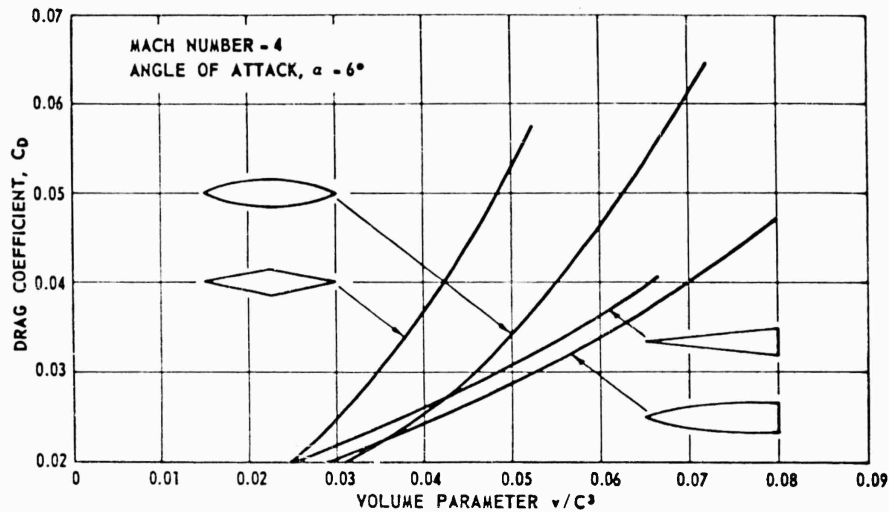


Figure 3.2.10. Estimated Variation of Drag Coefficient With Volume Parameter.

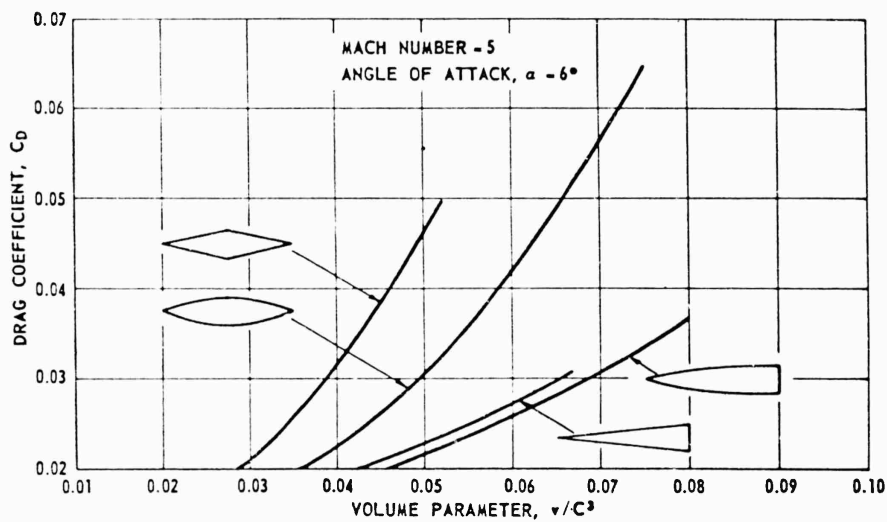


Figure 3.2.11. Estimated Variation of Drag Coefficient With Volume Parameter.

3.2.2 EXPERIMENTAL

Tests on three basic models and a blunted leading edge model were performed in the experimental phase of this study. The models tested are described in detail below. The Model I body (symmetrical lenticular) was tested to correlate results of these tests with the results of previous tests on lenticular bodies. The cross section of the Model III body was a result of the analytical study, presented in

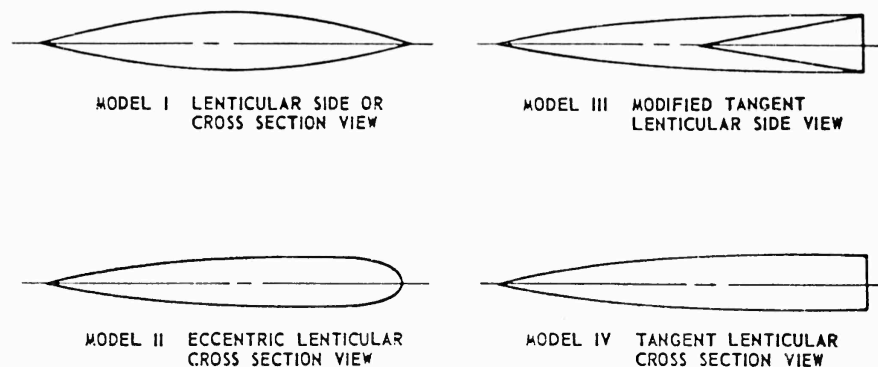


Figure 3.2.12. Cross Section Shapes.

paragraph 3.2.1, above, which indicated that for the optimum cross section shape, the maximum thickness should be located at the aft most point on the body. The Model II body is a slight variation of Model III and was tested to determine if the most favorable cross section did not fall between the two extremes investigated (i. e., the symmetrical Model I body with maximum thickness at the midchord and the Model III with maximum thickness for every chordwise cross section located at the aft most point of the section).

MODEL III. As determined in paragraph 3.2.1, above, a blunt trailing edge parabolic arc cross section offered the most promise from a lift, drag, and stability standpoint. In the arc of curve involved in the centerline profile, circular and parabolic equations both "fit" closely. In the machining of all models a circular arc profile was used for simplicity. Figure 3.2.13 presents a sketch of the layout of Model III. Figure 3.2.14 presents a photograph of Model III partially fabricated and illustrates the contour profile lines of this model. Figure 3.2.15 gives a top view of the completed model and shows the outline of the filler plates and plugs. Removal of these filler plates and plugs allowed the attachment of the forward (upper and aft) lower pitchwators (described below); the pins used to attach the model to the internal six-component balance; and the lateral roll control surfaces (described below). Figure 3.2.16 gives a side view illustrating the blunt trailing edge of the model.

MODEL II. Model II is best described as one in which the contour profile lines are made up of circles tangent to the model circumference at the aft end. It is best envisioned as "clam shell" shaped. Figure 3.2.17 illustrates the difference in Model II chordwise cross sections for various spanwise locations. A description of the surface contour lines is illustrated in Figure 3.2.18 which is a photograph taken during fabrication. A side view of Model II is shown in Figure 3.2.19.

SECRET

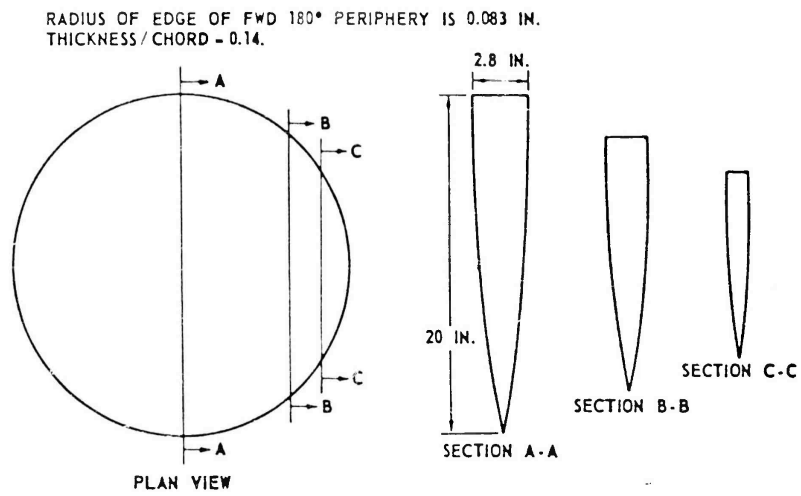


Figure 3.2.13. Model III.

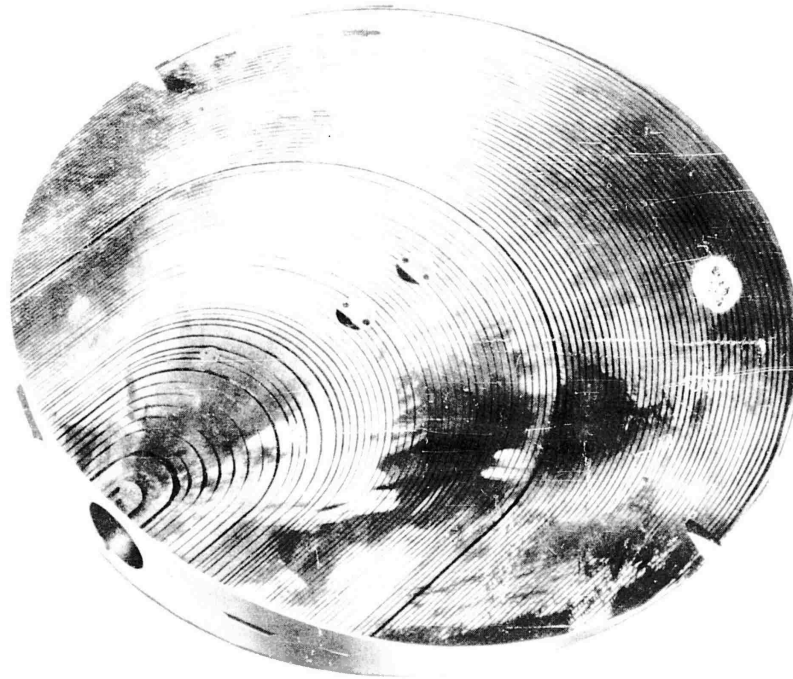


Figure 3.2.14. Model III, Partially Fabricated.

SECRET

SECRET

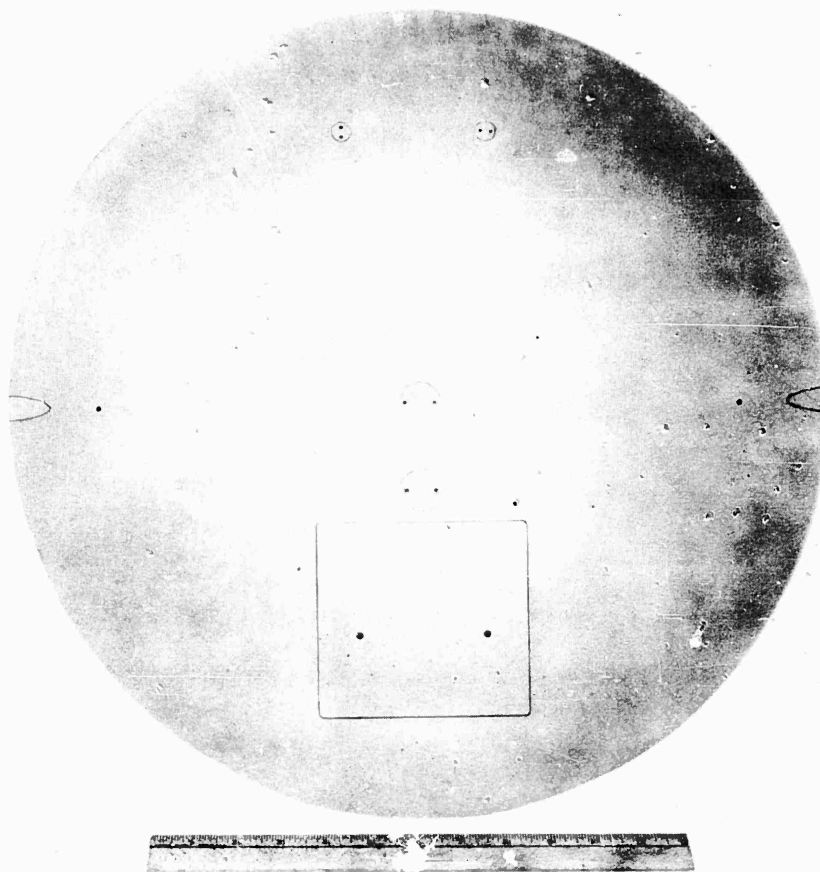


Figure 3.2.15. Model III, Top View.



Figure 3.2.16. Model III, Side View.

3.2.16

SECRET

SECRET

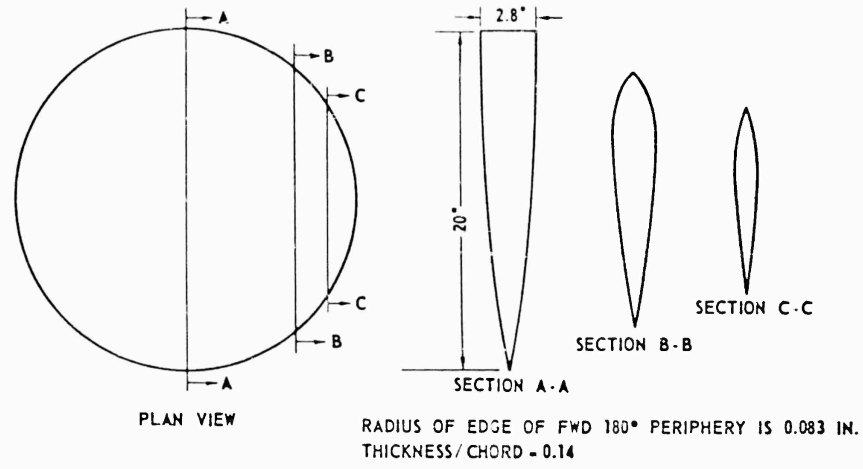


Figure 3.2.17. Model II.

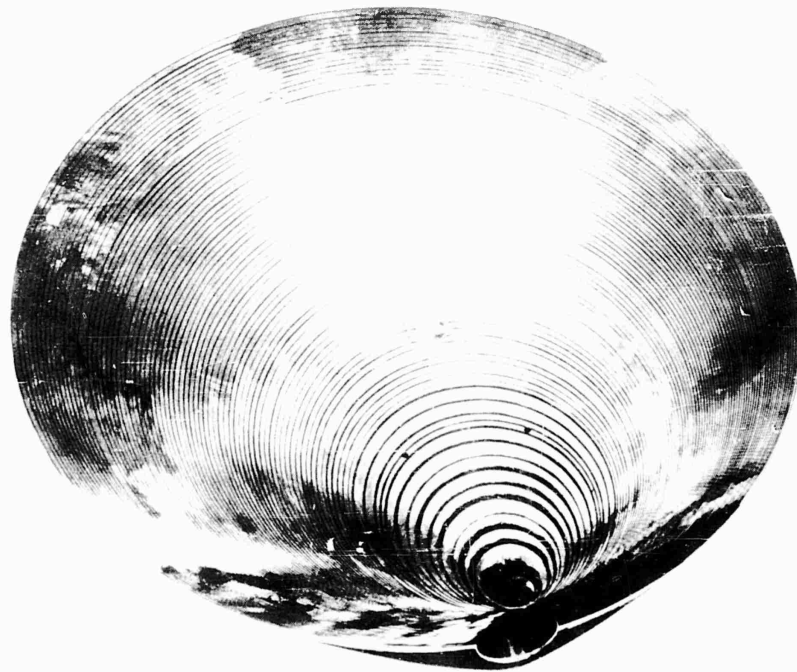


Figure 3.2.18. Model II, Partially Fabricated.

SECRET

3.2.17



Figure 3.2.19. Model II, Side View.

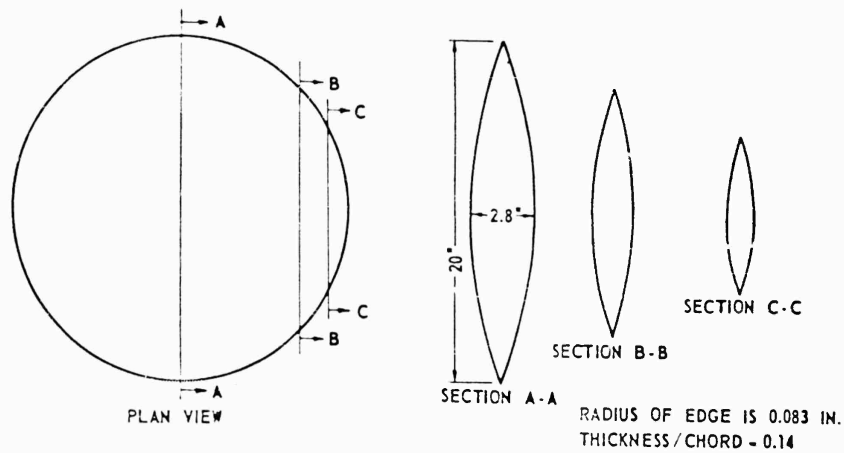


Figure 3.2.20. Model I.

MODEL I. Model I was a symmetrical lenticular body. Except for the fact that the circumferential edges had a leading edge radius of 0.083 inch, this model is identical to the shape tested by APGC. Figures 3.2.20 and 3.2.21 present detailed information on this model.

MODEL IV. Model IV is a symmetrical lenticular body with a circular plan-form 19.14 inches in diameter. This model was obtained by machining the circumferential edges of Model I to a radius of 0.25 inch. The resulting reduction in area was 26.4 IN^2 . This induced no error in the coefficients because the reduced area was used in reduction of the force and moment data. There resulted a slight discrepancy in the thickness ratios. The thickness ratio for Model IV was 14.63 percent compared to 14 percent for the three other models tested.

SECRET



Figure 3.2.21. Model I, Side View.

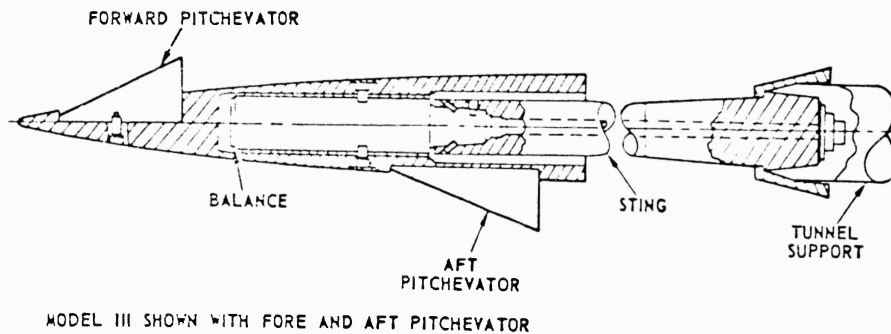


Figure 3.2.22. Test Article Arrangement.

A sketch of the model balance sting combination with pitchvators is presented in Figure 3.2.22

Pitchvators, (P). Pitchvators were spoiler type flaps located on the forward, upper and/or aft-lower surfaces, of the body for pitch control. Deflection of these control surfaces from the body into the airstream was simulated by wedges (see Figure 3.2.22). The plate covering the recession in the bodies for securing these wedges can be seen in the photograph of Figure 3.2.15.

Several different pitchvators, varying in size and aspect ratio as described in Table 3.2.1 were tested.

SECRET

Table 3.2.1
PITCHEVATOR GEOMETRICAL CHARACTERISTICS

Pitchevator	P ₁	P ₂	P ₃
Chord, IN.	5	5	7
Span, IN.	5	7	5
Area, IN. ²	25	35	35
Location of forward pitchevator leading edge, body station, IN.	1.0	1.0	1.0
Location of aft pitchevator leading edge, body station, IN.	12.8	12.8	12.8
Deflection angles, degree	20° Models I, II & III	20° Model III	20° Model III
	15° and 25° Model III		

Conevators, (C). The conevators were a pair of cones of 30 degrees included angle, 5.47 inches in altitude, and with a 2.94 inch diameter base. The cones were mounted at the lateral extremities of Model III and were rotatable about the lateral body axis to achieve roll control.

Wedgevators, (W). The wedgevators were a pair of wedges, 3 inches in chord and 2 inches in span, mounted at the lateral extremities of Model III. With an included angle of 15 degrees each, the wedges were rotated about the lateral body axis to achieve roll control. For yaw control one wedge angle had a larger magnitude than the other to produce differential drag. Wedge angles of 15, 30, and 45 degrees were provided.

Tests were conducted in the Arnold Engineering Development Center's wind tunnel "A" for a Mach number range of 2 to 6 to determine the drag and longitudinal and lateral stability characteristics of several lenticular configurations. Longitudinal, lateral, and roll control devices were also investigated as well as the effects of blunted leading edges. References 3.2.20 and 3.2.21 present, in detail, the planning for all the wind tunnel testing performed during this program.

SECRET

The primary objectives of this test program were: (1) to determine the most favorable cross-sectional shape for a circular planform body and (2) to determine the feasibility of controlling a circular planform body in pitch, roll, and yaw by using pure aerodynamic controls. In addition, the effect of blunting the leading edge to withstand aerodynamic heating was determined.

The models, with and without the various controls, were tested at angles of attack from -5 to 15 degrees for roll attitudes of 0 , ± 90 , and 180 degrees at five Mach numbers; $M = 2, 3, 4, 5$, and 6 (very little data for the configurations with controls were obtained at $M = 6$). In addition a Reynolds number variation was run at each Mach number at low angles of attack (-5 to $+5$ degrees) for the bare body configurations.

The cross sections of the models tested to determine optimum cross section during the experimental program are illustrated in Figures 3.2.13, 3.2.17, and 3.2.20.

The wind tunnel test results obtained for the bare body models are discussed in this section. The results obtained for the body with various controls are discussed in subsection 3.7.

Presented in Figures 3.2.23 through 3.2.30 are samples of the Schlieren photographs taken during this test program. These Schlieren photographs are of the profile aspect of the models. The shock waves shown are primarily in the vertical plane of the centerline of symmetry of the models. Actually, the shock wave field is three-dimensional and the bow shock is a curved one following the leading edge. It must also be noted that the Schlieren sensitivity was not a constant in these photographs. All pictures were taken at zero degree angle of attack. Figures 3.2.23 and 3.2.24 concern Models I and III, respectively, at Mach number 3.0. A similar set of pictures is presented in Figures 3.2.25 and 3.2.26 for Mach 6.0. In general the photographs indicate unseparated flow over the length of the body. It should be noted that not all lines shown in the photographs are indicative of flow but are due to blemishes on the window or tunnel wall. These figures show that the shock wave angle of Model III at both Mach numbers is less than that of Model I, indicating that the wave drag of Model III is less than that of Model I.

Figures 3.2.27 through 3.2.30 are to illustrate the drag effects of blunting the leading edge of Model I at Mach number 2.0. Figures 3.2.27 and 3.2.28 are side view Schlierens of Models I and IV, respectively, while Figures 3.2.29 and 3.2.30 are top views of Models I and IV, respectively. These figures indicate an increased shock wave intensity as the leading edge of the model was increased from 0.083 inch (in the case of Model I) to 0.25 inch (in the case of Model IV).

SECRET

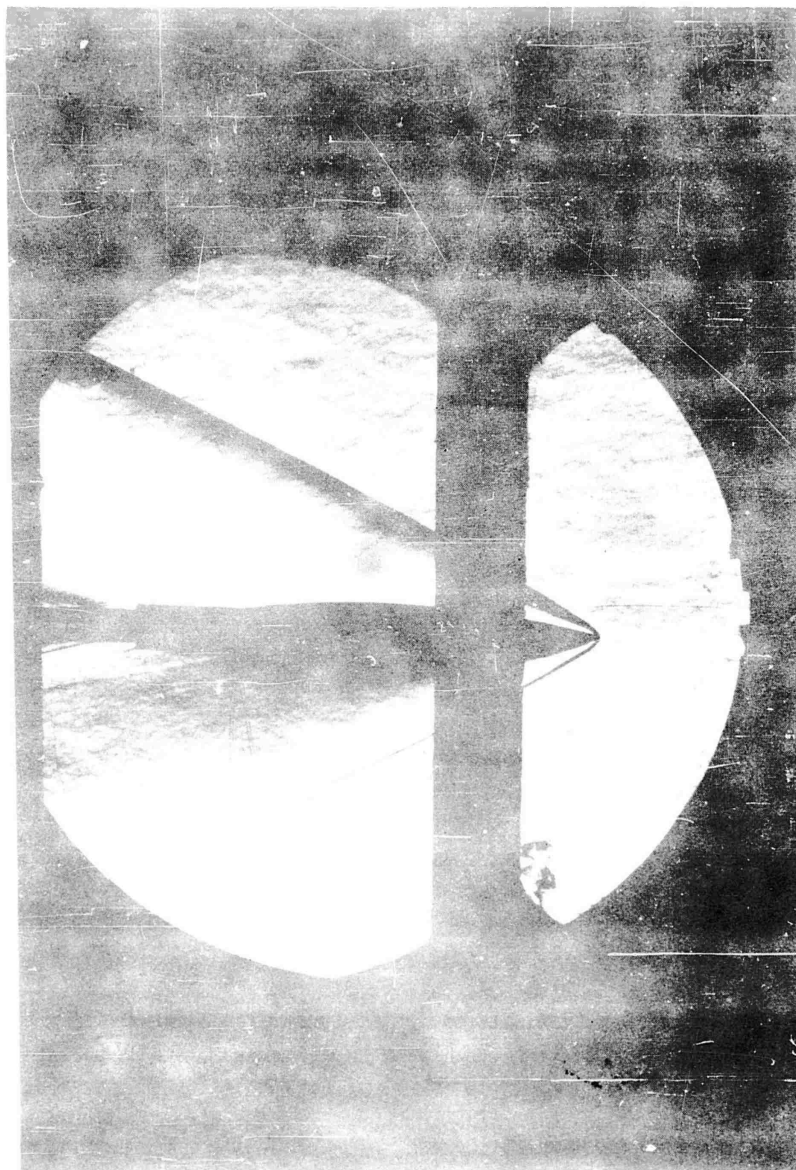


Figure 3.2.23. Metal I, Mach Number 3.

SECRET

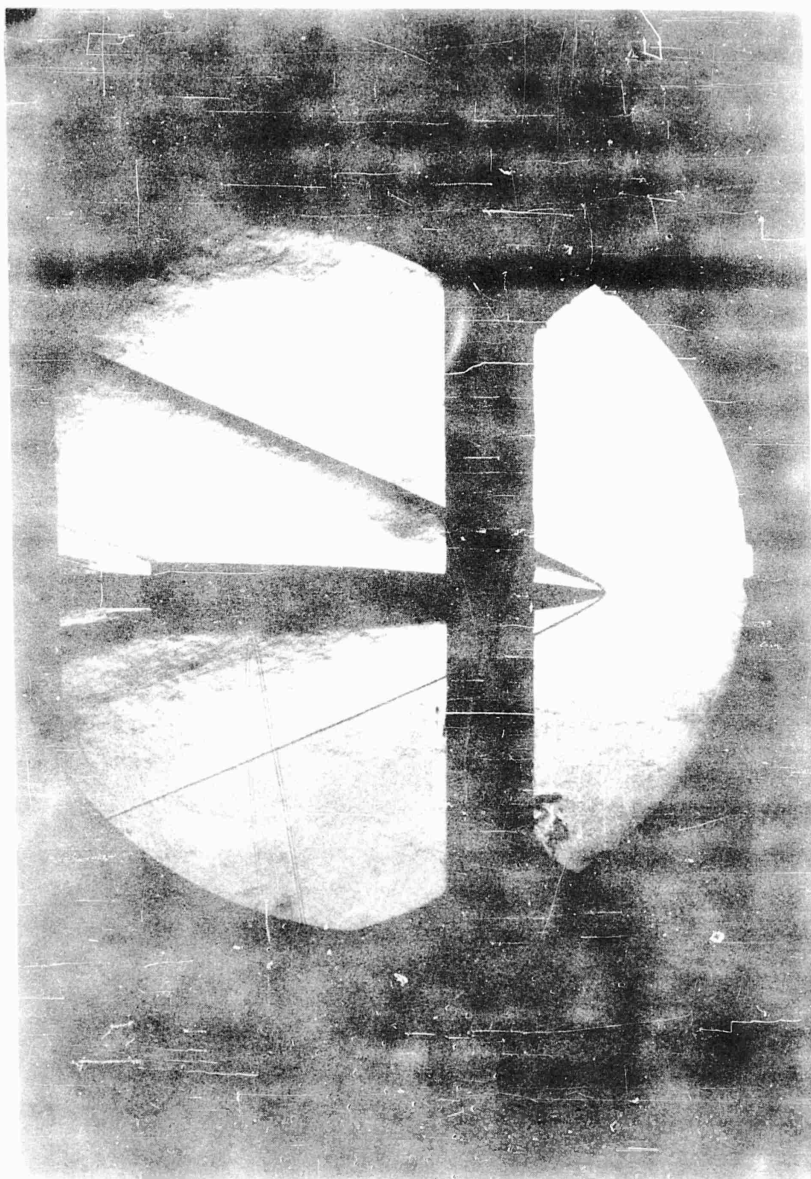


Figure 3.2.24. Model III, Mach Number 3.

SECRET

3.2.23

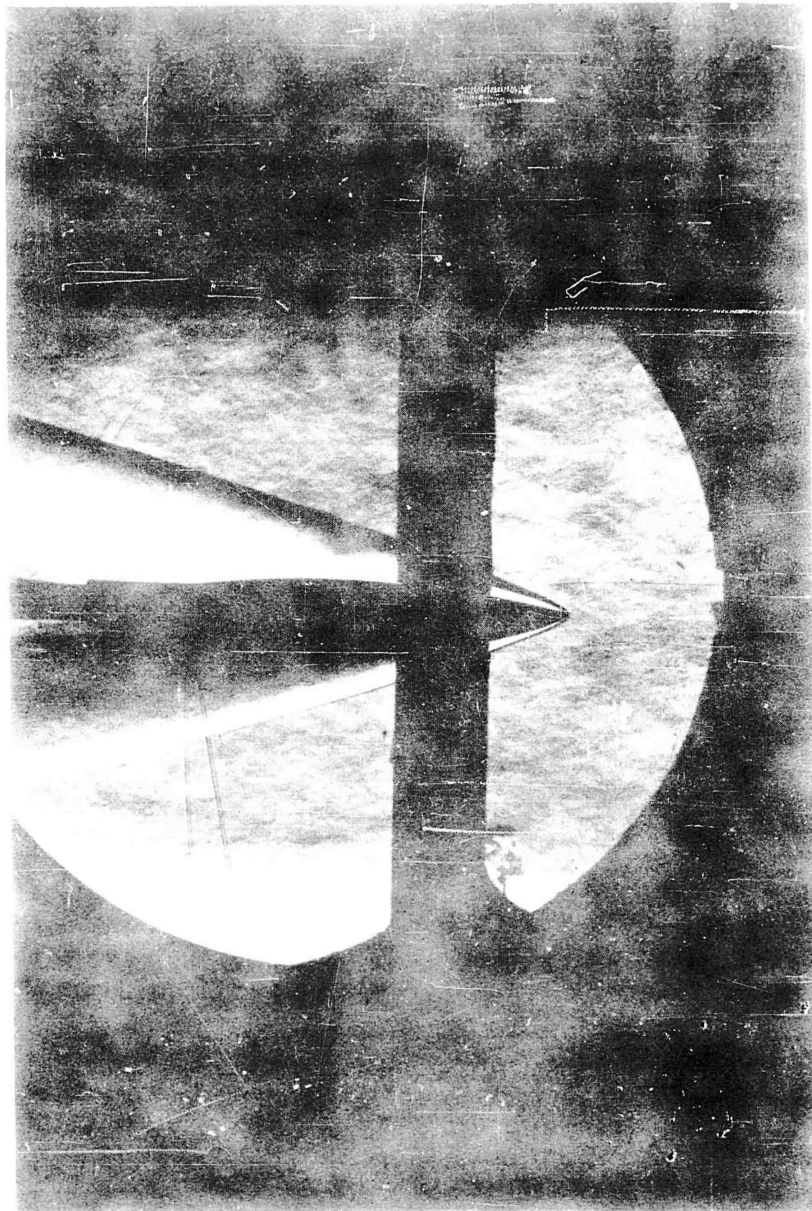


Figure 3.2.25. Model I, Mach Number 6.

SECRET

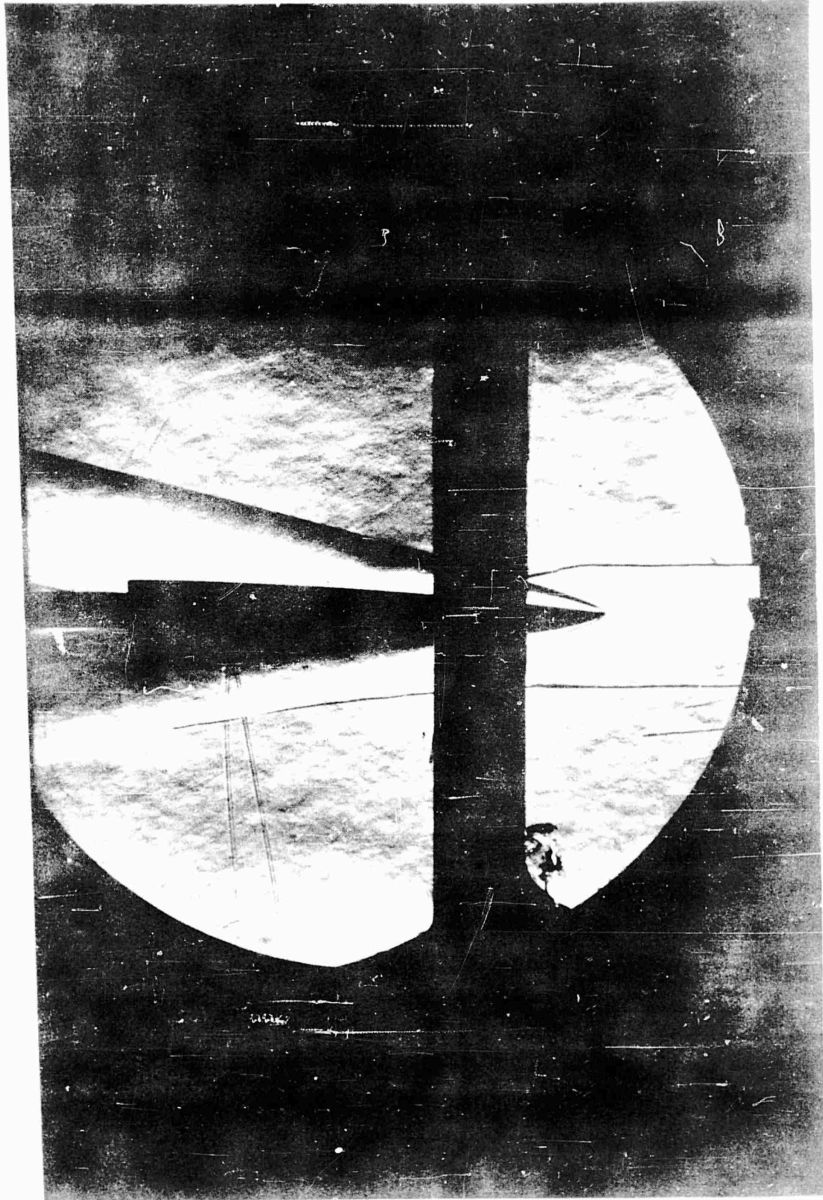


Figure 3.2.26. Model III, Mach Number 6.

SECRET

3.2.25

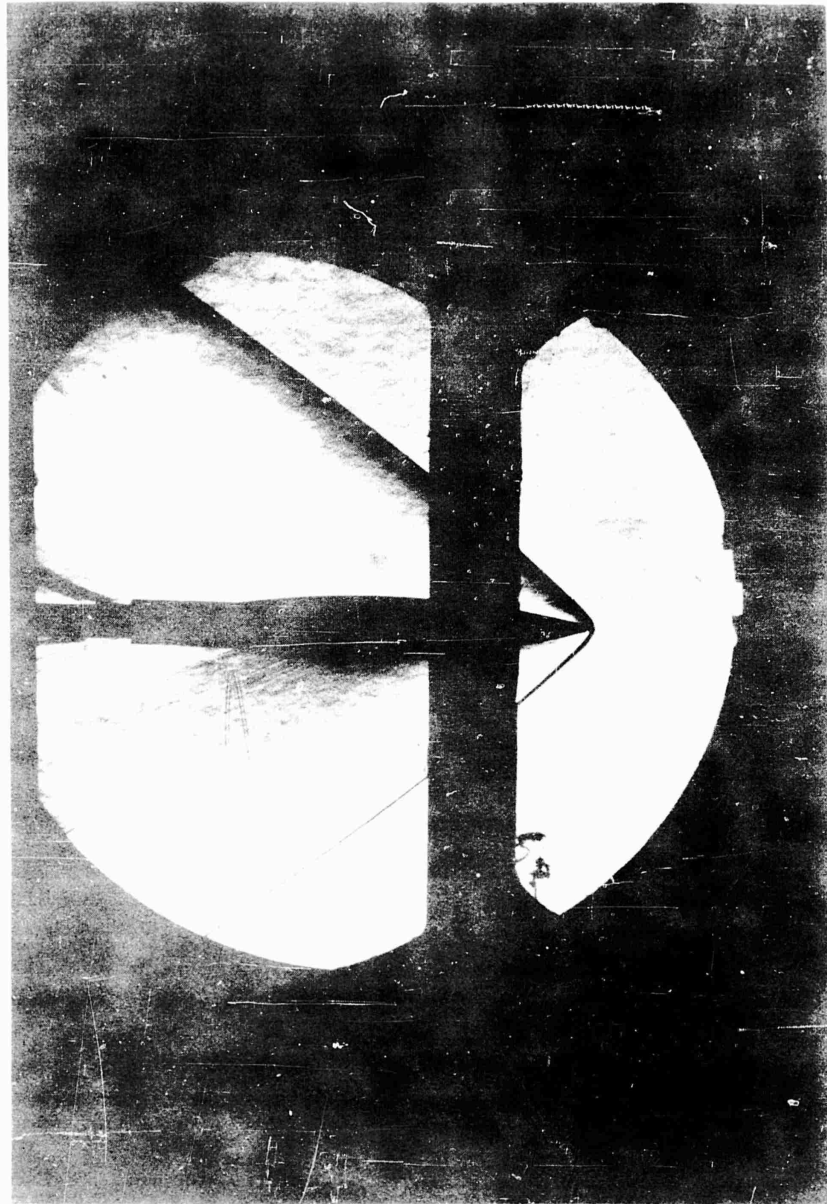


Figure 3.2.27. Model I, Mach Number 2.

SECRET



Figure 3.2.26. Model IV, Mach Number 2.

SECRET

3.2.27

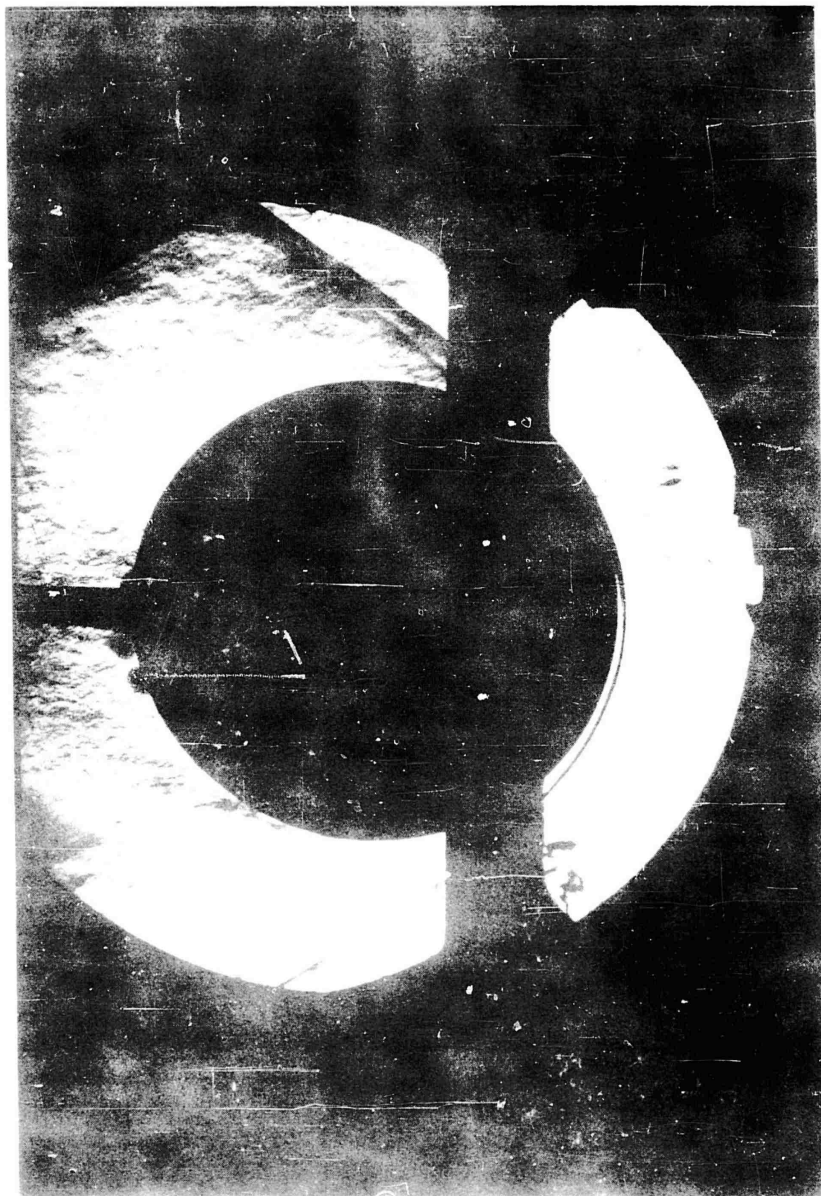


Figure 3.2.29. Model I, Mach Number 2.

SECRET



Figure 3.2.30. Model IV, Mach Number 2.

SECRET

3.2.29

Presented in Figures 3.2.31 through 3.2.35 are plots comparing the C_L and C_D variation with α for Models I, II, and III for Mach numbers 2, 3, 4, 5, and 6, respectively. As can be seen, the lift characteristics of Model III are superior to that of Models I and II at all Mach numbers. For instance, at Mach 2, Model III produces 3 percent more lift than Model I at 15° angle of attack. At Mach 6 Model III produces 13 percent more lift than Model I at the same angle. Thus as Mach number increases the advantage of Model III over Model I also increases as predicted.

A similar advantage is indicated in zero lift drag. At Mach 2 Model III has 82 percent of the zero lift drag of Model I while at Mach 6 it has only 64 percent of the zero lift drag of Model I. It is also worthwhile noting that the performance characteristics of Model III are equal to or greater than Model II although the latter configuration has considerably less volume.

A somewhat more revealing comparison of the relative aerodynamic performance of the three models is made in Figures 3.2.36 through 3.2.40 which present lift-to-drag ratio (L/D) versus angle of attack for the same Mach numbers listed above. Model III has the most favorable L/D for all angles of attack and Mach numbers investigated.

Thus, as predicted by Reference 3.2.4 and the analytical investigation of paragraph 3.2.1 above, a blunt trailing edge configuration exhibits considerably better aerodynamic performance as Mach number increases. It should be noted that base drag was included in the above comparisons. However, due to the inaccuracies involved in wind tunnel base drag measurements, the drag comparisons at Mach 2 and 3 may not be exactly valid due to the dominant role of base drag in this region. As Mach number increases, this term becomes less important; therefore, the results from Mach 3 through 6 are felt to be valid.

Reynolds number has an influence on base pressure but the effect is very small at the high Reynolds numbers for which the test was performed. For example, in Reference 3.2.22, it was shown that Reynolds number variation has a very small effect on base pressure for turbulent boundary layers (Reynolds numbers greater than 6×10^6). Conversely, Reynolds number has a very large effect on base pressures with a laminar boundary layer (Reynolds numbers less than 2×10^6). For the tests performed at the Arnold Engineering Development Center, the Reynolds numbers ranged from 2×10^6 to 9.75×10^6 . The data taken at the lower Reynolds numbers were specifically for the purpose of obtaining Reynolds number effect. All the stability and control data were taken at the maximum Reynolds number at each Mach number. These values ranged from a minimum at $M = 2$ of 4.25×10^6 to the maximum at $M = 5$ of 9.75×10^6 . From this Reynolds number range, it can be seen that the Reynolds number effects on base pressure for the test data are reasonably small. The drag scale effect $\left(\frac{\partial C_D}{\partial R_N}\right)$ for the complete configurations ranges from .00025 to .0005 per million

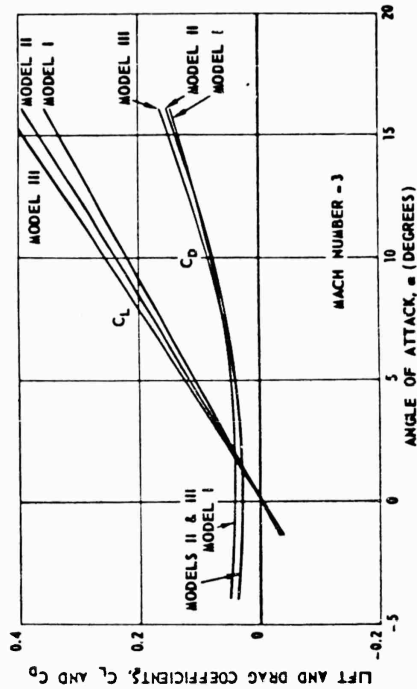


Figure 3.2.32. Comparisons of Lift and Drag Coefficients.

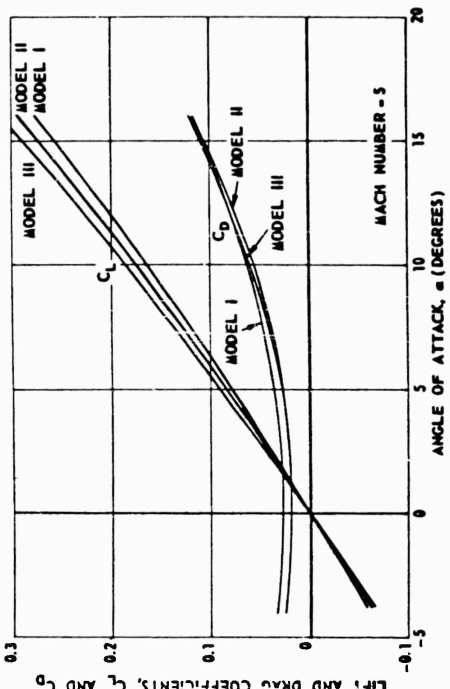


Figure 3.2.34. Comparisons of Lift and Drag Coefficients.

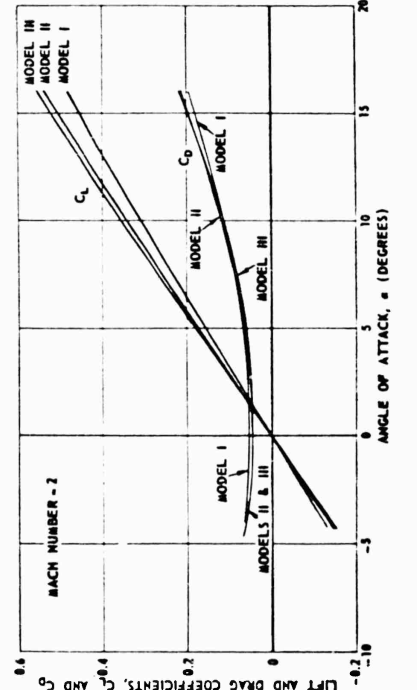


Figure 3.2.31. Comparisons of Lift and Drag Coefficients.

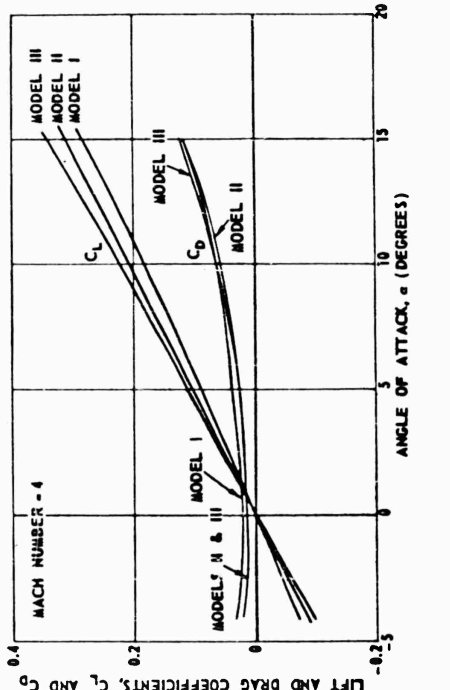


Figure 3.2.33. Comparisons of Lift and Drag Coefficients.

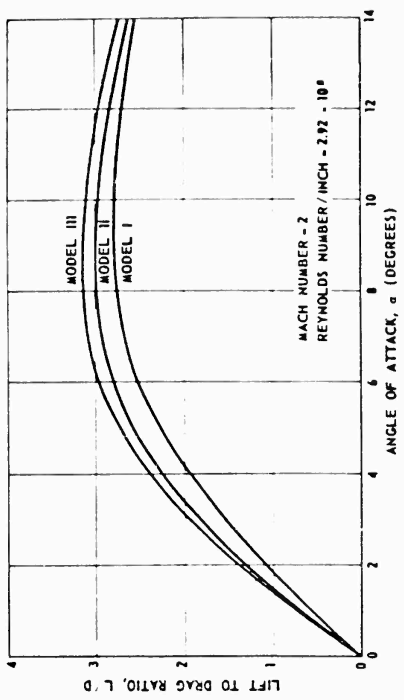


Figure 3.2.36. Comparison of Lift-to- Drag Ratio.

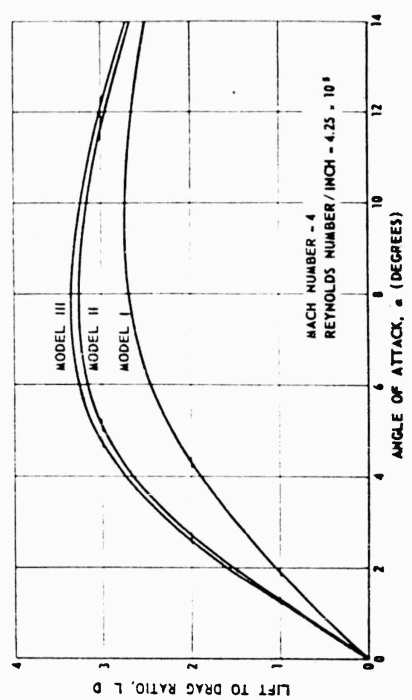


Figure 3.2.38. Comparison of Lift-to- Drag Ratio.

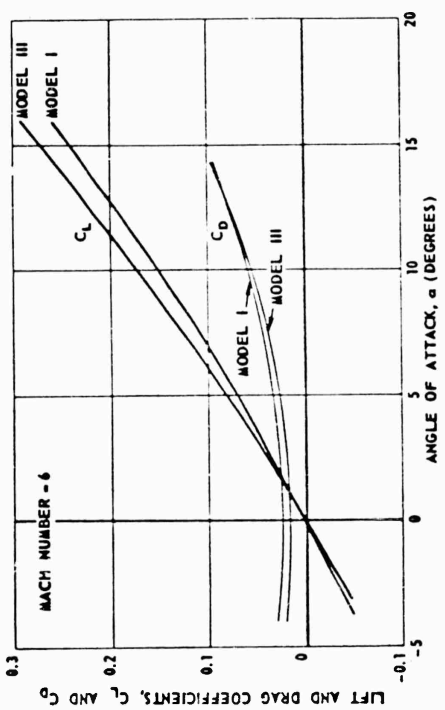


Figure 3.2.35. Comparisons of Lift and Drag Coefficients.

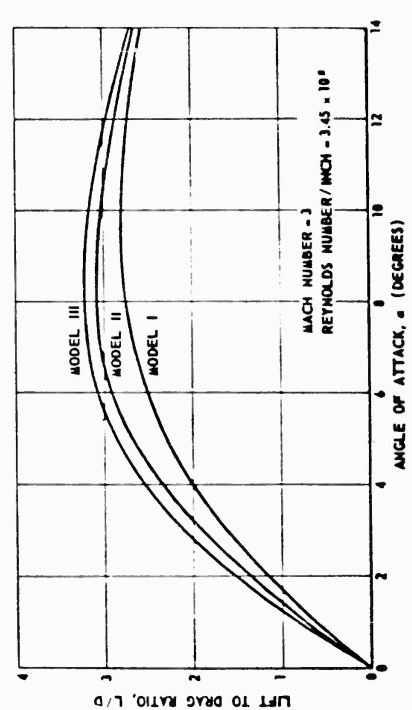


Figure 3.2.37. Comparison of Lift-to- Drag Ratio.

SECRET

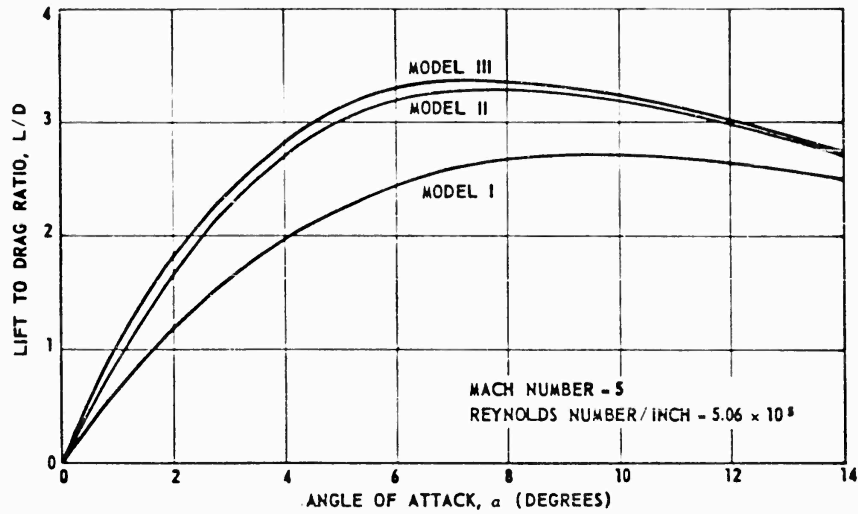


Figure 3.2.39. Comparison of Lift-to-Drag Ratio.

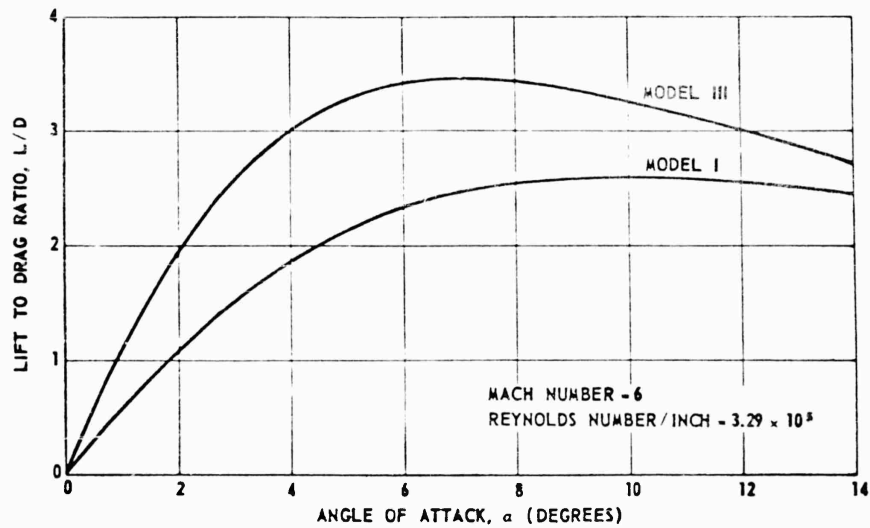


Figure 3.2.40. Comparison of Lift-to-Drag Ratio.

change in Reynolds number. At $M = 2$, for Model II this represents a one percent change in C_{D_0} for each Reynolds number change of one million.

The full scale altitudes simulated in the testing represented heights of 65,000 to 95,000 feet. The majority of the data were taken in the range of altitudes of 65,000 to 85,000 feet full scale.

SECRET

No correction was made for support interference in the base pressure data. This is because of the three-dimensional base on the models. Reference 3.2.23 indicates a maximum error of 16 percent in base pressure results on a body of revolution for a support to base diameter ratio $d/D = .5$ over the range of Reynolds numbers of 10×10^6 to 40×10^6 . For the tests performed at the Arnold Engineering Development Center the ratio of the base height to support diameter was $d/h_B = .536$ in one plane and in the other plane it was $d/h_B = .075$.

Plots of the lift curve slope at zero angle of attack versus Mach number and the zero-lift drag coefficient variation with Mach number are presented in Figures 3.2.41 and 3.2.42 for Models I, II, and III. As shown, the $C_{L\alpha}$ of the Model III is most favorable and the C_{D_0} of Model III is less than that for Model I and is identical to that of Model II.

From experimental data it was found that for all three bodies the variation of C_m with α was essentially linear for the angle of attack range investigated (i. e., $\alpha = -5$ to $+15$ degrees). Therefore, presented in Figure 3.2.43 is a comparison of $C_{m\alpha}$ (referenced to the midchord of the models) versus Mach number for Models I, II, and III. As shown, the $C_{m\alpha}$ for all three bodies is unstable (i. e., $C_{m\alpha}$ is positive); however, the moment coefficient slope of Model III is considerably less than those of Models I and II.

A more revealing comparison of the relative stability of the three models is contained in Figure 3.2.44 which presents a comparison of the stability margins of the three bodies near zero angle of attack. The stability margin is defined as the aerodynamic center of pressure location, measured from the midchord of the model, divided by the chord (or diameter) of the model. As in the case of pitching moment coefficient, a positive stability margin indicates an unstable moment (i. e., center of pressure forward of the midchord of the model).

Figure 3.2.44 indicates that Model III is less unstable than the other two models over the Mach number range from 2 to 6. Figure 3.2.44 shows that Model III has an aerodynamic center of pressure that lies between 5 and 6 percent ahead of the midchord of the model except for Mach number 2 where a 7 percent location is indicated. Of primary importance is the fact that the center of pressure location is fairly constant with Mach number over the range investigated. This considerably simplifies the problem of control design in that an overdesigned condition need not exist over the majority of the flight time due to a critical narrow Mach number range.

The conclusion of the evaluation is, that of the cross section shapes considered, Model III is again the most favorable. It is felt that the ability to achieve rearward shifts in the aerodynamic center of pressure and missile volume are the most important gains experienced from Model III. As noted earlier, References 3.2.15 and 3.2.16 gave some indication of this, however, the magnitude of the shift of the aerodynamic center of pressure was more than expected and considerably improved the control aspect for the circular planform configuration.

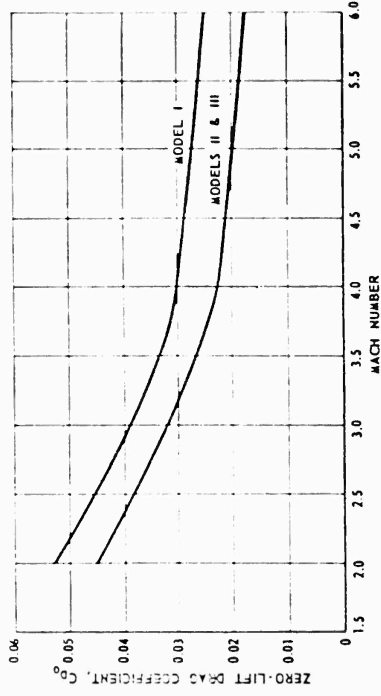


Figure 3.2.41. Comparison of Lift Coefficient Slope.

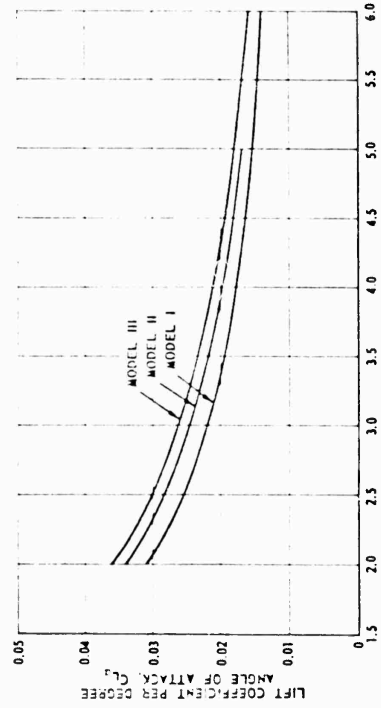


Figure 3.2.42. Comparison of Zero-Lift Drag.

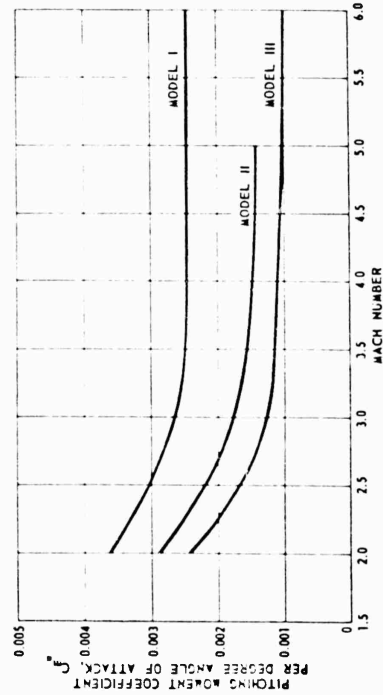


Figure 3.2.43. Comparison of Pitching Moment Coefficient Slope.

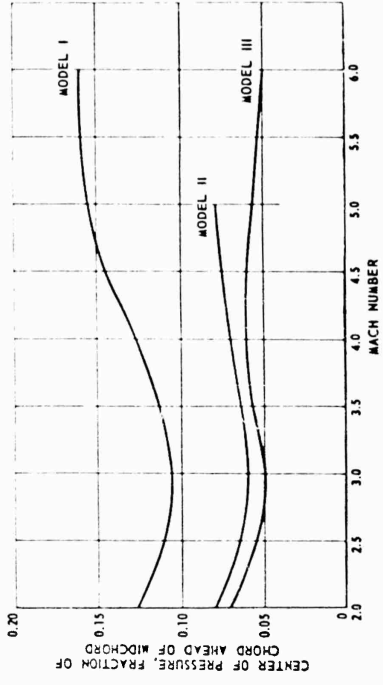


Figure 3.2.44. Variation of Center Pressure Location.

Comparisons of the experimental and predicted data variation with Mach number for Model III are shown in Figures 3.2.45 and 3.2.46. As can be seen, for Mach numbers less than 5, the predicted $C_{L\alpha}$ values were slightly lower (4 percent) than experimental data. The predicted C_{D0} is quite close to experimental data at Mach numbers 3 and 4 but is considerably lower than experimental data at Mach 5.

3.2.3 AERODYNAMIC CHARACTERISTICS

This section presents the aerodynamic characteristics of Model III over the Mach number range of zero to 10. Experimental data for this body with a thickness ratio of 14 percent were obtained, as discussed above, for the Mach number range of 2 to 6. Characteristics presented in this section for Mach numbers below 2 and 6 and for thickness ratios other than 14 percent were obtained by utilizing various other sources as noted. Only Model III will be discussed since the above analysis concluded that this shape was the most favorable of all the shapes considered and probably approaches the optimum shape possible for a circular planform body.

The variation in zero-lift drag coefficient with Mach number for Model III is presented in Figure 3.2.47 for thickness ratios (t/C) of 14 percent with a leading edge radius equal to $1/240$ of the planform diameter. The values for the 14 percent body between Mach numbers 2 and 6 are based on PYE WACKET experimental data; all dashed curves indicate the values have been calculated. The zero-lift drag values shown from $M = 0$ to 2 were estimated utilizing the data presented in References 3.2.24 through 3.2.30. The zero-lift drag was extended to Mach numbers above 6 using the data of References 3.2.24, 3.2.31 and 3.2.32.

Also contained in Figure 3.2.47, are the drag breakdown data for the 14 percent configuration. Computed skin friction drag coefficients are presented for altitudes of sea level, 50,000 feet, and 100,000 feet for a 60-inch diameter missile. These were computed using Reference 3.2.19. A computed base drag curve is presented which was determined from Reference 3.2.18. The computed skin friction drag and base drag were removed from the experimental data to obtain the wave drag coefficient data shown in the breakdown.

The C_{D0} versus Mach number curve for $t/C = .21$, presented in Figure 3.2.48, and the variation of C_{D0} with t/C shown in Figure 3.2.49 were obtained by employing the combined supersonic - hypersonic similarity law (Reference 3.2.33) together with the experimental data for the 14 percent body from $M = 2$ to 6. The supersonic-hypersonic similarity law relates the Mach number and thickness ratio of bodies as follows:

$$\beta_1 \delta_1 = \beta_2 \delta_2 \quad (3.2.15)$$

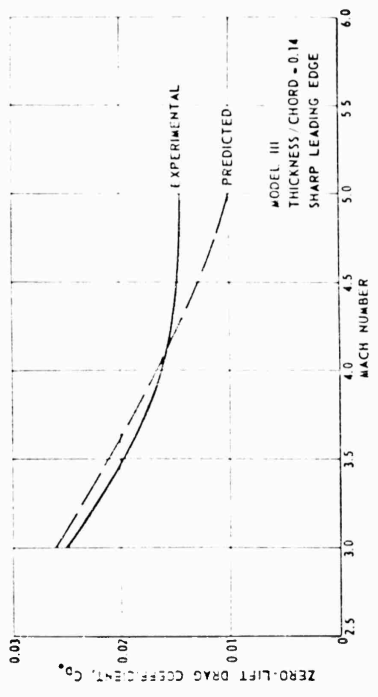


Figure 3.2.46. Comparison of Predicted and Experimental Zero-Lift Drag Coefficient.

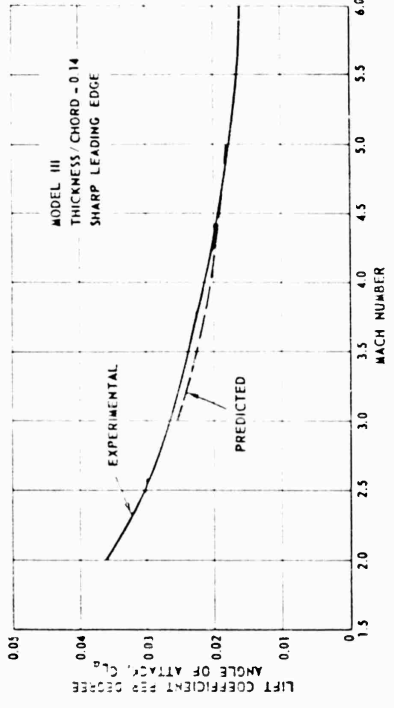


Figure 3.2.45. Comparison of Predicted and Experimental Lift Coefficient.

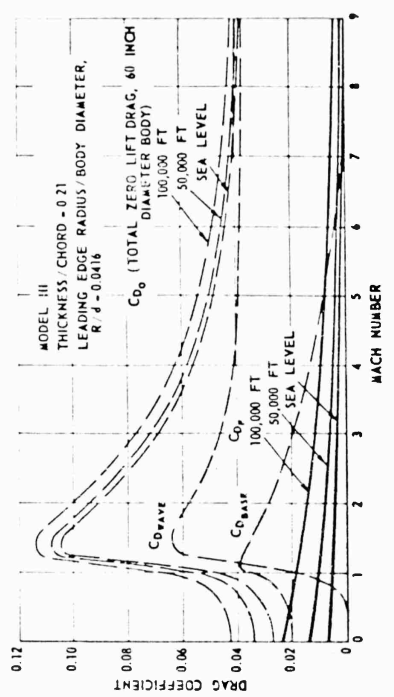


Figure 3.2.48. Variation of Skin Friction, Base, Wave, and Zero-Lift Drag Coefficients.

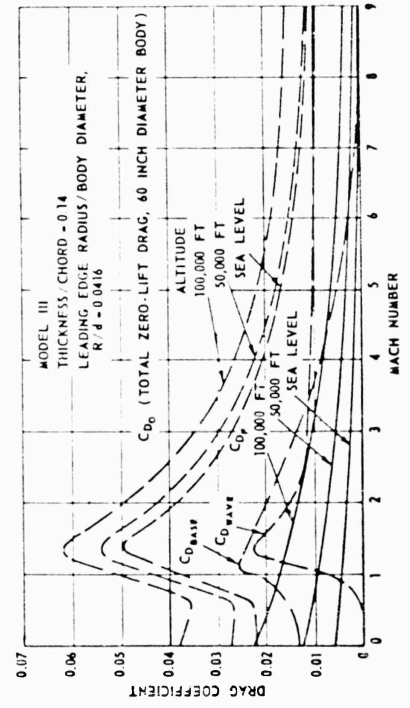


Figure 3.2.47. Variation of Skin Friction, Base, Wave, and Zero-Lift Drag Coefficients.

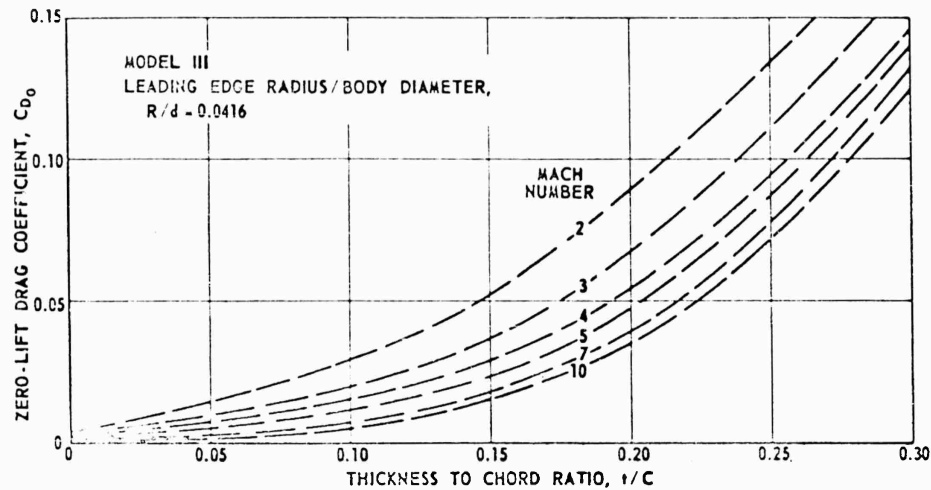


Figure 3.2.49. Variation of Zero-Lift Drag Coefficient With Thickness-to-Chord Ratio.

where

$$\beta = \sqrt{M^2 - 1} \quad \text{and} \quad \delta = \frac{t}{c}$$

which reduces to

$$M_2 = \sqrt{M_1^2 \left(\frac{\delta_1}{\delta_2} \right)^2 - \left(\frac{\delta_1}{\delta_2} \right)^2 + 1} \quad (3.2.16)$$

The wave drag coefficients were then determined for various thickness ratios, for the appropriate M_2 , where M_1 and δ_1 referred to the data for the 14 percent body, by the following equation:

$$\frac{C_{DW_2}}{C_{DW_1}} = \left(\frac{\delta_2}{\delta_1} \right)^3 \quad (3.2.17)$$

The C_{DW_1} for the 14 percent body was used in this computation to obtain wave drag for the other thickness ratios. The methods of Reference 3.2.18 were then used to obtain base drag for bodies having other thickness ratios and was added, along with skin friction drag, to the wave drag calculated by the supersonic-hypersonic similarity law.

SECRET

Along with the total zero-lift-drag coefficient for the 21 percent configuration, Figure 3.2.48 presents a breakdown of these data. Skin friction drag for altitudes of sea level, 50,000 feet and 100,000 feet are presented for a 60 inch diameter missile. Base drag data and wave drag data are also presented. The skin friction data were computed using Reference 3.2.19.

Presented in Figure 3.2.50 are curves of increases in wave drag due to blunting as a function of the leading edge radius divided by planform diameter. These values were obtained from experimental data at Mach numbers 3, 4, and 5.

The normal force coefficient per degree angle of attack is presented versus Mach number in Figure 3.2.51 for bodies having thickness ratios of 0.14 and 0.21. Normal force coefficients for angles of attack up to 45 degrees are presented in Figures 3.2.52 and 3.2.53 for thickness ratios of 14 and 21 percent, respectively. The values presented in the above plots for the 14 percent body between $M = 2$ and 6 and for angles of attack less than 15 degrees were obtained experimentally in the wind tunnel program discussed previously in this section. The data were extended to $\alpha = 45^\circ$ using the data of References 3.2.36, 3.2.44, and 3.2.24. From Reference 3.2.43, a normal force value at $\alpha = 45^\circ$ was computed and the variation of normal force with angle of attack determined. These data were then combined with the experimental data. Values for the subsonic and transonic regions were estimated utilizing the results of References 3.2.26 through 3.2.30 and 3.2.34 through 3.2.37; estimates for Mach numbers above 6 were based on results of References 3.2.31 and 3.2.38 through 3.2.43. Normal force values for the 21 percent thick body were calculated by utilizing the supersonic-hypersonic similarity law. M_1 and M_2 are related as discussed above for the drag calculations; C_N values for the 21 percent body were then calculated by the following relationship;

$$\frac{C_{N_2}}{C_{N_1}} = \left(\frac{\delta_2}{\delta_1}\right)^2 \quad (3.2.18)$$

where $\delta = t/C$ and subscripts 1 and 2 refer to the 14 and 21 percent bodies, respectively.

The variation of the pitching moment slope, C_{m_α} , with Mach number is presented in Figures 3.2.54 and 3.2.55 for the 14 and 21 percent thick bodies, respectively, for several center of gravity locations. The pitching moment coefficient data obtained for Model III varied linearly with angle of attack up to 15 degrees which was the maximum angle of attack at which data were obtained. A positive value of C_{m_α} , as presented in the above plots, denotes a longitudinally unstable configuration. The estimated values presented in Figures 3.2.54 and 3.2.55 for the 21 percent body were obtained utilizing the results of the same references discussed above for the normal force coefficients.

SECRET

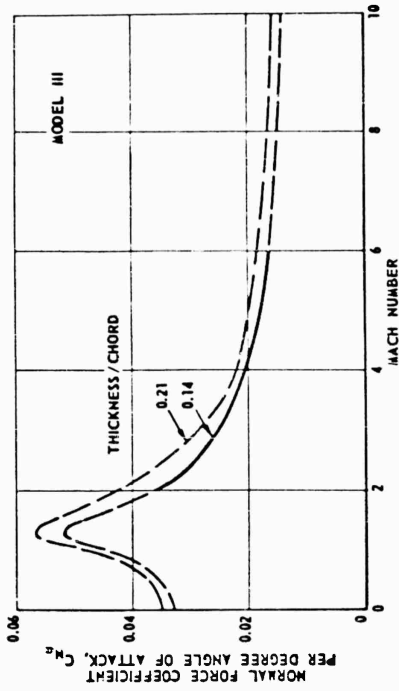


Figure 3.2.51. Variation of Normal Force Derivative With Mach Number.

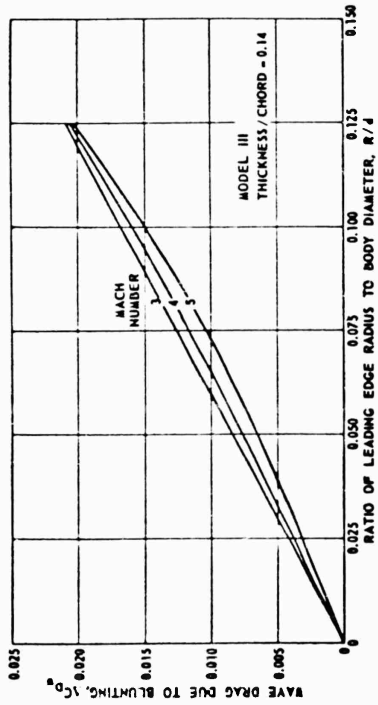


Figure 3.2.50. Drag Increment Due to Blunting Leading Edge.

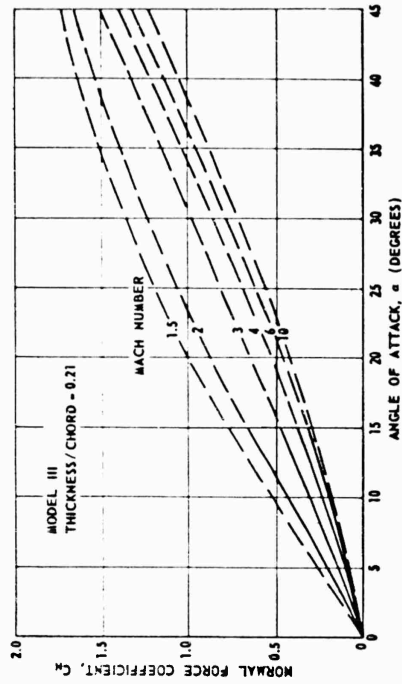


Figure 3.2.53. Variation of Normal Force Coefficient with Angle of Attack.

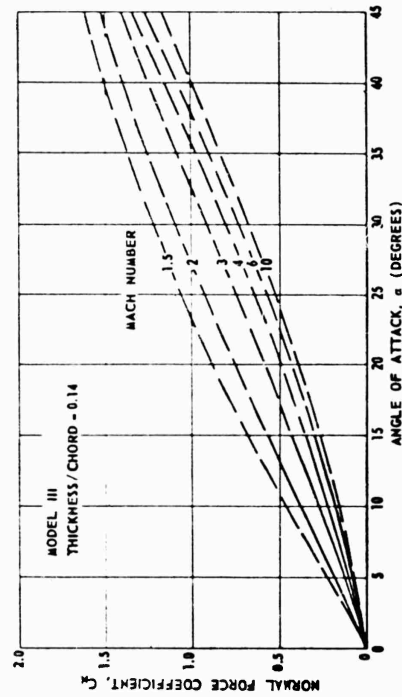


Figure 3.2.52. Variation of Normal Force Coefficient With Angle of Attack.

SECRET

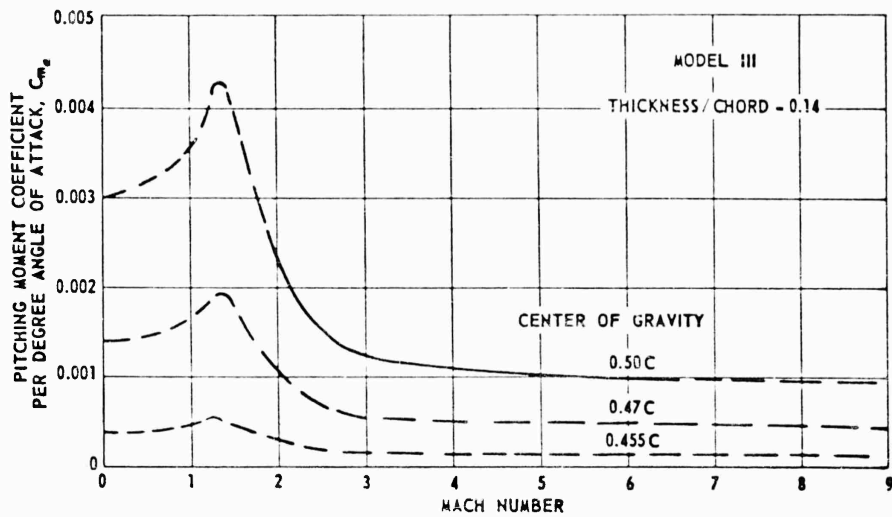


Figure 3.2.54. Variation of Pitching Moment Derivative - Thickness/Chord = 0.14.

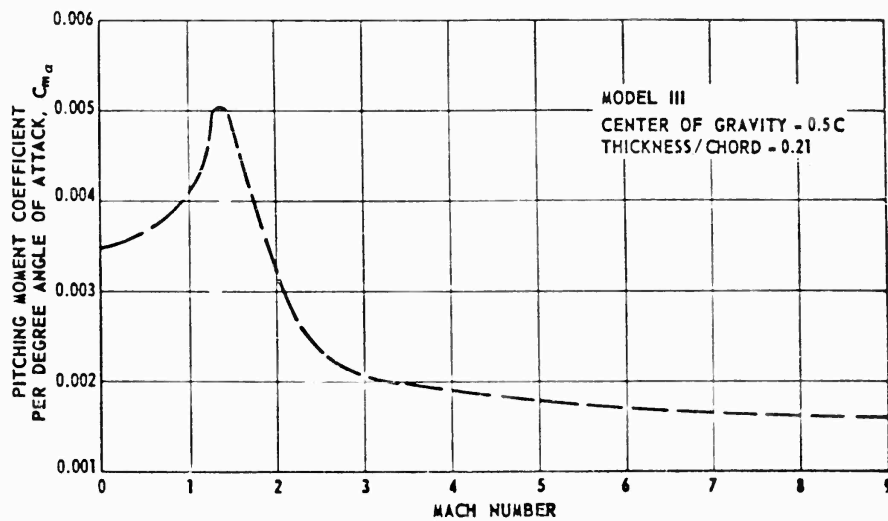


Figure 3.2.55. Variation of Pitching Moment Derivative - Thickness/Chord = 0.21.

The yawing moment coefficient per degree angle of yaw, $C_{n\psi}$, is presented in Figure 3.2.56, for Model III. This curve shows, that for a moment reference station at the midchord, the body is slightly stable in yaw. This $C_{n\psi}$ curve is based on data obtained at zero angle of attack and for angles of yaw varying from -5 to +15 degrees.

SECRET

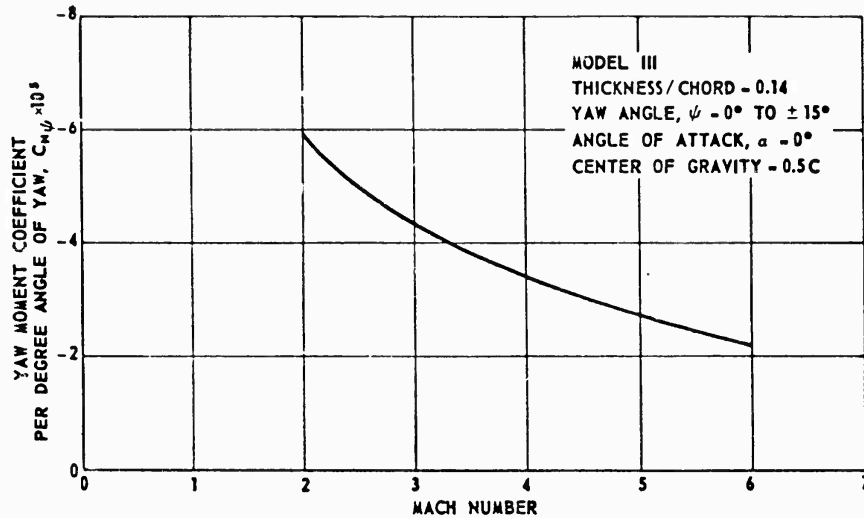


Figure 3.2.56. Body Yaw Moment Per Degree Yaw Angle.

Of considerable interest is the yawing moment that would exist at extremely large yaw angles. Since no data were obtained above 15° yaw angle, estimates were made of the yawing moment over a yaw angle range from 0 to 180° for Model III. Due to the blunted base, yaw moments will exist which will attempt to turn the missile. Since large angles of yaw, above 15 degrees, would exist only during an omnidirectional launch operation, a Mach number of 2.50 was picked for estimating yaw moment coefficients, since this represents the highest launch velocities anticipated in the near future.

The yawing moment due to yaw angle is the result of the drag distribution along the periphery of the body. As the body becomes thicker at the aft end, the drag distribution becomes asymmetrical (larger drag at the rear) and a yawing moment results. An estimated drag distribution was made in which the drag per unit periphery was computed as a function of the longitudinal station. This estimate was based on the differential drag along the periphery, due to local flow parameters. These parameters consist of the local dynamic pressure, local differential area normal to the periphery, and a local drag coefficient.

This procedure was carried out for a number of yaw angles to give the variation of yawing moment with yaw angle.

Figure 3.2.57 shows the variation of yaw moment coefficient with yaw angle calculated for a Mach number of 2.50 about a reference point at the midchord. Examination of this plot indicates that the yawing moment is asymmetrical with respect to yaw angle, the maximum yawing moment occurring at approximately 140 degrees of yaw angle. The ability of the control system to handle the above yawing moment is discussed in subsection 3.7 of this report.

SECRET

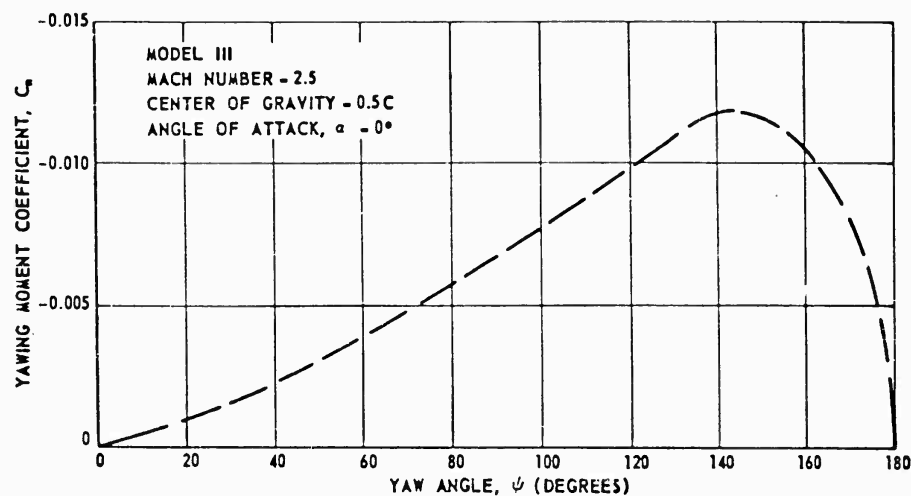


Figure 3.2.57. Estimated Variation of Yawing Moment Coefficient.

The aerodynamic design data presented above pertains to aerodynamically clean, bare bodies only. This, of course, is the ideal condition particularly from an aerodynamic drag standpoint. However, due to the launch, guidance and fabrication requirements of a functional missile, various protuberances, mismatches, etc., will undoubtedly be incurred. As an example of the effects protuberances can have on aerodynamic characteristics, various types of radar or infrared seekers were investigated.

Two possible methods of mounting seekers on Model III are shown in Figure 3.2.58. As shown for Case 1, two seekers, mounted top and bottom, are employed having an inclined flat plate for aerodynamic shielding. Seekers mounted at the lateral extremities having conical or pyramidal windshields are shown as Case 2. In both cases a seeker whose diameter was 1/24 of the missile planform diameter was assumed. The flat plate fairing for Case 1 was assumed to be inclined 30° with respect to the body centerline. The cones or pyramids for Case 2 were assumed to have an apex angle of 30 degrees and a tip radius of 0.5 inch, to alleviate the heating problem.

The zero-lift drag coefficients for the bare body and for the above two seeker configurations are presented in Figure 3.2.59. These drag values for the seeker configurations were obtained utilizing the conevector and pitchvector data from the PYE WACKET wind tunnel tests.

From the above discussion, the seekers mounted at the lateral extremities were shown to have the most severe effect on drag; however, this configuration decreases the instability of the bare body whereas the seekers mounted on the top and bottom contribute to the instability of the bare body. This is shown in Figure 3.2.60 which presents $C_{m\alpha}$ about the midchord versus Mach number for the bare body and for the two seeker configurations.

SECRET

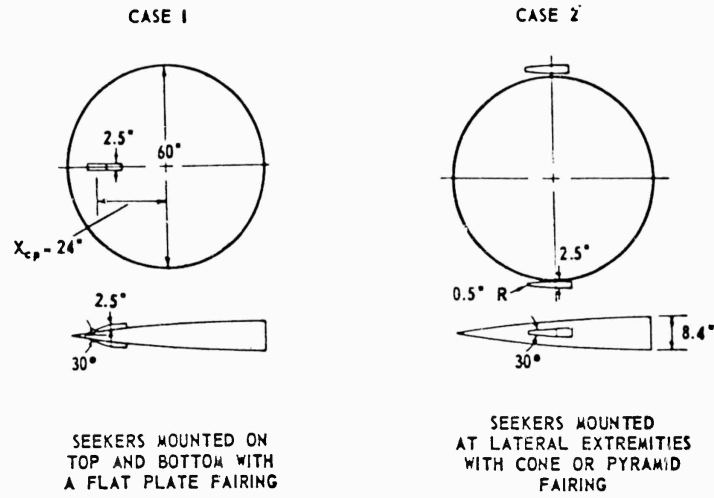


Figure 3.2.58. Typical Seeker Locations.

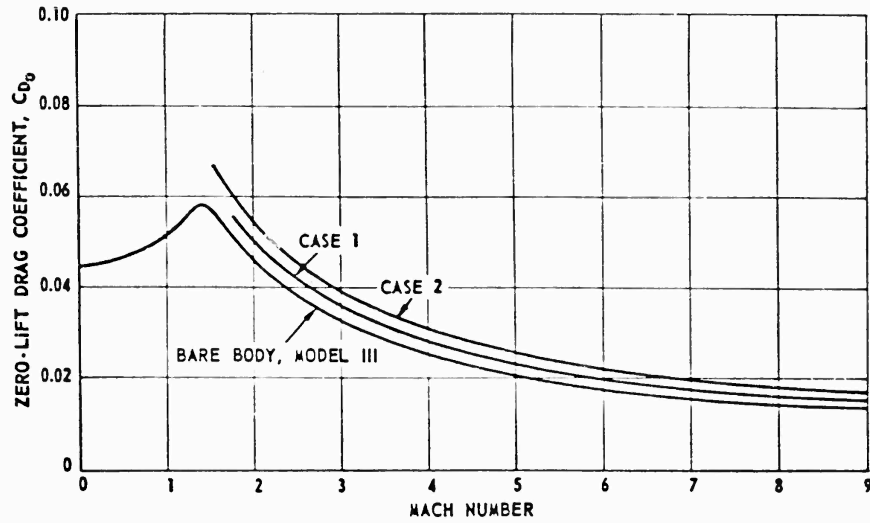


Figure 3.2.59. Effect of Seekers on Zero-Lift Drag.

Effects on zero-lift drag characteristics were calculated and are presented in Figures 3.2.61 and 3.2.62, respectively, for hemispherical and spherical protuberances, having various radii, located on both the top and bottom surfaces. As noted, even for small radii, large drag increases are incurred.

Figure 3.2.63 indicates the drag penalty for a more practical design where the spherical protuberance is located in the leading edge of the missile. Since only one element would be required at this location, a much more favorable drag picture results.

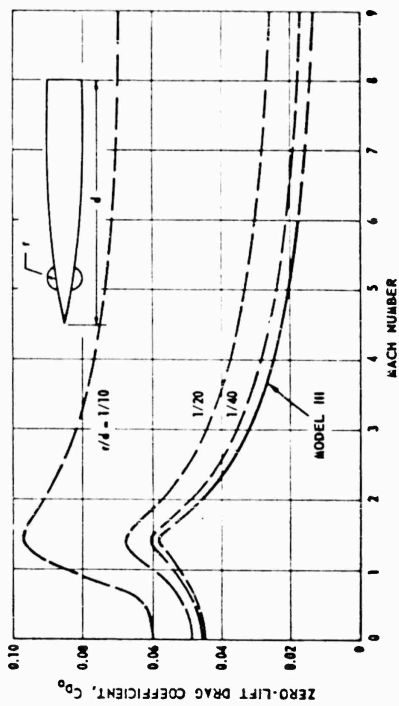


Figure 3.2.61. Variation of Drag Due to Protuberances.

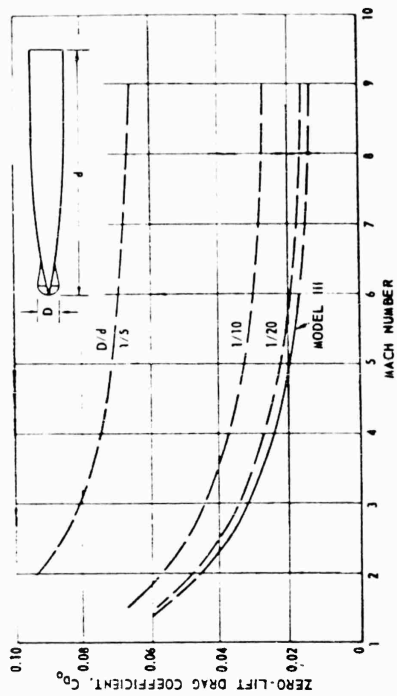


Figure 3.2.63. Variation of Drag Due to Protuberances.

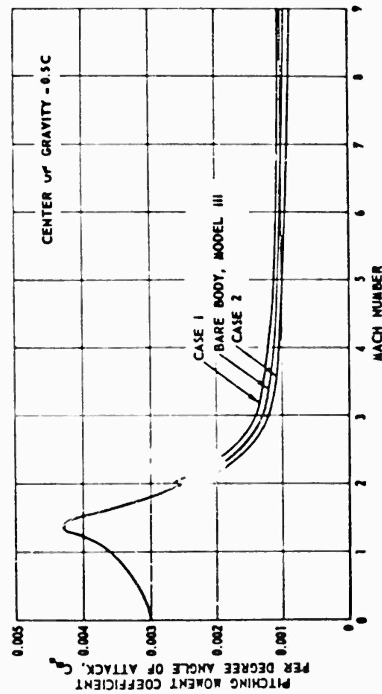


Figure 3.2.60. Effect of Seekers on Pitching Moment Derivative.

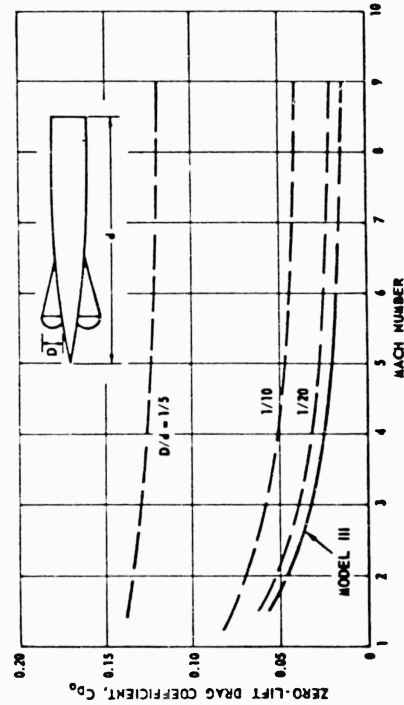


Figure 3.2.62. Variation of Drag Due to Protuberances.

3.2.4 AREAS REQUIRING INVESTIGATION

Although the present investigation along with the previous study of Reference 3.2.1 have considerably enhanced the knowledge of aerodynamics as pertains to circular planform configurations, a considerable need exists for additional study effort if omnidirectional launch is desired.

Perhaps the greatest need results from the omnidirectional launch concept. Experimental investigations to date have considered only the conventional straight ahead launch case, and have not touched upon the other possible launch attitudes. Prior to any development program a detailed experimental program would be necessary in order to obtain design information for establishment of nominal parameters. Yaw angles of zero to 180° should be considered in this program. The need for such data would extend from the subsonic range to the maximum Mach number obtained during the boost phase with particular emphasis on the transonic range.

A second area of equal importance is the determination of the jet interference effects from both control and main jets for the attitudes described above. Certain effects will exist, which may even be favorable; however, in any case, they should be determined for consideration in the missile design.

A third area of importance is the need for aerodynamic coupling data. Again these data are primarily required to assist in autopilot design. Coupling terms are aerodynamic effects which occur due to interference. In most instances, the longitudinal and lateral portions of any flight condition may be treated independently. When high angles of attack or other factors make it necessary to treat the two simultaneously, because of interactions, coupling exists. Coupling generally refers to a motion induced about one axis as a result of control about another axis.

Other desirable data are the aerodynamic characteristics at extremely large angles of attack with, and without, the interference effects of the control and main jets. Highly desirable are aerodynamic data above Mach number 6, preferably up to the peak Mach number envisioned for this type missile.

3.2.5 SUMMARY OF AERODYNAMIC INVESTIGATIONS

The results of the aerodynamic investigations of this study can be summarized as follows:

1. Based on analytical studies and wind tunnel tests, a vastly improved circular planform cross section shape was determined. This configuration is referred to as Model III. The drag, lift, and stability characteristics of this configuration are far superior to the symmetrical lenticular configuration (Model I). These performance improvements were achieved primarily by moving the maximum thickness point of the missile to the aft end.

SECRET

2. The most important advantage of Model III over Model I is that the aerodynamic center of pressure of Model III is located approximately 10 percent further aft than the aerodynamic center of pressure of Model I.

As concluded in Section 2, above, this advantage is not apparent for the fully loaded missile since the centroid of volume of Model III is 9 percent further aft than the centroid of Model I which, in the ideal case, would be located at the midchord of the body. Therefore, for the loaded case (i. e., at launch) the two configurations exhibit approximately the same stability margin, assuming that the loaded centers of gravity and centroids of volume are one and the same.

A considerably different picture exists when the rocket motor is burned out. Since the center of gravity of the propellant of Model III would be located considerably further aft than that of Model I, a much larger shift in center of gravity would occur for Model III. Since a large part of the total volume would be for propellant, there is no reason to assume any difference in the empty center of gravity locations for the two models. Therefore, Model III exhibits a considerable advantage in the glide phase of flight which normally lasts for a much longer time period than the powered phase of flight.

An appreciation of this advantage can be obtained from the following example. If the center of gravity of the missile is located at the midchord (50%C) then the control moments required for Model III would be only one-third of those required for Model I, since the aerodynamic center of pressure of Model III lies approximately 45%C aft of the leading edge while the aerodynamic center of pressure of Model I lies approximately 35%C aft of the leading edge.

It is felt that this advantage is the difference between a feasible and a marginal design. Model I would obviously require three times as much control force as Model III during the glide phase of flight assuming that the control units of both models had the same moment arm distance. In the case of reaction controls, Model I would therefore require three times as much fuel for the reaction jets as Model III. It should be noted that the possibility of achieving the same moment arm distance for Model I as for Model III is remote due to the lack of sufficient volume at the radial extremities of Model I.

3. It is true that the blunt based Model III incurs a yawing moment during the omnidirectional launch phase of flight, particularly when the wind vector is orientated between 90° and 160° with respect to the thrust vector (Figure 3.2.57). However, this penalty is small with respect to the gains experienced in pitching moment control.

It should be noted that yaw control will be required for any configuration during omnidirectional launch due to the existence of thrust vector misalignment, non-uniform flow fields in the vicinity of the launching

SECRET

3.2.47

aircraft and effects of the rocket motor jet. It should also be noted that, with a circular planform missile of the thickness ratios considered in this report, pitching moments will always be the dominant factor in control system requirements.

Because of the above, it is felt that the yawing moment incurred by moving the maximum thickness to the aft end of the missile is a small penalty to pay for the relief in pitching moment during the glide phase of flight.

4. Two very desirable features exist in the stability margin characteristics of Model III. These are small variations in stability margin with Mach number and angle of attack. This means that an optimum control system design is possible since a system which is over designed for the vast majority of the flight, in order to accommodate a narrow-critical flight range, is not necessary.
5. It is felt that a circular planform missile with Model III cross section is a superior configuration for achievement of omnidirectional launch capability. However, it is felt that further study, as outlined above, is required before stating that it is the optimum configuration. Prime consideration in the determination of the optimum configuration should be the minimization of control considering wind vector orientation from any direction around the periphery of the missile.

3.2.6 SYMBOLS AND DEFINITIONS

The following defined symbols appear in the equations of the Aerodynamics discussion.

M	Mach number
N	Normal force, LB
L	Lift, LB
D	Drag, LB
A	Axial force, LB
V	Velocity, FT/SEC
m	Pitching moment, FT/LB
Y	Yaw force, LB
YM	Yawing moment, FT/LB
RM	Rolling moment, FT/LB
d	Diameter, FT
t	Thickness, FT
C	Chord, FT
S	Reference area, planform, SQ FT
P	Ambient pressure, LB/FT ²
q	Dynamic pressure, $\frac{1}{2} \rho V^2$, LB/FT ²
I	Moments of inertia, slug-FT ²

SECRET

C_N	Normal force coefficient, $\frac{N}{qS}$
C_L	Lift coefficient, $\frac{L}{qS}$
C_D	Drag coefficient, $\frac{D}{qS}$
C_A	Axial force coefficient, $\frac{A}{qS}$
C_m	Pitching moment coefficient, $\frac{m}{qSd}$
C_n	Yawing moment coefficient, $\frac{YM}{qSd}$
C_l	Rolling moment coefficient, $\frac{RM}{qSd}$
v	Volume, FT^3
x/d	Stability margin, diameters
W	Weight, LB
γ	Ratio of specific heats, 1.4
ϵ	Pitchevator deflection, degrees
α	Angle of attack, degrees
ψ	Angle of yaw, degrees
ω_L/ω_R	Apex angle of left and right conevators or included angle of wedgevators, degrees
δ_L/δ_R	Deflection of left and right wedgevator or conevator for roll control, degrees
$\Delta\omega$	Difference in the included angles of the left and right wedgevators for yaw control, degrees
C_{N_α}	Variation of normal force coefficient per degree angle of attack
C_{m_α}	Variation of pitching moment coefficient per degree angle of attack

SECRET

SECRET

3.2.7 LIST OF REFERENCES

- 3.2.1 Experimental and Theoretical Investigations on Lenticular Rocket Shapes (U) Technical Planning Group--Directorate of Development--Air Proving Ground Center--Eglin Air Force Base, Florida (SECRET)
- 3.2.2 IC-334-231 "Visit to Convair Scientific Research Division," by E. J. Velton and W. Hatalsky, Convair, A Division of General Dynamics, Pomona, California, September 1959.
- 3.2.3 IC-334-248 "Trip Report on Consultation with Dr. A. J. Eggers at Ames Laboratory, Moffet Field, California," by E. J. Velton and W. Hatalsky, Convair, A Division of General Dynamics, Pomona, California, October 1959.
- 3.2.4 CPC-1393 "Proposal for Lenticular Rocket Feasibility Study," presented to Air Proving Ground Center, United States Air Force by Convair-Pomona, April 1959.
- 3.2.5 NACA TM 1324, "Steady Vibrations of Wings of Circular Planform and Theory of Wings of Circular Planform," by N. E. Kochen, dated January 1953.
- 3.2.6 NACA TR 1048, "A Study of Viscosity on Flow Over Slender Inclined Bodies of Revolution," by H. Julian Allen and Edward W. Perkins, dated 1951.
- 3.2.7 Report No. CAL-37, "The Aerodynamics of Low Aspect Ratio Wings and Wing-Body Combinations," by A. H. Flax and H. R. Lawrence, Cornell Aeronautical Laboratory, September 1941.
- 3.2.8 JAS Volume 19, No. 9, "Two Dimensional Airfoils at Moderate Hypersonic Velocities," by William H. Dorrance, dated September 1952.
- 3.2.9 NACA TN 3504, "Effect of Trailing--Edge Thickness on Lift at Supersonic Velocities," by Dean R. Chapman, and Robert H. Kester, dated June 1955.
- 3.2.10 NACA TN 2611, "Experimental Investigation of Base Pressure on Blunt--Trailing--Edge Wings at Supersonic Velocities," by Dean R. Chapman, William R. Wimbrow, and Robert H. Kester, dated January 1952.
- 3.2.11 NACA TN 3503, "Reduction of Profile Drag at Supersonic Velocities by the Use of Airfoil Sections Having a Blunt Trailing Edge," by Dean R. Chapman, dated September 1955.
- 3.2.12 NACA RM L52D21, "Effects of Planform, Airfoil Section, and Angle of Attack on the Pressures Along the Base of Blunt-Trailing Edge Wings at Mach Numbers of 1.41, 1.62, and 1.96," by Kenneth L. Goin, dated 16 September 1952.

3.2.50

SECRET

SECRET

- 3.2.13 NACA RM A53B02, "An Experimental Investigation of the Zero-Lift Drag Characteristics of Symmetrical Blunt-Trailing-Edge Airfoils at Mach Numbers from 2.7 to 5.0," by Clarence A Syvertson and Hermilo R. Gloria, dated 29 April 1953.
- 3.2.14 NACA RM L55D13, "Experimental Investigation of the Zero-Lift Wave Drag of Seven Pairs of Delta Wings with Constant and Varying Thickness Ratios at Mach Numbers of 1.62, 1.93, and 2.41," by Arthur Henderson, Jr., dated 3 June 1955.
- 3.2.15 NACA RM A52L02, "Lift, Drag, and Pitching Moment of Low-Aspect-Ratio Wings of Aspect Ratio 2 of Rectangular, Swept-Back, and Triangular Planform, Including Effects of Thickness Distribution," by Ronald C. Hightower, dated 16 February 1953.
- 3.2.16 NACA RM L53D13, "Effects of Trailing-Edge Bluntness on the Lift, Drag, and Pitching Moment Characteristics of Unswept, 45° Swept, and 45° Delta Wings at Mach Numbers of 1.41, 1.62, and 1.96," by Kenneth L. Goin and Gertude C. Westrick, dated 10 June 1953.
- 3.2.17 WADC TN 56-394, "Note on the Flow Fields on the Rear Part of Blunt Bodies in Hypersonic Flow," by Antonio Ferri and Adrian Pallon, dated July 1956.
- 3.2.18 Convair-Pomona, TM-334-337, "Compilation of Power-Off Base Drag Data and Empirical Methods for Predicting Power-Off Base Drag," by E. E. Honeywell, 23 June 1959.
- 3.2.19 North American Aviation, Inc., Report No. AL-958, "Turbulent Boundary Layer for Compressible Fluids on an Insulated Flat Plate," by E. R. Van Driest, 15 September 1949.
- 3.2.20 Convair-Pomona TM-334-375, "PYE WACKET Wind Tunnel Test No. I Pre-Test Report," by E. E. Honeywell and D. J. Giese, July 1959.
- 3.2.21 Convair-Pomona TM-334-385 and TM-334-385A, "PYE WACKET Wind Tunnel Test No. II Pre-Test Report," by E. E. Honeywell and D. J. Giese, September 1959.
- 3.2.22 NACA TN 2137 "An Analysis of Base Pressure at Supersonic Velocities and Comparison with Experiment," by Dean R. Chapman, July 1950.
- 3.2.23 Report No. 332 "The Effect of Support Interference on the Base Pressure of a Body of Revolution at High Reynolds Numbers," by Kenneth R. Sivier and Seymour M. Bogdonoff, Princeton University, October 1955.
- 3.2.24 "Fluid-Dynamic Drag," by Sigard F. Hoerner, 1958.
- 3.2.25 NACA RM L55D13, "Experimental Investigation of the Zero-Lift Wave Drag of Seven Pairs of Delta Wings with Constant and Varying Thickness Ratios at Mach Numbers of 1.62, 1.93 and 2.41," by A. Henderson, Jr., 3 June 1955.

SECRET

3.2.51

SECRET

- 3.2.26 NACA RM A7C10, "Aerodynamic Characteristics at Subcritical and Supercritical Mach Numbers of Two Airfoil Sections Having Sharp Leading Edges and Extreme Rearward Positions of Maximum Thickness," by A. J. Eggers, Jr., 6 November 1947.
- 3.2.27 NACA RM A52L02, "Lift, Drag, and Pitching Moment of Low-Aspect-Ratio Wings at Subsonic and Supersonic Speeds - Comparison of Three Wings of Aspect Ratio 2 of Rectangular, Swept-Back and Triangular Planform, Including Effects of Thickness Distribution," by R. C. Hightower, February 1953.
- 3.2.28 NACA TN 4039, "Investigation of the Effects of Profile Shape on the Aerodynamic and Structural Characteristics of Thin, Two-Dimensional Airfoils at Supersonic Speeds," by E. D. Katzen, D. M. Kuehn, and W. A. Hill, Jr., September 1957.
- 3.2.29 NACA RM A51L17D, "A Correlation by Means of the Transonic Similarity Rules of the Experimentally Determined Characteristics of 22 Rectangular Wings of Symmetrical Profile," by J. B. McDevitt, 25 February 1952.
- 3.2.30 NASA Memo 4-30-59L, "Transonic Aerodynamic Characteristics of Two Wedge Airfoil Sections Including Unsteady Flow Studies," by P. J. Johnson, June 1959.
- 3.2.31 NACA RM L52K19, "Aerodynamic Characteristics of Two Delta Wings at Mach Numbers 4.04 and Correlations of Lift and Minimum-Drag for Delta Wings at Mach Numbers from 1.62 to 6.9," by E. F. Ulmann and R. W. Dunning, 23 December 1952.
- 3.2.32 NACA RM A54B15, "Optimum Lifting Bodies at High Supersonic Airspeeds," by M. M. Resnikoff, 7 May 1954.
- 3.2.33 "The Dynamics and Thermodynamics of Compressible Fluid Flow," by A. H. Shapiro, The Ronald Press Company, New York, 1954.
- 3.2.34 NACA RM A7110, "Investigation of Wing Characteristics at a Mach Number of 1.53. I-Triangular Wings of Aspect Ratio 2," by W. G. Vincenti, J. N. Nielsen and F. H. Matteson, 19 December 1947.
- 3.2.35 NACA TN 3607, "Effect of Thickness, Camber, and Thickness Distribution on Airfoil Characteristics at Mach Numbers Up to 1.0," by B. N. Daley and R. S. Dick, March 1956.
- 3.2.36 R. A. E. Technical Note No. 2323, "The Lift Curve Slope and Aerodynamic Center Position of Wings at Subsonic and Supersonic Speeds," by A. Stanbrook, Royal Aircraft Establishment. Farnborough Hants, England, November 1954.
- 3.2.37 NACA RM A50J09, "Lift and Moment Characteristics at Subsonic Mach Numbers of Four 10-Percent-Thick Airfoil Sections of Varying Trailing-Edge Thickness," by J. L. Summers and W. A. Page, 20 December 1950.

3.2.52

SECRET

SECRET

- 3.2.38 NACA RM A54D19, "Pressure Distributions of Triangular and Rectangular Wings to High Angles of Attack at Mach Numbers 1.45 and 1.97," by G. E. Kaattari, 25 June 1954.
- 3.2.39 NASA Memo 5-12-59A, "Surface Pressure Distribution at Hypersonic Speeds for Blunt Delta Wings at Angles of Attack," by M. O. Creager, May 1959.
- 3.2.40 NASA Memo 12-26-58A, "The Effect of Leading-Edge Sweep and Surface Inclination on the Hypersonic Flow Field Over a Blunt Flat Plate," by M. O. Creager, 1959.
- 3.2.41 NACA RM L51D17, "An Investigation of Four Wings of Square Planform at a Mach Number of 6.86 in the Langley 11-inch Hypersonic Tunnel," by C. H. McLellan, M. H. Bertram and J. A. Moore, 29 June 1951.
- 3.2.42 NACA RM A54J12, "Pressure Distribution of Triangular and Rectangular Wings to High Angles of Attack at Mach Numbers of 2.46 and 33," by G. E. Kaattari, 18 January 1955.
- 3.2.43 NASA Memo 1-17-59A, "Estimation of Static Longitudinal Stability of Aircraft Configurations at High Mach Numbers and at Angles of Attack Between 0° and $\pm 180^\circ$," by D. W. Dugan, March 1959.

SECRET

3.2.53

SECRET

3.3 LAUNCH

The separation of any body from a flying aircraft involves complex and highly transient flow dynamics. The phenomena are even more severe when the omnidirectional launching of a missile is considered. In the prime defensive mission under consideration, the missile must be capable of maneuvering into intercept position to provide successful defense of the parent aircraft from attacks from any direction. During the launch, the missile must endure the high loads generated when ejected from the launching aircraft and must be able to operate in the non-uniform flow field existing in the vicinity of the launching aircraft. A brief treatment of the problems associated with this flight phase is presented below. It should be noted that without specific knowledge of the launching aircraft, launch environment and mission, no detailed analysis is possible.

3.3.1 PROBLEM AREAS

In flight, the parent aircraft has a non-uniform flow field about its surfaces and fuselage due to the deflection of the air flow from its original direction. Similarly, the missile will induce a flow field. When the launch operation is performed, the non-uniform flow field of the airplane will affect the missile and the non-uniform flow field of the missile will affect the airplane. The local flow quantities in the vicinity of the aircraft will govern the behavior of the missile until the missile leaves the airplane flow field. Reference 3.3.1 indicates that when the missile has moved forward to a location 1 to 1.5 wing chords distance ahead of the leading edge of the wing-fuselage combination, the influence of the airplane on the missile is negligible. Similarly, as the missile moves downward away from the airplane, its influence is considerably reduced. References 3.3.2, 3.3.3, 3.3.4, and 3.3.5 substantiate the data of Reference 1.

Figures 3.3.1 and 3.3.2 present data from Reference 3.3.6 showing the magnitude of the longitudinal angularity field and the dynamic pressure field about a lifting surface at 8 degrees angle of attack in incompressible flow. Similar conditions will exist at supersonic Mach numbers except that the magnitudes will be considerably larger.

The preceding indicated the magnitude and direction of the flow fields about a lifting surface. When the missile reaches the edge of the airplane flow field, there will be an abrupt change supersonically and a relatively rapid change subsonically. This change would result in a phenomenon commonly referred to as jump angle. Unless compensated for, it would tend to perturb the missile from a particular trajectory.

A supersonic launch is an intricate process in which the shock wave off the nose of the missile can intersect the under-surface of the airplane. Forward of the shock wave the pressure is low; aft of the shock wave the pressure is high.

SECRET

3.3.1

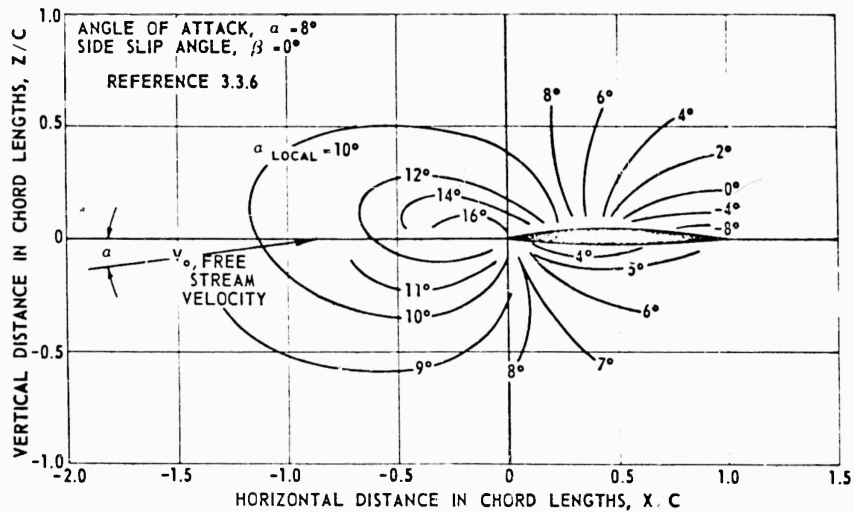


Figure 3.3.1. Longitudinal Angularity Field.

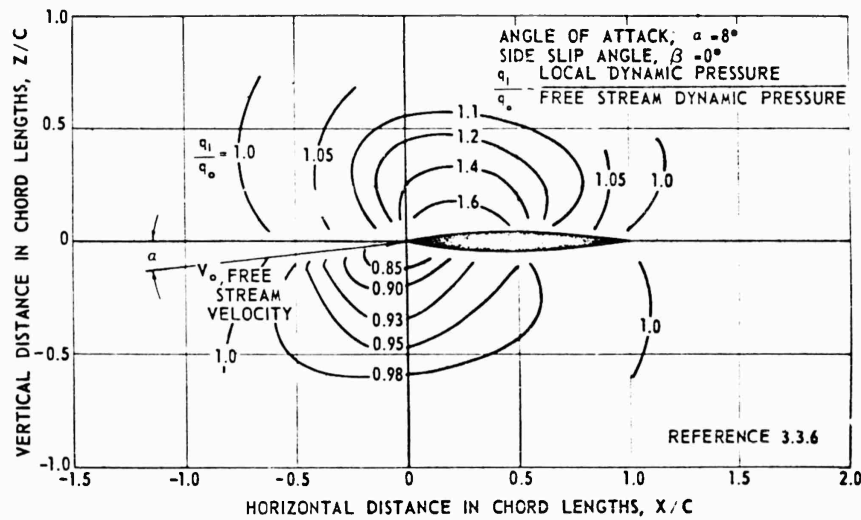


Figure 3.3.2. Dynamic Pressure Field.

As the shock wave travels the length of the airplane, it would load the skin in a concentrated fashion as shown in Figure 3.3.3.

A detailed investigation of these loadings would be mandatory before any flight tests.

Another interference problem concerns the effects of the missile on the launching aircraft. If the missile main propulsion system is ignited anywhere

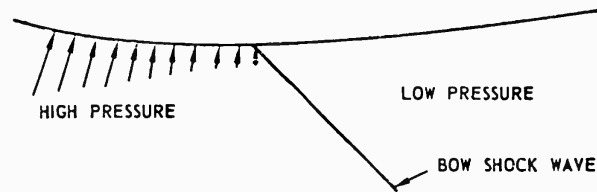


Figure 3.3.3. Shock Wave Loading.

in the vicinity of the airplane, the blast of the jet can impinge on the airplane/ and cause mechanical and thermal damage. It is, therefore, desirable that the ignition of the main propulsion rocket be delayed until the separation distance between the airplane and the missile and the attitude of the missile relative to the airplane, are such as to insure no damage to the airplane. The subsonic annulus surrounding the supersonic core of the exhaust jet has a large energy content but the energy level is sufficiently reduced so that no difficulties will be encountered. For example, the foot-pounds of energy contained by the annular air could be large, but the foot-pounds per cubic foot of air would be small. Figures 3.3.4, 3.3.5, and 3.3.6 present data from Reference 3.3.7 for a rocket exhaust supersonic core for a rocket motor with a nozzle exit Mach number of $M = 2.843$, exhausting into the atmosphere at an altitude of 50,000 feet. The nozzle has an area ratio of 5 to 1, a stagnation pressure at the exit of 340 PSIA, and a constant $\gamma = 1.225$. Figure 3.3.4 presents the Mach number profiles in the rocket supersonic core. The abscissa is downstream distance from the nozzle exit in terms of the nozzle radii. The ordinate is radial distance in terms of nozzle radii. Figure 3.3.5 presents the static pressure profiles for the same coordinates. Figure 3.3.6 presents the static temperatures. Examination of the data in these figures indicates that the rocket exhaust jet does not extend beyond three nozzle radii radially from the centerline of the rocket. As shown in subsection 3.4, the range of nozzle diameters is from approximately 5.0 to 10.0 inches. A conservative estimate for the maximum value of the supersonic core is 1 foot. However, since the subsonic annulus is quite large, and some heat is radiated from the jet plume, it would be well to use a safety margin. At an altitude of 50,000 feet, the missile should be displaced approximately 6 feet below the lowest point on the airplane, before the rocket motor is ignited. The data presented in Figures 3.3.4, 3.3.5, and 3.3.6 are for an altitude of 50,000 feet. Figure 3.3.7 presents the outer boundary for the rocket jet at other altitudes. It is seen that, as altitude increases, the outer boundary expansion reaches larger radial distances. At an altitude of 100,000 feet, the outer boundary of the jet reaches 12 nozzle exit radii radially. This would indicate the missile would have to be 12 feet below the airplane to clear all parts of the airplane.

3.3.4

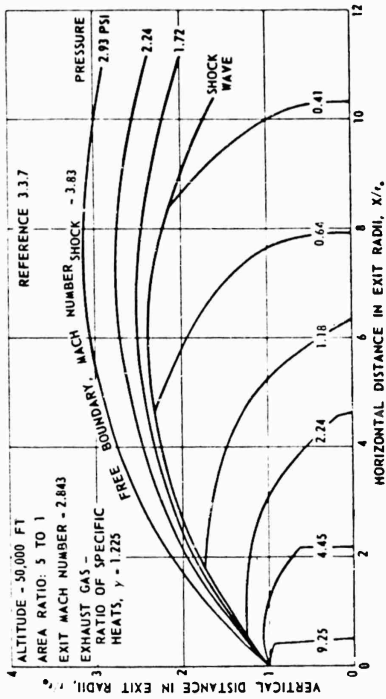


Figure 3.3.4. Rocket Jet Expanding to Ambient Pressure (Constant Mach Number Diagram).

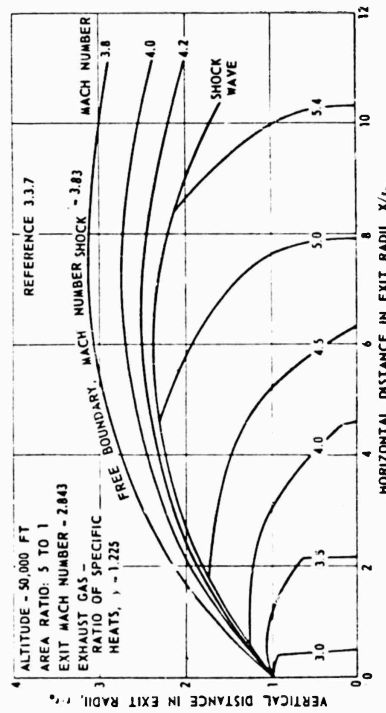


Figure 3.3.5. Rocket Jet Expanding to Ambient Pressure (Static Pressure Diagram).

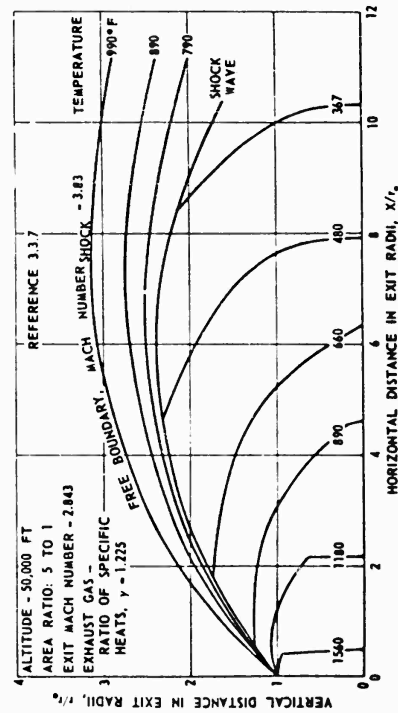
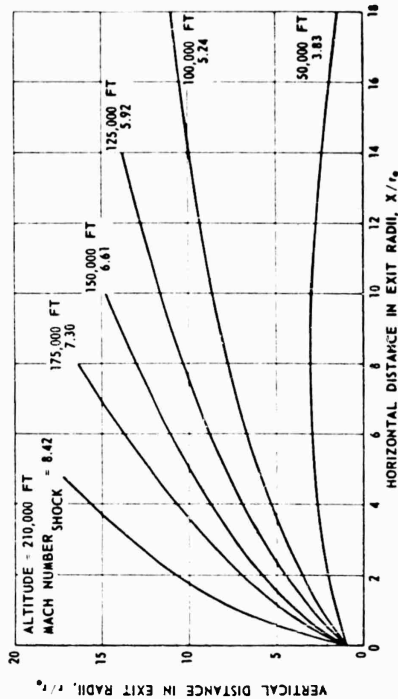


Figure 3.3.6. Rocket Jet Expanding to Ambient Pressure (Temperature Diagram).



SECRET

3.3.2 METHOD OF APPROACH

Two methods for separating the missile from the aircraft are immediately evident. These are gravity drop and ejection. A gravity drop separation would allow the missile to stay in the vicinity of the parent aircraft for too long a period of time. For example, it would take 0.61 seconds for the missile to reach a distance 6 feet from the airplane. During this period, the missile would be enveloped in the flow field of the airplane, and would be capable of generating 15 to 20 G's of acceleration if it developed an angle of attack ($\alpha = 6^\circ$, $M = 0.8$, $h = 30,000$ feet). Should such an acceleration be generated in a direction toward the parent aircraft, serious structural damage could result. Figure 3.3.8 presents a typical incidence field about a lifting surface; Figure 3.3.9 presents the effect on a trajectory of a missile in the vicinity of the lifting surface. These data from Reference 3.3.8 give an indication of the magnitude of the angle of attack the missile could encounter in the vicinity of the airplane and the violent maneuvers which could ensue using a gravity drop separation. The data presented are for a subsonic launch case. The conditions shown would be further aggravated at supersonic flight Mach numbers.

From the preceding discussion, it appears that a gravity drop launch for this application would be unsuitable.

Ejection launching of the PYE WACKET vehicle from the parent craft has the attraction of imparting an initial velocity which reduces the "dwell-time" in the flow field of the aircraft. If a vertical downward mode of launch for the missile is assumed, then the elementary equation describing the body displacement is:

$$Z = V_0 t + 1/2 g t^2$$

where

- Z = vertical displacement between aircraft and missile after ejection FT.
- V_0 = separation (or ejection) velocity, FT/SEC
- t = time after ejection, SEC

Figure 3.3.10 presents a plot of missile to parent aircraft separation distance as a function of time with the ejection velocity as a parameter. Providing the vehicle with an initial velocity greatly reduces the dwell time in the parent aircraft flow field. For example, an ejection velocity of 100 FT/SEC reduces the time increment required to reach a separation of 6 FT by a factor of 10.

To obtain this separation velocity, some device inside the aircraft must supply the accelerating force (i. e., a hot gas cartridge, or pneumatic or hydraulic actuator). The volume limitations in the aircraft require that the force must act over a short distance. This results in high accelerating loads. The elementary equations of motion express this acceleration as:

SECRET

3.3.5

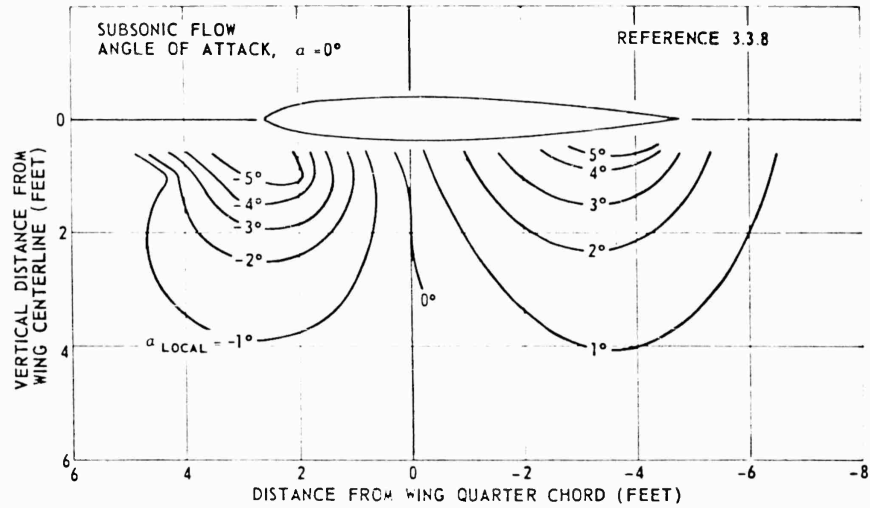


Figure 3.3.8. Flow Field About XF3D Wing Section.

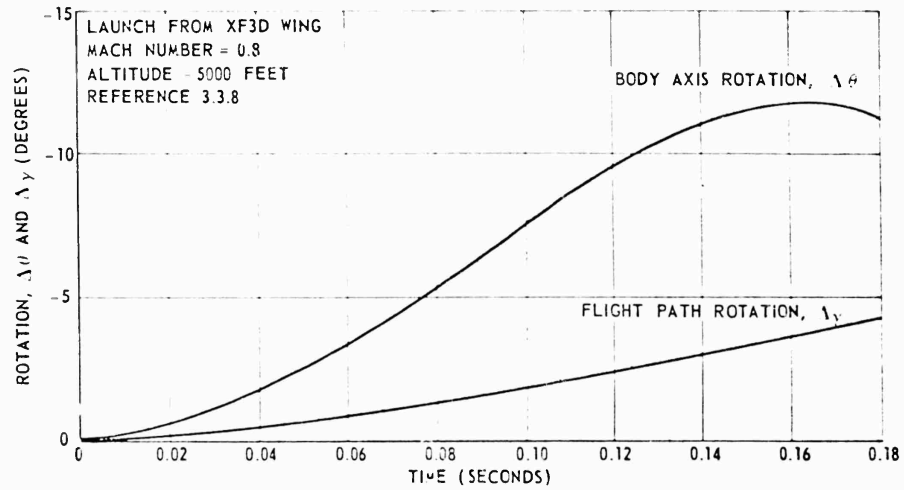


Figure 3.3.9. Pitching Deviation.

$$n = 1/2 \frac{V_o^2}{S}$$

where n = acceleration, FT/SEC²

V_o = separation velocity, FT/SEC

S = action distance of the accelerating force, FT

SECRET

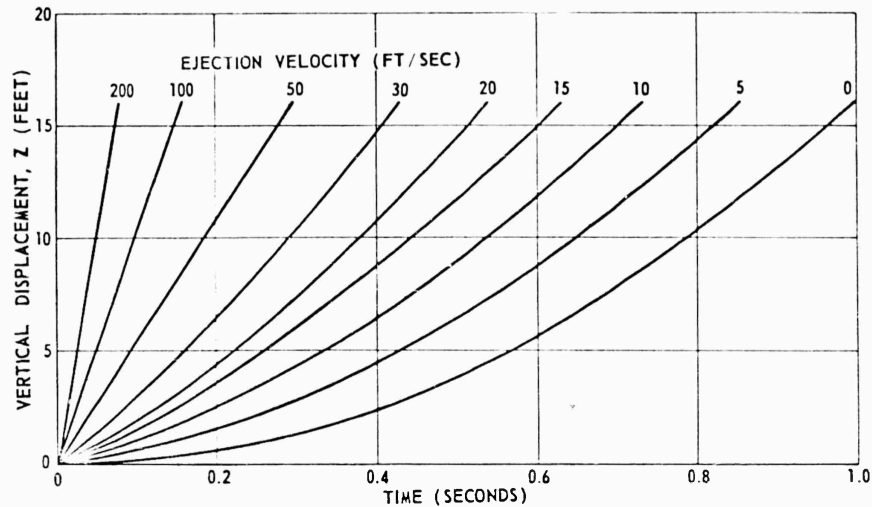


Figure 3.3.10. Displacement vs Time for Various Initial Ejection Velocities During Launch.

Plots of the accelerating force, in G's, as a function of action distance are shown in Figure 3.3.11 for several separation velocities. From these curves it can be concluded that, to minimize the launch loads on the vehicle, the ejection velocity should be as low as possible and the action distance should be maximized.

Figure 3.3.12 presents the impulse required to attain specific ejection velocities. For a 600 LB missile, a total impulse of 932 LB/SEC would be required to achieve an ejection velocity of 50 FT/SEC which would give a separation distance of 13.4 FT in 0.25 SEC.

In order to insure the safety of the launching aircraft and the maintenance of a proper course for the missile, the missile will be obliged to maintain a prescribed attitude during the launch phase. In a uniform flow field, separation of the missile could be accomplished by merely biasing the configuration such that a small maneuver away from the airplane would be insured. However, in the vicinity of the aircraft, large downwash and sidewash fields are generated by the aircraft surfaces and body. Upon separation, the missile will find itself in the midst of these flow gradients and will need to overcome these in order to achieve a safe and controlled separation. The magnitude of these gradients in the flow field will vary with attitude, velocity, maneuver and other factors. Hence, it would be difficult to define one missile configuration bias to cover all cases. Conversely, if the control system were in operation immediately after separation, the missile would overcome unfavorable gradients in the aircraft vicinity and perform a maneuver to increase the separation distance to a point where sufficient displacement between the missile and aircraft exists. At this instant, the missile could begin its maneuvering program toward the target. From the preceding discussion, it can be seen that a controlled launch phase beginning immediately after

SECRET

3.3.7

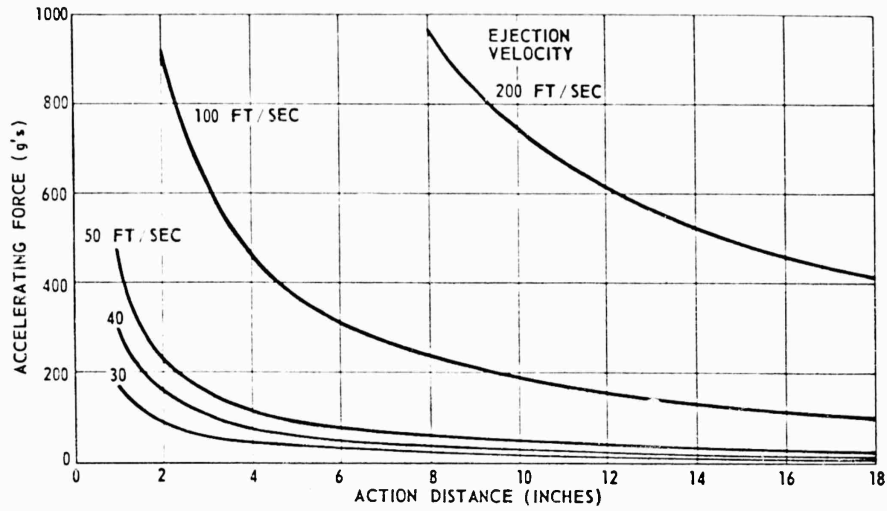


Figure 3.3.11. Accelerating Force Required as a Function of Action Distance and Ejection Velocity.

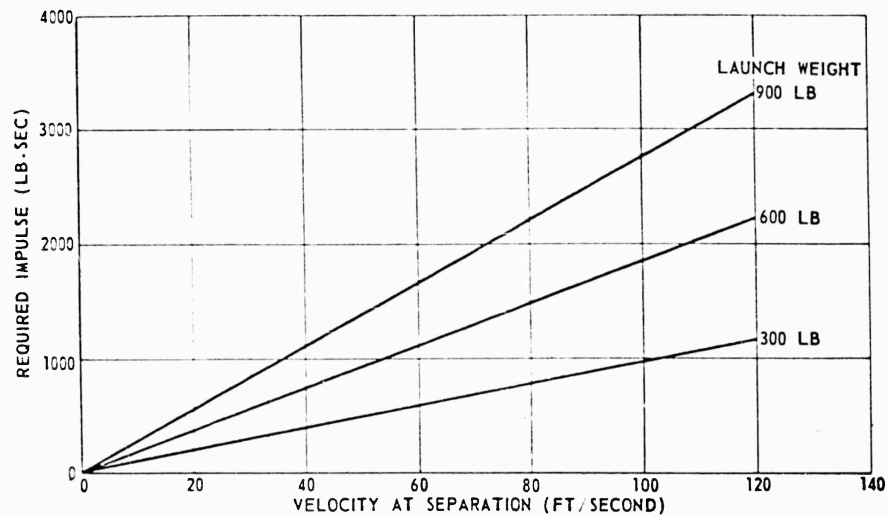


Figure 3.3.12. Impulse Requirements for Velocity and Distance at the End of Separation.

separation, ($t = 0.10$ SEC) would be the most direct method of overcoming the airplane's flow gradients and increasing the distance between the aircraft and the missile.

Figures 3.3.13, 3.3.14, and 3.3.15 present data from Reference 3.3.9 of attitude, altitude, and separation distance as a function of time for a controlled and free fall pod ($\delta_c =$ control deflection). Also, these data show the effects of

SECRET

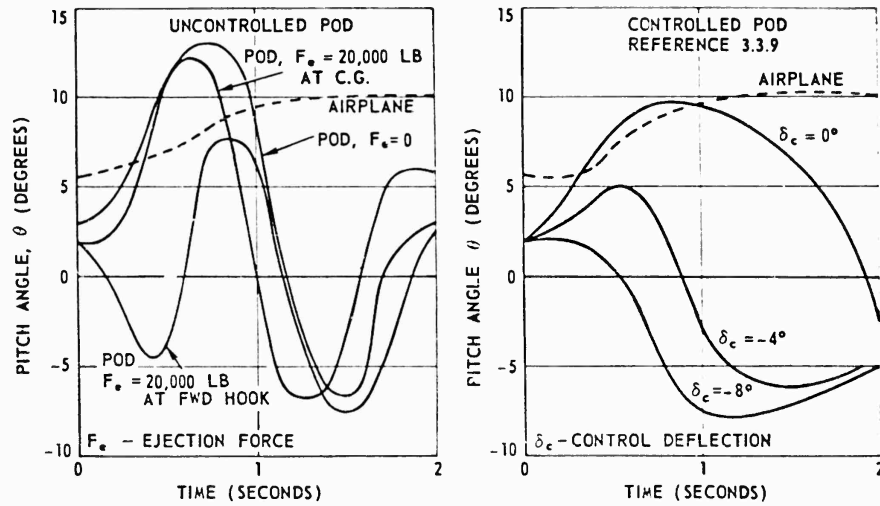


Figure 3.3.13. Typical Pitch Angle - Time Histories, Mach No. 2, Altitude = 50,000 Feet, B-58 Airplane.

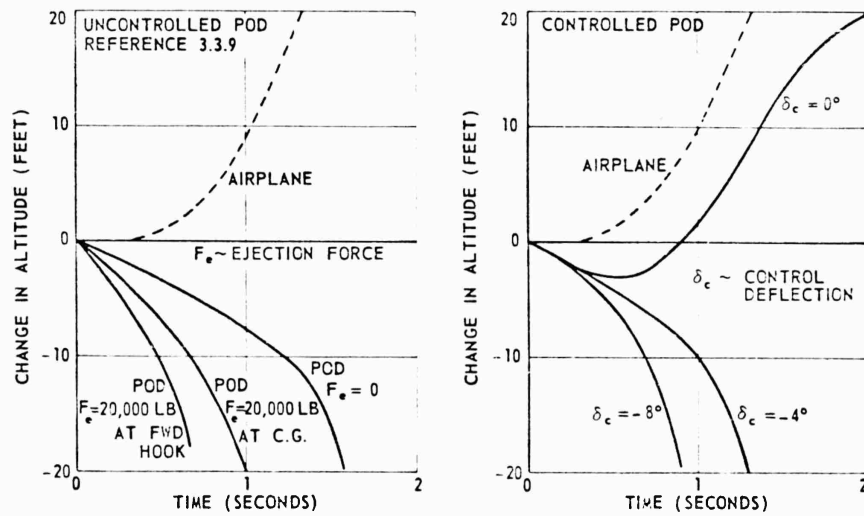


Figure 3.3.14. Typical Altitude - Time Histories, Mach No. 2, Altitude = 50,000 Feet, B-58 Airplane.

using ejection forces on the pod. These data are for $M = 2$ and 50,000 feet altitude. Similar data are available in Reference 3.3.9 for $M = 0.95$, Figure 12 presents the pitching angle as a function of time. For the uncontrolled pod, with a symmetrical ejection force, the data indicate the B-58 airplane and its pod can interfere during separation due to the pitching rotation. However, using an asymmetrical ejection force or a controlled pod will insure a satisfactory separation. Figure 3.3.14 presents the variation of altitudes as a function of time

SECRET

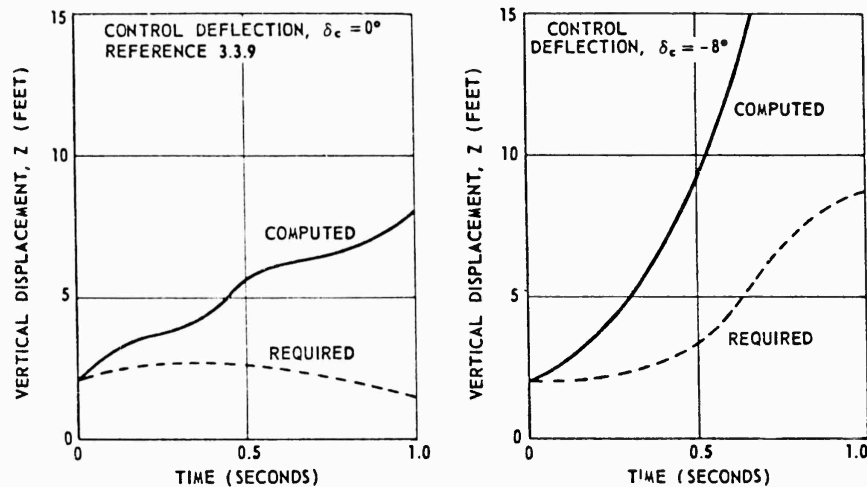


Figure 3.3.15. Vertical Displacement Between Airplane and Controlled Pod
Mach No. 2, Altitude = 50,000 Feet, B-58 Airplane.

of the B-58 airplane and its pod. Examination of these data, which are indicative of translation, indicates a reasonable separation in all cases, both controlled and uncontrolled. Figure 3.3.15 presents data for separation distance as a function of time between the B-58 airplane and its pod for the case when the pod is controlled. The dashed curve indicates the required minimum separation distance. In all cases for the controlled pod, a satisfactory separation distance is indicated.

Another factor to be considered in launch is the direction which would be most favorable toward intercepting the target. In general, launch above or below offers the best possibilities. Launch from either differs only in the projected surfaces of the airplane which must be cleared. Launch from above must clear the vertical stabilizer. Launch from below must clear the downwash field. The possibility of a horizontal launch (in a spanwise direction) has been dismissed for conventional aircraft because of the large area of lifting surface in this plane.

3.3.3 CONCLUSIONS

From the preceding discussion it appears that a vertical ejection system would be the most suitable for launching the PYE WACKET missile. However, a much more thorough treatment of the problem is required before a launching system can be designed. Vehicle acceleration limits, vehicle-parent flow interference, mode of control and separation distance must be investigated in some detail. These investigations must be performed for each type of carrier or parent aircraft and it is possible that the launching system design and method of operation might be unique to each.

SECRET

3.3.4 LIST OF REFERENCES

- 3.3.1 NACA RM L55A12, "Experimental Static Aerodynamic Forces and Moments at Low Speed on a Canard Missile During Simulated Launching From the Midsemispan and Wing-Tip Locations of a 45° Sweptback Wing-Fuselage Combination," by William J. Alford Jr., April 1955.
- 3.3.2 Report No. SM-27101, "A Study of the Aerodynamic Phenomena Arising from the External Carriage of Air-to-Air Missiles," by H. D. Froning, P. L. Munter, and R. M. Pedraglia, Missiles Aerodynamics Section, Douglas Aircraft Company Inc., August 1946.
- 3.3.3 NACA RM L54K11a, "Experimental Aerodynamic Forces and Moments at Low Speed of a Missile Model During Simulated Launching From the Midsemispan Location of a 45° Sweptback Wing-Fuselage Combination," by William J. Alford Jr., H. Norman Silvers, and Thomas J. King Jr., February 1955.
- 3.3.4 NACA RM L57B04, "Experimental Static Aerodynamic Forces and Moments at High Subsonic Speeds on a Missile Model During Simulated Launching From Unswept, Swept, and Modified-Delta-Wing-Fuselage Combinations at Zero Sideslip," by William J. Alford Jr., and Thomas J. King Jr., March 1957.
- 3.3.5 NACA RM L55D20, "Experimental Static Aerodynamic Forces and Moments at Low Speed on a Missile Model During Simulated Launching From the 25 percent-Semispan and Wing-Tip Locations of a 45° Sweptback Wing-Fuselage Combination," by William J. Alford Jr., H. Norman Silvers, and Thomas J. King Jr., May 1955.
- 3.3.6 NACA RM L55E10a, "Effects of Wing-Fuselage Flow Fields of Missile Loads at Subsonic Speeds", by William J. Alford Jr., June 1955.
- 3.3.7 ZJ-7-054, "Determination of the Envelopes and the Lines of Constant Mach Number for an Axially Symmetric Free Jet," by J. M. Bowyer Jr., Convair, A Division of General Dynamics, San Diego, March 1958.
- 3.3.8 "Some Aerodynamic Interference Effects of the Parent Aircraft on Air Launched Missiles," by M. W. Hunter and R. W. Luce Jr., Paper Presented at the Navy Symposium on Aeroballistics, May 1952.
- 3.3.9 FZA-4-206, "Comparative Bombing Performance With Proposed B-58 Free-Fall Bomb Pods," Convair, A Division of General Dynamics, Fort Worth, August 1955, (Secret).

SECRET

3.3.11

SECRET

3.4 PROPULSION

In the investigation of propulsion systems for the lenticular configuration air-breathing systems, liquid and solid propellant rocket systems were evaluated. From the initial parametric studies of liquid and solid rocket motor systems, feasible design configurations were found for each of the systems and the most promising designs were then analyzed over a range of vehicle thickness ratios. The systems were compared on various bases: initial weight, total impulse, mass ratio, maximum velocity, time to short-range target, and total down range.

All phases of the propulsion system study were directed toward systems which would be tactically and logistically acceptable (long-time storage capability, safe during storage and prior-to-launch, high reliability, etc.), and which would employ realistic performance parameters.

As outlined in subsection 3.1, the 60-inch diameter blunted lenticular configuration was chosen for major emphasis in this study. The blunted lenticular configuration is superior to the other types of lenticular bodies from the standpoint of propulsion system packaging. This is a relative comparison, however, since the essentially flat-plate skins do not make ideal pressure vessel shapes. This problem and other body-shape limitations are discussed below. These discussions describe the types of systems studies, compare the levels of performance to be obtained by the various systems, and indicate the kind of vehicle performance associated with various systems.

3.4.1 GENERAL DESCRIPTION OF SYSTEMS REQUIREMENTS

The dimensionless shape contours for the 14 percent thickness ratio blunted lenticular envelope are shown in Figures 3.4.1, 3.4.2, and 3.4.3. It should be noted that the thickest section of the missile is at the aft end, allowing space for a nozzle or nozzles, inside the aerodynamic envelope. It should also be noted that the thickness does not go to zero as the extremes of the diameter are approached on the aft half of the vehicle although the thickness does approach zero at the edge on the front half of the missile. The configuration is similar to a circular wedge with the top and bottom sides rounded off.

The volume inside the space envelope of the 60-inch diameter vehicle is shown in Figure 3.4.4, as a function of station for various thickness ratios. It is easily seen that the bulk of the volume is in the rear of the missile where it can be efficiently utilized for the propulsion system. The total missile volume available is shown in Figure 3.2, subsection 3.2, as a function of vehicle thickness-to-chord ratio. This curve demonstrates the very marked increase in volume with increase in thickness ratio.

SECRET

3.4.1

3.4.2

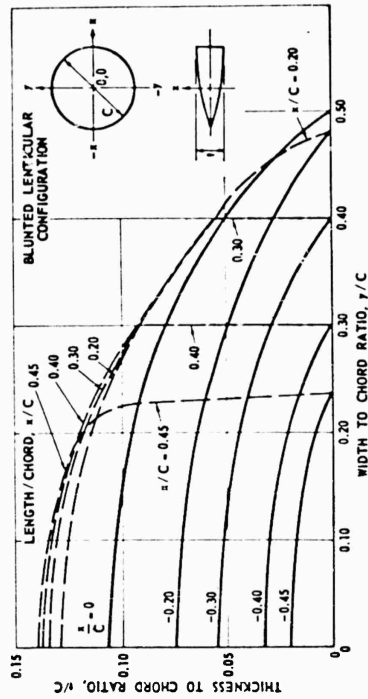


Figure 3.4.1. Dimensionless Shape Contours.

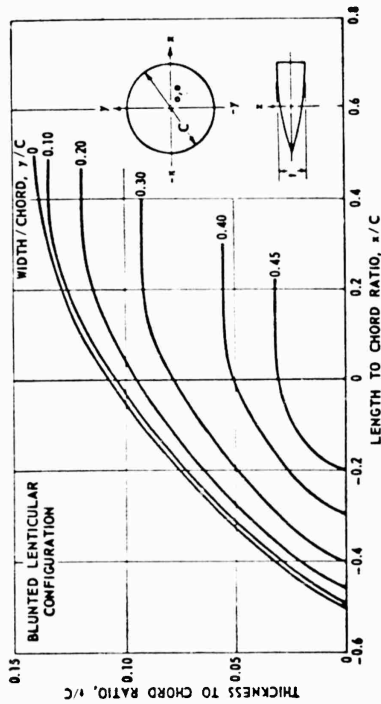


Figure 3.4.2. Dimensionless Shape Contours.

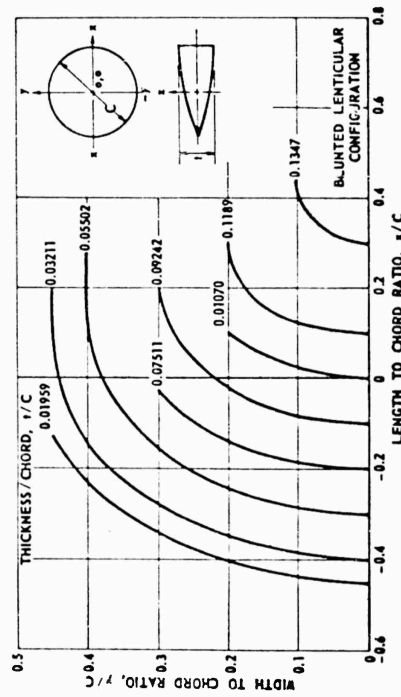


Figure 3.4.3. Dimensionless Shape Contours.

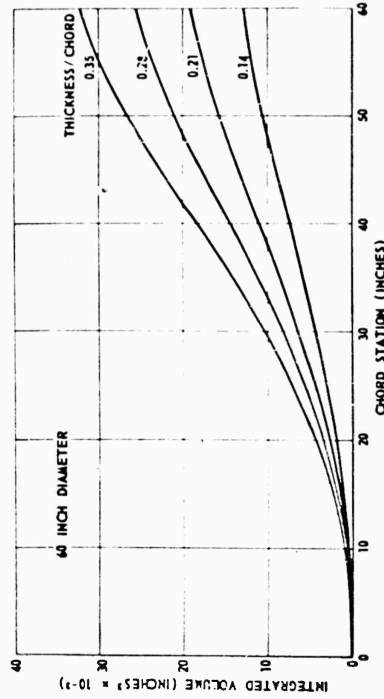


Figure 3.4.4. Integrated Volume Versus Chord Station.

SECRET

The packaging of small components does not present great difficulty, though packaging of propulsion components and other large items is somewhat complicated. The best packaging results when the external skin is used as the pressure vessel wall, though considerable effort is required to achieve a low-weight system (low weight plus sufficient weight of propellant for a given mission).

For the air-to-air mission chosen for specific investigations, a high performance vehicle is required. As employed in the propulsion studies, high performance means high acceleration capability (large g's), which dictates high thrust levels. Short flight times to close-in targets likewise means high thrust levels. On the other hand, for reasonable structure weights, pressure vessels integral with the basic lenticular vehicle should operate at low pressure. For high thrust and low chamber pressure, a large nozzle is required, but since a large nozzle cannot be efficiently packaged in the lenticular configuration, trade-off studies were required to determine satisfactory (and compatible) thrust levels, tank pressures, tank weights, and nozzle sizes.

In addition, air-breathing systems with their special problems (problems different from those associated with solid and liquid propellant rocket systems) were evaluated for the lenticular configuration.

3.4.2 AIR-BREATHING ENGINES

For any chemically powered vehicle operating within the earth's atmosphere it is of interest to evaluate propulsion systems which utilize the free oxygen available. For that reason, air-breathing systems were considered early in the study of the lenticular configuration. Three basic types for possible use are:

1. Turbojet or turbo rocket
2. Ramjet
3. External combustion ramjet

The current state-of-the-art of turbojet development is based on the design of a Mach 3 system. Future work with higher Mach number designs has been limited to "paper" analyses. Since the turbojet engine is a heavy, inefficient system for operation at Mach 3 to 4 and the current development effort does not appear to be pointed toward high Mach number operation, this system was not considered. Complexity, and development and production costs for missile application are additional factors for rejecting further consideration of turbojets.

Ramjet systems have been successfully developed for speeds of Mach 2 to 3. Current development efforts are directed toward engines which operate at Mach 4 at 80,000 feet, to be available about 1961. These latter design schemes were considered for the lenticular vehicle.

SECRET

3.4.3

INLET SYSTEMS. Several types of inlet systems considered for flight in the regime of Mach 4 to 7 (see Figure 3.4.5) are described below:

1. External Compression. The external compression inlet maintains the compression field external to the inlet duct as shown. This may be either a two-dimensional ramp, three-dimensional axi-symmetric cone or a three-dimensional half-cone center body. The inlet may have fixed or variable geometry features, may contain a boundary layer bleed system, and can utilize a bypass at off-design Mach numbers. These inlets have been extensively investigated experimentally at $M_0 = 2-3$. A bypass starting system is not required, although one is generally utilized to offset drag losses.

2. Internal Compression Inlet. The internal compression inlet may or may not have any projecting body (2 or 3 dimensional) outside of the duct wall, and the compression system at the operating Mach number is completely contained within the duct wall. The system generally is provided with a boundary layer bleed system and of necessity requires a large bypass system to start the inlet at high Mach numbers.

3. External-Internal Compression. The external-internal compression inlet utilizes an external surface in front of the duct to partially compress the air and internal compression within the duct to complete the cycle. The system requires boundary layer bleed control and a bypass system to start the inlet at high Mach numbers.

Design Parameters. The important design parameters for any inlet design are:

1. Pressure recovery
2. Mass flow ratio
3. Inlet stability and flow distortion
4. Cowl drag
5. Bleed drag
6. Bypass drag
7. Cooling and actuation requirements

The state-of-the-art pressure recovery characteristics for several inlet systems are shown in Figure 3.4.6 (References 3.4.1 and 3.4.2). Note that while the external compression inlet has a lower pressure recovery characteristic than the internal compression system, the attainment of these high recovery levels with the internal compression inlet is at the expense of very large inlet length requirements (compared to the external compression system).

The mass flow ratio characteristics of the inlet are affected by the operating Mach number region, the attitude α and ψ , and the geometric features (variable or fixed). For a fixed geometry system designed for operation at a high

SECRET

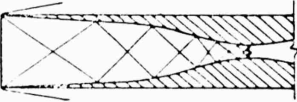
	$M_0 = 4$ INLET CHARACTERISTICS			
	H_2/H_0	VARIABLE GEOMETRY REQUIREMENT	BLEED REQUIREMENT	OVERALL LENGTH
 EXTERNAL COMPRESSION	0.55 TO 0.60	0	0.03 TO 0.05 m_0	MODERATE
 INTERNAL COMPRESSION	0.65 TO 0.75	LARGE	0.25 TO 0.30 m_0 AT $M_0 = 3$ TO 5	LONG
 EXTERNAL & INTERNAL COMPRESSION	0.62 TO 0.69	INTERMEDIATE	0.05 TO 0.10 m_0	MODERATE
			REFERENCE NO. 1	

Figure 3.4.5. Inlet Compression Systems.

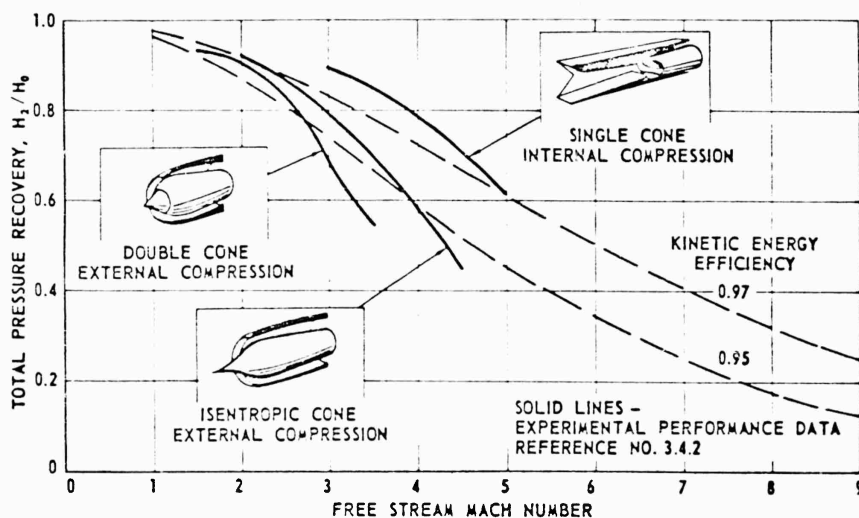


Figure 3.4.6. Inlet Efficiency Versus Mach Number.

Mach number, operation at lower Mach numbers causes the inlet to operate at lower mass flow ratios (airflow) and this in turn substantially increases additive drag.

In addition to the operating problem, there is the inlet starting problem, which is particularly acute for internal compression inlets where supersonic flow must be maintained within the duct walls up to the throat. For these systems the contraction ratio (A_t/A_i) required to operate at any Mach number is much lower

SECRET

than that required to swallow the initial normal shock as shown in Figure 3.4.7. Therefore, for an internal compression system with fixed-inlet geometry, some method, usually bypass, is used to "start" the inlet.

Inlet stability and flow distortion have long been problems with those vehicles which utilize air-breathing jet engines. For a fixed or variable geometry system, operation at less than the critical mass flow ratio will result in an unstable shock system with subsequent large variations in the duct pressures. This variation is in the form of both positive and negative changes with respect to the free stream total pressure and can occur at frequencies of 20 to 100 CPS. These rapid fluctuations naturally lead to unstable burning and can result in structural failure. It has been established in tests reported in Reference 3.4.3 on the SUPER TALOS program that the inlet instability propagated by the oscillating shock at off-design conditions affects the longitudinal stability of the vehicle. The SUPER TALOS vehicle is basically a boosted-ramjet surface-to-air missile with an inlet of the external compression type located at the nose of the vehicle. The design point for the system is about $M_0 = 4.0$.

The effect of inlet stability on the external longitudinal stability of a vehicle is appreciable. Figure 3.4.8 is a plot of the effects of the shock on pitching moment at a wing incidence angle of 0° and 10° on SUPER TALOS. Thus, from these data it can be seen that the vehicle will experience a change in characteristics dependent on the position of the inlet shock.

The location of the inlet at the nose of the vehicle tends to aggravate the stability problem. However, it will be shown that the inlet size requirements for the lenticular vehicle dictate a trapezoidal inlet shape which would have to be located along the side, or two separate pod-mounted engines would be required. The former would result in a problem similar to SUPER TALOS and the latter would result in high frontal drag.

Parameters 4 through 6 cannot in general be discussed independently of the type of inlet system. In general, bleed control of the inlet is necessary in order to obtain good pressure recovery. The performance increase due to bleed alone at high Mach numbers is in general difficult to isolate since the inlet models of necessity are provided with bleed systems. However, data from Reference 3.4.4 at $M_0 = 2.0$ show a 7.5 percent increase in pressure recovery due to 3.5 percent bleed. The model tested in Reference 3.4.5 was provided with an annular bleed system. One of the variables investigated was the effect on inlet performance of a constant area section in the subsonic diffuser. A reported increase in performance of almost 50 percent may be worth the additional inlet length.

The problem of the bypass system is the most critical area in inlet selection. Even with a fixed-geometry inlet system, operation of the inlet duct at off-design Mach numbers results in a large drag penalty unless a bypass control is employed. Figure 3.4.9 from Reference 3.4.1 is a plot of the drag effects due to spillage drag as compared to a bypass for a Mach 4 inlet design. Note that at $M_0 = 2$, the

SECRET

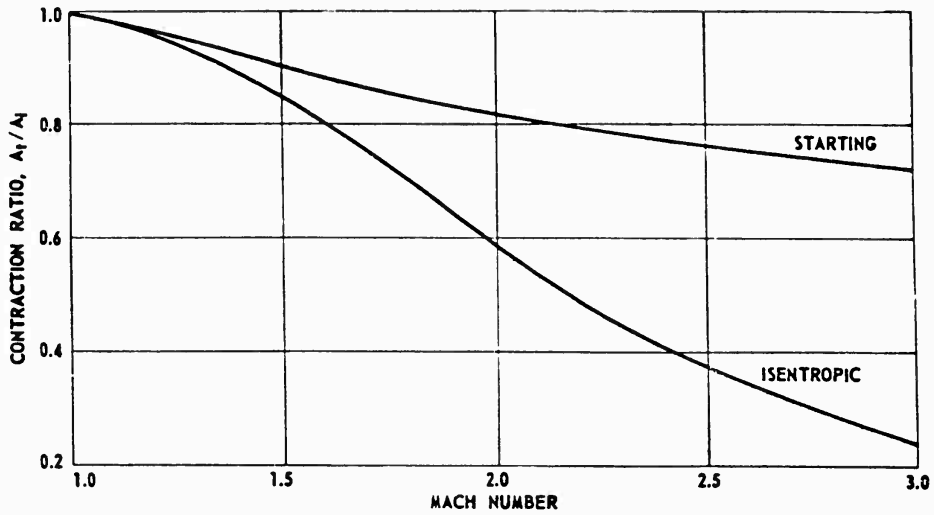


Figure 3.4.7. Contraction Ratio Versus Mach Number.

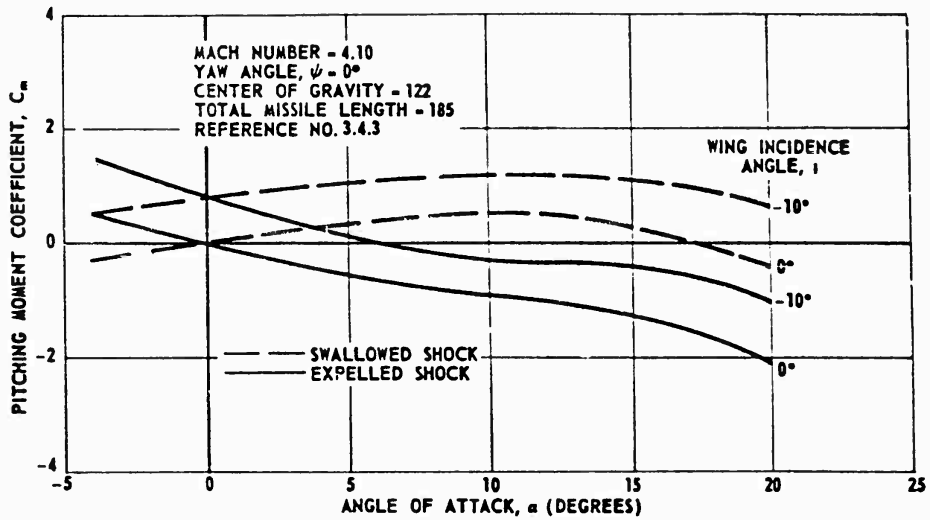


Figure 3.4.8. Pitching Moment Coefficient Versus Angle of Attack for Super Talos.

drag penalty with oblique shock spillage is five times that of the bypass system. It should also be noted that the use of a bypass at off-design Mach numbers greatly improves the pressure recovery and net thrust.

The last parameter listed above, 7, is a difficult one to evaluate. In general, at $M_0 > 4$ the weight and cooling requirements for a variable geometry system

SECRET

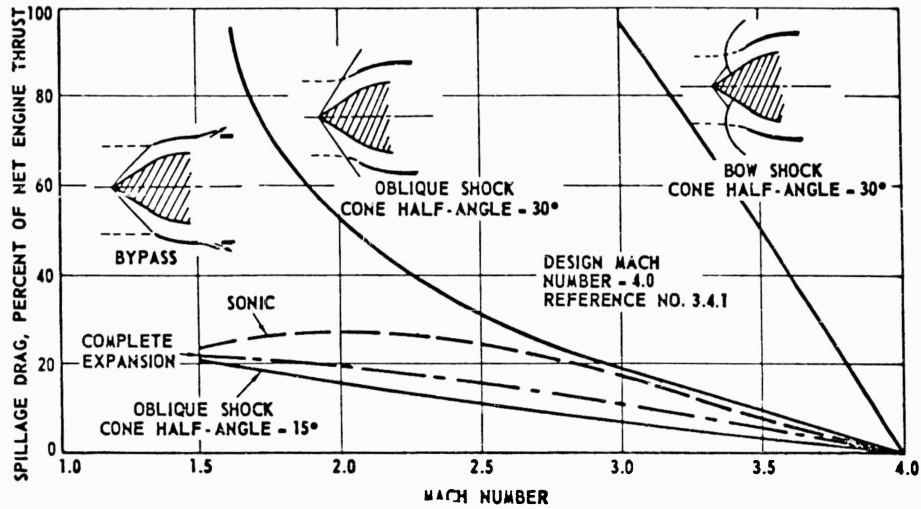


Figure 3.4.9. Turbojet, Matching Drag Penalties.

are very large. This is partially due to the high stagnation temperatures in the duct and the high duct pressures induced by the increased pressure recovery.

In summary then, for the lenticular application the use of an air-breathing system would almost certainly dictate a fixed, external compression system using bypass control at lower Mach numbers. Figure 3.4.10 from Reference 3.4.1 illustrates the size and length requirements for several typical inlet diffusers at $M_0 = 7$ and clearly indicates the simple external compression system to be the smallest.

Inlet Size Requirement. An evaluation of the approximate inlet size required was made for operation at $M_0 = 4.5$ and 6.0 at $60,000$ feet based on data obtained in References 3.4.6 and 3.4.7. The drag of the blunted lenticular body is shown in Figure 3.4.11 for a 21 percent missile. At $M_0 = 4.5$, the drag is 2400 pounds and the engine size was matched to this value as follows:

$$C_{T9} = 0.6 \text{ (Reference 3.4.8)}$$

$$A_9 = \frac{2400}{0.6 \times 2120} = 1.89 \text{ FT}^2 = 272 \text{ IN}^2$$

$$A_9/A_1 = 1.5$$

$$A_1 = 181.5 \text{ IN}^2$$

$$A_0/A_1 = 1.0$$

SECRET

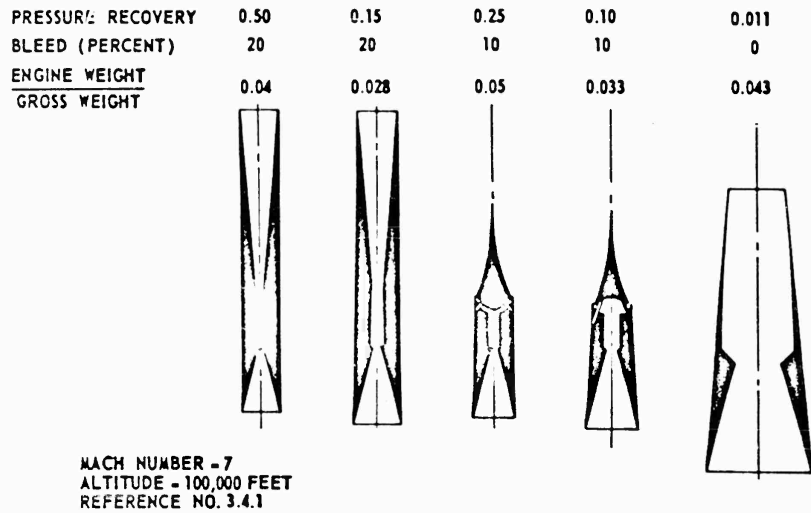


Figure 3.4.10. Relative Sizes for Ramjets With Equal Net Thrust.

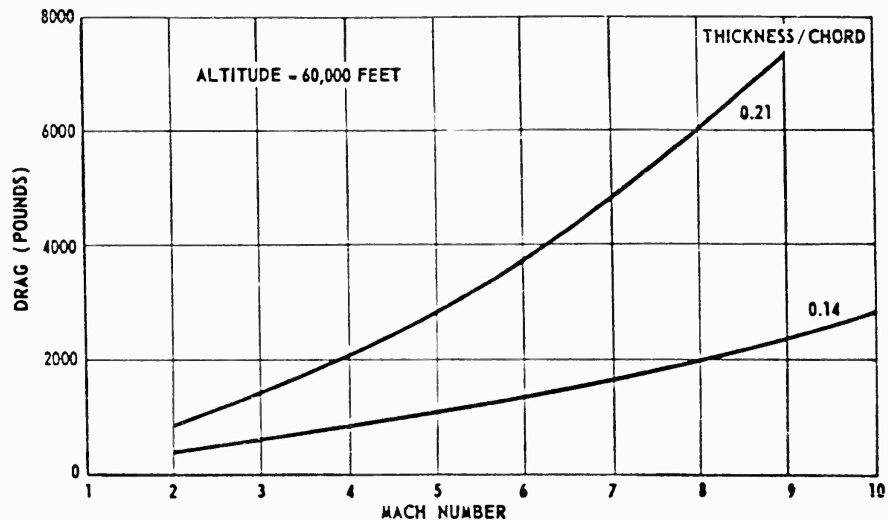


Figure 3.4.11. Body Drag Versus Mach Number.

Thus, an inlet diameter of 15.2 inches would be required. As a reference for comparison this is slightly larger than the thickest section of the vehicle. It is estimated that the engine would weigh about 400 pounds. In comparison, operation at $M_0 = 6$ at 100,000 feet would require an inlet of about 212-inch² or about 16.5-inch diameter, and would weigh about 500 pounds. It should be noted that these numbers are based on a design point engine.

SECRET

PROBLEMS IN USING RAMJETS. Considering that the emphasis of these design feasibility studies is directed to defensive missiles capable of omnidirectional launch from moving aircraft, additional propulsion problems arise such as: velocity transients of launch, effects of high angle of attack during maneuver, and the performance penalties of air density variations of a given mission altitude profile.

Figure 3.4.12 from References 3.4.8 and 3.4.9 is a typical plot of the degradation in performance for a fixed-design, at other than design Mach numbers. This can partially be offset by the use of a bypass system which will, however, result in added complexity and weight. Additionally, to boost a ramjet vehicle to near-design velocity requires a rocket engine. Minimizing the inner intercept boundary of the missile dictates high thrust levels for rapid acceleration and short-time-to target. Performance studies show (see subsection 3.9) that a glide or coast phase gives adequate range making additional propulsion for a cruise phase redundant.

The operation of an air-breathing system at high Mach number at angles of attack and yaw causes severe problems in performance and stability. From data reported in Reference 3.4.10 at yaw angles of 8° , the performance has decreased 30 percent. Figure 3.4.13 (from reference 3.4.10) is a plot of the effect of angle of attack to 11° on inlet performance. Also shown is the effect at $M_0 = 2.0$ from Reference 3.4.11. At angles of attack to 20° , performance is penalized over 30 percent.

Because of these limitations of ramjet propulsion systems, no further consideration was given to their possible useage in the design feasibility investigation. It is possible that in certain restricted applications of the PYE WACKET, ramjets could be of service.

EXTERNAL COMBUSTION. As a possible novel adaption of air-breather devices, an examination was made of research developments in external combustion. Interesting research on external-burning "ramjets" has been performed in the past few years. In this type of system, the fuel is injected into the boundary layer of the body and is burned externally. The resultant change in the pressure field produces both a positive thrust and lift force on the body.

Although of possible use in the future, progress is at a slow pace. From the data reported in Reference 3.4.12 it appears that only recently has there been any model testing accomplished on this system. In fact, it is stated in Reference 3.4.12 that. . . "it is doubtful that the over-all thrust efficiency of a pure external engine would ever be more than a small fraction of that obtainable with a conventional ramjet." Therefore, further analytical work was discontinued since the development of this system for actual vehicle propulsion seems to be some years in the future.

SECRET

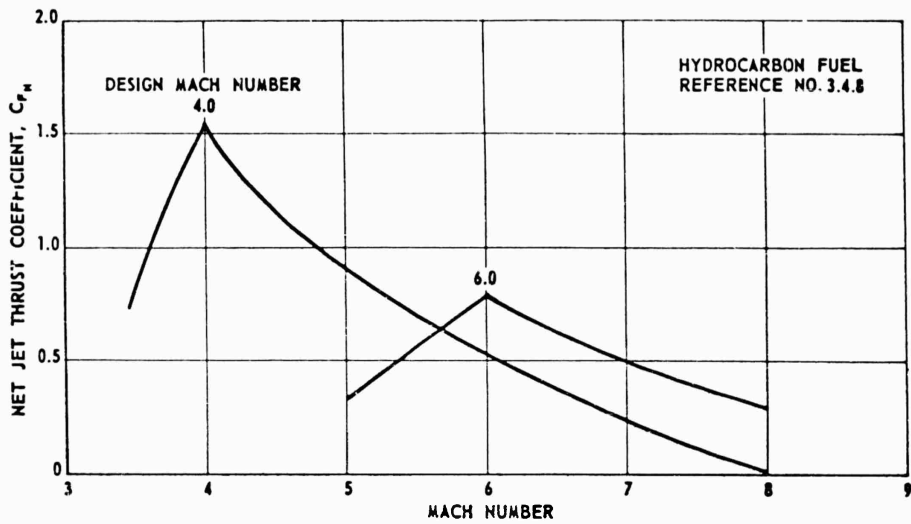


Figure 3.4.12. Net Jet Thrust Coefficient for Fixed Geometry Engines.

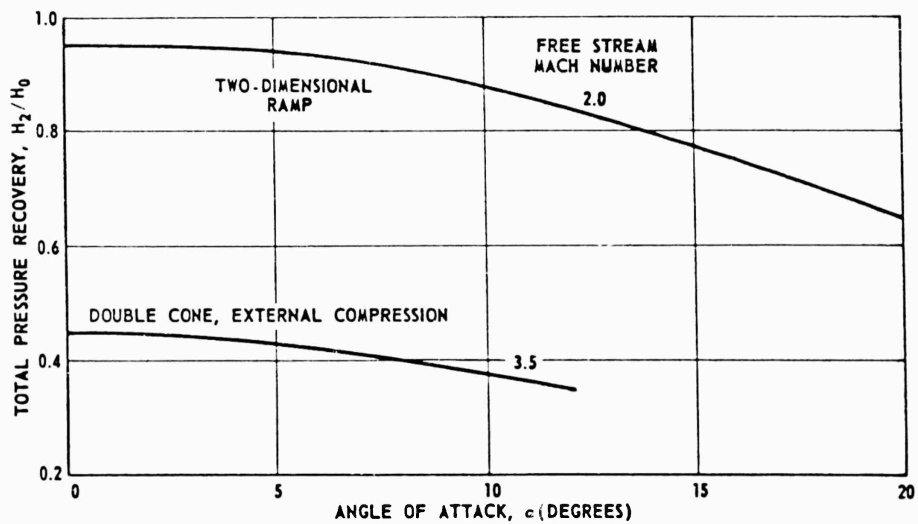


Figure 3.4.13. Effect of Angle of Attack on Inlet Performance.

3.4.3 ROCKET ENGINES

A preliminary examination of the rocket motor for PYE WACKET immediately revealed certain unique problems and limitations that prevented an immediate choice between a solid or liquid propellant system.

SECRET

Ordinarily, the rocket motor chosen for a missile that has a tactical mission (recently the trend has become similar for strategic weapons) would be a solid propellant unit. Design of an acceptable propulsion system would start with a determination of either an internal or end-burning grain. The present case requires a more involved study for two reasons. First, the unconventional geometry of PYE WACKET means either a low loading density, low impulse-to-weight ratio solid motor, or new intricate techniques of grain casting. Second, the rapid development, as flying hardware, of storable liquid propellant engines make them attractive to the unusual lenticular configuration. In the material, that follows, both solid and liquid engine possibilities are treated in some detail.

GENERAL NOZZLE CONSIDERATIONS. The blunted lenticular configuration, though superior to the other lenticular forms studied from a propulsion system standpoint, does place certain limitations on the range of rocket motor parameters (thrust level, chamber pressure, nozzle expansion ratio) which can be obtained. For instance, chamber pressure should be low to minimize case weight, (I_{sp} is still adequately high at altitude as shown later in Figure 3.4.14) and since a high thrust level is desirable for high acceleration capability, a large thrust area, hence, a large nozzle is required. Since these problems are common to both liquids and solids, both types of systems will be examined in this section.

It was assumed that the nozzle should not protrude outside the missile space envelope. This limitation, coupled with the high thrust requirement, means that an elliptical nozzle must be used rather than a conventional circular nozzle. Early in the study program thrust limitations were determined. The following tabulated values give the thrust available (based on the theoretical thrust coefficient-- C_F) as a function of thickness ratio for a 36-inch wide elliptical exit section, with an area ratio of 6, where the height of the ellipse is equal to the maximum thickness of the missile. It is possible that other packaging considerations (such as nozzles for jet control) may restrict the nozzle size and in turn the thrust level still further.

Thrust Limitations

Thickness ratio, percent	14	21	28	35
A_e/A_t	6	6	6	6
Nozzle exit width, IN	36	36	36	36
Nozzle exit height, IN	8.4	12.6	16.8	21.0
Throat area, A_t , IN ²	39.5	59.4	79.0	99.0
Thrust (solid at 150 PSIA, LB)	9,660	14,500	19,300	24,200
Thrust*(liquid) at 150 PSI, LB	4,670	7,010	9,340	11,700
Thrust (solid) at 250 PSIA, LB	16,280	24,420	32,520	40,800

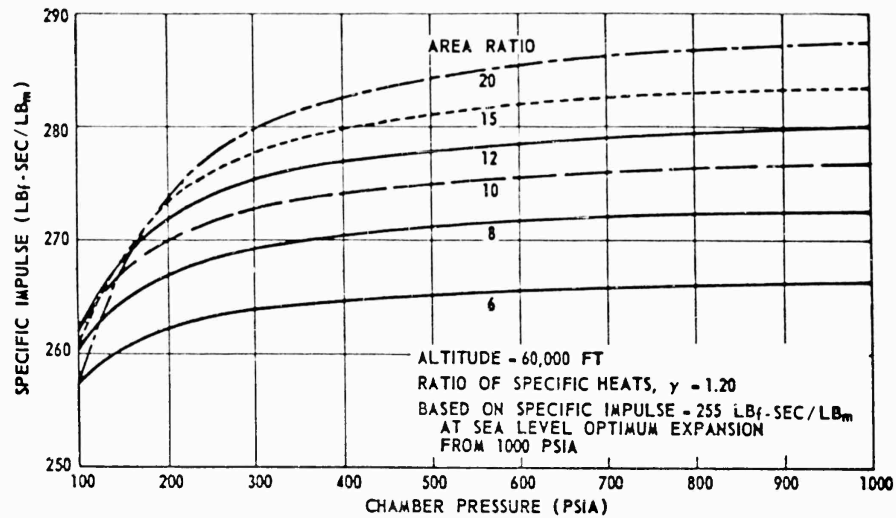


Figure 3.4.14. Specific Impulse Versus Chamber Pressure.

Thrust* (liquid) at 250 PSI, LB	11,200	16,900	22,420	28,200
Exit Area, IN ²	237	356	474	594
D', IN**	17.4	21.3	24.6	27.5

** D' = Diameter of circle with an area equal to exit area of elliptical nozzle
 * Liquid system assumes ΔP of 75 PSI from tank to chamber

The area ratio of 6, although not optimum expansion, is very near the optimum value considering overall performance, nozzle weight, etc. It can be seen from Figure 3 4. 15 that this area ratio gives good performance over nearly all the altitude range considered in this study. Since the exit section is elliptical, the throat section would be either circular with a transition duct, or also elliptical in shape. This would be finally determined from the nozzle losses which would be encountered with each configuration, and the extent of thrust vector control required.

For a multiple chamber solid propellant system, various designs are possible. Each cylinder could have a separate nozzle or the several chambers could be manifolded together to exhaust through a single nozzle. Individual nozzles result in simplicity of design, but some means of controlling the thrust level of each cylinder must be used. A simple pressure connection between nozzle entrance sections may be satisfactory. If only two cylinders are used, individual nozzles are desirable; if more than two are used the single nozzle will probably be superior.

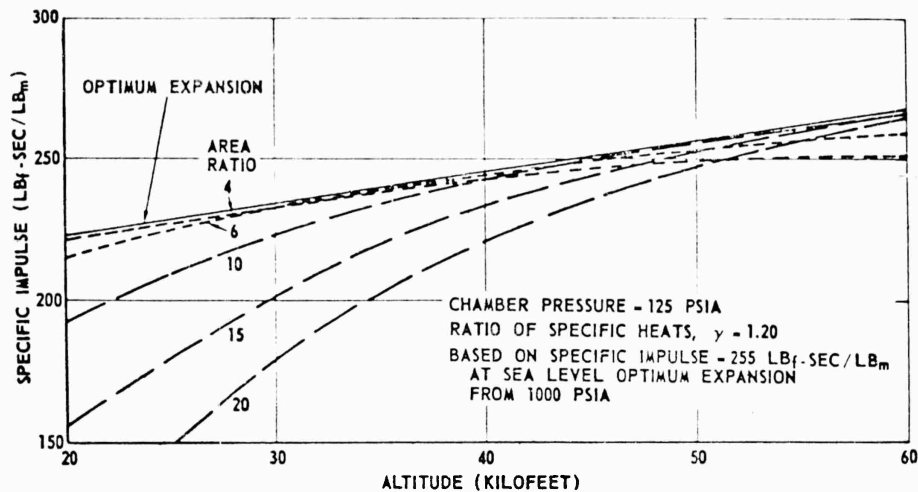


Figure 3.4.15. Specific Impulse Versus Altitude.

When the thrust vector must be controlled, swiveled or gimballed nozzles, jetevators, jet vanes, secondary injection, or some other method of flow control is required. Where large control forces are required, the single nozzle appears to be the best approach. (See subsection 3.7 for further discussion of this point.)

For the integral case or pancake type solid propellant motor, a single nozzle will be satisfactory. A swivel nozzle can be employed for thrust vector control or, depending on the magnitude of side force required and duration, secondary injection may be competitive with the mechanical systems.

In the liquid propellant system, the same thrust limitations are encountered due to geometry limitations--perhaps more severe than the solid (assuming a pressurized liquid tank system) since the injector pressure drop and line losses lower chamber pressure below that of the solid. A gimballed chamber appears to be the most effective way of attaining thrust vector control in the liquid system.

With these general nozzle limitations and maximum thrust limitations established as upper boundaries, the various configurations of solid and liquid propellant motors will be examined.

SOLID PROPELLANT SYSTEMS. In examining the possibilities of solid motor applications there are two approaches: (1) the use of conventional cylinders, which only partially fill the available space, or (2) the design of a grain and structure (non-conventional motor) that make the maximum volumetric use of available space.

Conventional Cylindrical Motors. The conventional cylindrical motor propulsion scheme can be described as a bank of motors mounted inside the allotted

SECRET

space envelope. Almost any number of cylinders can be used as long as they fit inside the space envelope. The cylinders can be either the conventional right-circular cylinders, or tapered cylinders which fit the space envelope more exactly. An analysis of each type was accomplished to determine the performance associated with each.

The cylindrical motor system delivers thrust by exhausting through individual nozzles or by manifolding the cylinders together so that they exhaust through a single nozzle. If individual nozzles were used, it would be necessary to provide some means of controlling the thrust of each motor so that the total thrust vector would be directed in the desired direction. Manifolding the inlet sections of the individual nozzles equalizes the pressures and equalizes the thrust from each nozzle.

For a given space envelope, the weight of propellant that can be packaged in cylindrical motors is obviously less than that which can be packaged by using the missile skin as the propellant tank, i. e., using the entire space envelope, (though this is partially offset by the higher I_{SP} realized by virtue of using higher chamber pressures). The volume between the cylinders is not available for propellant when using the cylindrical configuration.

Either internal-burning or end-burning grains can be used for this application, depending on the performance required. An end-burning grain requires more insulation and restriction than an internal-burning grain, but normally more weight of propellant can be packaged with the end-burning grain. Higher thrust levels and shorter durations are possible with the internal-burning grains.

Non-Conventional Motors. Two non-conventional solid-rocket designs were considered: (1) a pancake motor (designation of the flat pressure vessel where the chamber walls are integral with the vehicle outer skin) and (2) a flared end-burning motor.

1. Pancake Motor. Figures 3.4.16 and 3.4.17 illustrate the configuration of the pancake motor. This motor is a low chamber pressure, internal-burning, solid propellant motor. Since it is obvious that this shape is far from an optimum pressure vessel shape, low internal pressure is a requirement if a minimum weight structure is to be realized. Consequently the trade-off with propellant specific impulse must be carefully evaluated. These results are discussed below, under Determination of Preliminary Rocket Motor Parameters.

To obtain a high thrust level, a large propellant flow-rate is required, and if a low chamber pressure system is used, a large nozzle thereby results. It should be noted that with a large throat area, and an expansion ratio of 4 to 6, the nozzle exit cannot be circular if it is to remain inside the blunted lenticular space envelope. An elliptical exit section is shown in Figure 3.4.16, where the height of the ellipse is nearly the thickness of the missile at the rear end. This configuration utilizes most of the available area for the exit section, resulting in a reasonable nozzle area ratio.

SECRET

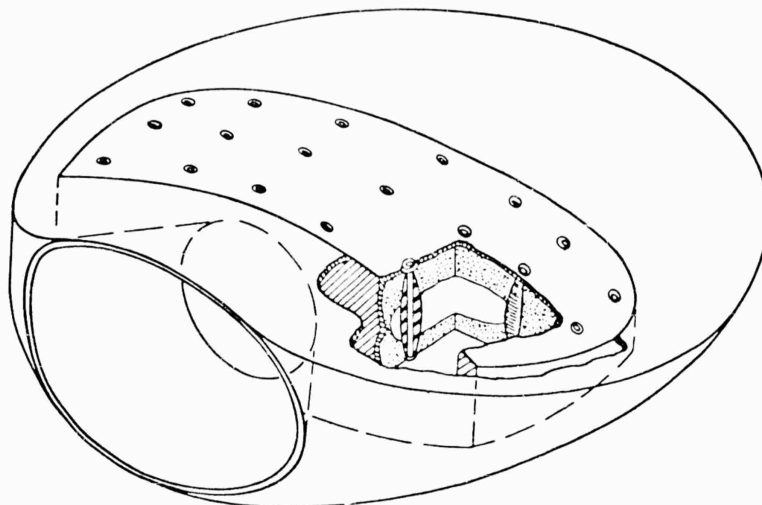
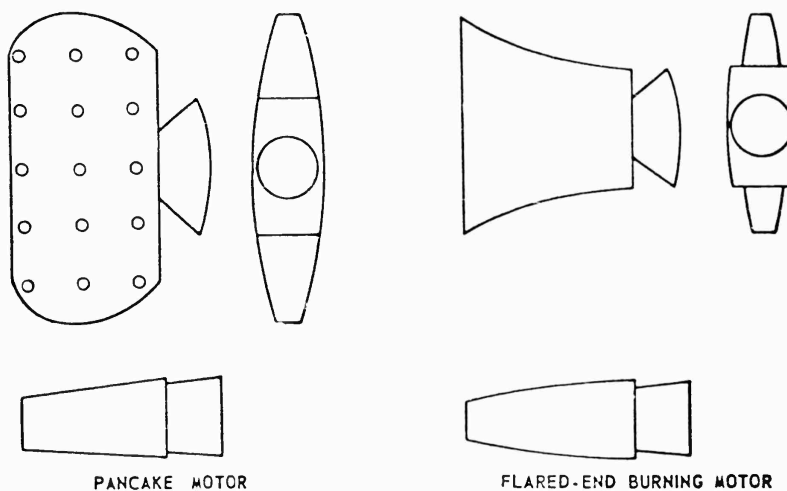


Figure 3.4.16. Lenticular Solid Propellant Rocket Motor Configuration.



PANCAKE MOTOR

FLARED-END BURNING MOTOR

Figure 3.4.17. Solid Propellant Motor Configuration.

The pancake motor shown in Figure 3.4.16 is constrained at the edges of the case, and additionally by internal stay-bars. The stay-bars are connected to the case at the top and bottom and are in tension when the case is pressurized. Other types of construction are possible, but since all metal parts inside the case must be insulated, a minimum exposed area is desired. This design results in a reasonable weight case and packages sufficient propellant to provide adequate missile performance.

SECRET

An internal-burning propellant grain requires a carefully designed grain perforation, such that the required thrust and burning time are developed. It is also necessary that the propellant burn out uniformly at the case wall to eliminate hot spots and possible burn-outs. For the flat-shaped motor a fairly complicated internal configuration is required; in addition, a method of forming the internal configuration must be realized. Collapsible mandrels, low melting point core material, forming the propellant in sections, and the usual removable mandrel are some of the methods that must be considered. A motor of this type could have a loading density of at least 70 percent, since conventional motors achieve loading densities of 90 percent.

2. Flared End-Burning Motor. An end-burner normally produces a constant burning area with a resulting constant thrust level. This flared end-burner motor has the required constant burning area, but must become wider as the missile becomes thinner. See Figure 3.4.17. This constant-area restriction, results in a curve-sided motor. As in a conventional cylindrical end-burner, the hot combustion gases are exposed to the case as the propellant burns. The case and any internal structural elements, therefore, must be well insulated to prevent structural failure towards the end of burning.

An end-burning grain is normally less complicated than an internal-burning grain, but in this case certain problems are anticipated. The changing cross section may require special propellant forming techniques. Casting the propellant in the case, though desirable, presents problems because of the internal stay-bars required in such a case. Obtaining even burning around these internal structural members may present some problems. However, this motor should achieve a high loading density if the other problems can be overcome.

DETERMINATION OF PRELIMINARY ROCKET MOTOR PARAMETERS.

Prior to consideration of liquid propellant rocket system it is desirable to discuss the determination of preliminary rocket motor parameters.

Conventional Cylindrical Motors. Two variations of the cylindrical motors were investigated: right circular, multi-cylinder motors and tapered multi-cylinder motors. The merits of each of these systems will be discussed in the following pages.

The maximum size cylinders that would fit the available space was determined initially. The dimensionless shape contours, Figures 3.4.1, 3.4.2, and 3.4.3, were used to determine the lengths and radii of cylinders that would fit the space envelope. As a first-order approximation, it was assumed that all the cylinders extended to the rear of the missile ($\frac{X}{C} = 0.50$) independent of the $\frac{Y}{C}$ position, as shown in Figure 3.4.18. It was then assumed that each cylinder had a nozzle attached to it. The nozzles extended outside the circular planform

SECRET

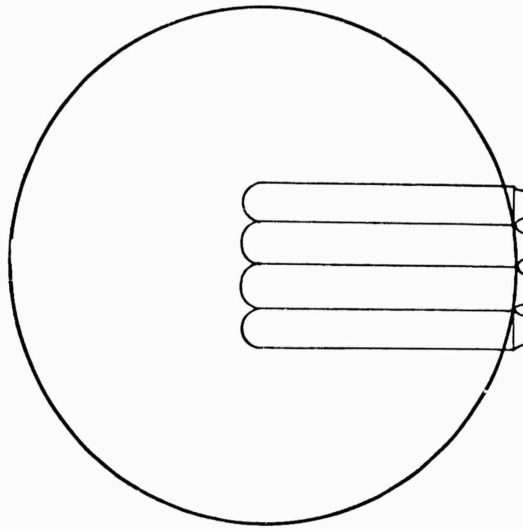


Figure 3.4.18. Right Circular Cylinder Motor Configuration.

of the missile. Three systems were then analyzed: the two-cylinder, three-cylinder, and four-cylinder systems. The three-cylinder system has one cylinder mounted along the centerline of the missile with two more mounted directly adjacent to the center cylinder. The four-cylinder system has two cylinders mounted on each side of the centerline.

At any $\frac{X}{C}$, $\frac{Y}{C}$ position within the space envelope of the missile, a thickness is defined. This thickness was taken to be the outside diameter of the cylinder, which would extend from that point back to the aft end of the cylinder. Since the aft end of the cylinder is located at $\frac{X}{D} = 0.50$ (aft end of vehicle), it follows that as the length of the cylinder increases, the radius decreases. This will be true for all right-circular cylinders mounted inside the space envelope.

Since the volume inside the cylinder is proportional to the radius squared times the length, there is an optimum position for the head of the cylinder so that it will house the maximum volume. Figure 3.4.19 shows the dimensionless volume as a function of the $\frac{X}{C}$ position of the head-end of the cylinder. It should be noted that the maximum volume occurs at $\frac{X}{C} = 0$ (center of vehicle) for both of the cylinders shown on the curve. Now, knowing the size of the cylinders as a function of the missile diameter, the weight of inert parts, weight of propellant, and resulting performance of the missile can be calculated.

Specific impulse (I_{sp}) versus chamber pressure for various area-ratios, is shown in Figures 3.4.19 and 3.4.20. These values were based on a specific impulse of 255 $LB_f SEC/LB_m$ at 1000 PSI chamber pressure and optimum sea-level expansion. The data shown in References 3.4.13, 3.4.14, 3.4.15, and 3.4.35

SECRET

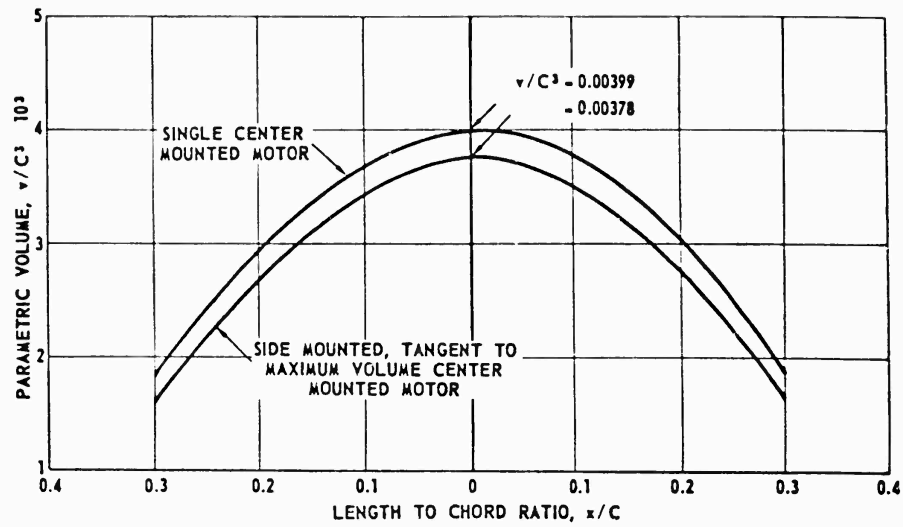


Figure 3.4.19. Available Volume With Three Cylinder Motor.

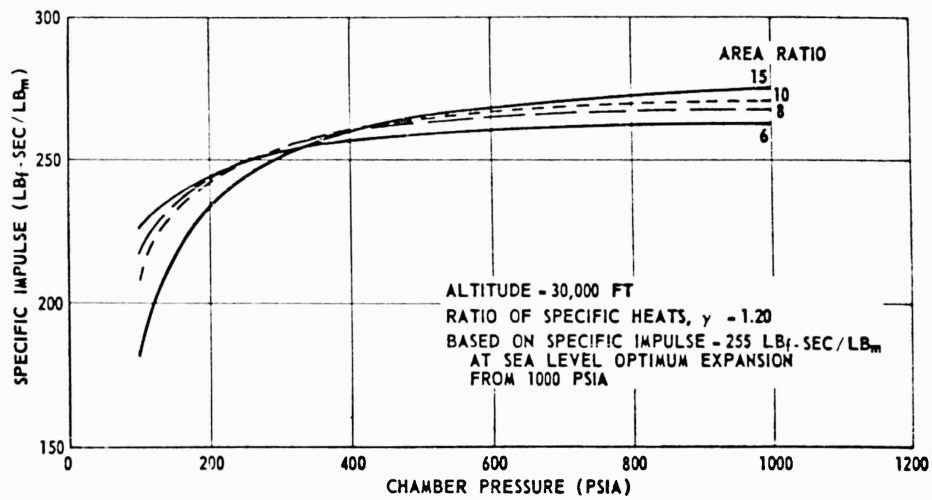


Figure 3.4.20. Specific Impulse Versus Chamber Pressure.

show that 255 LB_fSEC/LB_m is reasonable for the 1961-62 time period (for motors that will be beyond the development stage in this time period). This value was then ratioed to other altitudes and area-ratios, assuming that the characteristic exhaust velocity (C^*) remained constant. The specific impulse at any chamber pressure and altitude is then:

$$I_{sp} = \frac{C^* C}{g} \quad (3.4.1)$$

SECRET

$$I_{sp} = \frac{C^*}{g} \frac{C_{F2}}{C_{F1}} \quad (3.4.2)$$

$$\begin{aligned} I_{sp} &= 255 \text{ LB}_f\text{SEC/LB}_m \\ C_{F1} &= 1.595 \\ I_{sp2} &= 159.9 C_{F2} \end{aligned} \quad (3.4.3)$$

Where

$$C_{F2} = \sqrt{\left(\frac{2\gamma^2}{\gamma-1}\right)\left(\frac{2}{\gamma+1}\right)^{\frac{\gamma+1}{\gamma-1}} \left[1 - \left(\frac{P_e}{P_c}\right)^{\frac{\gamma-1}{\gamma}}\right]} + \left(\frac{P_e - P_0}{P_c}\right) \left(\frac{A_e}{A_t}\right) \quad (3.4.4)$$

The propellant density was assumed equal to 0.062 LB/IN³. Reference to Figure 3.4.21 shows this to be a typical value available in developed propellants. As reported in Reference 3.4.16 and 3.4.17, a delivered specific impulse of 240-245 is presently being obtained and, based on survey of the field recently accomplished by Convair, it was found that a delivered I_{sp} of 255 LB_fSEC/LB_m (standard conditions) could be obtained by 1962.

Table 3.4.1
PROPELLANT PROPERTIES

	Experimental C* FT/SEC	I_{sp} at 1000 PSI	Burning Rate at 1000 PSI and 70°F	Propellant Density LB/IN ³	γ
<u>Olin Mathieson</u>					
J-38 } 10 LB test data	4780	221	0.26	0.062	1.14
J-63 } not corrected	5110	225	0.315	0.063	1.15
J-66 } for optimum	5160	234	0.38	0.062	1.18
J-67 } expansion	5120	234	0.36	0.062	1.20
<u>Atlantic Research Corporation</u>					
Arcite 373	4880	242		0.065	1.18
with wires			1.9		
without wires			0.35		
Arcite 368	4670	230		0.062	1.22
with wires			3.01		
without wires			0.45		
Double base + NH ₄ ClO ₄ + AL				0.067	
<u>Grand Central Rocket Company</u>					
GCR-218	4900	238	0.45	0.062	1.23

3.4.20

SECRET

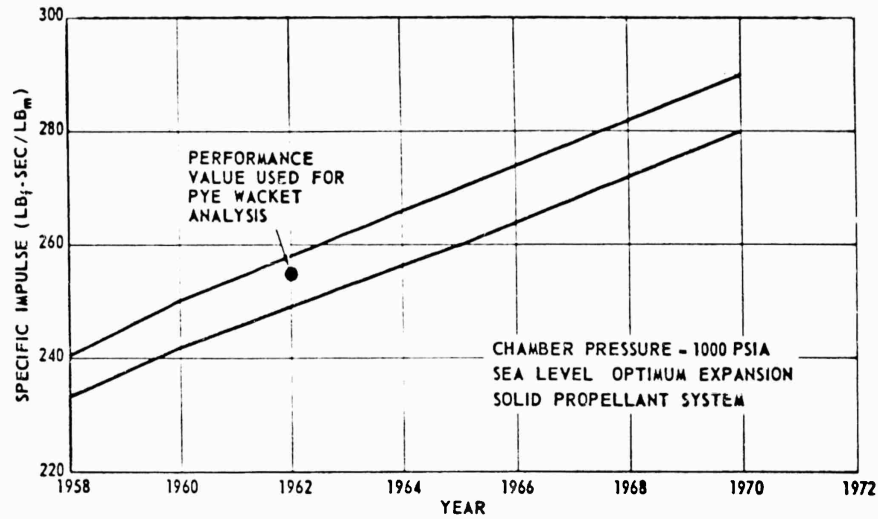


Figure 3.4.21. Predicted Delivered Specific Impulse Growth Trends.

	Experimental C* FT/SEC	I _{sp} at 1000 PSI	Burning Rate at 1000 PSI and 70°F	Propellant Density LB/IN. ³	γ
GCR-207	4850	236	0.45	0.063	1.20
CBAN	5150	239	0.32 - 0.70	0.062	1.21
<u>Goodrich</u>					
E-101		232	} Calculated	0.0611	
E-102		232			
C3967C	4900	226			
C3970C	5130	238			
<u>Aerojet General Corporation</u>					
2605 CD		238	0.26	0.0634	1.13
2619 R		244	0.41	0.0618	1.16
2621 B1		244	0.36	0.0610	1.18
2622 AF		233	0.41	0.0606	1.198
2633 FE		242	0.47	0.0615	1.17
2634 FE		244	0.18	0.0605	1.18

The polyurethane-aluminized propellants are currently being utilized in the Polaris and Minuteman engines. The high-impulse, composite, double-base propellants are also being used in Polaris, Minuteman and Vanguard. The PBAA

SECRET

polymers are being used for Minuteman, Pershing, Subroc and other vehicles. Over 20,000,000 pounds of polyurethane propellant have been manufactured and even more double-base propellant has been produced.

To provide an indication of future performance which might be anticipated, Convair conducted a survey of the leading propellant manufacturers. These findings are summarized in Figure 3.4.22. Some of the systems which could be used to obtain this performance are shown below in Table 3.4.2 from References 3.4.15, 3.4.19, and 3.4.20.

Table 3.4.2
ADVANCED PROPELLANTS

Components	I _{sp}
Lithium 14%, PFSA 86%	312
AlH ₃ 34%, NG 66%	316
Al 27%, BTNEN 73%	274
Polyurethane 14%, LiN (AlH ₂) ₂ 29%	275
NH ₄ C10 ₄ 57%	
Polyurethane 6%	304
C10 ₃ F 45%, NH ₄ C10 ₄ 14%	
Lithium aluminum hydride 35%	
Polyurethane 10%, NH ₄ C10 ₄ 68.18%	310
Beryllium hydride 21.82%	

One of the biggest problem areas here will be the encapsulation of the additives into the propellant system in such a way that they will not react during storage but will ignite with a nominal amount of input ignition energy. This area is presently being attacked by several organizations.

Insofar as the chamber or pressure vessel is concerned, the use of steel cases was assumed. Preliminary motor weights were computed as follows: (Refer to Figure 3.4.23 for the nomenclature.)

Hemispherical Head:

$$W_h = 2\pi \rho_c r_c^3 \frac{\rho_c}{S} \quad (3.4.5)$$

End Joints:

$$W_e = \frac{\pi R_c^2 r_c^3}{(500)S} \quad (3.4.6)$$

Case:

$$W_c = 2\pi r_c^2 \rho_c l \left(\frac{\rho_c}{S}\right) \quad (3.4.7)$$

SECRET

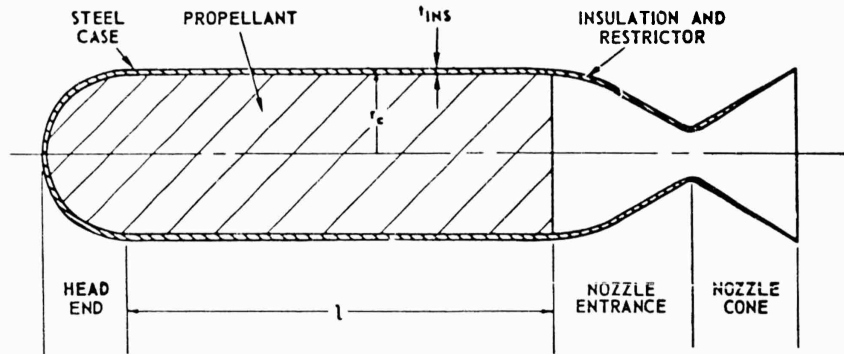


Figure 3.4.22. Configuration and Nomenclature.

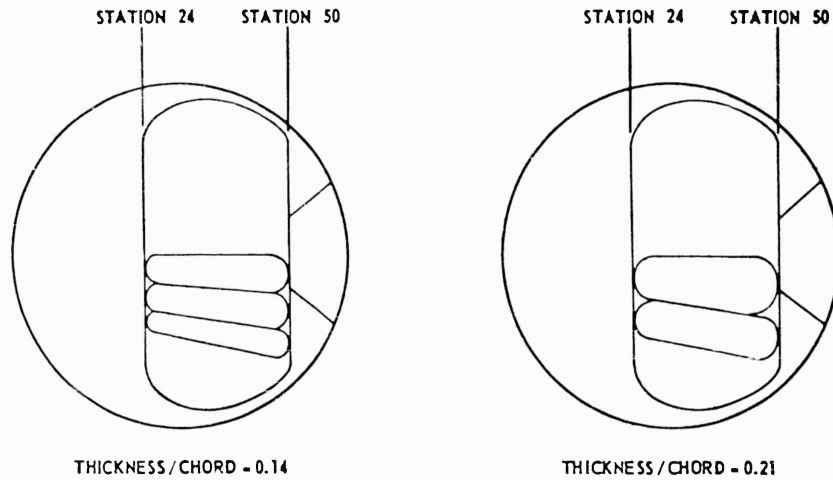


Figure 3.4.23. Tapered Cylinder Motor Configuration.

Insulation and Restrictor:

$$W_i = 0.35 \pi \rho_{INS} (r_s - t_{INS}) [2l + (r_c - t_{INS})] \quad (3.4.8)$$

Nozzle Entrance Section:

$$W_{N_1} = \sqrt{2} \pi \left(\frac{2.12 \rho_c \rho_c r_c + \rho_{INS} t_{INS}}{S} \right) ((r_c - t_{INS})^2 - r_t^2) \quad (3.4.9)$$

Nozzle Exit Cone:

$$W_{N_2} = \frac{A_t}{\sin \beta} \left[\frac{A_e}{A_t} - 1 \right] [K_1 + K_2] \quad (3.4.10)$$

SECRET

SECRET

Total Inert Parts Weight:

$$W_{IP} = W_h + W_e + W_c + W_i + W_{N_1} + W_{N_2} \quad (3.4.11)$$

Weight of Propellant:

1. End Burning Grain
$$W_p = \left[\pi (r_c - t_{ins})^2 \ell \right] \rho_p \quad (3.4.12)$$

2. Internal Burning Grain
$$W_p = \left[\pi (r_c - t_{ins})^2 \ell \right] \phi \rho_p \quad (3.4.13)$$

Assumptions:

- S = Maximum working stress = 150,000 PSI
- ρ_c = Steel density = 0.283 LB/IN³
- ρ_{ins} = Insulation density = 0.052 LB/IN³
- ρ_p = Propellant density = 0.062 LB/IN³
- t_{ins} = Insulation and restrictor thickness
 - 1. End-burner = 0.35 IN.
 - 2. Internal-burner = 0.10 IN.

P_c = Chamber pressure = 500 PSIA

From another Convair propulsion system study propellant fractions to be obtained in cylindrical motors compatible with the 60-inch diameter PYE WACKET configuration were computed as a function of total impulse for various chamber pressures. It was found that the propellant fraction (ratio of propellant weight to total motor weight) decreases with increasing chamber pressure since a heavier case is normally required as pressure increases. Since both a high propellant fraction and a high total impulse-to-weight ratio are desired, a compromise of each must be made to obtain the optimum chamber pressure.

The optimum pressure is a function of the propellant characteristics, operating altitude, size of the system, material properties, and the required performance for the particular mission. For cylinders of this size, and the performance of the propellants which were considered, the optimum chamber pressure was found to be approximately 500 PSIA. This pressure was used for all cylindrical motor calculations.

SECRET

SECRET

Table 3.4.3 shows the results of these calculations for the various systems.

Table 3.4.3
CYLINDRICAL MOTOR COMPARISON

$$t/C = 14\%$$

Vehicle Maximum Thickness-To-Chord Ratio = 0.14

Right Circular cylinders, 30 inches long
Vehicle diameter, 60 inches

End-Burning Cylinders

<u>Item</u>	<u>2 cylinders</u>	<u>3 cylinders</u>	<u>4 cylinders</u>
Propellant Weight, LB	64.1	93.9	119.9
Total Motor Weight, LB*	97.2	142.8	183.6
Propellant Fraction, W_p/W_r	0.659	0.657	0.653
Total Impulse, LB-SEC**	17,000	24,900	31,800
Cylinder Diameter, IN.			
Center	6.36	6.42	6.36
Outside	~	6.21	6.00

Internal-Burning Cylinders

Volumetric Loading Density = 0.90

<u>Item</u>	<u>2 cylinders</u>	<u>3 cylinders</u>	<u>4 cylinders</u>
Propellant Weight, LB	71.2	104.5	134.1
Total Motor Weight, LB*	89.24	131.2	168.2
Propellant Fraction W_p/W_r	0.798	0.796	0.796
Total Impulse, LB-SEC** ^r	18,900	27,700	35,600

<u>Item</u>	<u>2 cylinders</u>	<u>3 cylinders</u>	<u>4 cylinders</u>
Cylinder Diameter, IN.			
Center	6.36	6.42	6.36
Outside	~	6.21	6.00

* Includes nozzle and case only.

**For $I_{sp} = 265 \text{ LB}_f\text{-SEC/LB}_m$ at 60,000 FT.

SECRET

3.4.25

The thrust level at which the solid propellant rocket motor can be operated is governed by the equation:

$$F = I_{sp} \rho A_B r \quad (3.4.14)$$

The burning area of end-burning grains is a function of the cylinder cross-sectional area, while the burning area of internal-burning grains varies with the cylinder length and circumference. End-burners normally require very high burning rates while internal-burners usually require low burning rates. In both cases definite thrust limitations exist due to burning rate limitations. Table 3.4.1 shows a tabulation of burning rates available in present day propellants.

Figure 3.4.24 illustrates the total thrust available for end-burning cylinders as a function of burning rate. A burning rate of 3.00 IN./SEC was picked as a reasonable value for the present time period using wired charges. The REDEYE motor now being developed for Convair has a burning rate in excess of 3 IN./SEC. References 3.4.13, 3.4.14, 3.4.15, and 3.4.21, further show that propellants with this high burning rate are now feasible and that other rocket motors with this burning rate are being developed.

Conventional Multi-Tapered Circular Cylindrical Motor. Because of the increased section thickness at the rear of the missile, a tapered cylinder will obviously hold more propellant than a right-circular cylinder, when each is required to fit the blunted lenticular space envelope. As with the right circular cylinders the volume between cylinders is not available for propellant packaging.

This type of packaging was investigated for two thickness ratios, 14 percent and 21 percent of the 60-inch diameter configuration. Figure 3.4.25 illustrates these motors. A maximum volume cylinder does not occur at the mid point, $\frac{x}{C} = 0$, (as it does with right circular cylinders). For tapered cylinders, maximum volume results when cylinder lengths are the maximum possible within the space envelope allocated to propulsion. It was then necessary to define that part of the length (or volume) of the missile which could be used for the motor.

Analysis of the space required for guidance, controls, autopilot, inert structure, etc., resulted in a motor length boundary 24 inches behind the mid chord leading edge of the missile. The aft 10 inches were left for a nozzle which would fit inside the space envelope. The volume between Stations 24 inches and 50 inches behind the leading edge was then left for packaging of the tapered cylinders.

As can be seen from Figure 3.4.25 the cylinders are tangent to Station 24, Station 50, the internal skin, and each other at various points. After drawing the external and internal skin in three views, it was possible to pick the tapered cylinders that would fit the space envelope by interpolation of the drawings. The resulting cylinder sizes are shown in Table 3.4.4.

SECRET

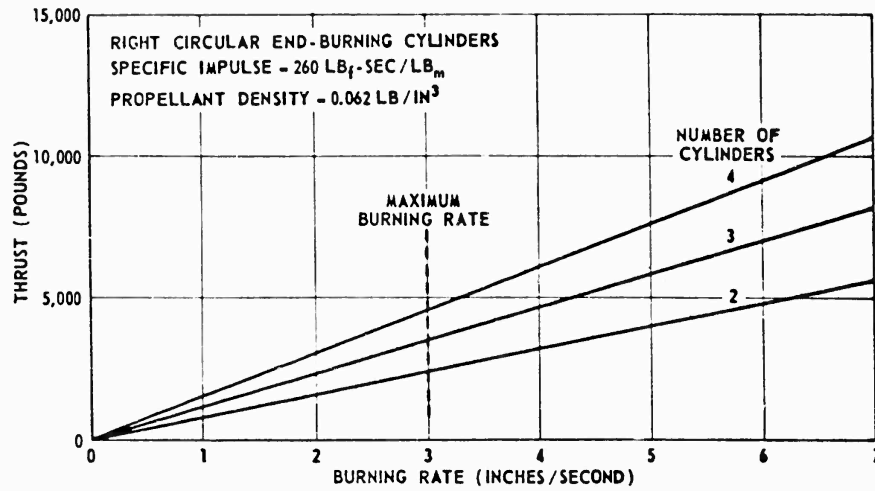


Figure 3.4.24. Thrust Versus Burning Time.

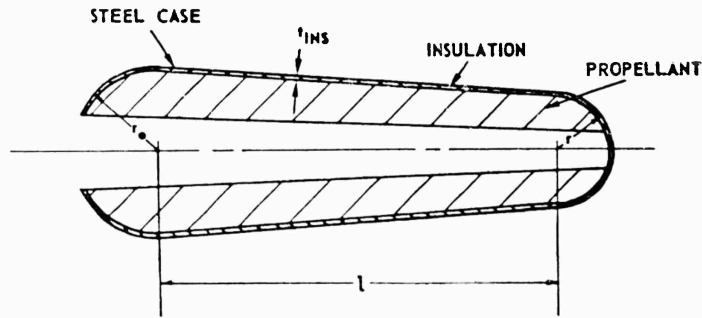


Figure 3.4.25. Configuration and Nomenclature for Tapered Cylinder.

Table 3.4.4
 TAPERED CYLINDER SIZES

Cylinder Location	Two Center Cylinders		Adjacent to Center Cylinders		Outside Cylinders	
Thickness ratio, percent	14	21	14	21	14	21
Length of cylindrical section, IN.	20.08	16.60	20.80	18.72	21.76	None
Large radius, IN.	3.50	5.32	3.13	4.18	2.50	None
Small radius, IN.	2.50	4.10	2.46	3.50	2.04	None

SECRET

It should be noted that the 21 percent thickness ratio vehicle will package four tapered cylinders and the 14 percent thickness ratio configuration will package six tapered cylinders. As noted from Table 3.4.4 the cylinder radii that fit the space envelope are larger for the 21 percent thickness ratio missile; hence, it requires fewer cylinders to make better use of the space envelope.

The propellant characteristics used in these calculations were the same as those used in the right-circular cylinder calculations and can be found in the preceding paragraphs.

It was assumed that steel cases were used. The weight of the motors was computed as follows. Refer to Figure 3.4.25 for the nomenclature.

Cylindrical Section:

$$t_c = \left(\frac{r_s + r_o}{2} \right) \left(\frac{\rho_c}{S} \right) \quad (3.4.15)$$

Hemispherical Heads:

$$W_H = 2\pi \rho_c t_c (r_o^2 + r_s^2) \quad (3.4.16)$$

Liner and Insulation:

$$W_{INS} = 2\pi \rho_{INS} \left[(r_o + r_s) \ell + (r_o^2 + r_s^2) \right] \quad (3.4.17)$$

Propellant Weight:

$$W_p = \phi \rho_p V_{CY} \quad (3.4.18)$$

$$V_{CY} = \frac{\ell}{3} \left[\pi (r_o - \delta)^2 + \pi (r_s - \delta)^2 + \pi \sqrt{(r_o - \delta)^2 (r_s - \delta)^2} \right] \quad (3.4.19)$$

Where

$$\delta = t_c + t_{INS} \quad (3.4.20)$$

The results of these calculations are shown in Table 3.4.5. It should be noted that, as expected, more propellant can be packaged in the tapered cylinders than in the right circular cylinders.

Table 3.4.5
TAPERED CYLINDER MOTORS

Vehicle Thickness Ratio	0.14	0.21
Number of cylinders	6	4
Propellant weight, LB	162.8	268.3

SECRET

Vehicle Thickness Ratio	0.14	0.21
Total weight, LB	216.0	323.0
Propellant fraction	0.75	0.83
Total impulse, LB-SEC	43,100	71,000

The advantages and disadvantages of individual and single nozzles have been discussed earlier. For the reasons given in that discussion only the single nozzle which fits inside the space-envelope was considered.

Non-Conventional Motors - Pancake. The configuration of the pancake motor is shown in Figure 3.4.15. As with the tapered-cylinder motor, the case fits between Stations 24 inches and 50 inches behind the leading edge of the 60 inch diameter missile, with the aft 10 inches left for a nozzle. A small amount of volume has been left on each side of the case for plumbing, and for electrical connections between the front and aft end of the missile. The pie-shaped volume on each side of the nozzle was allocated to control equipment.

For consistency, a brief discussion is given of the pancake construction; more detail can be found in subsection 3.6. Two types of case construction were considered: thick plate, and a special case of the thick plate type using sandwich construction. The sandwich material is made of thin, high density facings bonded to relatively thick, low density honeycomb.

The span of the case is relatively long, approximately 54 inches at the widest section. The deflections of the case are a problem in this design due to the large span, and a means of holding the deflections to a low value is necessary. Circular stay-bars connecting the top and bottom sides of the case are an efficient means of minimizing the deflection.

As a first approximation, the thickness of the plate and the plate deflection were computed, assuming a flat plate, point supported. The equations given in References 3.4.22 and 3.4.23 are:

$$S_{allow} = (0.222) \left(\frac{a^2}{t^2} \right) \rho_c \quad (3.4.21)$$

$$\varphi_{MAX} = 0.063 \left(\frac{a^4}{t^3} \right) \left(\frac{\rho_c}{E} \right) \quad (3.4.22)$$

Reference 3.4.24 shows the strength-to-weight ratio of titanium to be about 1.5 times greater than the strength-to-weight ratio of stainless steel. For this reason titanium was considered for the first approximation of the thick plate case. Reference 3.4.25 gives the data shown in Table 3.4.6, below, for welded and aged sheets of titanium.

SECRET

3.4.29

Table 3.4.6
TITANIUM CHARACTERISTICS

Density = 0.174 LB/IN³
Modulus of Elasticity = 14 x 10⁶ PSI

Test Temperature - °F	Yield Strength (0.2%) Elonga- tion PSI	Ultimate Tensile Strength PSI	% Elongation
70	165,000	170,000	5.0
600	128,000	150,000	8.0
800	120,000	145,000	8.0
1000	110,000	125,000	10.0
1200	56,000	62,000	10.0

A value of maximum allowable stress of 120,000 PSI was used, resulting in the following thickness and deflection:

$P_c = 150$ PSI (titanium case)

$a = 10$ IN.

Thickness $t = 0.167$ IN.

Deflection $\psi = 1.45$ IN.

It can be seen that the deflections are very large. Some of the methods to reduce these deflections are: (1) to increase the thickness of the plate, (2) decrease the distance between stay-bars, (3) use a high modulus of elasticity material, or (4) build up some structure to distribute the load. All these methods result in excessive case weights; therefore sandwich type construction was investigated.

Sandwich construction was analyzed according to References 3.4.22 and 3.4.23 for a continuous plate divided into square panels by circular supports. A stay-bar spacing of 10 inches was assumed for the first approximation. A variation of the stay-bar spacing was analyzed to determine its effect on case weight. The equations used for the sandwich analysis were as follows: (Refer to Figure 3.4.26 for the nomenclature.)

$$\frac{M}{a} = \text{moment per unit length} = K \left(\frac{L}{8}\right) (\rho_c) \left[L - \frac{2}{3} d_o\right]^2 \quad (3.4.23)$$

$$K = K_1, \text{ or } K_2 \quad (\text{whichever is largest})$$

$$K_1 = -0.5 - 1.5 \left(\frac{d_o}{a}\right)^2$$

$$K_2 = 0.46 \quad (3.4.24)$$

SECRET

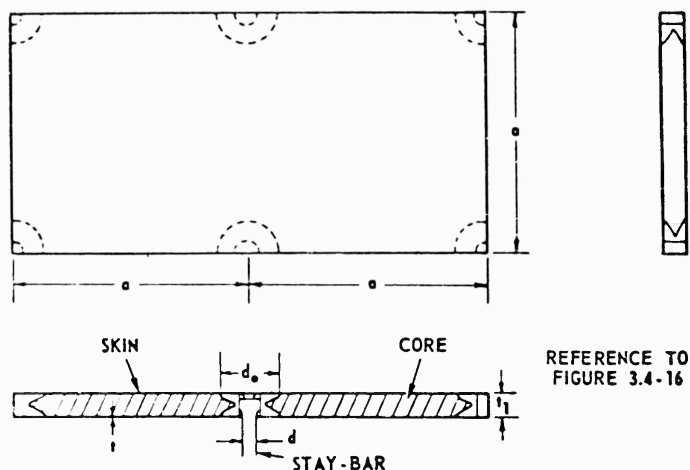


Figure 3.4.26. Configuration and Nomenclature for Sandwich Material and Stay-Bars of Solid Propellant Pancake Motor.

$$d_o = \frac{\rho_c a^2}{2\pi t_s} \quad (3.4.25)$$

$$d = \left(\frac{\rho_c a^2}{\pi/4 S} \right)^{1/2} \quad (3.4.26)$$

$$t = \left(\frac{M/a}{S t_s} \right) \quad (3.4.27)$$

$$W = (L^2 t_s \rho_c + \rho_t 2L^2 t) N \quad (3.4.28)$$

- N = number of panels
 ρ_k = core density = 15 LB/FT³
 ρ_t = titanium density = 0.174 LB/IN³

$$W_{STAYS} = \left(\frac{\rho_c a^2 \rho_t t}{S} \right) N_{STAYS} \quad (3.4.29)$$

It should be noted that the core thickness and the skin thickness are not given explicitly. They must be balanced against each other. A thicker core results in a thinner skin, and vice versa. A low-weight case design was formulated without unduly reducing the available volume for propellant. Edge closure weights and fitting weights were estimated. In the final design of a case of this type, the trade-off of core thickness versus skin thickness should be more closely examined.

SECRET

Deflections are not as great with this type of construction as compared to the flat plate type. The honeycomb core enables the case to have a large moment of inertia to resist bending while the weights remain small. The method of attaching the stays to the case can also be used to advantage to resist bending. One of these methods is shown in Figure 3.4.26. With proper design of a case of this type, deflections should not be prohibitive.

The estimated weights of sandwich type cases for the pancake motor are shown in Table 3.4.7 for two chamber pressures. These pressures are low in comparison to cylindrical configurations, but as stated above, the chamber pressure must be low to obtain a low case weight.

Table 3.4.7
CASE WEIGHTS AND DIMENSIONS

Thickness Ratio = 0.14

<u>Estimated Case Weights</u>		
Chamber pressure, PSIA	150	250
Sandwich weight, LB	40	51
Stay-bars weight, LB	4	4
Edge closure weight, LB	30	50
Fittings and miscellaneous, LB	<u>26</u>	<u>40</u>
Total weight, LB	<u>100</u>	<u>145</u>
<u>Estimated Case Dimensions</u>		
Sandwich thickness, IN.	0.500	0.852
Skin thickness, IN.	0.018	0.018
Stay-bar spacing, IN.	10	10
Stay-bar diameter, IN.	0.500	0.517
Number of stay bars	12	12
Material	B-120 Titanium	B-120 Titanium

It was found that increasing or decreasing the stay-bar spacing had little effect on the case weight. The only dimension affected markedly was the sandwich thickness, which of course, reduced the volume available for propellant. Reducing the stay-bar spacing reduced the sandwich thickness, but would make loading of the propellant quite difficult. A 10-inch stay-bar spacing appeared to be a near optimum configuration.

SECRET

Increasing the thickness of the missile increases the case weight somewhat, but also increases the weight of propellant that can be packaged. Since the case is quite flat, the top and bottom dimensions of the case do not change very much with a change in thickness ratio. The edge closure is the only weight affected appreciably by thickness ratio and varies approximately in direct ratio with thickness ratio.

The propellants considered here were high-performance, advanced-type propellants. These propellants have high combustion temperatures (above 5000° F) and necessitate the use of insulation on the stay-bar structure elements. The case wall is not exposed to the high temperature until burn-out so the insulation requirements at the wall are small. The burning times considered were short (approximately 4 to 8 seconds), which makes the stay-bar insulation requirement less severe. It was estimated that approximately 10 LB of insulation and restrictor would be required.

Table 3.4.8 shows the rocket motor performance characteristics determined for the internal-burning, solid propellant pancake-type motor.

Table 3.4.8
SOLID PROPELLANT PANCAKE MOTOR

Altitude = 60,000 FT
Chamber Pressure = 150 PSIA

Thickness ratio, percent	14	21	28	35
Propellant weight, LB	288.5	477.5	666	868
Motor case, nozzle, insulation, igniter weight, LB	122	137	152	167
Total weight, LB	410.5	614.5	818	1035
Propellant fraction	0.703	0.778	0.815	0.839
Total impulse, LB-SEC	75,010	124,150	173,160	225,680
Impulse to weight ratio, $LB_f\text{-SEC}/LB_m$	171.0	202.5	212.0	227.5

Altitude = 60,000 FT
Chamber Pressure = 250 PSIA

SECRET

Table 3.4.8 (Continued)

Thickness ratio, percent	14	21	28	35
Propellant weight, LB	237.5	426	610	819
Motor case, nozzle, insulation weight, LB	167	192	215	242
Total weight, LB	404.5	618	825	1061
Propellant fraction	0.588	0.689	0.739	0.770
Total impulse, LB-SEC*	62,463	112,038	160,430	215,397
Impulse to weight ratio, LB _f -SEC/LB _m	154.2	181.9	194.6	202.4

*Specific Impulse at 60,000 FT, at 150 PSIA
 Chamber Pressure, 260 LB_f-SEC/LB_m, at 250 PSIA
 Chamber Pressure, 263 LB_f-SEC/LB_m

Non-Conventional Motor. It was shown in the analysis of the pancake motor that internal structure is necessary, even when sandwich type construction is used. Using internal structure with an end-burning grain (flared-end-burner configuration) increases the weight of insulation required to a significant extent. Also, stress concentrations in the corners of this case make it unduly heavy.

The large insulation requirements, heavy weight, and construction problems involved in making a case for the flared-end-burner, dictated that no further work be done with this configuration. The pancake motor would be easier to realize, and lends itself more readily to the missile contour.

LIQUID PROPELLANT ROCKET SYSTEMS. The motor envelope developed for the pancake solid propellant motor was investigated for a liquid propellant application. This configuration makes maximum use of the available space.

In any liquid system, a means of transferring the fuel and oxidizer from the tanks to the combustion chamber is required. Two means of transferring the liquids are available: a tank pressurization system or a pumping system. For systems of this type where large flow rates and short burning times are required, and for total impulses less than approximately 200,000 LB-SEC (per another Convair study Reference 3.4.26) the incorporation of a pumping system is usually not desirable, considering weight, complexity, and reliability. The weight of the pump, turbine, gas generator, lines, valves and controls for a pumping system with a large flow rate capability is quite large when compared with the pressurization type system for the same low total impulse, high thrust motor. Even with a pumping system, case pressurization to approximately 50 PSIA is

SECRET

required to prevent pump cavitation. For this configuration, with a poor structural shape, the increase in case weight at 250 PSIA over a 50 PSIA case is about 100 LB. The 50 PSIA case design was not, however, analyzed in detail at this point for aerodynamic and inertail loads. These could possibly dictate a heavier structure.

The pumping rates for a thrust of 20,000 LB would be about 75 LB/SEC or a power rating of approximately 100 horsepower (assumed $\Delta P_{\text{pump}} = 500$ PSIA, propellant density = 0.054 LB/IN³). A gas generator, a turbine, and a pump that will deliver 100 horsepower would weigh about 50 LB while the pressurizing system weighs 5-10 LB. Even though the pump-type system weighs less than a pressurized system, the complexity and unreliability of the pumping system tend to degrade the weight advantage. For these reasons, it is evident that the pressurized system should be examined closely for the lenticular application.

Table 3.4.9 shows three propellant combinations which could be utilized in the engine for this vehicle. The theoretical data are shown for 1000 PSIA and sea level optimum expansion from References 3.4.27 and 3.4.28.

Table 3.4.9
STORABLE LIQUID PROPELLANT PERFORMANCE

Propellant	Specific Impulse (shifting) LB _f -SEC/LB _m	Weight Mixture Ratio		T _C (°F)	Density (LB/IN ³)	Density Impulse (LB _f -SEC/IN ³)
		$\left(\frac{\text{LB oxidizer}}{\text{LB fuel}}\right)$				
N ₂ O ₄ /N ₂ H ₄	292	1.32		5390	.044	12.8
N ₂ O ₄ /UDMH	285	2.6		5685	.043	12.3
ClF ₃ /N ₂ H ₄	295	2.77		6550	.054	16.0

It is easily seen that the performance for the ClF₃/N₂H₄ system is superior to the other combinations, due to the increased density and resultant smaller volume requirements.

The next parameter to establish was the expected delivered I_{sp}. Figure 3.4.27, is a plot of some experimental data obtained from Reference 3.4.29 for the ClF₃/N₂H₄ and N₂O₄/N₂H₄ system. It is seen that about 96-97.5 percent of the theoretical characteristic velocity is obtained. Since these data are based on small experimental engines, it was assumed that, for motors considered in this study, 96 percent of the theoretical C* could be obtained. It was further assumed that 95 percent of the theoretical C_F was obtained, which corresponded to a delivered I_{sp} of 267 at sea level.

SECRET

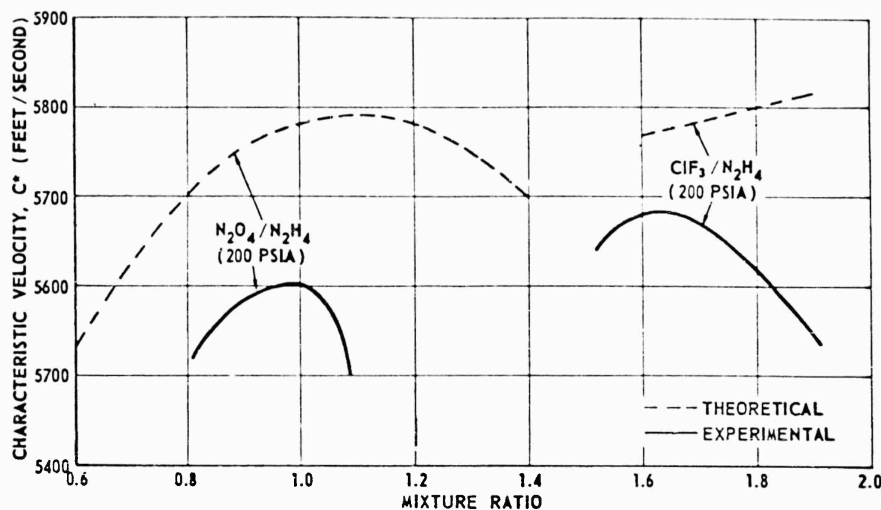


Figure 3.4.27. Comparison of Theoretical and Experimental Performance for Storable Liquid Propellants.

One of the disadvantages of $\text{ClF}_3/\text{N}_2\text{H}_4$ is the high freezing point, but it has been demonstrated in Reference 3.4.30 that additives can be used to depress the freezing point to -40°F at a loss of 1 percent in specific impulse.

To date, the $\text{N}_2\text{O}_4/\text{N}_2\text{H}_4$ system has been experimentally fired in thrust chambers to 150,000 pounds of thrust. The $\text{ClF}_3/\text{N}_2\text{H}_4$ system has been fired in engines to 5000 pounds of thrust and it is anticipated that firings at 100,000 pounds of thrust will be accomplished by the end of 1960.

Figure 3.4.28 shows the trend in expected performance for the storable liquid propellant system. Table 3.4.10 shows some of the formulations which might be utilized to obtain this increased performance.

Table 3.4.10
PERFORMANCE TRENDS
(Storable Liquid Propellants)

Propellant	Specific Impulse (shifting) $\text{LB}_f\text{-SEC}/\text{LB}_m$	Weight Mixture Ratio $\left(\frac{\text{LB oxidizer}}{\text{LB fuel}}\right)$	Density (LB/IN^3)	Density Impulse $(\text{LB}_f\text{-SEC}/\text{IN}^3)$
$\text{ClF}_3/\text{N}_2\text{H}_4$	295	2.77	0.054	16.0
$\text{N}_2\text{O}_4/\text{N}_2\text{H}_4+\text{A1}$	302	0.45	0.047	14.1
$\text{N}_2\text{H}_4/\text{B}_5\text{H}_9$	329	1.27	0.029	9.4

SECRET

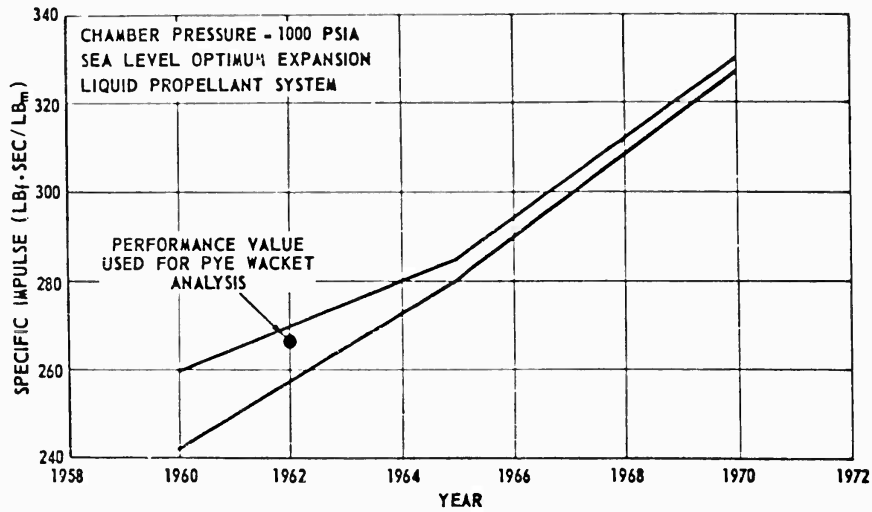


Figure 3.4.28. Predicted Delivered Specific Impulse Growth Trends.

Propellant	Specific Impulse (shifting) LB _f -SEC/LB _m	Weight Mixture Ratio ($\frac{\text{LB oxidizer}}{\text{LB fuel}}$)	Density (LB/IN. ³)	Density impulse (LB _f -SEC/IN. ³)
N ₂ O ₄ /N ₂ H ₄ +LiBH ₄	315 ± 10	-	-	-
N-F/N ₂ H ₄	320 ± 10	-	-	-
N ₂ O ₄ /N ₂ H ₄ and Metal hydrides	330 ± 10	-	-	-

The propellants chosen for evaluation in this study were high-performance, storable liquid propellants, including chlorine tri-fluoride and nitrogen tetroxide oxidizers, and hydrazine and unsymmetrical dimethylhydrazine fuels. Specific impulse versus chamber pressure for 30,000 feet and 60,000 feet altitude is illustrated in Figures 3.4.29 and 3.4.30, respectively. These curves were based on a specific impulse of 267 LB_f-SEC/LB_m at 1000 PSIA chamber pressure and optimum sea level expansion. The data given in References 3.4.31, 3.4.32, 3.4.33, and 3.4.34, show that the specific impulse of 267 LB_f-SEC/LB_m is reasonable for the propellant combinations chosen.

These data also demonstrate that a bulk density of 0.054 LB/IN.³ is a realistic, nominal value for computing propellant weights and was, therefore, used throughout the liquid propulsion system analysis.

SECRET

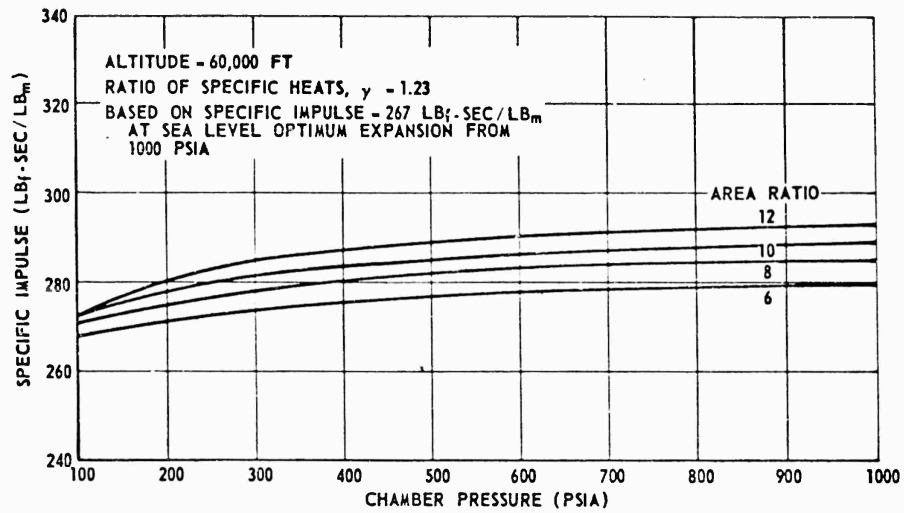


Figure 3.4.29. Delivered Specific Impulse Versus Chamber Pressure.

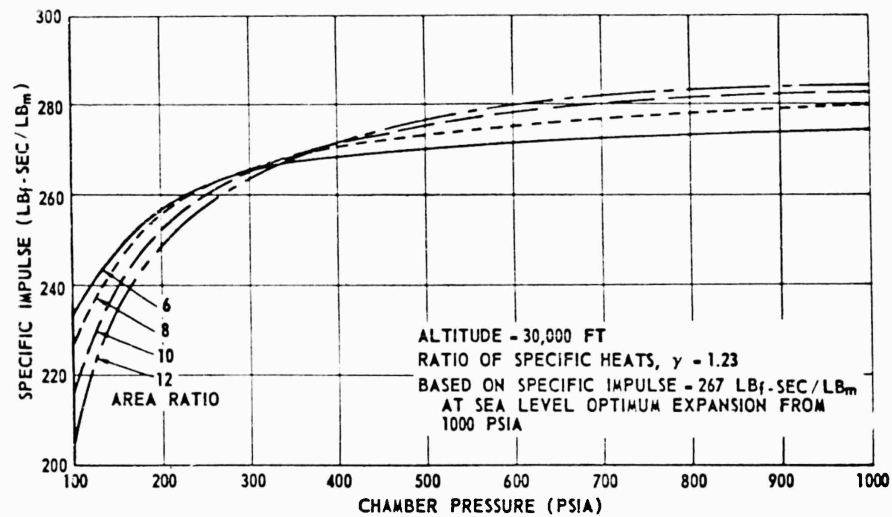


Figure 3.4.30. Delivered Specific Impulse Versus Chamber Pressure.

The volume of propellant was computed by assuming an 80 percent loading density based on the volume inside the missile between Stations 24 and 50, after the thickness of the tank has been subtracted. The plumbing inside the tank, the pressurization system components, and a cut-out on the rear of the tank for the

SECRET

thrust chamber, plus ullage and outage volumes were assumed to account for the other 20 percent of the available volume.

A solid propellant pressurization system was assumed (gas products compatible with the propellants selected) in which the gas generator exhausts directly into the propellant tank. If short durations are used, the hot pressurizing gas can be directly exposed to the propellants, though for longer durations a membrane separator would likely be required. Probably, no membrane would be required for the lenticular system, but it would be necessary to demonstrate the feasibility of such a system by actual test since g-effects, sloshing, etc., might present problems. The weight of a solid propellant gas generator pressurization system would be considerably less than that of a stored gas pressurization system.

The values of weights and performance that resulted from these calculations are shown in Table 3.4.11.

Table 3.4.11
STORABLE LIQUID PROPELLANT PANCAKE MOTORS

Tank Pressure = 150 PSIA Propellant Density = 0.054 LB/IN ³				
Thickness Ratio Percent	14	21	28	35
Tank weight, LB	101	112	123	134
Chamber, pressure system, valves, LB	26.5	32.6	38.9	45
Gimbal nozzle control, LB	20	20	20	20
Total inert parts weight, LB	<u>147.5</u>	<u>164.6</u>	<u>181.9</u>	<u>199.0</u>
Propellant, LB	<u>301</u>	<u>490</u>	<u>676</u>	<u>877</u>
Total weight, LB	488.5	654.6	857.9	1076.0
Propellant fraction	0.671	0.749	0.788	0.815
Total impulse, LB-SEC*	79,770	129,850	179,140	232,310
<u>Total impulse</u> Total weight	177.8	198.5	208.8	216.0
	LB _f -SEC/LB _m			

For P_c = 250 PSIA

Tank weight, LB	144.8	159.3	173.7	188
-----------------	-------	-------	-------	-----

SECRET

3.4.39

Table 3.4.11 (Continued)

Chamber, pressure system, valves, LB	27.2	34.1	41.1	48.3
Gimbal nozzle control, LB	<u>20</u>	<u>20</u>	<u>20</u>	<u>20</u>
Total inert parts, LB	192.0	213.4	234.8	256.3
Propellant, LB	251.5	439	628	827
Total weight, LB	443.5	652.4	862.8	1073.3
Propellant fraction	0.567	0.673	0.728	0.771
Total impulse, LB-SEC*	68,160	118,970	170,190	224,120
<u>Total impulse</u> <u>Total weight</u> LB _f -SEC/LB _m	153.7	182.4	197.3	208.9

*Assumed: $\Delta P_{inj} = 75 \text{ PSI}$
Specific impulse at 60,000 FT

$$P_c = 75 \text{ PSI}, I_{sp} = 265 \text{ LB}_f\text{-SEC/LB}_m \text{ at } 60,000 \text{ FT}$$

$$P_c = 175 \text{ PSI}, I_{sp} = 271 \text{ LB}_f\text{-SEC/LB}_m \text{ at } 60,000 \text{ FT}$$

The propellant fraction and impulse-to-weight ratio at 250 PSIA tank pressure are not especially high; however, if the tank pressure were raised much above the 250 PSIA level the missile performance would be degraded due to the high inert parts weight. This same result was also found for the solid propellant pancake motor.

3.4.4 VEHICLE PERFORMANCE STUDIES

When undertaking the study of a completely new missile, it is important to optimize the system as a whole. In accomplishing this goal it becomes necessary to optimize the various components, then evaluate trade-off among them in order to realize the best overall system.

Analysis of the propulsion system as a separate entity is a necessary and valuable part of the overall system study. In fact, propulsion system optimization is a requirement for any study, and is particularly important for an unconventional configuration such as the lenticular rocket. However, as is often the case when studying a complete missile or weapon system, the optimum propulsion system is not necessarily optimum for the vehicle as a whole. Therefore, compromises

SECRET

or trade-offs must be evaluated in the interest of securing the best overall system for the particular mission envisioned - considering the packaging arrangement or space limitations, and other factors such as reliability, simplicity, logistics, cost, and time for development.

Initial vehicle performance studies were undertaken on a parametric basis. At that point in the study detailed space allocations and weight estimates could not be made; therefore, missile weights were established for the 60-inch diameter vehicle (over a range of t/C ratios) based on an overall average missile density. In this case a density of approximately 0.055 LB/IN³ was employed, based on experience with other relatively small tactical missiles. Having established total vehicle weights, non-propulsive system weights (guidance system, warhead, controls, etc.) were estimated for a range of thickness ratios (14 to 50 percent); the difference of the two gave the propulsion system weight. A range of propellant fractions was assumed of 50 to 90 percent; and total impulse was thereby obtained on the basis of a delivered I_{sp} of 260 LB_f-SEC/LB_m at operating conditions. For these initial performance studies, burnout acceleration (ratio of thrust to burnout weight) was held constant at 50 g's for each case.

Preliminary drag data (C_{D0} versus Mach number) for the lenticular vehicle were employed for these initial comparative studies, and even though these data were somewhat optimistic for the larger t/C's (compared to final wind tunnel data), the preliminary vehicle performance results were quite valuable in narrowing down the ranges for the many parameters.

Performance evaluations of these systems were made, based on burnout velocity, range, and time to close-in targets, by solution of the basic equation of motion.

$$M \frac{dV}{dt} = F - \frac{1}{2} \rho V^2 C_D A \quad (3.4.30)$$

Analog computer solutions were obtained for the preceding input conditions for constant altitude flights at 30,000 feet and 60,000 feet.

Figure 3.4.31 is a plot of burnout velocity versus t/C for the range of rocket motor propellant fractions studied. These results exhibit normal trends until the thickness ratio of 40 percent is reached where burnout velocity of the 90 percent propellant fraction (PF) vehicle is lower than the 80 percent case. This crossover results from the assumption that thrust to burnout weight is constant. For the 90 percent PF case, thrust is lower than for the 80 percent PF case and for the example of a 50 percent t/C vehicle, thrust equals drag at approximately Mach 7.85 for the 90 percent PF case. On the other hand, thrust exceeds drag for the 80 percent PF case at Mach 7.85 thereby permitting it to accelerate to a higher burnout velocity.

SECRET

3.4.41

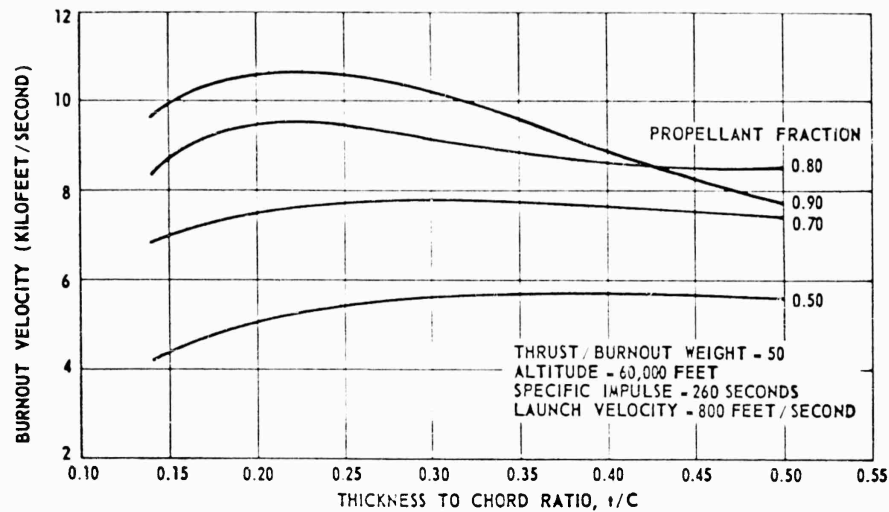


Figure 3.4.31. Burnout Velocity Versus Thickness to Chord Ratio.

Figure 3.4.32 illustrates range as a function of t/C considering ranges down to a Mach No. of 2.5. Thrust levels applicable to the various thicknesses and propellant fractions are superimposed. These thrust curves illustrate the effect of the 50 g burnout assumption - decreasing thrust with increasing propellant fraction - and further emphasize the importance of low drag (small t/C) and high propellant fraction.

Figure 3.4.33 shows the effect of t/C on time to a short range target. The thrust levels used here were dictated by the geometry limitations of the blunted lenticular configuration. Except for the very low t/C configurations (low thrust levels) time to target is not significantly affected by t/C variations. Thrust level, on the other hand, does affect this parameter.

These preliminary parametric performance results showed that adequate ranges could be obtained with thickness ratios less than 25 percent - ranges greater than 180,000 feet based on coast-down to Mach 2.5 at 60,000 feet. Further, it was shown that thrust levels could be varied over a significant range (keeping impulse constant) without serious effect on vehicle range. Also, burnout velocity changes very little at 60,000 feet for cases in which thrust level differs by a factor of two. At 30,000 feet burnout velocities for the higher t/C ratios decrease, though for the lower thickness ratios the change is not very great. For instance, for a thickness ratio of 25 percent, burnout velocity at 30,000 feet is reduced 17 percent if thrust is reduced 50 percent; at 60,000 feet the decrease is only 7 percent.

SECRET

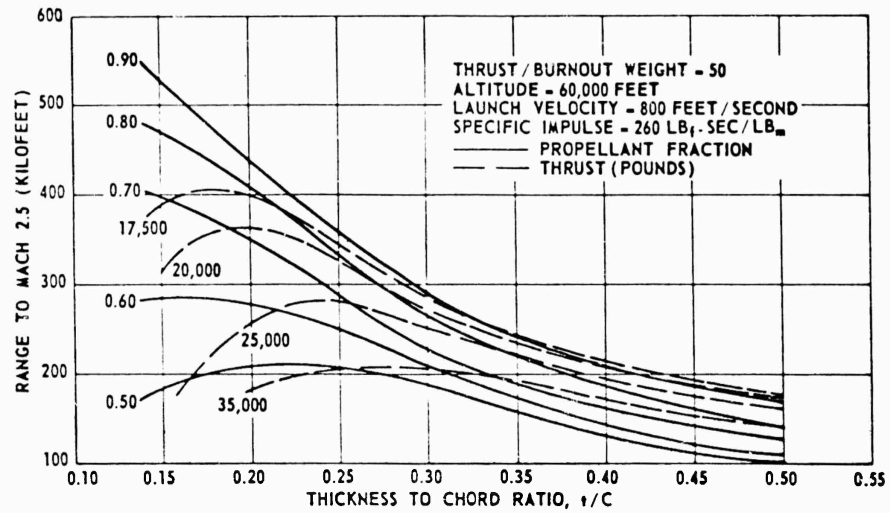


Figure 3.4.32. Range to Mach 2.5 Versus Thickness to Chord Ratio.

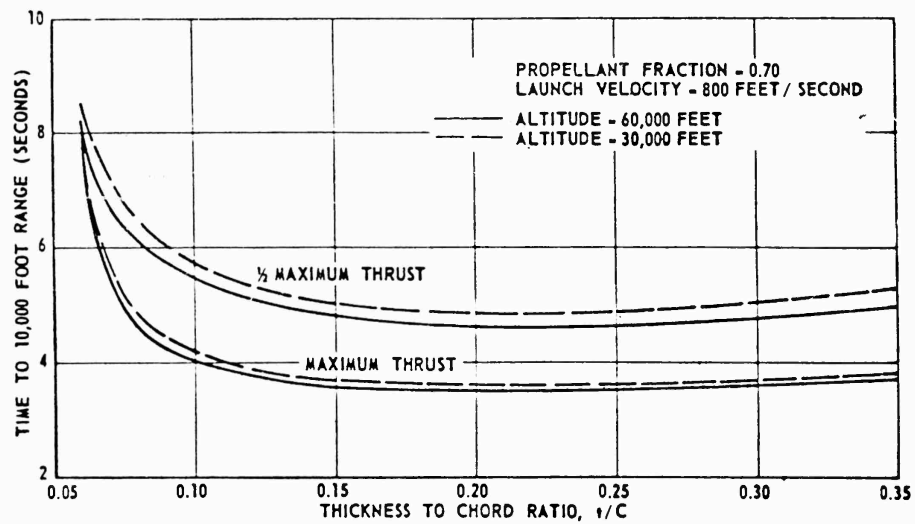


Figure 3.4.33. Time to 10,000 Feet Range Versus Thickness to Chord Ratio.

Altitude effects on range are, as might be expected, significant, particularly for the higher t/C vehicles. Much of the range is obtained after motor burnout, pointing up the importance of the parameter, burnout weight.

Based on the preliminary results obtained in the parametric performance studies, characteristics of three types of low-chamber pressure motors were

SECRET

3.4.43

defined for more detailed performance evaluations - solid propellant and liquid propellant designs using essentially all the space allocated for the propulsion system, and a solid propellant system utilizing a multiple-cylinder arrangement. The characteristics were described in previous paragraphs.

Vehicle performance calculations were made utilizing essentially the final 14 percent and 21 percent weight estimates and drag data based on the wind tunnel results. Iterative solutions of the familiar equation of motion for constant altitude flight

$$M \frac{dV}{dt} = F - \frac{1}{2} \rho V^2 C_D A \quad (3.4.31)$$

were made for the powered phase. During coast-down the following relations were used:

$$\Delta \text{ Range} = \frac{2Wc}{\rho g C_D A} \ln \frac{V_i}{V_f} \quad (3.4.32)$$

$$\Delta \text{ Time} = \frac{2WE}{\rho g C_D A} \left(\frac{1}{V_f} - \frac{1}{V_i} \right) \quad (3.4.33)$$

Figures 3.4.34 and 3.4.35 are plots of velocity and range versus time for the 14 percent t/C configuration. Similar plots for the 21 percent t/C vehicle are shown in Figures 3.4.36 and 3.4.37. It can be seen that the liquid and solid propellant motors produce approximately equal burnout velocities, somewhat greater than for the lower-weight cylindrical arrangement. The latter type, though lighter in weight, has a lower total impulse.

Figure 3.4.38 shows the time to a 10,000 foot range versus t/C. Here, the primary reason for different times is the variation in thrust levels applicable to each (and consequently acceleration capability). Figure 3.4.39 is a composite plot of range versus time for a range of t/C's. Superimposed are the Mach 2.5 and Mach 1 lines (coast-down). This plot further emphasizes the desirability of designing a vehicle in the approximate t/C range of 14 to 21 percent (as discussed in subsection 3.11. Considerations other than range and velocity, such as payload space, warhead size, etc., may dictate which end of this range to employ.

Performance obtained with the three types of propulsion systems - multi-cylinder solid propellant, and solid and liquid propellant pancake types - packaged in the blunted lenticular body is quite attractive and will, when combined with the omni-directional launch and high maneuver-g characteristics, produce an excellent overall system capability. Further discussion of the performance attainable with PYE WACKET may be found in subsection 3.9.

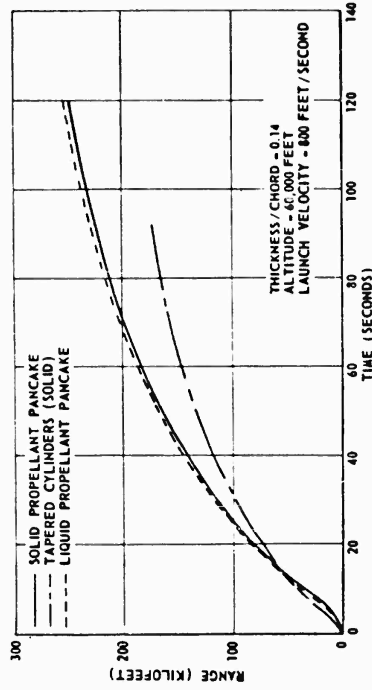


Figure 3.4.35. Range Versus Time.

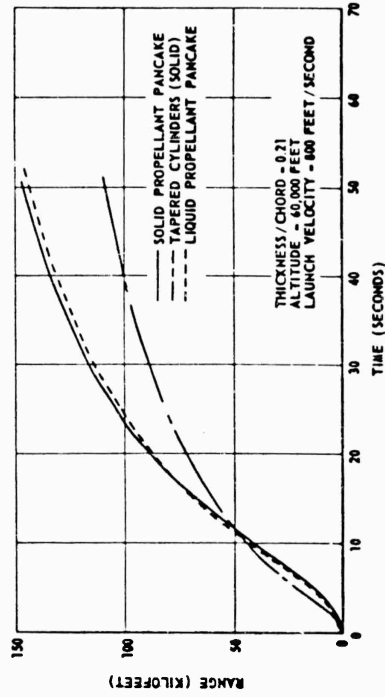


Figure 3.4.37. Range Versus Time.

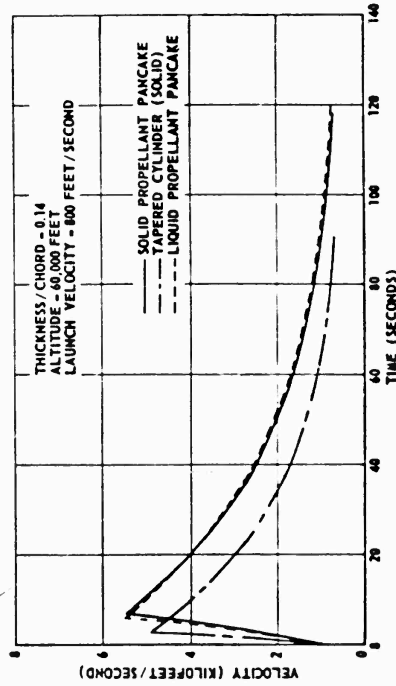


Figure 3.4.34. Velocity Versus Time.

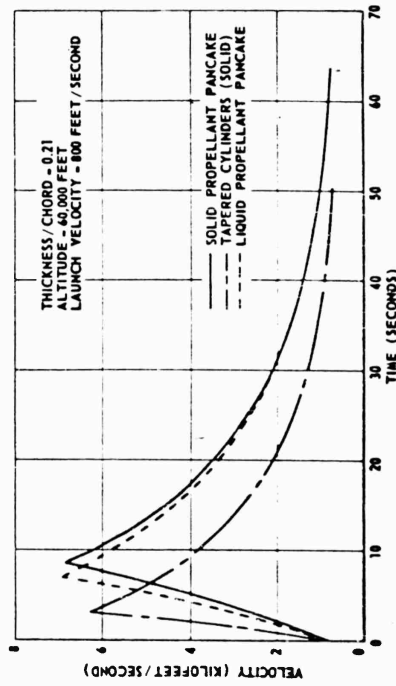


Figure 3.4.36. Velocity Versus Time.

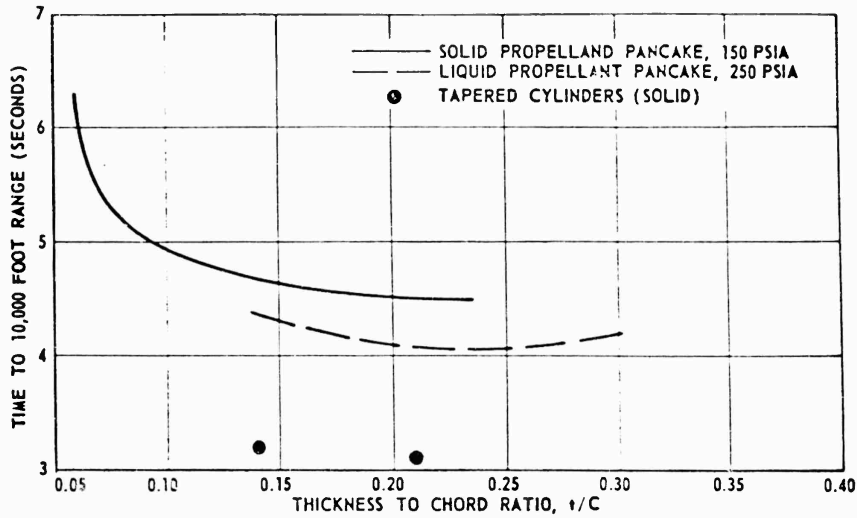


Figure 3.4.38. Time to 10,000 Feet Range Versus Thickness to Chord Ratio.

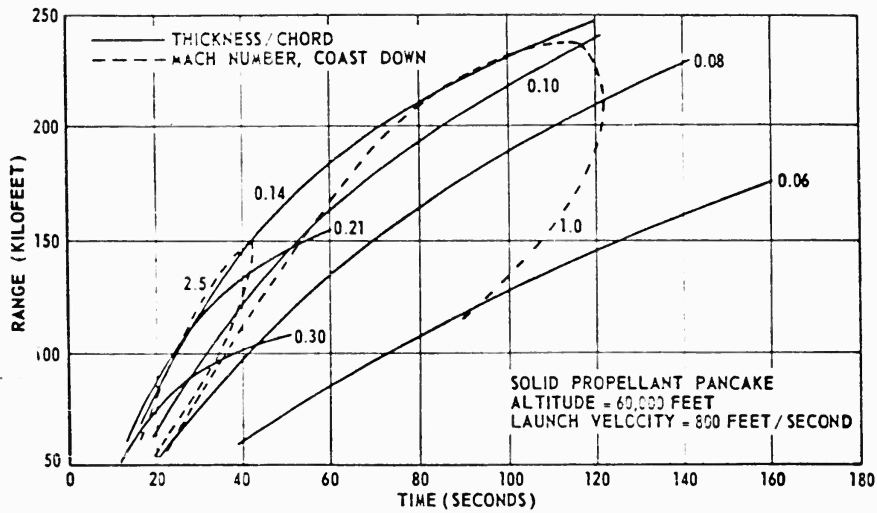


Figure 3.4.39. Range Versus Time.

3.4.5 CONCLUSIONS

The propulsion system studies have shown that several types of efficient propulsion systems can be packaged in the PYE WACKET configuration - systems which will produce very attractive vehicle performance for the air-to-air mission. There are variations in the performance of these systems and variations in the

3.4.46

SECRET

relative development times associated with each; for instance, considering solid propellant systems, the multiple cylinder configurations could be realized in a reasonably short development time. Available propellants and current processing techniques are adequate for this system. The nozzle manifold represents the only real extension in the state-of-the-art, and it should not be an unduly difficult task, considering present day construction materials and insulations. Recent advances in developing swivel nozzles will materially assist in overcoming this problem area.

The pancake solid propellant motor, on the other hand, represents a greater development task. Here a number of problems must be solved: (1) the design of a lightweight pressure vessel must be established, (2) a suitable grain configuration must be worked out, (3) methods of coring and casting such a grain must be developed. (Use of a collapsible mandrel or one made of a low-melting alloy are possible techniques), (4) a reasonable environmental temperature range must be achieved, and (5) ignition of this unusual configuration must be achieved reliably. The foregoing are all problems amenable to solution though more difficult to solve than those associated with the multiple cylinder system.

The liquid propellant system will be similar to current storable liquid systems using pressurized tanks such as the guardian series developed by the Reaction Motors Division of the Thiokol Chemical Corporation. The primary problems will likely (as in the pancake solid) be in the pressure vessel design. Another possible problem area is that of insuring positive expulsion of the propellants at all altitudes and under a g environment. Since engine operating duration is relatively short, an insulated chamber or one employing a simple cooling system such as film cooling should be adequate.

Stable operation at low chamber pressures might have been a questionable area, but recent work on propulsion systems for space vehicles has proved the feasibility of operating satisfactorily at pressures less than 100 PSI.

Insofar as actually achieving the impulses and engine system weights given in previous paragraphs, preliminary proposals obtained from a number of major rocket engine manufacturers substantiate the performance numbers quoted in this study. It is firmly believed that all of these performance numbers are realistic and attainable in the 1961-62 time period.

Future work should encompass detailed propulsion system analysis for the specific vehicle and mission envisioned for missile weapon system development. Though confidence in successfully igniting and launching rocket engines pointed into high velocity air streams has been gained by virtue of the Wagtail program, this area should be further investigated for the PYE WACKET missile.

SECRET

3.4.47

3.4.6 SYMBOLS AND DEFINITIONS

Propulsion System Analysis

I _{sp}	Rocket motor specific impulse, LB ₁ -SEC/LB _m $(F/\dot{w} \text{ or } \frac{C^* C_F}{g})$
F	Thrust, LB
\dot{w}	Propellant flow rate, LB/SEC
C*	Characteristic exhaust velocity, FT/SEC
C _F	Thrust coefficient $(F/P_c A_T)$
g	Gravitational constant, FT/SEC ²
P _c	Combustion chamber pressure, PSIA
A _T	Nozzle throat area, IN ²
γ	Ratio of specific heats-----
m	Molecular weight of exhaust gases
T _c	Flame temperature, °R
R	Gas constant, $\frac{FT - LB}{LB_m - °R}$
A _e	Rocket motor nozzle exit area, IN ²
P _e	Rocket motor nozzle exit pressure, PSIA
P _o	Atmospheric pressure, PSIA
H ₂	Ramjet diffuser exit total pressure, PSIA
H _o	Free stream total pressure, PSIA
H ₂ /H _o	Inlet total pressure recovery
M _o	Mach number
ρ_o	Atmospheric air density, LB/FT ³
ρ_c	Propellant gas density, LB/FT ³
ρ_p	Solid or liquid propellant density, LB/FT ³
V _o	Free stream velocity, FT/SEC
A _o	Ramjet airflow free stream tube area, IN ²
W _a	Ramjet airflow, LB/SEC
A _c	Inlet capture area - projection of inlet frontal area on plane perpendicular to velocity vector at zero angle of attack, IN ²
η_{KE}	Inlet kinetic energy efficiency

SECRET

Propulsion System Analysis (Continued)

A _i	Inlet flow area at inlet station, IN ²
r	Propellant burning rate, IN/SEC
A _B	Propellant burning area, IN ²
C _{T9}	Ramjet thrust coefficient $F/q_0 A_9$
A ₉	Ramjet nozzle exit area, IN ²
L*	Characteristic length (V_c/A_T) IN.

Weight Analysis

x	Stations along lenticular planform measured either side of centerline, IN.
y	Lenticular planform width, measured either side of centerline, IN.
D	Diameter, IN.
t	Missile thickness, IN.
c	Missile diameter, IN.
t/C	Thickness ratio
l	Length of propellant grain in cylindrical rocket motor case, IN.
t _c	Steel thickness, IN.
r _c	Outside radius of cylindrical rocket motor case, IN.
t _{ins}	Insulation and restrictor thickness, IN.
S	Working stress, LB/IN ²
ρ _c	Density of metal for motor, LB/IN ³
ρ _{ins}	Insulation density, LB/IN ³
K ₁	ρ _c × t _c , LB/IN ²
K ₂	ρ _{ins} × t _{ins} , LB/IN ²
B	Nozzle half-angle DEG
ρ _p	Propellant density, LB/IN ³
ϕ	Volumetric loading density-----
W _P	Propellant weight, LB
W _{ip}	Rocket motor inert parts weight (gimbal weight added for performance studies), LB
E	Modulus of elasticity, LB/IN ²
δ	Case deflection, IN.
a	Width of short side of flat plate, IN.

Vehicle Analysis

W _F	Missile launch weight, LB
W _e	Missile empty weight, LB
V	Missile volume, IN ³
W _{ps}	Propulsion system weight, LB

SECRET

3.4.49

SECRET

Vehicle Analysis (Continued)

M. F. Propellant mass fraction (WP/W_{IP})-----
 W_{IP} Rocket motor inert parts weight (no gimbal device), LB
 V_i Initial launch velocity, FT/SEC
 V_f Final missile velocity, FT/SEC
 C_D Drag coefficient
 A Reference area, IN²
 α Angle of attack, DEG
 Ψ Angle of yaw, DEG

3.4.7 LIST OF REFERENCES

- 3.4.1 Connors, J. R., Allen, J. L., Survey of Supersonic Inlets for High Mach Number Applications, NACA RME 58A20, April 1958
- 3.4.2 State-of-the-Art Inlet Pressure Recovery, Convair Fort Worth, October 1958
- 3.4.3 Bumblebee Aerodynamics Panel, University of Texas, October 1958, SECRET
- 3.4.4 Allen, J. L., Piercy, T., Performance Characteristics of an Under-slung Vertical - Wedge Inlet with Porous Suction at Mach Numbers of 0.63 and 1.5 to 2.0, NACA RME 56B15, August 1956
- 3.4.5 Stitt, J. E., Obery, L. J., Performance of an All-Internal Conical Compression Inlet with Annular Throat Bleed at Mach Number 5.0, NACA RME 58E14, August 1958
- 3.4.6 Mach 4.5 Ramjet Study, General Electric Company, September 1958
- 3.4.7 Mach 6 Ramjet Study, General Electric Company, June 1958
- 3.4.8 Hypersonic Ramjet Data, Marquardt Aircraft Company., December 1957
- 3.4.9 Fixed Geometry Ramjet at $Mo = 4.0$, General Electric Company, June 1959
- 3.4.10 Kepler, C. E., Performance of a Variable-Geometry Chin Inlet at Mach Numbers from 1.6 to 3.0, V.A.C. Report R-0455-24
- 3.4.11 Vargo, D. J., Parks, P. N., Davis, O. H., Investigation of a High-Performance Top Inlet at Mach Number of 2.0 and at Angles of Attack to 20°, NACA RME 57A21, March 1957
- 3.4.12 Bumblebee Report No. 284-B, Applied Physics Laboratory
- 3.4.13 Whitehurst, C. A., The Performance and Characteristics of Solid Rocket Propellants, MR-P-66, Convair Fort Worth, 20 March 1958
- 3.4.14 Bulletin of the Eleventh Meeting of the Joint Army-Navy-Air Force Solid Propellant Group, Volume 1, 18-19-20 May 1955
- 3.4.15 Polaris Power Plant Development, Report No. 3520-01M-16, Aerojet-General Corporation, January 1959
- 3.4.50

SECRET

SECRET

- 3.4.16 Hogan, B. T., Rosen, Evaluation of Certain Nitro Compounds as Ballistic Additives in Polyurethane Propellants, 15th JANAF Meeting, June 1959
- 3.4.17 Zimmerman, C. A., Polaris Propulsion Program, 15th JANAF Meeting, June 1959
- 3.4.18 Henderson, C. B. Scheffee, Simmons, Hotter and Runkel, Theoretical Performance of Selected Propellant Systems, Aluminum, Atlantic Research Corporation, July 1958
- 3.4.19 Henderson, C. B., Scheffee, Simmons and Runkel, Theoretical Performance of Selected Propellant Systems, Beryllium, Zirconium, Atlantic Research Corporation, September 1958
- 3.4.20 Compilation of Solid Propellant Theoretical Performance Calculations, Aerojet-General Corporation, August 1959
- 3.4.21 Proposal for the Design, Development and Production of a Solid Propellant Rocket Motor for Redeye, Atlantic Research Corporation, 26 December 1958
- 3.4.22 Seely, Fred B., and Smith, James O., Advanced Mechanics of Materials, John Wiley and Sons, Inc., Second Edition, 1952
- 3.4.23 Haytog, Den, Advanced Strength of Materials, McGraw-Hill Book Company, 1952
- 3.4.24 Lunsford, L. R., Smith, R. L., Stallings, J. P., Titanium Research Program Test Results, S. D. R. 9.14, Convair-Fort Worth, 21 May 1959
- 3.4.25 Materials and Processes Bulletin No. MPB-21, Convair-Pomona, 1 August 1959
- 3.4.26 Anderson, K. D., An Evaluation of Missile Powerplants, Convair-Pomona, TM-332-150, December 1959
- 3.4.27 Silverman, J., Hydrazine Based Storable Fuels, ARDC/Industry Symposium, January 1959
- 3.4.28 Recent Significant Advances in Storable Liquid Propellant Rockets, Aerojet-General Corporation, November 1959
- 3.4.29 Elverum, Jr., G. W. Massier and Lee, Research and Development at Jet Propulsion Laboratory on Storable Propellants Using Hydrazine as the Fuel, ARDC/Industry Symposium, January 1959
- 3.4.30 Thatcher, A. F., Pre-Packaged Liquid Propulsion Systems for Air-Launched Applications, ARDC/Industry Symposium, January 1959
- 3.4.31 Storable Propellants, Rocketdyne, A Division of North American Aviation, Inc.
- 3.4.32 Recent Significant Advances in Storable Liquid-Propellant Rockets, Report No. 1355, Aerojet-General Corporation, November 1957
- 3.4.33 Propellants for Large Liquid Rocket Engines, Report No. CR 110, Aerojet-General Corporation

SECRET

3.4.51

SECRET

- 3.4.34 Elvenum, G. W., Jr., Martinez, J. S., Gillispie, R. W., Results of Theoretical Rocket-Motor-Performance Calculations for Liquid-Propellant Systems, Jet Propulsion Laboratory, California Institute of Technology, 1 November 1957
- 3.4.35 Goldstein, R. E., Prototype Rocket Motor Study-Redeye, Convair-Pomona, TM-332-137, 20 April 1959, SECRET
- 3.4.36 Sechler, E. E. and Dunn, L. G., Airplane Structure Analysis and Design, John Wiley and Sons, Inc., 1942
- 3.4.37 Advance Excerpts from Hexcel Technical Brochure "D", Hexcel Design Testing Data, Hexcel Products, Inc.

3.4.52

SECRET

SECRET

3.5 AERODYNAMIC HEATING

The magnitude of the aerodynamic heating problem and possible solutions to this problem were analyzed for the lenticular vehicle. Primary emphasis in this section of the study was directed toward the establishment of conceptual structural feasibility of the lenticular vehicle while flying in the high heat input environment of supersonic-hypersonic flight.

Problems related to the leading edge, structure aft of the leading edge, and types of structure protection (ablative coverings and porous wall cooling) were first analyzed on a parametric basis. Thereafter, specific examples were evaluated to illustrate structural temperatures, weights of various protective systems, etc., for typical lenticular configurations.

3.5.1 THERMAL ENVIRONMENT

The thermal environment which a lenticular vehicle may experience depends on many parameters, e.g., mission, altitude, velocity, etc. In order to establish structural temperature extremes without resorting to specific velocity histories and material thicknesses, steady state (radiation equilibrium) temperatures were calculated. Reference to Figure 3.5.1 shows the temperature at which a flat plate would be in equilibrium with its surroundings (at a point 3 feet from the leading edge). Care must be taken in using radiation equilibrium temperatures computed for a flat plate since the heat input is lower than that found on a curved body such as the lenticular configurations. This is due to flow through the bow shock wave which results in a higher recovery temperature than that for a flat plate.

As an example of the thermal environment encountered, if the PYE WACKET were used in a skip glide or re-entry type mission, the radiation equilibrium temperature of the leading edge is given in Figure 3.5.2.

Although the lenticular vehicle appears attractive for several missions, emphasis in this study was directed toward the air-to-air manned aircraft defense mission. Where specific trajectories were required for transient heating investigations, flights at launching altitudes of 30,000, 60,000, and 90,000 feet were assumed. Figures 3.5.3 and 3.5.4 illustrate Mach number versus time histories for the two representative configurations, viz. 21 percent and 14 percent thickness-to-chord ratios. Launching velocities assumed were 2500 FT/SEC at 60,000 and 90,000 FT and 800 FT/SEC at 30,000 FT. It can be seen from Figures 3.5.3 and 3.5.4 that the 21 percent t/C version attains a burnout Mach number of 9 at 90,000 FT whereas the 14 percent t/C vehicle burns out at Mach 7.5. These very high speeds produce large thermal loads which are sufficiently high to dictate the need for some kind of protection for the load-carrying structure.

SECRET

3.5.2

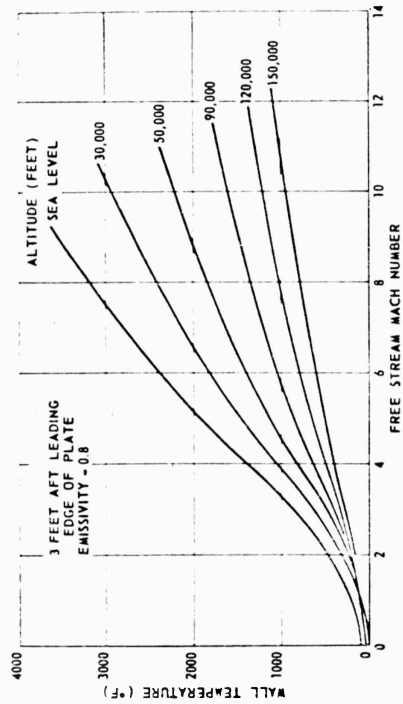


Figure 3.5.1. Radiation Equilibrium Temperature.

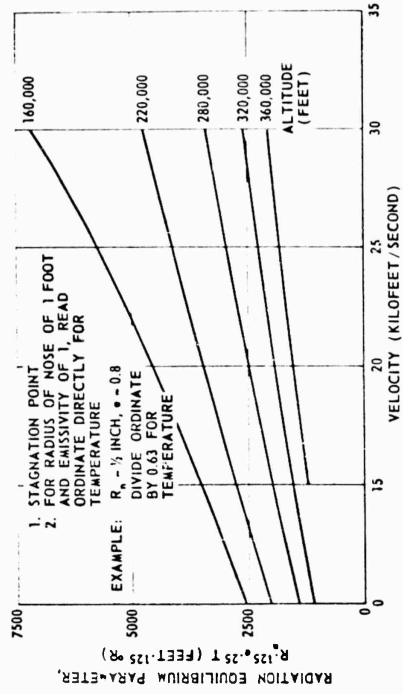


Figure 3.5.2. Radiation Equilibrium Temperature for Re-Entry Trajectories.

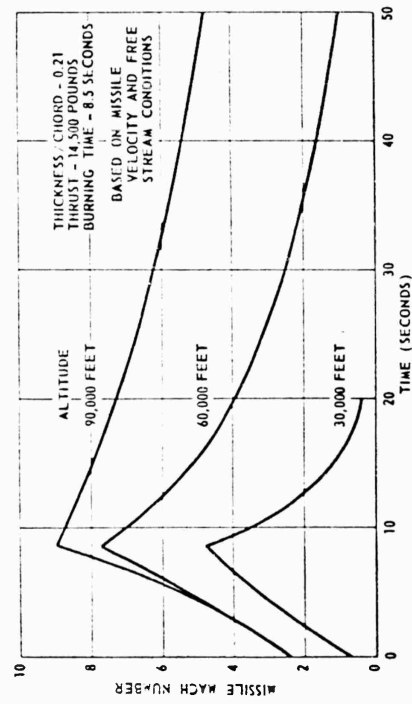


Figure 3.5.3. Mach Number vs Time.

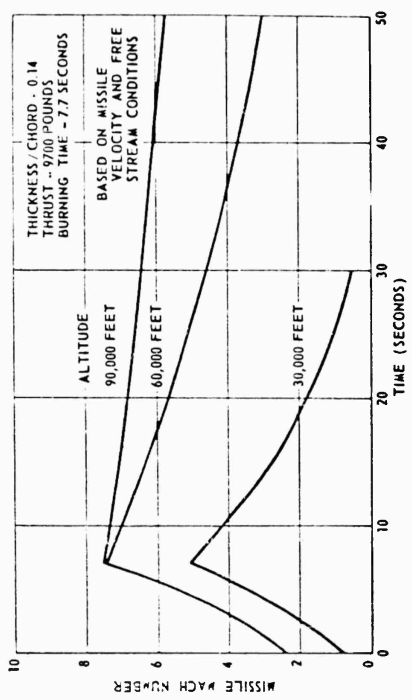


Figure 3.5.4. Mach Number vs Time.

SECRET

For the trajectories assumed, it was shown that aerodynamic heating input was a maximum for the 90,000 FT case where maximum velocity is achieved. Figure 3.5.5 illustrates the difference in adiabatic wall (recovery) temperatures for the range of altitudes studied, and Figure 3.5.6 shows the variation in total heat input as a function of altitude. Both figures indicate maximums at 90,000 FT. For purposes of comparison, total heat inputs were based on flight durations of 50 seconds (equivalent to a cutoff Mach number of one for the 60,000 FT case).

The primary vehicle structure assumed was one in which the outer skins were protected by a layer of ablating material (teflon was determined to be superior to several other possible materials). Heat flux calculations were based on missile temperatures equal to the sublimation temperature of teflon, 800°F. A second type of structure investigated was one employing transpirational cooling techniques.

Due to the air flow through an oblique bow shock wave and a favorable pressure gradient, heat input to the surface varies with axial position on the skin. Heat input also varies with time due to the time variation in velocity. An indication of the magnitude of heat input is obtained from Figure 3.5.7 where it is shown that typical integrated heat inputs for the 90,000 FT altitude case range from 950 BTU/FT² at Station 6 to 150 BTU/FT² at Station 48 for a 21 percent t/C case. The variation with station is less for a 14 percent t/C configuration. A further indication of the severity of the thermal environment is shown in Figure 3.5.8, which presents the time variation in heat input for the 90,000 FT trajectory; a maximum input of 57 BTU/FT²-SEC at Station 6 at 8.5 SEC is shown.

CALCULATION OF THERMAL ENVIRONMENTAL PARAMETERS. In order to determine the aerodynamic heat flux to the skin surface during flight, various parameters were computed. Although real gas effects were considered, these corrections were usually small and necessary only at the maximum velocities reached.

The expression for heat input along the surface is,

$$\dot{q}(t) = h'(t) [T_r(t) - T_w(t)] - \sigma \epsilon T_w^4(t) \quad (3.5.1)$$

At the stagnation point $T_T(t)$ replaces $T_r(t)$. In a non-ablating wall calculation, the most important parameter is the recovery temperature $T_r(t)$. When the wall ablates (or, sublimates) and the thickness decreases, the heat transfer coefficient, $h(t)$, becomes equally important since the ablation speed depends directly on it.

Total temperatures were computed by the use of

$$\frac{u^2}{2gJ} = \int_{T_s}^{T_r} c_p(T) dT \quad (3.5.2)$$

SECRET

3.5.3

3.5.4

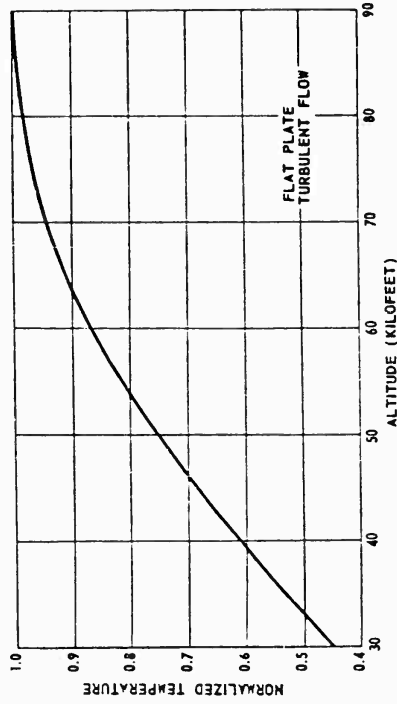


Figure 3.5.5. Normalized Heat Input vs Altitude.

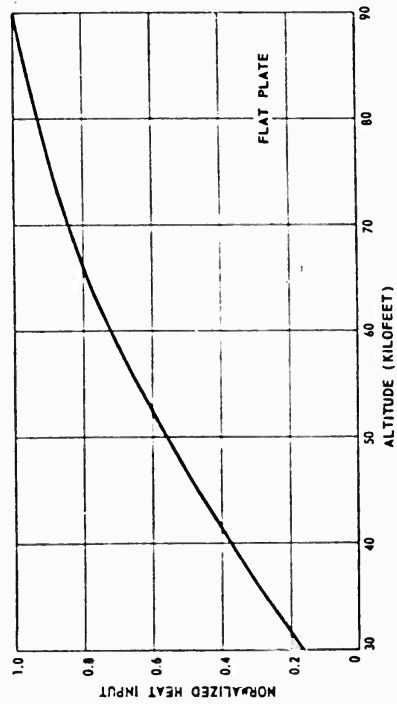


Figure 3.5.6. Normalized Maximum Recovery Temperature vs Altitude.

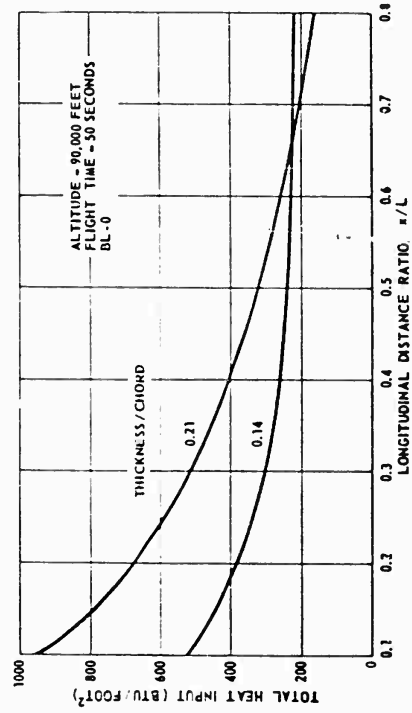


Figure 3.5.7. Total Heat Input vs Dimensionless Distance.

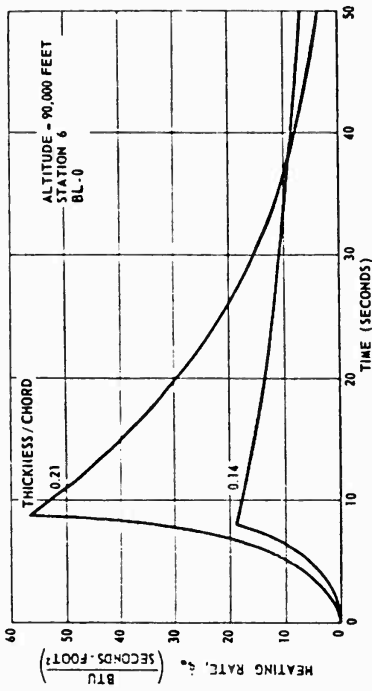


Figure 3.5.8. Aerodynamic Heating Rate vs Time.

SECRET

Real gas (rotation, vibration, and dissociation degree-of-freedom) effects appear in $C_p(T)$. In computing the total temperature on the flat plate, Figure 3.5.3, the free stream enthalpy was added to the enthalpy change, $U^2/2gJ$, and the resulting temperatures found from Reference 3.5.1 (or Reference 3.5.2 when the dissociation degree-of-freedom was excited). The variation of the recovery temperature in flat plate (shock free) flow with free stream velocity is shown in Figure 3.5.9, (dissociation effects begin at about Mach 6). At Mach 8 about 9 percent reduction in recovery temperature is found due to true dissociation degree-of-freedom. Where total temperature was computed behind an oblique shock, perfect gas laws (and tables) were used to obtain local values of pressure and temperature. Since the oblique shocks were somewhat weaker than a normal shock, $M_n < M_1 \sin \theta_w$, negligible error was found due to real gas effects.

Local flow conditions along the surface of the missile were computed from conditions just behind the bow shock wave by Prandtl-Meyer expansions. Recovery temperature was determined from

$$T_r(t) = T_g(t) + [T_r(t) - T_g(t)] N_r \quad (3.5.3)$$

where the recovery factor N_r , has been taken as 0.89 for turbulent flow (local temperature per Reference 3.5.3). The variation of recovery temperature along the surface of a 21 percent t/C ratio configuration is shown for conditions at 90,000 feet, (Figure 3.5.10) at Station 6. Maximum recovery temperatures were 4750°R for the 21 percent t/C and 3700°R for the 14 percent t/C. Flow conditions aft of a normal shock were strongly affected by dissociation, at the higher Mach numbers. A maximum error of 20 percent, at Mach 8.9, was found when comparing real and perfect gas calculations. Errors in local pressure ratio were within 5 percent. These errors, if not corrected, would tend to make the calculations too conservative (overestimate the magnitude of the heat input). Calculations were first made using the perfect gas laws, then corrections were made to real gas conditions, Reference 3.5.3. After the correct local pressures and temperatures were determined, total temperatures were obtained from total enthalpy values by means of real gas charts, Reference 3.5.2.

In order to determine the aerodynamic heat input, a coefficient, h , is computed. This coefficient is related to skin friction and is empirically determined. At the stagnation point, a laminar flow correlation due to Sibulkin, (Reference 3.5.4), was used;

$$\frac{hD}{k_g} = 1.14 \left(\frac{u_{\infty} D}{\mu} \right)_g^{0.5} \left(P_r \right)_g^{0.4} \quad (3.5.4)$$

SECRET

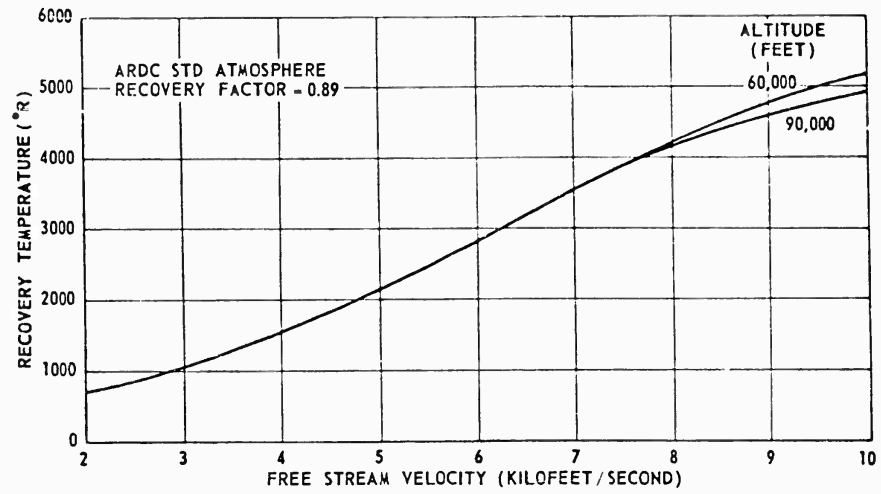


Figure 3.5.9. Flat Plate Recovery Temperature.

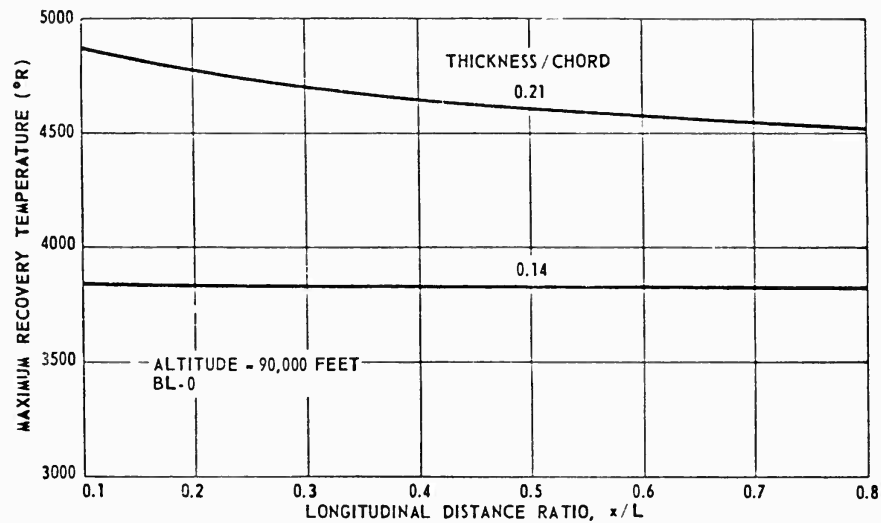


Figure 3.5.10. Turbulent Recovery Temperature vs Dimensionless Distance.

(where D is the diameter of the leading edge and the flow properties are evaluated just behind the bow wave). The coefficient, h, is defined at the stagnation point by

$$h \equiv + \frac{\rho + \rho E T_{ar}^2}{T_r - T_w} \quad (3.5.5)$$

SECRET

The leading edge bluntness has a large effect on the heat transfer to it. Reference to Equation 3.5.4 reveals that the heat transfer coefficient, h , is inversely dependent on the square root of the diameter, D . The variation in "h" with "D" is shown in Figure 3.5.11. The direct variation in heat flux with the heat transfer coefficient, Equation 3.5.1, shows leading edge bluntness to be important.

Along the missile skin surface, aft of the leading edge, a turbulent flow correlation was used. The Colburn-Eckert turbulent flow relationship used to determine the heat flow to a non-ablating surface is given as follows:

$$\frac{h'x}{k_s} = 0.0296 \left(\frac{u_{px}}{\mu} \right)_s^{0.8} (p_r)_s^{1/3} \left(\frac{T_f}{T'} \right)^{0.533} \quad (3.5.6)$$

$$h' = \frac{\dot{q} + \sigma \epsilon T_w^4}{T_r - T_w} \quad (3.5.7)$$

When modifying an incompressible flow correlation to compressible conditions, the properties are evaluated at a suitably determined reference temperature, T' . Compressibility, heat transfer, and real gas effects are included by evaluating the properties at the outer edge of the boundary layer and correcting them to the reference conditions through the temperature ratio $\left(\frac{T_f}{T'} \right)^{0.533}$. The expression used for determining the reference temperature was

$$T' = 0.178 T_r + 0.242 T_s + 0.58 T_w \quad (3.5.8)$$

It may be seen T' is weakly dependent on T_r , the parameter in which dissociation effects are found. In the use of the reference temperature ratio to obtain a heat transfer coefficient, it was assumed:

$$\frac{\mu'}{\mu_s} = \left(\frac{T'}{T_s} \right)^{0.67} \quad \frac{k'}{k} = \left(\frac{T'}{T_s} \right)^{0.87} \quad (3.5.9)$$

Sample calculations over the range of temperatures involved showed these relations to be within a few percent of actual measured values. Flow calculations, over the curved flight surface are described in the discussion of ablation calculations.

As an example of the magnitude of the heat transfer coefficient, at 90,000 FT, values shown in Figure 3.5.12 range to 0.025 BTU/FT²-SEC-°F.

SECRET

3.5.7

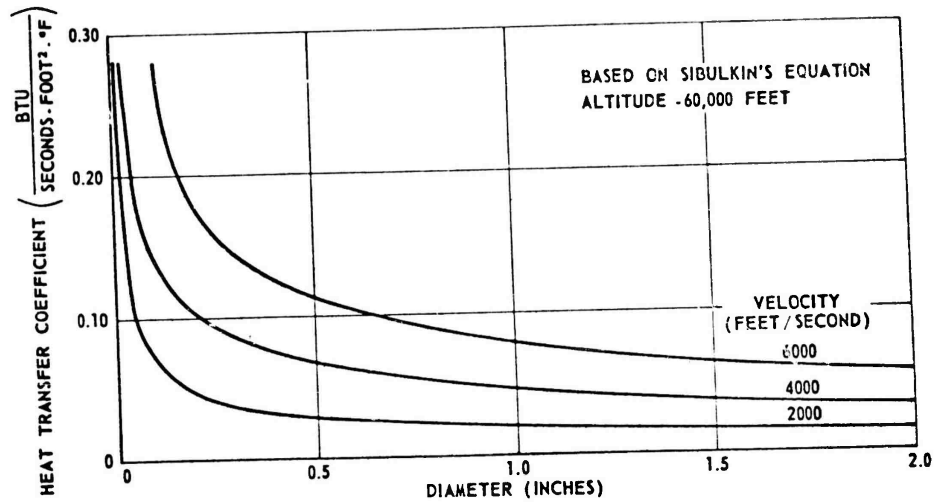


Figure 3.5.11. Heat Transfer Coefficient for Blunt Leading Edge.

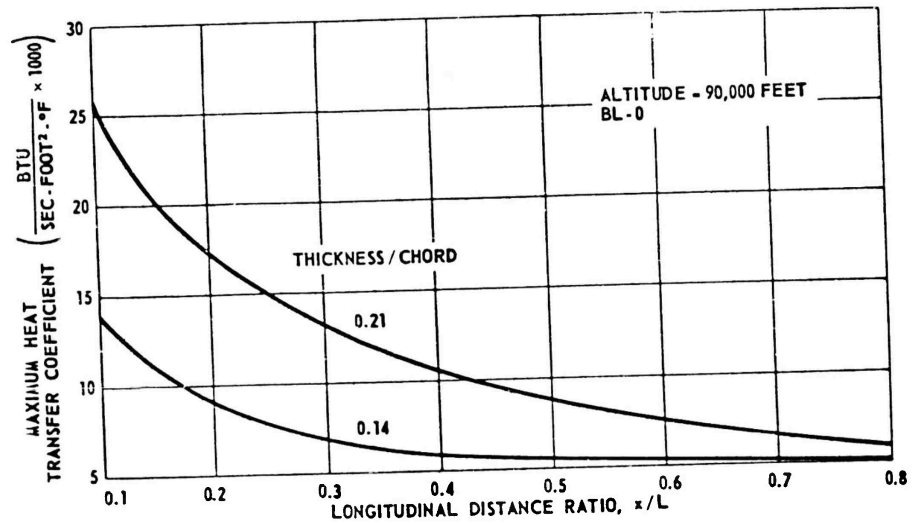


Figure 3.5.12. Heat Transfer Coefficient vs Dimensionless Distance.

3.5.2 STRUCTURAL PROTECTION

THERMAL EFFECTS ON STRUCTURES. To evolve an acceptable airframe structure for a hypersonic flight vehicle, such as the blunted lenticular example studied, careful consideration must be given to the high aerodynamic heating rates encountered. The heat flux history to which the vehicle is subjected will produce high temperatures, and large temperature gradients.

SECRET

Thermal effects on structures depend on temperature, time at temperature, and the temperature gradient. The strength of materials is temperature dependent; however, the reduction in strength is alleviated by short duration heating. The temperature gradient is important since thermal stresses produced in structural components can cause failures. A high temperature level reduces a structure's resistance to buckling in flight due to air loads, and thermal buckling may also be induced. Thermal deflection may change the aerodynamic shape which then causes a re-distribution of pressure over the surface creating, perhaps, increased aerodynamic heating and further deformation. In addition, unprotected structural materials may be heated to the melting point.

CLASSES OF STRUCTURES. Hypersonic flight vehicle structures may be separated into two general classes; hot and cooled structures. The hot structure concept implies the load bearing member is allowed to be heated and no protection is afforded. Adding a refractory covering to a metal surface protects it by reducing the heat flux to the load carrying members due to a low thermal conductivity in the protection material. Heat sink methods utilize a material which has a high heat absorption capacity and will withstand high surface temperatures. The use of an unprotected structure is impossible for many hypersonic missile applications because of the materials problem. The cooled structure may be one which is protected by various means. Two of the most widely studied protective schemes are the ablating wall technique, and the method of fluid injection through the structure. Re-radiation of heat energy is important when the heated surface is at high temperature.

The PYE WACKET leading edge may be a hot structural component, such as graphite; however, the surfaces aft of the edge should be protected.

COOLED STRUCTURE AFT OF LEADING EDGE. The structure aft of the leading edge may be cooled or protected in various ways. Two possible methods are: the use of an ablating material and the use of fluid injection into the boundary layer through the load carrying structure. Various structural advantages indicate that ablation should be the more desirable of the two protection schemes. If a fluid is injected through the load bearing structure, fine porosity is necessary for uniform injection, and a reduction in strength-to-weight ratio results. In addition, control of the injected coolant mass rate is required, plus a mechanism to control and deliver coolant to the surface, which may result in a loss of available space for component packaging, and further increase the total vehicle weight.

Another cooling method that may be considered is the use of a hollow structure containing a liquid which may be heated to the boiling point. The heat absorbed by this coolant reduces the outer skin temperature. After the liquid changes phase, it is ejected from the missile near the aft end. Structural advantages which are gained include the omission of a porous skin.

SECRET

Studies were made to determine the weight penalty incurred by the use of structural protection. First, an ablation analysis was performed, and then an air-to-air injection study was made for comparison. Details of the ablation calculations and results are discussed below.

Ablating Wall, Parameters and Materials. The ablating wall scheme consists of protecting the load bearing structure with a material which will melt, or sublime, at a suitable temperature. The incident aerodynamic heat flux is attenuated by the following means in this type of protection: (1) as the wall sublimates, energy is absorbed in the amount ρh_v BTU/FT²-SEC, (2) as the material issues from the wall in vapor form, it partially blocks the aerodynamic heat input, and (3) sensible heat is absorbed in the conduction layer of the protection that remains. In order to obtain a complete solution for the temperature history of an ablating heat shield metal skin combination, the latent heat of fusion, h_v , the ablation speed, \dot{S} , and the vapor injection cooling effect must be known. Calculations based on an "exact" approach would be extremely lengthy, and physical property data, e. g., latent heat of fusion, are not always available. To facilitate computations, a simplified approach has been used in the present study based on an experimentally determined parameter, "effective heat of ablation," H_{eff} . This parameter enables the calculation of the mass loss of the ablating surface. Using H_{eff} , the remainder of the solution is simplified to a conduction problem in which the heated surface moves with a known ablation speed and at a constant (ablation) temperature. In the following paragraphs the H_{eff} parameter, experimental data, and the choice of ablation heat shield materials are discussed. Some insight into the H_{eff} concept, may be gained by use of simple equations. If the heat diffusion equation is integrated over the wall thickness

$$\int_s^\delta \rho c_p \frac{\partial T}{\partial t} dy = \int_s^\delta \kappa \frac{\partial^2 T}{\partial y^2} dy \quad (3.5.10)$$

and use is made of the boundary conditions,

$$-\kappa \frac{\partial T}{\partial y}(s,t) + \rho h_v \frac{ds}{dt} = h(t) [T_r(t) - T(s,t)] \quad (3.5.11)$$

(at heated surface)

(where radiation is omitted since at low $T(s,t)$ values it is small compared to aerodynamic heating)

$$\frac{\partial T}{\partial y} = 0 \quad (3.5.12)$$

(at inside surface)

SECRET

and the assumed temperature distribution is through the boundary layer,

$$\frac{T}{T_s} = \left[1 - \frac{y-S}{\delta-S} \right]^n \quad (3.5.13)$$

it follows that

$$S = \frac{\dot{q}}{\rho h_v} \frac{\phi}{1+\phi} \quad \phi = \frac{h_v}{c_p T_v} \quad (3.5.14)$$

after a transient period, for times longer than

$$t \gg \frac{n}{n+1} \frac{\phi+1}{\phi} \left(\frac{\rho h_v}{\dot{q}} \right)^2 \alpha \quad (3.5.15)$$

After a short transient period, Equation 3.5.15, the mass rate of ablation is a linear function of aerodynamic heat input \dot{q} , (and of material physical properties C_p , T_v , h_v)

$$\dot{m} = \frac{\dot{q}}{h_v} \left(\frac{1}{1 + \frac{c_p T_v}{h_v}} \right) \quad (3.5.16)$$

Using the definition of H_{eff} and Equation 3.5.16, an expression for H_{eff} is given by Equation 3.5.17. This expression was employed to permit use of laminar flow data in turbulent flow calculations.

$$H_{eff} = \frac{\dot{q}_a}{\dot{m}} = \frac{\dot{q} - \dot{q}_o}{\dot{m}}; \quad \text{where } \frac{\dot{q}_o}{\dot{q}} \text{ is small,} \quad (3.5.17)$$

$$H_{eff} = h_v + c_p T_v + \frac{\dot{q}_o}{\dot{m}}$$

In this analysis q_B/\dot{m} is the blowing term and has been shown to be $\beta(\Delta i)$ in Reference 3.5.5. In turbulent flows, β is about 1/3 the value for laminar flow; experimental data, however, are available only for laminar flow.

An assumption made in the analysis, is that no heat is transferred past the unheated side of the ablating wall. Since this assumption is not absolutely true in an actual case, an indication of its effect is given here. From

$$\dot{q}_o = \dot{m} \left[h_v + c_p T_v + \beta(\Delta i) \right] \quad (3.5.18)$$

it is seen that all the incident aerodynamic heat input is absorbed in the ablating wall, and

$$H_{eff} = \frac{\dot{q}_a}{M_{CALCULATED}} \quad (3.5.19)$$

SECRET

If the heat transferred to the metal load bearing skin is accounted for

$$\dot{q}_o - \dot{q}_{SKIN} = \dot{m}_{ACTUAL} [h_V + C_p T_V + \beta(\Delta i)] \quad (3.5.20)$$

then the mass ablation rate will be overestimated by

$$\frac{\dot{m}_{CALCULATED}}{\dot{m}_{ACTUAL}} = \frac{1}{1 - \frac{\dot{q}_{SKIN}}{\dot{q}_o}} \quad (3.5.21)$$

which may be a large factor when almost all the ablation material is gone. This error tends to underestimate the efficiency of the protection by ablation, therefore making the results conservative.

The choice of an ablation material is predicated on availability of experimental H_{eff} data and on its physical and thermal properties. Many materials may be adequate from the standpoint of good bonding characteristics; however, few have been completely evaluated (experimentally determined data issued for H_{eff}). A large part of the available data are for materials used for higher temperature and higher heat flux conditions (e.g. re-entry bodies). In selecting a material for the blunted lenticular configuration a relatively low ablation temperature is necessary (under $\approx 800^\circ\text{F}$) thereby preventing the basic structure from experiencing large temperature rises. For instance if a material had an ablation temperature of the order of 2000°F , the under-structure would likely reach this temperature. For PYE WACKET, it was desirable from a materials selection standpoint (lightweight structure) and due to protection of internal components, to restrict skin temperatures to under 800°F . This requirement led to the choice of materials such as nylon and teflon. If a material is to be used efficiently, the heat absorbed in diffusion should be small compared to that absorbed in sublimation. Sublimation is desirable, in place of melting, for several reasons. If a material is melted, it may run, or flow, and never be injected into the boundary layer to partially block heat input. The flowing material could conceivably interfere with other missile functions (e.g., aerodynamic control, guidance windows, etc.).

An estimate of the relationship of material properties may be obtained from the ratio-of-heat absorbed in conduction to the total heat absorbed.

$$\frac{Q_c}{Q_i} = \frac{\rho H_{eff} k T_a}{\dot{q}_o^2 t} \quad (3.5.22)$$

A large H_{eff} is desired so as to minimize the ablation weight necessary; however, this increases the heat absorbed in conduction. The ratio Q_c/Q_T must be minimized by a low product of density, conductivity and ablation temperature, $\rho k T_a$. These products for nylon and teflon are as follows:

$$\begin{aligned} \text{nylon} & (71)(3.4 \times 10^{-5})(600) = 1.66 \\ \text{teflon} & (130)(3.3 \times 10^{-5})(800) = 3.44 \end{aligned}$$

SECRET

Nylon is shown to be superior to teflon insofar as the conduction to total heat absorbed ratio is concerned; however, other factors show teflon to be superior. Data exists by which H_{eff} may be estimated in turbulent flow, Reference 3.5.5.

$$H_{eff} = f(\Delta i)_o$$

by subtracting $(h_v + C_p T_v)$ from laminar flow experimental data to obtain the blowing component $\beta(\Delta i)$. After reducing the laminar blowing term, $\beta_L(\Delta i)$, to the turbulent blowing term, $\frac{\beta_L(\Delta i)}{3}$, an H_{eff} for teflon was available. The use

of nylon is less attractive than teflon, one reason being the scarcity of valid data. Also nylon does not sublime but melts. Nylon-binder combinations retain the melt until it is vaporized; however, the surface temperatures necessary are too high for the present application. Another practical advantage of teflon over nylon is that there is greater industrial experience in bonding it to metal.

Methods of Computing Ablation Cooling. The calculation of the time rate of ablation has been accomplished in two ways: estimates made by hand calculations and more accurate computations by numerical methods programmed on a digital computing machine.

1. Hand Solution. The hand computations were used in parametric studies. These calculations were of sufficient accuracy to obtain the relative mass ablated at various altitudes. A flat plate model was assumed to be heated according to the trajectories of Figures 3.5.3 and 3.5.4. The mass rate of ablation was obtained by Equations 3.5.1 and 3.5.19.

The heat flux as a function of time, $\dot{q}_o(t)$, is that heating a non-ablation body receives in the same environment with the same surface temperature T_a . The results of these calculations yielded the total (and time rate of) mass loss, but did not include the structural temperature response. Since the aerodynamic heating conditions were obtained for flow over a flat plate, the ablation rates computed did not agree closely with the more refined machine calculations where flow conditions along the actual surface were found. These results were useful, however, in establishing preliminary ablation weight requirements.

2. Computing Machine Solutions. In computing the temperature history of the metal load bearing structure, a more refined solution was necessary. The metal skin temperature was obtained by solving the transient heat conduction equation for the composite geometry of ablating wall and metal skin. The aerodynamic heating parameters (see paragraph 3.5.1, Thermal Environment) were computed with properties evaluated at the outer edge of the boundary layer along the curved surface, approximated by a series of wedges. After the flow computations through the oblique bow wave were completed, local flows along the surface were computed by use of the Prandtl-Meyer expansion. The perfect gas computations were checked for real gas effects and were found to be accurate.

SECRET

Temperature histories at various positions through the ablating wall and metal skin were obtained by numerical techniques using a medium sized digital computing machine. A brief description of the numerical analysis follows.

The equation defining temperature between the surfaces of the ablation material was

$$\rho c_p \frac{\partial T}{\partial t}(y, t) = k \frac{\partial^2 T}{\partial y^2}(y, t); s < y < \delta \quad (3.5.23)$$

A constant thermal conductivity, k , was used, (linearizing the heat conduction equation). The boundary conditions at the heated surface were (when $T(s, t) < T_a$):

$$-k \frac{\partial T}{\partial y}(s, t) = h'(t) [T_r(t) - T(s, t)] - \sigma \epsilon T^4(s, t) \quad (3.5.24)$$

When the heated surface reached the ablation temperature, $T(s, t) = T_a$, the H_{eff} concept was used, Equations 3.5.1, 3.5.19 and 3.5.23. A non-catalytic wall was assumed in cases where dissociation was present.

The boundary condition at the unheated surface

$$\left[-k \frac{\partial T}{\partial y}(s, t) \right] = \left[\rho c_p \delta \frac{dT}{dt} \right]_{\text{METAL}} \quad (3.5.25)$$

TEFLON

A one dimensional numerical analysis was used in solving the ablation problem. The heated surface was allowed to reach the ablation temperature, at which time increments of mass were removed according to Equation 3.5.19. The experimentally determined data, H_{eff} , was stored in the machine as a function of heat input to a non-ablative wall.

The conduction of heat through the remaining solid material was computed in the usual manner using the ablation temperature as the heated surface boundary condition. As is usual, in solving problems on a digital computer, the calculus of finite differences was used. This involved the replacement of a continuum by a lumped parameter system. A node or lump, at which the surface temperature was computed, contained an amount of mass proportional to the weight of the ablation material and the number of lumps. The incremental mass removal due to ablation had been summed and stored in the machine. When the sum of the incremental masses lost to ablation equaled the mass of the surface lump; this lump was removed.

The technique described in the preceding paragraph enabled economical and adequately accurate computations. The computer code was checked by comparison with analytical results under the assumption that the interior boundary of the ablating wall does not experience a temperature change. Figure 3.5.13 shows the results of a code check.

SECRET

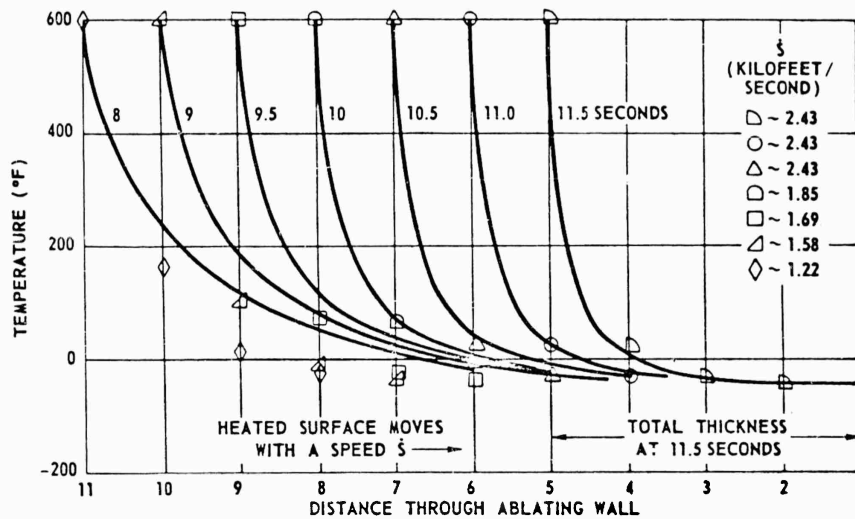


Figure 3.5.13. Ablating Wall Example Used to Check Numerical Computation Against Analytical Solution.

It may be seen that better agreement results after a period of ablation. The temperature gradient is very steep (in this case) during steady ablation and is proportional to

$$e^{-s\sqrt{y}/\alpha}$$

For a large ablation velocity, \dot{S} , or low thermal diffusivity, α , a large gradient is established. In the case of the code check, the incident heat flux was sufficiently high, such that most of the heat is absorbed in the ablation process.

Results and Discussion of Ablating Heat Shield Calculations. The results of the ablating heat shield calculations are presented in Figures 3.5.14 through 3.5.24. The principal results of the analysis have been the determination of: (1) the altitude for which aerodynamic heating is most severe, (2) the amount of ablation material required at the extreme condition, and (3) the load bearing skin temperature histories.

Before the determination of the load bearing structure temperatures, parameteric studies revealed the 90,000 foot altitude trajectory to be more severe with respect to aerodynamic heating than the 30,000 or 60,000 foot trajectories. The amount of ablation material needed at 60,000 feet was 65 percent of that required at 90,000 feet; and, at 30,000 feet, 25 percent of the 90,000 feet requirements (Figure 3.4.14). The variation in ablative material required, was due to unequal missile launching velocities, and higher thrust-to-drag ratios at increased altitude.

SECRET

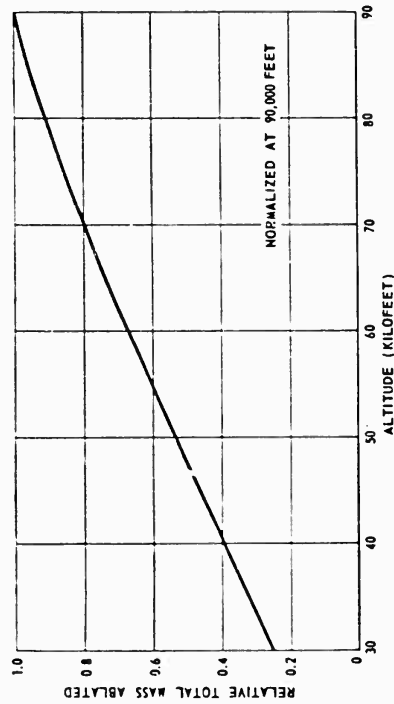


Figure 3.5.14. Total Ablation Mass Loss vs Altitude.

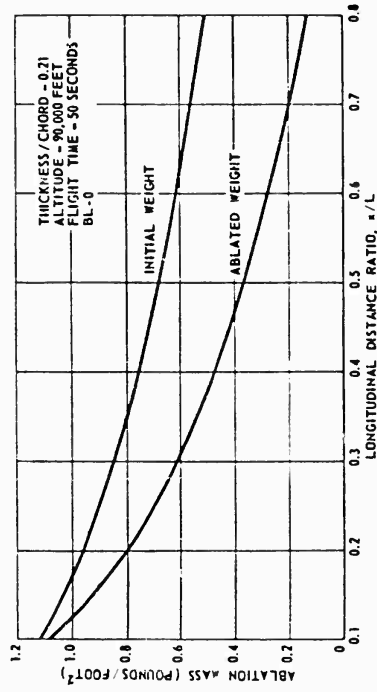


Figure 3.5.15. Ablation Mass vs Dimensionless Distance.

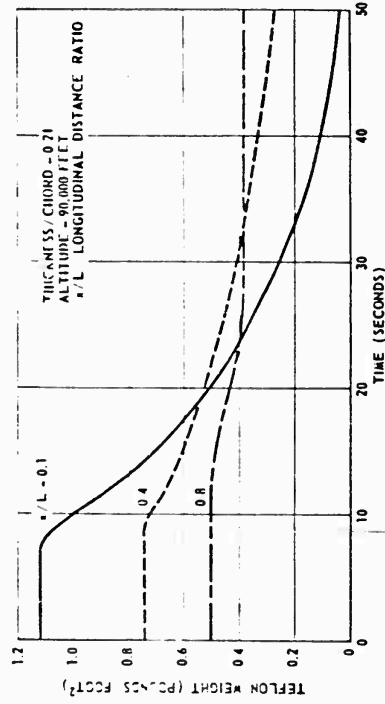


Figure 3.5.16. Ablation Mass vs Dimensionless Distance.

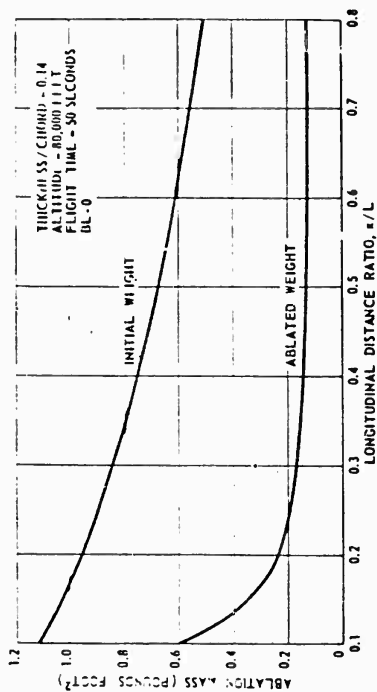


Figure 3.5.17. Ablation Weight vs Flight Time.

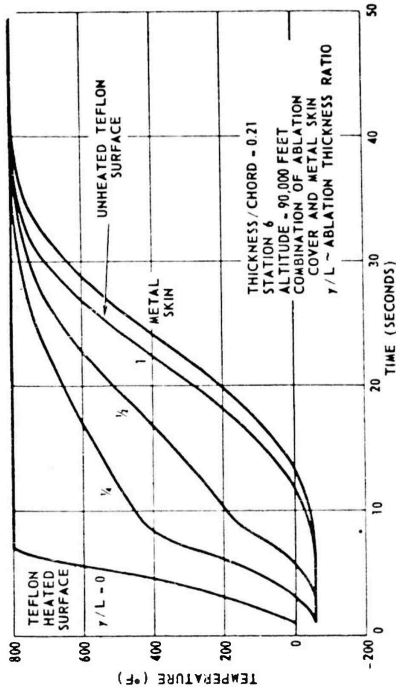


Figure 3.5.19. Temperature Distribution vs Time.

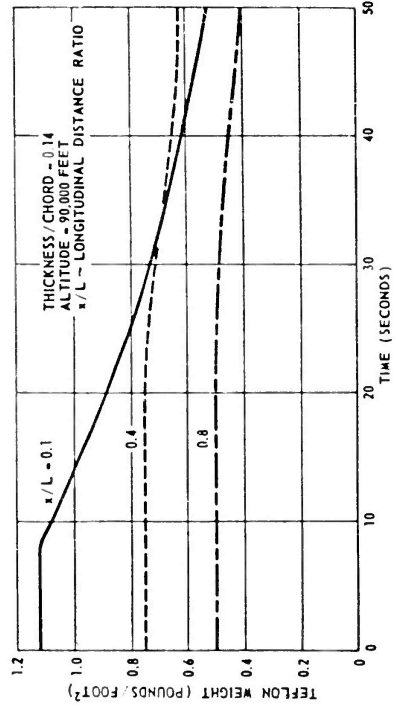


Figure 3.5.18. Ablation Weight vs Flight Time.

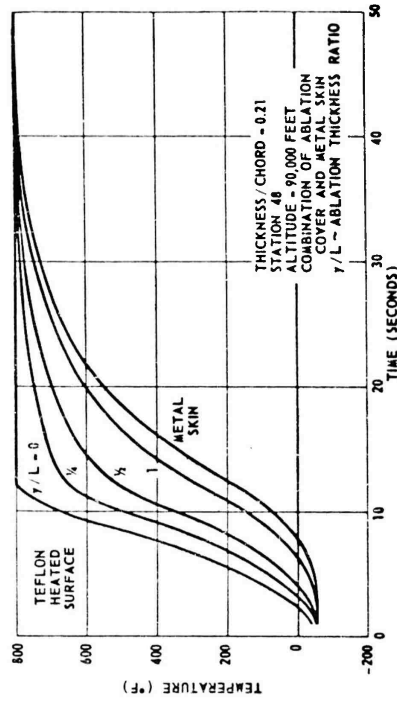


Figure 3.5.21. Temperature Distribution vs Time.

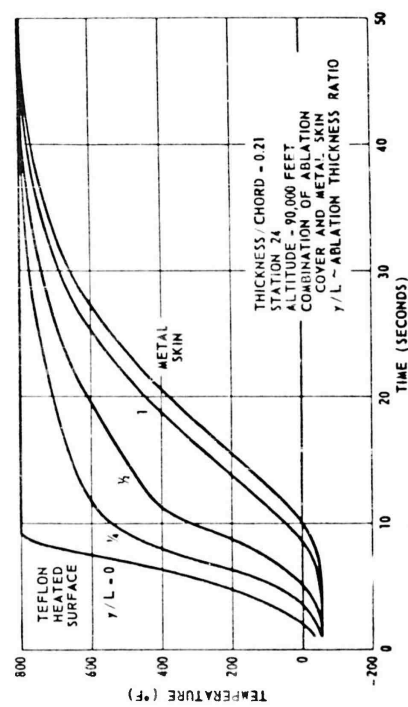


Figure 3.5.20. Temperature Distribution vs Time.

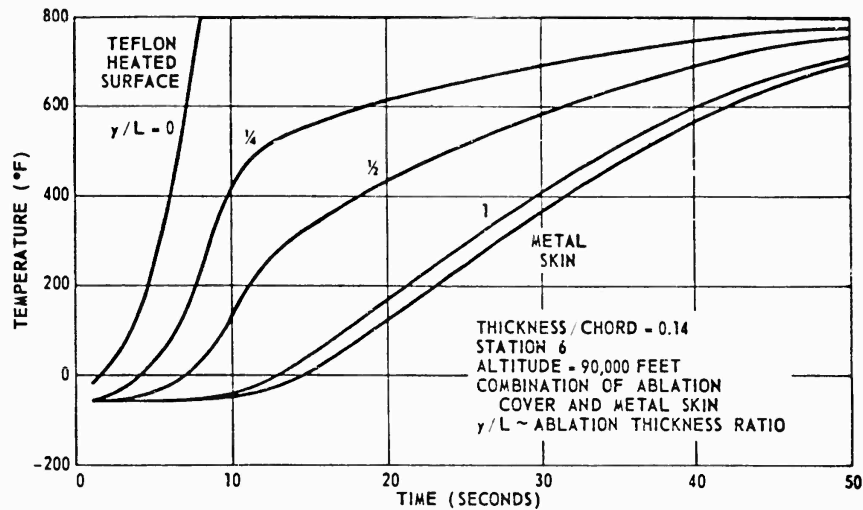


Figure 3.5.22. Temperature Distribution vs Time.

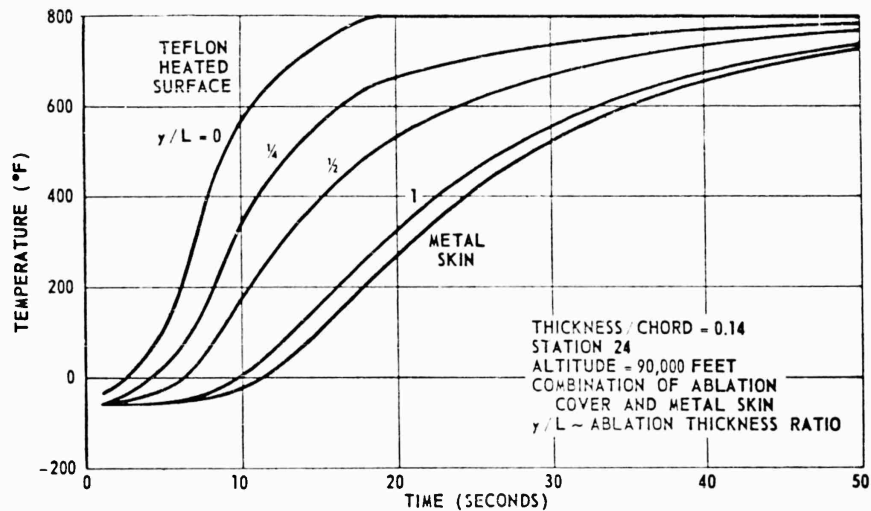


Figure 3.5.23. Temperature Distribution vs Time.

Numerical calculations, performed with the aid of the digital computing machine, were carried out at the maximum heating conditions in order to evaluate the extent of protection necessary to prevent the load bearing skin from exceeding 800°F under this very severe environment. An initial weight of teflon was estimated at 30 pounds, and the temperature history was found through the combined heat shield (teflon) and load bearing skin (0.018 inch titanium). The teflon was not completely removed during the 50 seconds of flight studied. The

SECRET

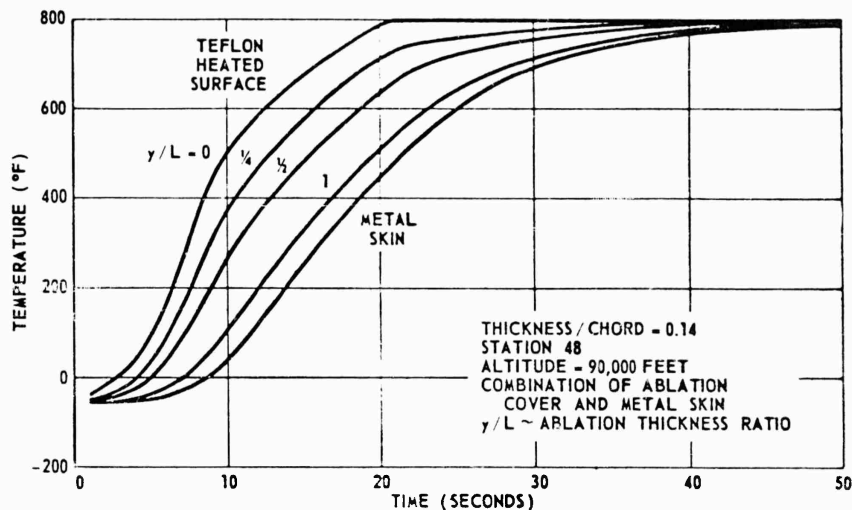


Figure 3.5.24. Temperature Distribution vs Time.

distribution of the initial teflon shield is given for the 21 percent t/C version, Figure 3.5.15, and for the 14 percent t/C version, Figure 3.5.16. The distribution of the teflon remaining at the end of the 50 second flight is shown on the same two figures. The total teflon ablated was found to be 21 pounds for the 21 percent t/C and 10 pounds for the 14 percent t/C version. The initial thickness of the teflon shield was 0.087-inch at Station 6, 0.063-inch at Station 24, and 0.026-inch at Station 48. Since the temperature of the titanium skin did not reach 800°F at 50 seconds at all stations of the 14 percent t/C version, an estimated weight of 15 to 20 pounds of teflon will result in sufficient protection from aerodynamic heating. The amount of teflon remaining at the three stations at various times, during the 50 second flight, is shown in Figure 3.5.13 for the 21 percent t/C case and in Figure 3.5.14 for the 14 percent t/C version. It may be noted that the teflon does not ablate a sufficient amount to remove a surface lump at some stations (e.g., Figures 3.5.17 and 3.5.18). The protection afforded by the teflon at these stations is that of a resistance layer that attenuates heat input by virtue of a low thermal diffusivity.

The temperature histories of the load bearing skin (0.018-inch titanium) and the teflon heat shield are shown in Figures 3.5.19 through 3.5.24. The 21 percent t/C version temperature history is presented in Figure 3.5.19 (at Station 6) in Figure 3.5.20 (at Station 24) and, in Figure 3.5.21 (at Station 48). The same temperature information, for the 14 percent t/C version is shown in Figure 3.5.22 (Station 6), Figure 3.5.23 (Station 24), and Figure 3.5.24 (Station 48).

Temperature gradients through the teflon and titanium skin combination may be obtained from Figures 3.5.19 through 3.5.24. If the temperature distribution through the teflon and titanium combination wall were required (for thermal

SECRET

stress calculation) at Station 6 for the 21 percent t/C version at 10 seconds, a vertical line passed through 10 seconds on the horizontal scale of Figure 3.5.19 enables the spacial variation in temperature to be obtained. Since the heated surface has moved toward the load bearing skin, the teflon thickness is obtained from Figure 3.5.17.

Thermal Stresses in the Ablating Wall. The thermal stresses in the ablating teflon heat shield were calculated, based on the assumption that the teflon behaves as an elastic material. As the material approaches the sublimation temperature, partial stress relief will occur, and any estimates, made using elastic considerations will be conservative. In order to obtain an indication of the stress levels involved, thermo elastic equations were used as a design approximation. The mathematical model chosen for the ablating wall was a slab, restrained in bending, and heated on one side. The thermal stress in a flat plate, restrained in bending, is given by the expression:

$$\sigma_x \frac{(1-\nu)}{\bar{\alpha} E_y} = \frac{1}{\delta} \int_{-\delta/2}^{\delta/2} T(y) dy - T(y) \quad (3.5.26)$$

The temperature distribution through the teflon (Figures 3.5.15 through 3.5.20) may be expressed by an equation of the form, where the exponent "n" is determined by curve fitting the numerically computed results.

$$T(y) = T(\delta) + [T(s) - T(\delta)] \left(\frac{\delta - y}{\delta} \right)^n \quad (3.5.27)$$

Insertion of the expression for temperature, at any time t, into the thermal stress equations result in the following simple stress expressions. The stress will act in the tangential direction, at time t.

$$\sigma_c(s,t) = - \frac{\bar{\alpha} E_y n}{1-\nu} \left[\frac{T(s,t) - T(\delta,t)}{n+1} \right] \quad \text{(compressive stress at the heated surface)} \quad (3.5.28)$$

$$\sigma_r(\delta,t) = + \frac{\bar{\alpha} E_y}{1-\nu} \left[\frac{T(\delta,t) - T(\delta,t)}{n+1} \right] \quad \text{(tensile stress at the cooled surface)} \quad (3.5.29)$$

It was found that the maximum thermal stresses occurred, for both the 14 percent and 21 percent configurations, at about 13 seconds. The stresses calculated at these times were of the order of 2,000 PSI, maximum. The tensile strength for teflon ranges between 1500 and 3000 PSI, thereby indicating the need for a careful stress investigation in an actual design.

The interfacial bond between the teflon and metal wall has not been considered in the simple analysis described here. More exact calculations would include the metal skin, and result in the forces acting on the fibers of the teflon

SECRET

at the bond surface but exerted by forces set up by the temperature distribution through the teflon. It would seem advisable to study the bonding problem analytically and experimentally to assure the designer of a strong joint. Teflon properties used in the calculation were:

$$E_y = 5.8 \times 10^{-6} \text{ PSI}$$

$$\alpha = 10 \times 10^{-5} \text{ IN/IN } ^\circ\text{C}$$

$$\nu = 0.25$$

Structural Protection by Transpiration Cooling. Transpiration cooling is accomplished by blowing a fluid into the external-free-stream through a porous external missile skin. Since fairly reliable data on supersonic heat transfer with air-to-air injection is available, air was chosen for the coolant. Due to heat absorption in vaporization, coolant weight would be saved using water or some other liquid. The principal disadvantages of the system are the same for both coolants, however. The structural disadvantages and storage, pumping, and distribution pose as great a problem for water as for air. These disadvantages are the principal reason that injection cooling is considered to be inferior to the ablation method.

Transpiration rates were calculated (assuming air as the injected gas) by means of steps outlined below:

1. A heat balance on a unit area of the porous surface results in:

$$St (\overline{T}_r - T_w) = \frac{\rho_w U_w}{\rho_s U_s} (T_w - T_c) \quad \text{Reference 3.5.6} \quad (3.5.30)$$

re-arranging terms:

$$\frac{\overline{T}_r - T_w}{T_w - T_c} = \frac{\rho_w U_w}{\rho_s U_s} \frac{1}{St}$$

where St is the Stanton number including the transpiration cooling. The dependence of St/St_0 on $\left(\frac{\rho_w U_w}{\rho_s U_s}\right) \frac{1}{St_0}$ for air as the injected gas, is

found in References 3.5.6 and 3.5.7. It has been found, that this plot does not vary appreciably with Mach number.

2. The information found in References 3.5.6 and 3.5.7 were replotted as (See Figure 3.5.25)

$$\frac{St}{St_0} = f\left(\frac{\rho_w U_w}{\rho_s U_s} \frac{1}{St_0}\right) \quad (3.5.31)$$
$$\left(\frac{\rho_w U_w}{\rho_s U_s}\right) \frac{1}{St_0} = \frac{\overline{T}_r - T_w}{T_w - T_c}$$

SECRET

3.5.21

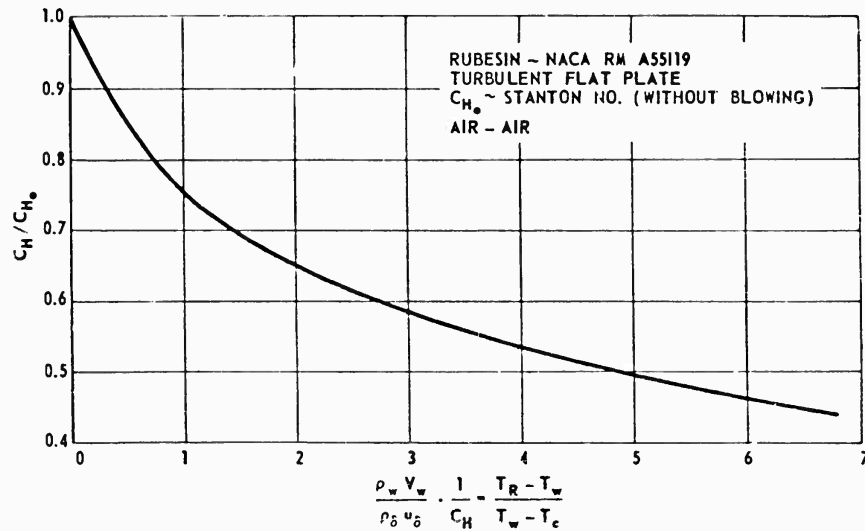


Figure 3.5.25. Mass Injection Effect on Station Number.

3. A coolant temperature at a constant value of 0°F, was assumed.
4. A wall temperature of 800°F (the maximum temperature the ablation cooled wall will attain), was assumed.
5. Previously calculated $T_p(t)$ values (to calculate the temperature ratio and consequently the abscissa of Figure 3.5.25, were used.
6. Values of St/St_0 , using (a) were obtained.
7. Previously calculated St_0 (Stanton number for no blowing) to find St , were used.
8. From (a) and previously determined $\rho_\delta u_\delta$, the blowing mass rate per square foot, $\rho_w v_w$, was found.

Air Cooling Results. The results of the transpiration cooling calculations outlined above are shown in Figures 3.5.26 and 3.5.27. These figures show a comparison of the mass rates of transpiration (or air) and ablation (of teflon). It was found that the air-to-air transpiration mass rates were higher than teflon mass loss rates, with an overall ratio of 2.5 to 1.

The necessary weight of air was found to be 50 pounds for the 21 percent t/C and 25 pounds for the 14 percent t/C configuration, based on a 50 second flight at 90,000 feet. The additional weight allocated for storage and delivery of air was estimated to be 50 pounds.

THE LEADING EDGE STRUCTURE. In order to reduce drag, a small diameter leading edge is desired; however, aerodynamic heat input increases with decreasing leading edge diameter. In addition, the temperature rise of a

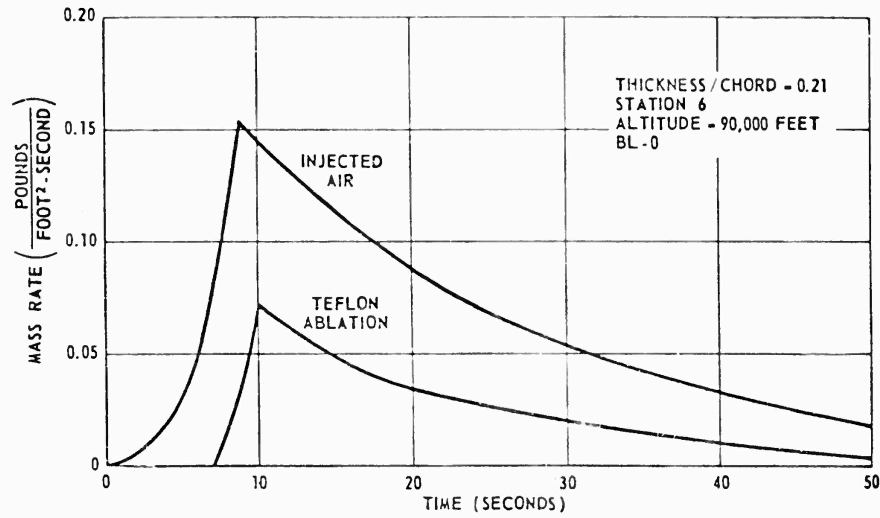


Figure 3.5.26. Mass Rates of Transpiration and Ablation vs Time.

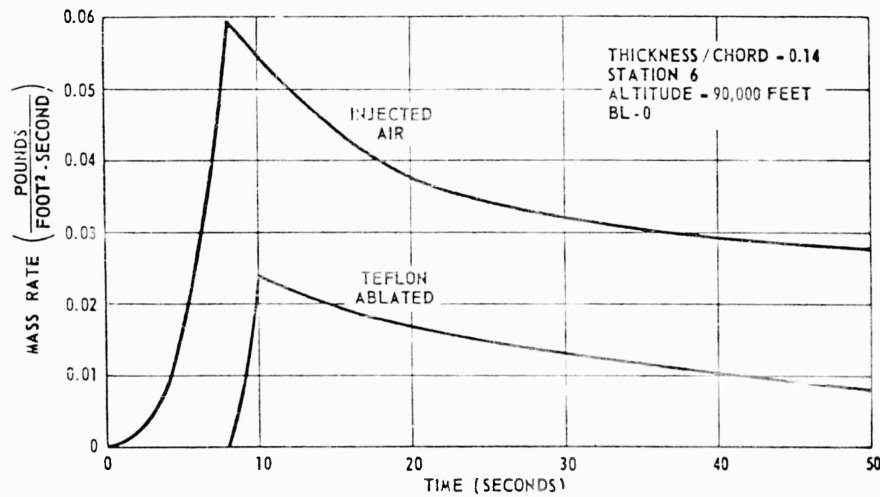


Figure 3.5.27. Mass Rates of Transpiration and Ablation vs Time.

leading edge increases with decreasing mass available to absorb the incident heat input. In view of these facts, the diameter of the leading edge of a hypersonic vehicle surface must be based on compromises.

The design of a leading edge, from thermal considerations, may be approached from both the hot and the cooled structure point of view. The hot structure may be made of a material which will withstand high temperatures and resulting thermal stress. The material should have a high emissivity (so as to

re-radiate much of the energy gained due to aerodynamic heating), be adequately strong, and be easy to fabricate. The cooled structure may be made of teflon, to utilize the ablation mechanism, or consist of a metal structure cooled by fluid injection. Calculations for cooled structures, have been made in the section devoted to areas aft of the leading edge. Disadvantages in the use of cooling schemes at the leading edge are: (1) a possible change in edge diameter in the case of ablating teflon, and (2) weight addition and loss of packaging volume in the case of the injection of cooling fluids.

In the following paragraphs the design of a graphite leading edge is discussed.

Leading Edge Materials, and Construction. Graphite has been examined as the material of leading edge construction due to its high temperature tolerance, emissivity, and thermal conductivity. The strength of graphite, especially in some of its advanced forms, e. g., pyrographite, was felt to be adequately high to withstand the air loads.

The Raytheon Corporation has produced pyrographite which differs strikingly from ordinary graphite. The basal planes in the crystal structure of pyrographite are arranged in a different manner than in the ordinary material. No well defined position relative to neighboring layers occurs in the new material, rather they are arranged in a random fashion. A high degree of anisotropy is effected. Thermal conductivity in one plane is two orders of magnitude higher than in another direction. From a heat conduction point of view, this would tend to isolate the cooler from hotter sections of the leading edge in a peripheral direction. A comparison of the physical properties of graphite and pyrographite is given below. Temperature and thermal stress calculations were completed using the material properties for graphite.

	<u>Graphite</u>	<u>Pyrographite</u>
E_y	= 1.1×10^6 PSI	
$\bar{\alpha}$	= 1.15×10^{-6} °F ⁻¹	= 0.09×10^{-6} °F ⁻¹
ν	= 0.25	
ρ	= 96 LB/FT ³	= 125
k	= 2.24×10^{-2} BTU/SEC-°F/FT-FT ²	= 4.5×10^{-2} (along basal planes) = 4.5×10^{-4} (normal to basal planes)
C_p	= 0.18 BTU/LB-°F	= 0.23
ϵ	= 0.8	= 0.81 - 0.9
Tensile strength	= 2-4,000 PSI	= 15-20,000 PSI

In comparing the physical properties of the two graphite materials, it is found that the strength of pyrographite is the most important difference in this application. The tensile strength is 15 to 20,000 PSI for pyrographite, 5 times

SECRET

as high as the ordinary material. Although the usual form of graphite is felt to be adequate, the improved material may be used because of its higher strength. It may be noted that the densities and specific heats differ, such that temperature calculations using pyrographite would result in lower values than were obtained in Figures 3.5.25 and 3.5.26.

Leading Edge Temperature Estimations. Early in the study program, prior to the calculation of the final trajectories, a diameter of about 0.5-inch for the leading edge was determined to be the smallest that would be thermally adequate. Subsequently, a parametric study was conducted to determine the variation, with altitude, of the leading edge temperature. The geometry of the leading edge, for which the following temperature estimations were made, is shown in Figure 3.5.28. The temperature was computed for a stagnation point on the centerline of the missile, through the thinnest section of graphite, 0.125-inch. The trajectories used are shown in Figures 3.5.3 and 3.5.4. For the parametric study, a simplified hand solution has been performed. In this solution the following assumptions were made:

1. The graphite temperature was uniform through a small thickness.
2. Re-radiation could be neglected.
3. Ideal gas relationships could be used.

In view of the assumptions, the results of this study are used for a comparison only. After it was determined that maximum temperatures occurred at 90,000 feet altitude, the computer solutions were performed using this trajectory, Figures 3.5.3 and 3.5.4. In the computer solution, none of the aforementioned assumptions were made. The hand solution has been obtained in the following manner.

The equations used have been derived in previous studies, References 3.5.8 and 3.5.9. Using a stagnation temperature history shown in Figure 3.5.29 and suitably averaged heat transfer coefficient, the temperature of the graphite at times t such that, $t_1 < t < t_2$ is given by

$$T(t) = T_r(t) - \left(\frac{l}{l + \frac{hL}{2K}} \right) \frac{G}{h} \left\{ \left[\frac{T_r(t) - T_r(t_1)}{t_1} \right] e^{-ht/G} \left(e^{\frac{ht}{G}} - 1 \right) + \right. \\ \left. \left[\frac{T_r(t_1) - T_r(t_2)}{t_2 - t_1} \right] \left[e^{h(t-t_1)/G} - 1 \right] \right\} \quad (3.5.32)$$

SECRET

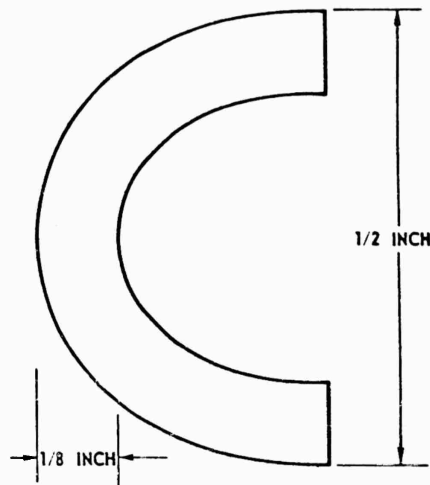


Figure 3.5.28. Leading Edge Geometry.

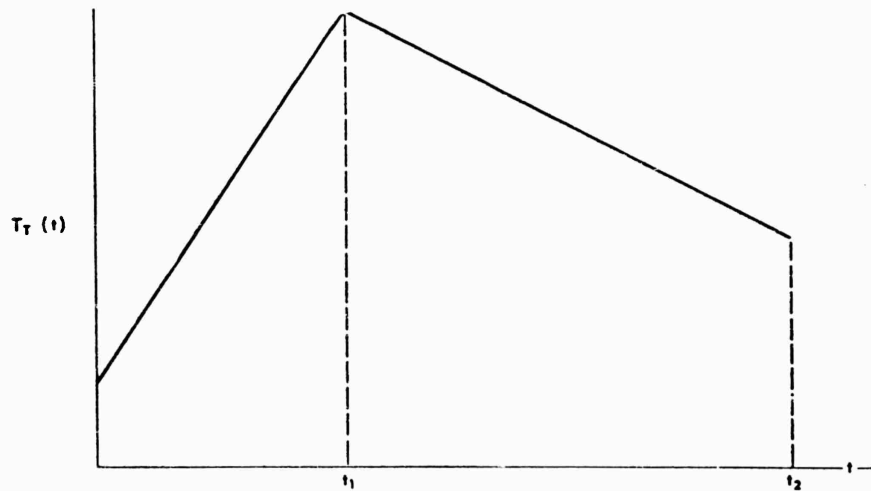


Figure 3.5.29. Stagnation Temperature History.

The maximum temperature experienced by the graphite, over the trajectory in question, occurs at time t_m given by

$$t_m = -\frac{G}{h} \ln \left\{ \frac{\left[\left(1 + \frac{hL}{2K} \right) \left[\frac{T_T(t_1) - T_T(t_2)}{t_2 - t_1} \right] \right]}{\left[\frac{T_T(t_1) - T_T(0)}{t_1} \right] \left[e^{ht_1/G} - 1 \right] + \left[\frac{T_T(t_2) - T_T(t_1)}{t_2 - t_1} \right] e^{\frac{ht_1}{G}}} \right\} \quad (3.5.33)$$

SECRET

The maximum leading edge temperature was computed, using the equation previously described, at time t_m . The results of the computations are graphically presented on Figure 3.5.24, showing 90,000 feet to be the extreme case.

Leading Edge Temperature Solutions. Based on work described above, the material and diameter of the leading edge was determined. Since the temperature, reached by the aerodynamically heated leading edge, will depend upon its diameter and material of construction, more refined calculations were performed for a verification of the design. The final temperature calculations were performed with the aid of a digital computing machine. In the following paragraphs a description of the methods used in the analysis have been presented.

The geometry chosen for the machine calculations was at the thickest section such that maximum temperature gradients and thermal stress would result. A simple leading edge, shown in Figure 3.5.30, was designed. The rib was included for attachment to the missile structure. The thermal model shown in Figure 3.5.31 was used in the analysis since the maximum temperature gradient will occur at the thickest section. Calculations, based on the material and geometry described above, were performed for the maximum heating condition, 90,000 feet. (Refer to Figures 3.5.1 and 3.5.24.)

A multi-dimensional temperature distribution study was recognized as a possible approach to the analysis of the leading edge though such a lengthy and expensive study could not be justified during the present study. A two-dimensional analysis revealed that excessive digital computer time would have been necessary. This was due to the requirement for double precision in the matrix inversion code, caused by the extremely high conductance values of small pieces of graphite. In view of these facts a one-dimensional analysis was used.

In the transient one-dimensional heat conduction problem at the leading edge, the following equations were used. The heat diffusion equation in cylindrical geometry is

$$\rho c_p \frac{\partial}{\partial t} T(r,t) = k \frac{\partial}{\partial r} r \frac{\partial T}{\partial r}(r,t) \quad 0 < r < s \quad (3.5.34)$$

with boundary conditions at the heated surface (stagnation point)

$$-k \frac{\partial T}{\partial r}(t,s) = h(t) [T_f(t) - T(t,s)] - \sigma \epsilon T^4(t,s) \quad (3.5.35)$$

and the inner surface

$$\frac{\partial T}{\partial r}(0,t) = 0$$

The heat transfer coefficient and total temperature determination, which included real gas effects, is described in paragraph 3.5.1, Thermal Environment. The heat transfer coefficient is not corrected for a reference temperature,

SECRET

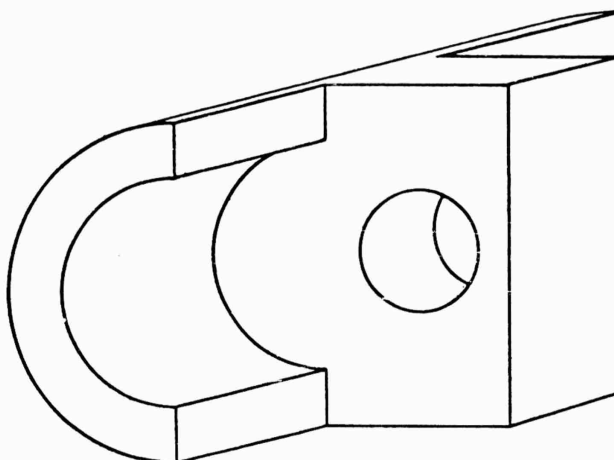


Figure 3.5.30. Simplified Leading Edge.

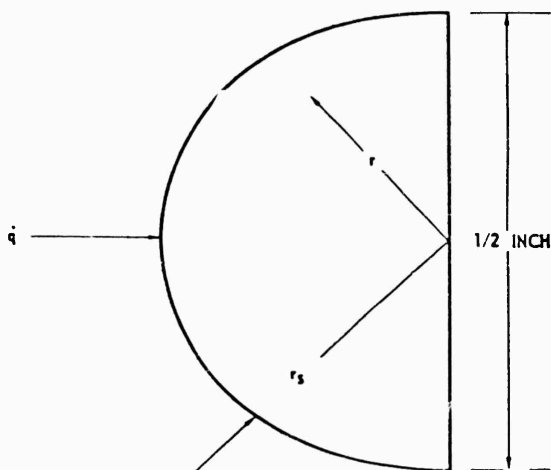


Figure 3.5.31. Thermal Model.

since at constant pressure the laminar flow heat transfer coefficient is weakly dependent on temperature. It may be noted that dissociation effects were included assuming a non-catalytic wall.

The heat conduction equation was expressed in finite difference form resulting in a recurrence equation for a general interior node

$$T(t+\delta t, r) = \left(\frac{k}{\rho c_p} \right) \frac{\delta t}{\delta r^2} \left[\left(1 + \frac{1}{2m} \right) T(r+\delta r, t) + \left(1 - \frac{1}{2m} \right) T(r-\delta r, t) \right] + \left[1 - \left(\frac{2k}{\rho c_p} \right) \frac{\delta t}{\delta r^2} \right] T(r, t) \quad (3.5.36)$$

SECRET

Similar equations expressing the temperature rise of the surface nodes were used. These equations were solved on the computing machine using a code described in Reference 3.5.10.

Results and Discussion of Leading Edge Temperature Calculations. The temperature histories of the heated surface of the graphite leading edge are shown in Figure 3.5.32 for the 21 percent t/C and in Figure 3.5.33 for the 14 percent t/C configuration. It may be seen that the maximum temperatures are 3300°F (at 11 seconds) for the 21 percent t/C and 2750°F (at 11 seconds) for the 14 percent t/C configuration. The average surface temperature over 50 seconds was 2000°F in both the 21 percent t/C and 14 percent t/C ratio cases. The temperature gradient has been plotted at the time at which it was found to be maximum, at 8 seconds after launching (Figure 3.5.34). The temperature difference between the heated surface and center portion of the graphite was about 60°F. Due to the high specific heat and density of pyrographite, calculations made using these material properties would result in lower temperatures.

Thermal Stresses in the Leading Edge. A simple infinite solid cylinder model has been used as a design approximation of the leading edge. The cross section is taken at the centerline of the missile and it has been assumed a rib used to attach the edge was placed at this point.

The equations relating thermal stress to temperature distribution may be found in Reference 3.5.11. The temperature distribution through the leading edge, (Figure 3.5.34), may be approximated by

$$T(r,t) = T(o,t) + [T(s,t) - T(o,t)] \left(\frac{r}{r_s}\right)^n \quad (3.5.37)$$

where "n" is determined by curve fitting. Insertion of the temperature distribution into the integral equations of thermal stress result in the following simple expressions, Reference 3.5.11.

$$\sigma_T(o,t) = \frac{\bar{\alpha} E}{1-\nu} [T(s,t) - T(o,t)] \frac{2}{n+2} \quad \text{tension at center} \quad (3.5.38)$$

$$\sigma_c(s,t) = -\frac{\bar{\alpha} E}{1-\nu} [T(s,t) - T(o,t)] \left[\frac{2}{n+1} - 1\right] \quad \text{compression at heated surface} \quad (3.5.39)$$

These stresses act in the circumferential direction.

The results of the calculations were that both compressive and tensile stresses were about 50 PSI, much below the allowable stress in graphite.

SECRET

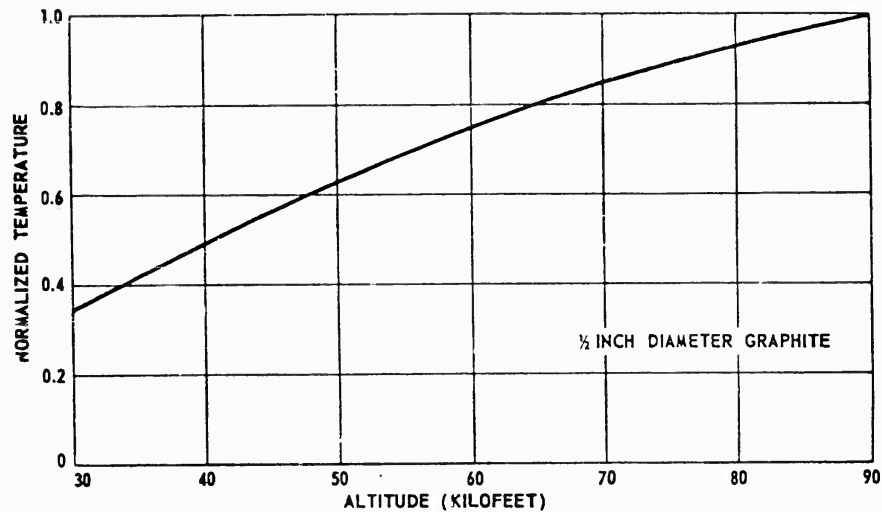


Figure 3.5.32. Normalized Leading Edge Temperature.

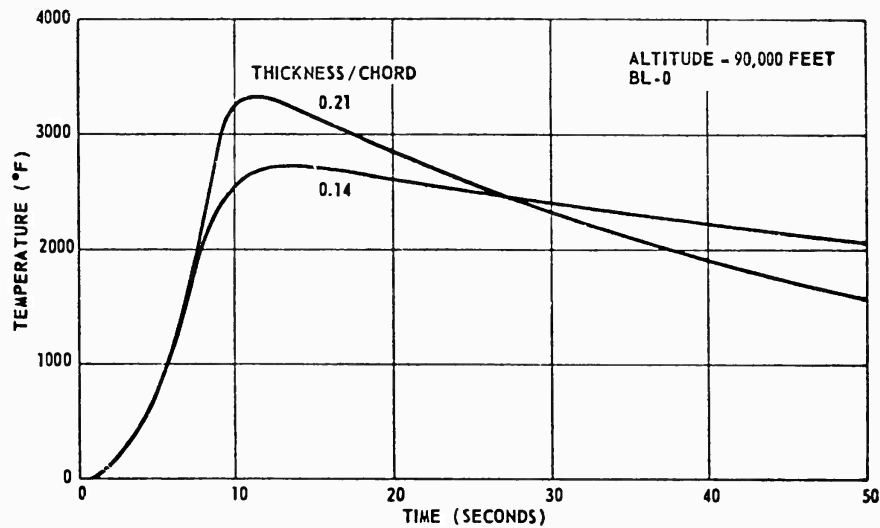


Figure 3.5.33. Leading Edge Surface Temperature vs Time.

3.5.3 SUMMARY

An analytical study has been made to determine the feasibility of the PYE WACKET configuration from a thermal point of view. A conceptual design approach has been used. Calculations have been made to determine the thermal environmental conditions to which the missile is subjected. Several means to

SECRET

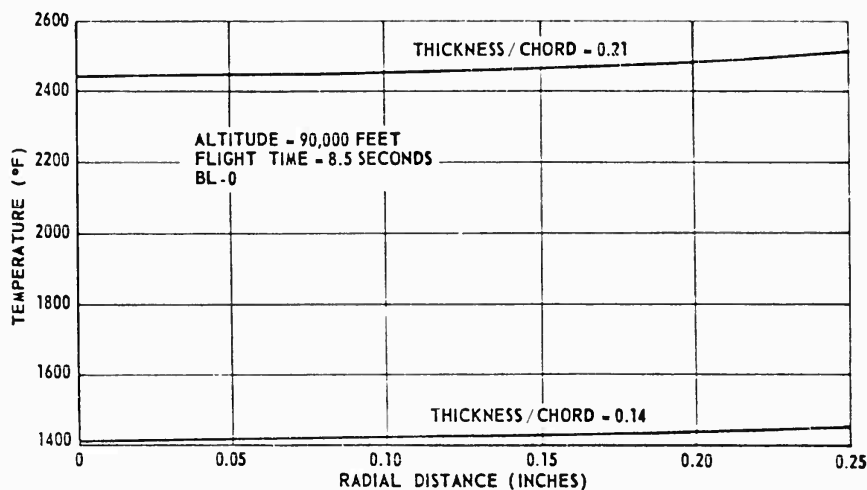


Figure 3.5.34. Temperature Gradient Through Leading Edge.

enable the structure to retain sufficient strength and stiffness were investigated. Temperature histories, computed for simple structural models and the example trajectories, have demonstrated that a moderate amount of thermal protection (a maximum of 30 pounds of teflon for a 60-inch diameter configuration) will allow the use of available engineering materials. Brief studies have shown the teflon ablation scheme to be superior to that of air-to-air transpiration cooling, from a simplicity and weight penalty standpoint. A heat sustaining graphite leading edge has been found to be adequate. Insofar as surviving the thermal environment, a blunt leading edge covered with an ablative material could be employed. This approach, however, would possibly increase drag, thereby lowering overall missile performance, and for this reason was not investigated further in this study.

This phase of the study has clearly shown that a composite structure (metal skin plus ablative covering) will satisfy the structural requirements of PYE WACKET while flying in the severe thermal environment of a high Mach number air-to-air mission. Certain problems may be encountered in a development program, e.g., thermal stress-buckling of structural elements, heating problems, radomes or IR domes (treated briefly in subsection 3.8) handling problems of an ablatively covered vehicle, etc.; however, all of these appear to be amenable to solution in a reasonably short development program.

A type of structure which also might be of interest for some PYE WACKET missions (though time did not permit a detailed evaluation in this study phase) is a double wall consisting of skin in which a liquid coolant is packaged. The coolant is allowed to boil-off as heat is absorbed. The vapor is ejected through the skin, but is ducted to the aft end of the missile to contribute propulsive thrust force.

SECRET

Future work would include detailed analyses of the various protective schemes considering cost as well as cooling efficiency. Experimental evaluation of the most promising techniques should be conducted in a "hot" wind tunnel where conditions can be carefully controlled and measurements made accurately.

3.5.4 SYMBOLS AND DEFINITIONS

C_H	Stanton number
C_p	Specific heat, BTU/LB
D	Diameter, feet
E_y	Young's Modulus
G	Heat capacity, BTU/FT ² -SEC
h	Heat transfer coefficient, BTU/FT ² -SEC-°F
h_y	Heat of fusion, BTU/LB
H_{eff}	Effective heat of ablation, BTU/LB
i	Enthalpy, BTU/LB
Δi	Enthalpy difference across boundary layer, BTU/LB
J	Mechanical equivalent of heat, LB/FT/BTU
k	Thermal conductivity, BTU/SEC-°F/FT-FT ²
L	Wall thickness, feet
M	Mach number
m	$r/\delta r$ - number of nodes in conduction
\dot{m}	Mass rate, LB/FT ² -SEC
n	Curve fitting constant
N_r	Recovery factor
\dot{q}	Heat flux density, BTU/FT ² -SEC
Q	Heat stored, BTU/FT ²
r	Radial distance, feet
s	Surface value of y , r , feet
St	Stanton number
t	Time, SEC
U	Velocity in x direction, FT/SEC
v	Velocity in y direction, FT/SEC

Greek

$\bar{\alpha}$	Thermal coefficient of expansion, IN/IN °F
α	Thermal diffusivity, FT ² /SEC
β	Blowing coefficient in ablation
ϵ	Emissivity
δ	Ablating wall thickness, feet
δ'	Load bearing skin thickness, feet
ρ	Density, LB/FT ³ , slugs/FT ³

SECRET

Greek

μ	Viscosity, slugs/FT-SEC
ν	Poisson's ratio
σ	Stephen Boltzman's constant, BTU/FT ² -°R ⁴ -SEC
$\sigma_{t,c}$	Stress, PSI
θ_w	Wave angle, degrees

Subscripts

o	No ablation, no transpiration
δ	Outside of boundary layer
W	Wall
r	Recovery
T	Total
n	Normal
v	Vaporization
B	Blockage by evaporated ablation material

Superscripts

'	At the reference condition
·	Differentiation respect to time

3.5.5 LIST OF REFERENCES

- 3.5.1 "Gas Tables," J. H. Keenan and Joseph Kaye, John Wiley & Sons, Inc., 1948
- 3.5.2 "Composition and Thermodynamic Properties of Air in Chemical Equilibrium," W. E. Moeckel and K. C. Weston, NACA TN 4265
- 3.5.3 "Tables and Graphs of Normal-Shock Parameters at Hypersonic Mach Numbers and Selected Altitudes," Paul W. Huber, NACA TN 4352, September 1958
- 3.5.4 "Heat Transfer Near the Forward Stagnation Point of a Body of Revolution," N. Sibulkin, Journal of Aeronautical Sciences, August 1952
- 3.5.5 "Recent Advances in Ablation," Mac C. Adams, American Rocket Society Journal, Volume 29, No. 9, pp. 625-632
- 3.5.6 "An Analytical Estimation of the Effect of Transpiration Cooling on the Heat-Transfer and Skin Friction Characteristics of a Compressible Turbulent Boundary Layer," M. W. Rubensin, NACA TN 3341
- 3.5.7 "The Effect of Fluid Injection on the Compressible Turbulent Boundary Layer - Preliminary Tests on Transpiration Cooling of a Flat Plate at

SECRET

3.5.33

SECRET

- M = 2.7 with Air as the Injected Gas," N. W. Rubesin, C. C. Pappas, and A. R. Okuno, NACA RM A55119
- 3.5.8 "Evaluation of Methods of Computing Aerodynamic Heat Input to Hypersonic Vehicles," W. A. McIntosh, and R. G. Shook, Convair-Pomona, TM-349-3
- 3.5.9 "Dimensionless Temperature and Thermal Stress Charts for use in Design Problems Requiring First Order Approximation Accuracy," W. A. McIntosh, Convair-Pomona, TM-332-124
- 3.5.10 "General 15 Lump Computer Solution for Aerodynamic Heating," Tinkham, E. I., TM-332-1235
- 3.5.11 "Theory of Elasticity," S. Timoshenko, McGraw - Hill Book Company, 1934
- 3.5.12 "The ARDC Model Atmosphere, 1956," Geophysics Research Directorate, USAF, December 1956, R. A. Minzer, and W. S. Ripley, ASTIA Document 110233

3.5.34

SECRET

3.6 STRUCTURES

Evaluation of the design feasibility of the FYE WACKET configuration required study of several other technical areas in addition to the basic investigation of aerodynamic feasibility. One of these areas included the study of structural problems associated with the rather unique configuration of the lenticular vehicle. Limitations imposed by the configuration, possible construction techniques, and selection of suitable materials were studied in order to evolve a satisfactory structural configuration for PYE WACKET.

The basic configuration studied was the blunted lenticular, or Model III in terms of the wind tunnel model designations. The details of this planform and cross section are shown in Section 2, Configuration Evaluation.

A liquid propellant rocket motor configuration was arbitrarily chosen for specific study; however, the techniques and results obtained are applicable to a solid propellant powered vehicle.

In the following paragraphs, the structure is analyzed first from static considerations alone, i.e., internal pressure and aerodynamic loads, and then is treated from a dynamic standpoint (aeroelastic considerations).

3.6.1 TYPES OF MATERIALS CONSIDERED

Three alloy materials were considered for the skin and the propellant pressure vessel. The strength-weight and stiffness-weight ratios of these titanium and stainless steel alloys are shown in the following tables for two temperatures. The titanium is an all beta alloy shown as B-120 or Ti-13V-11 Cr-3 Al. Other metals considered were PH 15-7 MO and 17-7 PH corrosion resistant alloys. The stresses shown in Table 3.6.1 are expected tensile yields in the welded condition.

Table 3.6.1
TENSILE YIELDS IN WELDED CONDITION

Material	Strength-Weight Ratio Comparison			
	Tensile Yield Strength-PSI		Strength-Weight Ratio	
	800°F	1000°F	800°F	1000°F
B-120 Ti	117,000	110,000	670,000	632,000
PH 15-7 Mo	166,300	121,000	555,000	400,000
17-7 PH	130,000	100,000	434,000	334,000

SECRET

Stiffness-Weight Ratio Comparison				
Material	Modulus of Elasticity-PSI		Stiffness-Weight Ratio	
	800°F	1000°F	800°F	1000°F
B-120 Ti	14×10^6	13×10^6	80.5×10^6	75×10^6
PH 15-7 Mo	26×10^6	24.5×10^6	87×10^6	82×10^6
17-7 PH	25.8×10^6	22.8×10^6	86×10^6	76×10^6

The data in Table 3.6.1 show that B-120 Ti is 20.7 percent and 58 percent superior in strength weight ratio to PH 15-7 Mo at 800°F and 1000°F, respectively. This more than offsets the superiority in stiffness-weight ratio of 15-7 Mo over B-120. B-120 Ti is 7.5 percent and 8.5 percent less in stiffness-weight ratio than PH 15-7 Mo at 800°F and 1000°F, respectively.

The above data indicates that for the alloys considered, B-120 Ti will provide the minimum weight for skin and tank material when based on the same strength and stiffness requirements.

CONSTRUCTION TYPES. The basic structure was divided into the following sections for analysis purposes: forward section (leading edge aft to the rocket motor), rocket motor end closures, rocket motor top and bottom plates, and rocket motor stiffening posts. A sketch of this configuration is shown in Figure 3.6.1.

In the process of determining the most efficient structure for the forward section of PYE WACKET, corrugated sections, solid sheets, and honeycomb skins were evaluated. For the rocket motor end closures, only solid sheets were studied in any detail. Three types of construction were examined for the large, relatively flat plates comprising the top and bottom of the rocket motor: solid sheets, grid skins, and honeycomb structure.

The analysis and the recommended structure for the various subsections are presented below.

3.6.2 STATIC CONSIDERATIONS

FORWARD SECTION. This portion of the structural analysis was performed to determine the minimum weight design possessing adequate load-carrying capability for the following three types of structures:

1. Corrugation stiffened sheet
2. Solid sheet
3. Honeycomb

3.6.2

SECRET

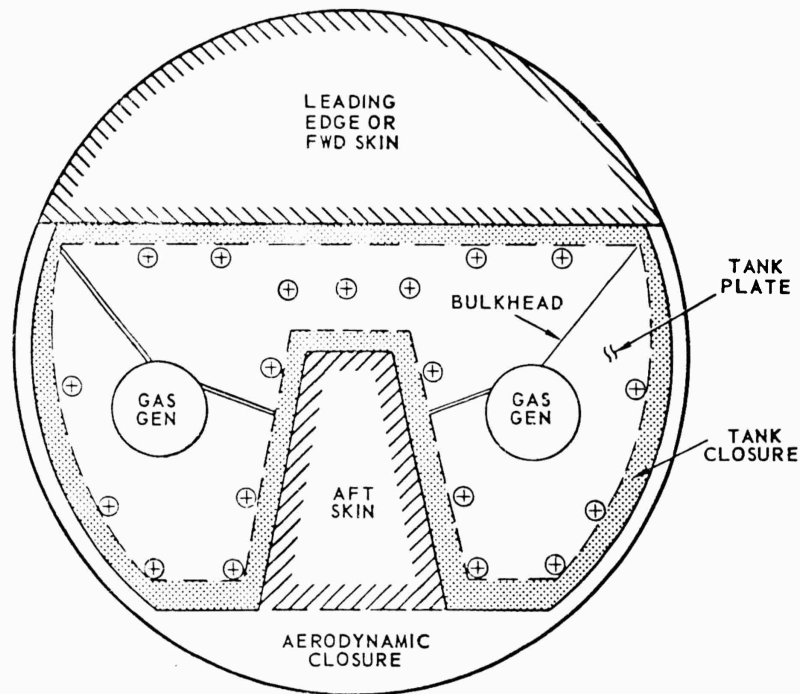


Figure 3.6.1. Basic Structure Configuration.

Basic parameters considered common to all three types of structures were:

1. Maximum bending moment (chordwise) at the aft end of the forward section is 35,000 IN-LB.
2. The forward structure will not buckle.
3. The material to be used is B-120 titanium alloy.

Corrugation Type. Figure 3.6.2 illustrates the type of structure analyzed. One object of the analysis was the determination of the optimum thickness (t_c) and pitch (L) for various skin thicknesses (t_s). Skin thickness required was then determined for various (t/c) ratios for an external net moment at Station 26 of 35,000 IN-LB. Dimension "b" on Figure 3.6.2 is 15.5 inches, taken from layouts of nominal configurations.

The pressure on the skin was taken to be the maximum aerodynamic pressure superimposed with the +10 PSI or -3 PSI induced due to angle of attack. The B-120 titanium was assumed to be 800°F. Of course, during most of the flight, skin temperatures would be much less than 800°F (tending to make some of the results conservative), only approaching this value near the end of a maximum duration flight at which time most of the ablative covering would have been depleted (Reference subsection 3.5).

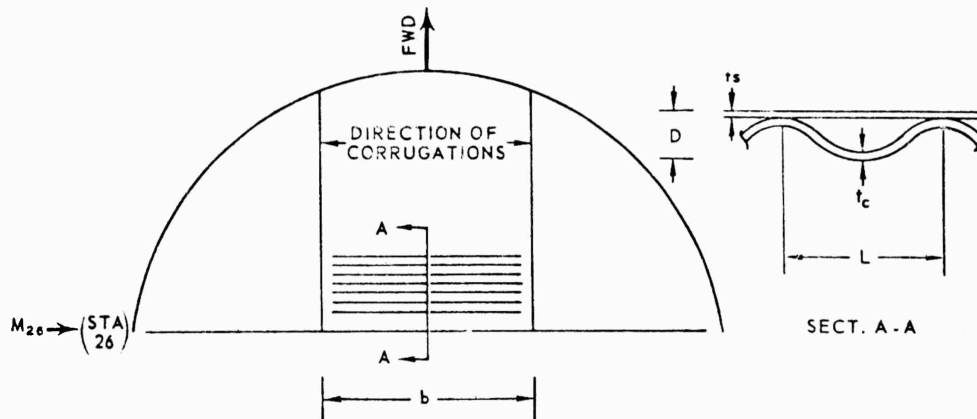


Figure 3.6.2. Corrugated Stiffener.

Referring to Figure 3.6.2 if b/L is very large the skin can be assumed to be a pure Euler column with no edge restraint. (Wavelength = $2L$)

$$F_{c_0} = \frac{C\pi^2 E}{(L/\rho)^2} \quad L \text{ is a function of } t_s \quad (3.6.1)$$

$$\rho = \sqrt{I/A} = \sqrt{t^3/12t} = 0.288t \quad (3.6.2)$$

$$F_{c_0} = \frac{(1.0)\pi^2(14 \times 10^6)}{(L/0.288t)^2} = \frac{(11.53 \times 10^6)t^2}{L^2} \quad (3.6.3)$$

Assuming a stress limit of $F_{ty} = 117,000$ PSI Figure 3.6.3 shows panel length, L , in terms of skin thickness versus panel stability stress.

It was assumed that the corrugations must distribute a 10 PSI aerodynamic pressure spanwise between nose ribs. Depth of the corrugations was assumed variable. Figure 3.6.4 illustrates the loading diagram.

$$M = \frac{ws^2}{8} = \frac{10KL(15.5)^2}{8} = 300KL \quad (3.6.4)$$

For a flat, square panel it can be shown that membrane effects will reduce bending stress by a factor of 2.50. Assuming conservatively that K (above equation) = 0.50 therefore yields,

$$M_{MAX} = 150L \quad (3.6.5)$$

SECRET

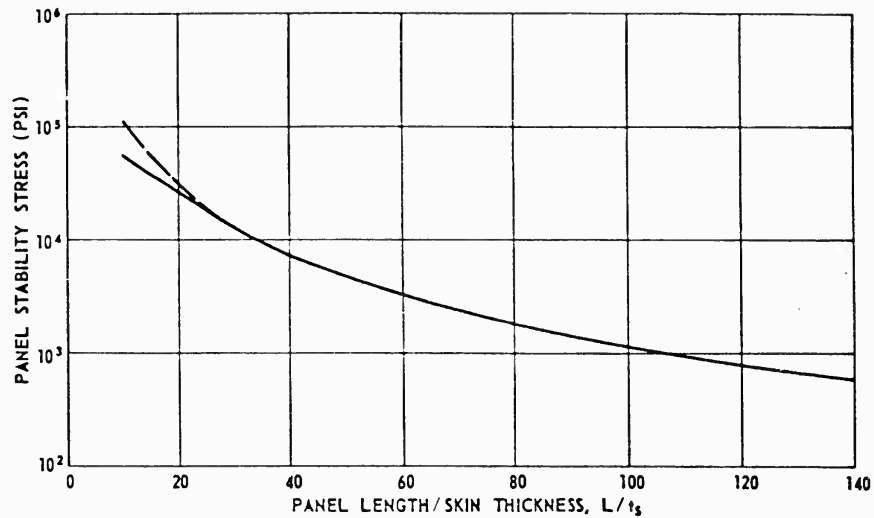


Figure 3.6.3. Panel Stability Stress Versus Ratio of Panel Length-to-Skin Thickness.

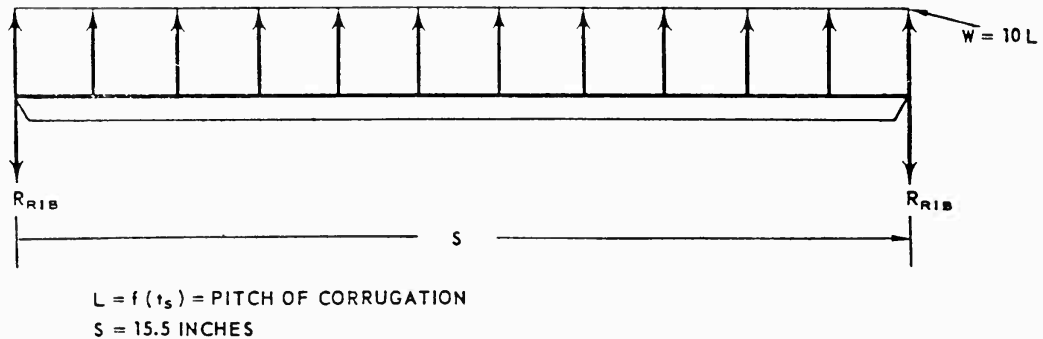


Figure 3.6.4. Leading Edge Corrugations.

From Reference 3.6.1, assuming $D = 1.0$, and plotting K_i/K_w versus L/D (refer to Figure 3.6.5), it can be seen that the maximum I_c per-unit-weight of corrugation occurs at an L/D of 4.50. Practical design considerations, such as clearance between valley and ridge for welding and optimum pitch to resist buckling, have shown an L/D of 3.30 to be a near optimum compromise. This ratio was used in the remainder of the structures study.

Figure 3.6.6 shows a plot of L/t_s versus D for various values of t_s . It should be noted that the minimum bend radius of solution heat treated B-120 titanium sheet is approximately $3t$. Thus these curves are cut off where values of t_c are too large for the D value. Also the R/t_c values will be limited to 60 (maximum) from buckling strength considerations. Figure 3.6.7 shows the

SECRET

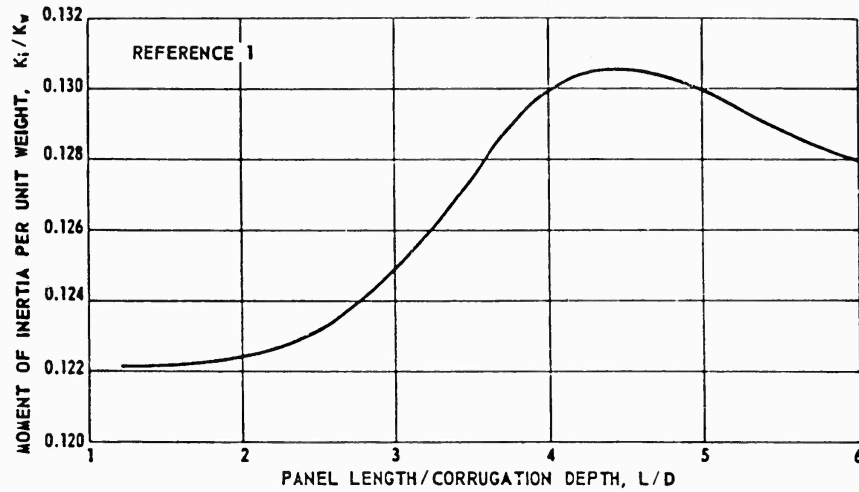


Figure 3.6.5. Optimization of Corrugation Stiffness.

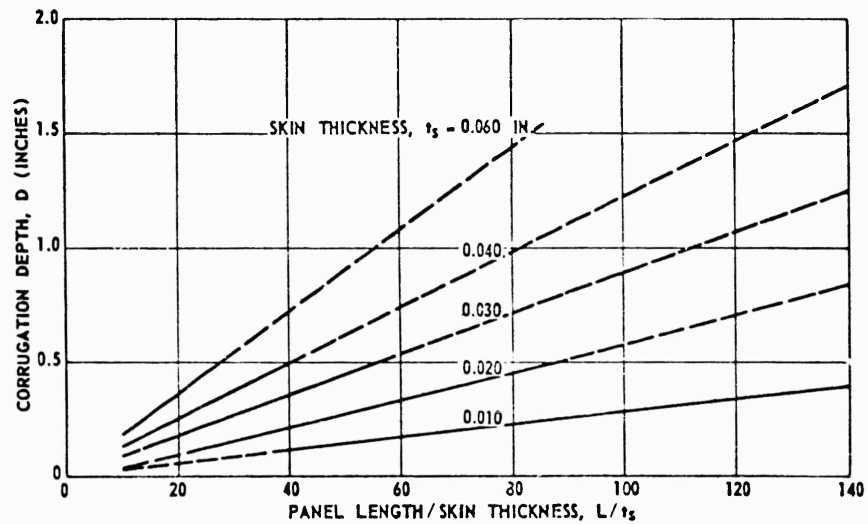


Figure 3.6.6. Corrugation Depth Versus Ratio of Panel Length to Skin Thickness.

L/t_s values for the boundaries of Figure 3.6.6; conversely Figure 3.6.6 plots the boundaries defined in Figure 3.6.7.

Reference 3.6.1 gives $K_w = 1.25$ and $K_i = 0.158$ for $L/D = 3.3$. Therefore

$$D = \frac{L}{3.3} ; I = \phi t_c (0.158 D^2) t_c \tag{3.6.6}$$

SECRET

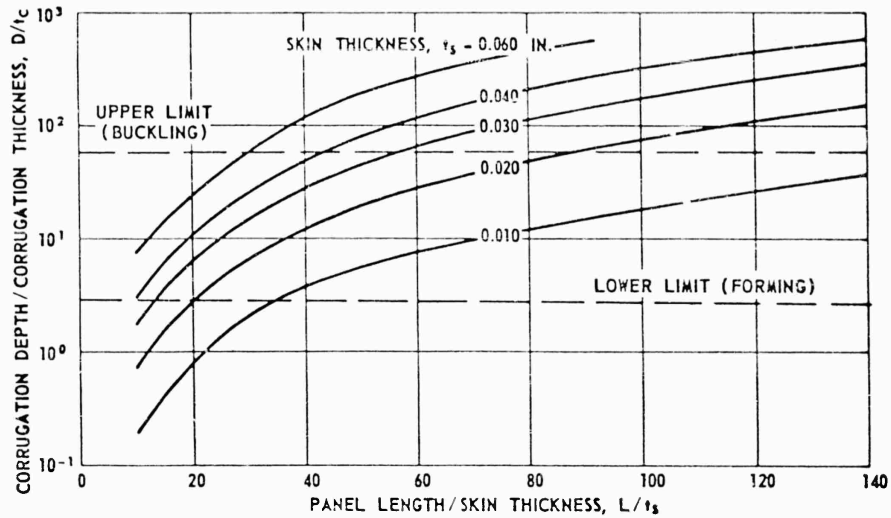


Figure 3.6.7. Corrugation Depth to Corrugation Thickness Ratio Versus Panel Length-to-Skin Thickness Ratio.

Using $F_{cr} = 100,000$ PSI for the corrugation

$$f_o = M_c/I ; 100,000 = \frac{150(L)(D)}{2(0.158D^2)t_c L} \quad (3.6.7)$$

Thus:

$$t_c = 75 \times 10^{-5} D/\phi \quad (3.6.8)$$

For a B-120 Ti density of 0.174 LB/IN.^3 , the weight of corrugation/ IN.^2 is

$$0.174(t_s + K_w t_c) = 0.174(t_s + 1.25 t_c) \quad (3.6.9)$$

Figure 3.6.8 plots the load-carrying capacity of the skin versus the L/t_s ratio. It should be noted that the effective load range for each t_s is taken from Figure 3.6.7 and that this range is shown between the D/t_c limits of 3.0 to 60.0 of Figure 3.6.8.

Figure 3.6.9 shows the optimum t_s to be used for a given loading.

Figure 3.6.10 approximates the cross section at Station 26 of the nominal 60-inch diameter missile of 21 percent thickness-to-chord ratio. The moment of inertia for this section is

$$I_{xx} = 2t_s R^3 [\alpha(1 + 2 \cos^2 \alpha) - 1.5 \sin 2\alpha] \quad (3.6.10)$$

SECRET

3.6.7

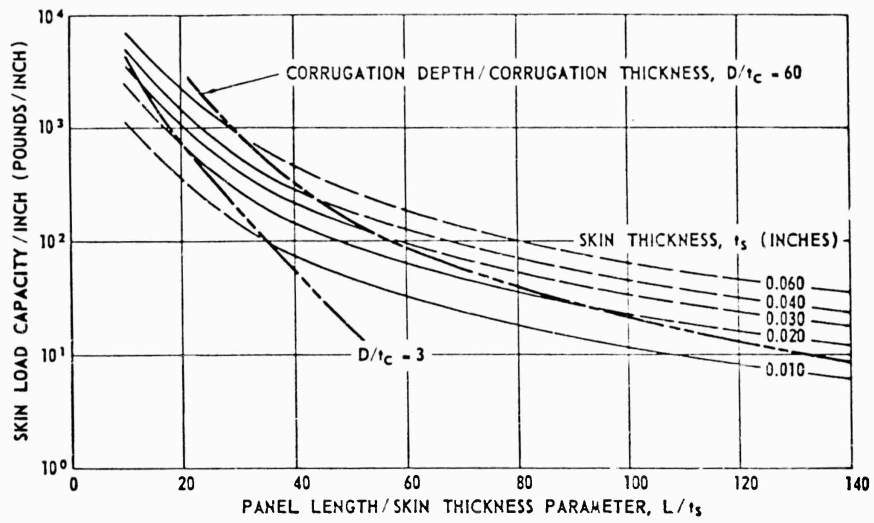


Figure 3.6.8. Skin Load Capacity Versus Ratio of Panel Length-to-Skin Thickness.

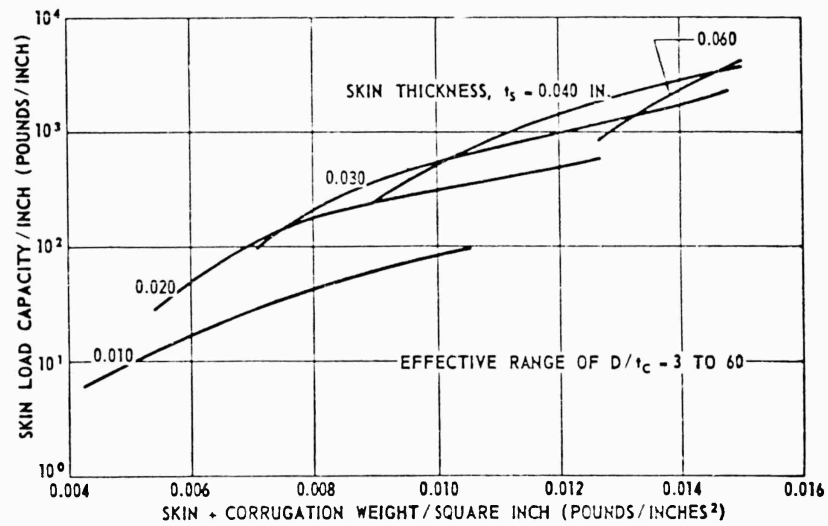


Figure 3.6.9. Skin Load Capacity Versus Skin and Corrugation Weight.

where

$$R = \frac{(\frac{h}{2})^2 + (\frac{a}{2})^2}{h}$$

$$\alpha = \sin^{-1} a/2R$$

(3.6.11)

3.6.8

SECRET

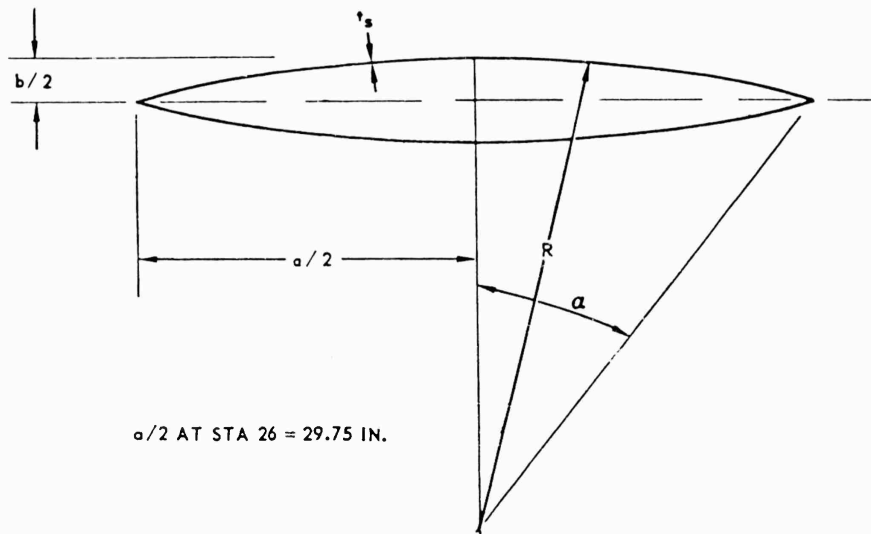


Figure 3.6.10. Determination of Skin Loading.

From previous calculations where $t_s = 0.060$ inch, and for the nominal 21 percent thickness-to-chord ratio missile,

$$I_{xx} = 6416 \text{ in.}^4$$

$$h/2 = 4.358 \text{ in} \quad (3.6.12)$$

Assuming $h/2$ for any thickness-to-chord ratio (t/c) is directly proportional to (t/c)

$$\frac{h}{2} = \frac{4.36}{.21} (t/c) = 20.75 (t/c) \quad (3.6.13)$$

Assuming I_{xx} is proportional to $(h/2)^2$

$$I_{xx} = \frac{64.6 t_s (h/2)^2}{0.060 (4.36)^2} = 62.1 (t_s) (h/2)^2 \quad (3.6.14)$$

The maximum load per-inch, W_{max} , due to the moment at Station 26 (35,000 IN-LB) is given by

$$W_{max} = \frac{35,000 (h/2) t_s}{I_{xx}} \text{ lb/in.} \quad (3.6.15)$$

Table 3.6.2 shows the results of the above calculation.

SECRET

3.6.9

SECRET

Table 3.6.2
EFFECT OF THICKNESS-TO-CHORD RATIO ON MAXIMUM WEIGHT

(t/C)	h/2	(h/2) ²	I _{XX}	I _{XX} /(h/2) (t _S)	W _{max} (LB/IN.)
0.10	2.075	4.32	268 t _S	129	271
0.14	2.91	8.46	525 t _S	180.5	194
0.21	4.36	19.00	1079 t _S	248.0	141
0.35	7.25	52.60	3265 t _S	450.0	78

The WT/IN.² versus (t/C) is determined from

$$wt/in.^2 = 0.174 [t_s + 1.25 t_c] \tag{3.6.16}$$

where

t_S is determined from Figure 3.6.9

L/t_S is determined from Figure 3.6.8

$$L = L/t_s \times t_s$$

$$D = L/3.3$$

D/t_c is taken from Figure 3.6.7

$$t_c = \frac{D}{D/t_c}$$

and is shown in Table 3.6.3.

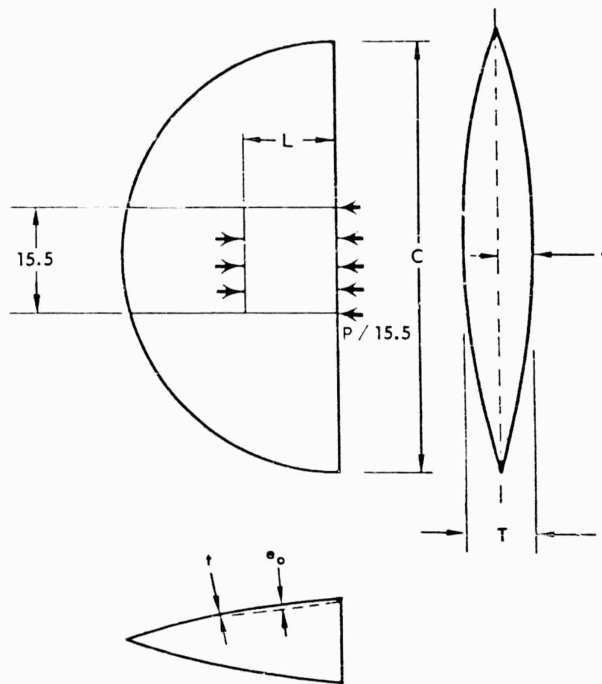
Table 3.6.3

EFFECT OF THICKNESS-TO-CHORD RATIO ON WEIGHT/SQUARE INCH								
t/C	t _S	L/T _S	L	D	D/t _C	t _C	t _S + 1.25 t _C	WT/IN. ²
0.10	0.030	36.5	1.095	0.332	23.5	0.0141	0.0476	0.0083
0.14	0.030	42.0	1.260	0.381	31.5	0.0121	0.0451	0.0079
0.21	0.030	49.0	1.470	0.445	43.0	0.0103	0.0429	0.0075
0.35	0.020	53.0	1.06	0.321	23.0	0.014	0.0375	0.0065

3.6.10

SECRET

SECRET



$$P = \frac{MctL}{I_T}$$

$$P_{CR} = \frac{K\pi^2 EI_1}{L^2}$$

$$e_f = \frac{e_o}{\cos \left[\frac{\pi}{e} \left(\frac{P}{P_{CR}} \right)^{1/2} \right]}$$

$$M_{MAX} = Pe_f$$

Figure 3.6.11. Leading Edge, Solid Skin.

Solid Skin. Figure 3.6.11 illustrates the type of section analyzed, a panel forward of Station 26 (referred to the 60-inch diameter nominal vehicle), and shows some of the relations employed in making the calculations. The following assumptions and definitions apply to this analysis:

- M = 35,000 IN-LB
- K = 3.5 (Reference 3.6.1)
- E = 13×10^6 PSI at 1000°F
- E = 14×10^6 PSI at 800°F
- F_{ty} = 110,000 PSI at 1000°F
- F_{ty} = 117,000 PSI at 800°F
- L = 15.5 inch
- I_T = Total moment of inertia of cross section
- I_1 = Moment of inertia of skin between ribs

SECRET

For a thickness-to-chord ratio (t/C), of 10 percent:

$$f_c = M_c / I_{1c} + P/A = 110,000 \text{ psi at } 1000^\circ F \quad (3.6.17)$$

$$f_c = \frac{276t}{2(1.292)(t^3) \cos 0.0685 \sqrt{1/t^3}} + \frac{4600}{15.5t} = 110,000$$

where

$$\begin{aligned} I_1 &= 1.292 t^3 & P_{cr} &= 2.41 \times 10^6 t^3 \\ I_T &= 244 t & P &= 4600 \\ e_o &= .06 & e_y &= \frac{0.06}{\cos 0.0685 \sqrt{1/t^3}} \\ c &= 2.07 & M_{max} &= \frac{276}{\cos 0.0685 \sqrt{1/t^3}} \end{aligned}$$

Solving graphically this gives a required skin thickness

$$t = 0.1285 \text{ IN.}$$

In a similar manner, solutions for other (t/C) 's were obtained.

$$\begin{aligned} (t/C) &= 14\%; t = 0.115 \text{ IN.} \\ (t/C) &= 21\%; t = 0.101 \text{ IN.} \\ (t/C) &= 35\%; t = 0.088 \text{ IN.} \end{aligned}$$

These results indicate that relatively heavy skins are required for the forward area (thicknesses that decrease as (t/C) increases). Figure 3.6.12 shows the skin-weight/ IN.^2 for the solid skin forward section.

Honeycomb Type. A schematic representation of the honeycomb section is shown in Figure 3.6.13. The analysis of the unit weight of this type of construction proceeded as follows:

$$I_{NA} = \frac{15.5 t_1 (t - t_1)^2}{2}$$

$$P_{CR} = \frac{K \pi^2 E I_{NA}}{L^2} = 14.49 t_1 (t - t_1)^2 (10^6)$$

SECRET

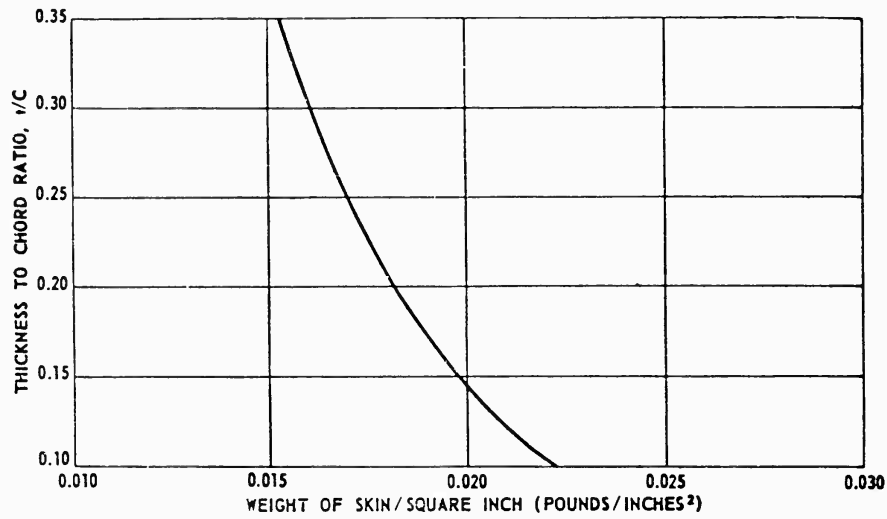


Figure 3.6.12. Thickness-to-Chord Ratio Versus Forward Section Solid Skin Weight.

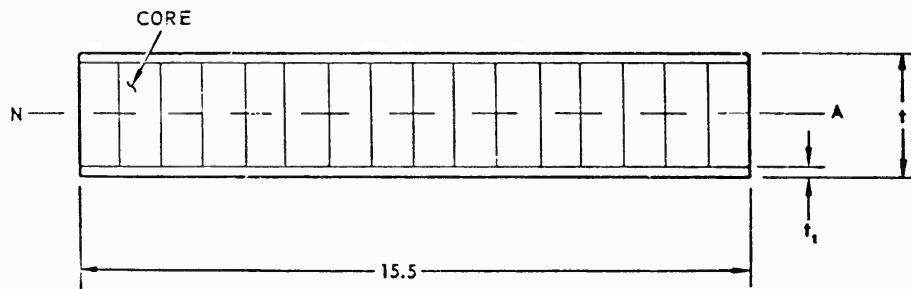


Figure 3.6.13. Leading Edge, Sandwich Skin.

For $(t/C) = 10$ percent; $P = 4600$

$$e_f = \frac{.06}{\cos \pi/2 \sqrt{\frac{4600}{14.49(10^6)(t_1)(t-t_1)^2}}}$$

$$M_{max} = P e_f = \frac{276}{\cos .0279 \sqrt{\frac{1}{t_1(t-t_1)^2}}}$$

$$f_c = \frac{M_c}{I_{MA}} + \frac{8}{A} = 110,000 = \frac{276 t}{2(7.75) t_1 (t-t_1)^2 \cos .0279 \sqrt{\frac{1}{t_1(t-t_1)^2}}} + \frac{4600}{31 t_1}$$

SECRET

3.6.13

which solved graphically gives

$$\begin{aligned} \text{for } t &= 0.25 \text{ IN.}; t_1 = 0.0065 \text{ IN.} \\ \text{for } t &= 0.1875 \text{ IN.}; t_1 = 0.0115 \text{ IN.} \end{aligned}$$

Referring back to the results on the solid skin forward section, it was seen that as (t/C) increased lighter skins were required, or for a given skin gage, the stiffness requirement is lowered as (t/C) increases. The practical lower limit of sheet thickness for the external skin in honeycomb or sandwich construction is 0.012 inch. The analysis for a (t/C) ratio of 10 percent and a sandwich skin thickness of 0.1875 inch indicates that an external skin thickness of 0.012 inch is adequate; this thickness will be sufficient for all (t/C) ratios greater than 10 percent.

The weight/IN.² of sandwich skin with titanium core and external skin is:

$$t = 0.1875 \text{ IN.}; t_1 = .012 \text{ IN.}; \text{WT/IN.}^2 = 0.00619 \text{ LB/IN.}^2$$

$$t = 0.25 \text{ IN.}; t_1 = .012 \text{ IN.}; \text{WT/IN.}^2 = 0.00638 \text{ LB/IN.}^2$$

A comparison of the unit weight of sandwich skins with corrugation-stiffened and solid skins is shown in Figure 3.6.14. The weight advantages of the honeycomb type of construction is readily apparent.

ROCKET MOTOR END CLOSURES. The parameters of significance in optimizing the weight and design of end closures for various (t/C) ratios and pressures are:

1. The shape of the closure, i.e., the amount of curvature of a cross section
2. The post spacing around the perimeter
3. The volume lost or gained in the tank by varying the amount of the end closure

In order that stress and weight can be reduced to useable values, the end closure must have some curvature between tank skins. For a given envelope or pressure vessel planform, less volume is lost in using more flat end closures, but flat closures create greater stresses and thus higher weights. The thickness required for the end closure is based on the governing condition of moment and tension at the tank edges or moment and tension in the closure. Since post spacing affects the moment at the tank edges, this parameter has to be optimized.

Several types of end closures were studied. The first of these was a half cylinder closure; definitions of this geometry are shown in Figure 3.6.15. Proceeding with the type of analysis shown on page 156 of Reference 3.6.2 in which the deflection due to pressure is equated to the deflection due to W gave

$$f = \frac{M t^{3/2}}{I} = \frac{2.14 p l}{t} \frac{t^{3/2}}{I} = 1.078 \quad (3.6.18)$$

SECRET

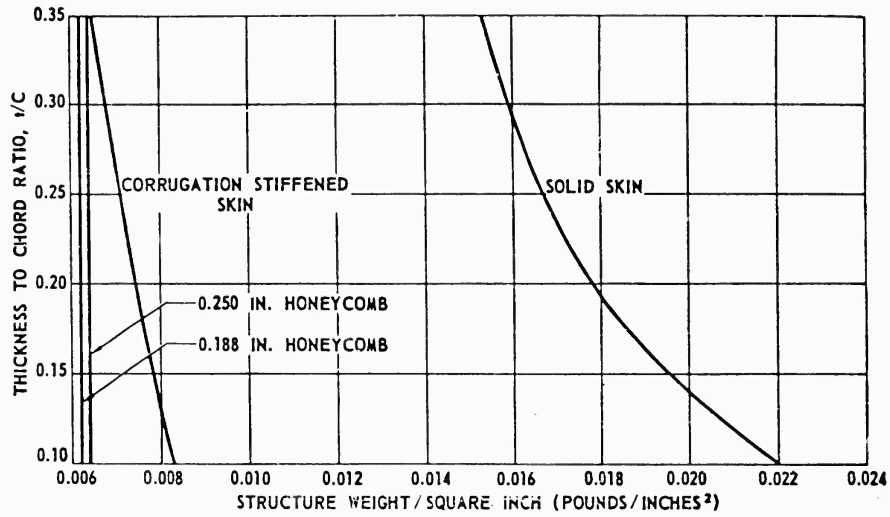


Figure 3.6.14. Weight Comparison of Forward Section Structure Designs.

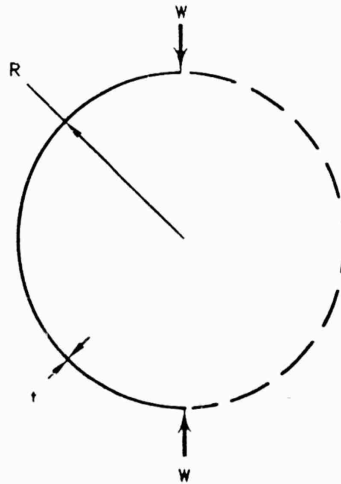


Figure 3.6.15. Half Cylinder Closure.

An elliptical closure will be restrained in the same manner as the cylinder. (Refer to Figure 3.6.16).

The deflection due to pressure is equal to:

$$D_{Y_2} = \frac{Pba}{tE} \quad (3.6.19)$$

SECRET

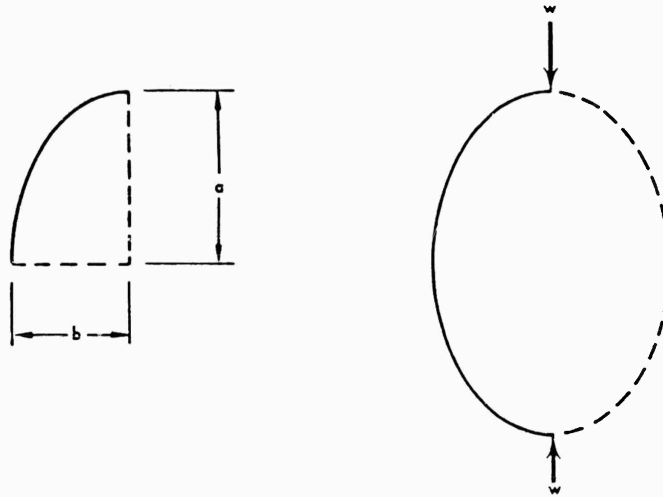


Figure 3.6.16. Elliptical Closure.

Assume the equation $D_{y_2} = 0.149 \frac{wR^3}{EI}$ (Reference 3.6.2 is appropriate if $R = b$ and 0.149 is increased by the proportion C_i/C_L , where C_i is the perimeter of 1/4 of an ellipse with 1/2 the minor axis of b , and 1/2 the major axis of $\frac{a+b}{2}$. (Refer to Figure 3.6.17).

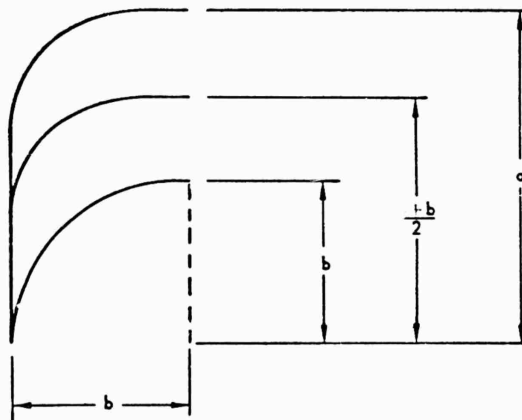


Figure 3.6.17. Edge Closure Nomenclature.

Following through with the above assumptions gives:

$$f_1 = \frac{M^2/2}{I} = \frac{K_w P a^2}{0.149 b \sqrt{2[b^2 + (\frac{a+b}{2})^2]}} \quad (3.6.20)$$

SECRET

An elliptical cylinder under restraint is subject to bending moments that are additive to those caused by the post restraint.

$$M_2 = K_p P_a^2 \quad (\text{Reference 3.6.2, page 156})$$

$$f_2 = \frac{M_2}{Z} \quad (3.6.21)$$

where

$$t = \frac{t^2}{6}$$

Both the elliptical and cylindrical closures are subject to tension stresses due to pressure

$$f_t = \frac{PR}{t} \quad (3.6.22)$$

where R = 1/2 tank thickness (spacing between = flat plates)

Conditions at the tank edge are shown in Figure 3.6.18.

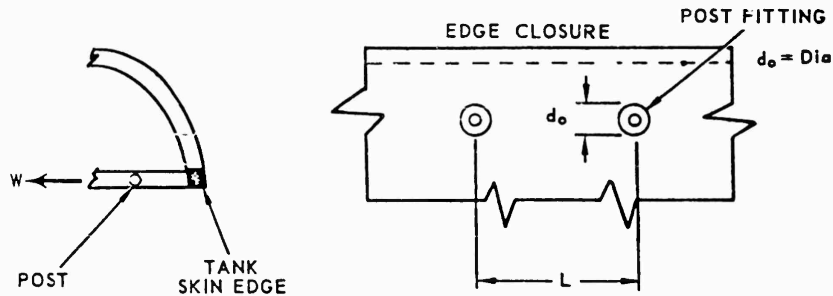


Figure 3.6.18. Tank Edge.

The average moment per unit width is (Reference 3.6.3)

$$M = \frac{W}{8} \left[1 - \frac{2}{3} \left(\frac{d_o}{L} \right) \right]^2 \quad (3.6.23)$$

$$f_1 = \frac{M}{Z} = \frac{6M}{t^2}$$

SECRET

Summarized, the pressure vessel or tank end closure stress conditions are:

1. Cylinder

$$f = f_i + f_t = 1.07P + \frac{PR}{t}$$

$$t = \frac{PR}{f - 1.07P}$$
(3.6.24)

2. Ellipse

$$f = f_1 + f_2 + f_t$$

$$= \frac{K_w P a^2}{0.149b \sqrt{2[b^2 + (\frac{a+b}{2})^2]}} + \frac{6 K_p P a^2}{t^2} + \frac{PR}{t}$$
(3.6.25)

3. Tank Skin Edge

$$f = f_i + f_t = \frac{6M + PRt}{t^2}$$

$$t = \frac{PR}{f} + \frac{\sqrt{(\frac{PR}{f})^2 + \frac{24M}{f}}}{2}$$
(3.6.26)

Table 3.6.4 summarizes the calculations of end closure weights. The calculations were based on 250 PSI internal pressure, 7.5 inch post spacing, and for each (t/C) ratio, a mean tank thickness.

Table 3.6.4
END CLOSURE WEIGHTS

t/C	Closure Thickness, IN., Ellipse Ratio			Closure Weight, LB, Ellipse Ratio			Post and Fitting Weight	Total Weight, LB, Ellipse Ratio		
	1	1.5	2	1	1.5	2		LB.	1	1.5
10	0.206	0.206	0.206	32.7	27.8	25.8	17.4	*50.1	*45.2	*43.2
14	0.206	0.206	0.206	45.8	38.8	36.3	18	*63.8	*56.8	*54.3
21	0.206	0.229	0.274	68.5	64.6	72.0	19	*87.5	**83.6	**91.0
35	0.206	0.383	0.457	114	180	200	21	*135	**201	**221

*Based on moment and tension at tank edges

**Based on moment and tension in closure

SECRET

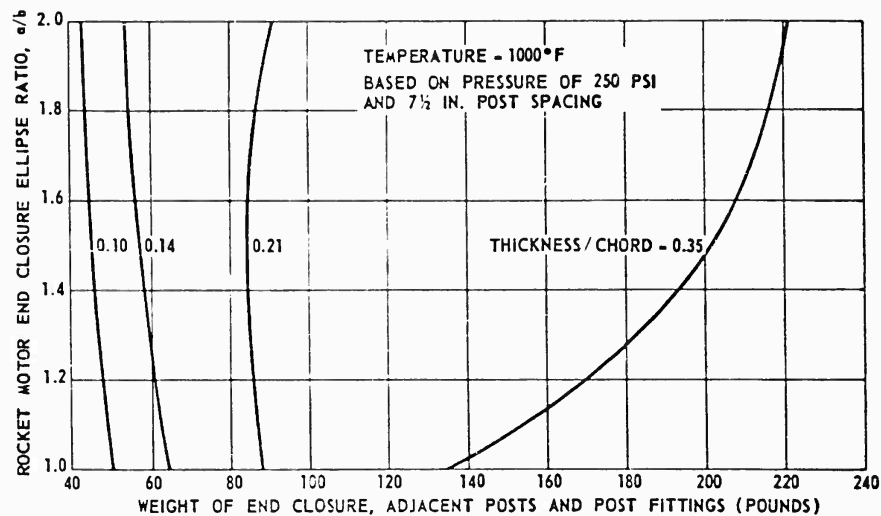


Figure 3.6.19. Optimization of Rocket Motor and Closure Ellipse Ratio.

Figure 3.6.19 is a plot of end closure weights versus end closure ellipse ratio for a range of (t/C)'s). It can be seen that for (t/C) ratios of 21 percent and less ellipse ratios do not appreciably affect the weight. For (t/C) ratios greater than 21 percent, a weight penalty can be expected. From the calculations, it is shown that for (t/C) ratios of 10 percent and 14 percent, moment and tension at the edges govern, and for (t/C) ratios of 21 percent and 35 percent, moment and tension in the closure govern. A small increase in post spacing would increase the weight for (t/C) ratios to 21 percent, but would not affect the weight for larger (t/C) ratios. A reduction in post spacing, on the other hand, would reduce the weight for 10 percent and 14 percent (t/C) ratios but would not affect the weights for 21 percent and larger (t/C) ratios.

Additional cases were studied in which tank pressures of 150, 250, and 500 PSI were assumed (temperature assumed = 1000°F; conservative since aerodynamic heating is not significant until after rocket motor burnout) for various (t/C) ratios. This analysis was based on the previous optimization of end closure ellipse ratio of 2 and post spacing of 7.5 inch. These results are shown in Figure 3.6.20.

It was determined that a post spacing of 7.5 inch gave best results because of the increase in weight in the lower and median ranges of (t/C) ratios for increased spacing and no decrease in weight for the 21 percent t/C ratio for decreased post spacing. Larger post spacing would also result in heavier tank skins because of greater loads in the posts.

SECRET

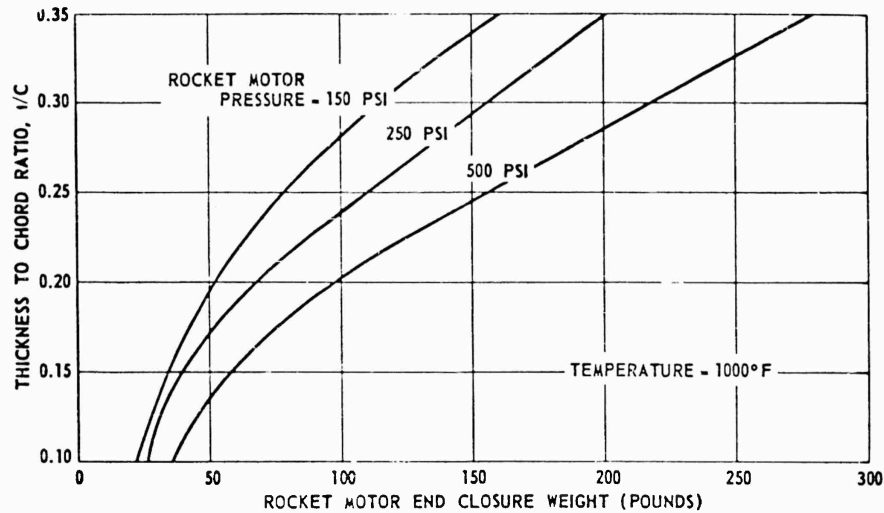


Figure 3.6.20. Thickness-to-Chord Ratio Versus Rocket Motor End Closure Weight.

TANK PLATE STUDY. The structure designated "tank plate" includes both top and bottom sections of the rocket motor pressure vessel. These are relatively flat sections as shown in Figure 3.6.21 below.

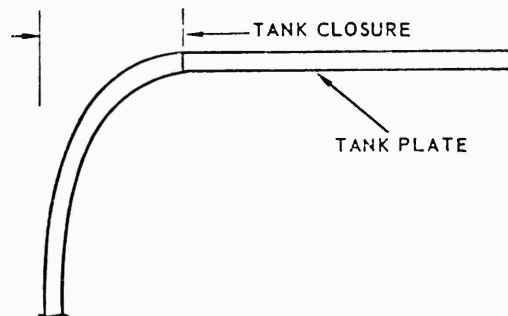


Figure 3.6.21. Tank Plate Cover.

Three basic types of B-120 titanium structure were considered for the pressure vessel walls:

1. Solid skin
2. Grid frame with thin membrane
3. Honeycomb

As established above, posts will be required to stabilize the plate and end closure; post spacing of 7.5 inch was found to be optimum. The structure

SECRET

requirements of the plate are independent of the t/C ratio; thus, the only variable is tank pressure.

Solid Skin. From Reference 3.6.3, pages 252-256, a theory for flat plates supported at intervals is developed. It is assumed that a disk reinforcement is placed at each post which serves as a base to anchor and seal each post. Approximate disk diameters, d_o , for various pressures are:

$$d_{o150} \text{ PSI} = 1.75 \text{ IN.}$$

$$d_{o250} \text{ PSI} = 2.25 \text{ IN.}$$

$$d_{o500} \text{ PSI} = 2.25 \text{ IN.}$$

It was assumed that a typical panel is supported at each corner by posts. This panel will be a portion of a much larger continuous panel. Utilizing the definitions shown in Figure 3.6.22.

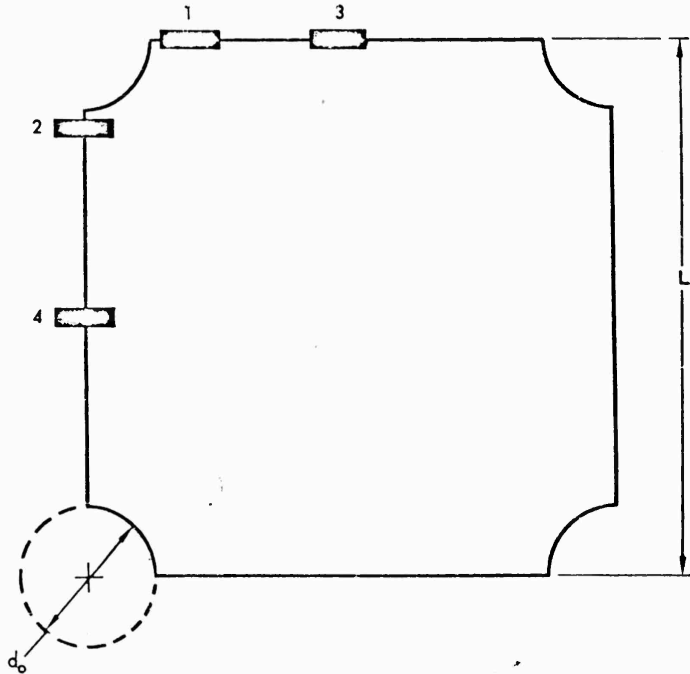


Figure 3.6.22. Plate Tank Cover, Solid Skin.

the moment-per-unit width at any point on the panel is:

$$M = \frac{KP}{8} (L - \frac{2}{3} d_o)^2 \quad (3.6.27)$$

SECRET

3.6.21

where $L = 7.50$ IN. and K is a function of q (d_o/L), and the place on the panel in question. The numbered bars shown in Figure 3.6.22 represent the moment directions at various directions on the plate. By combining 1 with 2 and 3 with 4, biaxial bending results at point adjacent to and between the posts. Using the very conservative assumption of a structure at 1000°F the following thicknesses are calculated based on

$$\left. \begin{aligned} F_{ty} &= 110,000 \text{ PSI} \\ F_{sy} &= 0.577 F_{ty} = 63,500 \text{ PSI} \end{aligned} \right\} \text{B-120 Ti} \quad (3.6.28)$$

Grid Skin. The preceding paragraphs examined solid plate tank covers. Figure 3.6.23 shows the same basic panel size with a thin membrane skin attached to a grid-stiffening frame. The configuration will have a variable number of grids per side, "n", and therefore n^2 grid squares.

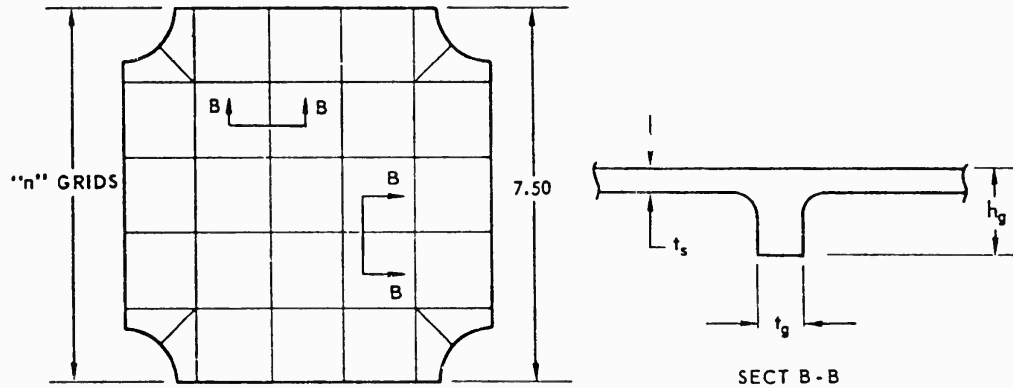


Figure 3.6.23. Tank Plate Cover, Grid Skin.

Assume: $30 t_s$ of skin effective with each grid

$$\text{Fillet radius} = h_g/2$$

Due to beam stability the h_g/t_g ratio should not exceed 5.0.

It can be seen that bi-axial stresses on the outer skin surface will produce compression in the membrane and tension in the grid due to bending. The combined stresses will make shear critical. Using $F_{sy} = 0.60 F_{ty}$ and designing the membrane to $F_{bmax} = F_{ty}$ means that F_b in the grid must be a low stress. This is demonstrated as follows:

$$F_{sy} = 0.60 (F_{ty}) = \frac{F_b \text{ membrane} + F_b \text{ grid}}{2} \quad (3.6.29)$$

SECRET

	<u>Point 1, 2</u>	<u>Point 3, 4</u>
P = 150 PSI	$t_s = 0.282$ IN.	$t_s = 0.139$ IN.
P = 250 PSI	$t_s = 0.30$ IN.	$t_s = 0.168$ IN.
P = 500 PSI	$t_s = 0.425$ IN.	$t_s = 0.238$ IN.

The above results show that very substantial skin thicknesses (with resulting large weights) result even with tank pressures as low as 150 PSI.

Since f_b membrane = F_{ty} ,

$$0.60 F_{ty} = \frac{F_{ty} + t_b \text{ grid}}{2} \quad (3.6.30)$$

$$f_{b \text{ grid}} = 0.20 F_{ty} = 0.20 (110,000) = 22,000 \text{ psi}$$

By virtue of the fillet and $30 t_s$ of skin the neutral axis will be shifted toward the surface. This reduces the grid tension bending stress at the surface. Assuming $30 t_s$ of skin a fillet radius, $R = h_g/2$, sample calculations show that a very close approximation of the required grid depth, h_g will be

$$h_g = \left[\frac{30 M_{MAX}}{F_{ty}} \right]^{1/3} \quad F_{ty} = 110,000 \text{ psi} \quad (3.6.31)$$

$$M_{MAX} = f(K_4) \times \frac{7.5}{n} \quad \text{where } n \text{ is the number of grids} \quad (3.6.32)$$

Having determined h_g , the skin thickness, t_s , must be calculated. From Reference 3.6.3, page 231 and Figure 131, the maximum bending stresses on the panel due to uniform pressure, w , is

$$F_{ty} = f_b = \frac{0.19 w b^2}{t_s^2} ; b = \frac{7.5}{n} - t_g - 2R = \frac{7.5}{n} - \frac{6 h_g}{5} \quad (3.6.33)$$

$$t_s = b \sqrt{\frac{.19 w}{F_{ty}}} = \left(\frac{7.5}{n} - \frac{6}{5} h_g \right) \sqrt{\frac{.19 w}{F_{ty}}} \quad \left\{ \begin{array}{l} h_g = \text{-----} \\ M_{MAX} = \text{-----} \end{array} \right. \quad (3.6.34)$$

Both a solid skin and a grid skin would require post support disks of equal size. Therefore, the disk support weight will be excluded for purposes of comparison. It should be noted that less bending material will be required in the center of the panel. This is offset, however, by increased shear requirements near the post disks.

SECRET

Assuming $t_{s\min} = 0.025$ inch due to practical fabrication limits, the weight is:

$$wt = \left[(7.5)^2 t_s + n^2 l_g A_g \right] (0.174) \quad (3.6.35)$$

$$l_g = \frac{30}{n} - 1.4 h_g \quad \text{and} \quad A_g = 0.1535 h_g^2 \quad (3.6.36)$$

The weights then for the various pressures will be:

	150 PSI	250 PSI	500 PSI
n			
2	1.216	1.565	2.24
3	1.106	1.423	2.08
4	1.150	1.405	2.04
5	-	-	2.10

For comparison the solid plate weights were:

150 PSI	250 PSI	500 PSI
1.36	1.64	2.33

Honeycomb Skin. Pressure on the skin results in high shear loads at the fittings which for honeycomb construction is undesirable because of the low shear allowables of the core. Stiffeners between post fittings are required to distribute shear loads and reduce them to values that cores can resist.

A sketch of the rocket motor planform which was analyzed is shown in Figure 3.6.24. The post fittings shown are 2.25-inch in diameter which is considered a maximum and will be used for the 500 PSI and 250 PSI designs. The diameter can be reduced to 1.75 inches for the 150 PSI design without sacrificing weight in the skin.

Sandwich thickness and core foil thickness were based on shear stresses with the sandwich thickness limited to 0.50-inch maximum. It was determined that the loss in volume due to the use of greater thicknesses was not sufficiently compensated by the reduced weight. Allowable shear stresses for cores of 3/16-inch cell size and various foil thicknesses are:

<u>Foil Thickness</u>	<u>Allowable Shear Stress</u>
0.0015 IN.	600 PSI
0.0020 IN.	800 PSI
0.0025 IN.	1000 PSI
0.0030 IN.	1200 PSI

SECRET

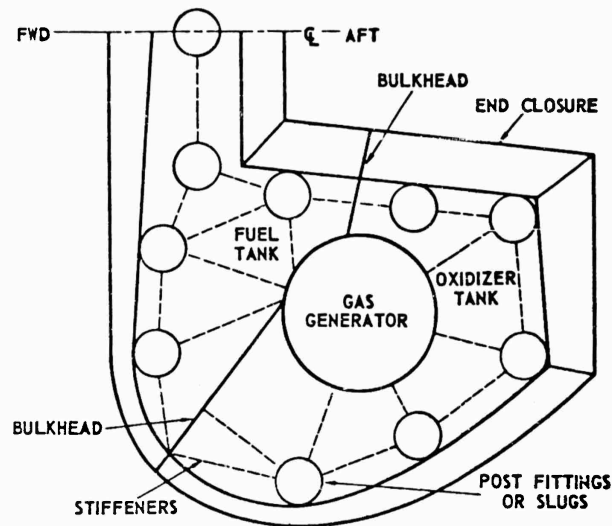


Figure 3.6.24. Planform Rocket Motor Honeycom Skin.

The stiffeners between post fittings were designed to resist shear and bending loads imposed by the skin. They will be made of solid metal and will be fitted between sandwich facings. The core shear attachment to these stiffeners is accomplished by brazing.

The honeycomb skin thickness was determined by using the type of analysis shown on page 255 of Reference 3.6.3. The calculations were based on the maximum moment within the panel at a position away from the stiffeners. The stiffeners were designed to resist moments at the panel edges.

For comparison with other types of structure, the panel weights were based on a 7.50-inch square honeycomb panel with one-half the weight of the adjacent stiffeners. A 3/16-inch cell size was used for all calculations. Results for the honeycomb skin are shown below:

Pressure PSI	Sandwich Thickness, IN.	Core Foil Thickness, IN.	Face Thickness, IN.	Stiffeners Width, IN.	Panel Weight, LB
150	3/8	0.0015	0.010	0.200	0.492
250	3/8	0.0020	0.010	0.340	0.609
500	1/2	0.0025	0.015	0.380	0.883

Figure 3.6.25 shows for comparison the weights of the three types of tank skins evaluated as a function of pressure. Post and disk weights are not included in the weights shown in Figure 3.6.25.

SECRET

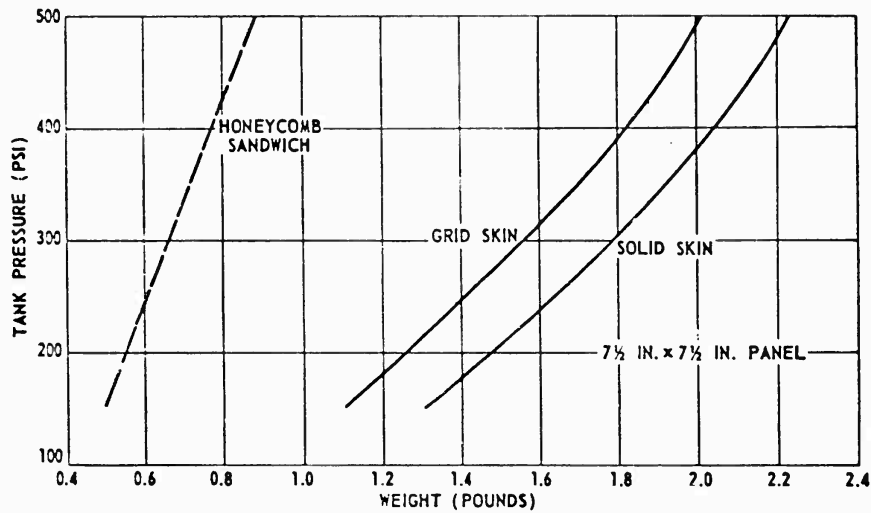


Figure 3.6.25. Weight Comparison of Fuel Tank Skin Structures.

ROCKET MOTOR POSTS AND POST FITTINGS. Each post is required to resist the pressure load on a 7.5-inch square panel.

$$\text{Post diameter} = 2 \sqrt{\frac{w}{\pi f_{ty}}} = D_p$$

where $w = (7.5)^2 \times \text{pressure}$

For $F_{ty} = 110,000$ PSI, the post sizes are

- 150 PSI; $D_p = 0.286$ IN.
- 250 PSI; $D_p = 0.368$ IN.
- 500 PSI; $D_p = 0.520$ IN.

Post fitting weights calculated for the grid skin were employed for the weight summary based on 19 posts, therefore 38 fittings. The combined weights are shown in Figure 3.6.26 as a function of (t/C) .

SUMMARY OF STATIC CONSIDERATIONS. The results presented in the preceding paragraphs were based on analyses of alternative designs of the individual sections. Now these components will be assembled and the weights shown for combinations of interest.

It should be noted that the basic configuration shown in Figure 3.6.1 is that of a liquid propellant vehicle. Weights applicable to a solid propellant vehicle will also be presented. The solid propellant motor pressure vessel will include the area of the aft skin shown in Figure 3.6.1. The weight

SECRET

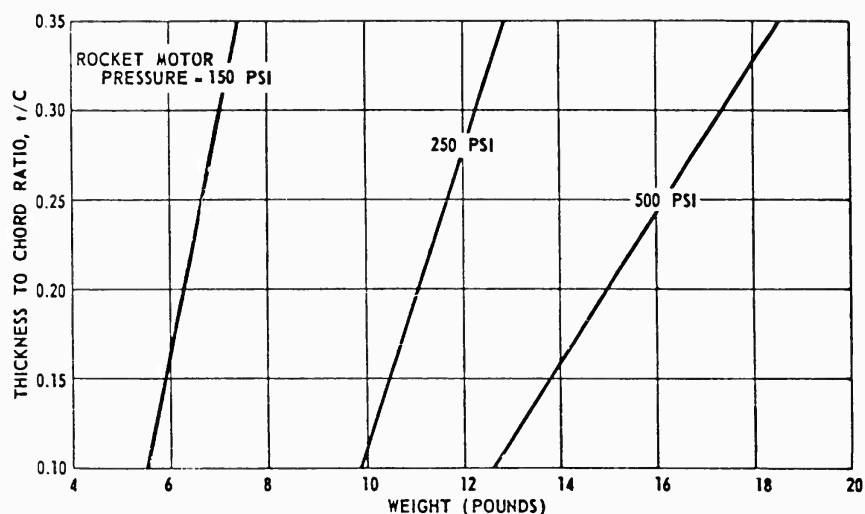


Figure 3.6.26. Thickness - to - Chord Ratio Versus Weight of Posts and Post Fittings.

comparison (liquid and solid propellant) will be for a 21 percent (t/C) ratio and 250 PSI tank pressure.

Since the forward and aft skin and the tank plates can be made of different types of structure, total weights will be computed for two types of design. Type I will be the minimum weight design, forward and aft skins plus the tank plate will be honeycomb. Type II will compromise weight for ease of manufacturing. Honeycomb sandwich will be excluded from this design and forward and aft skins will be corrugation stiffened. The tank plate will be grid skin. Weights of these structures are compared in Figures 3.6.27, 3.6.28, and 3.6.29 for the tank pressures of interest.

It should be noted that these weights include only the basic structure weights of the forward skins and propellant tank and do not include weights of nozzle, control system components, electronics, or other payload items.

Regarding the structure for a solid propellant vehicle (refer to Figure 3.6.30), the tank and closure would be modified, and gas generators and bulkheads eliminated. The tank plate would extend over the cutout space allocated for the liquid thrust chamber. Eleven extra posts would be required to stabilize the tank plate. Assuming honeycomb construction for the forward skin and tank plates, the solid propellant structure weights are:

Forward skin	13.9 LB
Tank end closure	51.0 LB
Tank plate	12.7 LB
Tank posts and fittings	17.5 LB
Tank stiffeners	9.4 LB
total	104.4 LB

SECRET

3.6.27

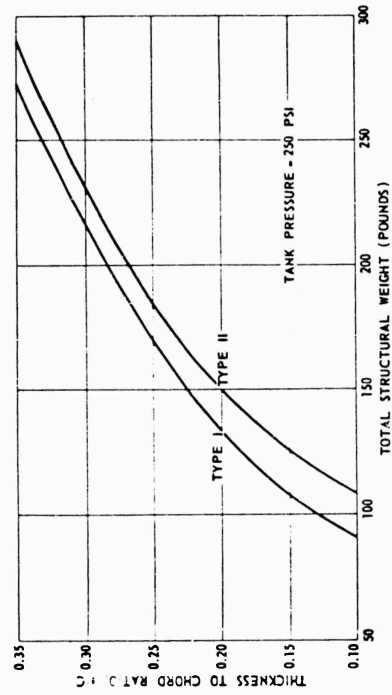


Figure 3.6.28. Thickness - to - Chord Ratio Versus Total Structural Weight.

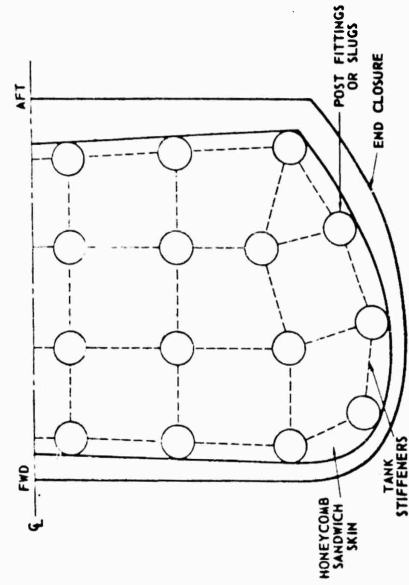


Figure 3.6.30. Planform of Solid Propellant Rocket Motor.

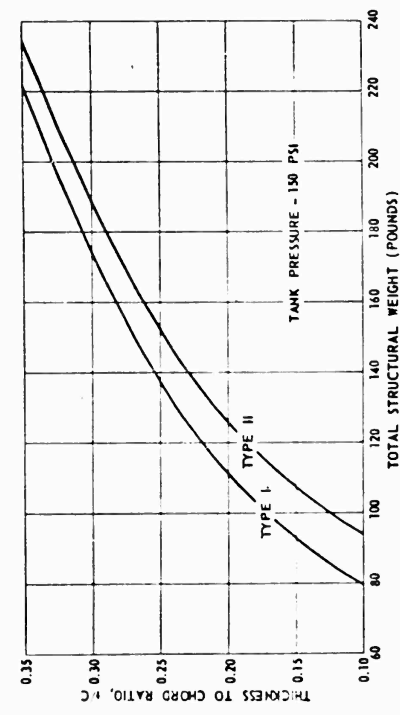


Figure 3.6.27. Thickness - to - Chord Ratio Versus Total Structural Weight.

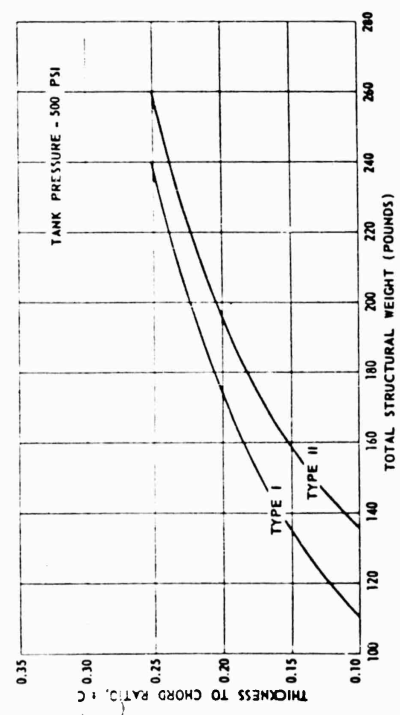


Figure 3.6.29. Thickness - to - Chord Ratio Versus Total Structural Weight.

SECRET

Reference to Figure 3.6.28 shows that the 250 PSI, 21 percent (t/C) liquid propellant structure would weigh approximately 140 pounds. Thus the integral solid propellant design is approximately 25 percent lighter, however some of this weight advantage would be lost due to insulation requirements (not included in this comparison).

3.6.3 AEROELASTIC CONSIDERATIONS

Initial aeroelastic studies of the PYE WACKET configuration have been directed toward parametric investigations in the following basic areas:

1. Vehicle structural dynamics - considering the effects of thickness ratio, geometric scale, and type of structure.
2. Panel flutter characteristics - in terms of panel thickness, geometry, support, and initial stress level.
3. Static aeroelastic effect on rigid body stability derivatives.

A reference configuration, based on a 60-inch diameter model with a thickness-to-diameter ratio of 21 percent is used as a focal point in these studies. Simplified scaling relationships are used to extrapolate the results obtained for the reference model to other configurations of interest.

A completely vigorous and detailed investigation of PYE WACKET aeroelastic characteristics was prohibitive due to the limited time and resources available for this study. However, in view of the importance of aeroelastic considerations to missile design, a limited study was conducted in this area. The purpose was to ascertain the significance of aeroelastic parameters on the PYE WACKET performance characteristics.

The method used to predict non-stationary airload distributions over the lenticular planform is described. For the limiting case of zero frequency rigid body translation and pitch, good agreement with respect to total lift and moment is shown between theory and corresponding wind tunnel data. Based on a qualitative analysis of the configuration, vehicle flutter as a result of aerodynamic coupling between primary surface modes is not considered to be likely within the required flight profile. For the purposes of this preliminary study, therefore, emphasis has not been placed on a quantitative flutter speed prediction. The method to be used, however, in mechanizing the flutter equations and obtaining a solution is presented.

NON-STATIONARY AERODYNAMICS. Non-stationary airloads are represented by means of an aerodynamic theory that is generally called Piston Theory. This theory makes the assumption that when an airfoil is travelling at supersonic speeds, the disturbance velocities in the air are perpendicular to the direction of travel. Thus it can be said that the air reacts just as though

SECRET

it were acted on by a series of pistons moving perpendicular to the flight direction. The pressure on the face of a moving piston can be expressed in terms of the piston velocity, or in the case of the airfoil, the perturbation velocity at any point. Ashley and Zartarian (Reference 3.6.4) show this relation to be

$$C_p = \frac{p - p_\infty}{q} = \frac{2wu}{MU} + \left(\frac{\gamma+1}{2}\right) \left(\frac{wu}{U}\right)^2 + \left(\frac{\gamma+1}{6}\right) M \left(\frac{wu}{U}\right)^3 + (\text{higher order terms}) \quad (3.6.37)$$

where

- M = Mach number
- w = Disturbance velocity, positive away from the surface
- μ = Free stream velocity
- q = Dynamic pressure
- γ = The ratio of specific heats

Since this theory does not take into account any finite span effects, and is generally limited to the case of thin airfoils, its applicability to the problem at hand might be questioned. In order to gain some insight of its usefulness, the theory was specialized to the case of steady state for the 14 percent thick blunt lenticular configuration, and the results were compared with wind tunnel data. Only the first two terms of the C_p equation were used. Figure 3.6.31 shows that the correlation between theory and experiment is quite good, especially between $M = 3$ and $M = 6$.

This agreement tends to justify the use of piston theory to calculate the airloads on the body.

FLUTTER-METHOD OF ANALYSIS. For aeroelastic purposes, one of the most convenient methods of describing the forced motions of an elastic body is by a summation of the natural modes of the free, unrestrained system plus the rigid body motions with respect to a reference plane. If this method is used, the elastic deflection of the body, $u(x, y, t)$ can be expressed as

$$u(x, y, t) = \sum_{r=1}^n \phi_r(x, y) \xi_r(t) \quad (3.6.38)$$

where $\phi_r(x, y)$ represents the deflection shape of the surface in the r th natural mode and ξ_r represents the time varying amplitude of the r th mode. If the pitch angles are small, this method can be extended to include the rigid body motion by letting

$$\begin{aligned} \phi_1 &= 1, \quad \xi_1 = h(t) \\ \phi_2 &= x, \quad \xi_2 = \theta(t) \\ \phi_3 &= y, \quad \xi_3 = \beta(t) \end{aligned}$$

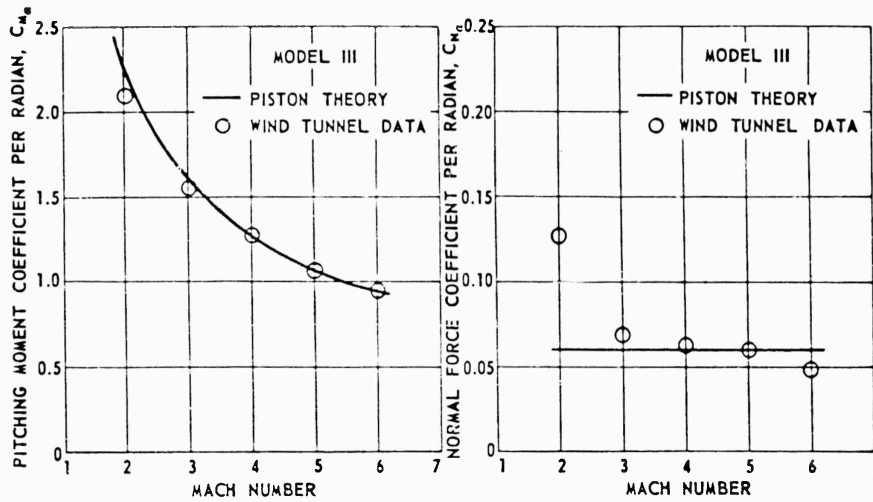


Figure 3.6.31. Stability Derivatives.

which represent vertical translation, pitch in the x direction and pitch in the y direction, respectively. Defining $z(x, y, t)$ as the z distance to any point on the body measured from an initial reference plane, it can be seen that

$$z(x, y, t) = \sum_{r=1}^n \phi_r(x, y) \xi_r(t) \tag{3.6.39}$$

The equations of motion for a system represented in such a manner and acted on by a force $F_z(x, y, t)$, can be found to be

$$M_r (\ddot{\xi}_r + \omega_r^2 \xi_r) = \Xi_r \tag{Reference 3.6.5} \tag{3.6.40}$$

where

$$M_r = \iint_S \phi_r^2(x, y) m(x, y) dx dy \tag{generalized mass},$$

$$\Xi_r = \iint_S F_z(x, y, t) \phi_r(x, y) dx dy \tag{generalized force},$$

$m(x, y)$ = Mass per unit area,

ω_r = The natural frequency of the rth mode,

$\omega_1 = \omega_2 = \omega_3 = 0$.

If F_z is aerodynamic loading,

$$F_z = \rho_{lower} - \rho_{upper} = g (C_{pl} - C_{pu}) \quad (3.6.41)$$

Applying second order Piston Theory to a symmetric airfoil, of thickness $\tau(x, y)$,

$$C_{pl} - C_{pu} = \left(\frac{4}{M} + [\gamma + 1] \tau'(x, y) \right) \left(\sum_{j=1}^n \left[\phi_j' \xi_j - \phi_j \frac{\ddot{\xi}_j}{U} \right] \right) \quad (3.6.42)$$

This gives

$$\Xi_r = g \sum_{j=1}^n \iint_s \left(\frac{4}{M} + (\gamma + 1) \tau' \right) \left(\phi_r \phi_j' \xi_j - \phi_r \phi_j \frac{\ddot{\xi}_j}{U} \right) dx dy \quad (3.6.43)$$

At the onset of flutter, the motion is a sustained oscillatory motion or

$$\xi_r = \bar{\xi}_r e^{i\Omega t} \quad (3.6.44)$$

Ω being the angular frequency of the oscillation. To determine the flutter boundary, the above relation is employed. Ξ_r may be rewritten as

$$\Xi_r = g \sum_{j=1}^n \left(f_{rj} - i \frac{\Omega}{U} g_{rj} \right) \bar{\xi}_j e^{i\Omega t} \quad (3.6.45)$$

$$f_{rj} = \iint_s \left(\frac{4}{M} + (\gamma + 1) \tau' \right) \phi_r \phi_j' dx dy \quad (3.6.46)$$

$$g_{rj} = \iint_s \left(\frac{4}{M} + (\gamma + 1) \tau' \right) \phi_r \phi_j dx dy \quad (3.6.47)$$

The equations of motion become

$$M_r (\omega_r^2 - \Omega^2) \bar{\xi}_r = g \sum_{j=1}^n \left(f_{rj} - i \frac{\Omega}{U} g_{rj} \right) \bar{\xi}_j \quad (3.6.48)$$

SECRET

or in matrix form,

$$[a_{rr}] [\bar{\xi}_j] - g [f_{rj}] [\bar{\xi}_j] + i g \frac{\Omega}{U} [g_{rj}] [\bar{\xi}_j] = 0 \quad (3.6.49)$$

where the elements of the a_{rr} matrix are

$$a_{rr} = M_r (w_r^2 - \Omega^2) \quad (3.6.50)$$

In order for the foregoing equation to always hold, the determinant of the coefficients of the $\bar{\xi}_j$ matrix must be equal to zero or

$$\left| a_{rr} - g f_{rj} - \frac{i\Omega}{U} g g_{rj} \right| = 0 \quad (3.6.51)$$

The solution of this determinant for its eigenvalues gives the flutter boundary.

Solving the foregoing determinant to obtain the flutter boundary is a straightforward but time consuming task, and it is felt that the limited time and uncertainty of the physical properties of the configuration did not warrant a complete analytical solution during this study.

PYE WACKET PRELIMINARY PANEL FLUTTER INVESTIGATION. The panel considered in this study is that indicated by the shaded area in Figure 3.6.32. For purposes of demonstrating the effect of internal stiffening, the panel is assumed to be divided into square cells; a 4-cell panel is shown in Figure 3.6.31 as an example. The following assumptions are made for purposes of this investigation:

1. The panel is initially flat (conservative).
2. "Steady" supersonic theory applies, i. e. $M_{\max} > 1.6 \mu > 10$ (These conditions are always satisfied for PYE WACKET configurations.)
3. The panel is not buckled.
4. No mid-plane compressive stresses exist. (unconservative)
5. The panel is simply supported. (conservative)
6. The panel material is titanium.
7. Panel aspect ratio = 1.0. (See Figure 3.6.32.)
8. No pressure differential exists across the plate. (conservative)

Further studies should encompass the effects precluded in this investigation by assumptions 1, 3, 4, 5, and 8.

The parameter governing oscillatory instability of a flat panel in "steady" supersonic flow is the dimensionless group

SECRET

3.6.33

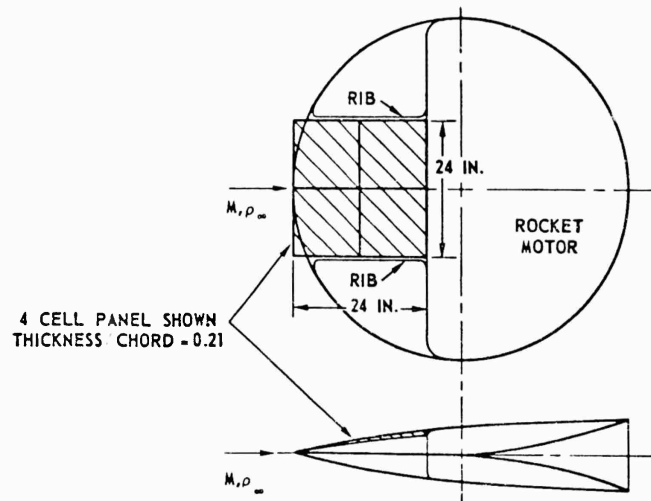


Figure 3.6.32. Sketch of Configuration.

$$\lambda = \frac{2q l^3}{D \sqrt{M^2 - 1}} \quad (3.6.52)$$

where D is the plate stiffness $D = \frac{E h_p^3}{12(1-\nu^2)}$

For given edge fixity and panel aspect ratio, a critical value of (λ) is defined. If (λ) exceeds this value (λ_{CR}), panel flutter is probable. By virtue of assumptions 5 and 7, λ_{CR} will have a fixed value throughout this study: $\lambda_{CR} = 475$.

From Equation 3.6.52 it can be seen that a value of λ_{CR} yields a panel flutter (or "critical") Mach number, M_{CR} , for fixed altitude, plate stiffness, and panel chord. Panel flutter is probable for any Mach number above M_{CR} .

The results of this study are presented in graphical form in Figures 3.6.33, 3.6.34, and 3.6.35, for the 60-inch blunted lenticular configuration with a t/C of 21 percent.

Figure 3.6.33 is a plot of M_{CR} versus altitude for a 4-cell panel, $h_p = 0.030$ inch, $l = 12$ inches. A maximum Mach number versus altitude curve for the 21 percent thick missile is superimposed on Figure 3.6.33 in order to show regions of panel flutter instability. Note that, for the example configuration supported in the manner shown, panel flutter will occur within the flight envelope for all altitudes below 64,000 feet.

Figure 3.6.34 shows the effect of plate thickness on M_{CR} for the 4-cell panel at sea level and at 60,000 feet. The strong influence of skin thickness on M_{CR} is evident. The sea level case would design the skin for a 4-cell panel.

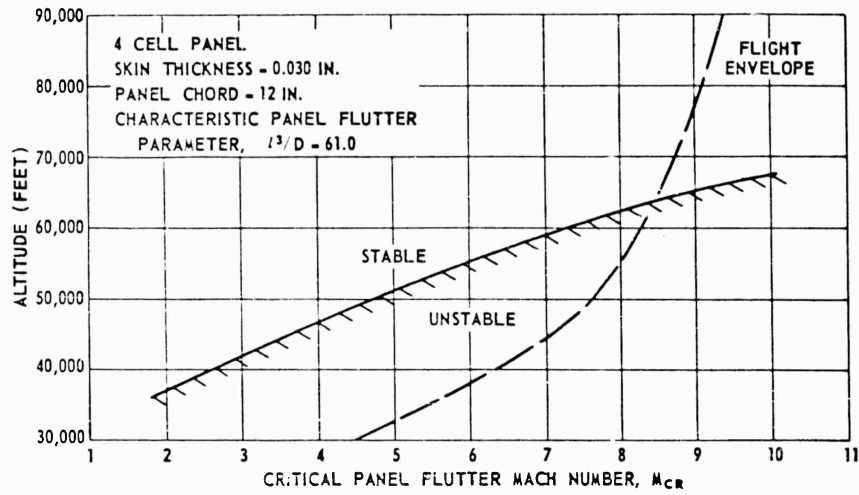


Figure 3.6.33. Altitude Versus Critical Panel Flutter Mach Number.

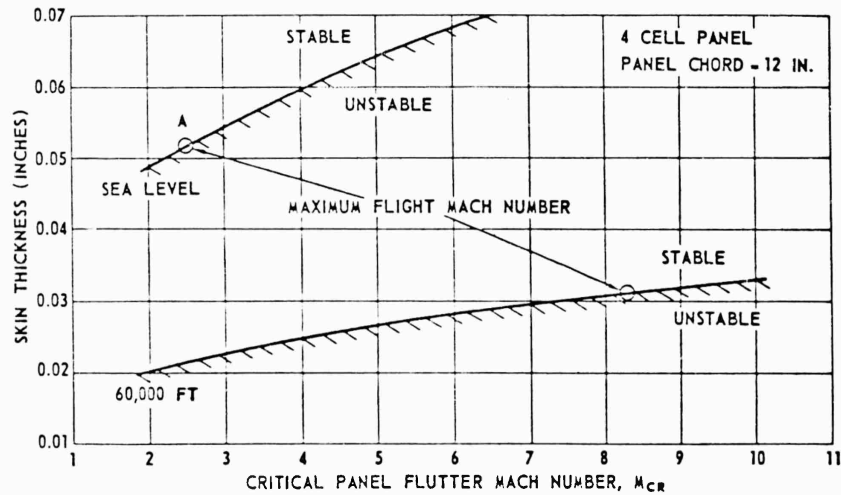


Figure 3.6.34. Skin Thickness Versus Critical Panel Flutter Mach Number.

Point "A" indicates maximum flight Mach number at sea level; thus panel flutter integrity would require at least $h_p = 0.052$ -inch for a panel 12 inches square.

Figure 3.6.35 illustrates the effect of internal stiffening on M_{CR} for a panel of 0.030 inch thickness at sea level. The need for internal stiffening is clearly indicated. It can be seen that, for $h_p = 0.030$ -inch, a 16-cell panel must be used to insure against panel flutter.^p

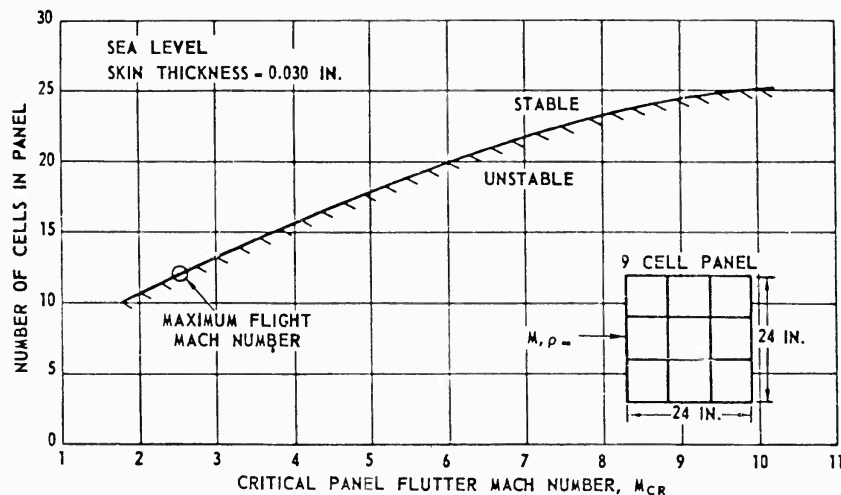


Figure 3.6.35. Effect of Internal Stiffening On Critical Panel Flutter Mach Number.

In the light of these preliminary results, it is recommended that some form of stiffening be used in the skin itself (honeycomb or chordwise corrugation), or in the missile internal structure (additional spanwise ribs added in order to reduce panel chord). This effect is depicted in Figure 3.6.35.

Compressive mid-plane stress and panel buckling, neglected in this study, have a significant effect on panel flutter. If mid-plane stress is allowed to approach the Euler buckling stress for the panel, a large reduction in critical Mach number may be expected.

STRUCTURAL DYNAMICS. The analysis of the structural dynamics of a body such as this is at best a complicated procedure. In order to obtain some first order estimates for use in other phases of this study, simplifying assumptions were made. The first two deflection shapes and their frequencies were calculated for a reference case. The configuration used had the following characteristics:

1. Diameter of 60 inches
2. 21 percent thickness-to-chord ratio
3. Skin on forward portion of missile is 0.060-inch titanium alloy sheet
4. Skin on tank area is 0.50-inch material of sandwich type construction having 0.020-inch thick facings

Plots of the mass and stiffness data that were used are presented in Figure 3.6.36.

The frequencies associated with the deflection shapes, which are presented in Figure 3.6.37, are 281 CPS and 652 CPS for the first and second modes, respectively. If they are considered to be representative, it is anticipated that

SECRET

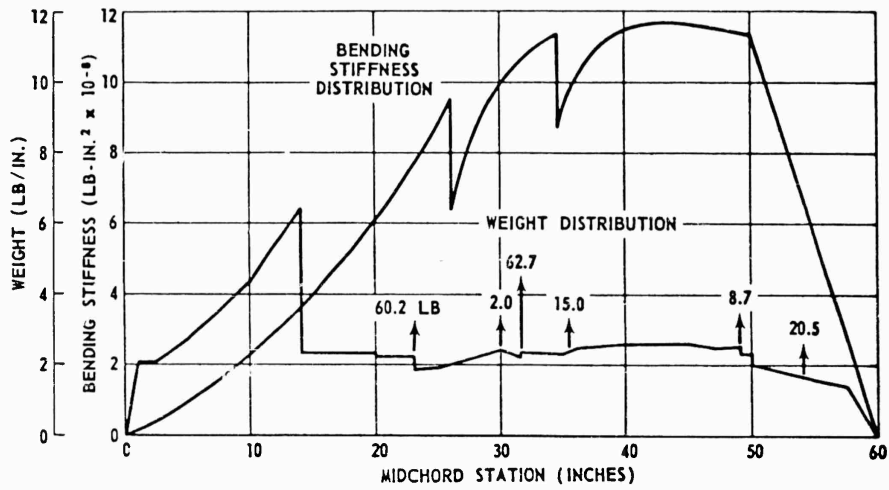


Figure 3.6.36. Physical Properties of Reference Vehicle.

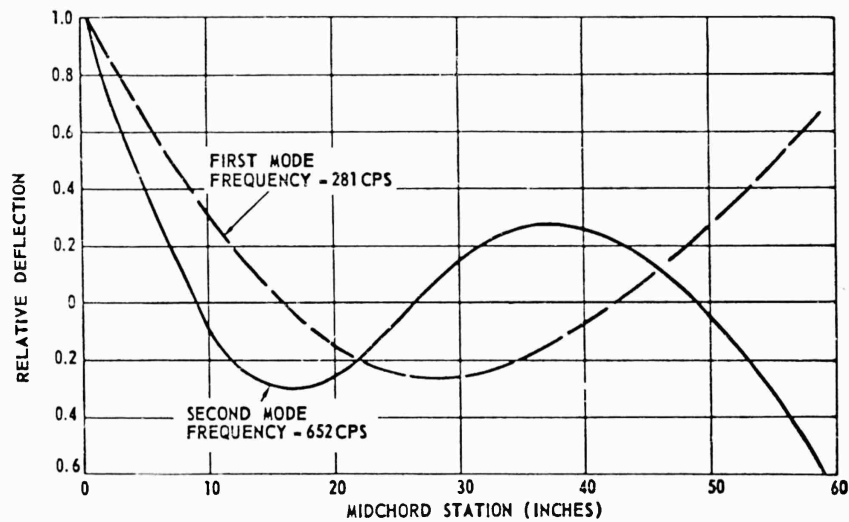


Figure 3.6.37. Deflection Shapes and Frequencies for Reference Configuration.

there will be no serious servo-elastic coupling problems to affect missile control since they are considerably above the frequencies associated with the autopilot-guidance system.

In Figure 3.6.38, plots can be seen which show the variation of the first mode frequency with change of overall dimensions and with change of thickness-to-chord ratio, assuming the mode shape to remain unchanged.

SECRET

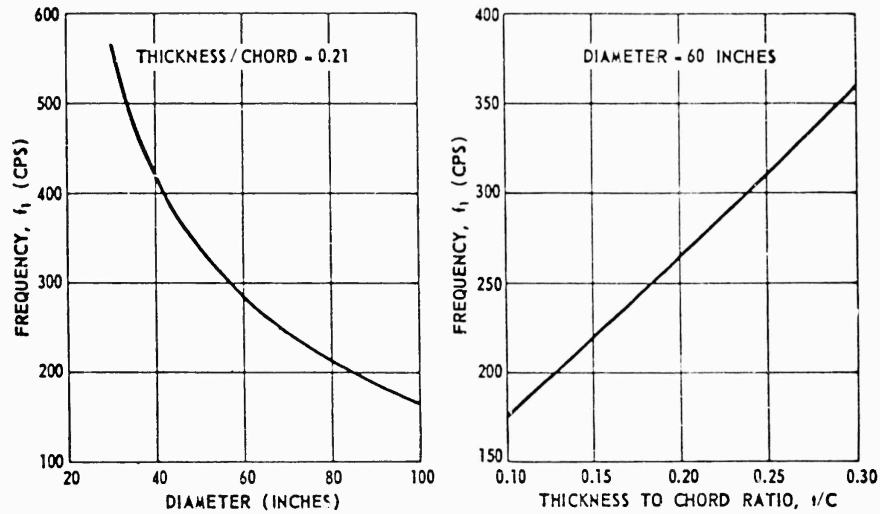


Figure 3.6.38. Variation of Frequency With Dimension Changes.

As an experimental check on the method of computation, the solid wind tunnel model (20-inch diameter, 14 percent thick) was vibration tested using an induction shaker setup shown in Figure 3.6.39. The first resonant frequency was found to be about 1000 CPS. The model analysis method used to compute frequencies for the reference configuration was then applied to the wind tunnel model. This resulted in a predicted fundamental frequency of 946 CPS which is considered to be in very reasonable agreement with the test value and suggests that the method of analysis is slightly conservative.

STATIC AEROELASTIC EFFECTS. The primary static aeroelastic characteristic of interest from the standpoint of autopilot design is the shift in effective aerodynamic center of pressure location as a result of airframe deformation under load. This effect has been estimated for the PYE WACKET configuration using a generalized coordinate method which permits a useful approximation to be obtained from the first elastic mode characteristics. This approximation for center of pressure shift due to static aeroelastic effects can be expressed as follows:

$$\Delta C_p = \left(\frac{A_{e\xi} A_{\xi h}}{A_{nn}} \right) \frac{q v^2}{2K_{\xi}} \quad (3.6.53)$$

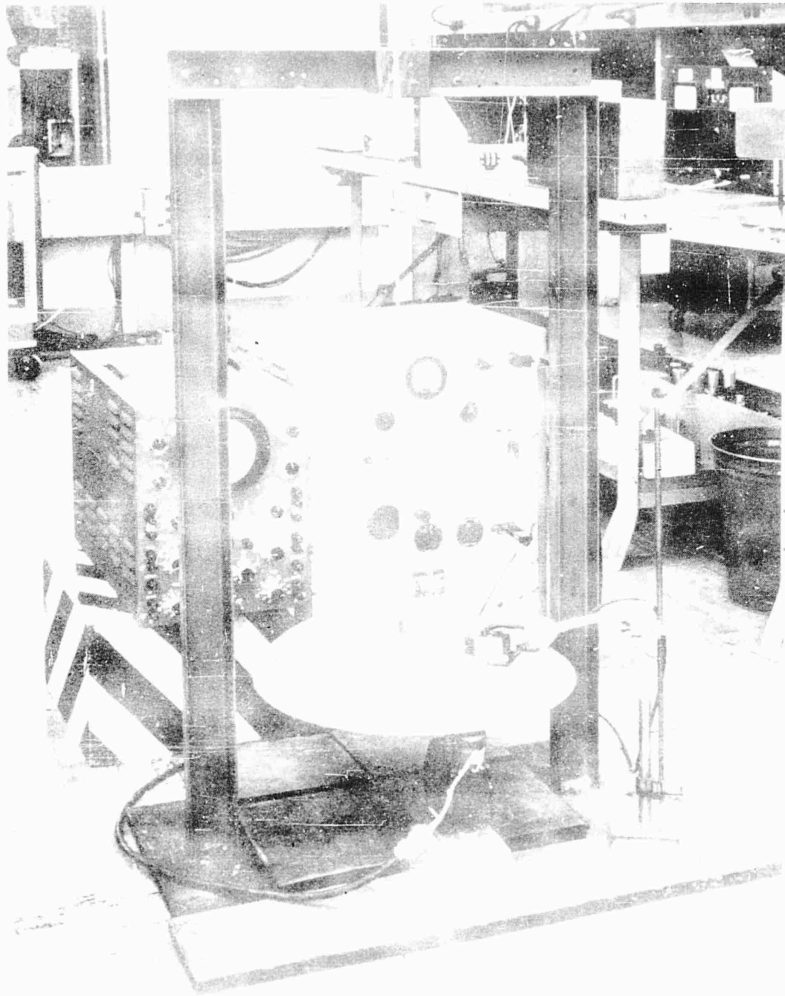


Figure 3.6.39. PYE-SACKET Vibration Tests.

where δ = diameter of platform, inches
 ρ = density of platform, lb./in.³
 ω = generalized frequency, rad./sec.
 ω_0 = natural frequency of platform, rad./sec.
 ω_0^2 = generalized first bending mode coordinate, inches
 R = radius of platform, inches
 k = spring constant of spring for the first bending mode, lb./in.

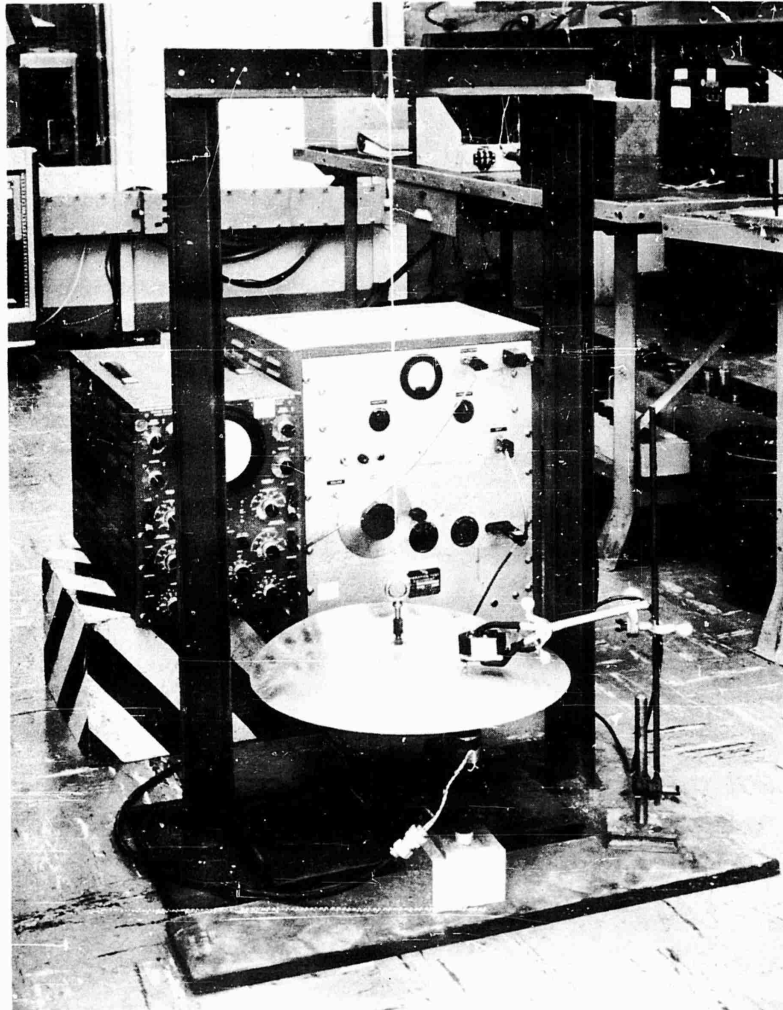


Figure 3.6.39. PYE WACKET Vibration Tests.

where

- Δc_p = Center of pressure shift in percent diameter
- A_{ij} = Generalized non-dimensional aerodynamic force produced on the i th coordinate by unit displacement in the j th coordinate
- ξ = Generalized first bending mode coordinate, inches
- r = Radius of planform, inches
- K_ξ = Generalized spring for the first bending mode, pounds/inch

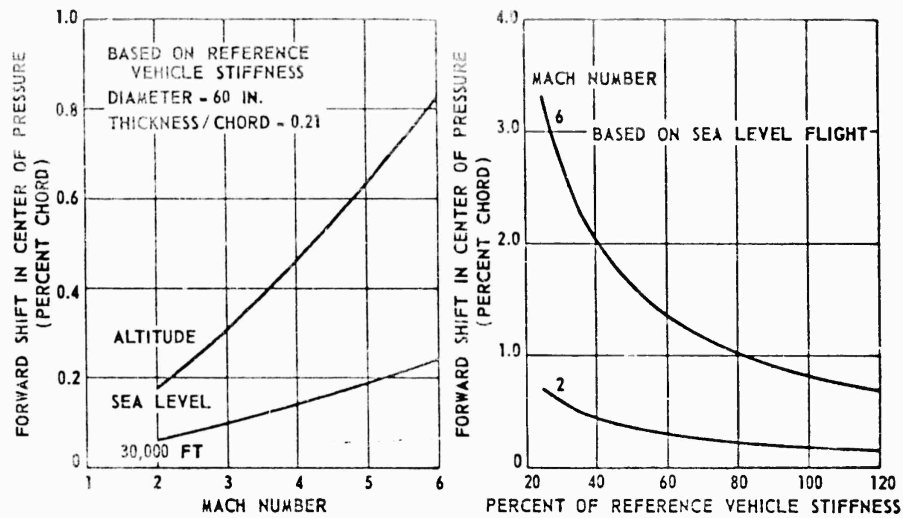


Figure 3.6.40. Static Aeroelastic Effect on Center of Pressure as Function Mach Number and Vehicle Stiffness.

The aerodynamic coupling, A_{ij} , between the rigid body coordinates of the vehicle and the first generalized elastic mode is computed by integrating the calculated sectional aerodynamic coefficients over the predicted mode shape. Figure 3.6.40 presents the estimated center of pressure shift as a function of Mach number for the reference configuration and also a curve showing the functional relationship with vehicle stiffness assuming no change in distribution. From an inspection of these curves it is evident that no appreciable shift in center of pressure will result from aeroelastic considerations within the expected flight environment.

3.6.4 SUMMARY OF STRUCTURES STUDY

MATERIALS AND STATIC CONSIDERATIONS. The material investigation showed a decided advantage for B-120 titanium. This material can be formed, machined, chemically etched, and molded. It possesses strength-to-weight advantages of 20 percent to 60 percent over 15-7 Mo stainless steel in the temperature range of 800°F to 1000°F.

Analysis of the forward skin showed honeycomb sandwich to be approximately 20 percent lighter than a corrugation stiffened skin.

Stabilization of the upper and lower pressure vessel surfaces was accomplished by posts. Posts were selected because they can be inserted after the tank is assembled, and they do not sectionalize the tank as would bulkheads.

SECRET

The tank edge closures proved to be the major weight factor for the tank. The extreme double curvature of the edge closure practically precludes the use of honeycomb sandwich in this area. Also, the solid plate could be welded at the mid-plane for final assembly of the tank.

The tank plates, or upper and lower surfaces, were studied for pressures ranging from 150 PSI to 500 PSI. Of the three types of construction evaluated; honeycomb, solid plate, and grid stiffened membrane, honeycomb again proved to be the lightest.

A comparison of weights for liquid and solid propellant structures was made for a 250 PSI and a 21 percent thickness-to-chord ratio case. The solid propellant structure was estimated to be approximately 35 pounds lighter based on metal parts weights alone, neglecting differences in insulation requirements.

No detailed structural analyses were made of multiple-cylinder solid propellant configurations (other than as presented in subsection 3.4, Propulsion) though these arrangements are sufficiently conventional to preclude any major structural problems. Such an arrangement appears completely feasible structurally.

While the PYE WACKET configuration is rather unusual, the overall structure studies conducted in this phase of the task indicated satisfactory structures could be designed with weights low enough to provide excellent missile performance. In fact, use of the 800°F temperature factor for the pressure vessel tends to make some of the weights conservative. Further detailed analyses and design studies should be conducted as part of the future PYE WACKET task to prove out optimum designs.

AEROELASTIC CONSIDERATIONS. As a result of the preliminary aeroelastic studies the following conclusions were reached:

1. The elastic mode frequencies will be sufficiently high to preclude serious coupling with the autopilot (guidance loop functions).
2. Static aeroelastic effects are not expected to be significant within the required performance boundaries for any of the configurations considered.
3. Some form of internal panel support either through use of a corrugated inner skin, additional ribs, and/or sandwich type construction will be required to prevent destructive panel flutter in a large portion of the flight profile. Expected stability margins for internally stiffened panels can be compromised if compression stresses, induced by temperature and flight loads, approach the value required for buckling. This effect should be more fully investigated in subsequent PYE WACKET studies.

3.6.5 SYMBOLS AND DEFINITIONS

Static Structural Study

A	Area, square inches cross section
a	

SECRET

3.6.41

b	Dimension, inches
C	Chord length, inches
	Distance, inches
c	Distance from neutral axis to outer fiber, inches
D	Corrugation height, inches
	Diameter, inches
	Deflection, inches
d	Diameter, inches
E	Modulus of elasticity, pounds per square inch
e	Eccentricity
°F	Degrees Fahrenheit
F	Allowable stress, pounds per square inch
f	Calculated stress, pounds per square inch
h	Height, inches
I	Moment of inertia, (inches) ⁴
K	Constant
(Ki/Kw)	Ratio denoting moment of inertia per unit weight
L	Length, inches
lb	Pounds
lg	Grid length, inches
M	Moment, inch-pounds
N	Number
P	Pressure, pounds per square inch
	Load, pounds
psi	Pounds per square inch
q	Load per unit length, pounds per inch
R	Radius, inches
STA	Station, inches
S	Dimension
t	Thickness, inches
(t/C)	Missile thickness-to-chord ratio
w	Load per unit length, pounds per inch
W	Force, pounds
Z	Section modulus, (inches) ³
α	Angle, radians or degrees
ρ	Radius of gyration
ϕ	Angle, radians or degrees
π	3.1416
c	Compression
	Corrugation
CR	Crippling
g	Grid
I	Sandwich skin

SECRET

max	Maximum
O	Outside
p	Pressure
	Posts
s	Skin
	Shear
T	Total
t	Tension
w	w load
x	x direction
y	y direction
	Yield

Dynamic Structural Study

C_{M_α}	Derivative of pitching moment coefficient with respect to angle of attack
C_{N_α}	Derivative of normal force coefficient with respect to angle of attack
C_p	$= \frac{p - p_\infty}{q}$ = pressure coefficient
CP	Center of pressure position
D	Plate stiffness (LB. IN.)
E	Young's modulus (LB/IN ²)
f	Frequency (cycles/SEC)
F_z	Aerodynamic force in the z direction
h	Rigid body translation (FT)
h_p	Panel thickness (IN.)
i	$= \sqrt{-1}$
I	Sectional moment of inertia (IN ⁴)
l	Panel chord (IN.)
M	Mach number
M_r	Generalized mass of the r th displacement mode (slugs)
p	Static pressure (LB/IN ²), (LB/FT ²)
q	$1/2 \rho_\infty U^2 = 1/2 \rho M^2 \gamma$ dynamic pressure (LB/IN ²), (LB/FT ²)
r	Radius of planform (IN.)
t	Time (SEC)
u	Elastic deflection of the body (FT)
U	Free stream velocity (FT/SEC)
w	Disturbance velocity, positive away from the surface (FT/SEC)
x	Coordinate direction
y	Coordinate direction
z	Coordinate direction
γ	Ratio of specific heats = 1.40 for air
ν	Poisson's ratio
Λ	Characteristic panel flutter parameter
μ	Density ratio $= \rho_m l / \rho_\infty h_p$

SECRET

3.6.43

ρ_∞	Free stream air density (slugs/IN ³), (slugs/FT ³)
ρ_m	Density of plate material (slugs/IN ³)
ϕ	Displacement shape or mode shape (dimensionless)
ξ	Generalized coordinate (FT), (IN)
ω	Angular frequency (RAD/SEC)
Ω	Flutter angular frequency (RAD/SEC)
r	Thickness of missile in z direction (FT)
θ	Rigid body pitch coordinate
β	Rigid body roll coordinate
Ξ	Generalized force (LB)

Subscripts

r	Referring to the r th displacement mode
j	Referring to the j th displacement mode

Symbols

\iint_s	Integral over the surface
$(\dot{})$	$\frac{\partial()}{\partial t}$ The partial derivative of a quantity with respect to time
$()'$	$\frac{\partial()}{\partial x}$ The partial derivative of a quantity with respect to x.

3.6.6 LIST OF REFERENCES

- 3.6.1 Bruhn, E. F., Analysis and Design of Airplane Structures, Tri-State Offset Company - Revised Edition, January 1952
- 3.6.2 Roark, R. J., Formulas for Stress and Strain, McGraw-Hill Book Company, 1954
- 3.6.3 Seeley, F. B., Smith, J.O., Advanced Mechanics of Materials, John Wiley & Sons, Inc., Second Edition, 1952
- 3.6.4 Ashley, H., and Zartarian, G., Piston Theory - A New Aerodynamic Tool for the Aeroelastician, Journal of the Aeronautical Sciences, December 1956
- 3.6.5 Dugundji, J., Panel Flutter, Chapter 6 of summer course notes for Aeroelasticity (16.919), presented at M.I.T., June 1958
- 3.6.6 Hedgepeth, John M., Flutter of Rectangular Simply Supported Panels at High Supersonic Speeds, Journal of the Aeronautical Sciences, August 1957
- 3.6.7 Fung, Y. C., On Two - Dimensional Panel Flutter, Journal of the Aeronautical Sciences, March 1958
- 3.6.8 Bisplinghoff, R. L., Ashley, H., and Halfman, R. L., "Aeroelasticity," Addison-Wesley Publishing Company, Inc., Cambridge, 1955

SECRET

3.7 CONTROL SYSTEMS

This subsection discusses the various control systems considered for PYE WACKET application. The primary objective is to determine the best control system to use on the PYE WACKET Model III configuration. The stability characteristics of this configuration are contained in subsection 3.2.

The contents of this subsection are enumerated below:

First, aerodynamic controls were treated in detail. The various aerodynamic controls considered included spoiler type flaps (pitchers), cones and wedges mounted at the lateral extremities of the body (cones and wedges), leading edge sector deflection and side sector deflection (side elevons). These were evaluated with regard to stabilizing and controlling capabilities as well as possible aerodynamic coupling effects. Such items as weight and actuation forces were also considered.

Next, a detailed treatment of non-aerodynamic controls was made. The non-aerodynamic controls considered were reaction jet types. These included the use of the main rocket jet and auxiliary control jets. These were evaluated as to design feasibility, available response time and adaptability to the PYE WACKET configuration.

Having treated both aerodynamic and non-aerodynamic controls, an investigation of autopilot systems was made. Both linear and non-linear systems were considered. Reaction and aerodynamic systems were evaluated for response times and autopilot simplicity.

Finally, the maneuver capabilities of both aerodynamic and reaction controls were considered over the operating Mach number and altitude ranges anticipated for PYE WACKET.

3.7.1 AERODYNAMIC CONTROLS

The following paragraphs discuss the use of aerodynamic surfaces for pitch, yaw, and roll control of a circular planform body. Aerodynamic controls are not suitable for use in the omnidirectional launch phase of flight due to the necessity of alignment with the relative wind and the requirement for sufficient dynamic pressure for proper control effectiveness. Reaction controls would obviously be required in that phase of flight. The utilization of aerodynamic controls for a missile system requiring omnidirectional launch capabilities is therefore restricted to the glide phase of flight. Hence, the consideration of aerodynamic controls automatically implies a dual control system if omnidirectional launch capability is a requisite. If omnidirectional launch is not a requisite, the feasibility of aerodynamic controls is of paramount interest. Therefore, a thorough investigation of their capabilities was warranted in this study. The use of aerodynamic controls for extremely long flight times in the lower atmosphere is a

SECRET

3.7.1

SECRET

distinct possibility. Special applications of PYE WACKET, which do not require omnidirectional launch, may find aerodynamic controls attractive and perhaps mandatory. It should be noted that the data obtained on aerodynamic controls are invaluable in an evaluation of the effects of surface protuberances on the force and moment characteristics of the missile.

Because the publication of all wind tunnel data obtained in the experimental program would make this volume too large to be useful, the presentation is limited primarily to the most indicative results of the data analysis. All data presented are for the blunt lenticular body unless noted otherwise.

CONTROL DEVICES INVESTIGATED. The controls investigated in this study are illustrated in Figure 3.7.1 and are described in detail in subsection 3.2. An application of the "bulk" controls considered in this section can be found in Reference 3.7.1.

For pitch control, the effectiveness of spoiler type flaps (pitchvators) was investigated. Figure 3.7.1 shows all four pitchvators (two forward surfaces and two aft surfaces) deflected. Figure 3.7.2 shows the directions for positive forces and moments. In order to generate positive (nose up) angular accelerations, only the forward lower and/or aft upper surfaces would be used. In other words, as illustrated in Figure 3.7.1, the negative incidence values would be used. Likewise, for negative (nose down) angular accelerations, the positive incidence values would be used. It should be noted that due to the instability of the missile (see subsection 3.2) positive incidence values would be required to maintain positive angles of attack. This is exactly opposite to the case where a stable configuration is involved. However, the art of flying unstable configurations is well advanced and, in many cases, unstable configurations are preferred to the slower responding stable configurations.

The procedure for maneuvering an unstable configuration is roughly as follows:

The missile is first perturbed by the application of a negative incidence deflection. Since the configuration is unstable, a rapid build up in angle of attack begins immediately. The control surfaces are adjusted by the autopilot to positive incidence settings in order to stop the missile at the angle of attack producing the called-for maneuver. Usually, a slight overcontrol is required in order to prevent overshoot in the desired angle of attack.

Three pitchvators were investigated in the wind tunnel program outlined in subsection 3.2. These are listed in Table 3.7.1.

SECRET

SECRET

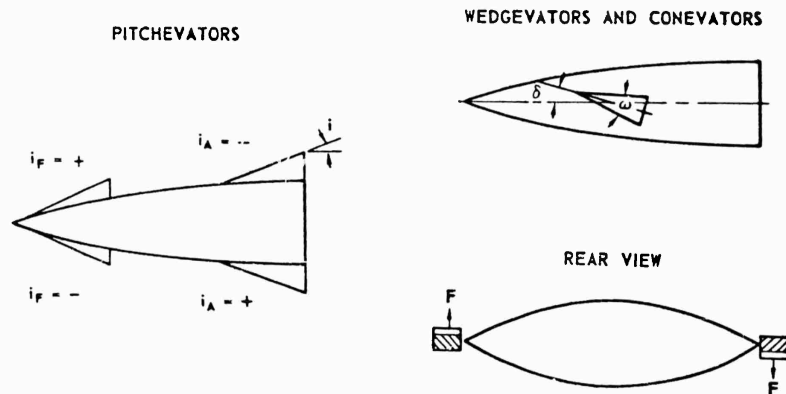


Figure 3.7.1. Configuration and Nomenclature for Aerodynamic Controls.

Table 3.7.1
PITCHEVATOR GEOMETRIC CHARACTERISTICS

Pitchevator	P ₁	P ₂	P ₃
Chord, IN.	5	5	7
Span, IN.	5	7	5
Area, IN ²	25	35	35
Location of forward pitchevator leading edge, body station, IN.	1.0	1.0	1.0
Location of aft pitchevator leading edge, body station, IN.	12.8	12.8	12.8
Deflection angles, DEG.	20° (Model I, II, & III)	20° (Model III)	20° (Model III)
	15° and 25° (Model III)		
Aspect ratio	1.0	1.4	0.714

SECRET

ALL FORCES AND MOMENTS SHOWN ARE IN POSITIVE SENSE

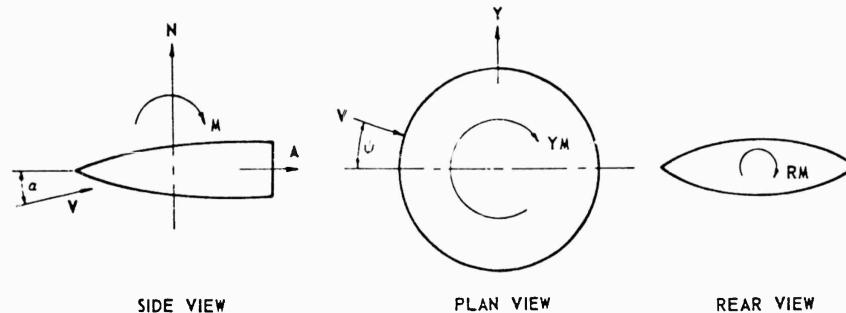


Figure 3.7.2. Aerodynamic Force, Moment, and Angle Notation.

The above control surface areas represent a relatively large percentage of the body surface area as compared to cone-cylinder type missiles with tail controls. This is due to the extremely short moment arm possible within the circular envelope. The location of the aft pitchvators could, however, be shifted further aft. This location was tested to be compatible with Model I. Model I could not have the pitchvators further aft due to the wind tunnel sting projecting through the body upper and lower surfaces.

Control of a circular planform body by means of aerodynamic surfaces located within the circular envelope poses mechanical design problems of considerable magnitude. As mentioned above, relatively large surfaces (i.e., large forces) are required due to short moment arms. Therefore, powerful actuator systems would be required for control surface operation. Flaps deflected from the surface do not permit aerodynamic balancing. Therefore, the combination of the flaps hinged at their leading edges, and the large forces which they are required to generate due to short moment arms, results in extremely large hinge moments.

Prior to discussing roll and yaw control devices, it is first worthwhile to discuss other possible means, not tested in this study, for achieving pitch control using aerodynamic surfaces. Leading edge deflection was proposed by the Air Proving Ground Center and was investigated in the APGC "in house" test program. The preliminary results of this test were forwarded to Convair-Pomona for consideration and are included in this report. Another possible method of control is by means of trailing edge deflection. This type of control was immediately dropped from consideration due to the thickness of the trailing edge of Model III. However, deflection of the upper and/or lower body surfaces near the aft end is a possible means of control which is quite similar to the operation of the aft pitchvator. A technique for supplementing pitch control at an angle of attack, which was also investigated in the APGC test program, would be

SECRET

the extension of flat plates from the aft end of the body; the further the extension of the plate, the less the degree of instability of the configuration. This technique was not pursued since design considerations precluded its application to the blunt base body, i. e., Model III.

For roll control, the effectiveness of cones (coneators) and wedges (wedg-evators) mounted at the lateral extremities was investigated. Other methods of obtaining roll control forces by aerodynamic surfaces were considered, but the testing time available was not sufficient to allow investigation of many possible roll control devices.

One method, which was suggested in Reference 3.7.2, is similar to that described above for pitch control (i. e., pitchevators). Spoiler type flaps could be mounted on the upper and lower surfaces near the lateral edges of the body. A clockwise rolling moment, for example, would be generated by deflecting the upper-right flap upward and the lower-left flap downward. The primary disadvantage of this system, from an aerodynamic point of view, would be the effect of body shielding on the leeward flap when the body was at an angle of attack. This would cause a decrease in the force on the leeward flap which would result in a yawing moment of large magnitude. For this reason, this method of roll control was not included in the experimental program.

Another promising method of obtaining roll control is by lateral tip deflection. This type of control was investigated in the APGC "in house" test program. The preliminary results of this test were forwarded to Convair-Pomona, and are included in this report.

As mentioned above, cones (coneators) and wedges (wedg-evators) mounted at the lateral extremities of the body were investigated for roll control characteristics. Rolling moments were obtained by differential deflection of the cones or wedges. As shown in Figure 3.7.1, the wedges are set at a positive differential deflection, i. e., deflection of the leading edge of the left wedge (δ_L) is up, producing a force up, and deflection of the right wedge (δ_R) is down, producing a force down.

The roll control data obtained during the experimental program were for a pair of cones having an apex angle of 30 degrees, a fineness ratio of 1.86, and a maximum diameter ratio, with respect to the body diameter, of 0.147. The pair of wedges have an included angle of 15 degrees, an aspect ratio of 0.66 and a maximum chord ratio, with respect to the body diameter, of 0.15.

Only one method of yaw control was investigated in this experimental program. This method employed wedges (wedg-evators) mounted at the lateral extremities of the body. Yawing moments were generated by setting the included angle of one wedge at a larger magnitude than the other, thereby producing differential drag. One reason for testing this method instead of other possible methods was that the wedges could be used for both yaw and roll control, as discussed above. It should be noted that the blunted lenticular is slightly stable in yaw, (see subsection 3.2).

SECRET

SECRET

The conventional method of obtaining yaw control, that is, by the use of movable vertical fins, was considered undesirable for use with a circular plan-form body. If only one fin were used (i. e., fin mounted only on the top or bottom) the fin would be quite ineffective when the missile is at an angle of attack with the fin located on the leeward side of the body where a disturbed region of flow exists. The use of only one fin is also impractical because any deflection for yaw control would produce a rolling moment. Therefore, two fins would have to be employed. Again, with two fins, rolling moments would be induced by yaw deflection if the missile were at an angle of attack causing the leeward panel to be less effective than the windward panel. The use of vertical tail fins even for the glide phase of an omnidirectional launch vehicle presents an additional aerodynamic problem. For any launch other than directly forward or aft, the vertical fins would tend to turn the missile into the relative wind. The only way to avoid this would be to fold the fins flush with the body until the wind velocity vector and the missile flight path were essentially parallel in the lateral plane of the body. Fin folding and the induced rolling moment discussed above make the consideration of vertical fins for yaw control very unattractive.

Another method of yaw control, which was suggested in Reference 3.7.2, would be the use of spoiler type flaps mounted as discussed above for roll control. Yawing moments would be generated by deflection of both the top and bottom flaps on one side of the body thus producing differential drag. The main disadvantage of this system is that, at angle of attack, the force on the leeward panel would be smaller, due to body shielding effects, than the force on the windward panel; this would result in a rolling moment. This approach was not included in the experimental program due to the limitations on model fabrication and testing time.

Pitch Control. Presented in Figures 3.7.3, 3.7.4, and 3.7.5 are side view Schlieren photographs of Model III with the aft P_1 pitchvator installed. These photographs were taken at Mach numbers 4, 5, and 6, respectively, at an angle of attack of zero degrees. The incidence of the pitchvator shown is 25 degrees at Mach numbers 4 and 5 and 20 degrees at Mach number 6. It can be seen in Figures 3.7.3, 3.7.4, and 3.7.5 that as Mach number increases the point of flow separation moves forward on the body. At $M = 5$ and 6 (Figures 3.7.4 and 3.7.5) it can be seen that the "dead air" wedge in front of the pitchvator causes separation to occur at about the 45 percent chord. This is undesirable because the pressure on the pitchvator is less than for the unseparated case.

Plots of pitching moment coefficient, referenced to midchord, versus angle of attack are presented in Figure 3.7.6 for the bare body and for the aft P_1 , P_2 , and P_3 pitchvators at both +20 and -20 degrees incidence. These data were obtained at $M = 3$ and are typical of the pitchvator wind tunnel data obtained at $M = 2, 4, \text{ and } 5$. As can be seen, the P_3 pitchvator is considerably more effective for longitudinal control than either the P_2 or P_1 pitchvator. As discussed

SECRET

SECRET

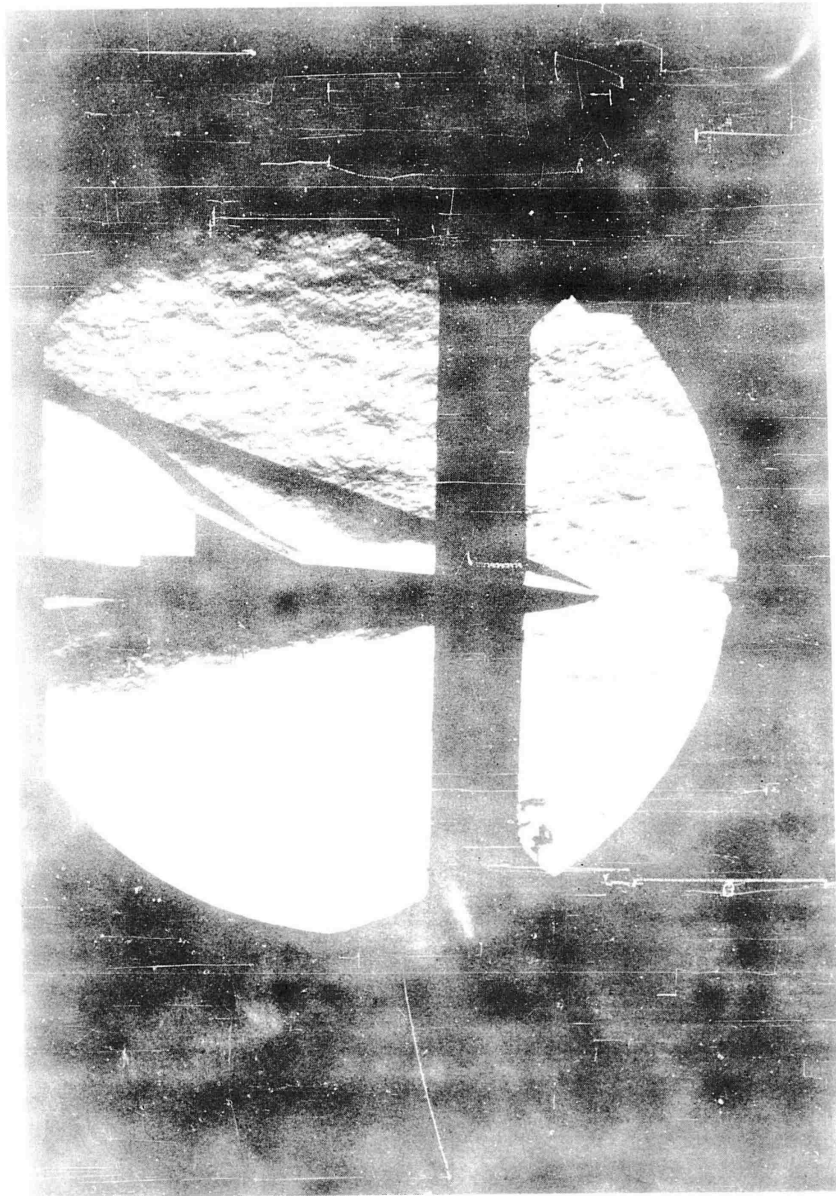


Figure 3.7.3. Side View of Model III With Aft P₁ Pitchvator
at -25° Incidence, Mach No. = 4.

SECRET

3.7.7

SECRET

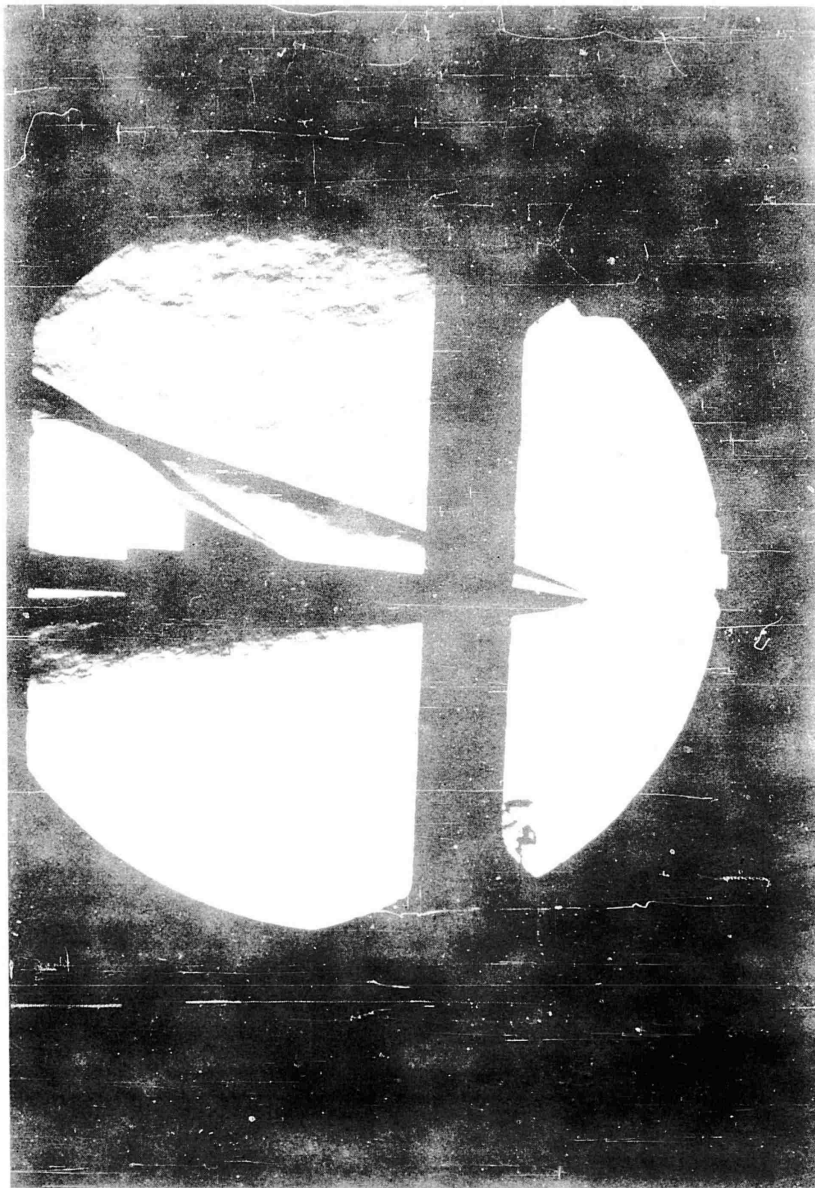


Figure 3.7.4. Side View of Model III With Aft P_1 Pitchevator
at -25° Incidence, Mach No. = 5.

3.7.8

SECRET

SECRET

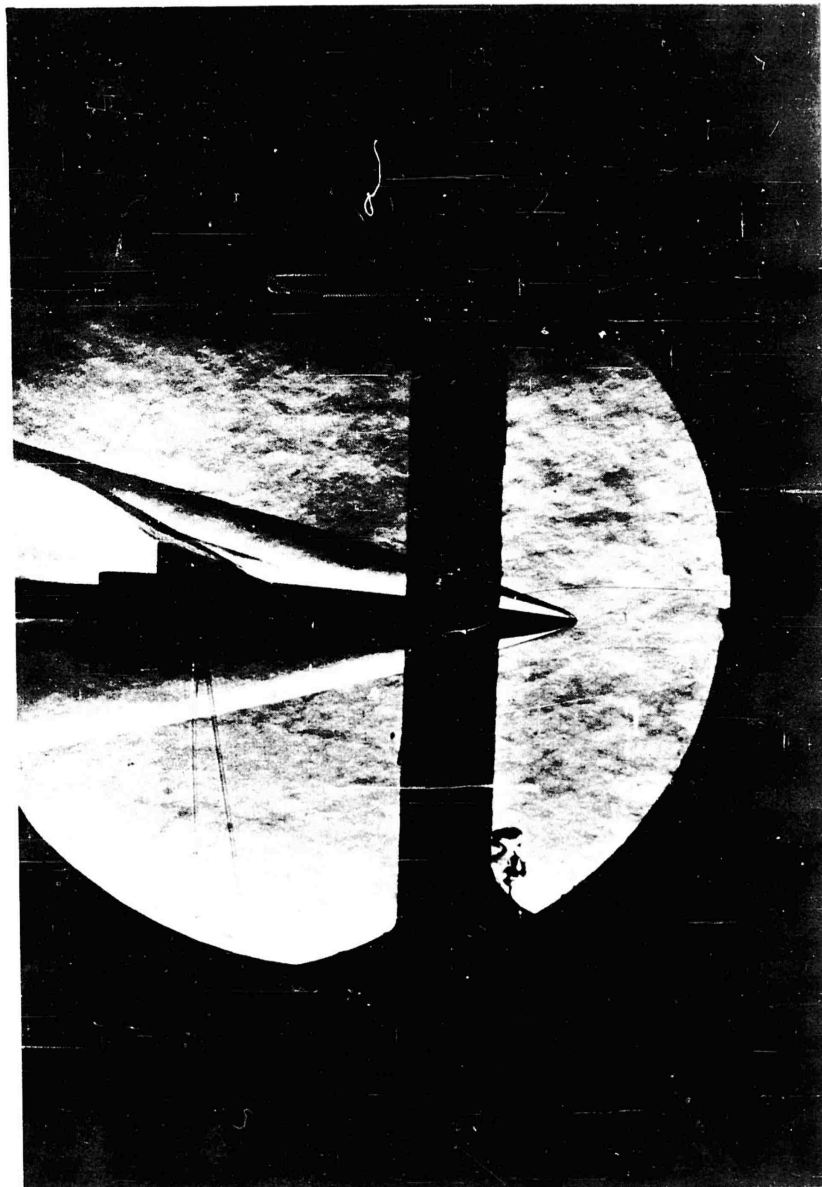


Figure 3.7.5. Side View of Model III With Aft P_1 Pitchevator
at -20° Incidence, Mach No. = 6.

SECRET

3.7.9

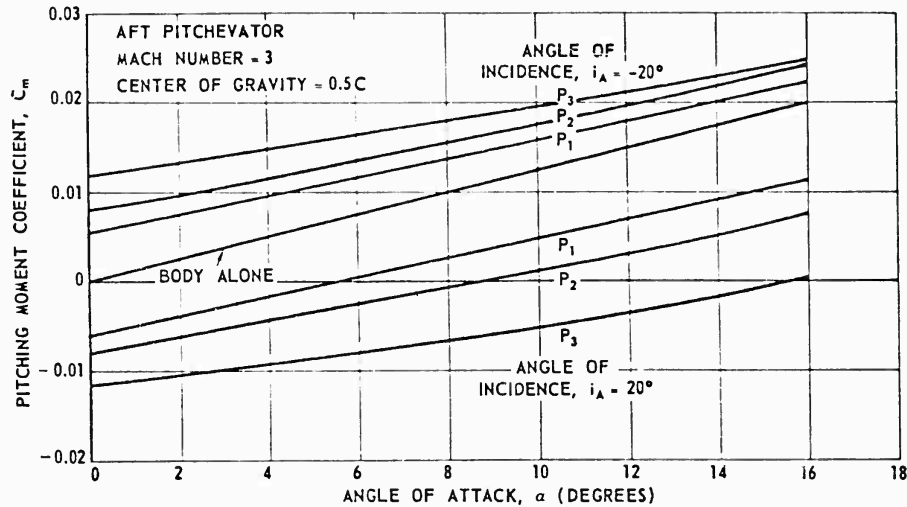


Figure 3.7.6. Variation of Pitchvator Effectiveness Due to Aspect Ratio and Area.

earlier, since the body itself is unstable, only a small unbalancing force is required to initiate desired angular accelerations. This requirement is much less severe than the requirement that the pitch controls be able to trim the configuration at the angles of attack necessary to produce the normal accelerations called for by the autopilot. Utilizing data obtained at the other Mach numbers, similar to that in Figure 3.7.6, curves of trim angle of attack versus Mach number for 20 degrees incidence are presented in Figure 3.7.7 for the P_1 , P_2 , and P_3 pitchvators.

As can be seen in Figure 3.7.7, the P_2 is more effective than the P_1 . This is due primarily to the P_2 having a larger area than the P_1 , with aspect ratio having a secondary influence. The P_3 can be seen to be even more effective than the P_2 . This is because the moment arm from the CP of the pitchvator to the reference station is greater for the P_3 than for the P_2 since the leading edge of both pitchvators was located at the same chordwise station, (i. e., 64 percent chord).

It could be argued that the P_2 is less effective than the P_3 due to a greater percentage of its area being immersed in the boundary layer where a region of dead air exists, as can be seen in the Schlieren photographs. An examination of typical normal force data presented in Figure 3.7.8, shows that the normal force on the P_2 is essentially the same as on the P_3 . Therefore, the decrease in P_2 normal force due to boundary layer immersion is probably partially off-set by the P_3 having more severe tip effects, since the P_3 aspect ratio is only 0.714 as compared to 1.4 for the P_2 . Consideration of boundary layer thickness and model scale indicate that this conclusion remains valid for a full scale body. The

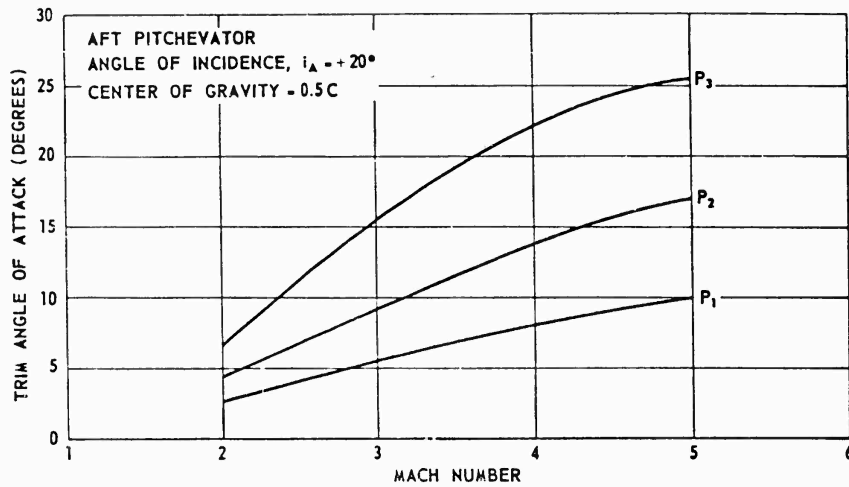


Figure 3.7.7. Effect of Pitchvator Aspect Ratio and Area on Control Capability.

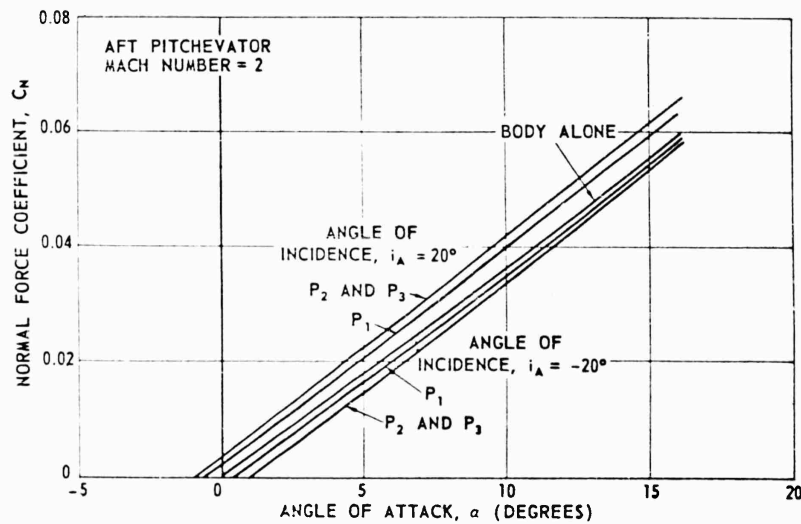


Figure 3.7.8. Effect of Pitchvator Aspect Ratio and Area on Normal Force Coefficient.

axial force on the pitchvator also contributes to the pitching moment, but, as can be seen in Figure 3.7.9, the axial forces due to P₂ and P₃ are very nearly the same. Hence, the margin of effectiveness of the P₃ over the P₂ is due almost entirely to the pitchvators' CP location with respect to the moment reference station.

As shown in Figure 3.7.9, the aft P_2 and P_3 pitchvators at 20° incidence increase the zero-lift drag of the configuration approximately 65 percent at $M = 4$. This effect exists for all Mach numbers and is approximately double in magnitude for the case of both fore and aft pitchvators.

The above discussion on relative effectiveness of the aft P_1 , P_2 , and P_3 pitchvators also applies to the configuration with both fore and aft pitchvators installed. A comparison of trim angle of attack obtainable for both fore and aft controls at 20 degrees incidence is presented in Figure 3.7.10. A comparison with Figure 3.7.7 shows that the use of both fore and aft controls produces only a small increase in trim angle of attack over aft controls for the Mach number range tested.

Presented in Figures 3.7.11, 3.7.12, and 3.7.13 are plots of C_m versus α at $M = 4$ for the P_1 , P_2 , and P_3 pitchvators, respectively. These plots contain data for the configuration having both the fore and aft pitchvator at 20 degrees incidence, and for the configuration having only the aft pitchvator at 20 degrees incidence. As can be seen, at low angles of attack the fore and aft pitchvators are almost twice as effective as the aft only. However, this advantage rapidly decreases at higher angles of attack. Examination of Figure 3.7.11 shows that the fore and aft pitchvators increase the trim angle of attack (and hence maneuverability) by less than 50 percent over that obtainable with the aft control alone. This decrease in the effectiveness of the fore and aft controls is because the upper one is partially shielded from the air stream by the forward portion of the body. It should be noted that, in order to gain this increased maneuverability, the design problems concerned are roughly doubled over that of a single control surface. Since the forward pitchvator would have to be located at the leading edge, where space is critical, it is concluded that the design advantages far outweigh any aerodynamic advantages for a configuration such as PYE WACKET.

The effects of varying the pitchvator incidence angle can be seen in Figures 3.7.14 and 3.7.15, which are plots of C_m versus α at $M = 4$ for various incidence settings. These data are for the configuration with P_1 aft pitchvator only (Figure 3.7.14) and the P_1 fore and aft pitchvators (Figure 3.7.15). The effects of incidence are better shown by the plots of trim angle of attack versus incidence presented in Figures 3.7.16 and 3.7.17. Comparison of Figures 3.7.16 and 3.7.17 reveals quite clearly the small advantage to be gained by using fore and aft controls as was discussed above.

Data for the P_2 and P_3 pitchvators for incidence angles other than 20 degrees were not obtained.

The effect of leading edge deflection on pitching moment, obtained from the APGC data at $M = 5$, is compared in Figure 3.7.18 with the effects of aft only and fore and aft P_1 pitchvators. The deflected leading edge data are for a

SECRET

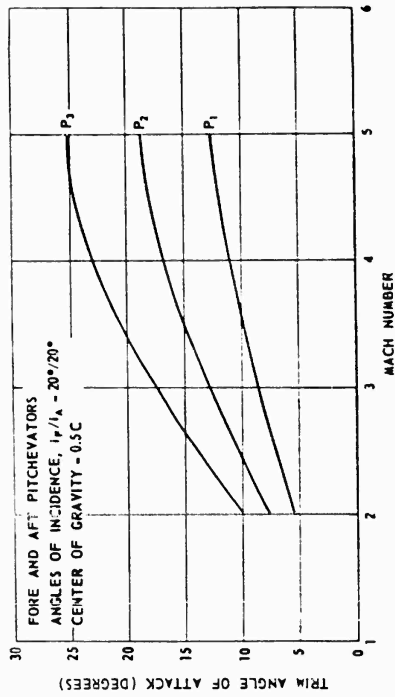


Figure 3.7.10. Effect of Pitcher Aspect Ratio and Area on Control Capability

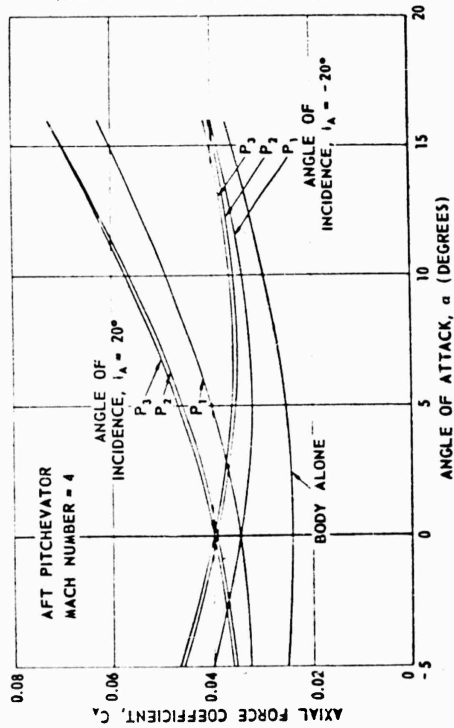


Figure 3.7.9. Effect of Pitcher Aspect Ratio and Area on Axial Force.

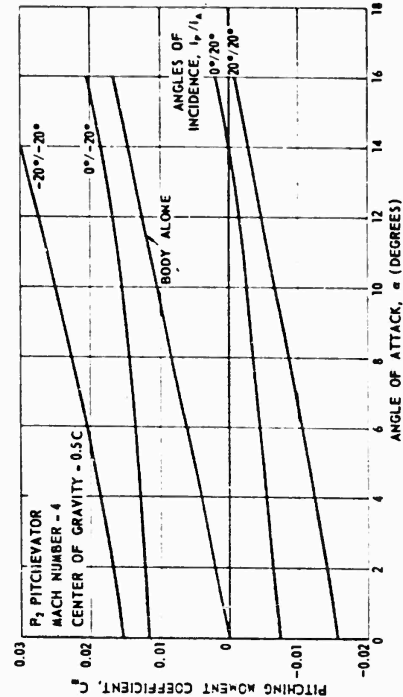


Figure 3.7.12. Comparison of Effectiveness of Fore and Aft Pitchers With Aft Pitcher Only.

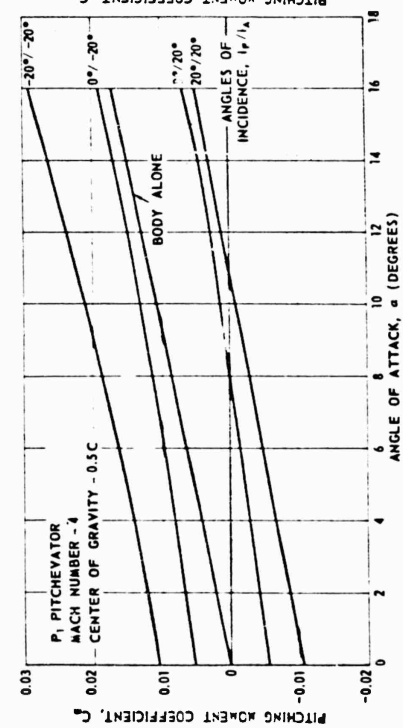


Figure 3.7.11. Comparison of Effectiveness of Fore and Aft Pitchers With Aft Pitcher Only.

SECRET

3.7.13.

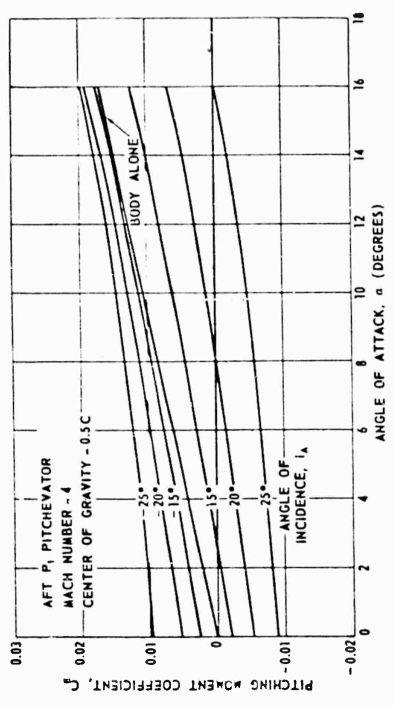


Figure 3.7.14. Variation of Pitcher Effectiveness Due to Incidence.

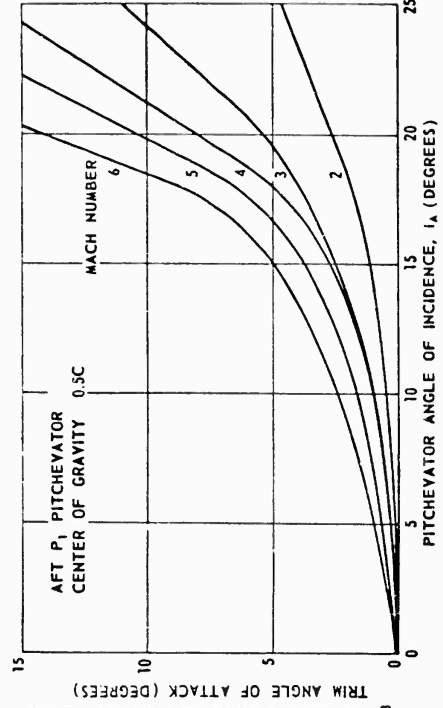


Figure 3.7.16. Variation of Trim Angle of Attack With Pitcher Angle of Incidence.

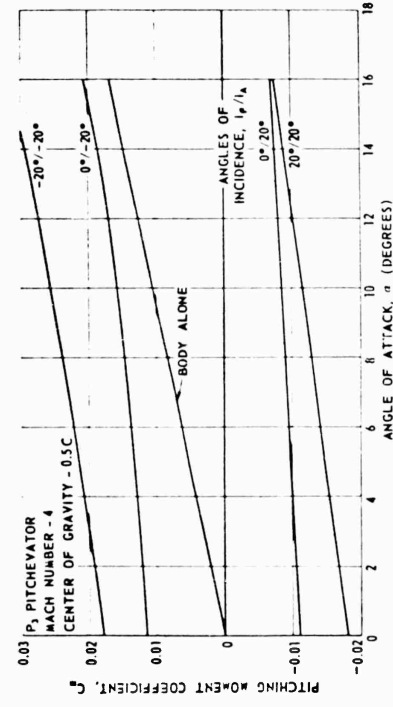


Figure 3.7.13. Comparison of Effectiveness of Fore and Aft Pitchers With Aft Pitcher Only.

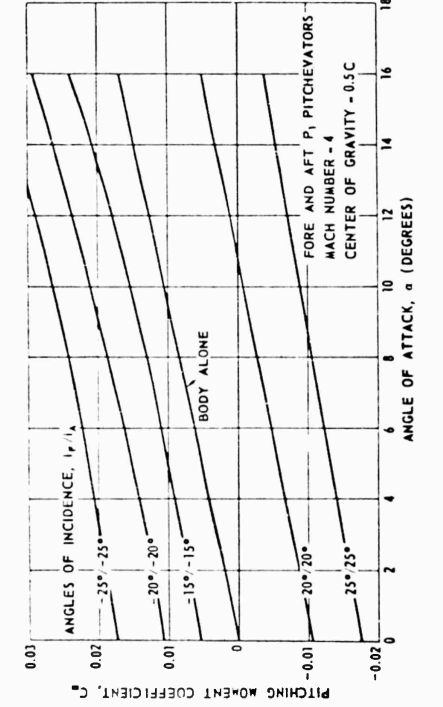


Figure 3.7.15. Variation of Pitcher Effectiveness Due to Incidence.

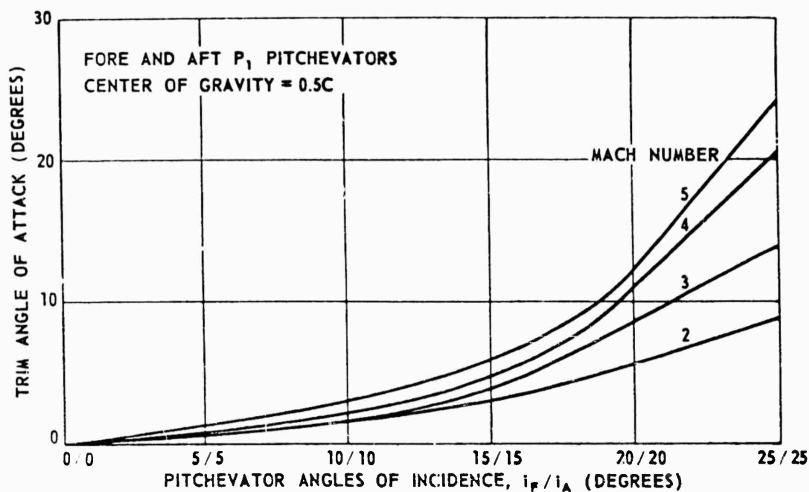


Figure 3.7.17. Variation of Trim Angle of Attack With Pitchvator Angles of Incidence.

symmetrical lenticular configuration with that sector of the circular body forward of the 12.5 percent chord deflected 10 degrees. This model was 8 inches in diameter and had a sharp leading edge. The Convair configuration was also a symmetrical lenticular body (Model I) but was 20 inches in diameter and had a leading edge radius of 0.083 inches. The differences noted for the body alone data in Figure 3.7.18 are probably due primarily to model scale although the difference in leading edge geometry would have some effect. It is believed that the data obtained on the Convair Model I are more accurate due to scale effects. This difference should be kept in mind when studying Figure 3.7.18. A leading edge deflection of 10 degrees would trim Model I at approximately 3.6 degrees angle of attack. An aft P_1 pitchvator at 20 degrees incidence would trim it at 2.7 degrees and fore and aft P_1 pitchvators at 20 degrees incidence would trim it at 4.2 degrees angle of attack.

The control capability of the pitchvators, in terms of configuration normal accelerations generated at various altitudes and Mach numbers, is compared in paragraph 3.7.4 with reaction-jet control capability.

Roll Control. As stated previously in the text, cones (conevators) and wedges (wedgenvators) were investigated to determine if roll control of a circular planform body by aerodynamic surfaces was feasible. This investigation considered not only roll control capability but the control coupling and induced drag effects due to the conevators and wedgenvators.

Figures 3.7.19 and 3.7.20 present top view Schlieren photographs of Model III, with conevators, taken at zero degrees angle of attack and at Mach numbers

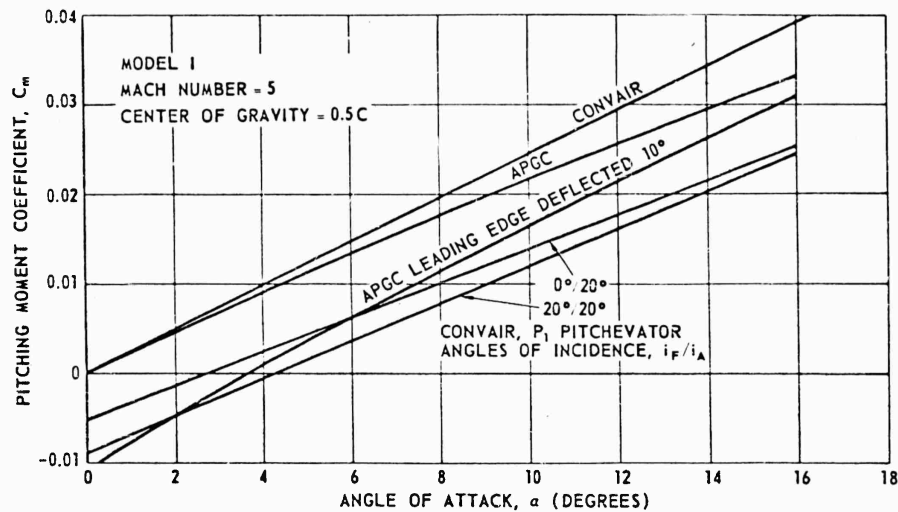


Figure 3.7.18. Comparison of Pitching Moment Effects Due to Pitchevators and Leading Edge Deflection.

2 and 5, respectively. The covevators shown in Figure 3.7.19 are at zero degrees deflection while those shown in Figure 3.7.20 are differentially deflected 20 degrees. An aft P_1 pitchevator at 20 degrees incidence is installed on the configuration shown in Figure 3.7.19. Note that the body leading edge shock impinges on the covevators near the apex for the $M = 2$ case and at about the midchord of the covevator at $M = 5$.

In other missile programs where shock wave impingement on control surfaces was experienced, the control surface hinge moment problem became quite severe. This is because the shock wave shifts the center of pressure, eliminating the possibility of designing the surface hinge line to coincide with the CP.

A plot of rolling moment coefficient per degree differential deflection of the covevators is presented in Figure 3.7.21 from Mach numbers 2 to 5. Analysis of the wind tunnel data shows that the C_l due to covevators varies linearly with δ up to deflection angles approaching 20 degrees. This effect of α on $C_{l\delta}$ is quite constant with angle of attack variations up to $\alpha = 10^\circ$. These approximate boundaries for the application of the $C_{l\delta}$ values presented are noted in Figure 3.7.21.

The effect of covevators on the zero-lift drag of the body alone is shown in Figure 3.7.22 for various deflections. A covevator deflection of 20 degrees increases the zero-lift drag by approximately 100 percent. Such increases in drag are of a magnitude sufficient to produce large decreases in performance. The effect of the covevators on pitching moment is presented in Figure 3.7.23.

SECRET



*Figure 3.7.19 - Top View of Model III with Air Pj. Distributor at 20° Incidence
and Cones at Zero Deflection, Mark No. - 2.*

SECRET

3.7.17

SECRET



SECRET

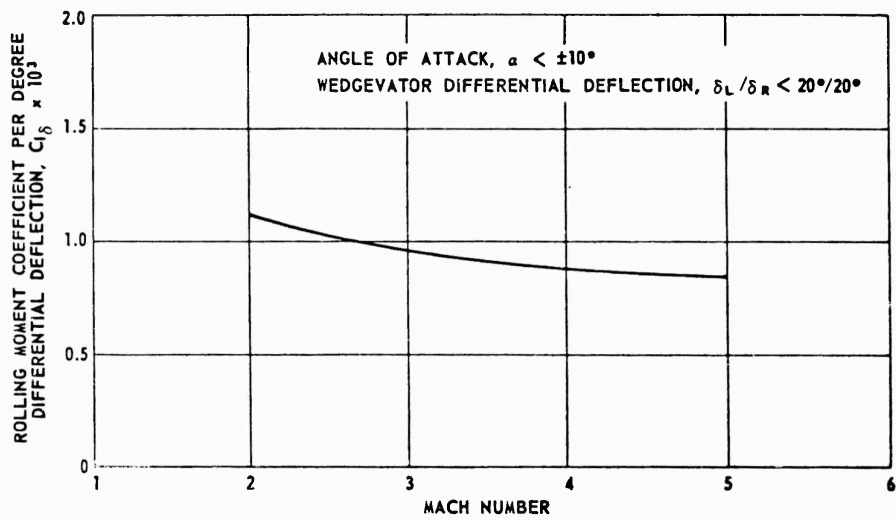


Figure 3.7.21. Rolling Moment Derivative Due to Conevators.

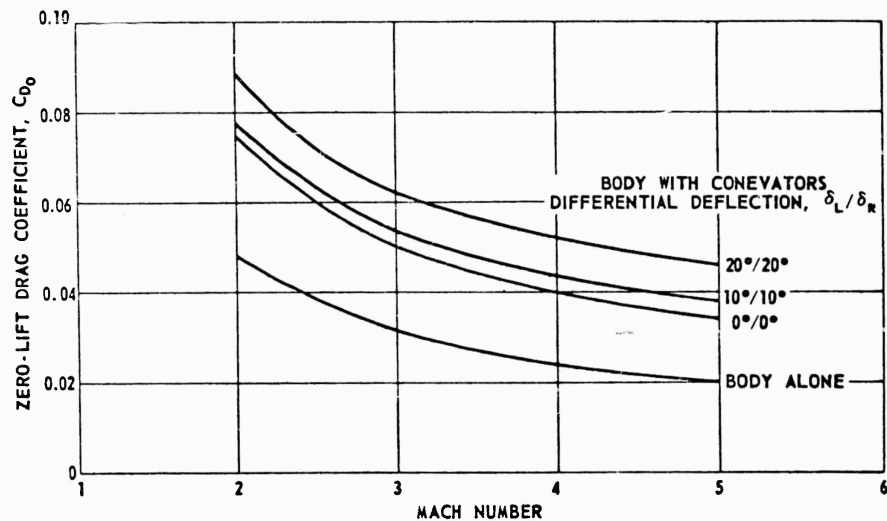


Figure 3.7.22. Comparison of Zero-Lift Drag Coefficient for Body With and Without Conevators.

The effect of the conevators, which is to reduce instability, was found to be essentially the same for all differential deflection settings.

The conevators were found to produce a small increase in the configuration normal force. The magnitude of this ΔC_N varied linearly with angle of attack. Therefore, this effect is presented as ΔC_N per degree angle of attack in Figure 3.7.24 for Mach numbers 2 to 5.

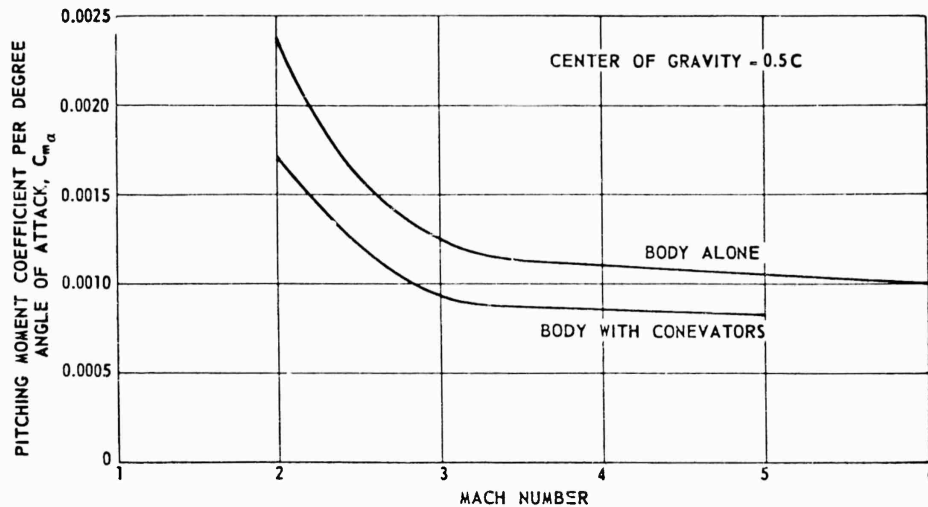


Figure 3.7.23. Comparison of Pitching Moment Derivative for Body With and Without Conevators.

Differential deflection of the conevators to produce a rolling moment also produces a yawing moment when the configuration is at an angle of attack. This can be readily visualized by considering a δ_L/δ_R of 15 degrees (i. e., left cone up 15° and the right cone down 15°) and an angle of attack approaching 15 degrees. A yawing moment will be produced when the drag of one cone is greater than the other. In the above example for $\delta = 15^\circ$, the right cone will have only zero-lift drag while the left cone will have a greater drag due to its position at approximately 30 degrees deflection to the airstream. Hence, a yawing moment is produced. Wind tunnel data show this roll control induced yawing moment to be linear with both differential conevator deflection angle and with angle of attack. The yawing moment per degree differential deflection and per degree angle of attack ($C_{n\delta\alpha}$) is presented in Figure 3.7.25. These induced yawing moments due to roll are as large or larger than the control yawing moments obtained in the experimental program by using the wedgevators. The values of roll control induced yawing moment shown in Figure 3.7.25 are, therefore, of sufficient magnitude to render infeasible the use of cones for roll control.

Presented in Figures 3.7.26 and 3.7.27 for $M = 2$ and 5, respectively, are top view Schlieren photographs of Model III with wedgevators. For these photographs the body was at zero degrees angle of attack and the wedgevator included angles were 15 degrees. The differential deflection of the wedgevators was 20 degrees at $M = 2$ and 15 degrees at $M = 5$. Note the change in the body leading edge shock wave impingement point on the wedgevators due to change in Mach number, as discussed above for the conevators. Such shock impingement creates severe control surface hinge moment problems.

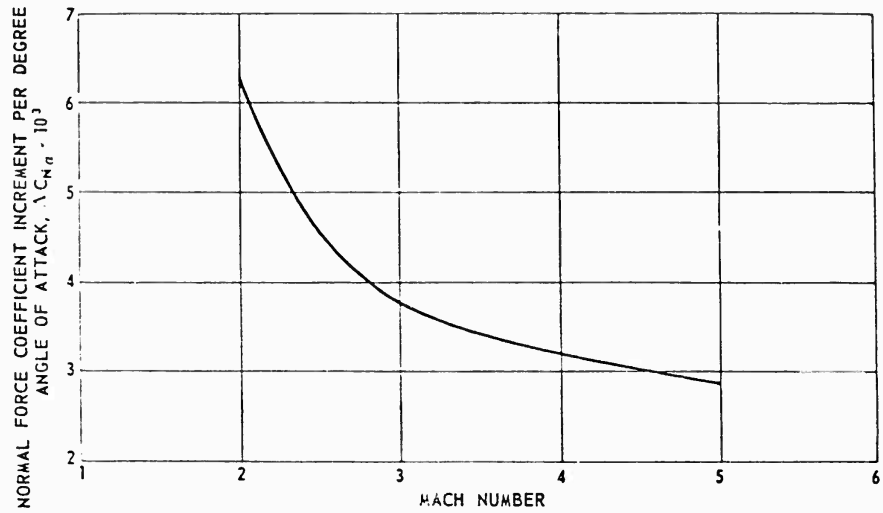


Figure 3.7.24. Increase in Normal Force Coefficient Per Degree Angle of Attack Due to Coneyators.

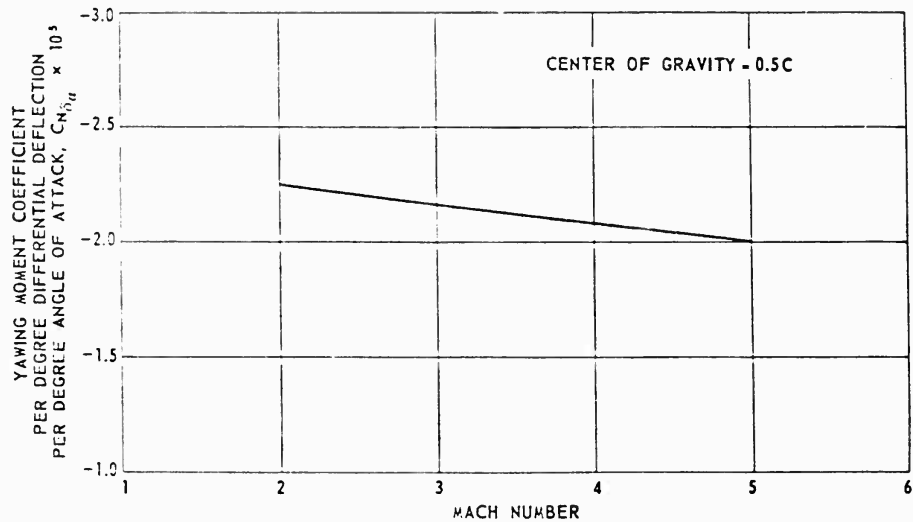


Figure 3.7.25. Roll Control Induced Yawing Moment Per Degree Differential Deflection per Degree Angle of Attack.

Shown in Figure 3.7.28 is a Schlieren photograph of the model rolled 20 degrees with respect to the horizontal. The wedgevators, as can be seen, are deflected to produce a rolling moment. This photograph was taken at $M = 4$ and zero degrees angle of attack with a differential deflection of 15 degrees.

The rolling moment produced by the differential deflection of the wedgevators (each wedge has an apex angle of 15°) is presented in Figure 3.7.29 as rolling

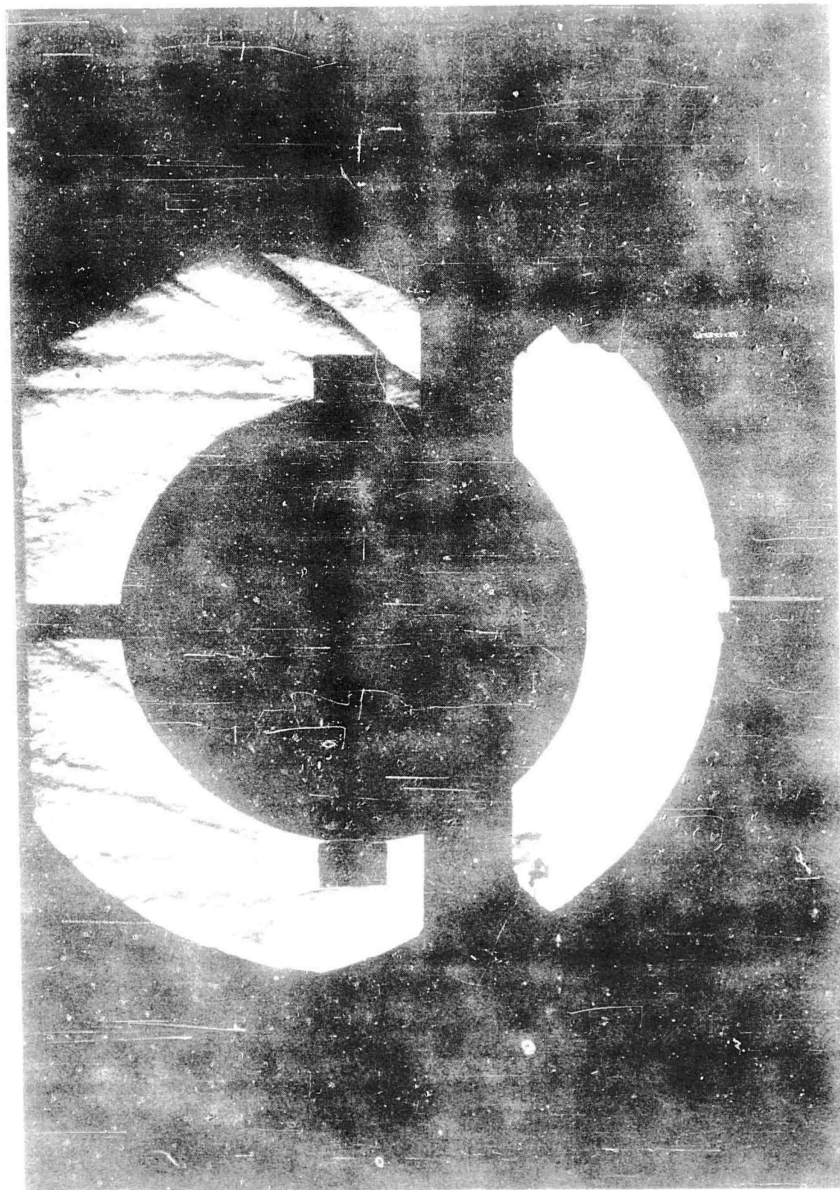
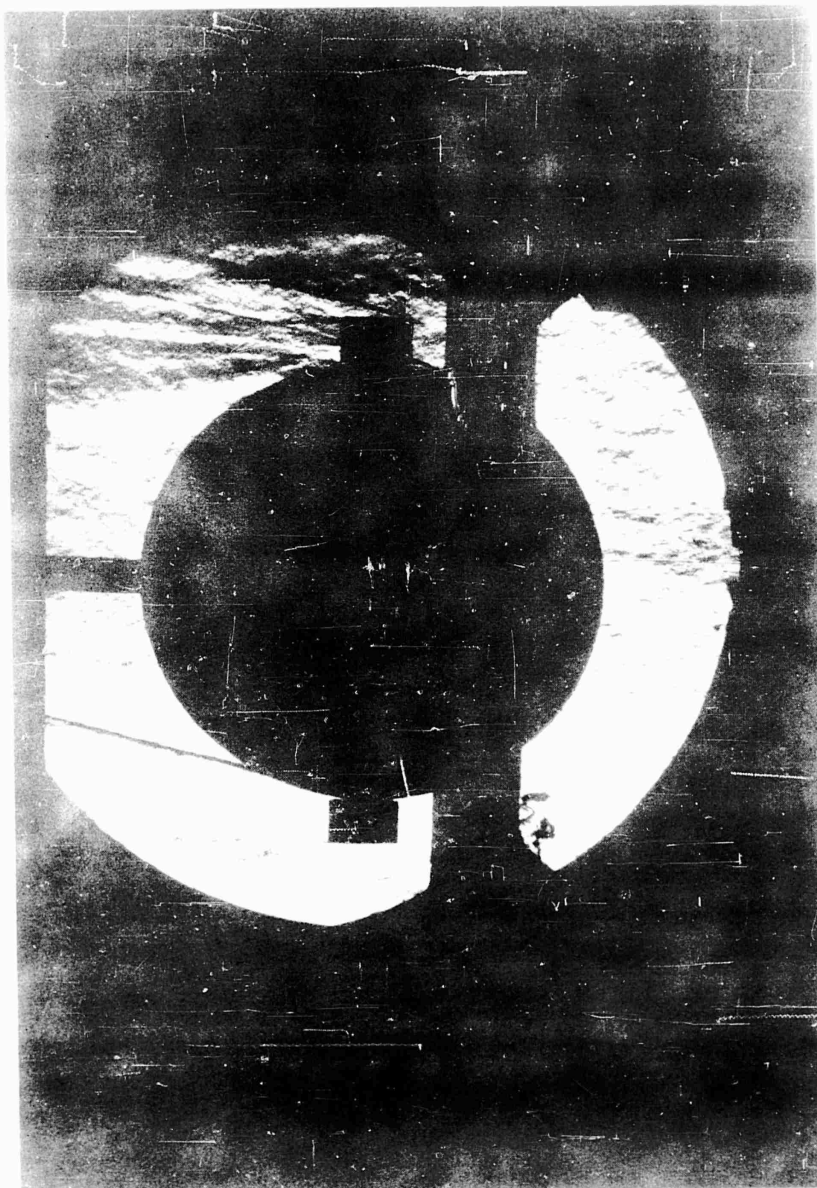


Figure 3.7.26. Top View of Model III With Wedgevators at 20°
Differential Deflection, Mach No. = 2.

SECRET



*Figure 3.7.27. Top View of Model III With Wedgevators at 15°
Differential Deflection, Mach No. = 5.*

SECRET

3.7.23

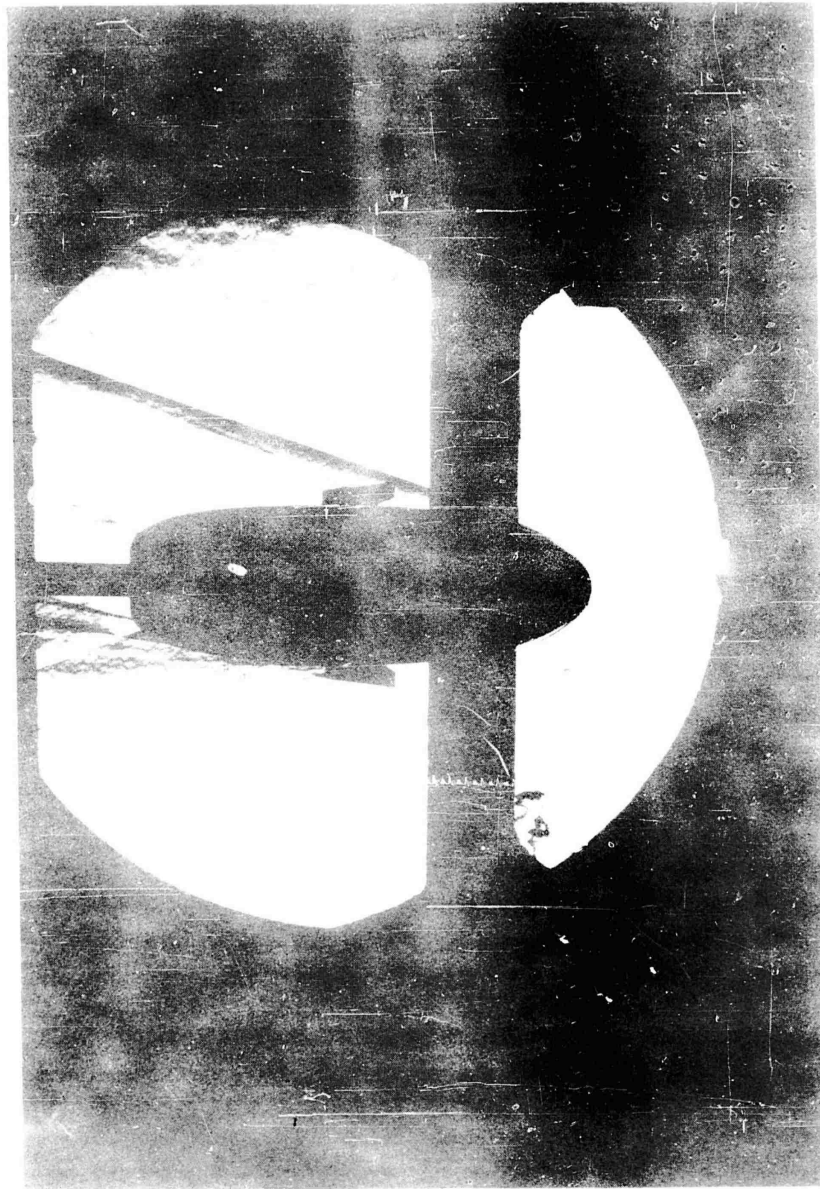


Figure 3.7.28. Side View of Model III Rolled 20° With Wedgevators at 15° Differential Deflection, Mach No. = 4.

SECRET

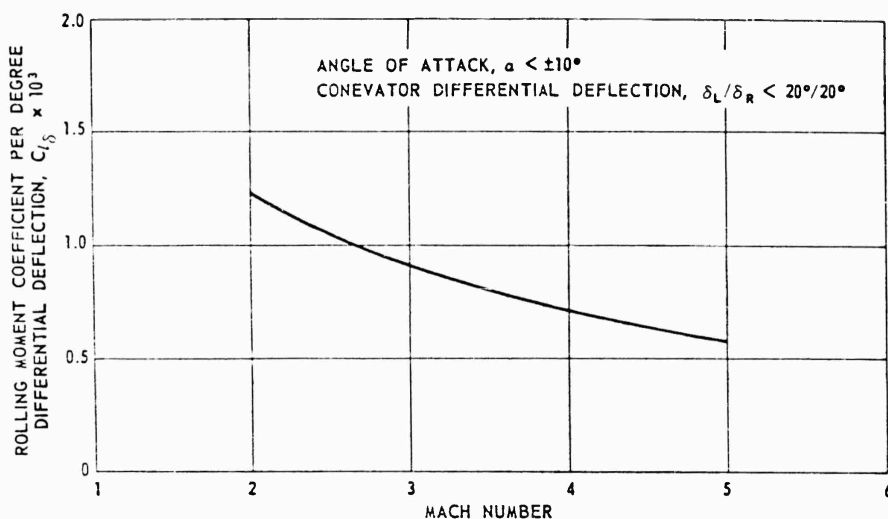


Figure 3.7.29. Rolling Moment Derivative Due to Wedgevators.

moment per degree differential deflection. As with the conevators, C_l varies linearly with δ up to δ approaching 20° and is constant with α up to approximately 10 degrees angle of attack.

The wind tunnel data show that the effects of the wedgevators on C_N , C_m , C_D and C_n while deflected for roll control, are similar to the effects presented above for conevators.

The rolling moment due to deflecting sectors of the body at the lateral extremities (outboard of lateral station $\frac{X}{d} = 81.6$ percent) are presented in Figure 3.7.30. These data were obtained from the APGC tests of Model I at Mach number 5 and are for differential deflections of 10 degrees. A comparison of the curves in Figure 3.7.30 shows that deflecting this particular portion of the body produces rolling moments essentially the same as the wedgevators tested and considerably less than the conevators for $M = 5$.

Yaw Control. The yawing moment resulting from differential drag produced when one wedgevator apex angle is greater than the other is presented in Figure 3.7.31. The C_n did not vary linearly with the wedgevator apex angles tested (i.e., $\omega_L/\omega_R = 45/15$ and $30/15$, giving $\Delta\omega$ of 30° and 15° , respectively). Therefore, a C_n per degree ω is not presented. The C_n produced by either of the yaw control settings did, however, remain constant with angle of attack.

The zero-lift drag for configurations with and without the wedgevators is presented in Figure 3.7.32. It should be noted that the increase in drag is less severe than with conevators.

SECRET

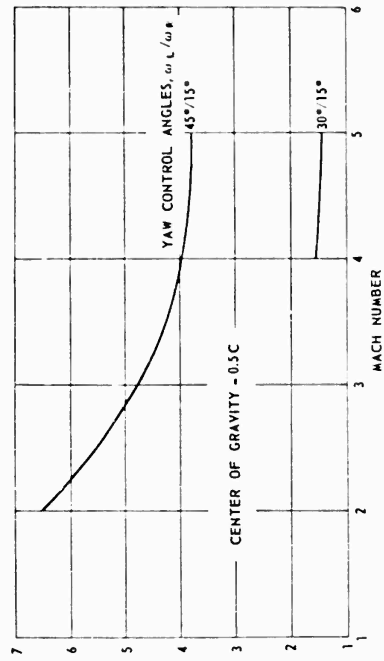


Figure 3.7.31. Variation of Yawing Moment With Mach Number for Different Yaw Control Angles of the Wedgevators.

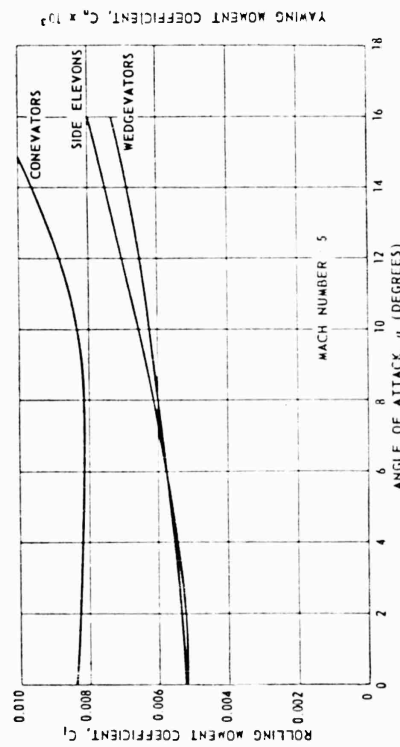


Figure 3.7.30. Comparison of Rolling Moment Coefficient for Conevators, Wedgevators, and Side Elevons.

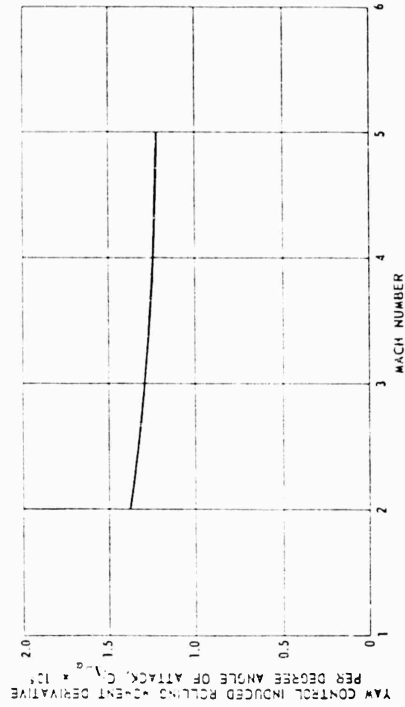


Figure 3.7.33. Yaw Control Induced Rolling Moment Coefficient per Degree Difference in Wedgevator Yaw Control Angle per Degree Angle of Attack.

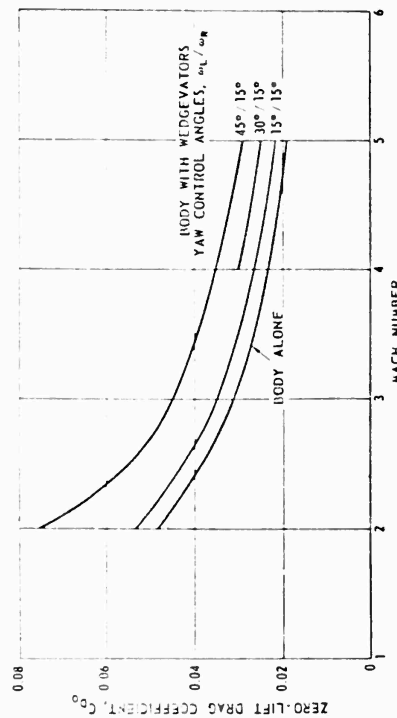


Figure 3.7.32. Comparison of Zero-Lift Drag Coefficient for Body With and Without Wedgevators.

SECRET

Because the wedgevators have a difference in apex angle for yaw control, one wedgevator will produce more lift than the other when the configuration is at an angle of attack. This difference in lift on the wedgevators will produce a rolling moment. From the wind tunnel data it was found that the yaw control induced rolling moment varies linearly with the difference in apex angles, and with the angle of attack. This yaw control induced rolling moment per degree difference in wedge apex angle and angle of attack ($C_{l\Delta\omega_\alpha}$) is presented in Figure 3.7.33.

The wedgevator characteristics presented above pertain to the wedgevator geometry tested at Arnold Engineering Development Center (AEDC) during the PYE WACKET wind tunnel tests. Obviously, the characteristics can be altered by varying the wedge geometry (i. e., vary aspect ratio, area, angles, etc).

SUMMARY OF AERODYNAMIC CONTROLS. The results of investigating aerodynamic surfaces for glide-phase control of an omnidirectionally launched vehicle, or for a vehicle restricted to forward launch, can be summarized as follows:

1. Adequate pitch control forces can be obtained by using spoiler type flaps (pitchvators) having large surface areas. However, pitch control induced drag forces are of a magnitude which would severely decrease the missile performance. Such a system would also present complex design problems such as large hinge moments and actuating mechanism packaging.
2. The use of either cones (conevators) or wedges (wedgevators) mounted at the lateral extremities of the configuration will provide sufficient rolling moment for control purposes as well as handling induced rolling moments due to aerodynamic coupling. However, large induced yawing moments result from deflection of the surfaces to produce roll. In addition, the conevators or wedgevators increase the configuration drag considerably. There are certain beneficial effects upon the missile aerodynamic characteristics which result from roll control, i. e., the configuration normal force is increased and the static instability is decreased.
3. Control forces needed for the yaw maneuvers necessary to maintain alignment between the missile centerline and the velocity vector can be provided by the wedgevators. However, the induced yaw moments resulting from aerodynamic coupling with roll control (mentioned above) are of a greater magnitude than the control moments produced by yaw control alone, thus nullifying their usefulness.
4. As a result of the body bow shock wave impinging on the conevators or wedgevators, large and unpredictable hinge moments will occur.
5. From consideration of all the above factors, it is concluded that aerodynamic controls are unsatisfactory except for the simple case of single degree of freedom maneuvers, unless they are supplemented by reaction controls.

SECRET

3.7.27

3.7.2 REACTION-JET CONTROL

It has been pointed out in the previous paragraphs that aerodynamic surfaces were not feasible for control during the launch phase of a missile possessing omnidirectional launch capabilities. It was also shown that control during the glide phase by aerodynamic surfaces presented many problems and disadvantages. It is felt that these problems and disadvantages render aerodynamic controls impractical for use on PYE WACKET. Therefore, non-aerodynamic control systems were investigated for application on a circular planform airframe and are discussed in this paragraph.

The systems investigated consisted of main propulsive jet control and secondary reaction jet controls. A brief analysis was conducted of the increased effectiveness of reaction jets due to interference between the jet flow and the body boundary layer.

MAIN PROPULSION SYSTEM. There are various methods of utilizing the main propulsion system to obtain missile control. These methods include the following:

- Jetevators
- Jet vanes
- Swivelled nozzles
- Jet paddles
- Nozzle deflectors
- Gimballed thrust chambers
- Secondary gas injection
- Nozzle throat control
- Rotating canted nozzles

Several of the control systems listed above are not feasible for the lenticular vehicle and therefore will be discussed only briefly.

The jet paddle has been briefly investigated by NACA (summarized in survey report, Reference 3.7.3). A typical design has a vane hinged near the nozzle exit, as shown in Figure 3.7.34. Test results with this type of system indicated that a very heavy actuating mechanism was required, and poor frequency response was obtained. A similar investigation on spoiler tabs, reported in Reference 3.7.4, indicated that low control forces are obtained whereas the vane area required to obtain the forces is high. Because of the obvious deficiencies, the jet paddle type of control system was not considered further.

A nozzle deflector design is illustrated in Figure 3.7.35 (Reference 3.7.3). With this type of control system, the deflector plates are extended or retracted in a line at the edge of the nozzle to obtain pitch and yaw control. Rolling moment can be obtained by differential operation of the pitch or yaw deflectors. This type of system, however, requires an excessive linkage weight, has poor frequency response, and results in poor control characteristics.

SECRET

REFERENCE 3.7.3

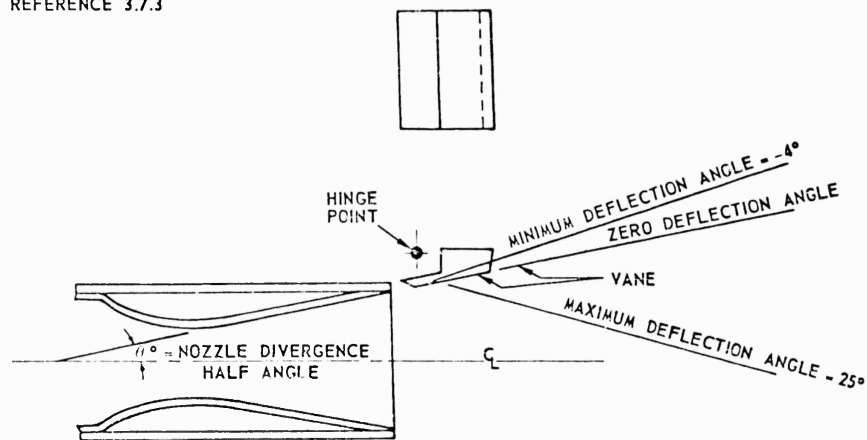


Figure 3.7.34. Schematic of Jet Paddles Relative to Rocket Nozzle.

REFERENCE 3.7.3

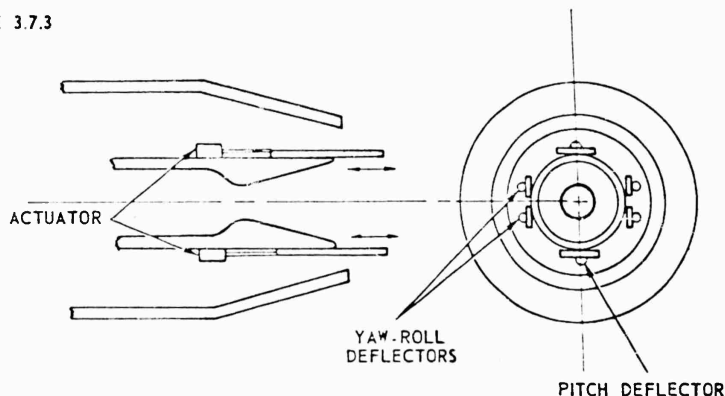


Figure 3.7.35. Extendable Nozzle Deflectors.

The gimballed thrust chamber is a system widely used for thrust vector control of liquid propellant rocket motors. To obtain directional control of the vehicle, the entire thrust-chamber-nozzle combination is allowed to move in two planes. Vehicles such as Atlas and Titan utilize this type of control system. A high hinge moment, with its associated large hydraulic actuating mechanism, is encountered with this type of system. The frequency responses obtainable with systems of this type to date do not appear to be adequate for the lenticular vehicle.

The utilization of secondary gas injection for thrust vector control has been studied in References 3.7.3, 3.7.5, and 3.7.6. Directional control of the vehicle is achieved by injecting gas into the main rocket motor exhaust stream,

SECRET

3.7.29

producing an oblique shock in the divergent section of the main nozzle, and diverting the direction of the rocket jet. A sketch illustrating this type of control system is shown in Figure 3.7.36. A preliminary study of the secondary gas injection control system, using cold air, is reported in References 3.7.3 and 3.7.5. Data obtained from Reference 3.7.3 on the variation of the nozzle side forces obtained with secondary flow are shown in Figure 3.7.37. Also shown in Figure 3.7.37 is a representation of the results obtained in Reference 3.7.5. The data from both references are in close agreement and indicate that relatively large secondary gas injection rates are required to obtain large jet deflections. Hot gas test data (Reference 3.7.5) are compared with nitrogen gas injection data (Reference 3.7.3) in Figure 3.7.38, and show reasonable agreement. It will be noted in this figure that approximately a 10 percent gas weight flow ratio is required in order to obtain a 7 percent force ratio. As indicated in Reference 3.7.6, the magnitude of the secondary gas flow required is too high to obtain satisfactory performance with a minimum weight system except for transient conditions. In addition, this type of control may or may not be adequate for roll control (depending on nozzle configuration). It is possible however that for short operating times the use of an inefficient secondary injection system would result in a lower system weight than that of a swivel nozzle design.

Another control method briefly investigated in Reference 3.7.3 utilized nozzle throat buttons to displace the location of the center of the nozzle throat, thereby deflecting the gas as it was expanding through the nozzle. Drag losses are apparently severe with this type of system and the material erosion problem might prove insurmountable, since heat flux is maximized at the nozzle throat. This system does not appear feasible at the present time.

The rotating canted nozzle system, like the jetevator system, requires four nozzles with the associated activating mechanisms to achieve pitch, yaw, and roll control. This arrangement did not appear promising for PYE WACKET due to space and configuration limitations and overall complexity.

On the basis of the foregoing discussion, it does not appear that jet paddles, nozzle deflectors, swivelled thrust chambers, nozzle throat control or rotating canted nozzles would be feasible as control systems for the lenticular vehicle. The secondary gas injection system likewise does not appear feasible for PYE WACKET unless a requirement for very short duration is established. The control systems which seem most promising are the jetevator, jet vane, and swivelled nozzle. A schematic of these systems is shown in Figure 3.7.39 (from Reference 3.7.7).

Jet Vanes. A jet vane control system normally consists of a set of blades installed at the exit section of the rocket nozzle. These blades remain in the rocket exhaust stream at all times, and are singularly differentially operated to deflect the exhaust gas. The system is relatively light in weight and will provide

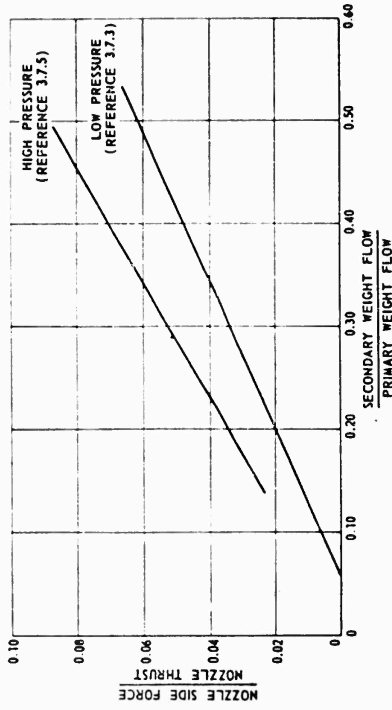


Figure 3.7.37. Variation of Nozzle Side Force With Secondary Flow.

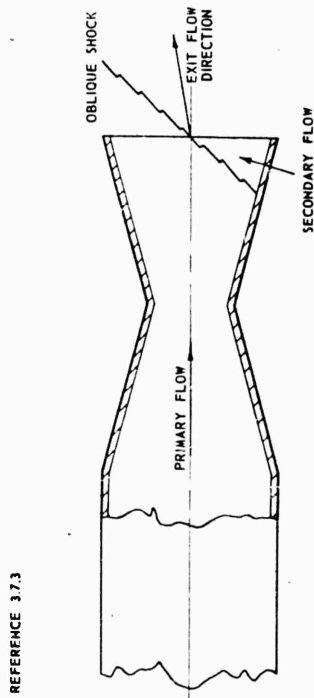


Figure 3.7.36. Lateral Forces Developed From the Introduction of a Secondary Jet of Gas.

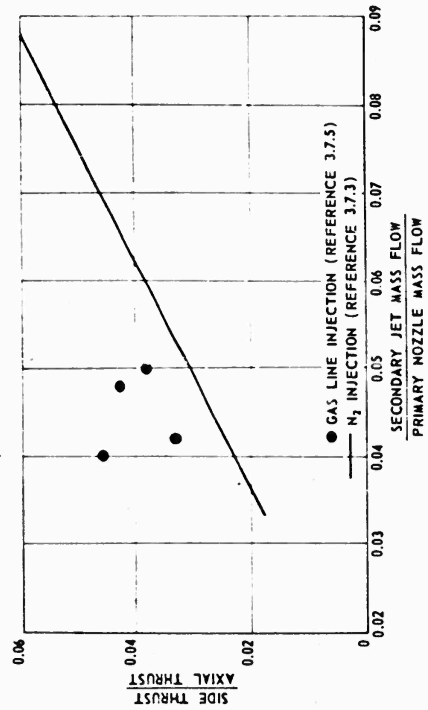


Figure 3.7.38. Variation of Side Force With Secondary Flow.

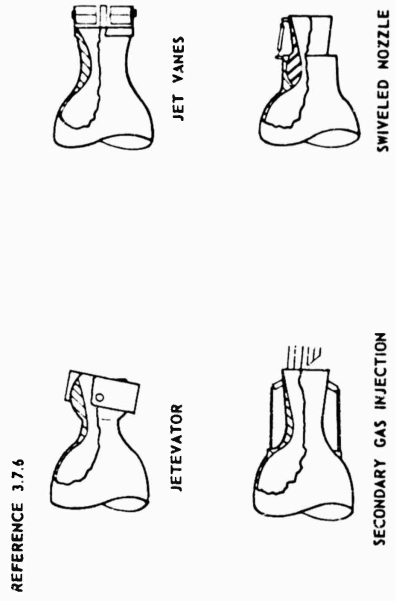


Figure 3.7.39. Methods of Thrust-Vector Control.

large control force with a high rate of response. There are several disadvantages to the jet vane system however. The vanes produce a definite loss in rocket motor thrust due to the projected area (drag) of the vane itself. The durability of the vane material is also extremely critical due to the extreme temperature of the rocket exhaust and the normally erosive effect of particles in the gas stream. In addition, vane "flutter" can occur throughout rocket motor operation with a subsequent induced flutter of the vehicle.

For the lenticular vehicle, large jet vane deflection angles may be required during boost operation. It may, therefore, be necessary for the jet vanes to operate in a deflected position throughout the majority of the rocket motor burning time - with resultant severe drag penalties.

Jetevators. The jetevator is a jet deflection device normally consisting of a right-circular cylindrical ring around the diverging portion of the nozzle. The hinge line is normal to the nozzle center line when in a neutral position. A typical jetevator assembly is shown on Figure 3.7.40 (Reference 3.7.6). A jetevator system mounted on multiple rocket motor nozzles can be used to supply pitch, yaw, and roll control.

Results of tests performed in Reference 3.7.3 and 3.7.6 are shown in Figure 3.7.41 to illustrate the jet deflection angle which can be achieved as a function of jetevator deflection angle. It can be seen in this figure that a jet deflection of 10° is obtained with a jetevator ring deflection of approximately 25° . This jet deflection would result in a side force ratio of about 12 percent.

A major disadvantage of the jetevator system is the problem of hot gas "blow-back" between the outside of the nozzle exit cone and the jetevator ring. The occurrence of "blow-back" would tend to erode the actuating mechanism and freeze the system. Up to the present time, the jetevator method for thrust vector control has not been completely satisfactory on missiles which have attempted to use it.

Swivel Nozzle. The swivel nozzle for thrust vector control is being utilized in several large missile programs. A sketch of a typical swivel nozzle design is shown in Figure 3.7.42. This type of system has the advantages of linear control characteristics and no loss in rocket motor impulse due to drag. A single system could be used to obtain pitch, yaw, and roll control (with dual nozzles).

The swivel nozzle design of particular interest utilizes a bellows-seal downstream of the nozzle throat, thereby minimizing the loads on the bellows and seal and reducing the required actuating moments. The nozzle materials problem, though always critical in a high impulse propellant system, appears capable of being solved with available materials for the relatively short burning times studied.

SECRET

REFERENCE 3.7.6
THRUST-VECTOR
CONTROL

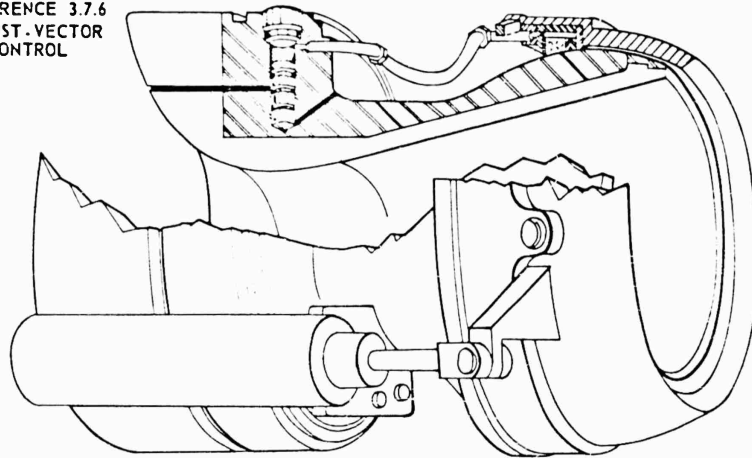


Figure 3.7.40. Typical Jetvator and Nozzle Assembly With Blowback Seal.

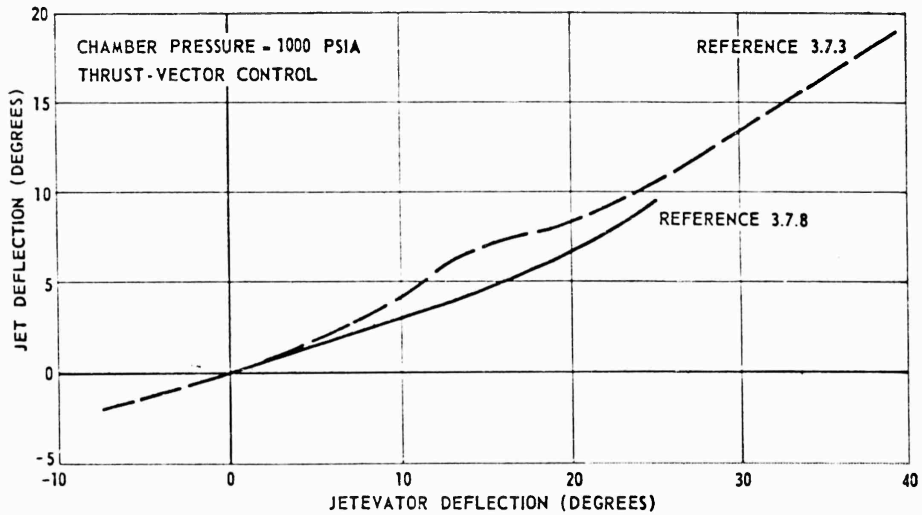


Figure 3.7.41. Jet Deflection Versus Jetvator Deflection.

Of the three most promising methods for obtaining jet control, the swivel nozzle appears to be the most attractive. A relative comparison is shown in Table 3.7.2 to support this conclusion.

A comparison of the thrust losses associated with the use of the various types of control systems is shown in Figure 3.7.43. It can be seen in this figure that

SECRET

3.7.33

REFERENCE 3.7.6
THRUST-VECTOR CONTROL

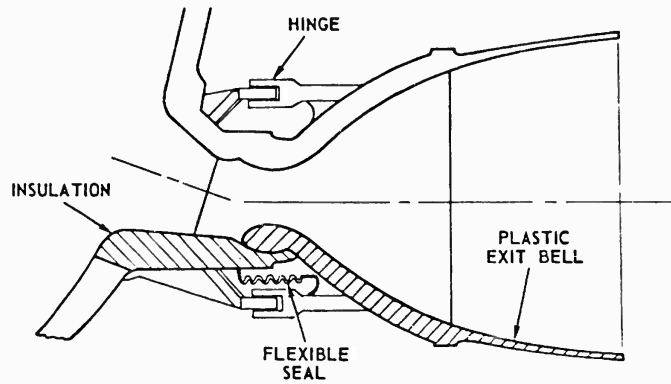


Figure 3.7.42. Flexible Seal Nozzle Design.

Table 3.7.2
COMPARISON OF REACTION-JET CONTROLS

Note: S = Satisfactory
U = Unsatisfactory

Requirements	Jet Vane	Control System Jetevector	Swivel Nozzle
Available forces	S	S	S
Hinge moment	S	S	S
Controlability	S	S	S
Drag	U	S	S
Erosion	U	S	S
Sealing	S	U	S
Weight	S	S	S
Materials (critical)	U	S	S
Duty cycle life	S	U	S

the jet vane and jetevector losses are excessive for a control force ratio of 12 percent. Thus, if main engine control is necessary, the use of swivel nozzles appears desirable. Whether or not main engine control is actually required for a particular design is dependent on stability margin, "g" requirements, and the weight trade-off resulting when use of main motor control is compared with use of the secondary jet control system.

SECRET

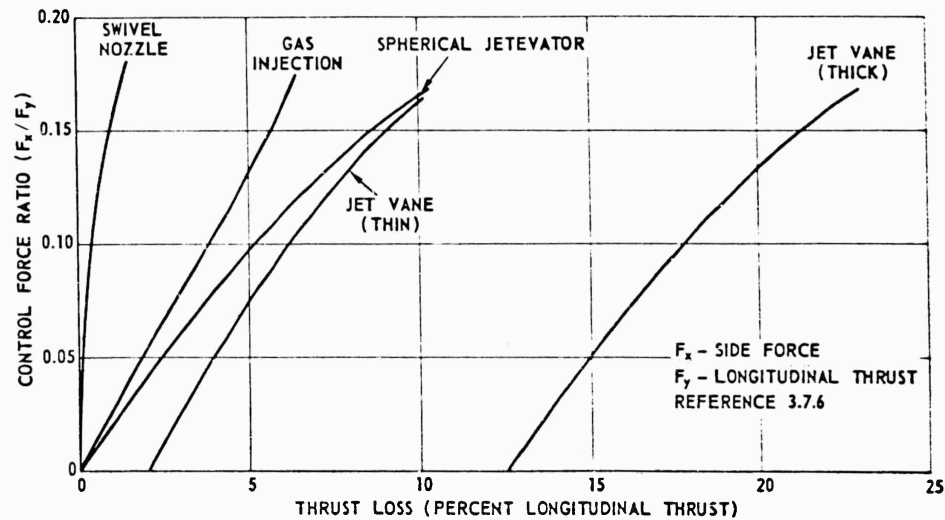


Figure 3.7.43. Comparison of Performance of Various Methods of Jet Deflection.

The adequacy of the main propulsion control system is dependent upon the response time of the actuating system used for the control device. In general, however, high response rates such as are needed for high "g" maneuvers have not been needed for previous missiles using thrust vector control, and little work has been directed toward the attainment of the high response rates which would be required by the lenticular vehicle. It should be noted that the main propulsion control system will be used, if needed, to supplement secondary controls during the boost phase of flight. In such a capacity the response rate demands may be less than if the main propulsive control system were the sole source of control.

Approximately 0.030 second will be required to initiate the main nozzle movement after signals are obtained from the autopilot. This is due to the basic delays inherent in the valving and fluid damping effects of a pressurized hydraulic system. For a typical thrust vector control system it appears possible to obtain a jet deflection of 10° in 0.075 second.

SECONDARY CONTROL. The PYE WACKET vehicle (primarily investigated as an air-to-air weapon in this study) has a relatively short duration of powered flight followed by a coast period to the target. During the non-propulsive flight phase of the vehicle, a secondary control system must be utilized which will provide pitch, yaw, and roll control throughout the coast flight. Pitch control of the vehicle can be obtained by a thrust force in the vertical direction from a secondary control system. Yaw control is obtained with a horizontal side force, and roll control utilizes a differential vertical pitch vector separated by a

SECRET

moment arm. Small liquid or solid propellant rocket motors could be utilized to supply the required thrust forces in the pitch, yaw, or roll planes, with nozzles aligned in the vertical and horizontal directions. If a set of canted nozzles were used to supply the control forces, two basic methods of control are available:

1. Movable nozzles
2. Fixed nozzles - variable thrust

Both systems were considered for this application. However, as will be shown later, in order to minimize system weight it is imperative that a modulating flow system be utilized. Therefore any advantage which would accrue from a movable nozzle would be due strictly to the small thrust increment obtained with the nozzle aligned at 90° to the velocity vector for pitch (for example) versus a fixed system aligned at a slightly smaller angle to provide for both pitch and yaw control. A brief analysis indicated a torque of 500 inch-pounds would be required by the 60-inch diameter vehicle to obtain a response time of 20 milliseconds with a movable system. The weight and complexity of the equipment required to adjust the movable nozzle is not warranted by the slight ($\approx 4\%$) increase in thrust capability. Therefore all further work was limited to the fixed nozzle, modulated flow system.

Description. A reaction-jet control system basically consists of a propellant-combustion chamber-nozzle system for producing thrust forces from chemically stored energy. For the lenticular vehicle, it was necessary to establish the type of system which could be utilized.

From previous consideration given to the main propulsion system, it was found that in order to obtain satisfactory performance the rocket motor nozzle must extend to Station 60 and would occupy an appreciable part of the volume in that area. Therefore it was decided to divide the secondary jet system into two packages on either side of the main nozzle. For purposes of maintaining high reliability, each side was designed as a separate system connected via electrical harnesses to the autopilot.

A pressurized, storable liquid propellant system was selected from the standpoint of reliability and tactical readiness. The propellant (either bi or monopropellant) would be stored in a cylindrical tank and pressure fed from a solid propellant gas generator into a thrust chamber. To obtain a modulated flow and resultant variable thrust, the propellant flow rate would be varied as required through use of an electrically operated valve between the propellant tank and the gas generator. Since forces in both positive and negative direction are required, two nozzles per side are needed. It will be shown later that the duration requirements are such that the use of a single thrust chamber and valve-controlled dual nozzles would probably not survive the thermal environment (produced by the hot gas) so that twin thrust chamber-nozzle systems on

SECRET

each side of the vehicle were employed. A schematic is shown in Figure 3.7.44. The thrust chamber nozzles would probably be regeneratively cooled with some internal insulation provided due to the diminished cooling effect at low flow rates. It is seen in this figure that in order to obtain pitch control, nozzles 1 and 2 or 3 and 4 are used. For roll control, nozzles 1 and 3 or 2 and 4 are used. For yaw control nozzles 1 and 4 or 2 and 3 are used.

In order to study the characteristics and performance of the secondary control system a reference volume and weight were required. The results of the packaging study indicated that approximately 800 cubic inches of propellant could be accommodated in a 21 percent t/C vehicle. This is equivalent to about 40 pounds of bipropellant similar to nitrogen-tetroxide and hydrazine. This was then arbitrarily established as a reference system weight and volume to obtain preliminary performance evaluation data.

Secondary Control Characteristics. As stated previously only the storable propellant systems were considered; either monopropellant or bipropellant such as hydrazine, or nitrogen tetroxide-hydrazine, respectively.

Assuming that the propellant flow rate to the combustion chamber would be controlled by solenoid actuated valves which would permit a flow corresponding to the thrust required for any given missile maneuver, the propellant flow rates required under various conditions were determined from the following equation:

$$\dot{W} = F/I_{sp}, I_{sp} = C^* C_F/g_c$$

where:

$$C_F = \sqrt{\left(\frac{2\gamma^2}{\gamma-1}\right)\left(\frac{2}{\gamma+1}\right)^{\frac{\gamma+1}{\gamma-1}}\left[1 - \left(\frac{P_e}{P_c}\right)^{\frac{\gamma-1}{\gamma}}\right] + \left(\frac{P_c - P_g}{P_c}\right)\frac{A_e}{A_T}}$$

Based on data reported in References 3.7.7, 3.7.8, and 3.7.9, the following parameters were used for the monopropellant and bipropellant systems.

	<u>Monopropellant</u>	<u>Bipropellant</u>
C*, FT/SEC	4050	5600
γ	1.27	1.24

In addition, a nominal nozzle expansion ratio of 5:1 was utilized, and it was assumed that the control system would operate at a chamber pressure of 200 PSIA to produce a thrust force of 50 pounds. The increased thrust forces required would thereby result in proportionally increased chamber pressure, and also a higher delivered specific impulse. The propellant flow rates required under the assumed conditions are shown in Figure 3.7.45. Figure 3.7.46 shows the durations which would result if all four nozzles were fired at a constant

SECRET

3.7.37

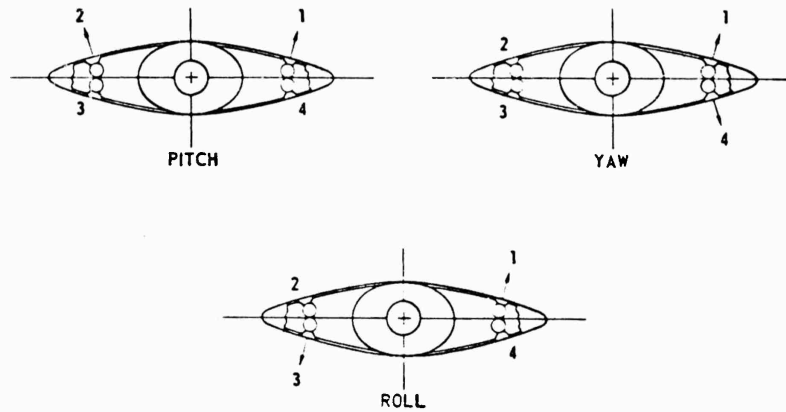


Figure 3.7.44. Diagram for Reaction Controls.

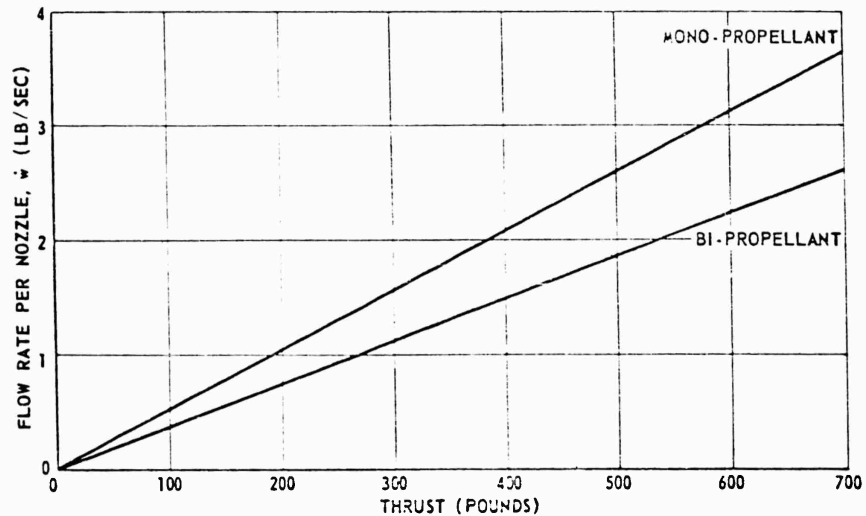


Figure 3.7.45. Nozzle Flow Rates for Secondary Control System.

thrust force as shown in Figure 3.7.44. Actually, only a pair of nozzles are required to fire at the thrust level required for maneuvers, but these data point up the necessity for flow modulation if adequate system duration is to be obtained.

The modulating requirements are naturally a function of the total duration required for the maximum thrust level and the flight duration required. An analysis was made of two design conditions:

1. Maximum thrust = 500 LB, minimum = 50 LB
2. Maximum thrust = 200 LB, minimum = 50 LB

SECRET

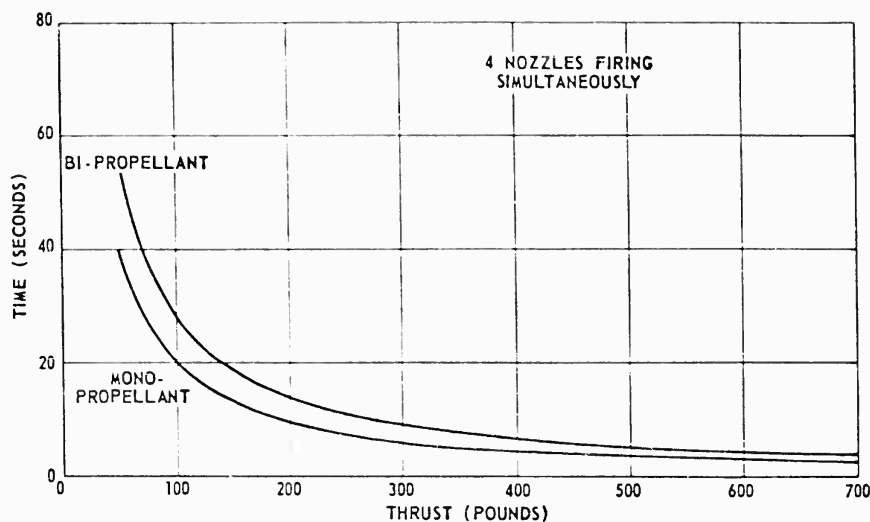


Figure 3.7.46. Duration for Secondary Control System.

A plot of the duration obtainable with each scheme is shown in Figures 3.7.47 and 3.7.48, respectively. The thrust capability of 200 pounds might be utilized in a system with a stability margin of about 0.02-0.025. The 50-pound thrust is for four nozzles and the high thrust level in each case is for two nozzles.

The two main conclusions are:

1. A bipropellant system is superior to a monopropellant system considering I_{sp} and resulting thrust-duration combinations.
2. To maintain a flight duration of 40 seconds, 3.7 seconds of maximum thrust capability of 500 pounds can be realized with a bipropellant.

The 200-pound thrust level can be used for 4.5 seconds and a total flight time of 50 seconds is realized. For the type of lenticular vehicles studied, and their associated trajectories, these durations appear to be adequate.

It is seen that to obtain both pitch and yaw control with this system, the nozzles must be canted at an angle with the vertical. As the angle increases from zero degrees, the effectiveness of the pitch vector is decreased. To determine the most effective cant angle, it was assumed that yawing moments of 70 and 260 FT-LB at 30,000 and 60,000 FT altitudes, respectively, were required, based on a preliminary aerodynamic analysis. Using a duty cycle of 3 seconds for yaw control, 3.5 seconds for maximum maneuver control, and 40 seconds for the total flight time, an optimization study was made as shown in Figure 3.7.49. A compromise angle of 20° was selected.

Allowing 0.030 second for actuation delay time, the total time to complete the control process can be determined by summing the response times inherent

SECRET

3.7.39

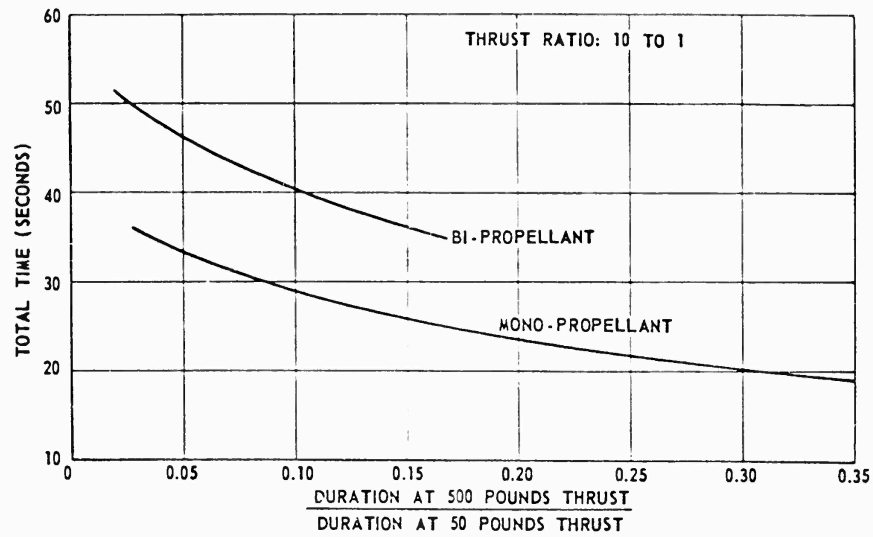


Figure 3.7.47. Duration for Modulated Secondary Control System.

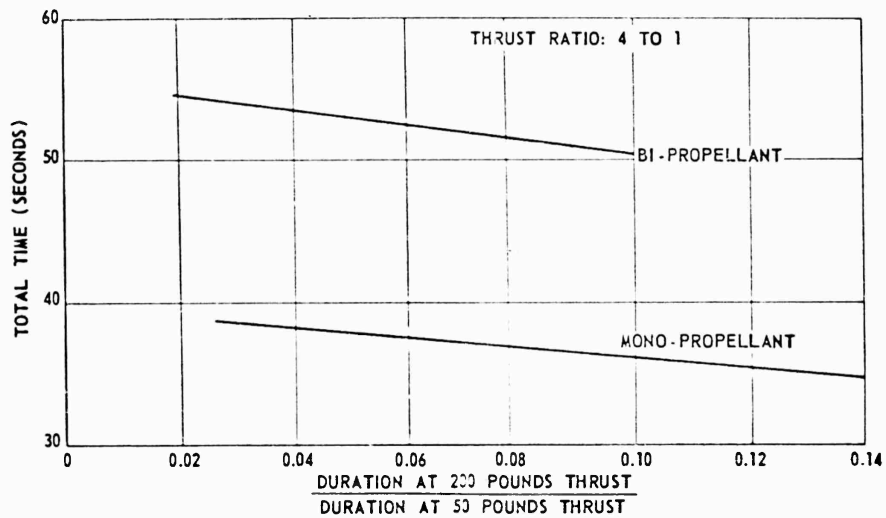


Figure 3.7.48. Duration for Modulated Secondary Control System.

in the control system. For a typical thrust vector control system, it appears possible to obtain a jet deflection of 7° in 0.075 second.

For a variable propellant flow control system, the transient response times of the propellant valves were investigated using the following basic assumptions:

1. The propellant flow through the valve instantaneously increases, i. e., valve actuation delay is not considered.

SECRET

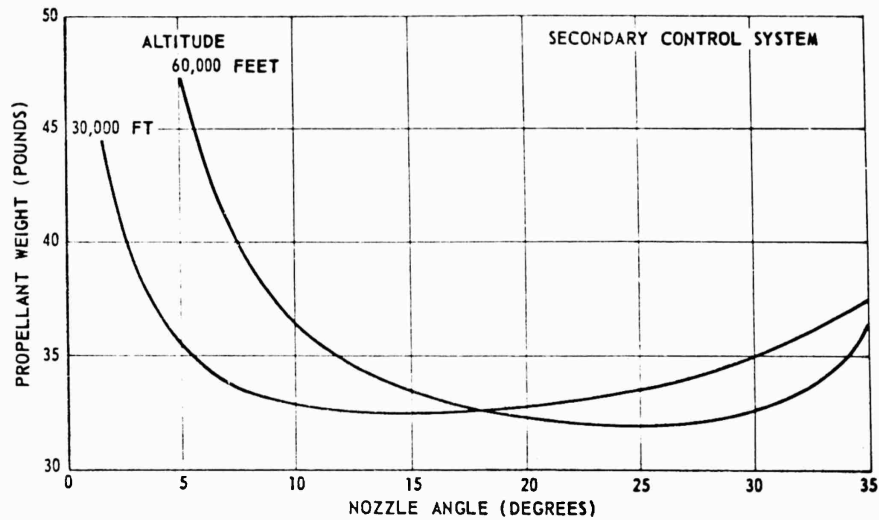


Figure 3.7.49. Optimization of Nozzle Angle Based on Minimum Flow for 3 Seconds Yaw Plus 40 Seconds Pitch.

2. Gas properties are uniform.
3. The nozzle flow process is steady.
4. The gas processes are isentropic.
5. The perfect gas law applies.

The mass flow of combustion gas through the nozzle can be expressed as a function of chamber pressure increase by the following relationship:

$$\dot{W} = A_T \rho_c a_o \left(\frac{2}{\gamma+1} \right)^{\frac{\gamma+1}{2(\gamma-1)}} \left(\frac{P_{c_t}}{P_{c_o}} \right)^{\frac{\gamma+1}{2\gamma}} \quad (3.7.1)$$

subscript t = final conditions
o = initial conditions

The mass of gas in the combustion chamber at any time is:

$$W = V_c \rho_c \left(\frac{1}{P_{c_o}} \right)^{\frac{1}{\gamma}} (P_{c_t})^{\frac{1}{\gamma}} \quad (3.7.2)$$

Equation 3.7.2 can now be differentiated to obtain the change in mass in the combustion chamber.

$$\frac{dW}{dt} = \rho_c V_c \left(\frac{1}{P_{c_o}} \right)^{\frac{1}{\gamma}} \left(\frac{1}{\gamma} \right) (P_{c_t})^{\frac{1-\gamma}{\gamma}} \frac{dP}{dt} \quad (3.7.3)$$

SECRET

3.7.41

SECRET

The sum of Equations 3.7.1 and 3.7.3 represents a step change in the propellant flow through the valve, or

$$\left(\frac{P_{ct}}{P_{c0}}\right)^{\frac{\gamma+1}{2\gamma}} + \frac{L^*}{a_0 \left(\frac{\gamma}{\gamma+1}\right)^{\frac{\gamma+1}{2(\gamma)}}} \left(\frac{1}{P_{c0}}\right)^{\frac{1}{\gamma}} \left(\frac{1}{\gamma}\right) (P_{ct})^{\frac{1-\gamma}{\gamma}} \frac{dP}{dt} = C \quad (3.7.4)$$

Equation 3.7.4 now can be used to determine the time response associated with changes in mass flow. Substituting the bipropellant and monopropellant values of γ and R, Equation 3.7.4 becomes:

Monopropellant

$$\left(\frac{P_{ct}}{P_{c0}}\right)^{.894} + 0.00181 \left(\frac{1}{P_{c0}}\right)^{.788} (P_{ct})^{-.213} \frac{dP}{dt} = C \quad (3.7.5)$$

Bipropellant

$$\left(\frac{P_{ct}}{P_{c0}}\right)^{.916} + 0.00142 \left(\frac{1}{P_{c0}}\right)^{.835} (P_{ct})^{-.167} \frac{dP}{dt} = C \quad (3.7.6)$$

These equations are not readily integrated, but can be iteratively solved by

letting $\frac{\Delta P}{\Delta t} = \frac{dP}{dt}$. The solution to these equations, as in Figure 3.7.50, indicates that approximately 5 milliseconds are required for the pressure to achieve the new equilibrium value.

An estimate was made of the response time for the secondary control system in order to study the vehicle maneuverability characteristics on the computer. The results are shown in paragraph 3.7.4 and indicate satisfactory response and maneuver capability for the vehicle.

Jet Interference Effects. The secondary control system discussed herein basically consists of jet nozzle devices which supply a reaction force to the vehicle. The performance of the control system, however, is only partially described by the jet reaction forces obtained from the nozzles. Of equal importance to the missile system is the effect induced on the pressure field about the body by the interference between the nozzle jet and the airstream flowing over the body. In addition to these considerations, it is important to know how the jet penetrates the boundary layer about the body in order to evaluate the effects of the hot gas on the surface(s) over which it passes. If the exhaust gas from the control jets contains any large percentage of corrosive or erosive products, it is important that the missile body structure be designed to withstand this type of environment.

It is not possible to obtain an exact solution to the jet interference problem, although the effects can be estimated. In Reference 3.7.10, the problem of the

SECRET

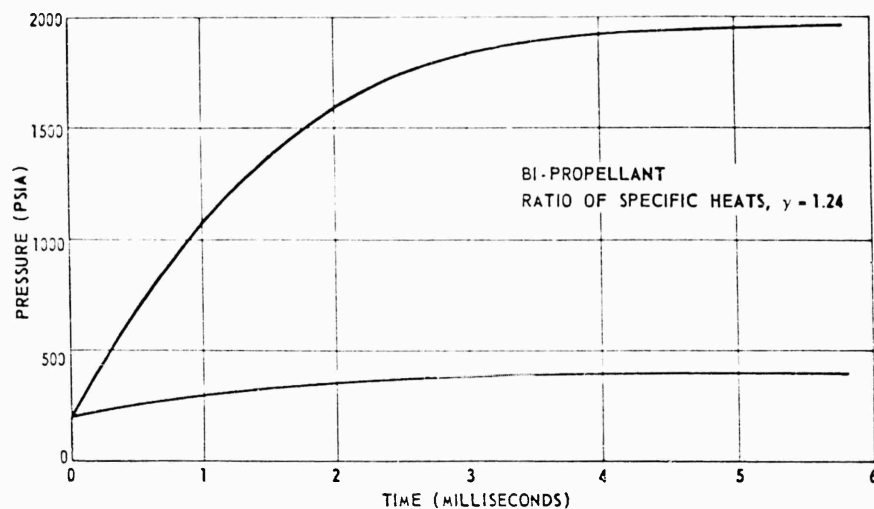


Figure 3.7.50. Transient Response Characteristics for Lenticular Control Nozzles.

shape of the jet exhausting into a high velocity airstream is treated with the simplifying assumption that any boundary layer separation phenomena will not effect the size and shape of the jet core, or the area over which the jet effect is realized. In this case, it was assumed that all interference effects occur between the jet and the detached shock wave which exists in front of the jet. This assumption is logical since the pressure forces exerted by the separated boundary layer (in practice) are small compared with those obtained by perfect fluid theory. The analytical work in Reference 3.7.10 was confined to the case of the simple convergent nozzle placed at right angles to the airstream. The analysis proceeded from the basic equations of momentum, energy, and continuity to develop the equations for describing the jet penetration into the free stream, considering both a constant area jet and a toroidal shape jet. The simplifying assumption of Newtonian flow was used to describe the characteristics of the shock wave surface and the shock stand-off distance. It was also assumed that the conditions which exist at the shock plane can be directly applied to the surface (this assumption was based on experimental data). A typical plot of the ratio of the interference forces to the jet forces is shown in Figure 3.7.51 (from Reference 3.7.10).

Up to the present time, experimental work on jet interference has concentrated on the use of a cold air source (References 3.7.11, 3.7.12, and 3.7.13). Although the data so obtained indicates the gross effects of jet interference, the effect of air line loads in the balance and instrumentation simplicity degrade the accuracy of the data. The original theoretical work on jet interference was

SECRET

3.7.43

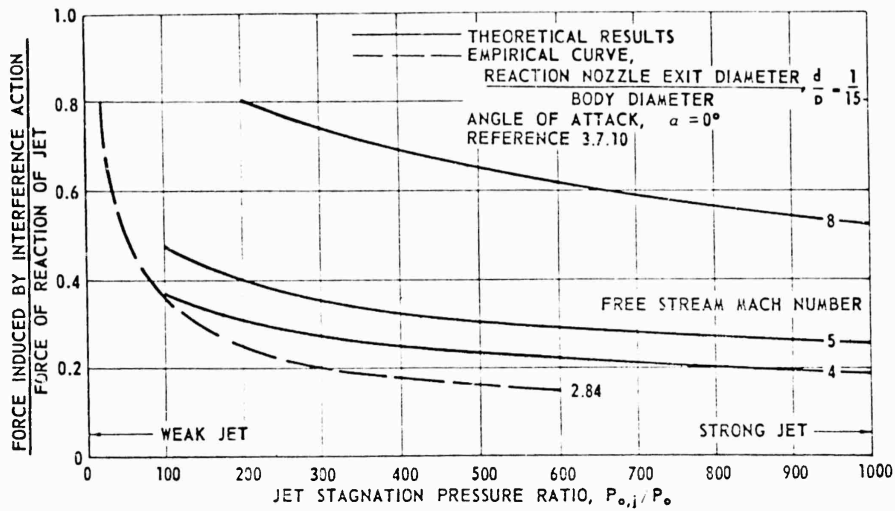


Figure 3.7.51. Jet Interference Produced by Side-Exhausting Jet Issuing From Cylindrical Body.

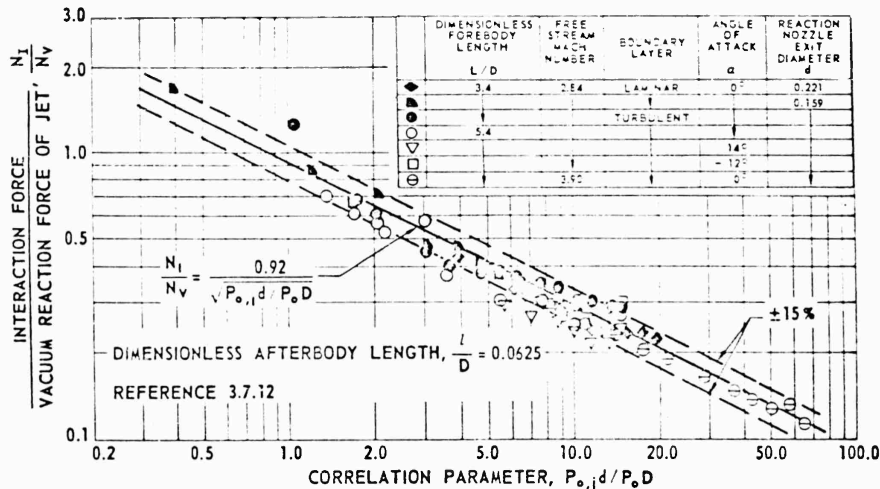


Figure 3.7.52. Jet Interference Correlation of Experimental Data.

based on two-dimensional isentropic expansion theory. As indicated in References 3.7.11 and 3.7.12, the early experimental data at Mach 2.84 and 3.90 did agree with the simple two-dimensional theory. From these data, shown in Figure 3.7.52, the following empirical equation was proposed:

$$\frac{N_i}{N_v} = \frac{0.92}{\left[\frac{(P_{o,i})(d)}{(P_o)(D)} \right]^{1/2}}$$

SECRET

Although at $M_0 = 4$ the two theories on jet interference effects agree fairly well, the correlation falls off as shown in Table 3.7.3.

Table 3.7.3
CORRELATION BETWEEN COMPUTED AND EMPIRICAL RESULTS

M_0	$p_0/p_{0,j}$	σ
4	0.010	0.987
4	0.005	1.03
4	0.001	1.08
5	0.010	1.051
5	0.005	1.105
5	0.001	1.191
8	0.005	1.412
8	0.001	1.519

The lack of correlation shown above may result either from the hypersonic theory overestimating the effect of Mach number, or the proposed equation based on the experimental data is not valid at $M_0 = 4$. However, the data of Reference 3.7.12 does indicate the relatively small effect of the boundary layer on the interaction force under conditions of laminar and turbulent flow.

Normal force versus stagnation pressure ratio data for jets at various angles normal to the airstream is shown in Figure 3.7.53 (from Reference 3.7.13). Also shown in Figure 3.7.53 are data obtained with a nose jet inclined 11° from the normal to the missile axis. A comparison of these data indicates the aft jet is far superior to the nose jet (for ogive-cylinders), possibly due to the body bow-shock disturbance of the nose jet which may tend to reduce the overall forces on the body. Although these data are not directly applicable to a lenticular body, it can be presumed that the aft jet location is at least equal in effectiveness to a nose jet and, in addition, has the advantage of not unduly complicating the packaging problem.

Normal force data for multiple jets is compared to single jet data in Figure 3.7.54 (from Reference 3.7.13). These data indicate that the effectiveness of the jets decreases as the number of jets is increased. At high pressure ratios, however, the multiple jet configurations approach the effectiveness of the single jet configuration.

Based on available information, the effect of jet interference on the performance of the secondary control system may be summarized as follows:

1. There is a substantial increase in force over and above the jet thrust, on the order of 20 percent at $M_0 = 4$ and possibly up to 60 percent at $M_0 = 8$.

SECRET

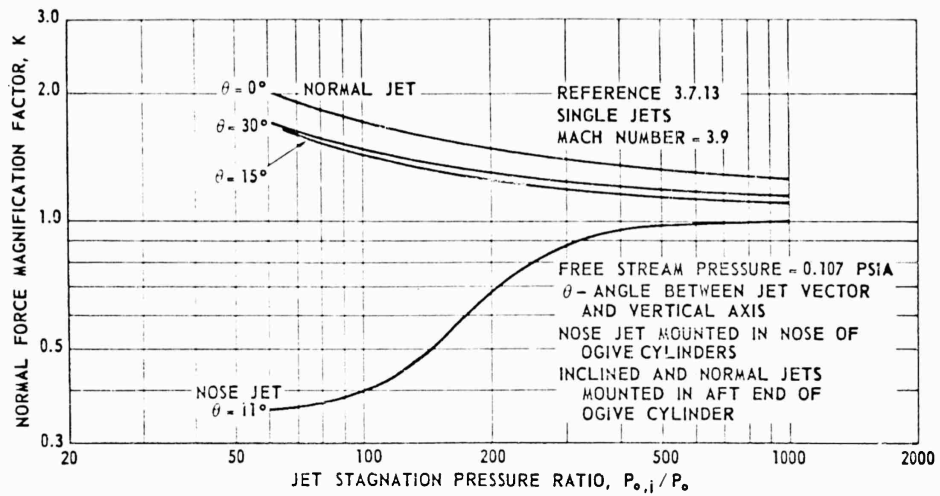


Figure 3.7.53. Normal Force Magnification Factor Versus Jet Stagnation Pressure Ratio.

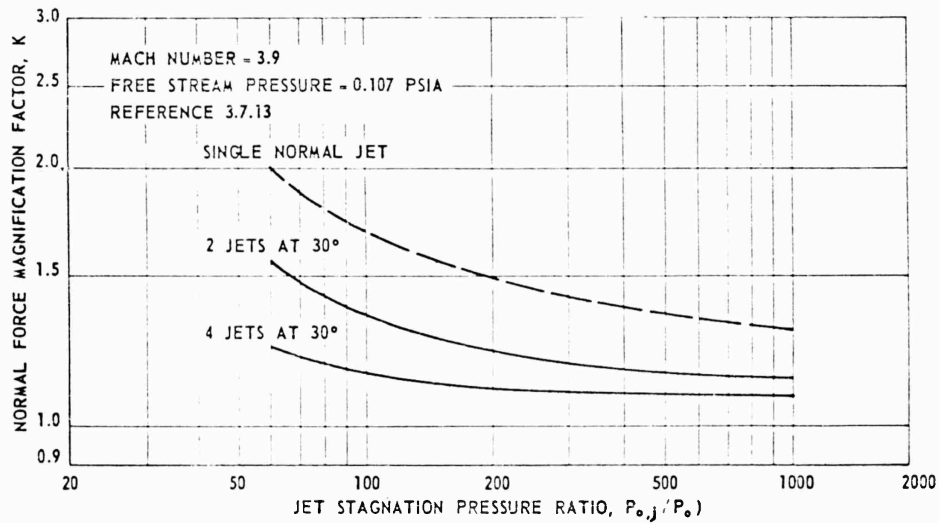


Figure 3.7.54. Normal Force Magnification Factor Versus Jet Stagnation Pressure Ratio.

2. The jet interference effect has been substantiated with cold air tests at $M_0 = 2.84$ and 3.90 , and it is presumed that hot gas would result in at least an equal effect.
3. Aft jets are superior to jets located at the forward end for the lenticular configuration.

SECRET

Although at $M_0 = 4$ the two theories on jet interference effects agree fairly well, the correlation falls off as shown in Table 3.7.3.

Table 3.7.3
CORRELATION BETWEEN COMPUTED AND EMPIRICAL RESULTS

M_0	$p_o/p_{o,j}$	σ
4	0.010	0.987
4	0.005	1.03
4	0.001	1.08
5	0.010	1.051
5	0.005	1.105
5	0.001	1.191
8	0.005	1.412
8	0.001	1.519

The lack of correlation shown above may result either from the hypersonic theory overestimating the effect of Mach number, or the proposed equation based on the experimental data is not valid at $M_0 = 4$. However, the data of Reference 3.7.12 does indicate the relatively small effect of the boundary layer on the interaction force under conditions of laminar and turbulent flow.

Normal force versus stagnation pressure ratio data for jets at various angles normal to the airstream is shown in Figure 3.7.53 (from Reference 3.7.13). Also shown in Figure 3.7.53 are data obtained with a nose jet inclined 11° from the normal to the missile axis. A comparison of these data indicates the aft jet is far superior to the nose jet (for ogive-cylinders), possibly due to the body bow-shock disturbance of the nose jet which may tend to reduce the overall forces on the body. Although these data are not directly applicable to a lenticular body, it can be presumed that the aft jet location is at least equal in effectiveness to a nose jet and, in addition, has the advantage of not unduly complicating the packaging problem.

Normal force data for multiple jets is compared to single jet data in Figure 3.7.54 (from Reference 3.7.13). These data indicate that the effectiveness of the jets decreases as the number of jets is increased. At high pressure ratios, however, the multiple jet configurations approach the effectiveness of the single jet configuration.

Based on available information, the effect of jet interference on the performance of the secondary control system may be summarized as follows:

1. There is a substantial increase in force over and above the jet thrust, on the order of 20 percent at $M_0 = 4$ and possibly up to 60 percent at $M_0 = 8$.

SECRET

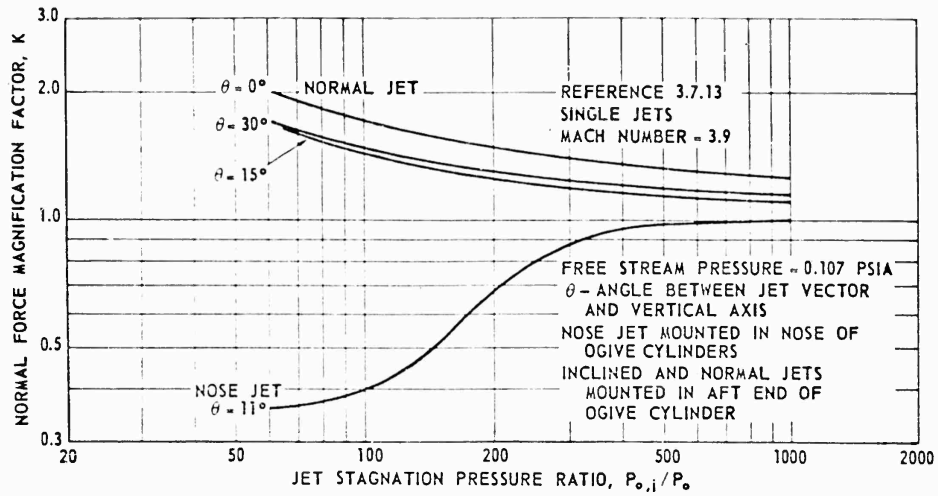


Figure 3.7.53. Normal Force Magnification Factor Versus Jet Stagnation Pressure Ratio.

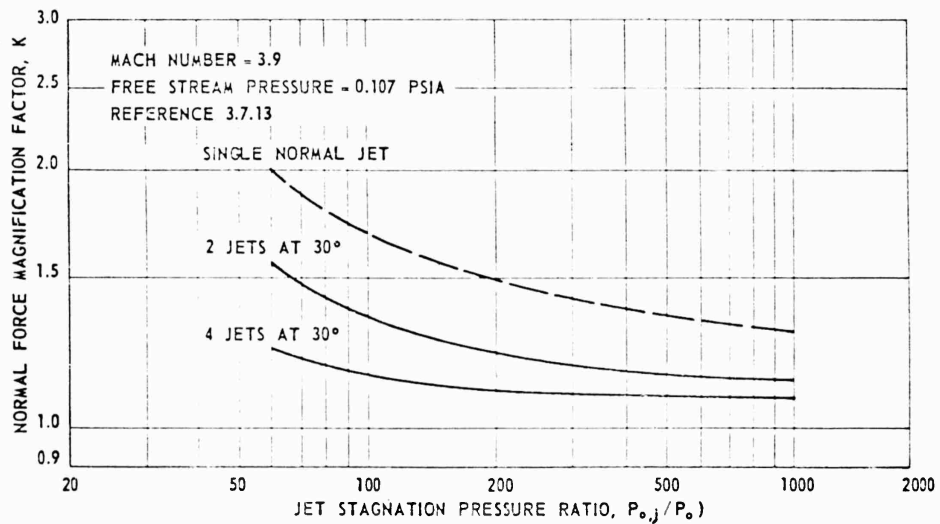


Figure 3.7.54. Normal Force Magnification Factor Versus Jet Stagnation Pressure Ratio.

2. The jet interference effect has been substantiated with cold air tests at $M_0 = 2.84$ and 3.90 , and it is presumed that hot gas would result in at least an equal effect.
3. Aft jets are superior to jets located at the forward end for the lenticular configuration.

SECRET

SUMMARY OF REACTION-JET CONTROL INVESTIGATION. The most feasible method for control utilizing the main propulsive jet appears to be a swivel nozzle, although secondary injection could be employed for short duty-cycle requirements.

The most feasible control scheme for a secondary jet system is to use a pair of nozzles on either side of the aft end of the vehicle, at approximately Station 54, and 12 inches from the vehicle centerline, in the case of the 60-inch diameter vehicle. Two nozzles are positioned 20° from the vertical in the upward direction and two are positioned 20° from the vertical in the downward direction, pointing away from the vehicle longitudinal centerline.

A significant additive force is obtained due to interference effects of the jet over the body. This effect was not considered in this analysis or in subsequent computer studies in determining the performance effectiveness of the secondary control system. Therefore, the results of the study are conservative in this respect. Roll and yaw control coupling effects were not considered in the computer studies and are believed to be very small compared to the coupling resulting from the use of aerodynamic control surfaces.

The use of a bipropellant system for the secondary control system produces a minimum weight system; however, a slightly more complex system results than if a monopropellant system is used. Both types of systems appear to be feasible.

3.7.3 AUTOPILOT

In this subsection, consideration is given to the design of PYE WACKET autopilots with emphasis on transient response times and steady-state errors to commands in the pitch, roll and yaw planes.

The autopilots which control movement of the missile are defined as having the following input-output characteristics:

1. Pitch:
 - a. The input is command acceleration.
 - b. The output is actual acceleration.
2. Roll:
 - a. The input is a command roll angle.
 - b. The output is actual roll angle.
3. Yaw:
 - a. The input is a command yaw angle.
 - b. The output is actual yaw angle.

In general, autopilot requirements are the same for all three types. These requirements include:

1. Stability. The requirement that the system remain stable with all flight conditions and possible inputs is paramount.

SECRET

3.7.47

2. Response Time. The system should have as fast a response as is compatible with stability requirements. This invariably corresponds to little or no overshoot of the output for a step input.
3. Steady State Error. The amount of steady-state error allowable is a function of the particular system under study. Generally speaking, of course, it should be kept at a minimum value compatible with stability requirements. In particular, it presently appears that roll and yaw steady-state errors should be made as near zero as possible. In pitch, where it is more difficult to satisfy this requirement, the guidance system may permit some relaxation. This relaxation is tolerable if the over-all guidance system can operate fast enough not to require a unity gain autopilot.
4. Disturbances. The outputs of the three types of autopilots should remain insensitive to disturbance inputs. A disturbance input is defined here as any input other than one provided by the guidance system. Examples are:
 - a. Electronic or aerodynamic noise.
 - b. Aeroelastic vibration pickup through the instruments.
 - c. Aerodynamic and geometric coupling between planes of motion.
5. Simplicity and Hardware Feasibility.

The following types of autopilots were given consideration in this study:

1. Linear wedgevator controlled roll system.
2. Non-linear reaction motor controlled roll system.
3. Non-linear reaction motor controlled yaw system.
4. Linear pitchvator controlled pitch system.
5. Non-linear reaction motor controlled pitch system.

Only single plane conditions were considered in the design for each autopilot.

It should be noted that, as determined in paragraph 3.7.1, aerodynamic forces are not considered feasible as a sole source of control. The primary reason for this conclusion is that the aerodynamic coupling terms would be excessive and, in the case of yaw motion, would exceed the control available. Nevertheless, roll and pitch control by aerodynamic means were investigated primarily to form a basis for evaluating the control characteristics of the reaction systems.

Paragraph 3.7.2 discusses the design feasibility of reaction controls. Paragraph 3.7.4 examines the steady-state performance available from the reaction controls. Paragraph 3.7.3 is concerned primarily with the response and transient characteristics available from the reaction control systems outlined above.

ROLL CONTROL. The design of a roll control system for PYE WACKET begins by assuming that the decoupled rolling moment equation adequately describes the aerodynamics. There are coupling conditions that exist, for example, between roll and yaw systems which should be considered from the absolute stability standpoint, but for the purposes for analyzing transient behavior the decoupled equation will suffice.

SECRET

Two methods for the missile to obtain control forces were studied, wedgevators and reaction jets. In each case there is a definite saturation level. With wedgevator control, this level is the maximum angle that the control surfaces are allowed to deflect. With reaction control, the saturation level is determined by the maximum thrust delivered from the reaction motors. The electronic analog computer was used for design of the closed loop system.

Aerodynamic Control. Wedgevators were initially considered as a means for obtaining the desired control forces in order to provide a basis for comparison with the reaction control system. The corresponding roll moment equation is as follows:

$$\ddot{\phi} = F\dot{\phi} + G\delta \quad (3.7.7)$$

where ϕ = angular rotation about the missile centerline, degree
 δ = wedgevator angle with respect to the plane of the missile, degree
F = roll damping factor, 1/SEC
G = roll control acceleration factor, 1/SEC²

The equations for F and G are given below and the estimated variation of roll moment derivatives versus Mach number are shown in Figures 3.7.55 and 3.7.56.

$$G = \frac{180}{\pi} \frac{1481 \lambda S d M^2 C_{l\delta}}{I_R}$$
$$F = \frac{1481 \lambda S d^2 M^2 C_{l\dot{\delta}}}{2 I_R V}$$

where S = reference area, 19.634 FT²
d = reference diameter, 5 FT
M = Mach No.
 λ = static pressure ratio, pressure at altitude/pressure at SL
 I_R = roll moment of inertia, slug-FT²
V = velocity, FT/SEC
 $C_{l\delta}, C_{l\dot{\delta}}$ = the roll moment derivatives

The control equation for the linear roll system is

$$\delta_c = K_1(\phi_c - \phi) + K_d \dot{\phi} \quad (3.7.8)$$

where δ_c = called for wedgevator angle into the position servo, degree
 ϕ_c = called for roll angle
 K_1, K_d = roll autopilot gains

SECRET

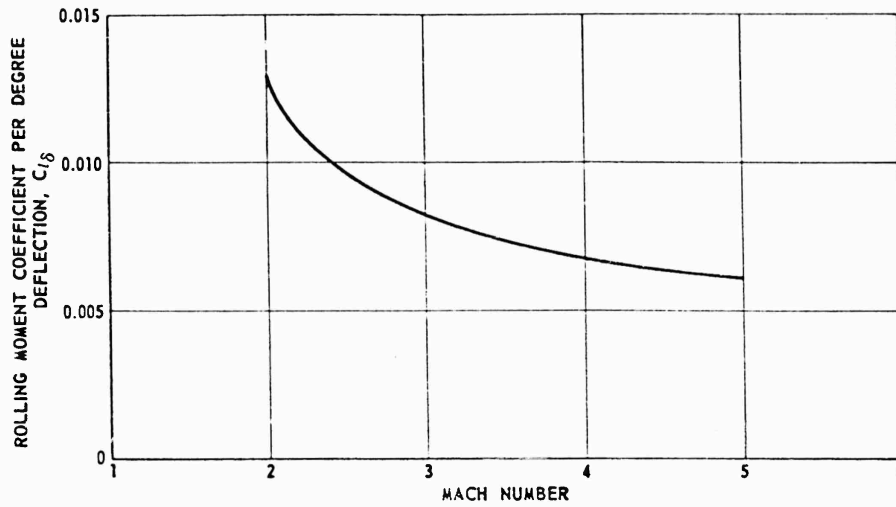


Figure 3.7.55. Roll Moment Derivative Due to Roll Deflection Versus Mach Number.

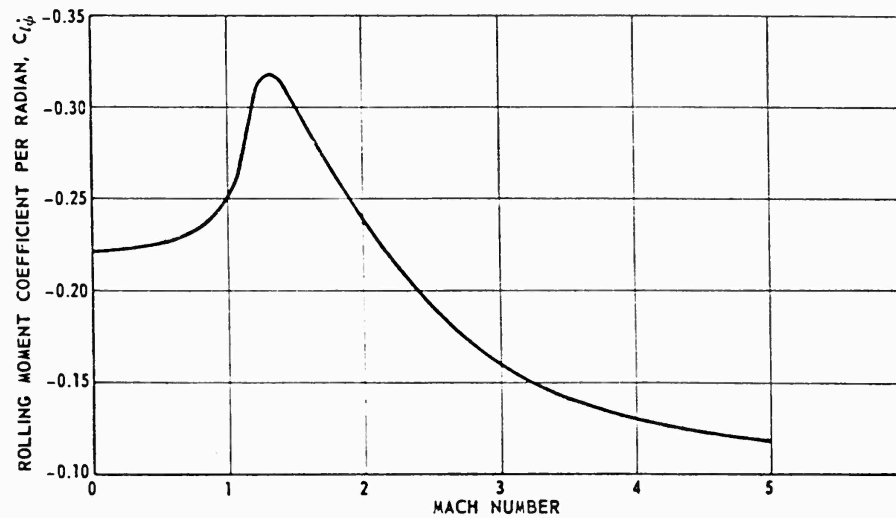


Figure 3.7.56. Roll Moment Derivative Due to Roll Angle Rate Versus Mach Number.

The wedgevator angular deflection is obtained with a position servo whose transfer function is assumed to be

$$\frac{\delta}{\delta_c} = \frac{1}{1 + 0.05s}$$

SECRET

The servo has the following characteristics:

1. The time constant of 0.005 second was chosen to be compatible with existing servos of this type as exemplified by those used in operational Convair missiles.
2. Investigations at Convair have shown that hydraulic servos are satisfactory for deflection control. Hydraulic forces are applied to pistons which are linked mechanically to the wedgevator surfaces through involute cams. This arrangement leads directly to two limitations. First, the maximum deflection rate is assumed to be about 300 DEG/SEC, limited by the available hydraulic pressure. Secondly, the maximum wedgevator deflection is taken as 30 degrees from the level position. This limit is necessary from the standpoint of mechanical linkage geometry and also from consideration of the maximum available effort that can be exerted by the servo in causing wedgevator deflection. These limits were incorporated in the analog computer simulation. A block diagram of the system described above is shown in Figure 3.7.57. Command step inputs of 30° and 90° were used as a criteria for selection of K_I and K_D . The transient responses were obtained from the analog computer and are shown in Figures 3.7.58, 3.7.59, 3.7.60, and 3.7.61 for various flight conditions. The roll moment of inertia used was 27.5 slug-feet². It should be noted that the maximum control torque which can be developed is a function of flight condition. Specifically, at higher Mach No. and lower altitudes the wedgevators are able to deliver greater torques and thereby decrease the response time to a called-for roll angle. This can be seen analytically by inspection of the closed loop transfer function

$$\frac{\phi}{\phi_c} = \frac{1 + K_D S}{1 + (K_D - \frac{F}{K_I G}) S + (\frac{1 - T F}{K_I G}) S^2 + \frac{T}{K_I G} S^3} \quad (3.7.9)$$

As the aerodynamic parameter G increases, the bandwidth of the system increases resulting in a faster transient response. The transient response times and control torques are summarized below in Table 3.7.4. The variations of K_I and K_D with altitude are presented in Figure 3.7.62.

A non-linear wedgevator control system was also investigated as a means of roll control. This system calls for either maximum positive or negative wedgevator angular position (δ_c) depending upon the sign of an input control function, Δ_c . Mathematically, this is stated as follows:

$$\delta = |\delta_{MAX}| \text{ Signum } \Delta_c \quad (3.7.10)$$

SECRET

3.7.51

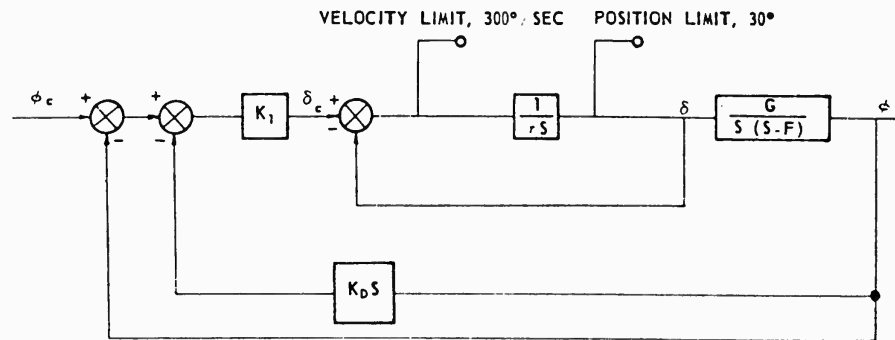


Figure 3.7.57. Simplified Block Diagram of a Linear Roll System.

Table 3.7.4
SUMMARY OF TRANSIENT RESPONSE TIMES
AND CONTROL TORQUES

Flight Condition Mach No. Altitude	Transient Response (Time of the output to equal 63 percent of a 90° step input, (SEC))	Maximum Available Torque (FT-LB)
2 30K	0.15	6450
	0.22	1690
	0.37	375
5 30K	0.1	20,200
	0.15	4860
	0.25	1175

(References 3.7.14, 3.7.15, and 3.7.16 present a detailed treatment of bistable control theory). Control systems consisting of position and rate servos coupled with this bistable device were studied on the analog computer. Briefly, the results indicate that for small errors the non-linear system transient response is faster than the comparable linear system. For large errors response times are about the same. The small error advantage is due to maximum corrective forces being applied in the non-linear system rather than proportional corrective forces in the linear system. The non-linear system also has the advantage of having a smaller number of parameter changes in the roll computer as compared to the linear system. For example, an adequate non-linear control equation is Equation 3.7.8 with $K_1 = 1$ for all flight conditions. A non-linear system employing reaction jets instead of wedgevators is presented next.

SECRET

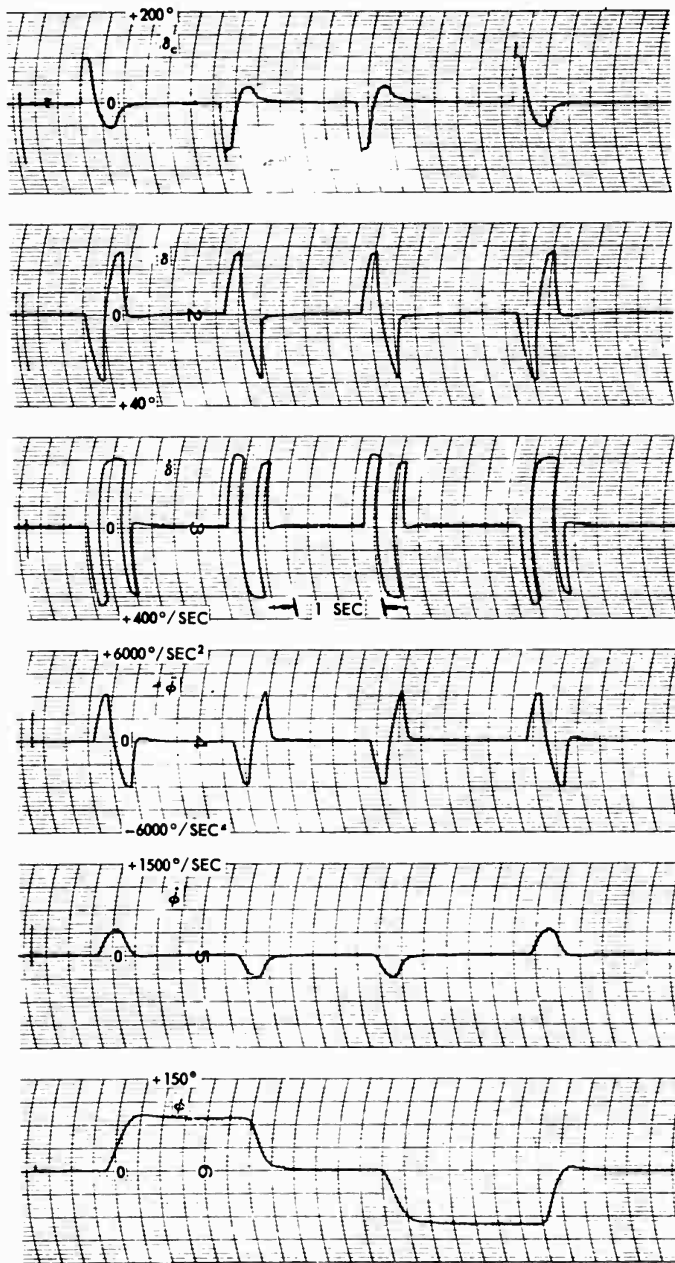


Figure 3.7.58. Transient Responses Mach 2
Altitude 60K $\phi_c \pm 90^\circ$.

SECRET

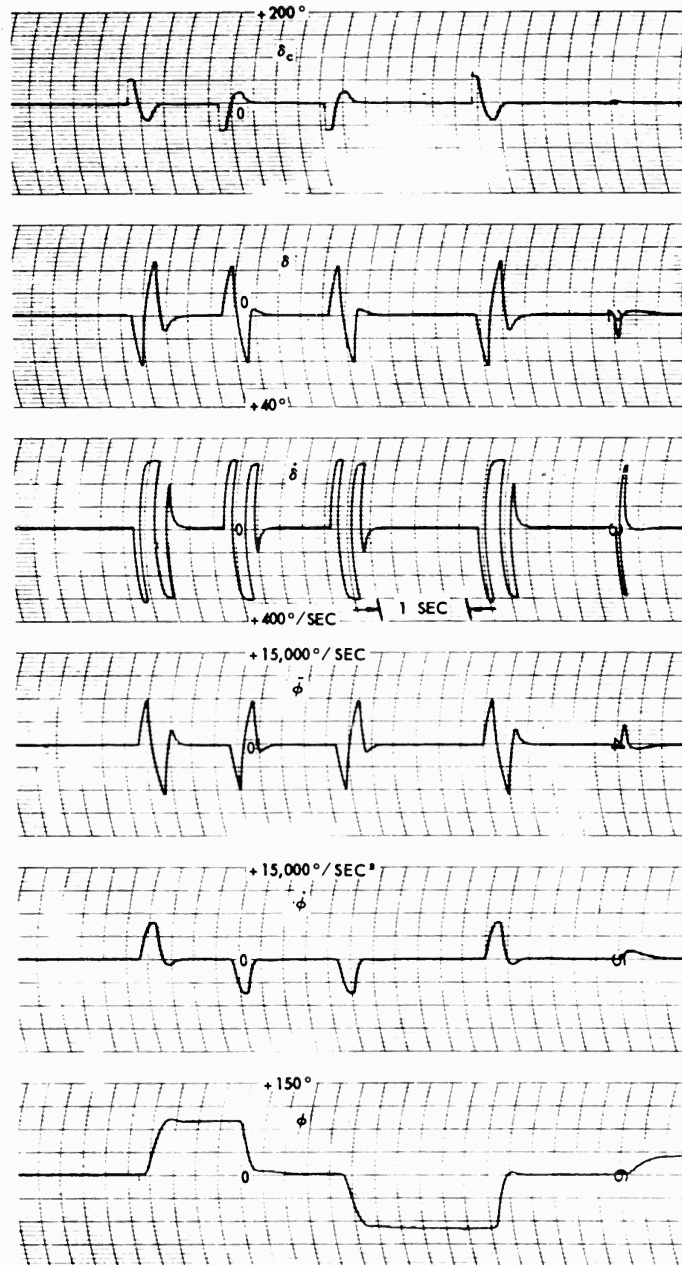


Figure 3.7.59. Transient Responses Mach 5
Altitude 60 K $\phi_c \pm 90^\circ$.

SECRET

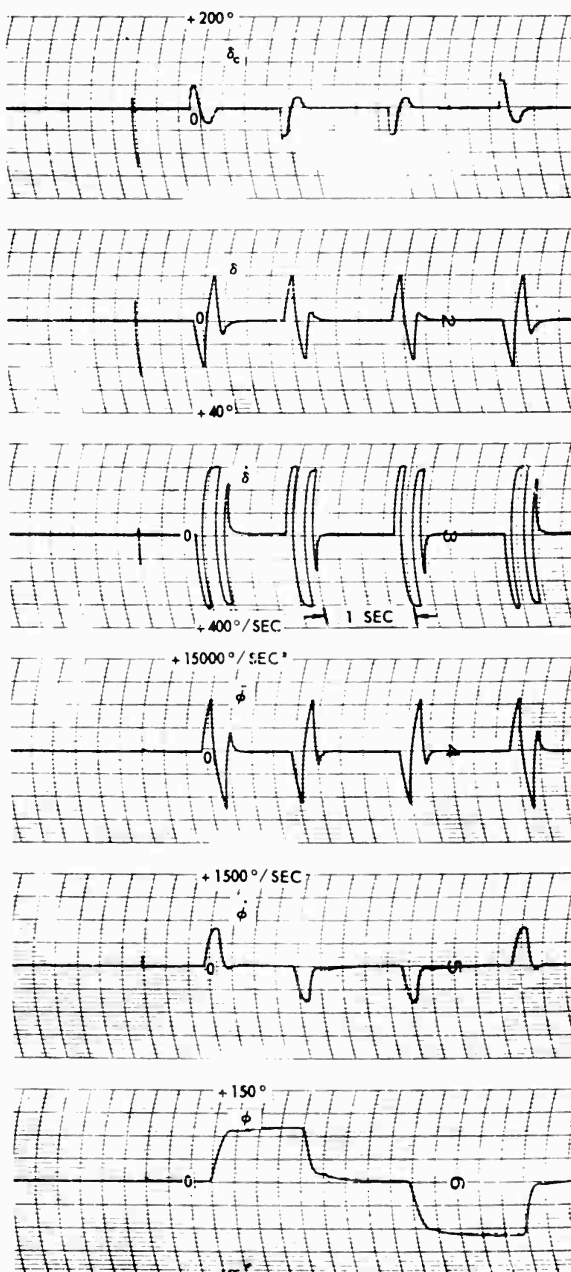


Figure 3.7.60. Transient Responses Mach 2
Altitude 30 K $\phi_c \pm 90^\circ$.

SECRET

3.7.55

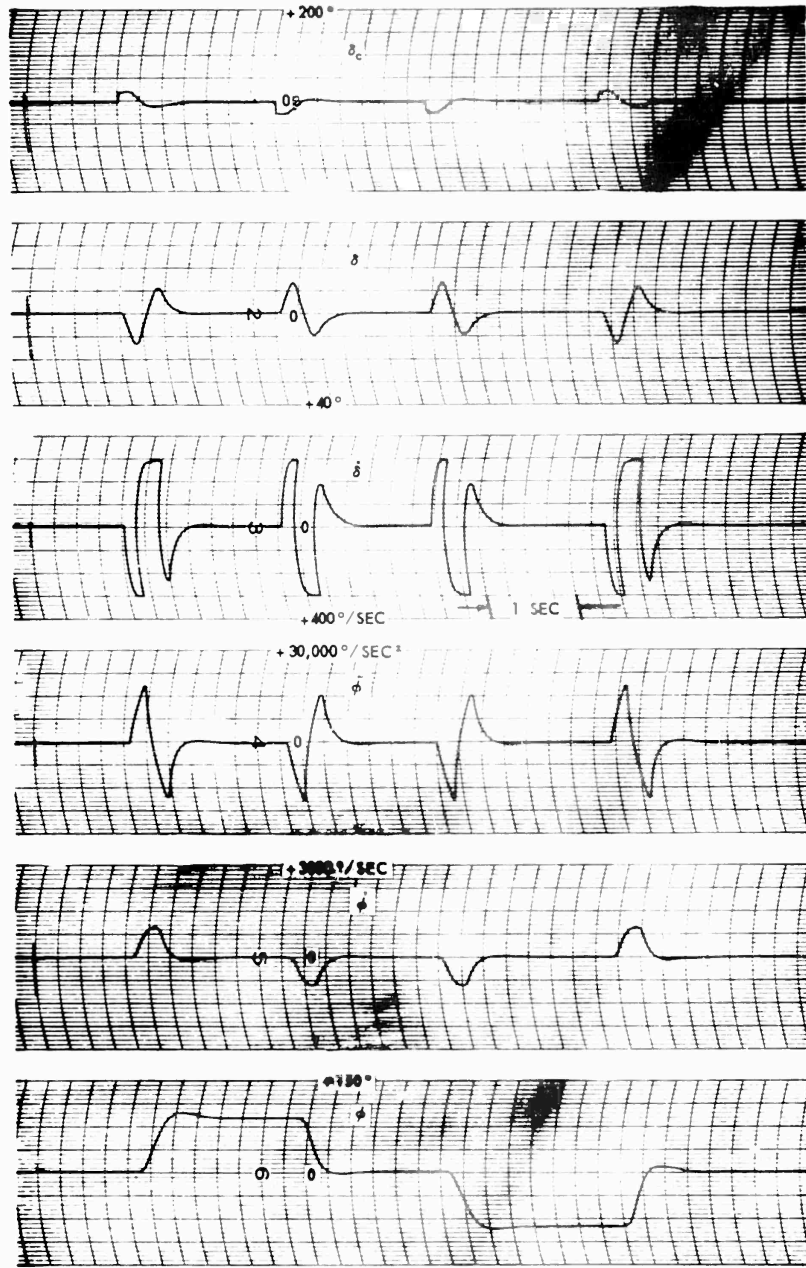


Figure 3.7.61. Transient Responses Mach 5
Altitude 30 K $\phi_c \pm 90^\circ$.

SECRET

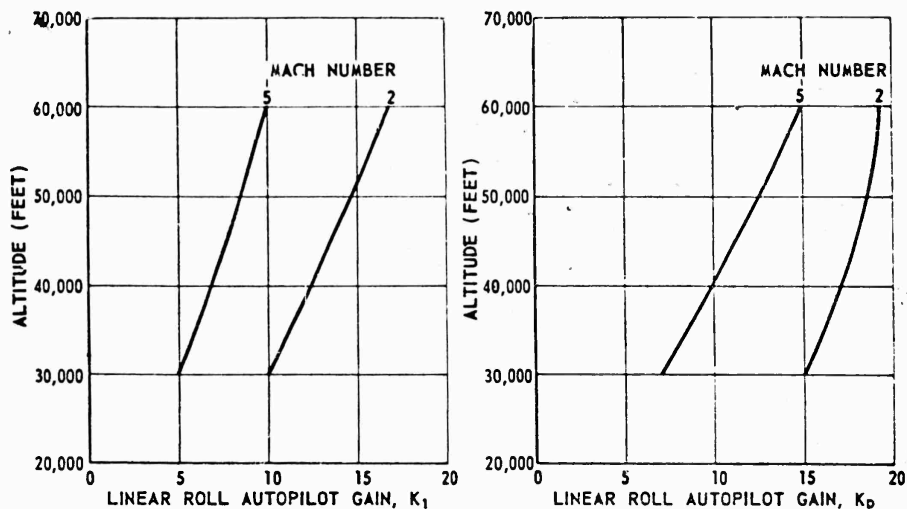


Figure 3.7.62. Linear Autopilot Gain Variations.

Reaction Control. Another form of obtaining roll control corrective forces is by the use of reaction jets instead of wedgevators. The roll moment equation now becomes

$$\ddot{\phi} = F\dot{\phi} + \frac{180k}{\pi I_R} f \quad (3.7.11)$$

- where k = moment arm, FT
 I_R = roll moment of inertia, 15.3 slug-FT²
 f = reaction thrust, LB

The response time of all contributing factors (reaction-jet valve, ignition, and thrust buildup) was considered as a lumped first order lag. Thrust delivered for roll control is given mathematically as follows:

$$f = f_c / \left(1 + \frac{r}{T_S} \right) \text{Signum } \Delta_c \quad (3.7.12)$$

- f_c = called-for thrust, LB
 r = time constant of the first order lag = 0.02 second
 Δ_c = the control function
 Signum Δ_c = "sign of" Δ_c , which can be ± 1

An adequate control equation is:

$$\Delta_c = \phi_E + K\dot{\phi}_E \quad (3.7.13)$$

SECRET

where

$$\phi_e = \phi_c - \phi$$

K = roll autopilot gain

A block diagram of this non-linear system is given in Figure 3.7.63.

The maximum available thrust (f) can have two values, depending upon the magnitude of the control function Δ_c . When $|\Delta_c|$ is less than a value approximately corresponding to a roll error of 30° , the applied thrust for roll control is taken as 200 pounds. When $|\Delta_c|$ is larger, (f) is 1000 pounds.

The non-linear element controlling the magnitude and sign of f_c is shown in the block diagram of Figure 3.7.64.

The system design is based on a transient response to a step input of 15° and 90° . These responses are presented in Figures 3.7.65, 3.7.66, and 3.7.67. Variation of K with altitude is shown in Figure 3.7.68. Since the linear dynamics of the system is an integral plus a first order time constant, an analytical method known as the phase plane technique may be used for verification of the transient response. The response to a 15° step input is shown in Figure 3.7.69 plotted in the ϕ_e versus $\dot{\phi}_e$ phase plane. Trajectories of the first and second applied forces compared well with the analog computer runs of Figure 3.7.67. Resulting equations used for phase plane trajectories are given below:

$$\phi_e = C_1 e^{-Ft} + C_2 - K f_c \left[\frac{t}{F} - \frac{1}{F^2} - \frac{K_2 e^{-t/\tau}}{\tau(F-F)} \right] \text{Signum } \Delta_c \quad (3.7.14)$$

$$\dot{\phi}_e = -FC_1 e^{-Ft} - K f_c \left[\frac{1}{F} + \frac{K_2 e^{-t/\tau}}{\tau(F-F)} \right] \text{Signum } \Delta_c \quad (3.7.15)$$

$$K_2 = 1 - \frac{f}{f_c} \text{Signum } \Delta_c$$

where

$$C_1 = -\frac{\phi_{e0}}{F} - \frac{K f_c}{F} \left[\frac{1}{F} + \frac{K_2}{\tau(F-F)} \right] \text{Signum } \Delta_c$$

$$C_2 = \phi_{e0} + \phi'_{e0} + \frac{K f_c}{F} \left[K_2 \tau \right] \text{Signum } \Delta_c$$

The average high frequency motion which is evident after the second switching on the analog computer run of Figure 3.7.67 is approximated in the phase plane by setting Equation 3.7.13 to zero. The error variable as a function of time, which results from the solution of Equation 3.7.13, is plotted in the phase plane giving a complete check of the transient response.

SECRET

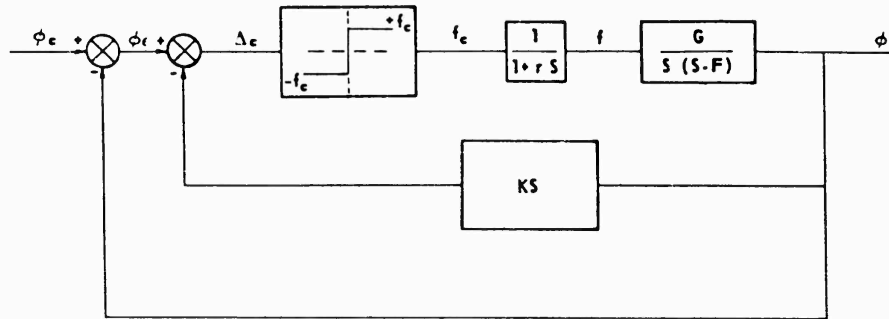


Figure 3.7.63. Simplified Block Diagram of a Two-State Non-Linear Roll System.

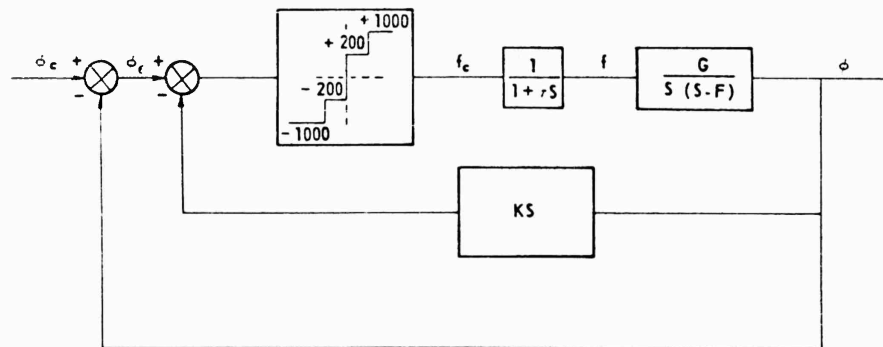


Figure 3.7.64. Simplified Block Diagram of a Four-State Non-Linear Roll System.

The high frequency oscillation on the analog computer runs "called-for force" trace, attempts to linearize the applied force. When the steady-state error and its derivatives are reduced to zero, the applied force is zero. This high frequency oscillation is caused by power supply ripple on the output of the operational amplifier preceding the bistable element. Actual measurement of this "dither" indicated the frequency to be 1200 cycles per second. The describing function technique (Reference 3.7.17) can be used to predict possible oscillation modes. The roll system was investigated for low frequency oscillation by attempting to filter the noise into the signum computer. A first order lag with a time constant of 0.0063 second was added to the system, which in turn produced a low frequency mode of approximately 40 cycles per second. Analytical verification is achieved by plotting the describing function of the non-linearity along with the linear elements in a plot known as a Nyquist diagram (Reference 3.7.17). The intersection of the above two curves, as shown in Figure 3.7.70, reveals a stable limit cycle occurring at $\omega = 210$ radians/second. Equations and definitions used in the analysis are:

SECRET

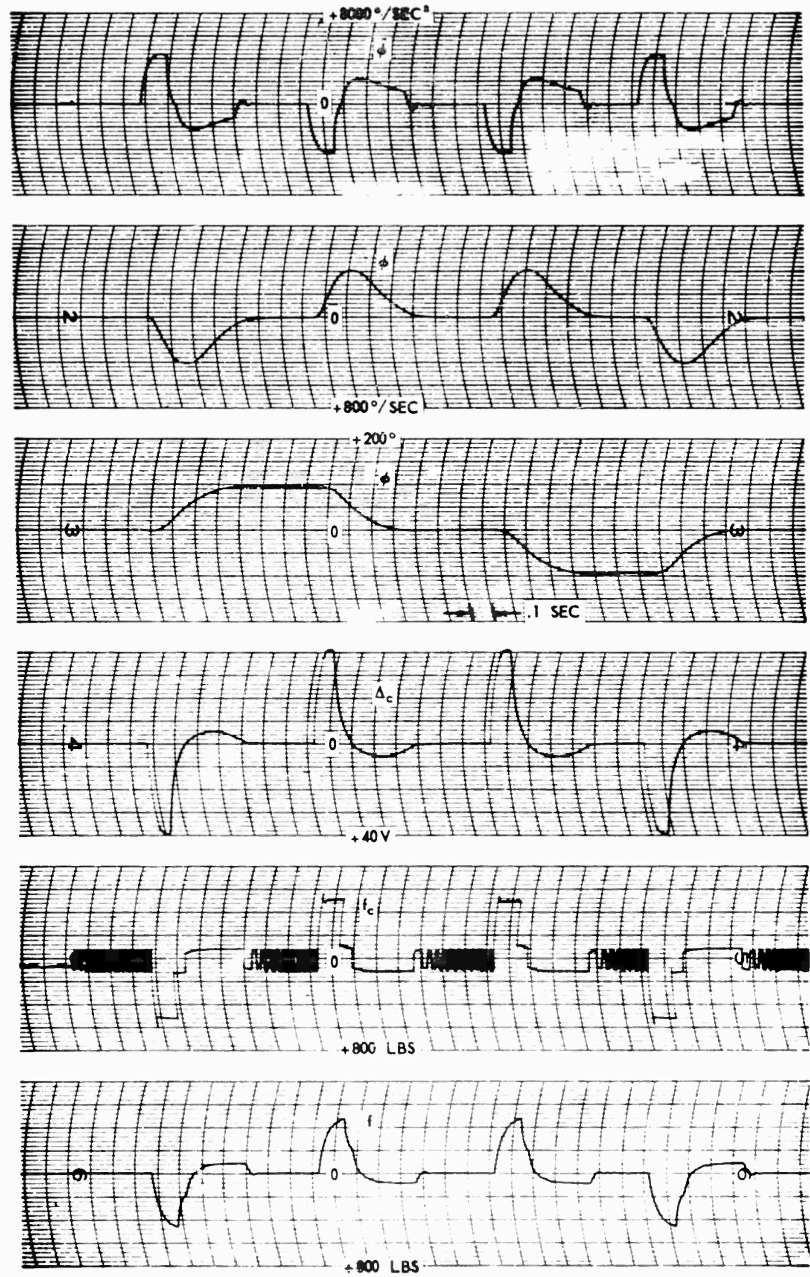


Figure 3.7.65. Transient Responses Mach 5 Altitude 30K $\phi_c \pm 90^\circ$.

SECRET



Figure 3.7.66. Transient Responses Mach 5 Altitude 60 K $\phi_c \pm 90^\circ$.

SECRET

3.7.61

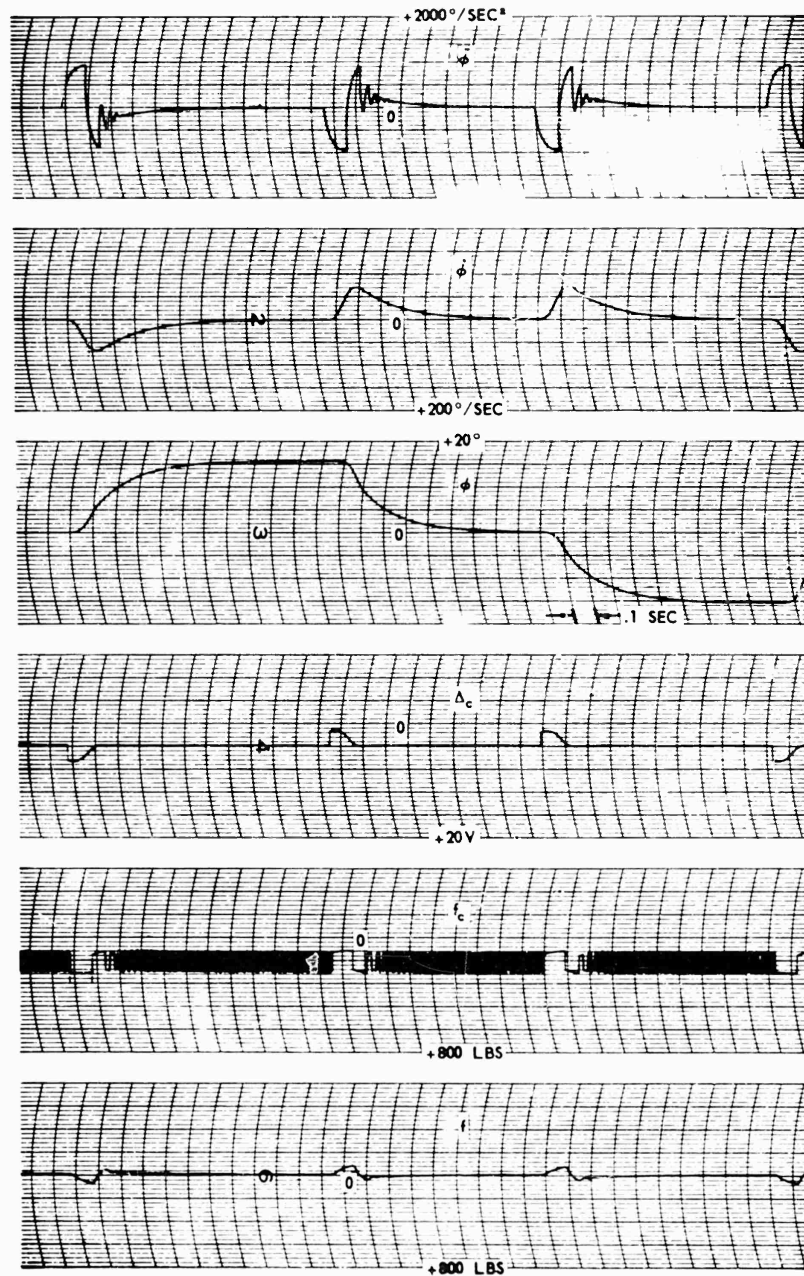


Figure 3.7.67. Transient Responses Mach 5 Altitude 60K $\phi_c \pm 15^{\circ}$.

SECRET

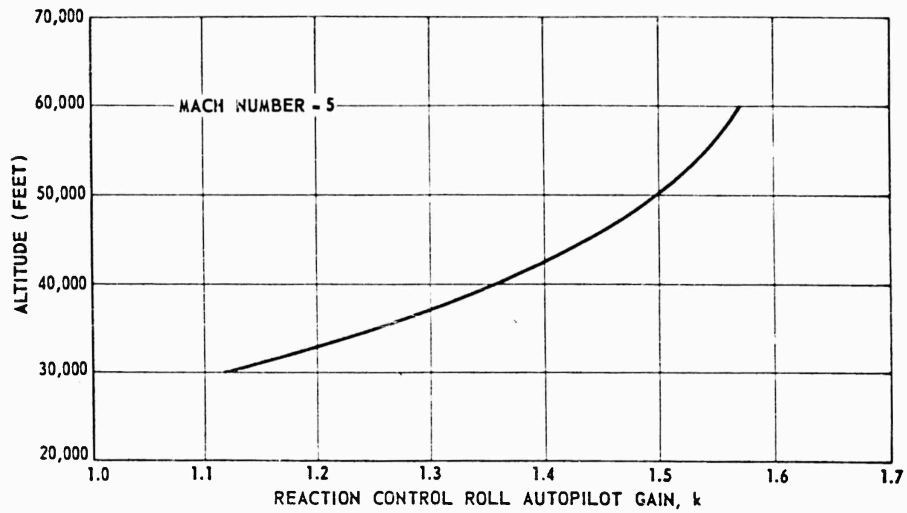


Figure 3.7.68. Reaction Control Autopilot Gain Variation.

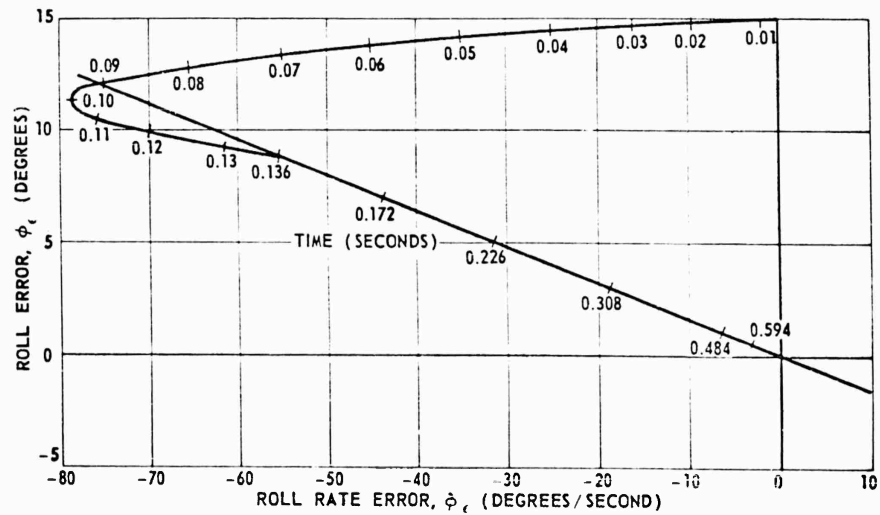


Figure 3.7.69. Phase Plane Plot of a 15 Degree Step Input.

Open loop transfer function

$$G(s) = \frac{K(1+s)}{s(1+\tau s)(s+f)(1+\gamma s)} = \frac{11.24(1+.16s)}{s(1+.02s)(s+1.14)(1+.0033s)}$$

SECRET

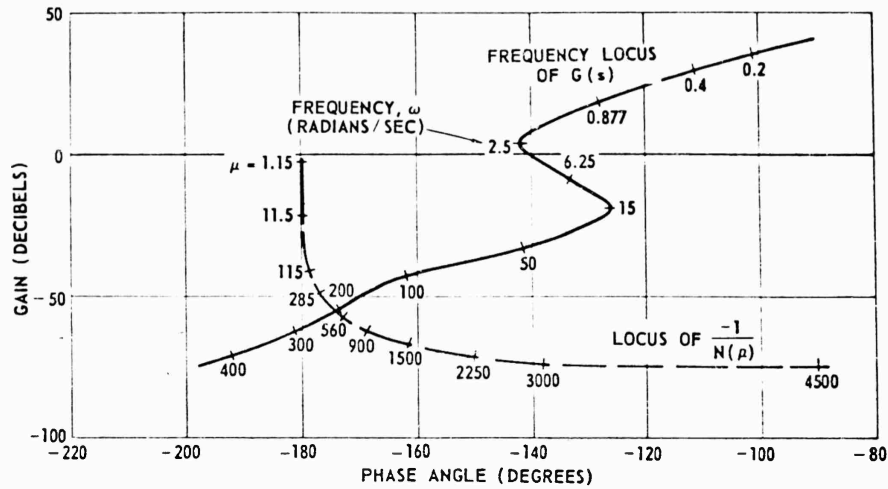


Figure 3.7.70. Stability Analysis of Roll System Utilizing the Describing Function.

Describing function of the signum computer with hysteresis

$$N(\alpha) = \frac{4\alpha}{\pi} \left[-\sin^{-1} \left(\alpha \frac{h}{f_c} \right) \right]$$

Condition for oscillations

$$G(s) N(\alpha) = -1$$

where hysteresis = 0.03 LB
 maximum force $f_c = 100$ LB

$$\alpha = \frac{f_c}{a}$$

	<u>Measured Results</u>	<u>Theoretical Results</u>
peak input amplitude of 4 CPS sine wave to the bistable element	a 0.25 LB	.224 LB
frequency	ω 251 RAD/SEC	210 RAD/SEC

The measured values compared well with the theoretical results. Only one flight condition (Mach = 5, h = 60K) was checked for limit cycle, however, it is reasonable to assume the other cases would yield similar results. It is not too

SECRET

important to know the exact frequency of oscillation because the valve and thrust responses were only approximated. If the low frequency mode is undesirable then a shift in frequency can be obtained by inserting a high frequency signal or possibly noise into the bistable element (Reference 3.7.18 and 3.7.19).

Summary of Roll Autopilot Investigation. At this time, very little work has been done in the way of analyzing imperfections of the servo, such as dead time, hysteresis, and higher order lags. The transient responses have been purposely designed on the overdamped side, thus allowing for the imperfections which often degrade the response times of simplified systems. In a future study, these various higher order effects should be analyzed in more detail with respect to stability and transient response. This study might include investigation of an adaptive system which would be insensitive to environmental conditions. Reaction jet control plays a favorable role in the design by minimizing the loop gain changes as a function of flight conditions.

Response times using non-linear control of the reaction jets have been shown to be at least as rapid, if not more rapid, than the linear aerodynamic control system for comparable force levels. Stability will depend on further investigation relative to reaction jets, such as the thrust build-up times and valve imperfections. Possible vibration oscillation modes and coupling conditions should also be considered in future studies. In conclusion, non-linear controls, as employed by reaction jets, are not only feasible but practical and economical as a means of obtaining roll control for PYE WACKET.

YAW CONTROL. There are two types of yaw control required by PYE WACKET. First, during boost or launch phase, it may be necessary to use the thrust of the main rocket engine in order to direct the missile toward the target. This is the so-called omnilaunch maneuver. In this case, the missile is either directed prior to launch or else launched in the forward direction and yawed in the air. Either scheme demands a space reference in yaw to maintain proper orientation of the missile centerline. The required control forces will be provided at least in part by swivelling the main rocket engine nozzle. Secondly, during the guidance or mid-course, and terminal phase of flight, the guidance system will provide signals to the roll and pitch autopilots in order to maneuver the missile toward its target. This will be a combined maneuver so as to maintain the target in a plane which lies along the missile centerline and normal to the missile planform. In the yaw plane, the function of the autopilot will be to maintain alignment between the missile centerline and the velocity vector. An autopilot is necessary because of misalignment resulting from the following:

1. Aerodynamic coupling from pitch and roll maneuvers. It has been shown in paragraph 3.7.1 that, with reaction controls, coupling will be significantly less than with aerodynamic controls.

SECRET

3.7.65

SECRET

2. Initial misalignment at the end of boost phase.
3. Disturbances such as wind gusts and instrument drift.

Coordinates and Transfer Functions. The coordinate system of the yaw plane is shown in Figure 3.7.71. The side-slip angle is measured positive as a counterclockwise rotation of the missile centerline from the velocity vector, as shown. Aerodynamic yaw moment is defined as positive if it causes positive sideslip angle acceleration. Figure 3.7.71 shows the reaction rocket motor orientation to produce yaw control moments and forces. Reaction motor thrust is defined as positive if it yields positive $\ddot{\beta}$. Therefore, since the observer is looking at the rear of the missile in the view shown, a positive yaw thrust would correspond to the left motor active and the right motor idle. The amount of thrust, f , available for yaw control is given by

$$f = \frac{2f_{max}}{2} \sin \theta \quad (3.7.16)$$

where f_{max} is the maximum available thrust from each rocket motor and θ is the angle from each nozzle centerline to the vertical.

In the development of the yaw equations of motion, the assumption was made that the yaw aerodynamic and control forces are unimportant, that is, missile motion parallel to itself, in yaw, is small. This results in the single moment equation:

$$\ddot{\beta} = c\beta + \frac{180}{\pi} \frac{fk}{I_y} \quad (3.7.17)$$

where

$$c = \frac{180}{\pi} \frac{1481 \lambda S d M^2 C_{n\beta}}{I_y}, 1/sec^2$$

- f = applied control thrust to produce yaw, in pounds
- k = yaw moment arm from rocket motors to CG, FT
- I_y = yaw moment of inertia, slug-FT²
- $C_{n\beta}$ = yaw moment derivative, per degree
- λ = static pressure ratio, pressure at altitude/pressure at S. L.
- S = reference area, 19.634 feet²
- M = Mach number
- d = reference diameter, 5 feet

The yaw thrust component, f , used for yaw control was taken as 40 pounds for the low level and 200 pounds for the high level capacity corresponding to a normal thrust vector per jet of 100 and 500 pounds. Recent reaction motor developments have revealed that these levels can be made close to two times larger. The 40- and 200-pound levels were based on a cant angle, θ , of 11.5

SECRET

SECRET

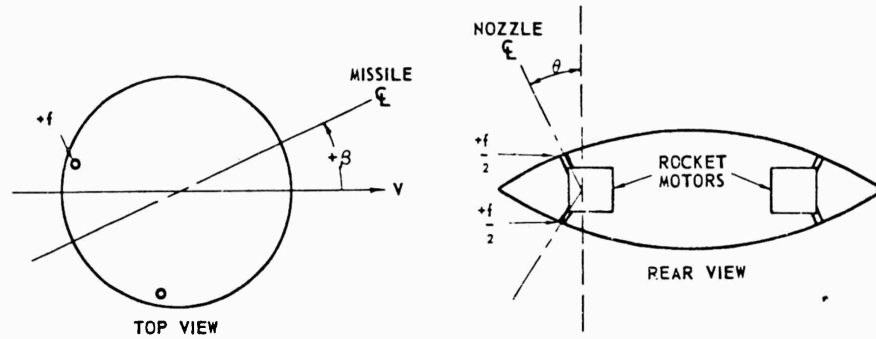


Figure 3.7.71. Yaw Reaction Control System Geometry and Force Sign Convention.

degrees in Equation 3.7.16. This angle should now be taken as 20 degrees, as described in paragraph 3.7.2. The results of these yaw control studies may be regarded as conservative. An increased thrust capability will decrease both response times and steady-state error and increase the maximum attainable yaw angle, β . This will result in an overall performance improvement. The simplified transfer function of the yaw airframe follows directly from Equation 3.7.17. It is

$$\frac{\beta}{f} = -\frac{180}{\pi} \frac{k}{Cl_y} \frac{1}{-\frac{s}{c} + 1} \quad (3.7.18)$$

The significant features of this transfer function are:

1. The steady-state gain is a function of flight condition.
2. The yaw moment coefficient, C ; is always negative, corresponding to a restoring torque. The airframe is then a second order system with zero damping. In actuality, the neglected force equation provides some amount of damping. Without control, the response to a step input of force, f , will be a bounded oscillation of β with a DC magnitude equal to $\frac{180 kf}{\pi Cl_y}$

Control System. The control equation used is:

$$\Delta_c = \beta_c - \beta - K_1 \dot{\beta} \quad (3.7.19)$$

where Δ_c = the control function

β_c = the called-for yaw angle

K_1 = the rate feedback gain

The called-for thrust, f_c , is given by:

$$f_c = |f_c| \text{Signum } \Delta_c \quad (3.7.20)$$

SECRET

where

Signum $\Delta_c =$ "sign of" Δ_c , which can be ± 1

The value of f_c is made to depend upon the magnitude of the control function Δ_c . When Δ_c exceeds a value corresponding to an error in β of approximately 2° , the thrust called for switches from the low level (40 pounds) to the high level (200 pounds).

The first order lag which approximates valve response and thrust build-up is represented by:

$$\frac{f}{f_c} = \frac{1}{0.02 S + 1} \quad (3.7.21)$$

The yaw autopilot block diagram is shown in Figure 3.7.72. The system was simulated on an analog computer in order to observe the response times as a function of K_1 . The significant factors are:

1. The control function Δ_c contains the following terms:
 - a. $\beta_c - \beta$ to provide measure of sideslip error. The sideslip angle, β , can be measured in flight using pressure probes mounted in the front of the missile on either side of center. A pressure differential will occur when there is misalignment between the velocity vector and missile centerline.
 - b. $K_1 \dot{\beta}$ to provide a measure of the rate of change of β . This gives the system damping. The signal, $\dot{\beta}$, is obtained from a rate gyro.
2. The system was tested at fixed flight conditions with two types of inputs:
 - a. Step commands in β_c . In actual flight, β_c is always zero. However, it is useful to examine these types of inputs for observation of response times, steady-state error, and thrust capability.
 - b. Initial conditions on β and $\dot{\beta}$ with β_c equal to zero. Such conditions are likely to be encountered at the end of launch phase.
3. The instruments which sense β and $\dot{\beta}$ are assumed perfect. In actuality the rate gyro dynamics exhibit second order roll-off and the pressure probe device will undoubtedly have a non-linear output for large β 's.
4. The control function, Δ_c , drives the bistable element to any of its four states, depending upon sign and magnitude. When Δ_c is greater than the value, c , (corresponding to 2 volts in the simulation), thrust called-for switches from low level to high level.

Transient Responses. Samples of yaw autopilot responses obtained from the analog simulation are presented in Figures 3.7.73, 3.7.74, 3.7.75, and 3.7.76 for the flight conditions shown. The variables plotted are listed below for convenience:

- Channel 1 - sideslip angle β in degrees.
- Channel 2 - sideslip rate $\dot{\beta}$ in degrees/second.

SECRET

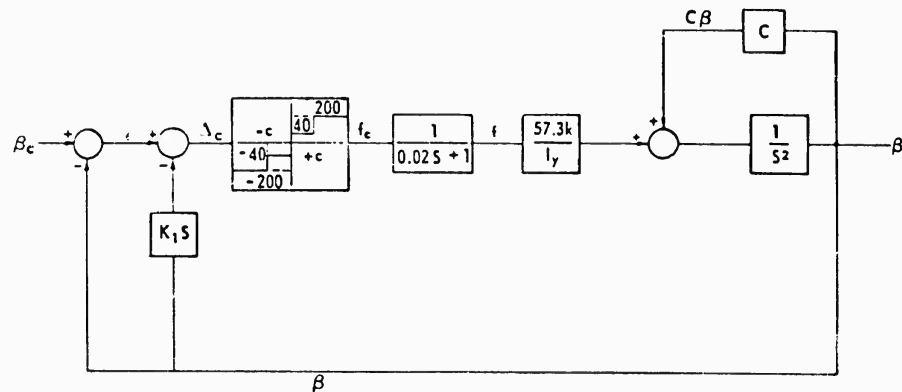


Figure 3.7.72. Yaw Autopilot Block Diagram.

Channel 3 - sideslip acceleration $\ddot{\beta}$ in degrees/second²

Channel 4 - control function Δ_c in volts.

Channel 5 - called-for thrust in pounds.

Channel 6 - actual thrust in pounds.

The significant features of the simulation study are:

1. The constants used were:
 - $W = 300 \text{ LB}$
 - $I_y = 22.6 \text{ slug-FT}^2$
 - $k = 1.675 \text{ FT}$
 - $C_{n\beta} = 0.000035 \text{ at Mach 5}$
2. The gain K_1 was chosen to give fast response to initial conditions on β and $\dot{\beta}$. It was necessary to vary this gain as a function of altitude, as shown in Figure 3.7.77.
3. In response to a step command, β_c (Figures 3.7.73 and 3.7.75) it is necessary to have a steady-state error in order to provide thrust to maintain $\dot{\beta}$ equal to zero. The magnitude of error varies as the yaw moment coefficient, C . The time constant (time to reach 63 percent of final value) decreases with increasing altitude as shown in Figure 3.7.78.
4. The responses to initial conditions, Figures 3.7.74 and 3.7.76, are shown for β_f and $\dot{\beta}_f$ both positive, which is considered the most severe case. No structural limits were assumed to exist on yaw rate or acceleration. The time constants for these cases do not exceed about 0.2 second, although there is some overshoot.
5. The system is limited in the number of degrees of β which can be maintained by the requirement that there be enough control thrust available to counteract the aerodynamic yaw moment. This value of β_{max} can be found from Equation 3.7.17 by setting $\dot{\beta}$ equal to zero. For example, at Mach 5 and 30,000 feet:

SECRET

$$|\beta_{MAX}| = \frac{180}{\pi} \frac{f_{MAX} \ell}{CI_y} = \frac{180}{\pi} \times \frac{200 \times 1.675}{22.6 \times 95.8} = 8.9^\circ$$

This limitation may not be severe since, as previously mentioned, the guidance phase yaw autopilot will function to maintain zero β in the presence of disturbances.

PITCH AUTOPILOT CONTROL SYSTEM. The function of the pitch autopilot is to translate command acceleration from the guidance computer to actual missile acceleration. Two types of systems were studied: linear aerodynamic control and reaction control. As with the roll system studies, an aerodynamic control system was used as a basis for comparison with the reaction system. Design considerations given to each of these systems will be discussed in the following paragraphs.

Linear Aerodynamic Controlled Autopilot. In the pitch plane, the motion of the missile in space consists of a rotation about the CG and a translation parallel to the missile centerline. For control it is necessary to produce counteracting forces and moments due to the unstable aerodynamics. For aerodynamic control, four pitchvators were proposed. They are located fore and aft, top and bottom. The capability of these surfaces to produce moments and forces was determined by wind tunnel tests.

1. Geometry and Transfer Functions. The reference system used to define the equations of motion is shown in Figure 3.7.79. Forces and moments are derived in coordinates fixed to the body and directed along, and normal to, the longitudinal axis of the missile. The equations of motion are:

$$n = A \alpha \quad \text{force equation} \quad (3.7.22)$$

$$\ddot{\psi} = B \alpha + E \delta \quad \text{moment equation} \quad (3.7.23)$$

$$\psi = \alpha + \delta \quad \text{geometry} \quad (3.7.24)$$

$$n = \frac{\pi V \delta^2}{180g} \quad \text{geometry} \quad (3.7.25)$$

In these equations:

$$A = \frac{1481 \lambda S M^2 C_{n\alpha}}{W} \text{ g's/degree}$$

$$B = \frac{180}{\pi} \frac{1481 \lambda S d M^2 C_{m\alpha}}{I_p} \text{ 1/sec}^2$$

$$E = \frac{180}{\pi} \frac{1481 \lambda S d M^2 C_{m\delta}}{I_p} \text{ 1/sec}^2$$

SECRET

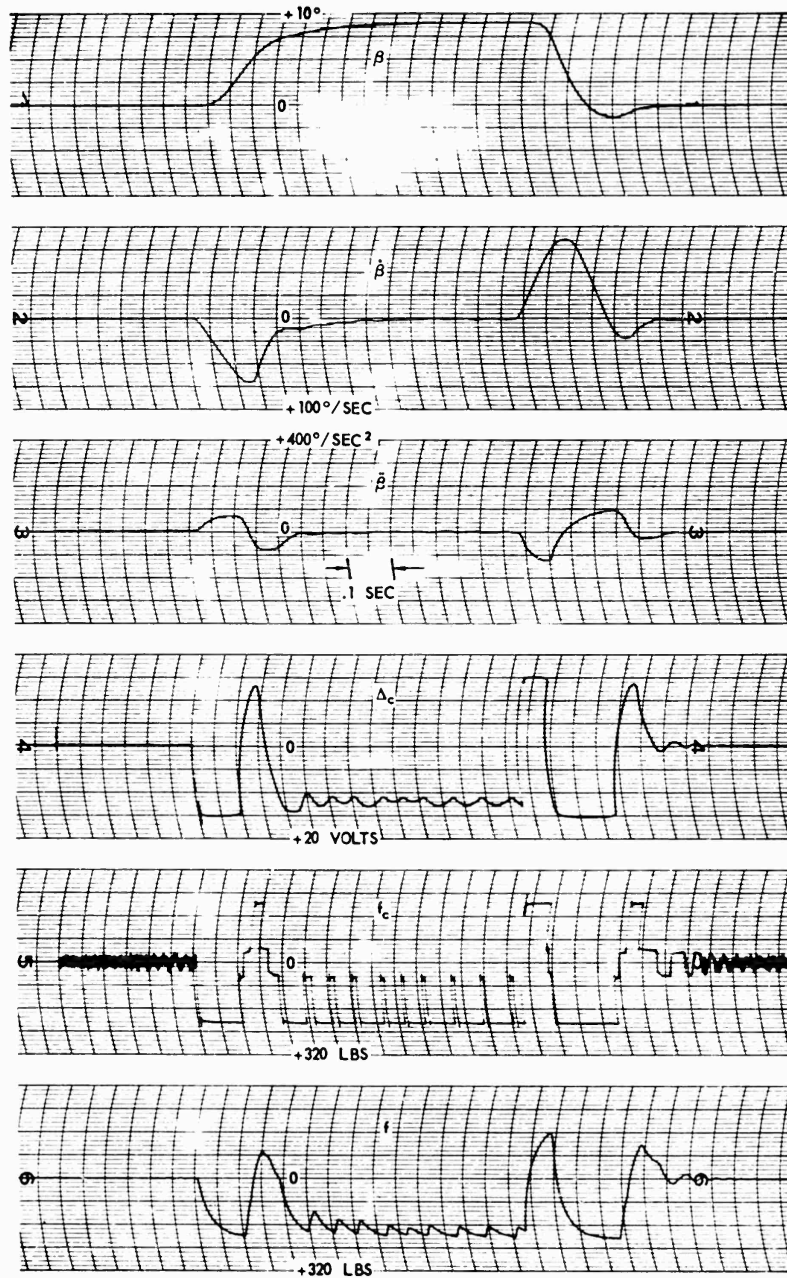


Figure 3.7.73. Transient Response Mach 5 Altitude 30 K $\beta_c + 10^\circ$.

SECRET

3.7.71

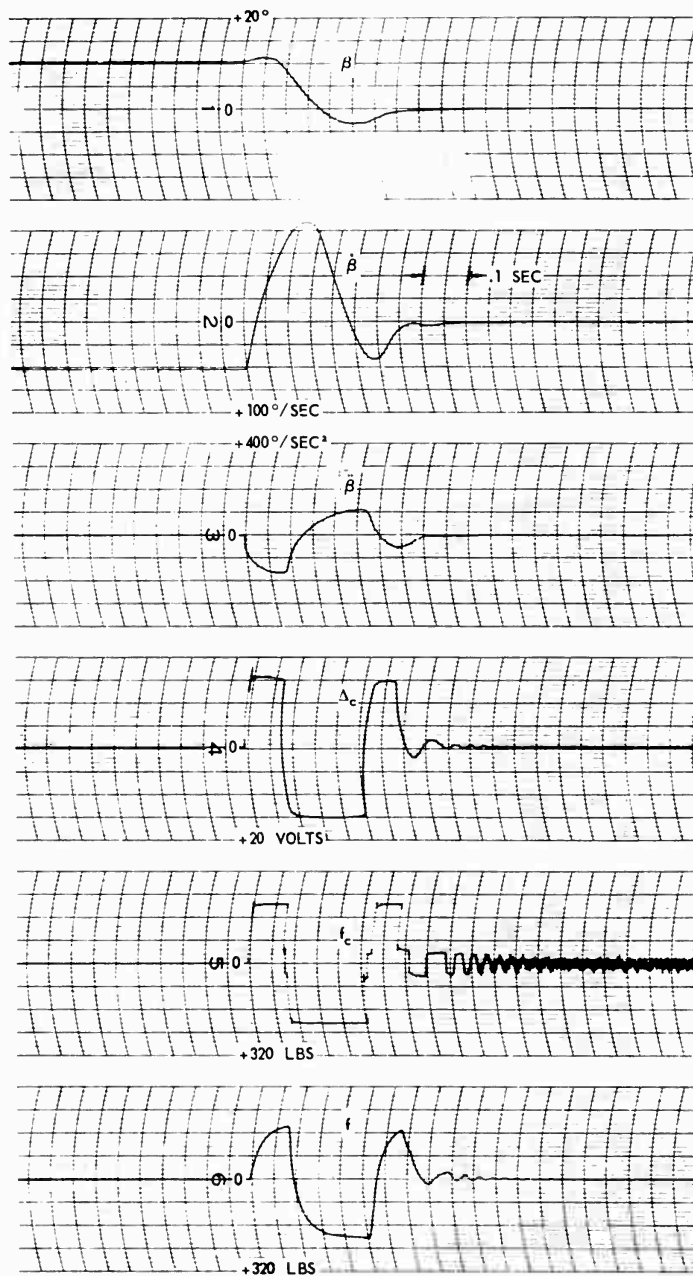


Figure 3.7.74. Transient Response Mach 5 Altitude
 $30 K \beta_1 + 10^\circ, \beta_1 + 100^\circ/\text{SEC}.$

SECRET

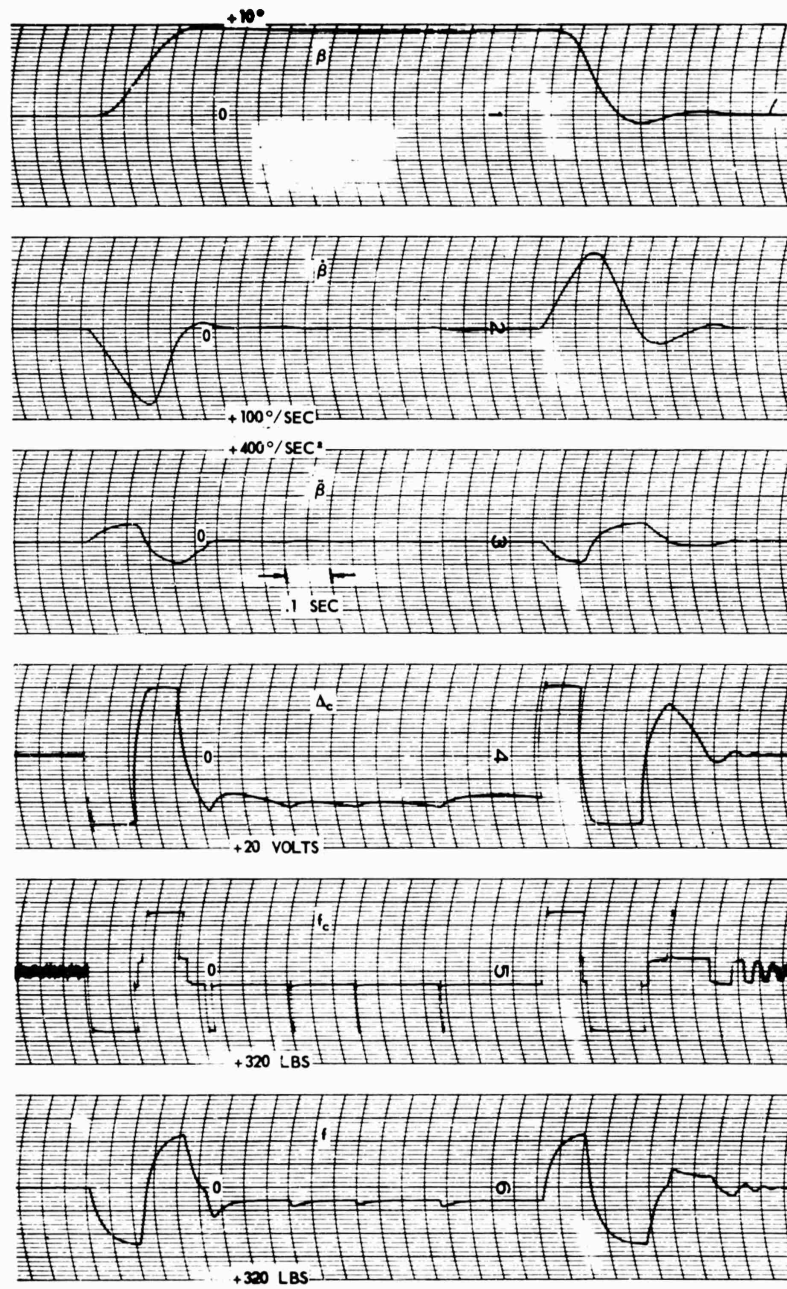


Figure 3.7.75. Transient Response Mach 5 Altitude 60K $\beta_c + 10^\circ$.

SECRET

3.7.73

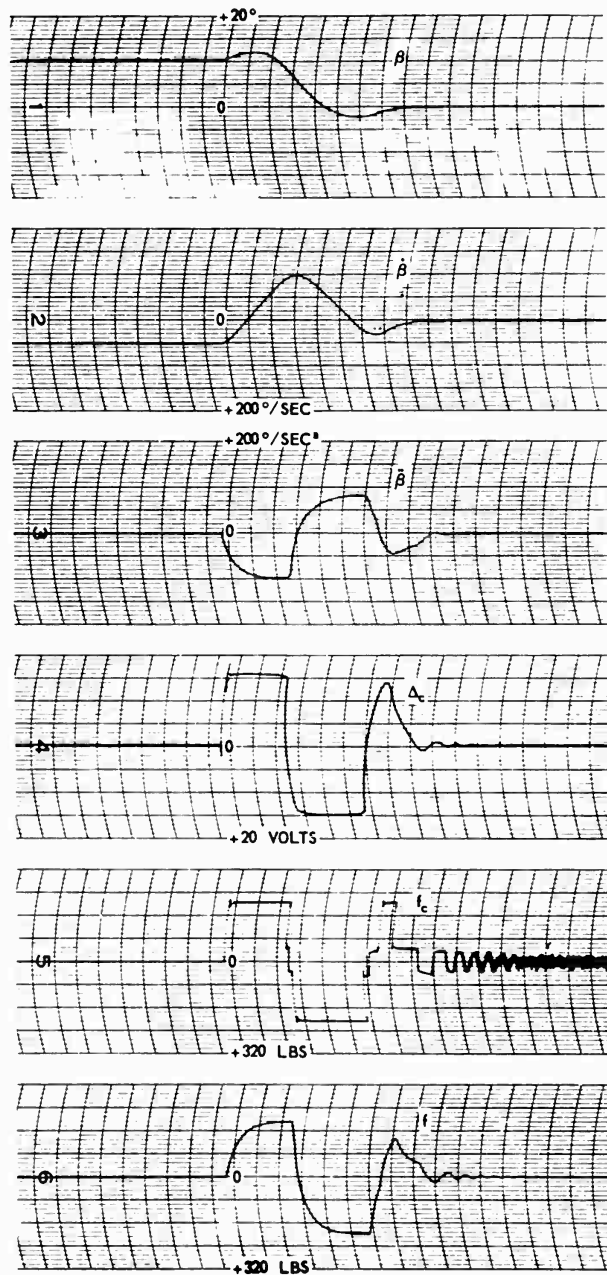


Figure 3.7.76. Transient Response Mach 5 Altitude
 $60K \beta_1 + 10^\circ, \beta_1 + 50^\circ/\text{SEC}.$

SECRET

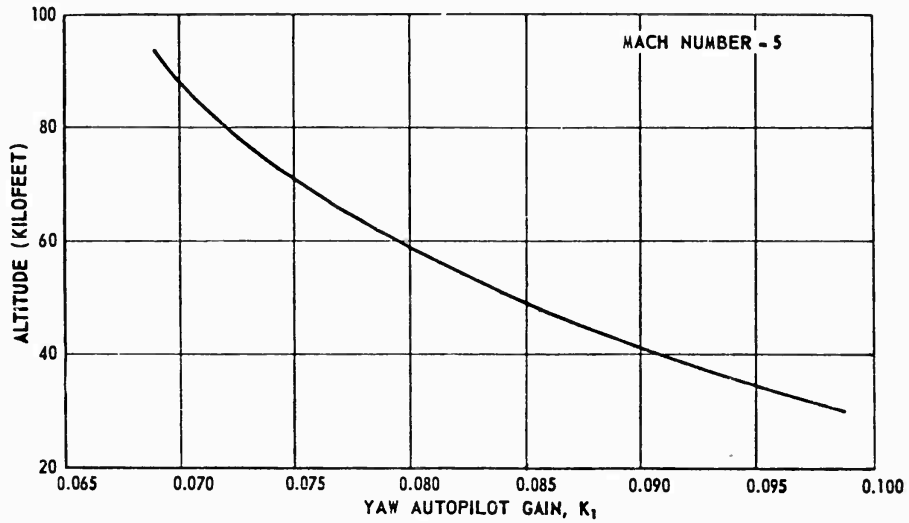


Figure 3.7.77. Yaw Autopilot Gain Variation.

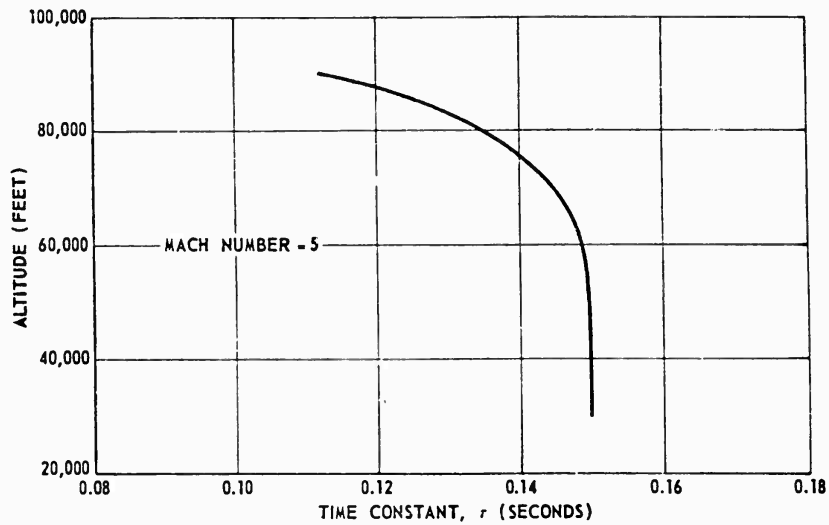


Figure 3.7.78. Yaw Autopilot Time Constant Variation.

- λ = static pressure ratio (pressure at altitude/pressure at S. L.)
- S = reference area, 19.634 FT²
- M = Mach number
- d = reference area, 5 FT²
- I_p = pitch moment of inertia, in slug-feet²
- W = missile weight, in pounds

SECRET

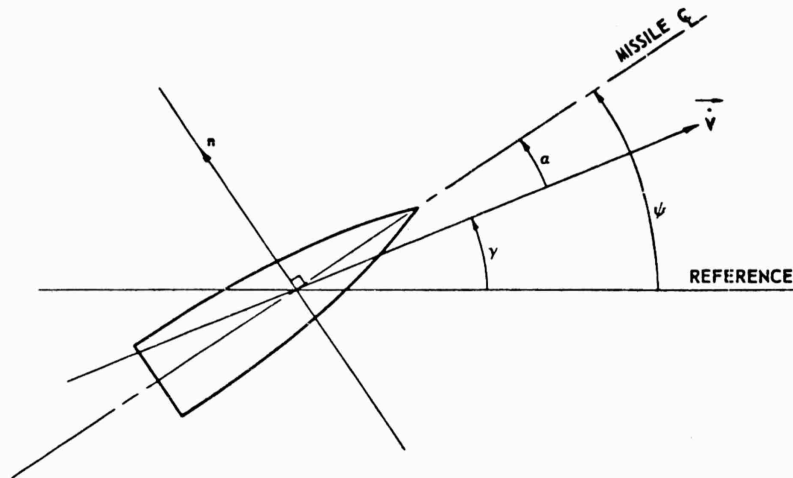


Figure 3.7.79. Pitch Geometry.

- $C_{m\alpha}, C_{m\delta}$ = pitch moment derivatives, per degree
- $C_{N\alpha}$ = pitch force derivative, per degree
- V = missile velocity, FT per SEC
- g = acceleration due to gravity, 32.2 FT per SEC²
- n = missile lateral acceleration, g's
- α = angle between velocity vector and missile centerline (angle of attack), in degrees
- γ = angle between reference and velocity vector, in degrees
- ψ = angle between reference and missile centerline (pitch angle), in degrees
- δ = pitch evator deflection angle, in degrees

The pitch evator deflection is defined as positive if it causes the missile to pitch upward. The airframe transfer functions which can be derived from the above equations are:

$$\frac{n}{\delta} = -\frac{AE}{B} \left[\frac{1}{-\frac{s^2}{B} - \frac{180g}{\pi V} \frac{A}{B} s + 1} \right] \quad (3.7.26)$$

$$\frac{\dot{\psi}}{n} = \frac{180}{\pi} \frac{g}{V} \left[\frac{\pi V}{180g} \frac{1}{A} s + 1 \right] \quad (3.7.27)$$

$$\frac{\dot{\psi}}{\delta} = -\frac{180}{\pi} \frac{g}{V} \frac{AE}{B} \left[\frac{\pi V}{180g} \frac{1}{A} s + 1 \right] \left[\frac{1}{-\frac{s^2}{B} - \frac{180}{\pi} \frac{A^2}{BV} s + 1} \right] \quad (3.7.28)$$

SECRET

The significant features of these equations are:

- Without any control, the airframe is a second order monotonically unstable system since B is always positive (CG aft of CP).
- The zero frequency gain is a function of flight condition.
- The pitch rate, $\dot{\psi}$, is a measure of the rate of change of n and can, therefore, be used to provide damping for the system.

CONTROL SYSTEM. The control equation used for the linear autopilot is:

$$\dot{\delta}_c = K(n_c - n) - K_1 \dot{\psi} - K_2 \ddot{\psi} \quad (3.7.29)$$

where

$$\begin{aligned} \dot{\delta}_c &= \text{called-for pitchvator deflection rate} \\ n_c &= \text{called-for acceleration} \\ K, K_1, K_2 &= \text{pitch autopilot gains} \end{aligned}$$

This form of control equation is very similar to that used in present Convair-Pomona missiles. The integrating pitchvator servos are also assumed to have first order lags expressed by the transfer function:

$$\frac{\delta}{\dot{\delta}_c} = \frac{1}{s} \frac{1}{.005s+1} \quad (3.7.30)$$

A complete block diagram of the linear pitch autopilot is given in Figure 3.7.80. The system was simulated on an analog computer in this form. The essential features are:

- The control equation approximately provides integral plus proportional plus derivative compensation. The signals are sensed with an accelerometer and a rate gyro.
- The departure from ideal integration by the pitchvator servos is assumed to be given in Equation 3.7.30. A rate limit of 300 DEG/SEC, and a deflection limit of 30 degrees was also used. These servos are assumed to be of the same type as described in the roll control section.
- The system is tested with application of step commands, n_c , at fixed flight conditions of Mach number, altitude, weight and moment of inertia.
- The instruments used to sense acceleration and pitch rate are assumed to have unity gain with no phase shift for all frequencies.

Transient Responses. Samples of linear pitch autopilot responses are given in Figures 3.7.81 through 3.7.83 for the flight conditions shown. The variables plotted are:

SECRET

3.7.77

SECRET

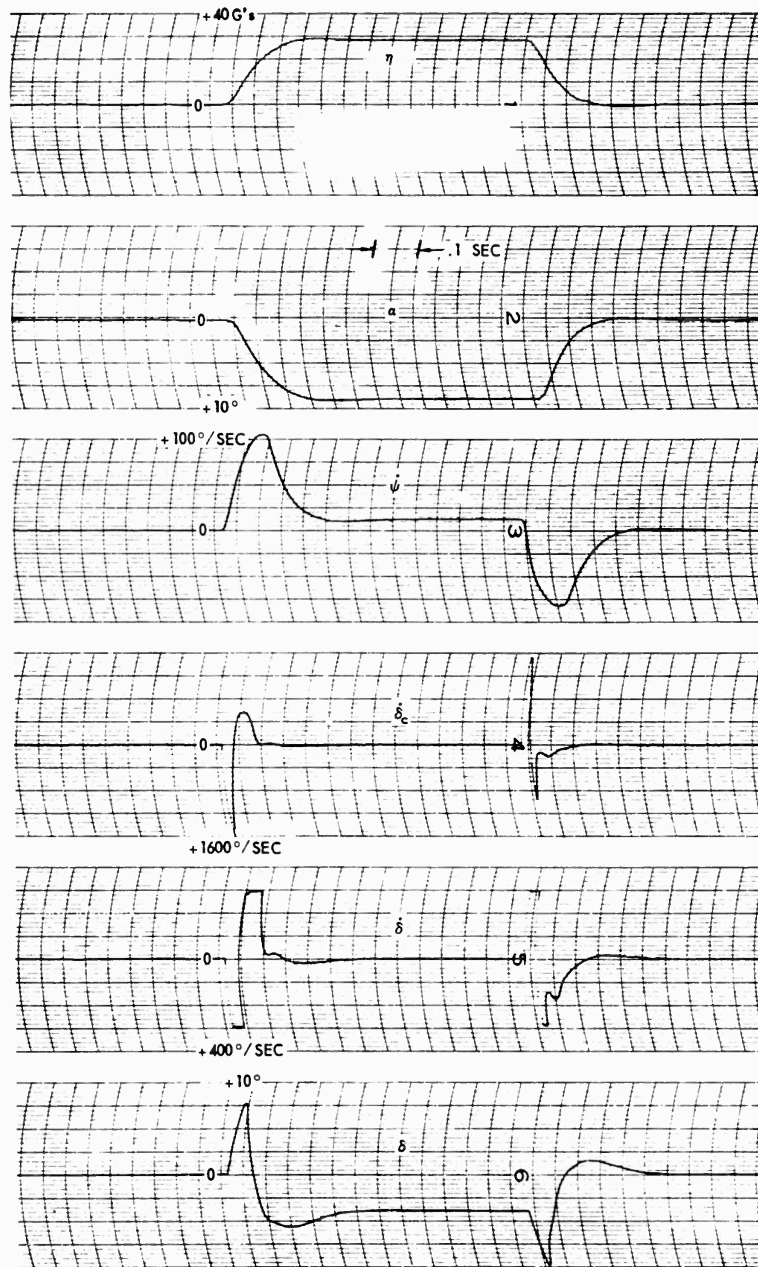


Figure 3.7.81. Transient Responses Mach 5 Altitude 60K $\eta_c + 30g's$.

SECRET

3.7.79

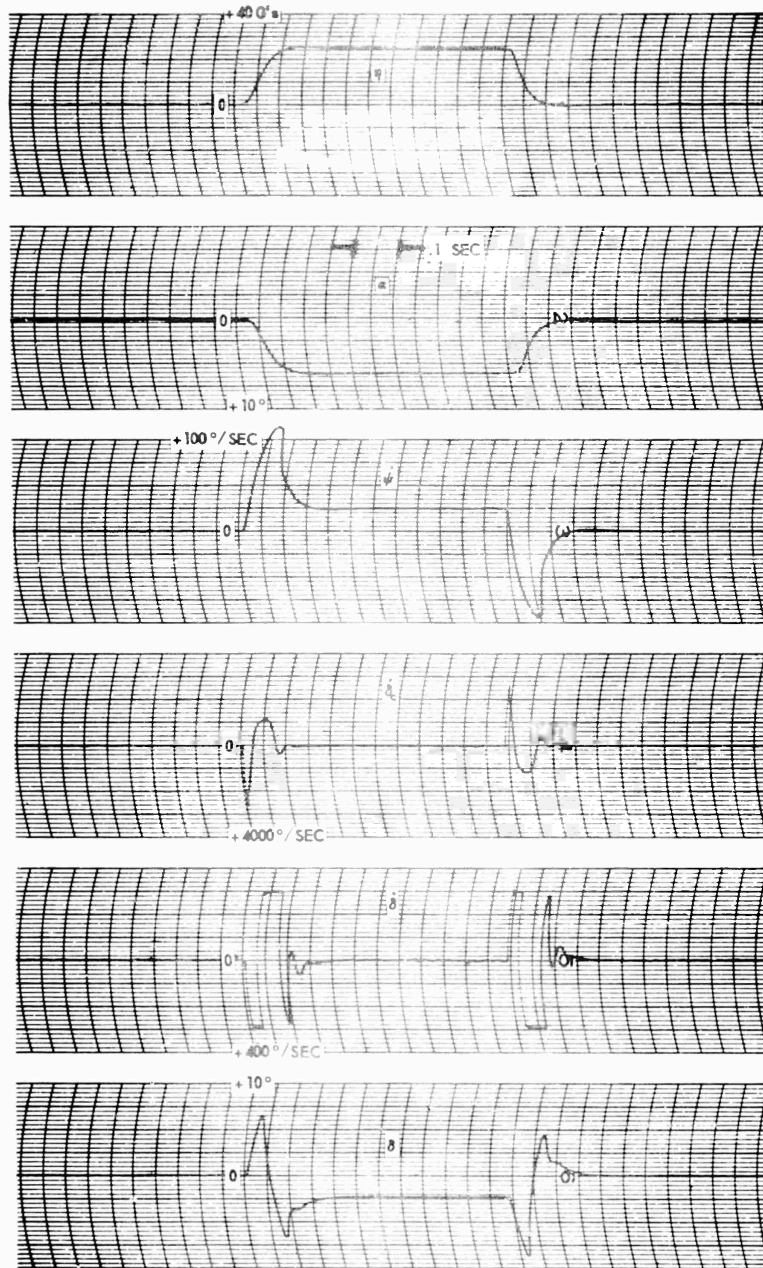


Figure 3.7.82. Transient Responses Mach 2 Altitude 30 K $\eta_c + 30g's$.

SECRET

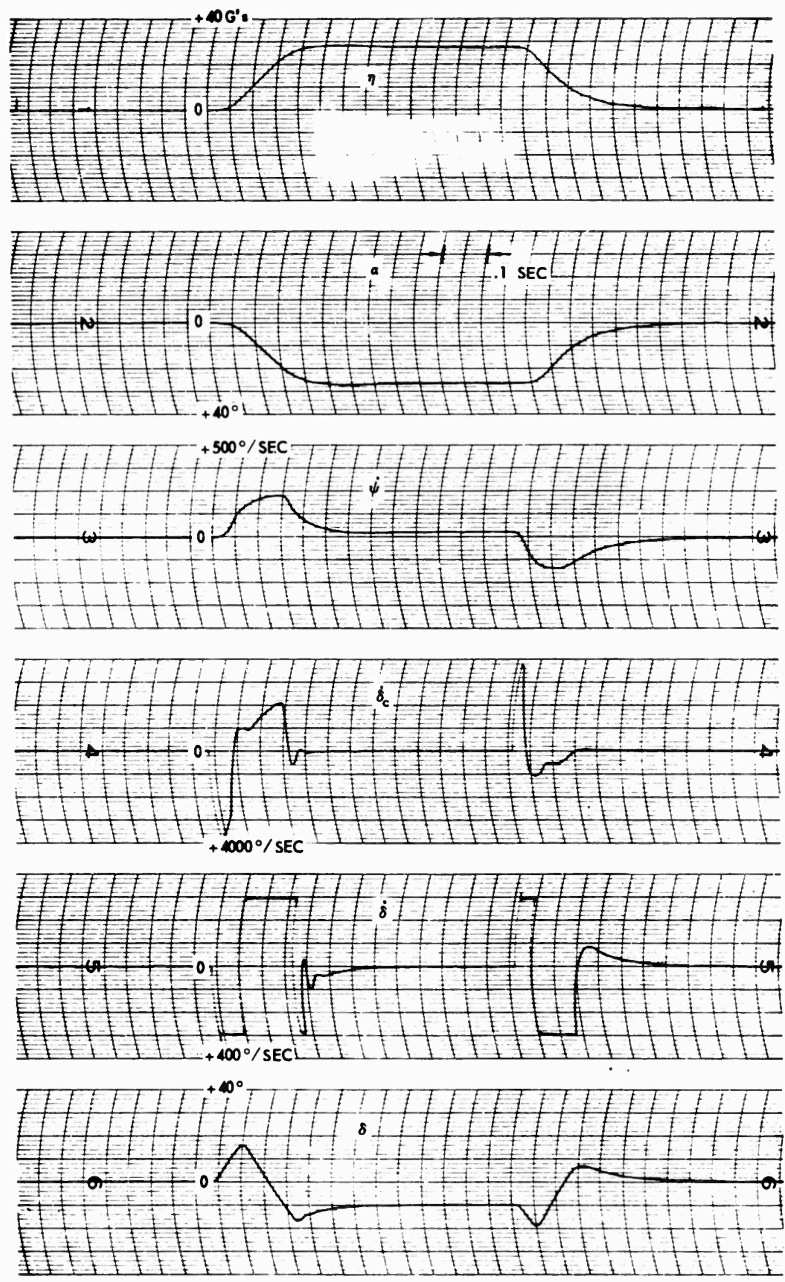


Figure 3.7.83. Transient Responses Mach 2 Altitude 60K $\eta_c + 30g^2s$.

SECRET

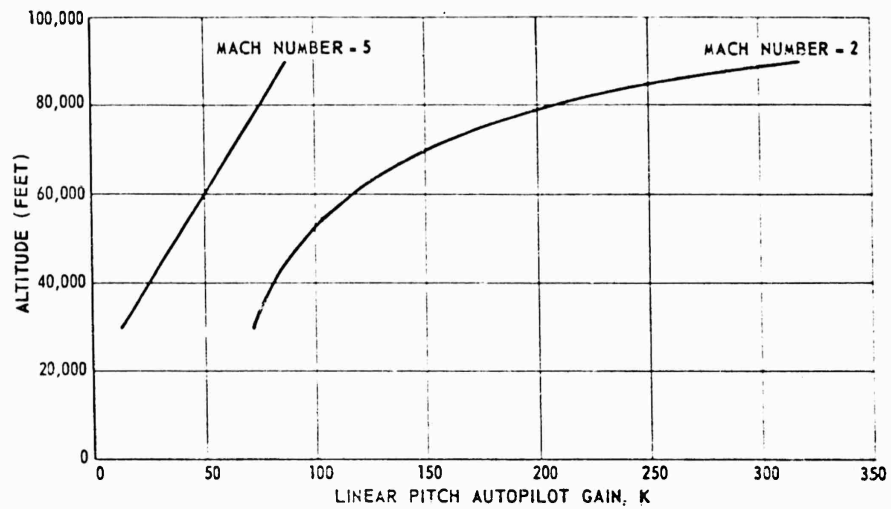


Figure 3.7.84. Linear Pitch Autopilot Gain Variation K.

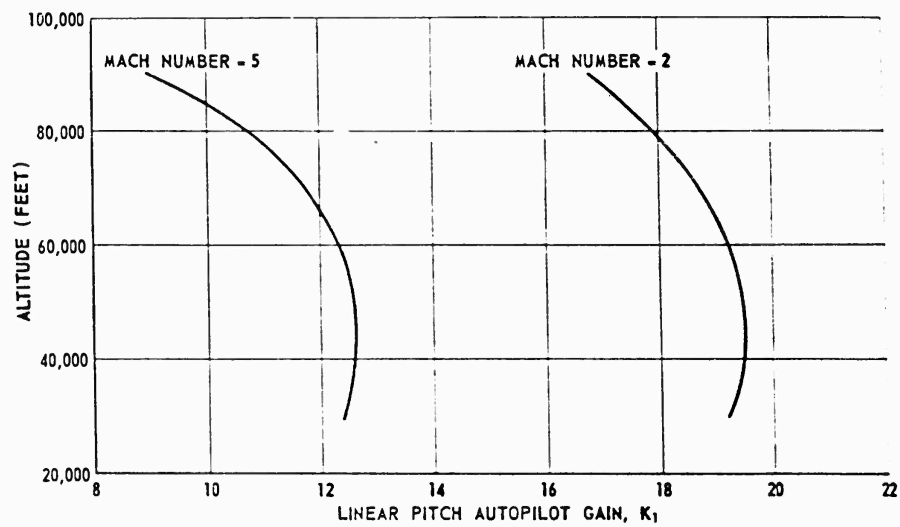


Figure 3.7.85. Linear Pitch Autopilot Gain Variation K₁.

Also in steady-state, the pitch error deflection rate must be zero. From Equations 3.7.29 and 3.7.31,

$$\dot{\delta}_c = 0 = K(n_c - n) - K_1 \dot{\psi}$$

or

$$\epsilon = \frac{n_c}{1 + \frac{K_1 V}{K_2} \frac{\pi}{180}}$$

SECRET

where ϵ is the steady-state error, $n_c - n$. Thus the steady-state error is a function of n_c and flight condition.

- c. The response time constants (time to reach 63 percent of final value) are shown in Figure 3.7.95. They increase with higher altitudes and lower Mach numbers. This is to be expected since the effectiveness of the pitch surfaces and the force coefficient, A , is reduced.
- d. A plot of the $C_m(\delta)$ used in this study is shown in Figure 3.7.86. The other aerodynamic coefficients used are presented in subsection 3.1.

Non-Linear Reaction Control Autopilot. With a reaction motor controlled autopilot, control forces and moments are provided by thrust from the two reaction rocket motors located in the aft section of the missile. Referring to Figure 3.7.71, when the rocket supplies thrust through the top set of nozzles, the missile will pitch upward. This is defined as negative thrust, f . When the bottom nozzles are operative, the missile will pitch downward. This is defined as positive thrust, f . As with the roll and yaw systems, there are two levels of thrust available. In the reaction autopilot these levels are taken as 200 and 1000 pounds for the combined forces (100 and 500 pounds per jet).

1. Aerodynamic Equations and Transfer Functions.

$$n = A\alpha + f/W \quad \text{force equation} \quad (3.7.32)$$

$$\ddot{\psi} = B\alpha - \frac{180}{\pi} \frac{fk}{I_p} \quad \text{moment equation} \quad (3.7.33)$$

$$\psi = \alpha + \delta \quad \text{geometry} \quad (3.7.34)$$

$$n = \frac{v \dot{\delta}}{\frac{180g}{\pi}} \quad \text{geometry} \quad (3.7.35)$$

where

- f = reaction control thrust, in pounds
 k = pitch moment arm from reaction motors to CG, in feet

SECRET

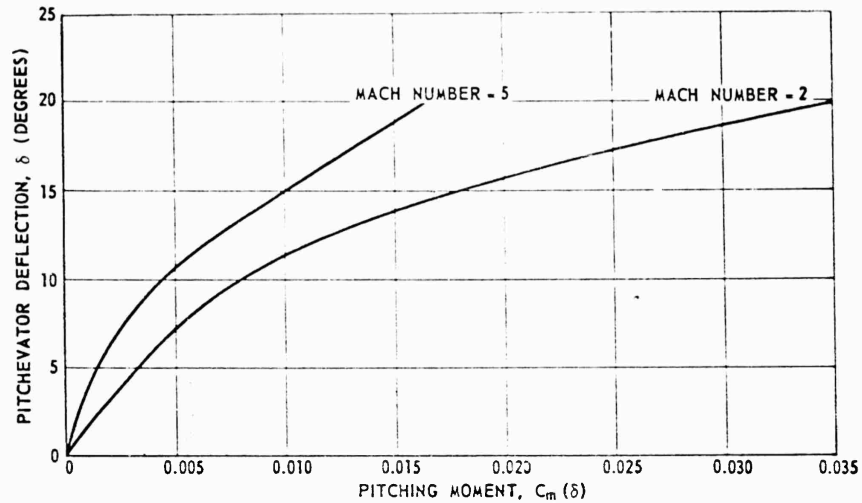


Figure 3.7.86. Linear Pitch Autopilot Pitchchevator Deflection Versus Pitching Moment.

The other symbols appearing have the same definitions as given under Equations 3.7.22 through 3.7.25. The airframe transfer functions which are derived from the above equation are:

$$\frac{\eta}{f} = \left[\frac{1}{W} + \frac{180}{\pi} \frac{k}{I_p} \frac{A}{B} \right] \left(\frac{1 + \frac{S^2}{B + \frac{180}{\pi} \frac{k}{I_p} AW}}{-\frac{S^2}{B} - \frac{180}{\pi} \frac{g}{V} \frac{A}{B} S + 1} \right) \quad (3.7.36)$$

$$\frac{\dot{\psi}}{f} = \frac{180}{\pi} \frac{g}{V} \left[\frac{1}{W} + \frac{180}{\pi} \frac{k}{I_p} \frac{A}{B} \right] \left(\frac{1 + \frac{\pi}{180} \frac{V}{g} \frac{S}{A + \frac{\pi}{180} \frac{I_p B}{k W}}}{-\frac{S^2}{B} - \frac{180}{\pi} \frac{g}{V} \frac{A}{B} S + 1} \right) \quad (3.7.37)$$

$$\frac{\dot{\psi}}{n} = \frac{180}{\pi} \frac{g}{V} \left(\frac{1 + \frac{\pi}{180} \frac{V}{g} \frac{S}{A + \frac{\pi}{180} \frac{I_p B}{k W}}}{1 - \frac{S^2}{B + \frac{180}{\pi} \frac{k}{I_p} AW}} \right) \quad (3.7.38)$$

The remarks pertinent to Equations 3.7.26, 3.7.27, and 3.7.28 apply here also.

SECRET

CONTROL SYSTEM. The control equation used is:

$$\begin{aligned} \Delta_c &= \Delta_c = n_c - n - K_1 \dot{\psi} - K_2 \ddot{\psi} & (3.7.39) \\ \Delta_c &= \text{control function, in volts} \\ n_c &= \text{called-for acceleration, in g's} \\ K_1, K_2 &= \text{autopilots gains} \end{aligned}$$

The called-for thrust level f_c is given by:

$$f_c = |f_c| \text{signum} \Delta_c \quad (3.7.40)$$

where

$$\text{signum } \Delta_c = \text{"sign of"} \Delta_c, \text{ which can be } \pm 1$$

The value of f_c is made a function of the magnitude of Δ_c . When $|\Delta_c|$ exceeds a value corresponding to an error in acceleration of about 2 g's, the thrust called for switches from the low level (200 LB) to the high level (1000 LB). The lag between called-for thrust, f_c , and actual thrust, f , is composed of value response lag and thrust build-up time. These lags are approximated by the transfer function:

$$\frac{f}{f_c} = \frac{1}{.025s + 1}$$

This approximation is compatible with existing estimates.

The complete reaction autopilot block diagram is presented in Figure 3.7.87, and represents the form in which the system was simulated on the analog computer. The essential features are:

- a. The control function, Δ_c , contains the following components:
 - (1) The term, $n_c - n$, which measures the error between desired and actual acceleration. The signal, n , is obtained from an accelerometer.
 - (2) The term, $K_1 \dot{\psi}$, which, by Equation 3.7.38, approximately measures the rate of n . This signal is obtained from a rate gyro.
 - (3) The term, $K_2 \ddot{\psi}$, this portion of the control equation provides lead around the lag network and speeds up the dither frequency. The signal, $\ddot{\psi}$, is obtained by electronic differentiation.

SECRET

3.7.85

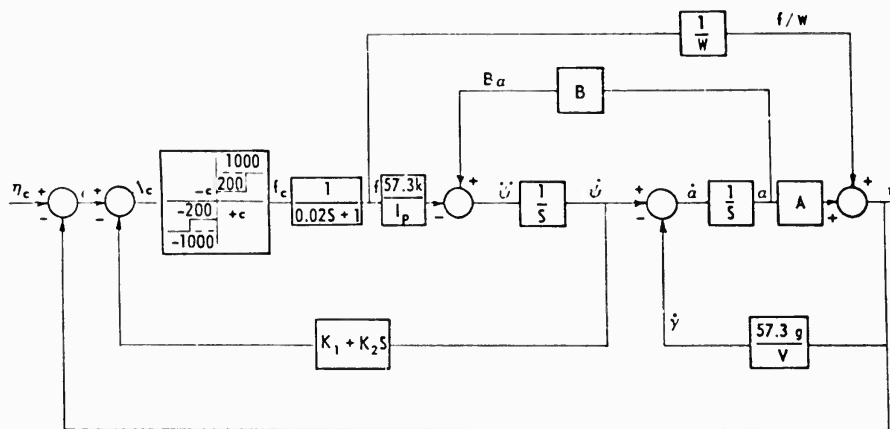


Figure 3.7.87. Nonlinear Reaction Control Pitch Autopilot Block Diagram.

- b. The system is tested with application of step commands, η_c , at fixed flight conditions.
- c. The instruments are assumed to have unity gain with no phase shift at all frequencies.
- d. Only the effects of differential application of thrust are considered. In actuality, four rocket motors deliver thrust and the applied thrust is taken as the sum of these. The rocket motors are assumed to have identical response times and outputs.
- e. The output of the bistable element assumes any one of the four values indicated in Figure 3.7.87 depending upon the sign of Δ_c . If $|\Delta_c|$ exceeds the value c , the called-for thrust switches from the low level to the high level. As previously noted, c is taken as 2 volts, corresponding to about a 2g error. The bistable element is an electronic circuit, and effects of hysteresis, non-symmetry, and time lag have been held at a minimum through judicious design. This circuit can be employed in the actual missile to serve the same purpose as it does in the simulation. The output voltage of the circuit can be used to drive the valve to the correct position for required thrust.

Transient Responses. Samples of autopilot responses obtained from the analog computer simulation are shown in Figures 3.7.88 through 3.7.92 for the flight conditions shown. The variables plotted are:

- Channel 1 - acceleration, n , in g's
- Channel 2 - angle of attack, α , in degrees
- Channel 3 - pitch rate, $\dot{\psi}$, in degrees/second
- Channel 4 - control function, Δ_c , in volts
- Channel 5 - called-for thrust, in pounds
- Channel 6 - actual thrust, in pounds

SECRET

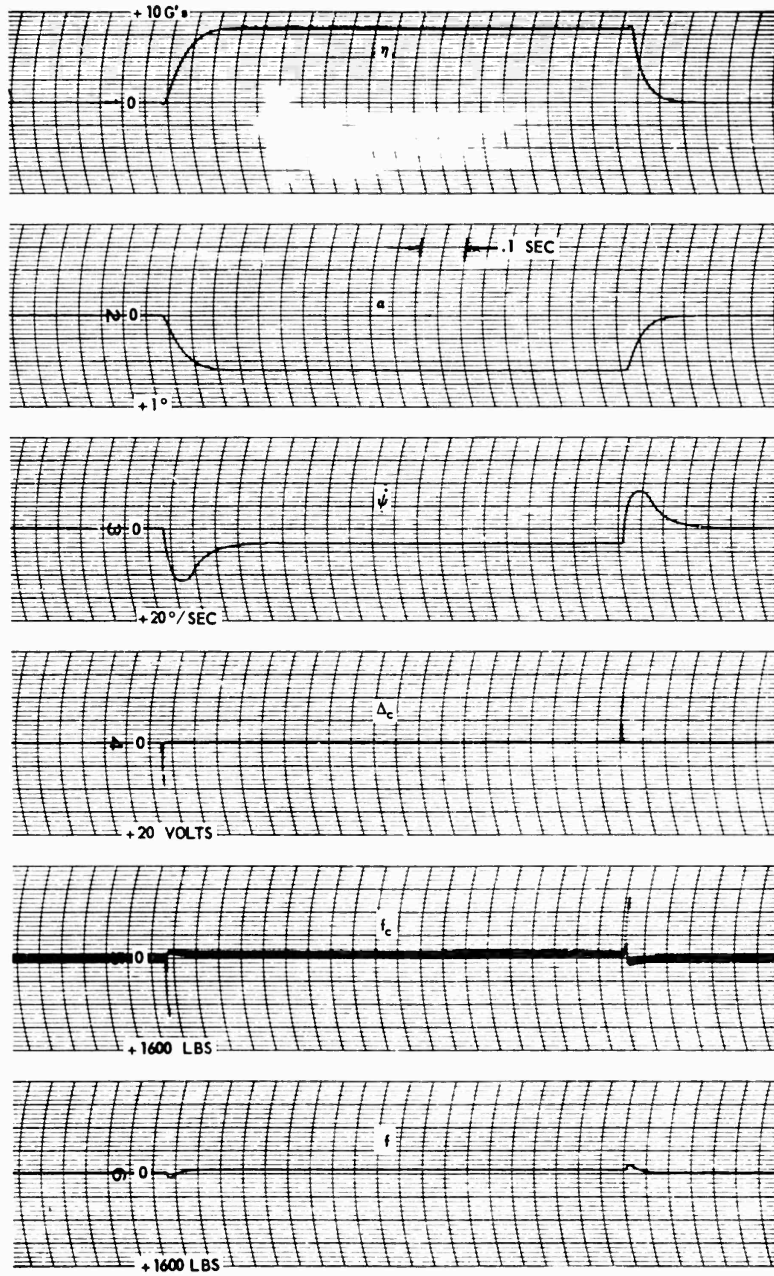


Figure 3.7.88. Transient Responses.

SECRET

3.7.87

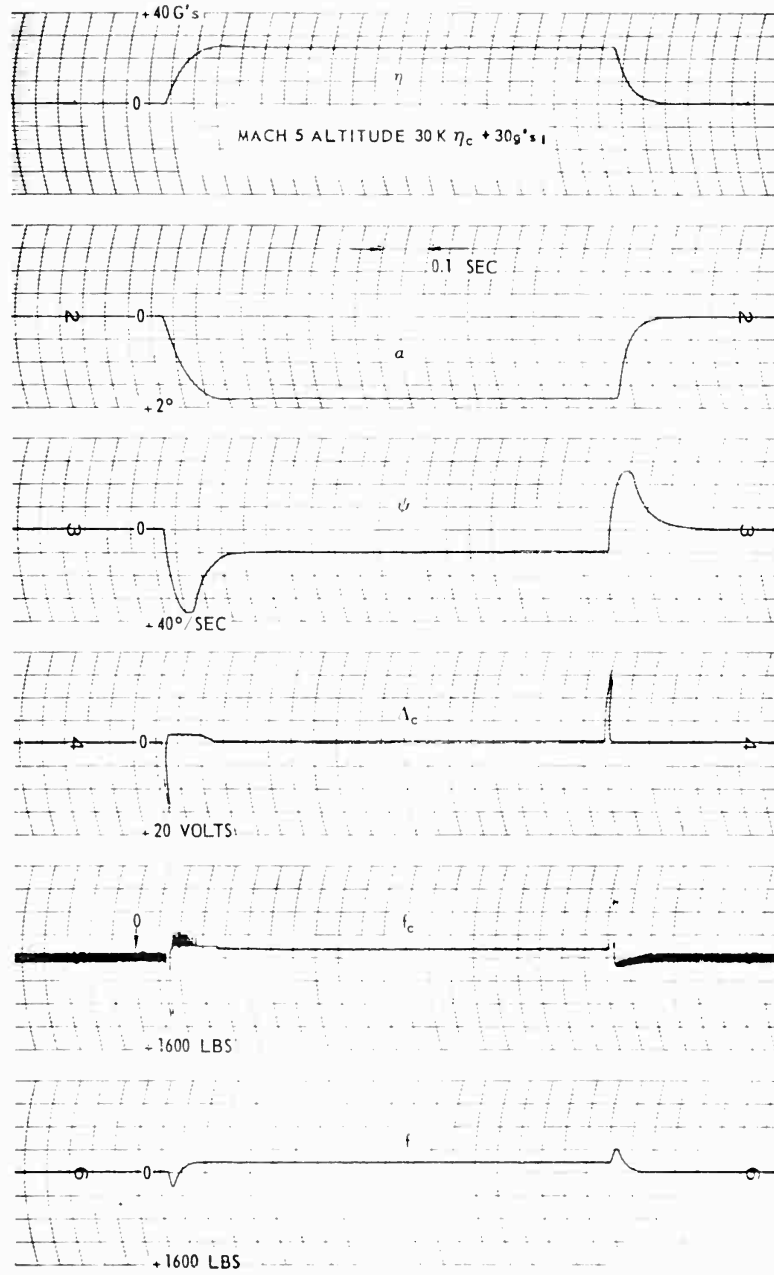


Figure 3.7.89. Transient Responses.

SECRET

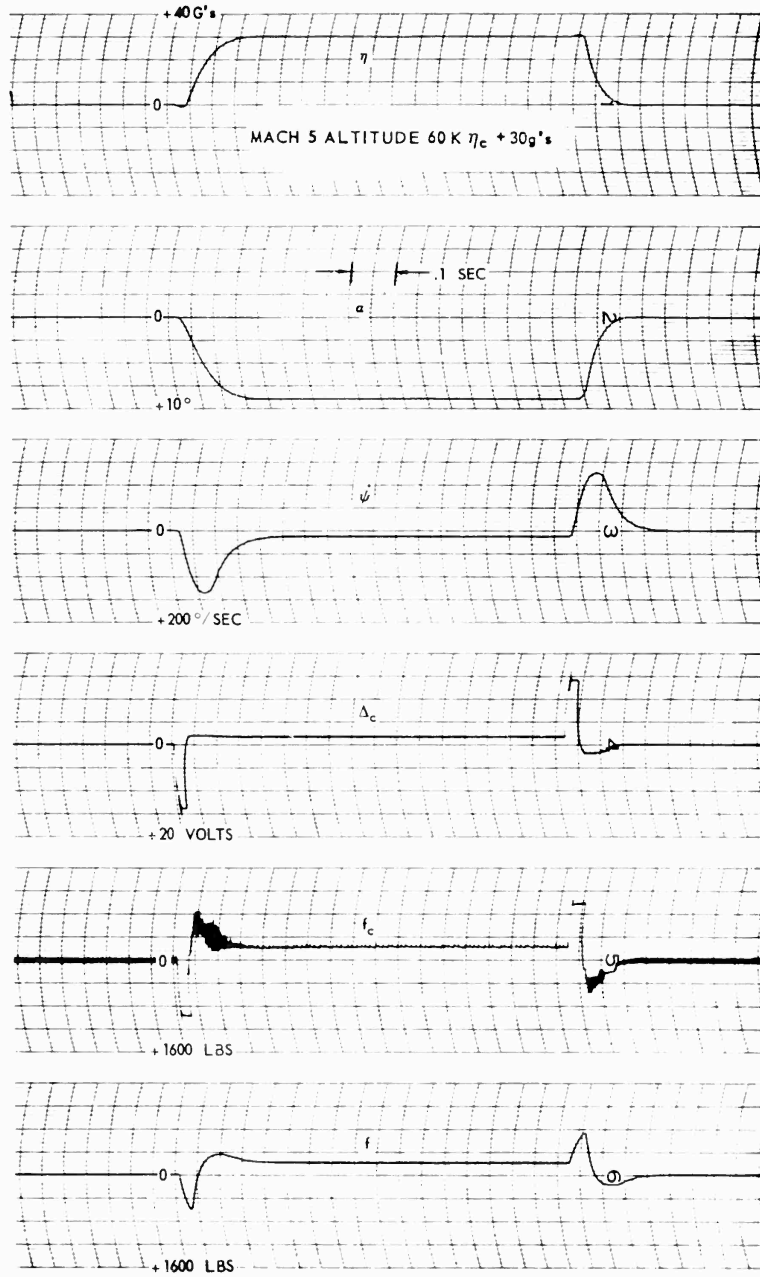


Figure 3.7.90. Transient Responses.

SECRET

3.7.89

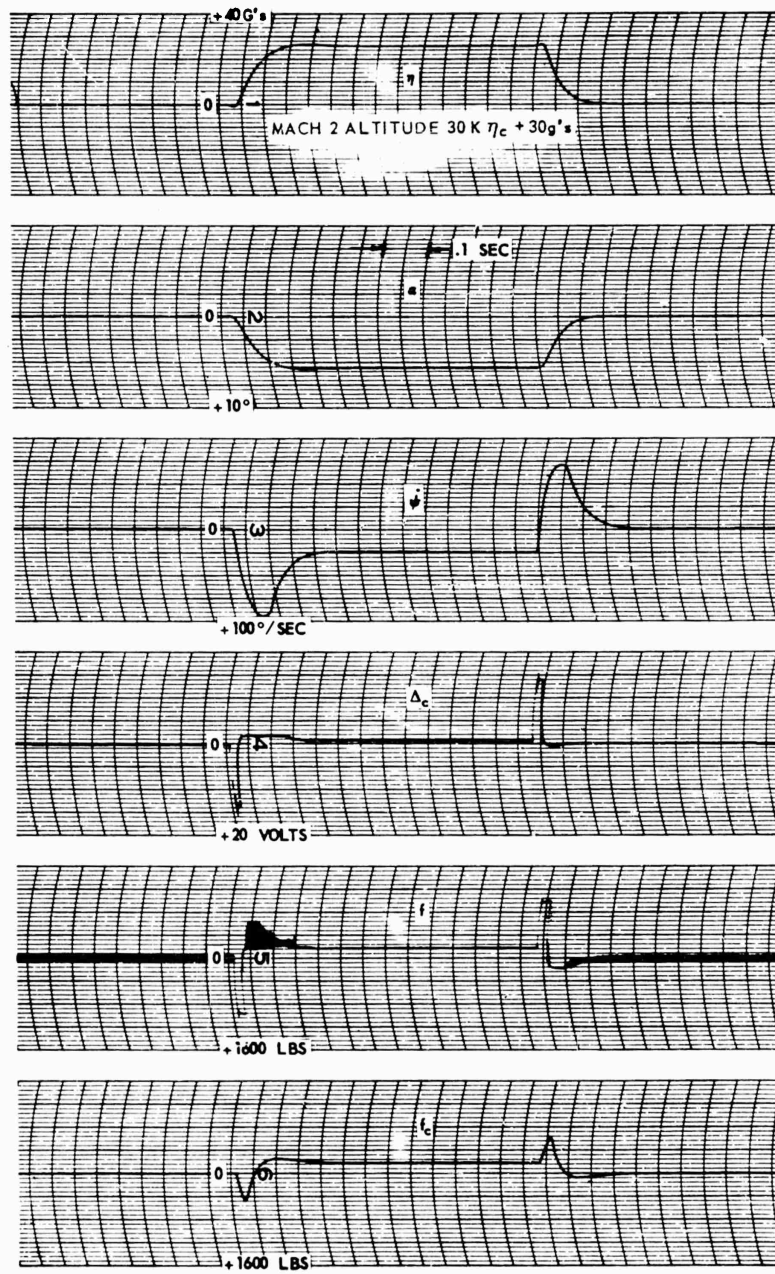


Figure 3.7.91. Transient Responses.

SECRET

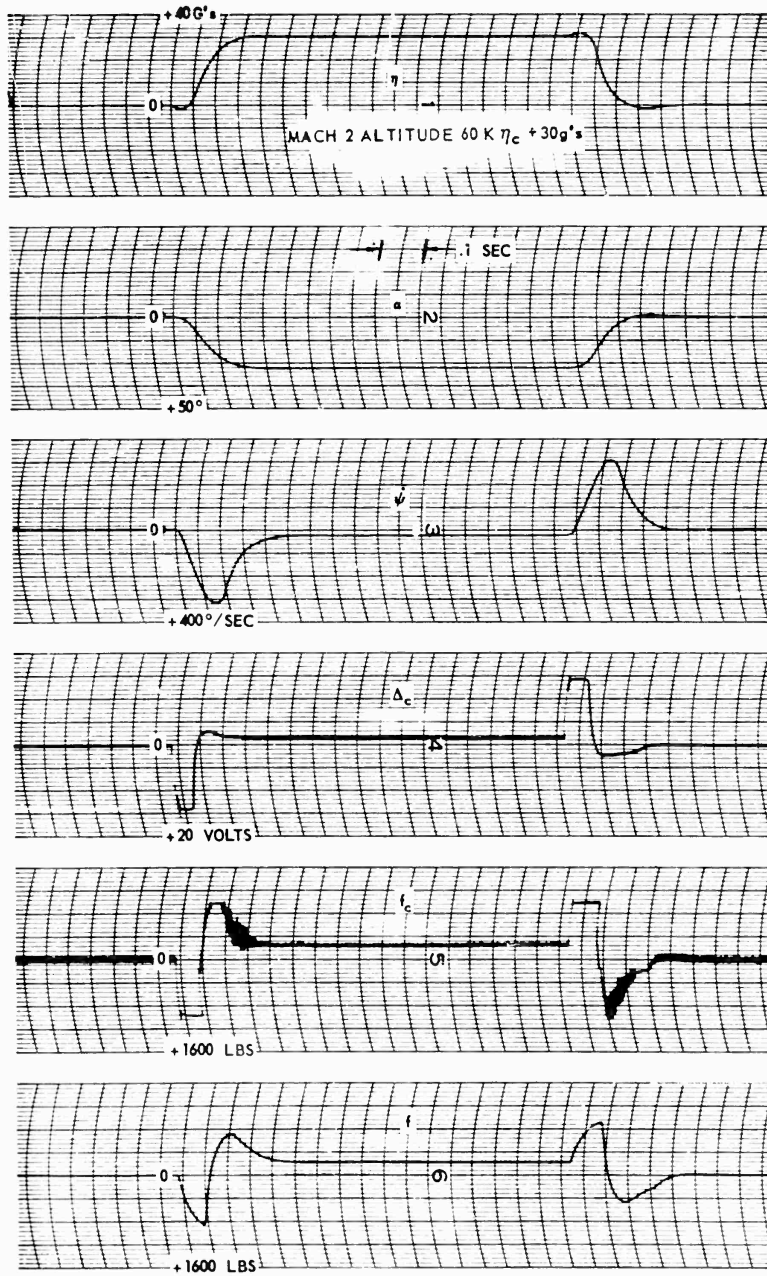


Figure 3.7.92. Transient Responses.

SECRET

The constants used for the transient responses were:

$W = 300$ pounds
 $I_p = 11.3$ slug-feet²
Stability margin $\bar{\tau}/d = 0.01$
 $k = 1.675$ feet

- a. The time constants of the system were obtained and are plotted in Figure 3.7.95. There is an increase in τ , with increasing altitude and decreasing Mach number, but, for the range considered, the time constants were no greater than 0.11 second.
- b. There is always a steady-state error between n_c and n , due to the steady-state $\dot{\psi}$ and the fact that it is necessary to have a non-zero value of the control function, Δ_c , in order to maintain $\ddot{\psi}$ at zero. The values of the error is a function of the flight condition. The amount of error which can be permitted is dependent upon a statement of the quality of autopilot demanded by the guidance system.
- c. In order to maintain a uniform response over the range of Mach numbers and altitudes considered, it was necessary to vary the gains K_1 and K_2 . Plots of these variations are shown in Figures 3.7.93 and 3.7.94. In actual implementation of these gain changes, a function is needed which varies in the same manner as the aerodynamic coefficients. Total pressure is such a quantity.
- d. A comparison between channels 5 and 6 on all responses shows that in steady state, the called-for thrust, f_c , dithers between levels allowed by Δ_c , whereas the actual thrust obtained remains at the average value required to maintain $\ddot{\psi}$ at zero. This is due to the filtering action provided by the lag simulation and means physically that in steady state the valve delivers an average flow of fuel to the reaction motors for combustion through the proper nozzles.
- e. The maximum number of steady-state g's that can be held is a function of the maximum thrust capability and the difference between the CP and CG. From the transient response point of view, there is a negligible change in response time as this distance decreases from 3.3 to zero inches; corresponding to stability margins of 0.055 and 0, respectively.

SUMMARY OF PITCH AUTOPILOT INVESTIGATION. Evaluation of the two types of control systems considered in this study reveal that, for the pitch system, the reaction control type has certain advantages in single plane performance. For the roll system, the two types were about equivalent from the performance standpoint.

SECRET

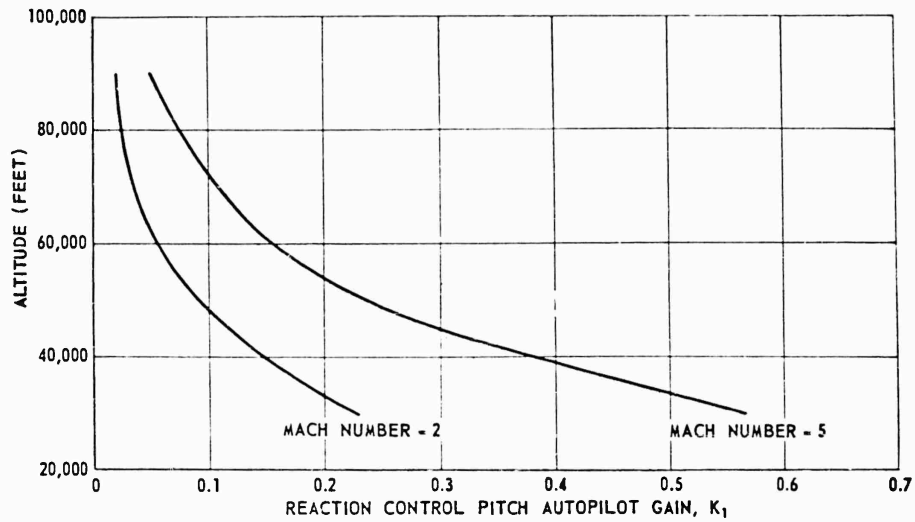


Figure 3.7.93. Reaction Control Pitch Autopilot Gain Variation K_1 .

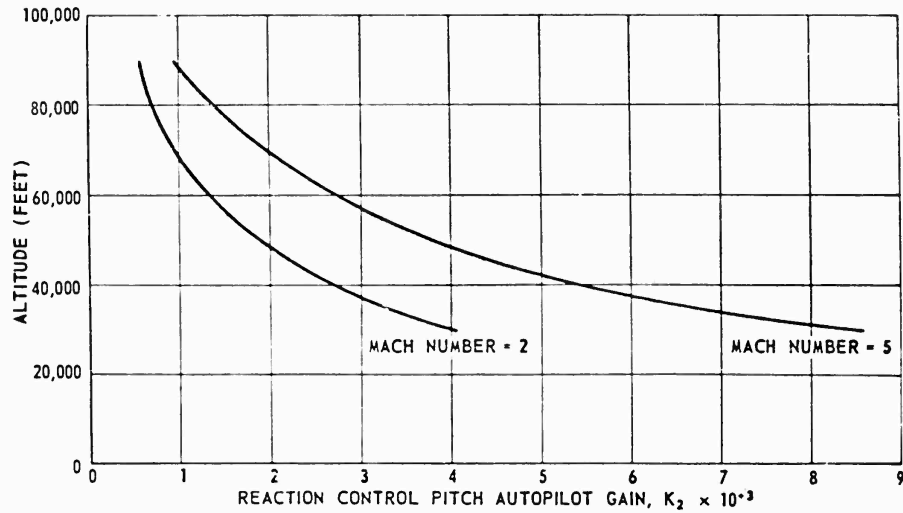


Figure 3.7.94. Reaction Control Pitch Autopilot Gain Variation K_2 .

Performance. The reaction controlled pitch system has the following advantages:

1. Response Times. Shown in Figure 3.7.95 are the variation of time constants with altitude for both the linear aerodynamic and reaction control systems. It is clear that the reaction control system responds faster to the types of inputs considered. At still higher altitudes, the aerodynamic control would be far less efficient.

SECRET

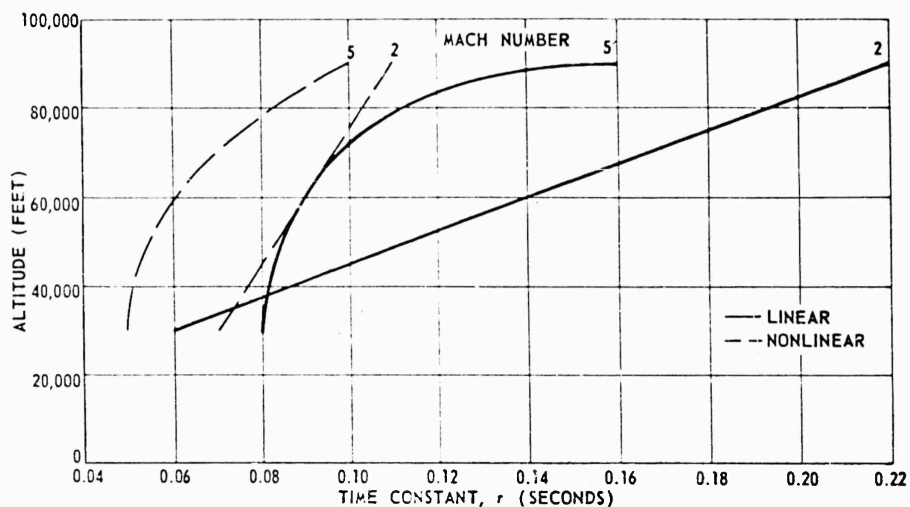


Figure 3.7.95. Pitch Autopilot Response Times.

2. Variation of Gains. The reaction control autopilot requires the variation of gains, K_1 and K_2 , as shown in Figures 3.7.93 and 3.7.94. Two statements regarding these variations are in order. First, although they were necessary for the reaction control system as simulated, there remains the possibility that, with further refinement of the control equation, gain variations can be considerably reduced, if not altogether eliminated. The simplifications in autopilot implementation gained thereby are substantial. For this study, only a relative comparison between the two systems was attempted. Secondly, if variations are necessary, Figures 3.7.93 and 3.7.94 show that the trend of variation with Mach number and altitude is the same and there is a possibility that a relationship between them can be established. With the linear system, where gain variations are absolutely necessary (Figures 3.7.84 and 3.7.85), there appears to exist little or no correlation as flight conditions change.
3. Steady-State G's Available. Reaction control moments and forces are essentially constant for all flight conditions up to the angle of attack where the aerodynamic normal force becomes extremely non-linear. A discussion of maneuver capabilities is presented in subsection 3.7.4 and therefore will not be treated here.

There are other advantages of reaction control related to the combined pitch, roll, and yaw systems. These are:

- a. Effects of aerodynamic coupling between pitch, roll, and yaw are appreciably decreased by eliminating control surfaces.

SECRET

- b. With four reaction nozzles, control is achieved in three dimensions by combination of actuating signals from each autopilot. With aerodynamic control, it is necessary to have four deflecting surfaces for pitch control alone, and two more for combined roll and yaw control, the result being an increase in hardware and complexity.

Recommendations. For the above reasons, it is presently recommended that a reaction motor control system be given the most consideration for use in PYE WACKET. Further investigations need to be made in the following areas:

1. Further study of the control equation is needed to determine the possibility of greatly reducing or eliminating autopilot gain variations.
2. Reaction control operation for combined maneuvers in pitch, roll, and yaw with activating signals applied through the same rocket motors must be considered.
3. As indicated previously, the output thrust, f , to maintain any steady-state condition is an average of the called-for thrust, f_c . The implication is that it is not necessary to provide two levels of control thrust from the standpoint of reaction propellant conservation because the average amount of fuel consumed is the same regardless of whether there are two magnitudes of control thrust available - in addition to the idling level - or just one. Consequently, in order to evaluate the possibility of eliminating the low level control capability, a complete statement must be made of reaction thrust system dynamics, with the input taken as the called-for control thrust and the output taken as the thrust exerted at the rocket motor nozzle.
4. An evaluation of the effects of aerodynamic coupling is required. As mentioned at the outset, the control system designs are valid for motion only in the plane being directly controlled. Interaction between planes of motion must be considered and a study of these effects calls for further wind tunnel testing and a three-dimensional analog computer simulation.
5. A detailed consideration of boost phase control problems is required, especially in the design of a boost phase yaw autopilot.
6. An evaluation of the effects of feedback loops created by aeroelastic body vibrations is needed.
7. Effects of instrument dynamics must be considered in autopilot responses.
8. Hardware requirements and feasibility must be determined.

3.7.4 MANEUVER CAPABILITIES

Prior to a discussion of maneuver capabilities, it is first necessary to review the findings of the control system investigations. These investigations consist of treatments of aerodynamic controls, reaction controls, and autopilot designs. Briefly, the pertinent findings of these investigations were:

SECRET

3.7.95

1. Aerodynamic controls are not feasible for control in the omnidirectional launch phase of flight. Moreover, it is felt that aerodynamic coupling problems are of such magnitude that control during the glide phase of flight, where proper wind vector orientation is assumed, is only a bare possibility. In particular, the yawing moments induced by roll control exceed the limited yaw control available. In addition, the relatively large pitchvator areas required for effective pitch control induces large drag, hence, range penalties.
2. Reaction controls using fixed auxiliary jets of variable thrust offer a mechanically feasible design of adequate duration. This control system can be supplemented by swivelling the main nozzle if additional control during the boost phase is required. Such a requirement may exist due to the extreme aft center of gravity location of the loaded (full) missile. As the propellant burns, the center of gravity moves forward and decreases the aerodynamic moments which the control system must overcome.
3. Autopilot studies indicate that the reaction controls respond faster than aerodynamic controls to commanded motions. This advantage increases as the flight altitude increases. Also, the autopilot design for the reaction system can be greatly simplified by the reduction of gain variations. Conversely, gain variations are absolutely necessary with aerodynamic controls.

As a result of the above findings, only the maneuver capabilities of the reaction controls are of importance. However, as a matter of interest and to provide some basis for comparison, the maneuver capabilities of a typical aerodynamic control system are also included.

The main concern of the following discussion is, therefore, the determination of the maximum maneuver capabilities of the reaction control system. For purposes of this determination, reaction jets of 500 pounds thrust were assumed, since, as shown in paragraph 3.7.2, this is a reasonable maximum thrust level for the flight times required. It should be noted that approximations of maximum maneuverability available from other levels of thrust can be obtained by ratioing the results presented in Figures 3.7.96 and 3.7.97. In other words, maximum maneuverability at thrust (T_1) is equal to the maximum maneuverability at thrust (500 pounds/jet) times the ratio of $T_1/500$. This approximation is very accurate at altitudes below 60,000 feet and within 10 percent at all altitudes.

Figures 3.7.96 and 3.7.97 present the maximum available normal acceleration as a function of altitude, with stability margin as a parameter. Stability margin is defined as the distance between the missile center of gravity and the aerodynamic center of pressure, divided by the missile diameter. Figure 3.7.96 concerns Mach 2 and Figure 3.7.97 concerns Mach 5. Both aerodynamic and reaction controls are considered. The weight of the PYE WACKET assumed for

SECRET

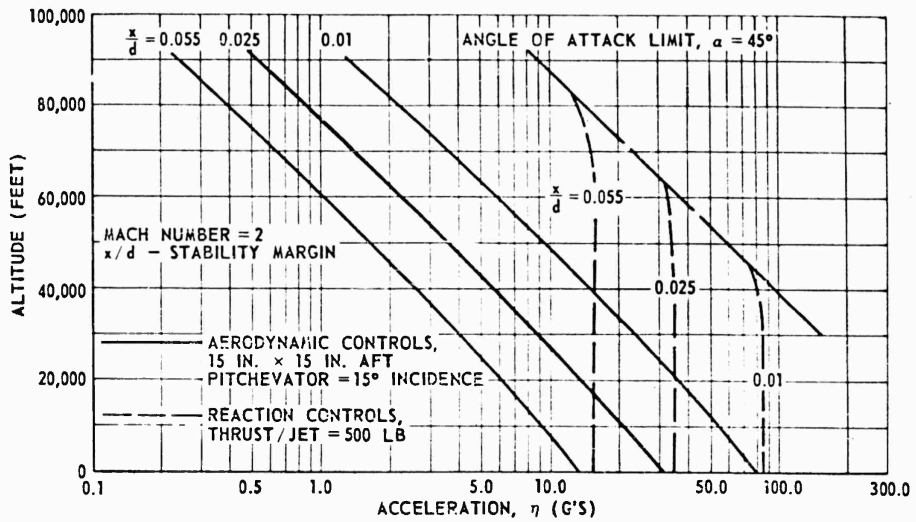


Figure 3.7.96. Available Normal Acceleration, Mach 2.

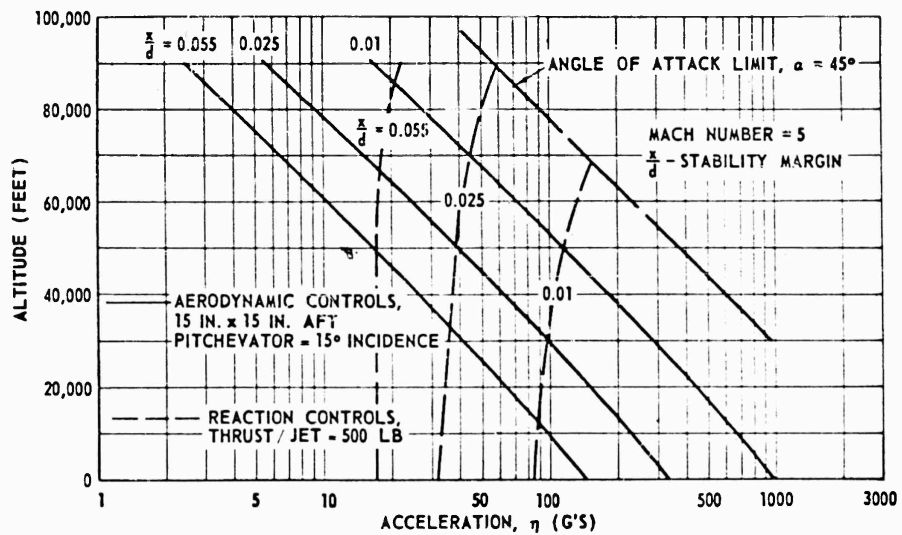


Figure 3.7.97. Available Normal Acceleration, Mach 5.

this analysis was 300 pounds. The aerodynamic curves of subsection 3.2 were used in computing maneuverability and trim moment.

Figure 3.7.96 indicates that, as the stability margin decreases from 0.055 to 0.01, the sea level maneuverability available with 500 LB reaction jets increases from approximately 15.5 to 84 g's. Moreover, this maneuverability is approximately constant with altitude up to the altitude where the missile reaches

SECRET

45 degrees angle of attack. This is due to the fact that, except for interference effects between the reaction jets and the free stream, the force produced by reaction jets is almost independent of altitude. It should be noted that the above mentioned interference effects - not considered in this study - would increase the control effectiveness of the reaction jets at lower altitudes.

Figure 3.7.96 indicates that the maximum maneuverability available from aerodynamic controls decreases rapidly with altitude. For instance, for a stability margin of 0.025, the available maneuverability decreases from 78 g's at sea level to 1.5 g's at 90,000 feet.

In summary, Figure 3.7.96 indicates the superiority of reaction controls over aerodynamic controls at Mach number 2. This superiority increases as the altitude increases.

Figure 3.7.97 indicates that, as the stability margin decreases from 0.055 to 0.01, the sea level maneuverability available with 500 LB reaction jets increases from 17 g's to 84 g's. Here again, the available maneuverability is approximately constant with altitude up to the altitude where the missile reaches 45 degrees angle of attack. Aerodynamic controls are shown to produce very high g's at low altitudes. However, as was shown in Figure 3.7.96, the g's available with aerodynamic controls decreases rapidly as altitude increases. Above approximately 50,000 feet, reaction controls offer more maneuverability than aerodynamic controls. At all altitudes, reaction controls offer adequate maneuverability if reasonably low stability margins are maintained.

Some mention of the order of magnitude of stability margins expected from realistic designs is warranted at this time. Subsection 3.10 treats the design feasibility of several PYE WACKET missiles in detail and includes weight and balance statements. Empty center of gravity positions, which range between 45 and 48 percent of the missile diameter aft of the leading edge, are indicated for the various diameters and thickness ratios considered in subsection 3.10. Since, as shown in subsection 3.2, the aerodynamic center of pressure of PYE WACKET varies from 43 percent of the diameter at Mach 2 to 45 percent of the diameter at Mach 5, stability margins in the range of 0.05 to 0.02 can be expected. Therefore, as indicated in Figures 3.7.96 and 3.7.97, maneuver capabilities that probably exceed the missile structural capabilities are possible at end of boost (high Mach numbers). As Mach number decreases, maneuverability also decreases. At Mach 2, 20 to 40 g's would be available from the 500 LB reaction jets up to the altitude where the missile reaches 45 degrees angle of attack. For the PYE WACKET missile with the furthest aft center of gravity (CG at 48 percent), additional control force would be required if more than 20 g's terminal maneuver were required. For the PYE WACKET missile with the center of gravity at 45 percent, the resulting 40 g's would probably be adequate.

SECRET

3.7.5 SUMMARY

The results of the PYE WACKET control system investigation are as follows:

1. Aerodynamic controls are unsatisfactory for application to a circular planform missile (see paragraph 3.7.1).
2. Reaction controls using fixed auxiliary jets of variable thrust are mechanically feasible (see paragraph 3.7.2).
3. Reaction controls provide acceptable response times and afford a relatively simple autopilot design (see paragraph 3.7.3).
4. Reaction controls provide sufficient maneuver capability over the ranges of altitude and Mach number envisioned for PYE WACKET (see paragraph 3.7.4).
5. Maneuvers unobtainable with conventional configurations, are possible with PYE WACKET using reaction controls at extremely high altitudes.

3.7.6 SYMBOLS AND DEFINITIONS

The symbols employed in subsection 3.7.1 (Aerodynamic Controls) are defined below; forces and moments are shown acting on the configuration in the positive sense in Figure 3.7.2.

M	Mach number
N	Normal force, LB
L	Lift, LB
D	Drag, LB
A	Axial force, LB
V	Velocity, FT/SEC
M	Pitching moment, FT/LB
Y	Yaw force, LB
YM	Yawing moment, FT/LB
RM	Rolling moment, FT/LB
CP	Center of pressure location, percent chord
d	Diameter, FT
t	Thickness, FT
c	Chord, FT
S	Reference area, planform, FT ²
P	Ambient pressure, LB/FT ²
q	Dynamic pressure, $\frac{\gamma P M^2}{2}$, LB/FT ²
I	Moments of inertia, slug-FT ²
C _N	Normal force coefficient, $\frac{N}{qS}$
C _L	Lift coefficient, $\frac{L}{qS}$

SECRET

3.7.99

C_D	Drag coefficient, $\frac{D}{qS}$
C_A	Axial force coefficient, $\frac{A}{qS}$
C_m	Pitching moment coefficient, $\frac{M}{qSd}$
C_n	Yawing moment coefficient, $\frac{YM}{qSd}$
C_l	Rolling moment coefficient, $\frac{RM}{qSd}$
X/d	Ratio of center of pressure location with respect to body diameter
W	Weight, LB
γ	Ratio of specific heats, 1.4
i_F/i_A	Deflection angles of fore and aft pitchvator with respect to body centerline, degrees
α	Angle of attack, degrees
ψ	Angle of yaw, degrees
ω_L/ω_R	Apex angle of left and right conevators or included angle of wedgevators degrees
δ_L/δ_R	Deflection of left and right wedgevator or conevator for roll control, degrees
$\Delta\omega$	Difference in the included angles of the left and right wedgevators for yaw control, degrees
$C_{N\alpha}$	Variation of normal force coefficient per degree angle of attack, $\left(\frac{\partial C_N}{\partial \alpha}\right)$
$C_{m\alpha}$	Variation of pitching moment coefficient per degree of angle of attack, $\left(\frac{\partial C_m}{\partial \alpha}\right)$
$C_{l\delta}$	Variation of rolling moment coefficient per degree differential deflection, $\left(\frac{\partial C_l}{\partial \delta}\right)$
$C_{l\Delta\omega\alpha}$	Yaw control induced rolling moment coefficient per degree difference in wedgevator yaw control angle per degree angle of attack, $\frac{\partial^2 C_l}{\partial \omega \partial \alpha}$
$C_{n\delta\alpha}$	Roll control induced yawing moment per degree differential deflection per degree angle of attack, $\frac{\partial^2 C_n}{\partial \delta \partial \alpha}$

The symbols employed in subsection 3.7.2 (Reaction Jet Controls) are defined below:

I_{sp}	Specific impulse, LB _f -SEC/LB _m
F	Thrust, LB
\dot{W}	Propellant flow rate, LB/SEC
C_F	Thrust coefficient (F/P _c A _t)
P_c	Chamber pressure, PSIA
A_t	Nozzle thrust area, IN ²

SECRET

A_c	Nozzle exit area, IN ²
e	Expansion ratio (A_e/A_t)
C^*	Characteristic exhaust velocity, FT/SEC
γ	Specific heat ratio
F_x	Side force exerted by main propulsive jet, LB
F_y	Thrust force out of main propulsive jet in direction of velocity vector
g	Acceleration of gravity, FT/SEC ²
P_e	Nozzle exit pressure, PSIA
P_o	Atmospheric pressure, PSIA
P_{oj}	Stagnation pressure of jet, PSIA
a_o	Speed of sound, FT/SEC
V_c	Volume of combination launcher, IN ³
L^*	Characteristic length, IN.
D	Diameter of body over which reaction jet is acting, IN.
d	Exit diameter of reaction nozzle, IN.
N_I	Interaction force $N = N_v$, LB
N	Normal-force increment due to jet (normal force on model with jet on minimum force due to main stream only)
N_v	Normal force due to jet exhausting into vacuum
σ	Ratio of interference force calculated by method in Reference 3.7.10 to that computed by empirical results of Reference 3.7.12
M	Mach number
K	N/N_v

3.7.7 LIST OF REFERENCES

- 3.7.1 APL/JHU-TG-14-37, "An Investigation of Bulk Controls for Stabilization and Control of Slender Bodies of Revolution at Hypersonic Speeds," by R. C. Brown, published in Minutes of 40th Bumblebee Aerodynamics Panel Meeting, 12-13 May 1959, SECRET
- 3.7.2 CPC-1393, "Proposal for Lenticular Rocket Feasibility Study," presented to Air Proving Ground Center, United States Air Force by Convair-Pomona, April 1959, SECRET
- 3.7.3 Brandemin, D. S., Goldbeck and Jackson, Survey of Methods for Deflecting Exhaust in Missile Control, NARTS Report No. 60
- 3.7.4 Hunter, P. A., "An Investigation of the Performance of Various Reaction Control Devices," NASA Memo 2-11596, March 1959
- 3.7.5 Bankston, L. T., Larsen, "Thrust Vectoring by Secondary Injection in the Nozzle Exhaust Cone," Bulletin of the 15th JANAF Meeting, June 1959
- 3.7.6 Pippin, D. R., Advanced Wizard Ballistic Missile Defense System, Aerojet Report No. SRP-122, September 1958

SECRET

3.7.101

SECRET

- 3.7.7 Ellis, H. E., Rapp, L. R., "Studies of Storable Propellant Systems," ARDC Industry Symposium on Storable Liquid Propulsion Systems, January 1959
- 3.7.8 Elvenum, G. W., Massier, P. F., Lee, D. A., "Research and Development at Jet Propulsion Laboratory on Storable Propellants Using Hydrazine as the Fuel," ARDC Industry Symposium on Storable Liquid Propulsion Systems, January 1959
- 3.7.9 Liquid Propellant Handbook, Volume I, October 1955
- 3.7.10 Ferrari, Carlo, Interference Between a Jet Issuing Laterally From a Body and the Enveloping Supersonic Stream, Bumblebee Series Report No. 286, April 1959
- 3.7.11 Liepman, H. P., "On the Use of Side-Jets as Control Devices," ARS Journal, Volume 29, Number 6, June 1959
- 3.7.12 Vinson, P. W., Amick, J. L. Liepman, H. P., On the Interaction Effects Produced by a Jet Exhausting Laterally Near the Tail of an Ogive-Cylinder Model In a Supersonic Stream, NASA Memo 12-5-58W, February 1959
- 3.7.13 Bumblebee Activities, Quarterly Review, January-March 1959
- 3.7.14 "Discontinuous Automatic Control," Flugge Lotz, Princeton Press, 1953
- 3.7.15 "Studies of Second and Third Order Contact Control System," Lindgren and Flugge Lotz, Stanford University Division of Engineering Mechanics, T.R. No. 114
- 3.7.16 "On the Bang-Bang Control Problem," Bellman, Quarterly of Applied Mathematics, April 1956
- 3.7.17 "Control System Synthesis," John C. Truxal, McGraw-Hill
- 3.7.18 "Fundamental Theory of Servomechanics," L. A. Mac Coll, D. Van Nostrand
- 3.7.19 "Frequency Analysis of a Control Loop Containing a Bi-Stable Element," R. E. Gorozdos, APL-HJU CF-2750
- 3.7.20 Polaris Power Plant Development, Aerojet-General Corporation, May 1959
- 3.7.21 Rodeau, H. C., "Rocket Thrust Termination Transients," ARS Journal, Volume 29, Number 5, June 1959
- 3.7.22 Honeywell, E. E., Giese, D. J., Preliminary Results of PYE WACKET Wind Tunnel Tests, Convair Pomona, TM-334-409, November 1959

3.7.102

SECRET

SECRET

3.8 GUIDANCE

The PYE WACKET feasibility study does not specifically call for an investigation of methods of vehicle guidance, however, it was decided that a brief examination of possible guidance systems would be useful in developing missile concepts. Because of a lack of a specific mission and target definition, the several types of guidance systems can only be discussed in a qualitative manner. The information presented here has been obtained from independent Convair studies as well as from investigations related to other programs. As the concept of a PYE WACKET vehicle evolves, considerable effort must be directed towards making the guidance system compatible with other systems, especially the missile control system autopilot and the fire control system of the launching aircraft when employed in airborne weapon applications.

3.8.1 INERTIAL

An inertial guidance system for the air-to-air missile is not satisfactory for the complete flight trajectory due to the unpredictability of the target course after the missile is launched. This means that inertial guidance could be used only in the initial and midcourse flight phase with another type of guidance required for the terminal phase of flight.

A disadvantage of such a system is that the alignment and computing equipment required on the launching vehicle would be somewhat complex. For attainment of the final position in space, the accurate establishment of the initial position is required. Another disadvantage is that the missile instrumentation and computer circuitry would be complex and expensive. There may also be problems of packaging the inertial components within the PYE WACKET configuration. However, miniaturization techniques currently in progress may reduce the space requirements. An advantage of this system is, of course, the lack of radiation for enemy detection and countermeasures.

A simplified version of inertial guidance is proposed for the initial guidance phase for PYE WACKET. As described in a later section, for the conditions stated, a simple gyro reference can be used in the launch phase.

3.8.2 BEAMRIDING

The beamriding system of guidance is feasible in the general sense. In this type of guidance, a radar on the launching vehicle continuously tracks a target. The missile is launched into the radar beam and "rides" the beam to target intercept. A receiver in the missile obtains information from the radar beam which is used to control the missile in such a way as to remain in the beam.

SECRET

3.8.1

SECRET

The beamriding guidance system has both advantages and disadvantages. For the ranges that were considered in this study phase for PYE WACKET, the size and complexity of the radar tracking unit is not unrealistic for installation in the launching vehicle. In order to track more than one target, additional units are required or a time-sharing system is necessary. The latter is realizable. A further advantage of this type of guidance is that the missile receiver and control loop is relatively simple. A disadvantage is that the system is active and is therefore subject to rather simple countermeasure techniques. Another possible major disadvantage is that this type of system would necessarily have blind spots, as it is impractical to have spherical coverage, with only one transmitter.

The missile trajectory of the beamrider requires inherently more g capability than, say, a homing or ballistic trajectory. This, in itself, is not necessarily a deterrent so long as the g's required for intercept do not exceed missile capability.

The miss distance which might be expected for a beamriding system within the ranges and the target conditions under consideration, would not be prohibitive. The sources of error in this type of guidance are:

1. Radar noise
2. Radar tracking lags
3. Missile beamriding error

Radar noise is inherent in the mechanics of the radar tracking loop and the false signals from target reflection. Radar lag is also a characteristic of the tracking loop. Missile errors are attributed to the dynamic lags of the missile control loop, the missile g capability, and non-linearities of the control system. Typical miss distance figures for a beamriding missile against a Mach 2 target at about 40,000 foot range might be:

1. $\bar{y} = 20$ feet
2. $\sigma = 30$ feet

where:

\bar{y} is the average (or bias) miss distance and, for a normal distribution about the bias, σ is the RMS miss.

3.8.3 SEMIACTIVE HOMING

Guidance of PYE WACKET could be achieved through the use of a semiactive homing system. Basically, this system consists of a radar transmitter located in the launching aircraft and a receiver mounted in the missile. The target is illuminated by the aircraft's radar with the missile using the reflected energy as a homing signal.

3.8.2

SECRET

SECRET

One advantage of this system is that it provides an "all-weather" capability since radar is not greatly affected by ordinary atmospheric conditions. For an air-to-air missile, ground clutter would be a negligible problem. Another advantage is that this homing system is less susceptible to countermeasure techniques than the comparable "beamriding" missile. Search and detection systems currently favor radar because of long range use during adverse weather conditions and the fact that much knowledge has been accumulated with respect to system design. As long as radar detection is used, semiactive homing offers an excellent method of guidance.

A mechanically directed missile homing antenna in a semiactive system would present a number of problems. Among these are limitations on dish size due to the missile configuration, the additional power required to drive the gimbals, and the additional instruments required to stabilize the antenna. Most of these problems could be avoided by the use of fixed antennas. These fixed antennas could consist of an array of radiating elements connected through ferrite phase shifters so that the beam can be scanned electronically. A monopulse array, or two crossed fan beam arrays might be suitable for PYE WACKET.

The look angle possible with a ferrite-scanned array would be limited by the distortion of the beam shape and the allowable reduction of sensitivity. A monopulse system would require additional complexity in the missile receiver, as would the crossed beam system.

Convair is currently producing Tartar, which is a semiactive homing missile employing a proportional navigation guidance technique. Theoretically, a missile with this form of navigation would require a lateral acceleration capability equal to twice that of the target. The maximum acceleration is then a function of structural limitations which are common to both missile and target.

The miss distance of a semiactive homing missile is determined by a number of noise sources:

1. Fading noise
2. Glint noise
3. Receiver thermal noise

Fading noise is caused by variation of the radar cross section with the viewing angle. Noise dependent on the target range and dimensions is called glint noise. Receiver thermal noise is only significant when the receiver power level is below a specific minimum value, which is usually the case for long intercept times. Typical values of average miss distance (\bar{y}) and standard deviation (σ) for a semiactive homing missile are given below for an intercept condition of:

Missile velocity-M = 2, slant range R = 42K feet

$\bar{y} = 4$ feet

$\sigma = 18$ feet

SECRET

3.8.3

3.8.4 COMMAND

The command system has perhaps the most freedom for optimizing the guidance trajectory. The missile portion of the guidance system can be very simple since it needs only the capability of receiving information that will operate the controls in the correct directions upon command. The launcher-based equipment, on the other hand, may be quite complex. The target, or targets, must be tracked and so must the missile. Relative positions of target and missile must be computed continuously and appropriate signals sent to the missile to correct the trajectory for intercept. Another disadvantage is that the system radiates signals which could be used by the target. The system is also susceptible to jamming.

Except for the case in which the missile is commanded to fly a course similar to that of a beamrider, accurate range data is required for both target and missile. Since range information is the most susceptible to all radar data to enemy countermeasures, other trajectories are likely to be degraded by enemy action.

3.8.5 INFRARED

Based on current knowledge of the missile design and anticipated objectives, infrared appears to be the most attractive of the possible choices of guidance systems. It has the following desirable features:

1. IR appears to have the range capability for the targets which a manned-aircraft defensive missile may encounter.
2. It could be made to fit within the physical dimensions of PYE WACKET.
3. The stabilized head (gyroscopic) IR system is quite simple and reliable.
4. The system is passive.

The arguments against the IR system are that it is not an all-weather system, and target acquisition is heavily dependent upon target radiation characteristics which are subject to large variation.

The following paragraphs describe an IR guidance concept for the PYE WACKET defensive missile. The configuration used as a model for the calculations is the same as for the Convair-designed Redeye seeker and optics. The objective of this guidance system is to arrive at a simple design which might lend itself to early flight testing. A convenient assumption which contributes greatly to the simplicity is that target acquisition can occur prior to launch. This concept is not unrealistic but does require more engineering study before acceptance. With this concept, the stringent search, detection, and tracking requirements are on the launcher-based system and not on the missile. Full utilization of the omnidirectional launching capability is realized in this instance.

SECRET

IR SEEKER. The Redeye seeker, although by no means optimum for the present application, does present certain desirable features of size and simplicity which make the system attractive. The seeker uses a folded optical system with primary and secondary mirrors. From the secondary mirror, the energy passes through a spectral filter, is modulated by a reticle chopper, and is incident on a lead sulfide cell. Except for the cell, these components operate as a gyro assembly and are gimballed to permit target tracking.

The output of the lead sulfide cell, after amplification and detection, provides a signal to the precession coils and to the guidance section demodulators. For PYE WACKET, two reference coils provide a phase reference to two demodulators. The filtered outputs of the demodulators are error signals proportional to the rate of change of the seeker line of sight.

The characteristics of the Redeye seeker are:

1. Outside diameter-2.75 inches
2. Primary mirror-1.8 inches diameter, secondary mirror-1.06 inches diameter
3. Field of view-2°
4. Look angle-40° in any plane
5. Tracking rate-10° per second (Which can be increased by raising the power level)

Based on these general characteristics, the problems of an IR "window," target detection limitations, and improvement techniques are discussed in the following paragraphs.

IR Dome. There are two shapes of IR domes that are acceptable from the stand-point of the optics of an IR system; one is spherical, and the other is flat (plane).

The use of a spherical dome in the lenticular missile would require the addition of one or two protuberances. Due to look-angle requirements, the seeker must be mounted directly behind the dome. Use of a single seeker would require that the seeker and dome be set into the center of the leading edge of the missile. This would require a cylindrical protuberance with a spherical nose (the dome) with the resulting aerodynamic compromises. Another possibility is to place two domes (top and bottom) farther aft. This does not seem particularly promising because of the large drag forces that two domes would generate. Moreover, the use of two independent IR systems (domes and seekers) represents a redundancy that probably cannot be afforded in a smaller missile. For these reasons, a study has been made of the possibility of using flat IR domes. A configuration was found that might be more suitable for the PYE WACKET configuration.

Figure 3.8.1 shows how a single seeker might be used that looks through two flat IR windows (top and bottom). The two plane windows are set into the skin of the missile, in the center, just behind the leading edge. The curvature of the

SECRET

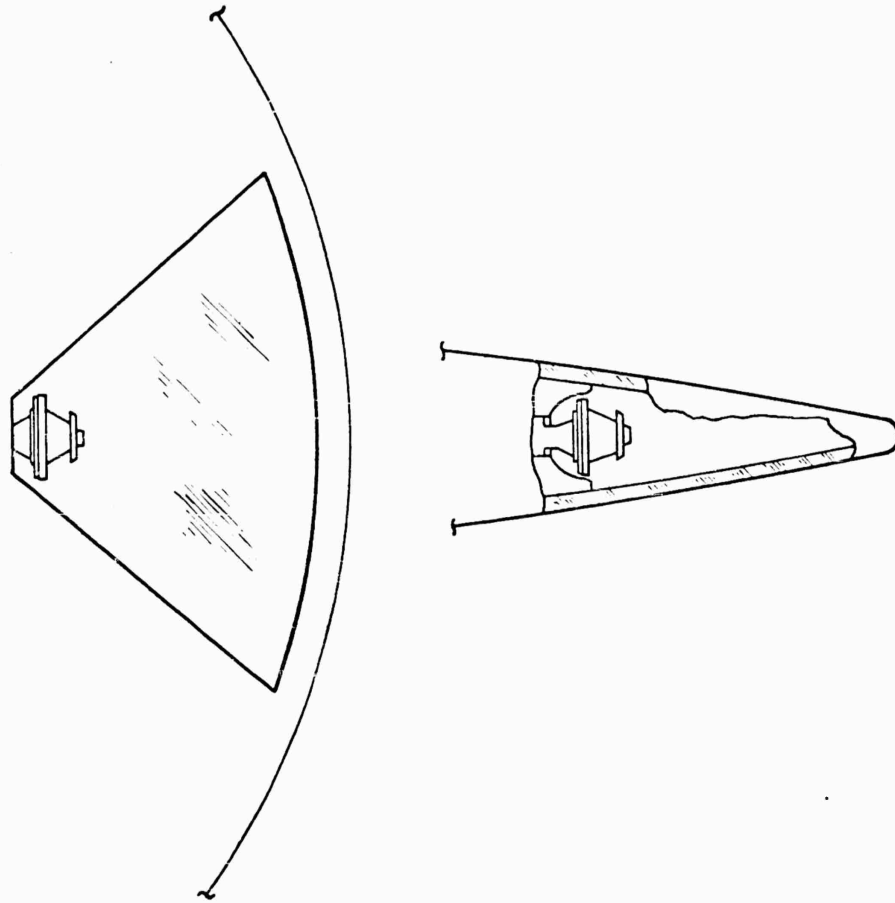


Figure 3.8.1. IR Window.

skin in this location is so slight that the windows are nearly flush with the skin. Masking of the seeker by the leading edge of the missile would occur only when the seeker looks in the plane of the missile. This masking is not as detrimental as it might appear, since, with a folded optical system, the center of the primary mirror is already masked by the secondary mirror. The 1.8-inch diameter Redeye mirror, for instance, is masked by the 1.06-inch diameter secondary mirror. For a mirror of this size, the additional masking by a 1-inch strip (typical of the feasible Designs in subsection 3.10) would be 50 percent in the worst case. For look angles out of the plane of the missile (the ordinary case), this masking would disappear.

A study has been made of the feasibility of cooling this type of window. The results were very encouraging. Among other things, it appears that the flat

SECRET

window is much easier to cool by mass injection than a spherical dome (Reference 3.8.1). This is especially true for large aerodynamic angles of attack of the missile.

The primary disadvantage of the flat window is the reflection loss that can occur. As the angle between the incident IR radiation and the normal to the window increases, the reflection loss increases. The amount of reflection loss for a given angle of incidence depends upon the index of refraction of the window. This, in turn, depends upon the material used for the window, and the wavelength of the IR radiation. The worst reflection for the window proposed here would occur for look angles in the plane of the missile. The total reflection loss for an index of refraction of 1.5, for example, could be as high as 60 percent. This, however, is again a worst case. For more ordinary look angles, out of the plane of the missile, the reflection losses would drop rapidly. Furthermore, optical coatings could help to reduce the reflection losses.

The advantages and disadvantages of the proposed plane windows, compared to spherical domes, may be summarized as follows:

1. Advantages:

- a. The flat window is aerodynamically "clean." It would produce little or no additional drag, or unstable moments.
- b. The flat window is comparatively easy to cool.
- c. Use of two flat windows permits the use of a single seeker.

2. Disadvantages:

- a. The leading edge in front of the windows partially masks the seeker for look angles in the plane of the missile.
- b. Reflection losses for the flat windows are higher than for a spherical dome, especially for look angles in the plane of the missile.

These masking and reflection losses, while significant, are not prohibitive. The apparent advantages of the flat windows make them especially attractive for further consideration for application to the PYE WACKET configuration.

IR PERFORMANCE CAPABILITY. A comprehensive discussion of the performance capability of an IR system for a lenticular rocket is beyond the scope of this feasibility study. Before an IR system can be designed for a missile, the performance requirements for the overall missile system should be defined. The targets must be defined, along with the tactical conditions under which the missile will be employed. Therefore, it is not practical to try to define a complete IR system for a lenticular missile at this time. It is worthwhile, however, to take a broad, qualitative look at IR system capabilities.

The field of view of an IR seeker is very small. Acquisition after launch would require extremely accurate inertial guidance in the missile, as well as imposing difficult search requirements on the seeker. To estimate the possibility of IR target acquisition in the missile before launch, some assumptions must

SECRET

SECRET

be made. As an example, assume that the target is a 6-inch, Mach 4 missile. Assume further that the target is seen in a "head-on" aspect. Due to this aspect (and the probable short duration of the powered phase of the target flight), the only IR radiation that can be relied upon is that due to aerodynamic heating. The radiation below 3 microns is insufficient for detection over desirable ranges. In the 8-13 micron region, detectors are not as well developed as for the shorter wavelengths. Moreover, background radiation in the 8-13 micron region is generally worse than at shorter wavelengths. For these reasons, we will consider only the radiation in the 3-5 micron atmospheric window.

For the hypothetical 6-inch diameter, Mach 4 target, at altitudes between 30,000 and 60,000 feet, the radiation intensity in the forward direction is of the order of 30 watts/steradian, in the 3-5 micron band. This includes the effect of atmospheric attenuation over a 100,000 foot range. An additional assumption is that the target is at equilibrium temperature at the Mach 4 speed.

The method for arriving at this figure is as follows: The equilibrium skin temperature at Mach 4 between 30,000 and 60,000 feet will be between 800 and 1000°K (Reference 3.8.2). Black body radiant emittance between 3 and 5 microns at 900°K is 13,400 watts/m².

$$W = \int_3^5 \frac{3.74 \times 10^8 \lambda^{-5} d\lambda}{e^{15.98/\lambda - 1}}$$

If the nose is assumed to emit as a grey body Lambert radiator with an emissivity of 0.5 the radiant intensity in the forward direction of the nose is

$$W_s = \frac{\epsilon A W_{m^2}}{\pi}$$

where

- ϵ = emissivity
- A = projected area (6-inch diameter)
- W_s = radiant intensity, watts/steradian
- W_{m^2} = radiant emittance, watts/square meter

This gives a radiant intensity of 39 watts/steradian.

It is assumed that the target launcher has been previously detected, and that sophisticated detection equipment aboard the defending bomber has detected

SECRET

SECRET

the target launching. The bomber, then, is able to direct the PYE WACKET missile seeker at the target.

Now the possibility of the missile seeker detecting the target will be determined. Assuming a nominal detection range of 100,000 feet, a seeker the size of the Redeye seeker (1.8-inch diameter mirror with a 1.06-inch diameter secondary mirror) intercepts approximately 10^{-12} steradian at a distance of 100,000 feet from the IR source:

$$(\pi/4) (1.8^2 - 1.06^2) / (12 \times 10^5)^2 \approx 10^{-12}$$

Assuming 66 percent losses, the 30 watt/steradian target would produce the order of 10^{-11} watt at the detector. This seems to be within the sensitivity that may be expected of a 3-5 micron detector within a reasonable development time.

Obviously, this represents a grossly simplified example. A more detailed discussion, however, would involve a thorough study of possible targets, along with a better definition of the range requirements. Such an involved study would be impractical at the present stage of the lenticular missile study. As was pointed out above, the IR system considerations can be refined as the PYE WACKET program becomes better defined.

The major omissions in this simplified example are the effects of background radiation (in the field of view of the seeker), time-lag in the aerodynamic heating of the target, and emission characteristics of the heated air between the missile and its shock wave. These effects should at least be mentioned here.

Radiation intensity gradients in the background will produce false signals in the seeker. It can be shown that, for elementary scanners, the edge of a cloud will produce a false signal that will "swamp" the target signal in the case given as an example above. However, improved scanner designs, such as the checkerboard, greatly reduce this tendency. There is no accurate data, to show just how often an intensity gradient of a given magnitude will appear in the field of view of the seeker. Moreover, it is not known at this time just what improvements can be expected in the techniques of background rejection. A large variety of scanning techniques are being studied, as well as other methods for attenuating the effects of backgrounds.

The assumption that the hypothetical Mach 4 target is at equilibrium temperature is a poor one. Actually, the target may be internally stored before launch. In this case, the level of radiation intensity in the 3-5 micron band would still be 20 DB below the 30 watt/steradian level given, 20 seconds after launch at 60,000 feet. On the other hand, a 12-inch diameter, Mach 6

SECRET

3.8.9

target, for example, would have a 15 DB higher radiation level at 3-5 microns than the 6-inch diameter, Mach 4 target.

Two of the fundamental limitations of an IR detection system are the background radiation and the detector noise. Operation of the seeker while the missile is still on the launcher represents a favorable environment. Since the seeker may be pointed accurately toward the target, a very small field of view may be used, which is favorable from the standpoint of reducing the background. Moreover, (to compensate for pointing errors) searching can be performed by control from the aircraft, with no added complication in the missile. In addition, very sophisticated circuitry might be employed in the aircraft to improve the background discrimination.

The effect of detector noise may be reduced to a minimum. A very accurate scanning rate may be maintained while the missile is on the launcher, permitting the use of very narrow bandwidths. Development of narrow band width tracking filters is being pursued. This would permit a narrow seeker bandwidth during flight.

Finally, the most important factor in the target detection picture is the progress that is being made in the field of IR techniques. All aspects of the problem are being studied in detail by many organizations and the field is in a state of rapid growth. In the text that follows, the major areas where improvement may be expected are discussed.

Areas for Improvement. As was mentioned previously, the two major limitations to IR systems are background radiation and detector noise. Scanning methods, signal and spectral filtering, and signal processing techniques are the main approaches under way for the reduction of background effects. Three different approaches to this problem are being studied at Convair-Pomona. In the detector field, methods of cooling, and basic solid-state research are among the approaches to the reduction of detector noise and the improvement of detector sensitivity.

One of the handicaps encountered in IR work is lack of adequate data describing the radiation characteristics of targets and backgrounds. Much work is being done to improve this situation.

Other areas of work involve the materials and the components involved in IR optics, such as domes (and windows), filters, and objective and field optical systems.

Three different approaches to the problem of discriminating the target from the background targets are now being studied at Convair-Pomona. One is a two-color system. Another is the combination of a special scanning reticle with an integration technique. The third is a combination of a special reticle with electronic filters. Only the first of these approaches is discussed below, since development is further along on the two-color system.

SECRET

The two-color system which is currently being developed and tested will be operable in the Redeye missile. This system detects sources in either the IR or the ultraviolet spectrums. Such a system will:

1. Permit tracking of targets (during daytime conditions) whose emitted energy is not sufficient to give a positive contrast signal.
2. Increase the useful range of the seeker against all targets.
3. Improve the seeker's ability to discriminate against various backgrounds.
4. Serve as a counter-countermeasure.

It is possible to detect targets by negative contrast in the 2.0 to 2.7 micron band under certain conditions. Operation at shorter wavelengths, however, appears to be more attractive. Background energy from the sky and clouds is considerably higher in the ultraviolet and visible spectra. At the same time, target energy is much lower, affording good contrast of the target against its background. The choice of the exact spectral band of operation is governed by available detectors and suitable filters.

The Convair Physics Laboratory is developing a series of two-color photocells, one of which is of "club sandwich" construction which is sensitive in both the 0.35-0.8 micron region and the 2-2.7 micron region. See Figure 3.8.2.

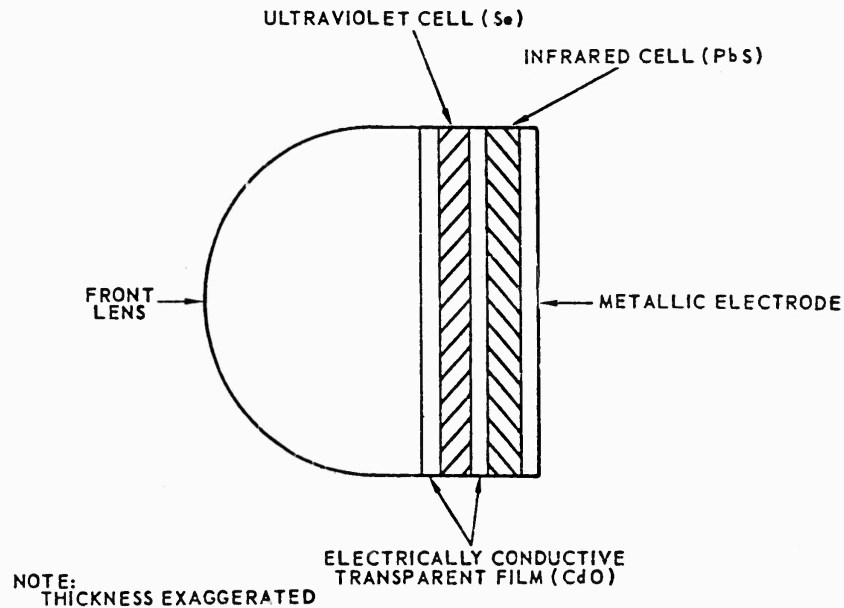


Figure 3.8.2. Two-Color Photocell.

The results of preliminary field tests using a two-color system to track a commercial helicopter are shown in Figure 3.8.3. In the first group of traces, the

SECRET

3.8.11

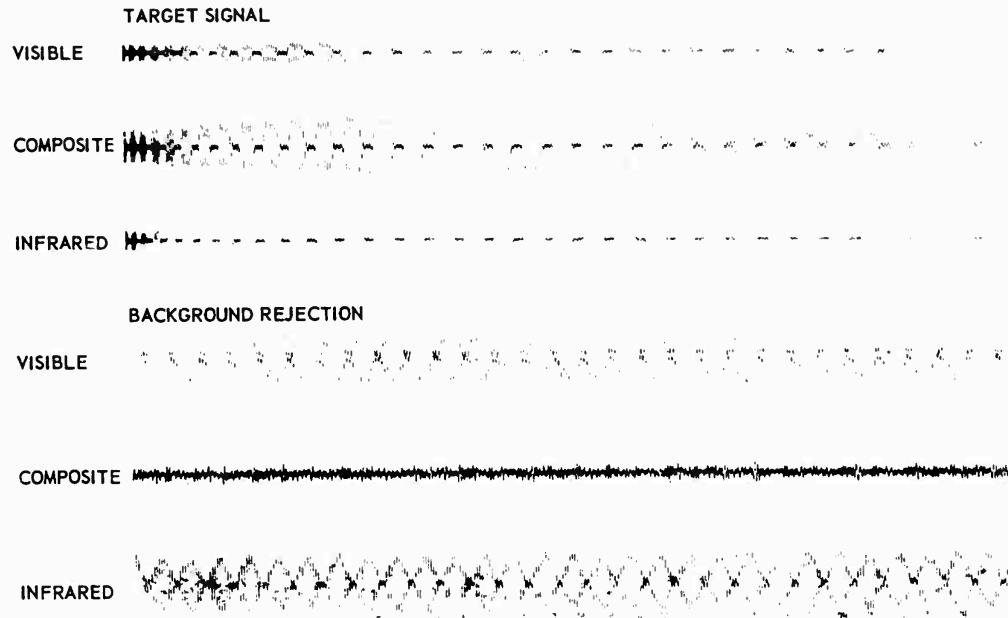


Figure 3.8.3. Target Test and Background Reduction.

composite target signal is greater than either individual signal. In the second group the composite signal from a "hot spot" on a small cirrus cloud is much reduced illustrating the background noise reduction.

3.8.6 CONCEPTUAL SYSTEMS

In subsection 3.7, reaction controls and autopilot concepts were developed. The previous discussion has emphasized the possibilities of IR guidance. These concepts are now combined and a description of the operations, from the launching of the defensive missile until it approaches the target, is presented.

Control of the vehicle, Figure 3.8.4 will be by means of four reaction jets. Differential thrust between jets will provide control torques about all three axes. At the present time, it is planned to use "bang-bang" control. One system studied employs four small rocket motors (two left and two right). The thrust level in each motor can be varied to produce forces for pitch, yaw, and roll control.

The roll and yaw axes will be essentially position controlled, with rate-gyro feedback for damping. The pitch axis, however, will be acceleration controlled. Due to the near-neutral stability of the vehicle in pitch, accelerometer and rate gyro feedback will be used. Convair has had extensive experience in the development and use of this type of autopilot in missiles.

SECRET

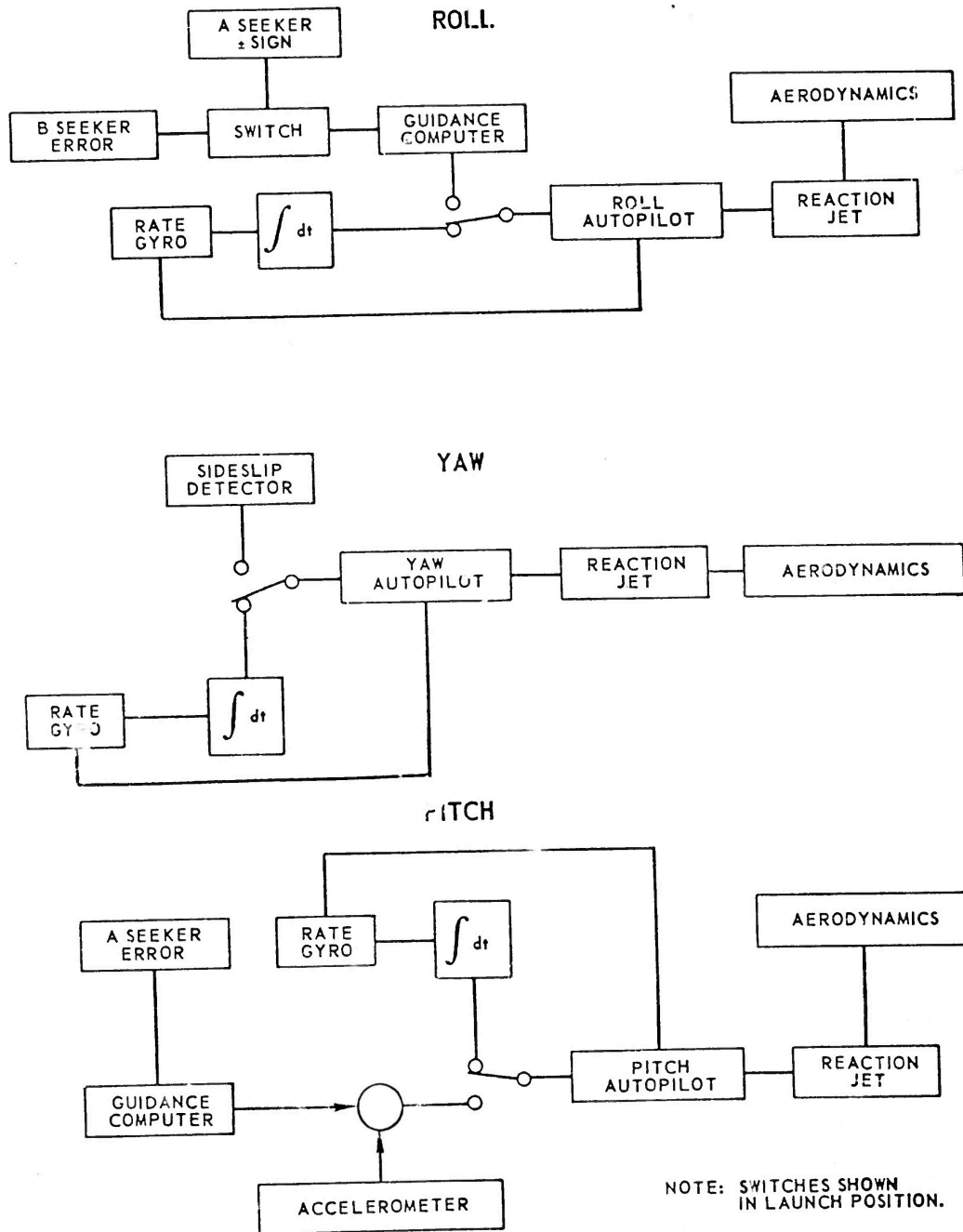


Figure 3.8.4. Guidance and Control Schematic.

SECRET

SECRET

Before launch, the missile will have been oriented in azimuth, on the launcher, so that the seeker may be pointed at the target. After the seeker has locked onto the target, the missile will be ejected from the launcher. At this time, the missile may see a very large angle of aerodynamic yaw (up to 180°). For this reason, the missile is stabilized by inertial reference until thrust from the rocket motor builds up forward speed. The inertial reference will be obtained by electronic integration of all three rate gyros. This will give stabilization of the missile at nearly constant angles of pitch, roll, and yaw, in space.

After the missile has achieved sufficient forward velocity to reduce the aerodynamic angle of yaw within reasonable limits, guidance will be switched over to the terminal mode.

Aerodynamic yaw will be sensed by differential pressure measurements. This signal will be fed into the yaw autopilot, maintaining the aerodynamic yaw (sideslip) of the missile at a minimum.

Signals from the seeker will be used to provide guidance in roll and pitch. "B" plane (yaw plane) signals will be the roll error signal. This will cause the missile to roll so that the plane of the required homing maneuver is in the pitch plane of the missile. The sign of the roll error signal may be switched according to the sign of the signal in the "A" plane (pitch plane). This will prevent the missile from being required to roll more than 90° in order to effect any one maneuver.

The seeker signal from the "A" plane (pitch plane) is fed into the pitch autopilot. The seeker signal is proportional to the rate of change of the seeker line of sight. The pitch autopilot trims the missile to an acceleration level which is proportional to the input. Hence, this combination of seeker and autopilot give proportional navigation homing.

The proposed roll control system has the peculiar characteristic that the gain of the control loop is proportional to the magnitude of the homing error signal. For the correct collision course (zero error), the roll error signal vanishes altogether. This is not considered to be a serious problem, however, since "bang-bang" control has been shown to be capable of accommodating a wide dynamic range of gain change within the control loop. As for the vanishing of the roll error signal at small homing errors, experience has shown that there is usually sufficient drift or bias present in the overall system to give significant homing error. Finally, it would not be serious if the missile did occasionally lose roll position reference. It would roll at a slow rate, due to the rate gyro feedback, and would regain roll position as soon as a significant homing error developed.

As outlined above, the missile instrumentation includes, besides the seeker, a yaw-sensor and three rate gyros. In addition, in the launch phase, electronic integration of all three rate gyros is required.

SECRET

SECRET

It may be possible to obtain and use position information from the seeker. This information could replace the integrated pitch and yaw rate gyro signals. The time derivatives of this seeker position information, along with the normal seeker output, might be used to replace the pitch and yaw rate gyros themselves. Such a system might prove to be a desirable simplification. In general, infrared tracking signals are comparatively "clean," and the time derivatives might very well be clean enough to replace the rate gyro signals.

Moreover, further studies might prove it desirable to use seeker position information as part of the roll reference. At small homing error conditions, one particular plane might be "preferred," taking into account target maneuverability and/or speed variations of the target and/or missile.

3.8.7 SUMMARY

A brief discussion of the various types of missile guidance systems has been presented. General comments were made on the more obvious advantages and disadvantages of each system. Emphasis has been placed on infrared guidance systems for use in a manned-aircraft defense application of a PYE WACKET missile. Problem areas and techniques for improving IR systems are also discussed. Finally, the results of the controls, subsection 3.7, and the IR guidance method suggested in Section 2 are combined to show a possible intelligence and control system for a PYE WACKET missile for omnidirectional launch application to manned-aircraft defense.

It should be noted that the systems developed in this section are only possibilities. Actual decisions on a guidance system for a given missile will be greatly influenced by mission and development time period.

3.8.8 LIST OF REFERENCES

- 3.8.1 "Preliminary Investigation of Aerodynamic Heating Effects on an Infrared Window," December 1959, TM349-15 Convair-Pomona
- 3.8.2 "Infrared Study Summary and Conclusions," Volume V-A, Crosley Report No. 6654-58-11(V-A), Contract No. AF 33 (616)-5311
- 3.8.3 "Redeye Design Characteristics Inspection," 20-21 October 1959, Convair-Pomona
- 3.8.4 "Preliminary Study of Background Noise in the PbS Infrared Spectrum," TM-339-52-15, Convair-Pomona
- 3.8.5 "Redeye Target Radiation Test Report," TM-360-61, Convair-Pomona.

SECRET

3.8.15

SECRET

3.9 PERFORMANCE

This portion of the report deals with the performance characteristics of the PYE WACKET missile. These performance characteristics may be separated into two categories: (1) performance capabilities of PYE WACKET in the plane perpendicular to the missile planform and (2) performance capabilities of PYE WACKET in the plane of the missile planform. The first category deals with maximum maneuver capabilities. The second category deals with omnidirectional launch range capabilities. Since PYE WACKET is in the initial study stages, the performance criteria for these studies were flight time, range, Mach number, and maneuverability. In weapon system applications of PYE WACKET, performance would be evaluated in terms of kill probability against specific targets.

It should be noted that, in addition to this subsection, considerable performance data are spread throughout the other Design Feasibility subsection. In particular, subsections 3.4 and 3.7 contain performance analyses of importance. Subsection 3.4 investigates the effect of thickness-to-chord ratio on missile range and velocity-time history. Subsection 3.7 presents maneuver capabilities and transient flight conditions for feasible control systems.

3.9.1 NORMAL MANEUVERS

Normal maneuvers deal with performance capabilities of PYE WACKET in the plane of the missile planform as illustrated in Figure 3.9.1. The nomenclature used in the derivation of the normal maneuver equations is as follows:

- V = velocity vector, in feet per second
- T = thrust of the rocket engine, in pounds
- η_x = longitudinal acceleration, in g's
- η_z = acceleration normal to missile, in g's
- γ = angle between velocity vector and reference, in degrees
- ψ = angle between missile axis and reference, in degrees
- α = $\psi - \gamma$, angle of attack, in degrees
- A = normal acceleration, in g's per degree = $\frac{1481 \lambda M^2 C_{N\alpha} S}{W}$
- D = axial force, in pounds = $1481 \lambda M^2 S C_A$
- λ = static pressure ratio
- S = reference area, 19.634 FT²
- M = Mach number
- W = missile weight, in pounds
- $C_{N\alpha}$ = normal force coefficient, per degree
- C_A = axial force coefficient
- x-z = missile axes
- j-k = wind axes
- d-o = reference axes

SECRET

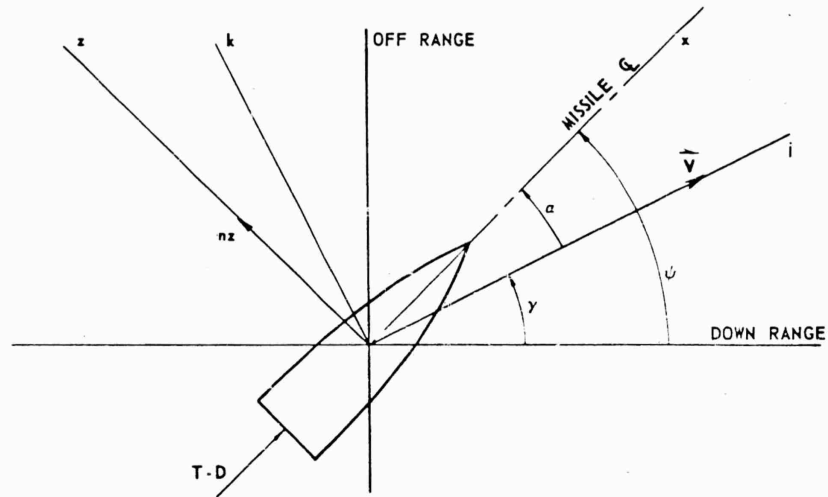


Figure 3.9.1. Missile Vertical Plane Geometry and Nomenclature.

The forces acting parallel to the missile thrust axis are

$$\sum F_x = ma_x = T - D \tag{3.9.1}$$

therefore acceleration, along the missile axis (η_x) is

$$\eta_x = \frac{T - D}{W}$$

The forces acting normal to the missile platform are

$$\sum F_z = ma_z = WA\alpha$$

therefore the normal acceleration (η_z) is

$$\eta_z = A\alpha \tag{3.9.2}$$

In Equation 3.9.2, the term, $A\alpha$, represents the normal acceleration, η_z , obtained aerodynamically from an angle of attack. Normal acceleration obtained from control forces is assumed to be negligible.

The transformation matrix from the missile axes, x-z; to wind axes, j-k, is

$$\begin{bmatrix} \eta_j \\ \eta_k \end{bmatrix} = \begin{bmatrix} \cos \alpha & -\sin \alpha \\ \sin \alpha & \cos \alpha \end{bmatrix} \begin{bmatrix} \eta_x \\ \eta_z \end{bmatrix}$$

where $\eta_j = \frac{\dot{v}}{g}$
 $\eta_k = \frac{v\dot{\sigma}}{g}$

SECRET

Performing the matrix expansion and substituting for η_j and η_k , there follows

$$\frac{\dot{v}}{g} = \eta_x \cos \alpha - \eta_z \sin \alpha \quad (3.9.3)$$

$$\frac{v\dot{\alpha}}{g} = \eta_x \sin \alpha + \eta_z \cos \alpha \quad (3.9.4)$$

The down-range and off-range are computed from the relationships

$$\text{down range} = \int v \cos \alpha dt \quad (3.9.5)$$

$$\text{off range} = \int v \sin \alpha dt \quad (3.9.6)$$

The independent input for lateral maneuvers is called-for acceleration. The autopilot simulation was kept extremely simple by assuming that the commanded and actual angle of attack were one and the same. In other words

$$\dot{\alpha} = \dot{\alpha}_c = K(\eta_{c\alpha} - \eta_\alpha)$$

where α_c = called-for angle of attack
 $\eta_{c\alpha}$ = called-for normal acceleration
 K = autopilot gain
 η_α = resulting normal acceleration

The closed-loop autopilot transfer function is then

$$\frac{\eta_\alpha}{\eta_{c\alpha}} = \frac{1}{\tau s + 1} \quad (3.9.7)$$

where, $\tau = \frac{1}{KA}$ = time constant. The gain, K , was chosen so as to make the system time constant no greater than 0.15 seconds over the range of the aerodynamic coefficient, A .

In summary, Equations 3.9.1 through 3.9.7 were utilized to simulate maneuvers in the plane perpendicular to the missile planform.

It should be noted that the effects of gravity were neglected for purposes of simplicity. Neglecting this one g normal force is within the accuracy to be obtained in a feasibility study of this nature. Also, the analog simulation was based on constant altitude maneuvers.

The analog computer simulation was set up in a manner to allow variations in all parameters associated with missile performance, both for normal maneuver and omnidirectional launch trajectories (to be discussed later). Figure 3.9.2 shows the analog patchboard mounted in the computer console and ready for operation. The Brush recorder on the right of the photograph is one of the two readout devices used. The other, not shown, is a two-dimensional plotting

SECRET

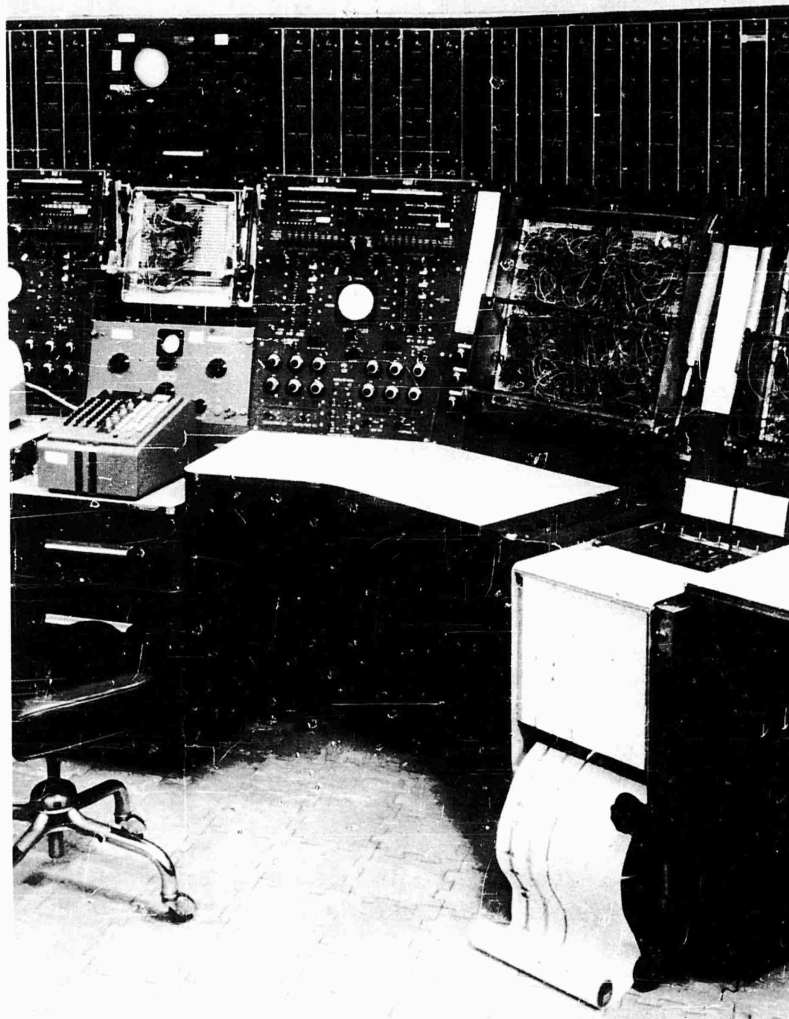


Figure 3.9.2. Analog Patchboard Mounted in Computer Console.

board. The switches and meters on the left are used to set the proper initial conditions, such as missile velocity, weight, altitude, and various flight angles, and to initiate the problem computation. The results of the analog computer studies were obtained from both readout devices. The plotting board presented the true single plane trajectory as a function of the single plane coordinates. Mach number and time were also shown on these traces. Brush recordings gave other detailed information of the missile angle of attack, acceleration, and flight geometry.

SECRET

Using the preceding equation maneuver trajectories were calculated on the analog computer for low altitude (30,000 feet), low launch velocity (800 FT/SEC), and high altitude (60,000 feet), high launch velocity (2500 FT/SEC) flight conditions. For these flight conditions, two 60-inch diameter missiles of 14 percent and 21 percent thickness ratio were investigated. These missiles correspond to the two 60-inch diameter feasible designs dealt with in subsection 3.10. Due to the necessity of programming the computer prior to the time that the final weights and balance statements were completed for the 60-inch diameter feasible design, first order estimates of the burnout (empty) missile weights were used in this study. These weights were 300 pounds for the 14 percent missile and 330 pounds for the 21 percent missile. In this study, the 14 percent and 21 percent missiles were flown at a maximum angle of attack limit of 30 degrees with a normal acceleration limit of 50 g's. Thus, at any instant during the trajectory, the angle of attack would be 30 degrees or less, compatible with a maximum of 50 g's of aerodynamic maneuver.

Figure 3.9.3 presents trajectories at an altitude of 30,000 feet for the 14 percent and 21 percent missiles when launched forward with an initial velocity of 800 FT/SEC. The 14 percent missile had a thrust of 9700 pounds with a burning time of 7.7 seconds. The 21 percent missile used a thrust of 14,500 pounds with a burning time of 8.5 seconds. From a maneuver standpoint, the 14 percent missile is slightly superior in that it can turn inside the 21 percent missile for the constraints placed on the missile (i.e., 30° angle of attack and 50 g's load factor). Two factors make it possible for the 14 percent missile to perform a tighter turn than the 21 percent missile. The first is the lower mass of the 14 percent missile; the second is the lower velocity of the 14 percent missile. In both the 14 percent and 21 percent cases, the normal force generated aerodynamically is approximately the same. It should be noted that, if the constraints (angle of attack and g limits) of the system were lifted or enlarged, the 21 percent missile would outperform the 14 percent missile. The times and Mach numbers at three points on each trajectory are noted. It can be seen that, for these cases, the missile turns through at least 270° before burnout.

Figure 3.9.4 presents data for 14 percent and 21 percent configurations at 30,000 feet with double the thrust and half the burning time of Figure 3.9.3. The total impulse is therefore identical for Figures 3.9.3 and 3.9.4. In Figure 3.9.4, the 14 percent configuration is again able to turn inside the 21 percent configuration due to the constraints placed on the system. Comparing Figures 3.9.3 and 3.9.4, it can be seen that the increased thrust increased the velocity and, as a result, there is a greater radius of turn for both configurations of Figure 3.9.4. A lower thrust over a longer period of time, will result in a lower velocity and smaller turning radius for the constraints imposed (i.e., $\alpha = 30^\circ$, $\eta_z = 50$ g's). As in the previous figure, removing the constraints could appreciably alter the form of these trajectories.

SECRET

SECRET

Figures 3.9.5 presents data for the 14 percent and 21 percent configurations with the low level thrust and longer burning time at 60,000 feet. The aerodynamic maneuver capability at the higher altitude is decreased by the ratio of the static pressures at 30,000 and 60,000 feet. Also, the velocity along each of the trajectories is increased due to the decreased drag. As a result of the decreased aerodynamic forces available, and the increased velocities, the turn radii are considerably increased for both configurations.

Figure 3.9.6 presents trajectory data for a maximum maneuver at 60,000 feet using the high level thrust and the shorter burning time. As at 30,000 feet, the ability to turn is reduced because of the increased velocities.

Figures 3.9.3 through 3.9.6 illustrate the maneuver capabilities of particular PYE WACKET designs. It is interesting to note that even with the PYE WACKET configuration, which is a very effective high-lift body, extremely long times are required to realize large turn angles. Moreover, large decreases in Mach number result from the penalty incurred by induced drag. In the analysis of omnidirectional launch capabilities that follows, it should be noted that a point in space can be reached much more rapidly and at less velocity loss by programming the direction of the thrust vector.

3.9.2 OMNIDIRECTIONAL LAUNCH TRAJECTORIES

Omnidirectional launch trajectories deal with performance capabilities of PYE WACKET configurations in the plane of the missile planform. Figure 3.9.7 shows the geometry used in the development of the equations simulated for omnidirectional launch. Definitions of variables used in these studies are as follows:

- T = thrust, constant between $t = 0$ and $t = t_B$, pounds
 C_D = zero lift drag coefficient = $\frac{D}{\frac{\rho}{2} V^2 S}$
 D = drag, pounds
 $\frac{D}{m}$ = $-KV^2 C_D$
 K = $\frac{\rho S}{2m}$ = constant for any trajectory
 a_s = speed of sound, feet/second
 t = time, seconds
 t_b = burning time, seconds
 V_0 = initial velocity, feet per second
 V = instantaneous velocity, feet per second
 V_B = velocity component due to thrust at end of boost, feet per second
 V_R = resultant velocity at end of boost, feet per second
 ϕ = angle between initial velocity and thrust centerline, degrees

SECRET

3.9.7

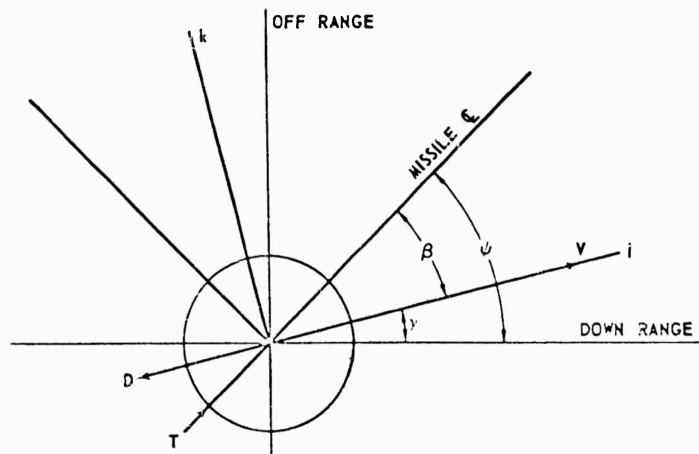


Figure 3.9.7. Missile Planform Plane Geometry and Nomenclature.

- γ = angle between velocity and initial velocity, degrees
 β = angle between velocity and thrust centerline, degrees
 W = missile weight, pounds
 m = instantaneous mass, slugs
 m_0 = initial mass, slugs
 m_f = final mass, slugs

The forces acting on the missile are: thrust, directed along the missile centerline, and drag which acts opposite to the instantaneous velocity vector. As in the previous derivation, gravity was neglected. Adequate control in pitch and roll was also assumed. The accelerations along the missile thrust axis may be expressed as

$$m_f = \frac{\dot{v}}{g} = \frac{T}{W} \cos \beta - \frac{D}{W} \quad (3.9.8)$$

The acceleration normal to the missile axis is

$$m_k = \frac{v\ddot{\epsilon}}{g} = \frac{T}{W} \sin \beta \quad (3.9.9)$$

The down-range and off-range values are computed from the relationships

$$\begin{aligned} \text{down range} &= \int v \cos \alpha dt \\ \text{off range} &= \int v \sin \alpha dt \end{aligned} \quad (3.9.10)$$

SECRET

The equation describing the omni-launch angle is the geometric relationship

$$\psi = \beta + \delta \quad (3.9.11)$$

Equations 3.9.8 through 3.9.11 were simulated on the analog computer to determine omni-launch performance.

An analytical calculation was also performed to determine the omni-launch trajectories in an idealized case of a missile propelled by an impulsive thrust, that is, infinite thrust for zero burning time. The results of this derivation are:

$$V = \frac{(AV_R + B)e^{-AK(t-t_B)} - B}{A}$$
$$R = \frac{1}{AK} \left[V_R - V + \frac{B}{A} \ln \left(\frac{AV + B}{AV_R + B} \right) \right]$$

where A, B, and K are constants used in the simulation of the vehicle drag

$$V_R = \sqrt{V_B^2 + V_0^2 + 2V_0V_B \cos \psi}$$
$$V_B = \frac{I}{m_p} \ln \left(\frac{m_0}{m_f} \right)$$

Using the above equations the velocity (V) at any time (t) may be determined as a function of the missile drag constants (A, K and B) and the resulting velocity at end of boost (V_R). Since burning time (t_B) is assumed equal to zero

$$t - t_B = t$$

The range at any time, t, may be determined as a function of the resulting velocity at end of boost, V_R, and the velocity, V, at the time, t. Since the burning time, t_B, is assumed equal to zero, the range during burning is zero.

The conversion from range to down-range and off-range is achieved as follows:

$$\text{down range} = R \cos \delta$$

$$\text{off range} = R \sin \delta$$

Using the above equations, the omnidirectional launch trajectories of PYE WACKET were investigated. The purpose of this investigation was to show the standoff distances available from feasible designs of the PYE WACKET employing omnidirectional launch. In addition, the velocity-time relationship was desired for any launch angle.

In this investigation, it was necessary to assume certain weights and total impulses. Three PYE WACKET missiles were selected for investigation. These three correspond to the three feasible designs dealt with in subsection 3.10. Due to the necessity of programming the computer prior to the time that the final weight and balance statements were completed for the feasible designs, first order

SECRET

estimates were used in this study. As it turned out, these estimates are fairly close to the actual weight and balance statements of subsection 3.10.

The characteristics of the three configurations used in this analysis are given in Table 3.9.1.

Table 3.9.1
PYE WACKET CONFIGURATION INVESTIGATED

Configuration	t/C (percent)	Diameter (inches)	W full (pounds)	W empty (pounds)	I total (LB-SEC)
A	14	60	600	300	74,600
B	21	60	850	330	123,250
C	21	36	200	100	26,000

Each of the three configurations was studied at three altitudes with a constant launch velocity. These conditions are given in Table 3.9.2.

Table 3.9.2
STUDY CONDITIONS

Condition	Altitude Feet	V _{Launch} (FT/SEC)
1	30,000	800
2	60,000	2500
3	90,000	2500

The conditions and objectives of the omnidirectional launch studies are summarized in Table 3.9.3. As noted, Figures 3.9.8 through 3.9.23 concern a 60-inch diameter missile and Figures 3.9.24, 3.9.25, and 3.9.26 concern one that is 36 inches in diameter.

Figures 3.9.8 through 3.9.15 show performance envelopes of the 14 percent and 21 percent missile for flight at altitudes of 30,000 and 60,000 feet. In these curves, the boost phase of flight receives special treatment due to the rapidly changing flight conditions during this phase of flight. As noted in Table 3.9.3, a fixed thrust and burning time was considered for each of the missiles.

SECRET

Table 3.9.3
OMNIDIRECTIONAL LAUNCH STUDY

Figure	Missile Characteristics		Propulsion Characteristics			Launch Conditions		Flight Time Covered	Comments
	Diameter (inches)	t/C (percent)	Total Impulse (LB/SEC)	Thrust (LBS)	Burning Time (SEC)	Altitude (feet)	Launch Velocity (FT/SEC)		
3.9.8	60	14	74,600	9,700	7.70	30,000	800	Total flight	60-inch diameter performance
3.9.9	60	14	74,600	9,700	7.70	30,000	800	Boost phase only	
3.9.10	60	21	123,250	14,500	8.50	30,000	800	Total flight	
3.9.11	60	21	123,250	14,500	8.50	30,000	800	Boost phase only	
3.9.12	60	14	74,600	9,700	7.70	60,000	2500	Total flight	
3.9.13	60	14	74,600	9,700	7.70	60,000	2500	Boost phase only	
3.9.14	60	21	123,250	14,500	8.50	60,000	2500	Total flight	
3.9.15	60	21	123,250	14,500	8.50	60,000	2500	Boost phase only	
3.9.16	60	14	74,600	Variable	Variable	30,000	800	Total flight	Effects of burning time

SECRET

Figure	Missile Characteristics		Propulsion Characteristics			Launch Conditions		Flight Time Covered	Comments
	Diameter (inches)	t/C (percent)	Total Impulse (LB/SEC)	Thrust (LBS)	Burning Time (SEC)	Altitude (feet)	Launch Velocity (FT/SEC)		
3.9.17	60	14	74,600	Variable	Variable	60,000	800	Total flight	Effects of burning time
3.9.18	60	14	74,600			90,000	800		
3.9.19	60	21	123,250			30,000	800		
3.9.20	60	21	123,250			60,000	800		
3.9.21	60	21	123,250			90,000	800		
3.9.22	60	14	74,600	9,700	7.70	30,000	800		Comparison of t/C;
		21	123,250	14,500	8.50	30,000	800		
3.9.23	60	14	74,600	9,700	7.70	60,000	2500		
		21	123,250	14,500	8.50	60,000	2500		
3.9.24	36	21	26,000	5,000	5.20	30,000	800		36 inch diameter performance
3.9.25	36	21	26,000	5,000	5.20	60,000	2500		
3.9.26	36	21	26,000	5,000	5.20	90,000	2500		

SECRET

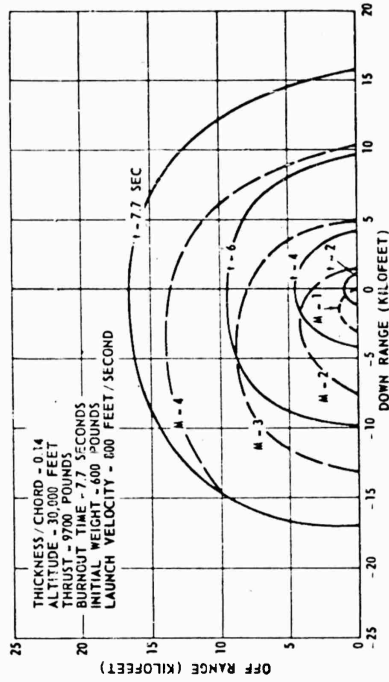


Figure 3.9.8. Omnidirectional Launch Thrust and Glide Phase Performance Envelopes.

SECRET

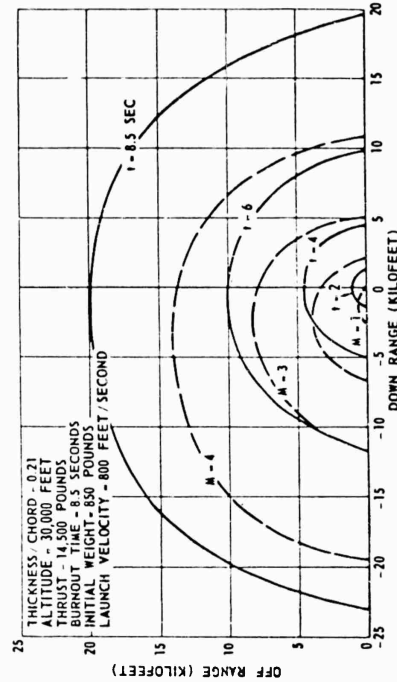


Figure 3.9.9. Omnidirectional Launch Thrust Phase Performance Envelope.

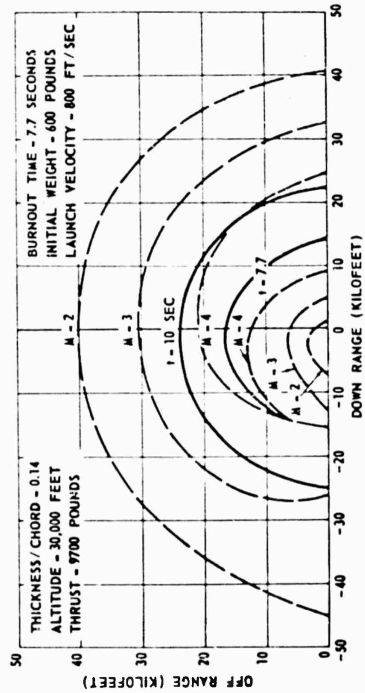


Figure 3.9.10. Omnidirectional Launch Thrust and Glide Phase Performance Envelopes.

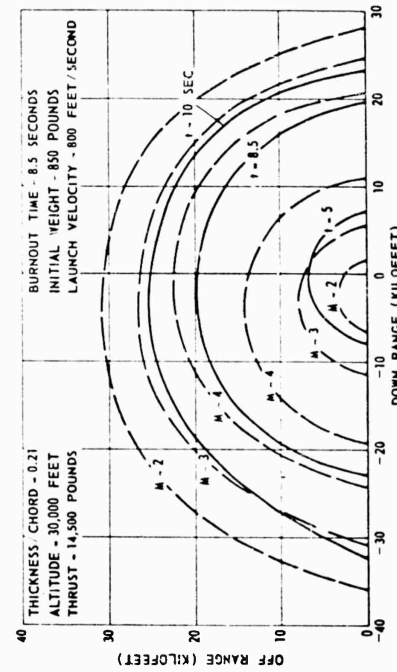


Figure 3.9.11. Omnidirectional Launch Thrust Phase Performance Envelope.

3.9.14

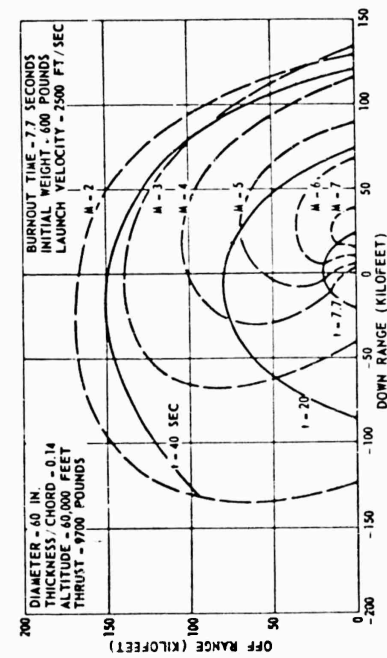


Figure 3.9.12. Omnidirectional Launch Performance Envelope.

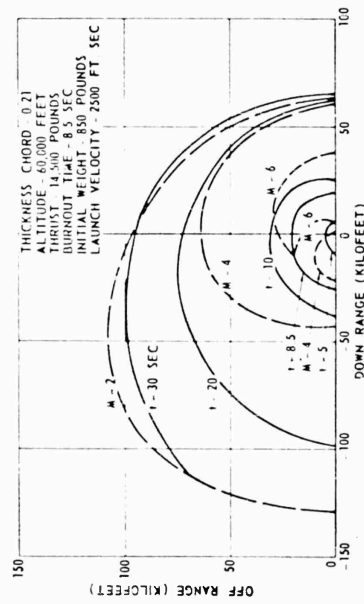


Figure 3.9.14. Omnidirectional Launch Thrust and Glide Phase Performance Envelope.

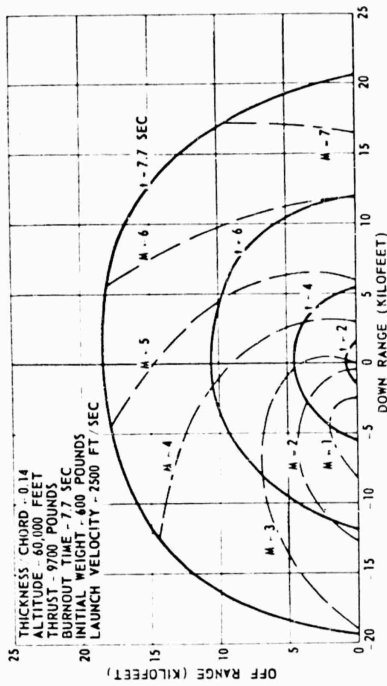


Figure 3.9.13. Omnidirectional Launch Thrust Phase Performance Envelope.

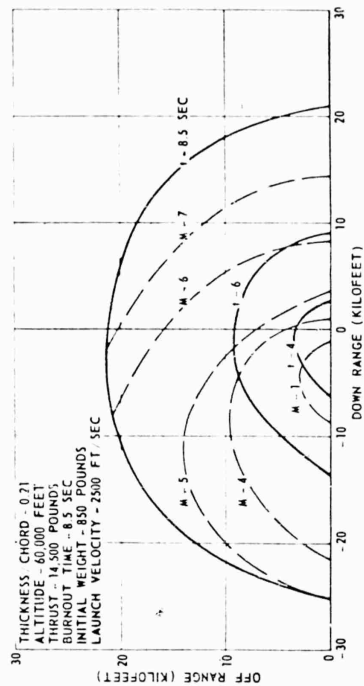


Figure 3.9.15. Omnidirectional Launch Thrust Phase Performance Envelope.

SECRET

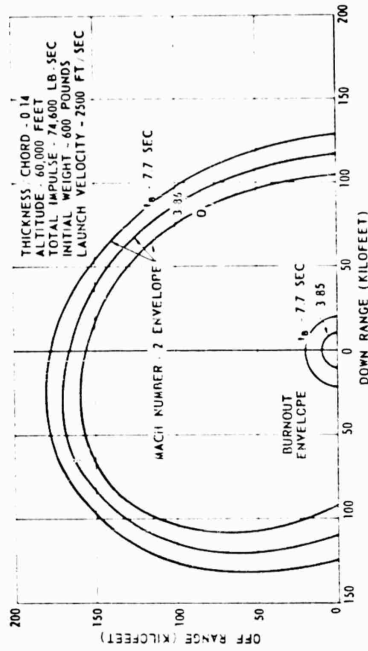


Figure 3.9.16. Omnidirectional Launch Thrust and Glide Phase Performance Envelopes for Various Burning Times.

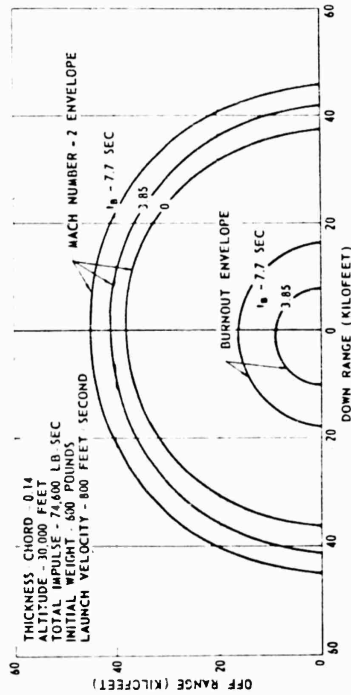


Figure 3.9.17. Omnidirectional Launch Thrust and Glide Phase Performance Envelopes for Various Burning Times.

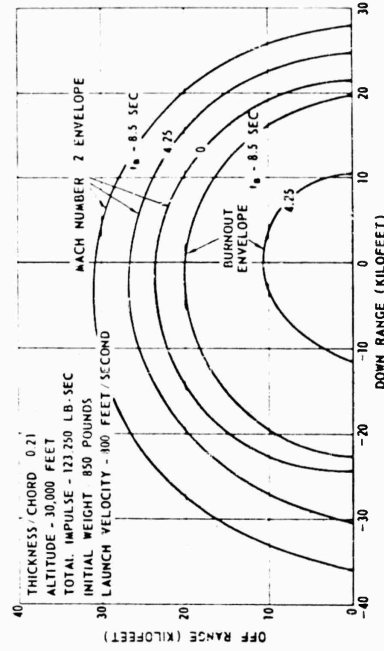


Figure 3.9.18. Omnidirectional Launch Thrust and Glide Phase Performance Envelopes for Various Burning Times.

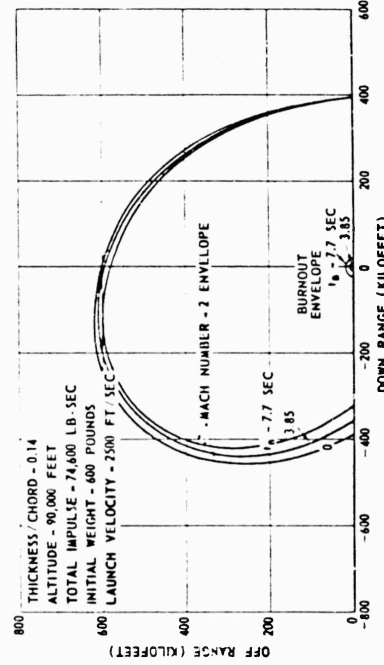


Figure 3.9.19. Omnidirectional Launch Thrust and Glide Phase Performance Envelopes for Various Burning Times.

SECRET

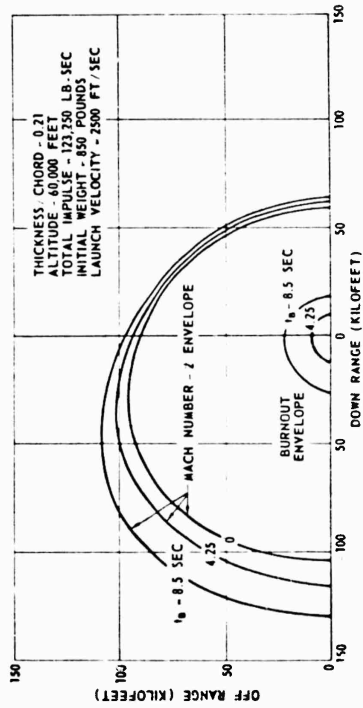


Figure 3.9.20. Omnidirectional Launch Thrust and Glide Phase Performance Envelopes for Various Burning Times.

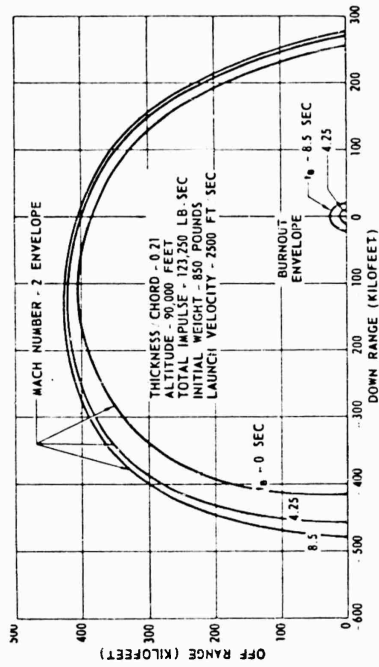


Figure 3.9.21. Omnidirectional Launch Thrust and Glide Phase Performance Envelopes for Various Burning Times.

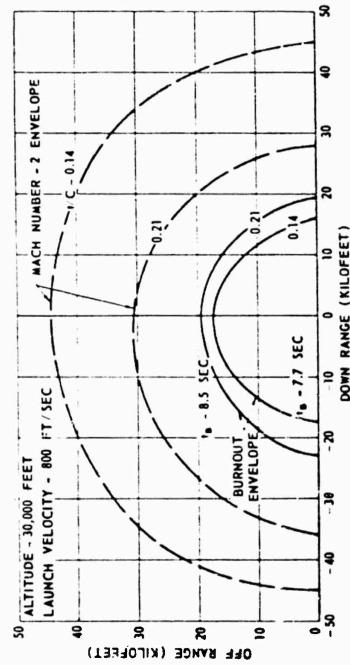


Figure 3.9.22. Omnidirectional Launch Thrust and Glide Phase Performance Envelopes for Different Thickness-to-Chord Ratios.

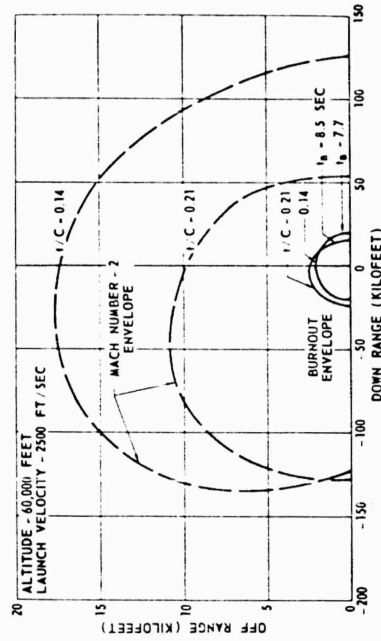


Figure 3.9.23. Omnidirectional Launch Thrust and Glide Phase Performance Envelopes for Different Thickness-to-Chord Ratios.

SECRET

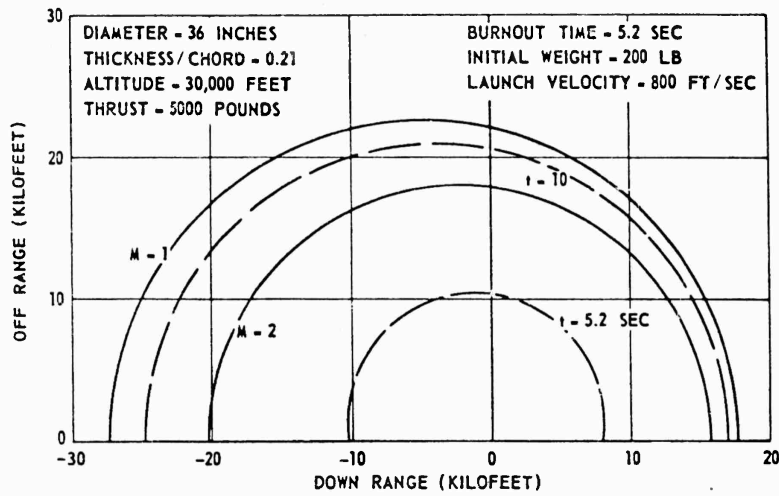


Figure 3.9.24. Omnidirectional Launch Performance Envelope.

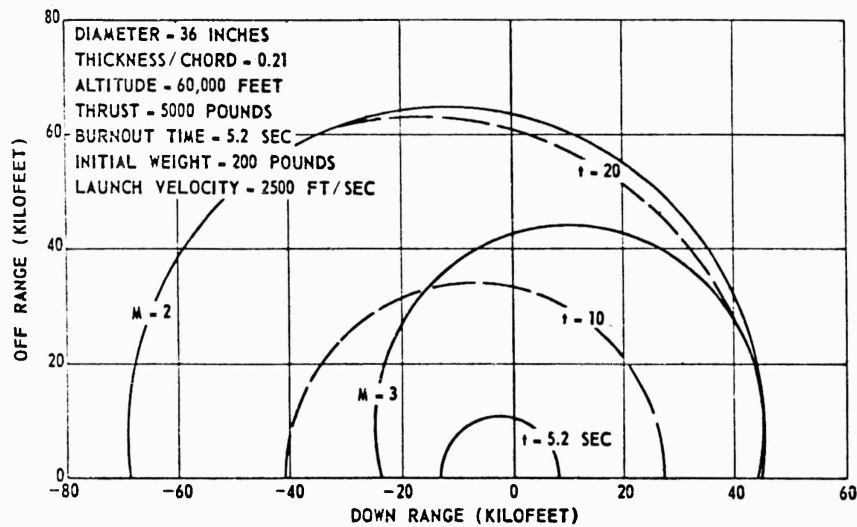


Figure 3.9.25. Omnidirectional Launch Performance Envelope.

Figures 3.9.16 through 3.9.21 present the effects of burning time on stand-off distance. Figures 3.9.16 through 3.9.18 are concerned with the 14 percent missile and Figures 3.9.19 through 3.9.21 are concerned with the 21 percent missile. Altitudes of 30,000, 60,000, and 90,000 feet are considered.

Figures 3.9.22 and 3.9.23 compare the performance envelopes of the two thickness ratios at altitudes of 30,000 feet and 60,000 feet respectively.

SECRET

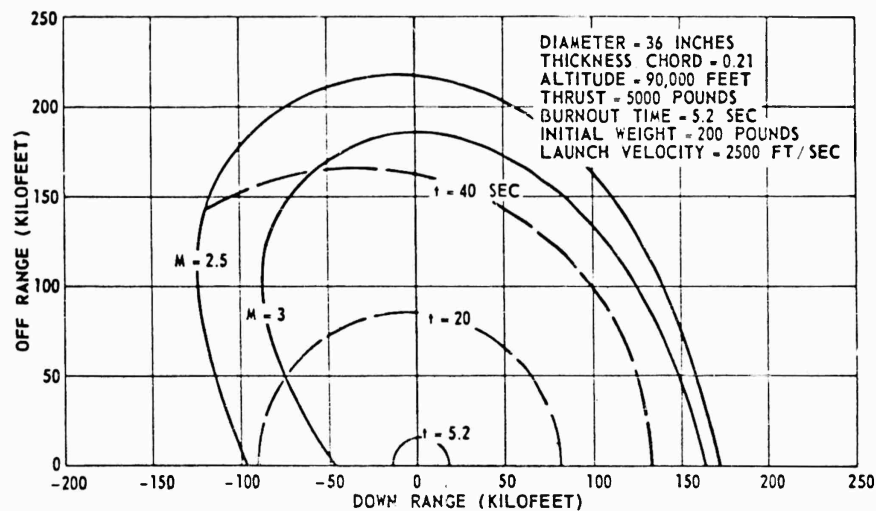


Figure 3.9.26. Omnidirectional Launch Performance Envelope.

Figures 3.9.24, 3.9.25, and 3.9.26 are concerned with a 36-inch diameter missile. These figures are intended to show the effects of altitude and launch velocity on the performance capabilities of the 36-inch diameter missile.

The performance data in the figures are presented in airplane coordinates. In these figures, the solid, circular lines represent constant time lines. The circular, broken lines represent constant Mach number lines. The data presented in each chart are a space-velocity-time history of the missiles. The areas contained within the Mach lines represent the space the missile can defend using the moving airplane as the origin. The exception is a small area immediately aft of the airplane marked, $M = 1$, in the performance charts covering the boost phase. In this area, the missile is operating below $M = 1$ and is in a region of rapidly changing stability margins and aerodynamic conditions.

Examination of the data in Figures 3.9.8 through 3.9.23 for the 60-inch diameter missile permits some generalizations to be made. Increasing burning time will increase the range at the end of boost. Increasing the altitude increases the range performance envelope for any one configuration. The performance envelopes are circular at the lower altitudes where lower launch velocities ($V_L = 800$ FT/SEC) are used. These become elliptical at the higher altitudes where launch velocities of 2500 FT/SEC are used. The slant ranges for the 14 percent configuration vary from approximately 40,000 feet to 120,000 feet. For the 21 percent configuration the ranges vary from approximately 25,000 feet to 60,000 feet.

Figures 3.9.16, 3.9.17, and 3.9.18 present the effects of propellant burning time on the performance envelopes for the 14 percent configuration at altitudes of 30,000 feet, 60,000 feet, and 90,000 feet. In these figures, total impulse was kept constant. At 30,000 feet, and 60,000 feet, reducing burning time reduces

SECRET

the outer performance envelope. However, at 90,000 feet, the situation is reversed. This reversal is due to the fact that, at 90,000 feet, the increased coast range due to the increased end-of-boost velocity for the shorter burning times exceeds the increase in longer boost ranges for the longer burning times, for the 14 percent missile. Also, at 90,000 feet, the effect of drag during the coast phase is much less than at the lower altitudes.

Figures 3.9.19, 3.9.20, and 3.9.21 present the effects of propellant burning time on the performance envelopes for the 21 percent configuration at 30,000 feet, 60,000 feet, and 90,000 feet. Again, total impulse was kept constant. For the 21 percent missile configuration, increasing the propellant burning time increases the range at all altitudes considered. This is because the drag of the 21 percent configuration is greater than the drag of the 14 percent configuration.

Figure 3.9.22 presents a comparison of the burnout range envelopes at $M = 2$ for 30,000 feet, for the 14 percent and 21 percent configurations. It can be seen that the range for the 14 percent configuration is greater by 65 percent, the increase in range is due to the significant effect of drag during the coast phase. The drag of the 21 percent configuration is approximately 2.5 times the drag of the 14 percent configuration. This increased drag offsets the advantage in total impulse. It should be noted, however, that the range at burnout is greater for the 21 percent missile as a result of its higher impulse and longer burning time.

Figure 3.9.23 is a comparison of the outer and burnout envelopes for the 14 percent and 21 percent configurations at a 60,000 foot altitudes. It can be seen in the figure, that there is very little difference in performance at burnout. The 14 percent configuration has a 4000 foot advantage in the forward launch while the 21 percent configuration has a 4000 foot advantage in the lateral and aft directions. The advantage exhibited by the 14 percent configuration in the forward direction, is due to its lower drag. As a result, it reaches a higher peak velocity, hence covers more distance. It should be noted that for aft launch, the drag acts in the same direction as the thrust. Hence, the larger drag of the 21 percent missile is an appreciable factor in nullifying the initial velocity. After the initial velocity is nullified, the 21 percent configuration still has sufficient impulse left to accelerate to a significant velocity and reach a greater range than the 14 percent configuration. In the outer performance envelope, the 14 percent configuration is significantly superior in all directions except directly aft. Again, the reduced drag of the 14 percent configuration is responsible for the range advantage. In the aft direction, the capabilities of the 14 percent and 21 percent configurations are equal.

Performance data for the 36-inch diameter, 21 percent missile are presented in Figures 3.9.24, 3.9.25, and 3.9.26. These data indicate the performance capabilities for smaller missiles.

Figure 3.9.24 presents the performance data for a PYE WACKET configuration launched at an altitude of 30,000 feet with a forward velocity of 800 FT/SEC.

SECRET

3.9.19

From the points of launch, these data show the $M = 1$ performance boundary to be from -27,200 feet to +17,600 feet down-range and $\pm 22,600$ feet off-range. The time to reach this envelope is approximately 11 seconds from launch. At burnout, $t = 5.2$ seconds, the missile would be capable of defending an area from -10,400 feet to +8000 feet down-range and $\pm 10,400$ feet off-range. Maximum Mach numbers on the order of $M = 3$ to 4.5 are achieved at this altitude.

Figure 3.9.25 shows the performance data for the 36-inch diameter configuration when launched at 60,000 feet with a velocity of 2500 FT/SEC. The $M = 2$ envelope in this performance chart extends from -68,000 feet to -45,000 feet down-range and $\pm 64,000$ feet off-range. The increased ranges at this altitude are the result of the increased launch velocity and the decreased drag. The flight times to reach this outer envelope range from approximately 12 to 22 seconds. The ranges at burnout extend from -13,000 feet to -8,000 feet down-range and $\pm 10,000$ feet off-range. Maximum Mach numbers of the order of 3 to 6 are achieved at this altitude.

Figure 3.9.26 presents data for launching the 36-inch diameter missile at a velocity of 2500 FT/SEC at an altitude of 90,000 FT. Examination of these data indicate a range capability from -97,500 feet to -175,000 feet for a terminal Mach number of $M = 2.5$. The flight times along this outer envelope range from 25 to 85 seconds depending on the direction of launch. The maximum Mach numbers achieved range from $M = 4$ to $M = 7$ at burnout depending on the launch direction.

3.9.3 SUMMARY

This portion of the report presents performance analyses that are not covered in sufficient detail in other subsections of the Design Feasibility Studies. As noted earlier, considerable performance data are spread throughout the other Design Feasibility subsections of the report. Due to the basic nature of these data it was not advisable to separate them from the dependent study areas.

This part of the report is limited to investigation of PYE WACKET maneuver capabilities and omnidirectional launch range capabilities. An investigation of aerodynamic and reaction controls is presented in subsection 3.7. Subsection 3.4 investigates the effects of thickness-to-chord ratio on missile range and velocity-time history.

The performance investigations have shown that:

1. Using omnidirectional launch, protection for manned aircraft can be obtained for all approaches of attack.
2. In the case of a 60-inch diameter missile, stand-off distances of the order of 40,000 feet to 120,000 feet can be obtained with a 14 percent configuration at altitudes of 30,000 and 60,000 feet, respectively. Stand-off distances of the order of 25,000 feet to 60,000 feet can be obtained with a 21 percent configuration at altitudes of 30,000 and 60,000 feet, respectively.

SECRET

3. A reduction in missile size from 60 inches to 36 inches can be made without an excessive penalty in stand-off distance if advanced techniques and materials are used. Stand-off distances of the order of 20,000 feet to 50,000 feet can be obtained at altitudes of 30,000 feet and 60,000 feet, respectively.
4. High maneuver capabilities are available from the PYE WACKET configuration at all altitudes studied.

SECRET

3.9.21

SECRET

3.10 FEASIBLE DESIGNS

In the previous subsections technical studies were carried to the point of determining the feasibility of specific concepts organic to a PYE WACKET vehicle. The reader has been cautioned that in reviewing these subsections the re-cycling of the parameters was taken only to the stage of determining technical feasibility. In a quantitative sense this has resulted in some inconsistency of detail that must be adjusted to a common basis when the design of an actual and specific vehicle is initiated. With this in mind, attention is now directed to possible design concepts that are a result of the technical feasibility studies.

The purpose of this subsection is to investigate the design feasibility of the PYE WACKET configuration by introducing component design layouts which consider not only the performance aspects of the configuration but also the practical aspects of component availability and packaging requirements.

These layouts, Figures 3.10.1 and 3.10.2 were limited to the blunted lenticular configuration (Model III) as determined by the studies reported in subsection 3.2 of this report. A nominal 60-inch diameter missile was selected for these layouts due to the emphasis placed on this dimension by R and D Exhibit PGEM 58-162. Only thickness-to-chord ratios of 14 percent and 21 percent were considered for these layouts since studies discussed earlier in subsection 3.4 indicate that the performance capabilities of missiles with these thickness ratios span the range of interest for PYE WACKET on the bases of maximum range capability, minimum time-to-target intercept, and packaging limits.

Using these two thickness ratios, approximate missile weights and performance capabilities were determined as functions of the missile diameter. The range of missile diameters considered was limited to 30 inches to 120 inches. The scaling was accomplished by utilizing the weight determination of the nominal 60-inch diameter missiles of 14 percent and 21 percent thickness ratios as the bases for all scaled weight determinations. It should be pointed out that data derived from scaling the 60-inch diameter vehicle gives approximate results only and should not be considered as firm design or performance data.

Figure 3.10.3 shows gross weight versus vehicle diameter based on the 60-inch diameter configuration. Range capability versus diameter is presented in Figure 3.10.4. Results of this feasibility design study of the 14 percent and 21 percent 60-inch diameter missiles have shown that the PYE WACKET configuration is feasible as an airborne weapon for manned aircraft defense and for other uses, where omnidirectional launch has particular advantages. The contents of this subsection are:

1. Nominal Missile Layouts. Detailed component breakdown and layouts of the nominal 14 percent and 21 percent, 60-inch diameter missiles.
2. Design Scaling. Design scaling techniques for each major missile component. The component groups were arranged as follows:

SECRET

3.10.1

- a. Structural Group
- b. Rocket Motor Group
- c. Control System Group
- d. Electronics Section
- e. Fuze System
- f. Battery Power Supply
- g. Ablative Surface Material
- h. Miscellaneous Weights Group

The warhead weight was not scaled but was treated parametrically since an adequate warhead can only be defined for the scaled missiles on the bases of specific missions and targets.

The design scaling techniques developed for each component group were applied to the determination of the variation of the weight of each group as a function of missile diameter within the scaling range of diameter from 30 to 120 inches.

3. Effect of Scaling on Performance. Effect of missile diameter on such performance characteristics as time to target, stand-off distances, and range at terminal velocity. The variations of missile performance with missile diameter were next determined using the results of the design scaling study.
4. Small Missile Configuration. The design scaling mentioned above employs the latest techniques and materials which can be applied to missile design immediately. Of additional interest is what can be accomplished by utilizing advance techniques and improved materials. As a result of this scaling it was apparent that a smaller diameter missile is feasible so that by employing advanced techniques and materials the performance of the nominal 60-inch diameter 21 percent missile could be approached by a missile of 36 inches diameter. To indicate what may be expected in an advanced design a detailed layout was made of a 36-inch diameter 21 percent missile.

This smaller size could reduce missile cost, increase the number of missiles which can be carried by a particular aircraft, and minimize the handling, stowage, and launching problems.

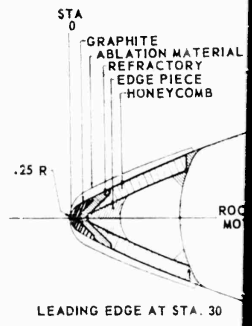
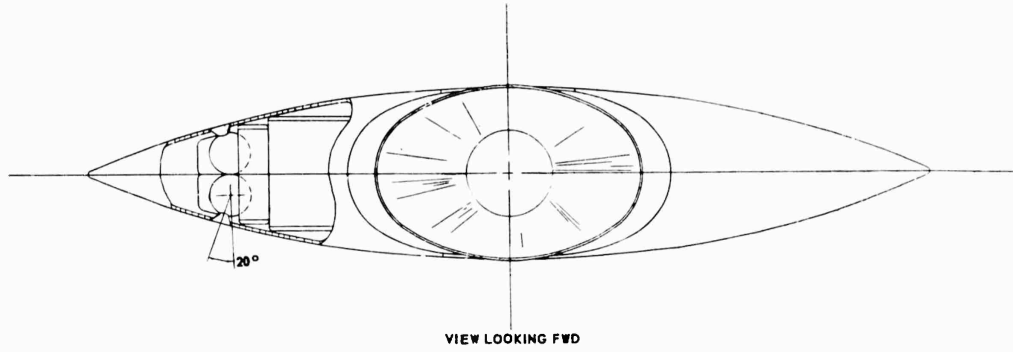
3.10.1 FEASIBILITY DESIGN OF NOMINAL MISSILES

Preliminary layouts were made of the 14 percent and 21 percent missiles having the nominal 60-inch diameter as outlined above. The purpose of these feasibility designs is to provide preliminary indications of what is achievable in tactical versions of the PYE WACKET configuration and to form a basis for the design and performance scaling study that follows.

A complete detailed preliminary design of the PYE WACKET missile could not be made during this study due to time limitations, but preliminary layouts

3.10.2

SECRET



1

SECRET

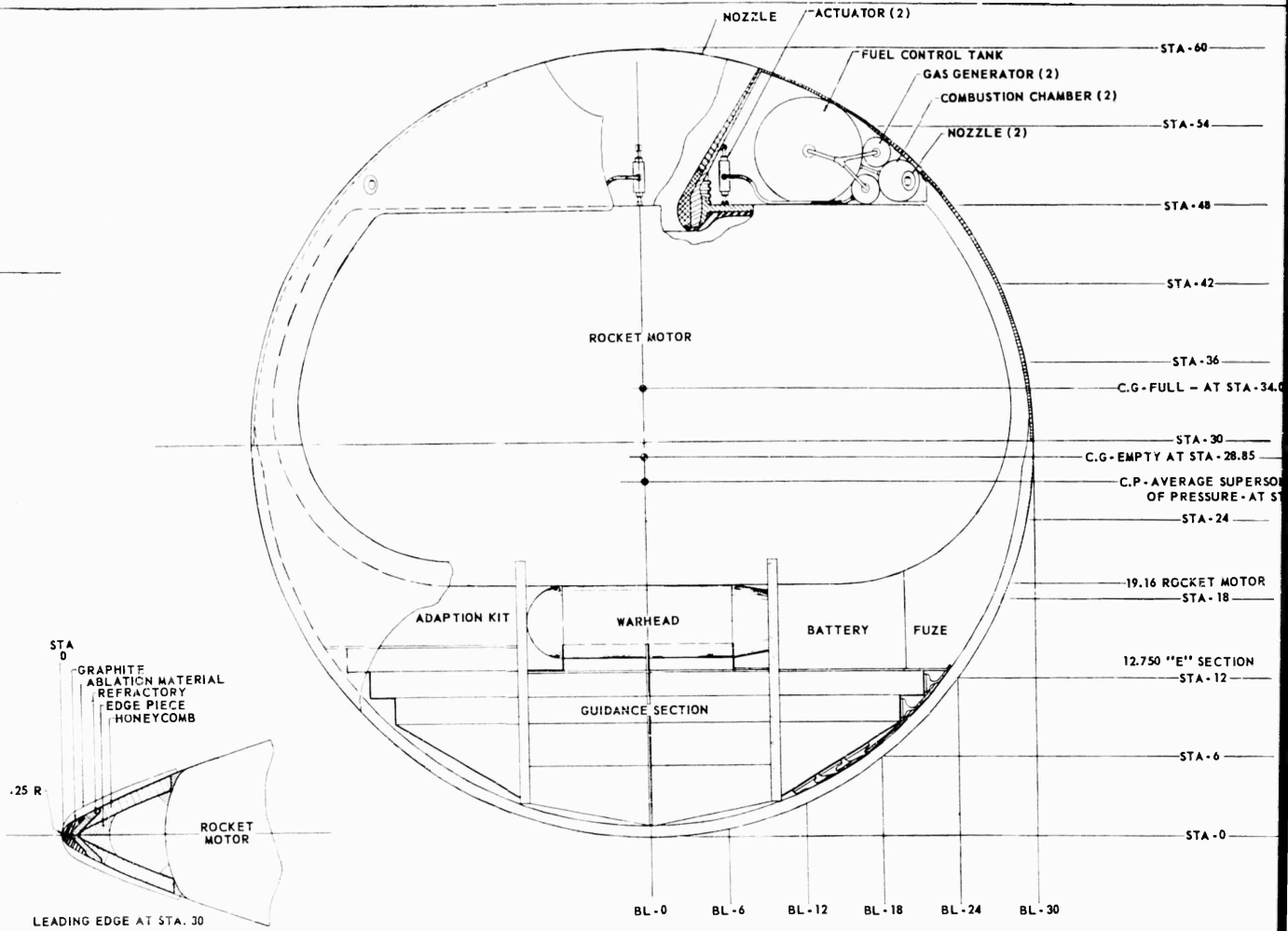


Figure 3.10.1. Feasibility Layout of 60-Inch Diameter

2

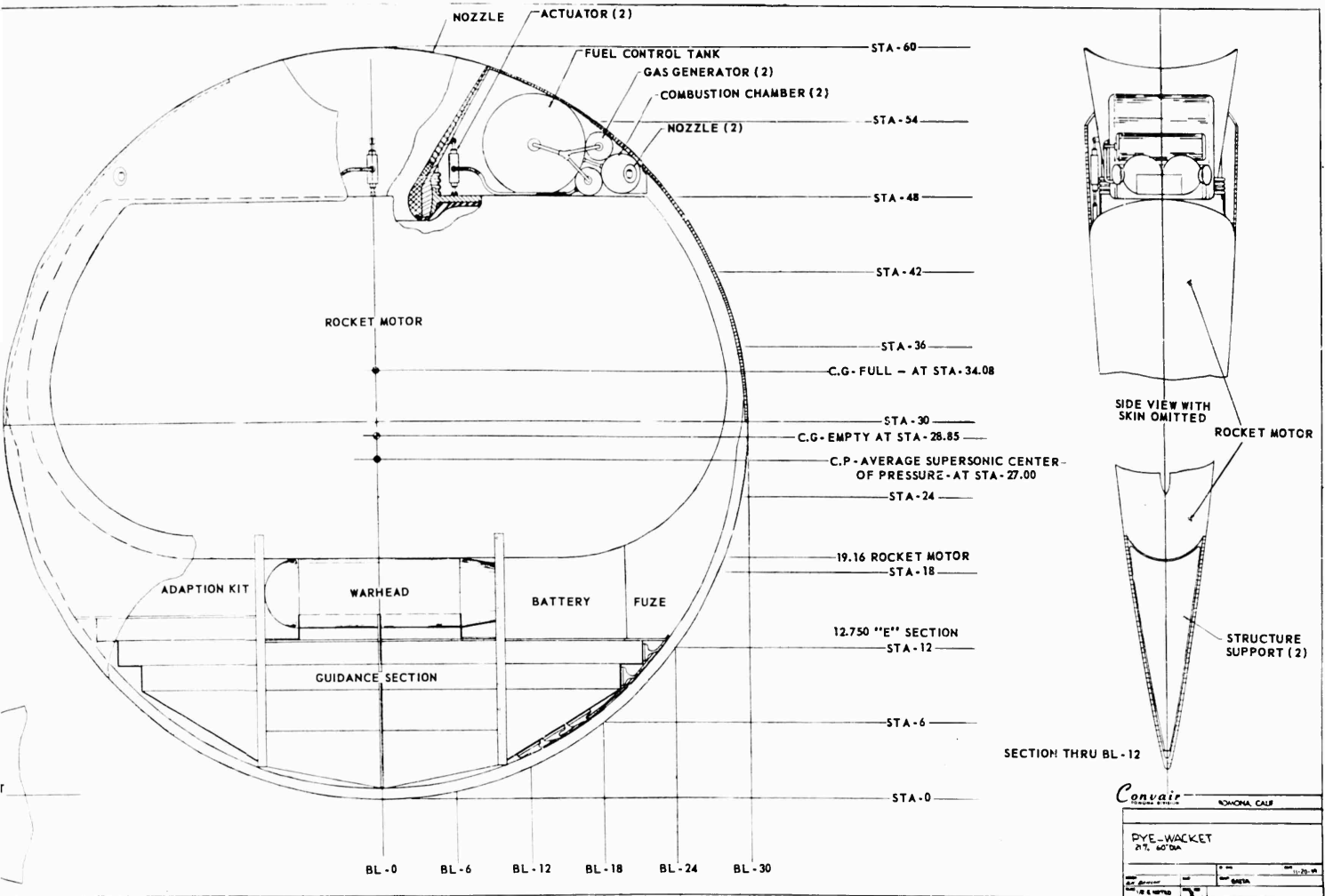
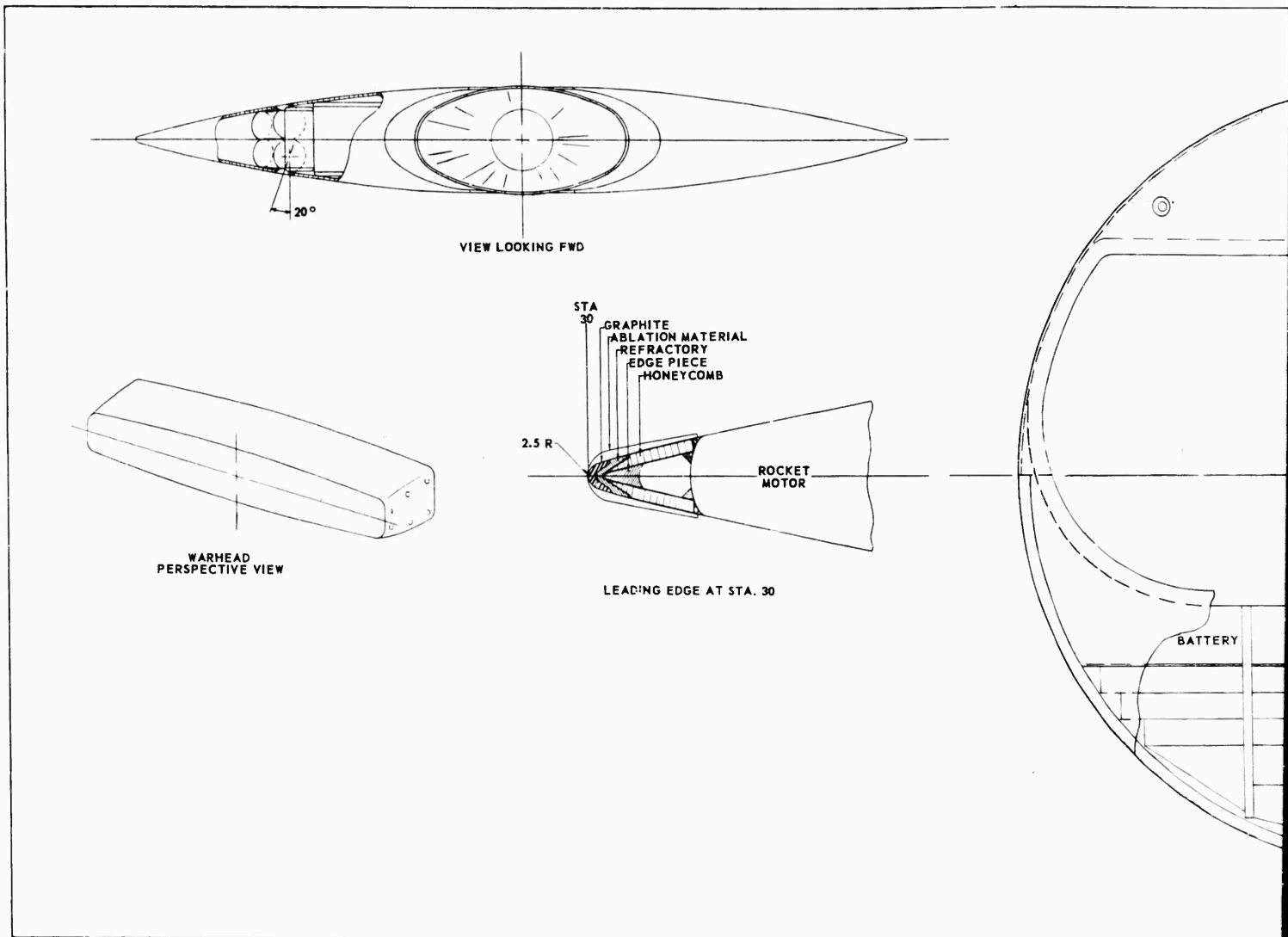


Figure 3.10.1. Feasibility Layout of 60-Inch Diameter 21 Percent PYE WACKET Missile.

3

SECRET



1

SECRET

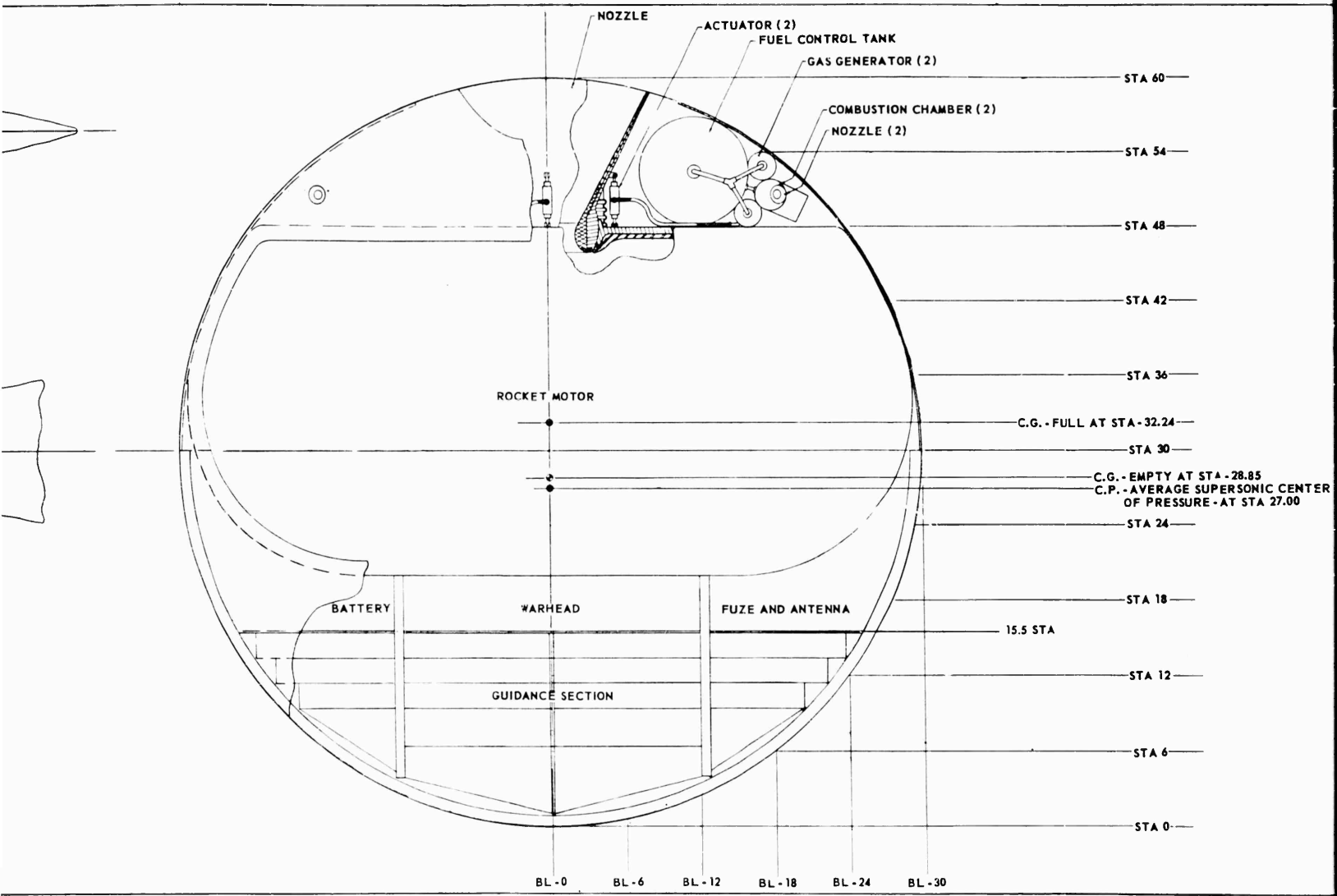


Figure 3.10.2. Feasibility Layout of 60-Inch

2

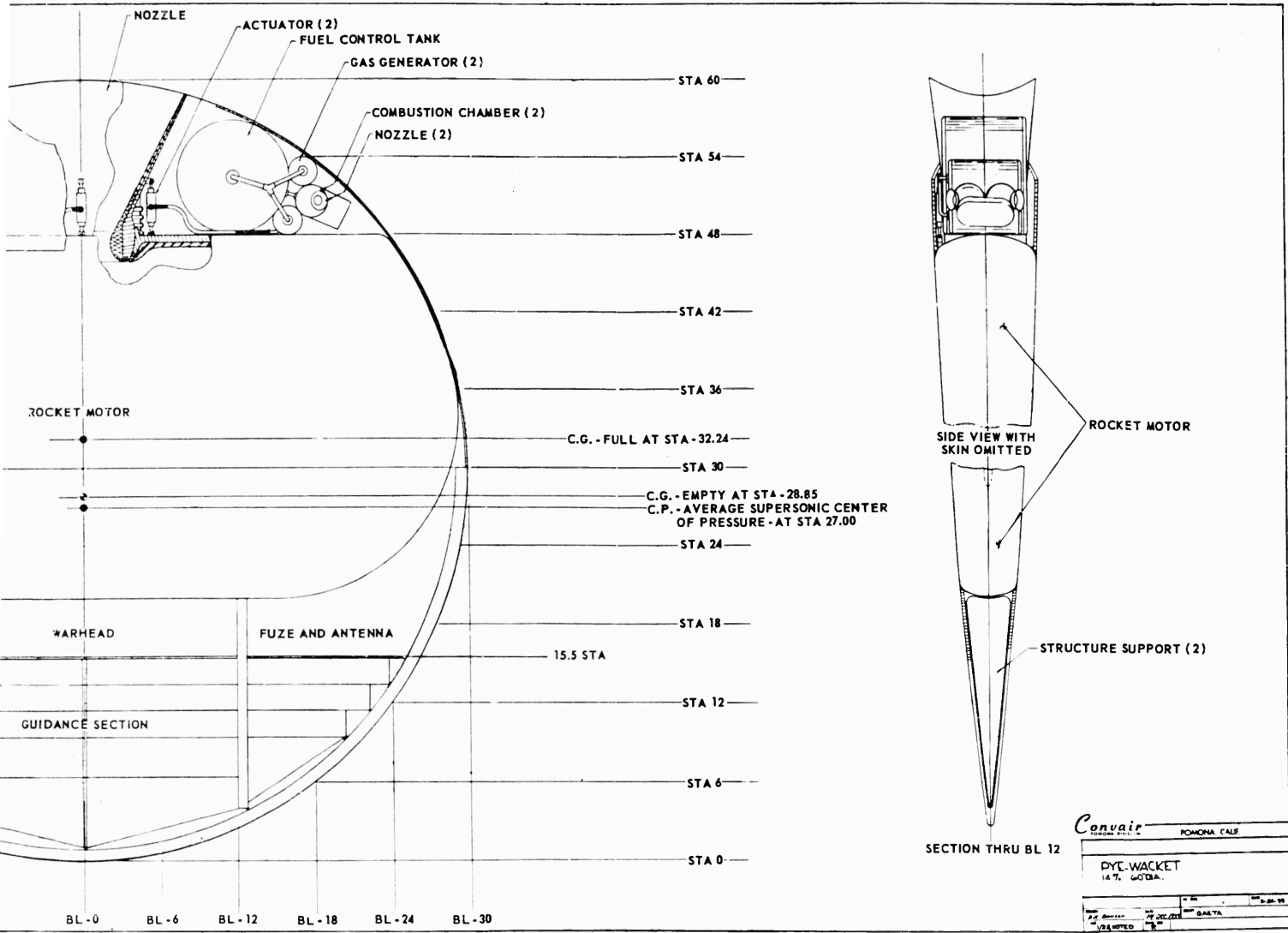


Figure 3.10.2. Feasibility Layout of 60-Inch Diameter 14 Percent PYE WACKET Missile.

3

SECRET

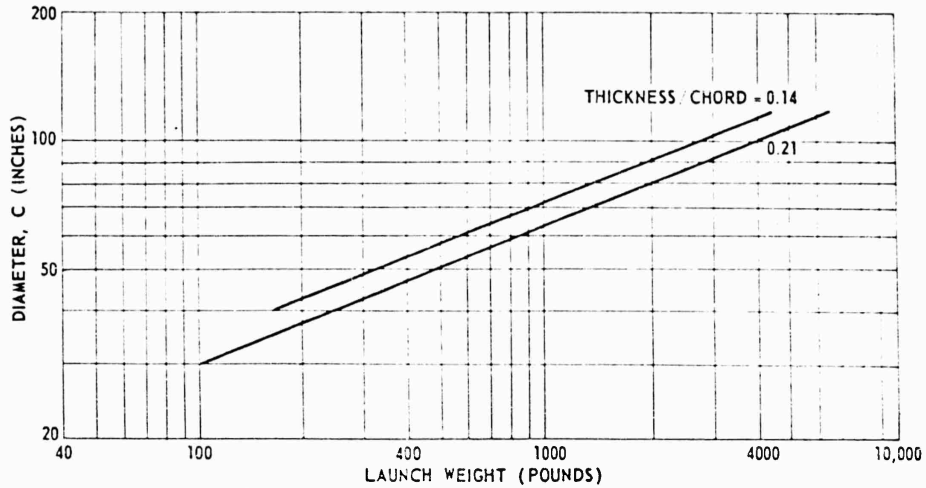


Figure 3.10.3. Scaled Launch Weights.

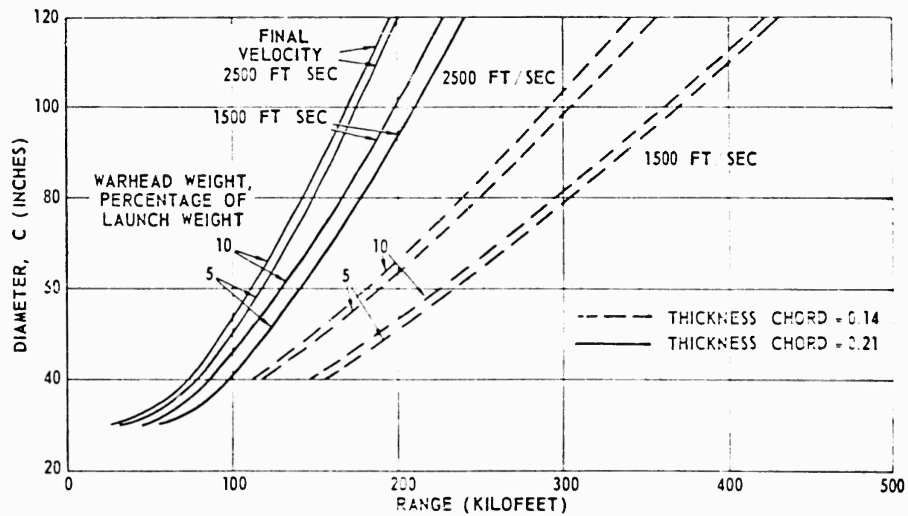


Figure 3.10.4. Scaled Range Performance.

indicate that the PYE WACKET concept is feasible, as an airborne weapon. All necessary components can be packaged in the PYE WACKET configuration to provide an airborne missile with unique performance capabilities.

60-INCH DIAMETER 21 PERCENT MISSILE. The packaging layout considered for the nominal 60-inch diameter missile, with a thickness-to-chord ratio of 21 percent, is shown in Figure 3.10.1. The volume available for

SECRET

SECRET

packaging is shown in Figure 3.10.5 which depicts the integrated volume of the nominal 60-inch diameter missiles. The electronics section, consisting of the guidance, autopilot, fuze, adaption kit (when a nuclear warhead is employed), and power supply sections is contained in the forward end of the missile. These components are best able to utilize the thin section afforded in this region. Furthermore, most guidance systems require location in this region for purposes of target observation during flight. Two structural beams extend from the leading edge to the rocket motor forward bulkhead to provide aeroelastic body stiffening and attachments for mounting packages in the forward section.

Interchangeable nuclear or conventional high explosive non-nuclear warheads are possible for this missile. Either a nuclear warhead or the high explosive warhead is centrally located and is suspended between the two forward beams. A contoured type high explosive warhead is a possibility for the PYE WACKET missiles. A perspective view of a contoured warhead is shown in the inset of Figure 3.10.2.

It was determined that a nuclear warhead could be made available during a PYE WACKET development time period which might be adapted to the 21 percent missile. In view of the possible usefulness of a nuclear capability, a nuclear warhead was shown with the layout to indicate that an interchangeable high explosive-nuclear capability is feasible for this missile.

The rocket motor for the nominal configurations, as shown in Figure 3.10.1, is a pancake type of basic thick skin construction. The chamber is intended to house a solid propellant burning at 250 PSI chamber pressure. It should be noted that this selection is somewhat arbitrary, because no positive decision was made between liquid and solid pancake engines in subsection 3.4.

This thick skin utilizes a honeycomb or waffle type construction as discussed in subsection 3.6. This results in reduced structural weight and increased strength since the external skins of the rocket motor form an integral part of the missile aerodynamic surface.

The leading edge consists of quasi-laminated construction as shown in the inset of Figure 3.10.1. The principal structural member is a steel edge to which the skins are attached by welding in the manner shown. Over the joint is added an insulating material which is attached to the steel section and supports the actual leading edge of carbon. The entire section is covered by ablation materials as discussed in Aerodynamic Heating subsection 3.5, and as shown in Figures 3.10.1 and 3.10.6.

For the nominal missile designs this leading edge extends over the forward 180° of periphery of the missile. The edge around the remaining aft portion of the missile is constructed of honeycomb material in the same manner as the skin.

The reaction control system shown in Figure 3.10.7 and discussed in Control Systems, subsection 3.7, is packaged in the aft end of the missile on both sides of the main nozzle. These reaction controls operate by means of

3.10.8

SECRET

SECRET

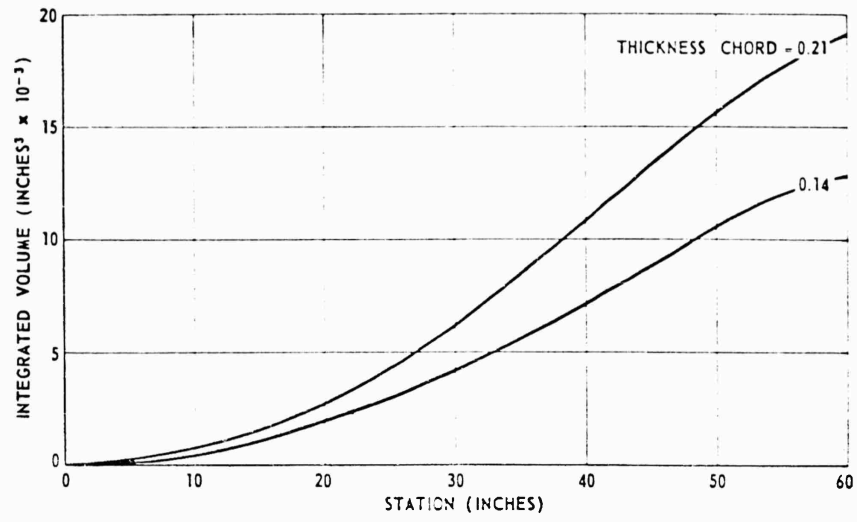


Figure 3.10.5. Integrated Missile Volume.

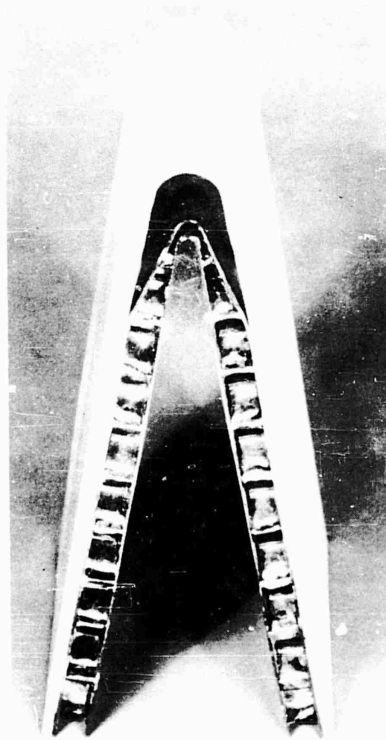


Figure 3.10.6. Leading Edge.

SECRET

3.10.9

four fixed nozzles which exhaust through the top and bottom aft surfaces. Pitch, yaw, and roll control are obtained by differential throttling of the propellant flow to the four fixed thrust chambers.

The entire reaction force system including propellant, pressurizing charge, servos, thrust chambers, etc., could be constructed as an integral package for installation into either side. Electrical signals to the control propellant flow system are transmitted from the autopilot located in the electronics section to the aft section by means of electrical harnesses inside the periphery of the missile.

A swivel nozzle having angular freedom of about $\pm 10^\circ$ of action in both pitch and yaw planes provides additional pitch and yaw control forces during the boost phase of flight. In a final, specific design, thrust vector control may only be needed in one plane. Furthermore, it is possible that for a particular missile, mass injection might substitute for nozzle swiveling. The details of a typical swivel nozzle and its method of attachment are shown in Figure 3.10.1. Gas pressurized actuators are shown as a means of controlling the swivel nozzle. Pressurized gas (provided from the propellant pressurization system of the control motor) is valved to the control piston and hence can control the position of the main nozzle. Similar systems are used for both pitch and yaw control. Openings in the top and bottom skins over the nozzle exit region allow the nozzle to extend outside the missile contour when deflected in the pitch plane.

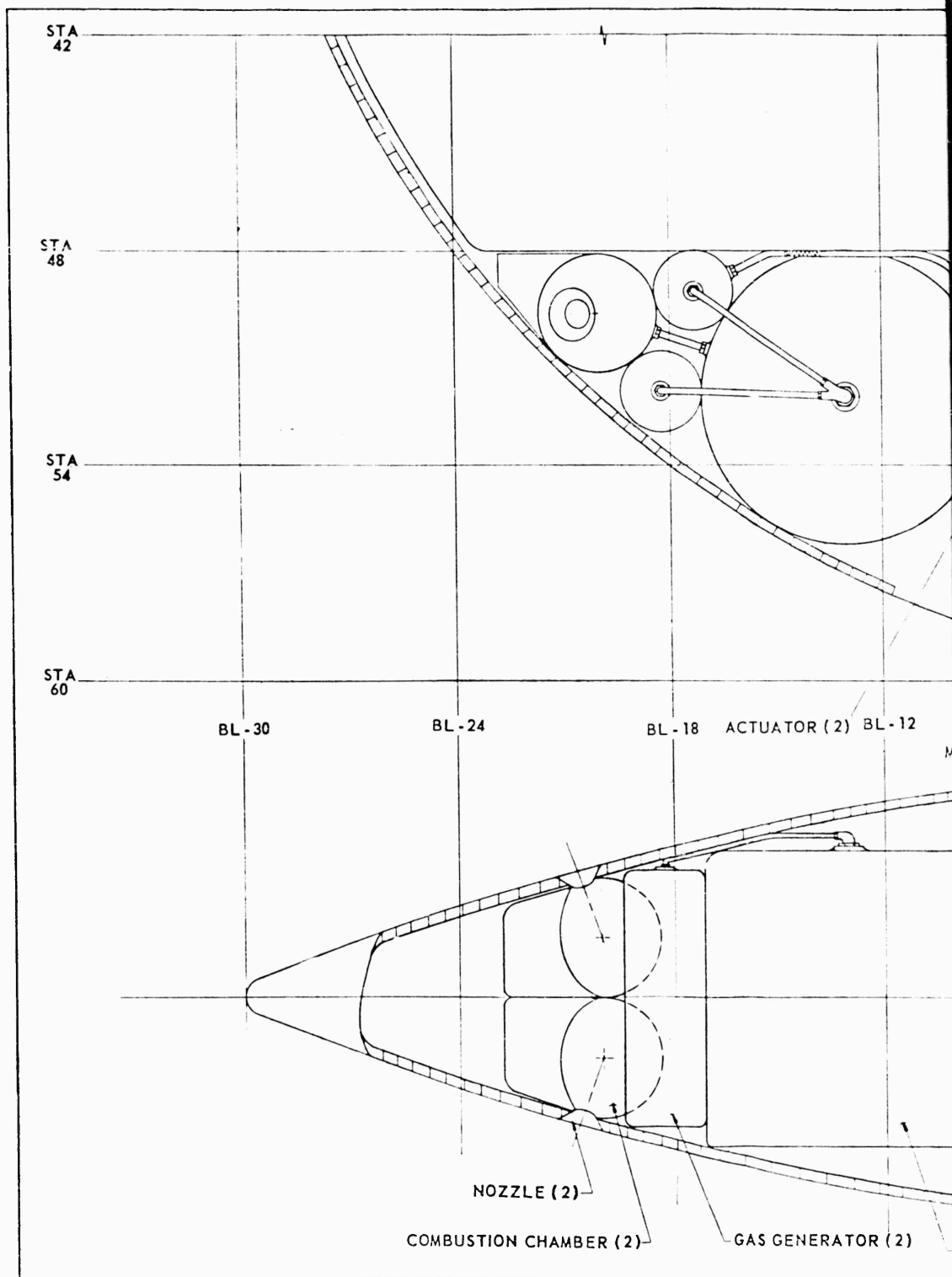
Electrical connection to the launcher and exact location of the umbilical connector and launching provisions will be dependent upon a more complete evaluation of launching conditions.

The missile skin can be easily removed in two major sections by disconnecting a main joint across the forward edge of the rocket motor. This will allow easy access to all components for assembly, test, checkout and servicing operations. To insure reasonable skin temperatures the entire external surface will be covered by an ablative material of varying thickness as required by aerodynamic heating considerations. Table 3.10.1 is a thickness chart for the layout of Figure 3.10.1 which gives the thicknesses at each station-butline intersection. Thicknesses are given from the center plane to the inner skin surface, the outer skin surface, and the ablation surface.

Table 3.10.2 is an estimated weight and balance statement for the configuration shown in Figure 3.10.1.

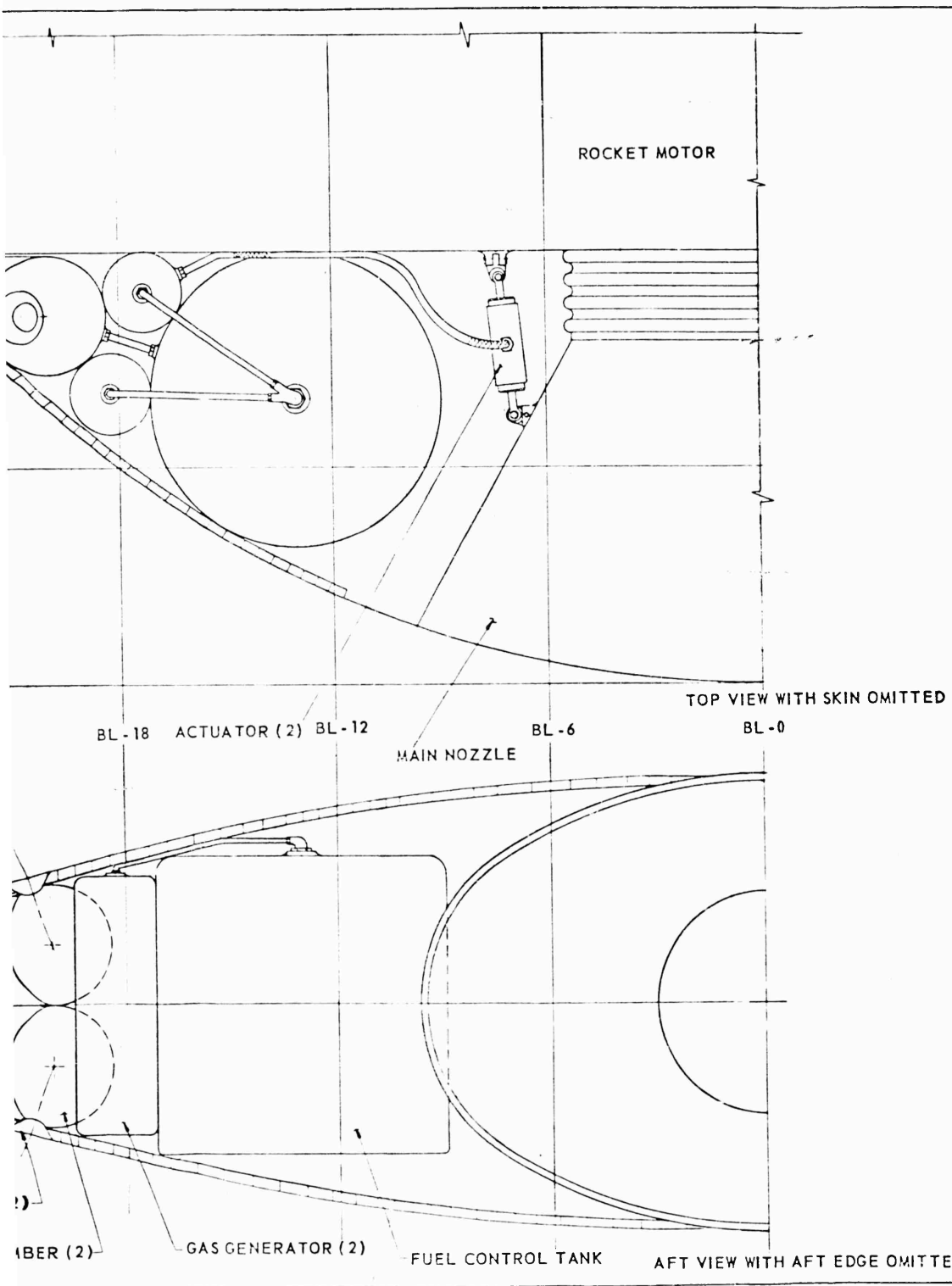
The 60-inch diameter 21 percent thickness ratio missile has a launch weight of 830.4 pounds with a center of gravity (c.g.) at Station 34.08 and an empty weight of 324.4 pounds with a c.g. at Station 28.85. The lateral center of gravity is located approximately at butline 0.000 throughout flight.

SECRET



SECRET

1



2

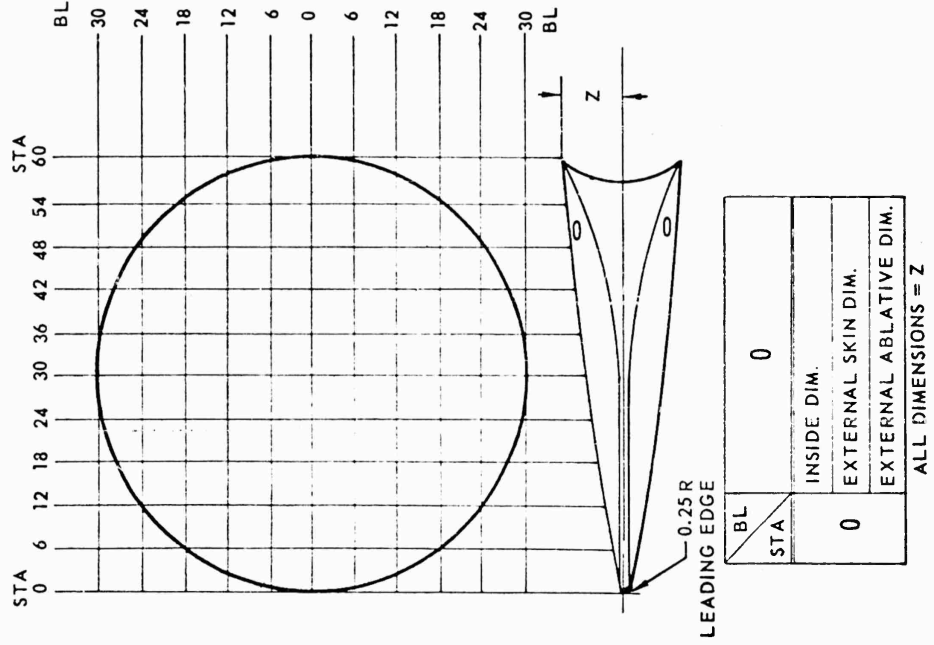
<i>Convair</i>	
FOR DATA CALL	
REACTION CONTROL SYSTEM	
6070-217	
DATE	BY
	GAETA
APP. -	REV.

Figure 3.10.7. Layout of Reaction Control System.

SECRET

Table 3.10.1
 PYE WACKET 21 PERCENT 60-INCH DIAMETER

		PYE-WACKET 21% 60" DIA					
BL STA	0	6	12	18	24	30	
0	.201 .299						
6	1.201 1.451 1.539	1.095 .954 1.455	.704 .299	.201			
12	2.237 2.487 2.565	2.103 2.353 2.433	1.239 1.989 2.071	1.074 1.324 1.412	.201 .298		
18	3.140 3.390 3.460	3.002 3.252 3.323	2.663 2.913 2.986	1.955 2.205 2.283	.915 1.165 1.251		
24	3.878 4.128 4.191	3.786 4.036 4.101	3.422 3.672 3.738	2.701 2.951 3.029	1.603 1.853 1.931		
30	4.569 4.819 4.874	4.452 4.702 4.758	4.065 4.315 4.373	3.304 3.554 3.617	2.049 2.299 2.369	0.000	
36	5.109 5.359 5.407	4.983 5.233 5.283	4.564 4.814 4.866	3.723 3.973 4.028	2.224 2.474 2.537		
42	5.523 5.773 5.815	5.410 5.660 5.704	4.925 5.175 5.210	3.903 4.153 4.101	2.235 2.485 2.530		
48	5.820 6.070 6.106	5.689 5.939 5.977	5.091 5.341 5.381	3.903 4.153 4.195	2.235 2.485 2.533		
54	5.950 6.200 6.230	5.786 6.036 6.071	5.091 5.341 5.380	3.903 4.153 4.189			
60	6.050 6.300 6.325						



SECRET

Table 3.10.2
WEIGHT AND BALANCE STATEMENT FOR 60-INCH DIAMETER
21 PERCENT PYE WACKET MISSILE

Item	Weight (LB.)	Arm (IN.)	Moment (IN/LB)
Structure Group			
Skins	25.5	16.9	430.9
Leading edge	10.9	8.9	97.0
Mounting structure	6.0	16.20	97.2
Joints	7.5	36.00	270.0
Rocket Motor			
Motor case	88.0	35.0	3430.0
Inhibitor	10.0		
Igniter	1.5	24.0	36.0
Nozzle (main)	37.4	49.0	1832.6
Nozzle controls	4.4	50.00	220.0
Guidance	7.6	10.1	76.8
Autopilot	18.2	10.1	183.8
Harnessing	14.0	9.2	128.8
Warhead	40.0	16.40	656.0
Adaption Kit	15.0	17.1	256.5
Fuzing and S/A	5.0	16.1	80.5
Power Supply	6.5	17.0	110.5
Ablation Materials			
End flight	10.0	20.0	200.0
Launch	30.0	20.0	600.0
Control System			
Fuel tanks and mounting	4.5	52.0	234.0
Pressurizing assembly	3.5	50.6	177.1
Combustion chambers	3.4	49.8	169.3
Control nozzles	1.0	49.8	49.8
Servos and valves	3.5	49.2	172.2
Plumbing	1.0	50.1	50.1
Control Propellant	46.0	52.00	2392.0
Rocket Propellant	460.0	35.1	16146.0
Launch Conditions	830.4	34.08	28296.9
Final Conditions	324.4	28.85	9358.9

The foregoing study summarized the component design feasibility of the 60-inch diameter, 21 percent thickness ratio missile configuration. It is now in order to examine the performance characteristics of this particular configuration equipped with reaction jet control.

SECRET

First consideration was given to maneuver capability as a function of the reaction jet thrust. Because of lack of wind tunnel data on the 21 percent configuration, the center of pressure was assumed to be the same as that for the 14 percent thickness configuration tested. Furthermore, for the purpose of this investigation it was assumed that the center of pressure did not vary with angle of attack; the wind tunnel results of subsection 3.2 show this is essentially correct, at least for the lower angles of attack.

Figure 3.10.8 presents the maneuverability (g's) as a function of reaction jet thrust for the 60-inch diameter, 21 percent thickness configuration. The empty weight and center of gravity as determined from Table 3.10.2 were used in Figure 3.10.8. This plot shows that maneuver capability in g's is directly proportional to the reaction jet thrust at a constant Mach number. In other words, doubling the reaction jet thrust will double the number of g's the missile is capable of achieving. The variation of g's with Mach number is due to the fact that the center of pressure varies with Mach number as determined in subsection 3.2. Examination of Figure 3.10.8 reveals that 500 pounds of reaction thrust per nozzle will yield 20 aerodynamic g's at Mach 2 and 33 g's at Mach 3. In order to obtain 50 aerodynamic g's a reaction thrust per jet of about 1100 pounds at Mach 2 and 675 pounds at Mach 3 would be necessary (for the stability margin obtained). It should be noted that alterations in packaging, resulting in a more forward center of gravity location, would appreciably increase the maneuver capability of the 21 percent missile.

Figure 3.10.9 presents the variation of range with altitude assuming a launch velocity of 800 FT/SEC. A thrust value of 14,500 pounds and a burning time of 8.5 seconds were assumed. As expected, the range increases considerably with altitude due to the lower air density.

Figure 3.10.10 presents the estimated yawing moment variation with yaw angle for the 60-inch diameter, 21 percent thickness configuration for launch conditions of Mach 2.5 at 60,000 feet altitude. This launching condition is shown because it is the most severe condition (highest velocity) anticipated for omni-launch in the near future. The launch weight and center of gravity as determined from Table 3.10.2 were used in Figure 3.10.10. The yaw moment capability of reaction jets is also shown on the plot for various thrust levels. This plot shows that about 220 pounds of thrust per jet is necessary for control in omnidirection launch. It should be noted that thrust vector control of the main propulsion system is available during the boost phase of flight and may be used to supplement reaction controls if needed.

The roll angular acceleration is shown in Figure 3.10.11 as a function of reaction jet thrust. This plot shows that the configuration is extremely maneuverable in roll. For instance, a reaction thrust per jet of 400 pounds will give the missile a roll acceleration of 76 radians per SEC².

Comparison of Figure 3.10.8 with 3.10.10 indicates that the critical design condition of the 21 percent missile reaction control system is due to the

SECRET

3.10.15

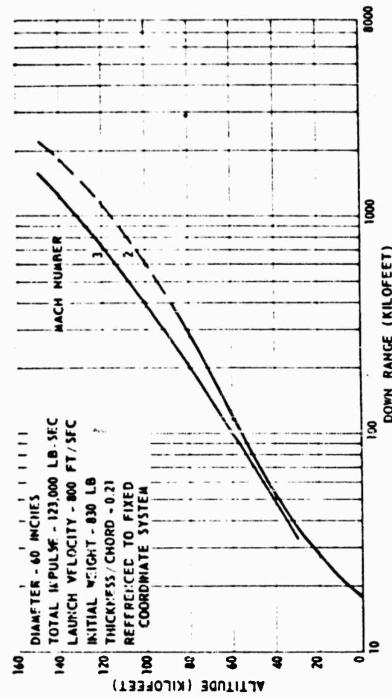


Figure 3.10.9. Effect of Altitude on Downrange.

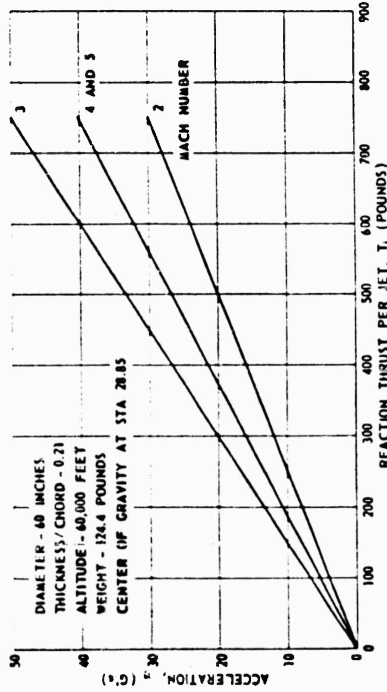


Figure 3.10.8. Variation of Maneuverability With Reaction Jet Thrust.

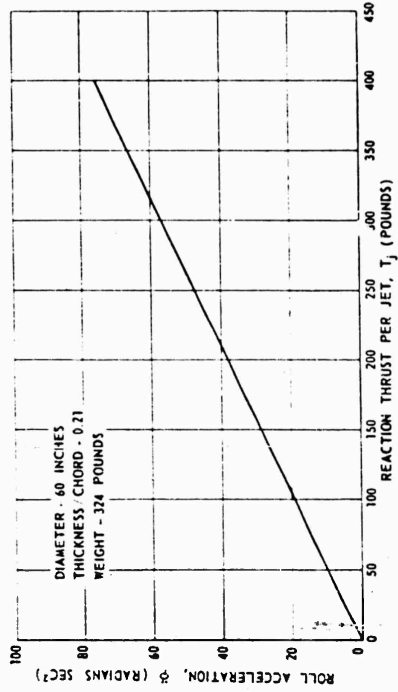


Figure 3.10.11. Variation of Roll Acceleration With Reaction Jet Thrust.

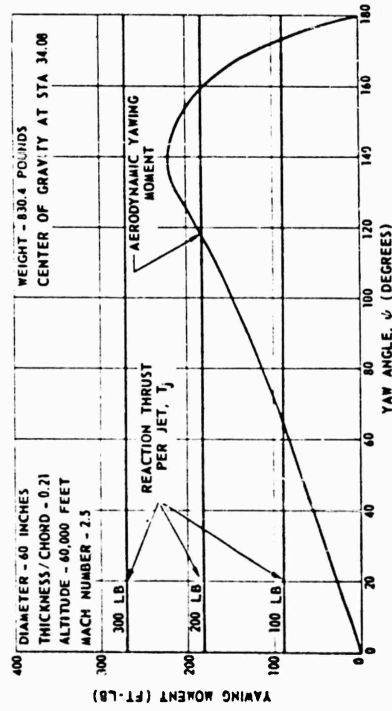


Figure 3.10.10. Required and Available Yawing Moment at Launch.

SECRET

requirement of high normal acceleration capability. A better balance between reaction force required for maneuverability during the glide phase of flight and yaw stabilization required during the omni-launch phase of flight could be achieved by shifting the center of gravity forward. This could be accomplished by alterations in packaging. Such a shift would appreciably increase the maneuver capabilities of the 21 percent missile.

60-INCH DIAMETER 14 PERCENT MISSILE. The nominal 60-inch diameter PYE WACKET missile with a thickness-to-chord ratio (t/C) of 14 percent is shown in Figure 3.10.2. This configuration is basically similar to the thicker missile shown in Figure 3.10.1. The leading edge and skins are constructed in the same manner explained above for the thicker missile and the rocket motor again forms an integral part of the missile aerodynamic surface. For purposes of this feasibility design the same guidance, autopilot and fuze are used for each configuration. The battery portion of the 14 percent missile is altered in size to accommodate the longer flight duration as determined in subsection, 3.9.

A contoured type high explosive warhead as mentioned earlier was considered, as shown in Figure 3.10.2. The control system for the 14 percent missile is similar to the one employed with the 21 percent missile except for the minor weight differences.

The rocket motor is a solid propellant pancake type which burns at 250 PSI chamber pressure. (Note again that this choice is somewhat arbitrary). The reduced thickness accommodates less propellant and results in a somewhat reduced ratio of launch-to-burnout weight.

The thickness chart for the 14 percent configuration is shown in Table 3.10.3. Three values are shown for each station-butline intersection which indicate the thickness at the internal skin, external skin and ablative surface. Assembly techniques are the same as for the 21 percent configuration.

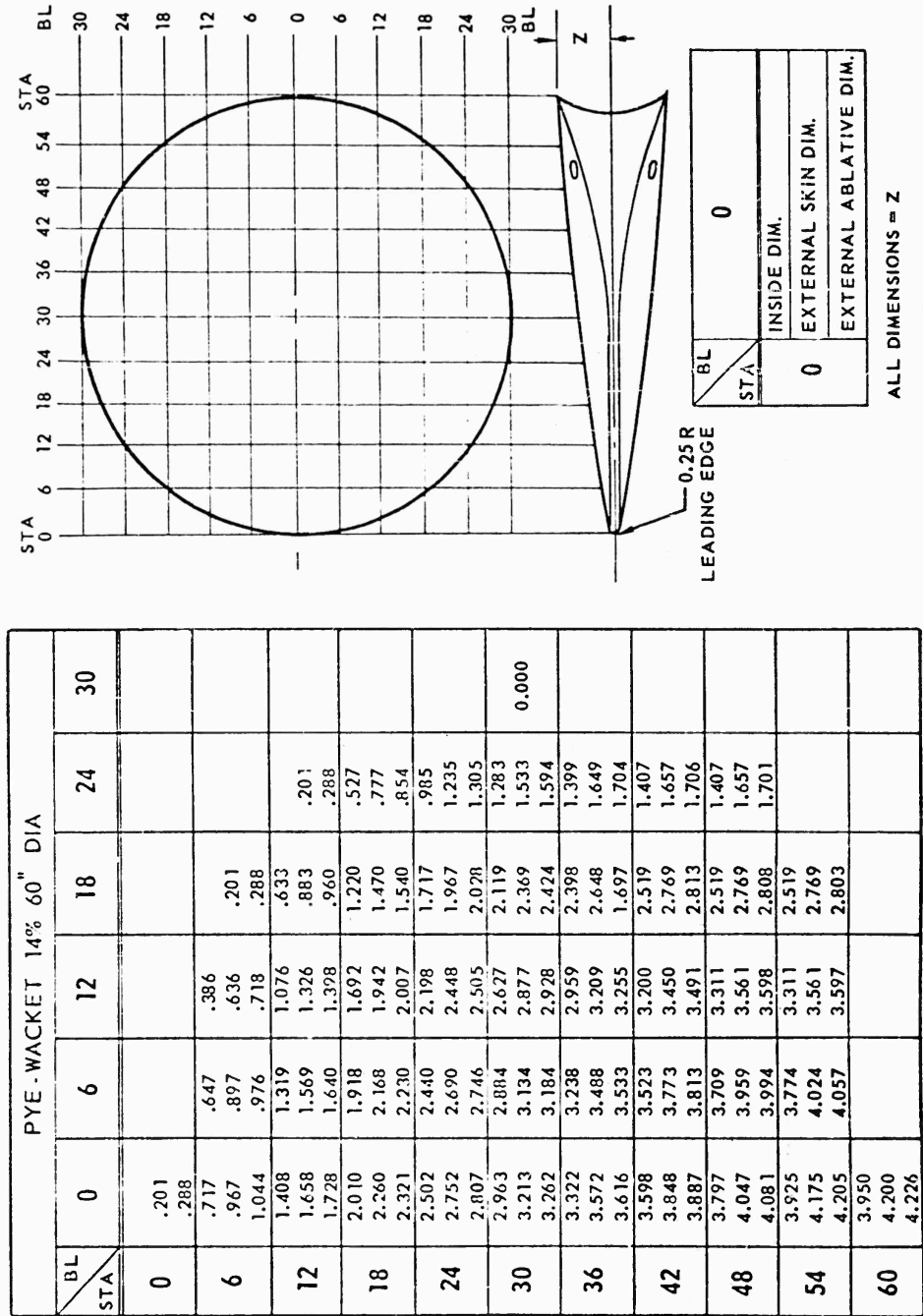
An estimated weight and balance statement is shown in Table 3.10.4 for the 60-inch diameter, 14 percent missile.

The 60-inch diameter 14 percent thickness-to-chord ratio missile has a launch weight of 581 pounds with the c.g. at Station 32.63, and an empty weight of 255.5 pounds with the c.g. at Station 27.18. The lateral center of gravity is located approximately at butline 0.00. The integrated volume from the forward edge to the aft edge is presented in Figure 3.10.5 for both the 14 percent and 21 percent missiles.

SECRET

3.10.17

Table 3.10.3
 PYE WACKET 14 PERCENT 60-INCH DIAMETER



SECRET

Table 3.10.4
WEIGHT AND BALANCE STATEMENT FOR
60-INCH DIAMETER 14 PERCENT PYE WACKET MISSILE

	Weight (LB)	Arm (IN.)	Moment (IN/LB)
Structure Group			
Skins	24.9	16.9	420.8
Leading Edge	10.1	11.0	111.1
Mounting structure	4.2	15.0	63.0
Joints	7.5	34.0	255.0
Rocket Motor			
Motor case	72.0	35.0	2520.0
Restrictor	10.0	35.0	350.0
Igniter	1.5	22.0	33.0
Nozzle (main)	26.0	48.5	1261.0
Nozzle controls	4.0	50.0	200.0
Guidance	7.6	10.0	76.0
Autopilot	18.2	10.0	182.0
Harnessing and Encapsulation	14.0	10.3	144.2
Warhead	20.0	18.0	360.0
Adaption Kit	None	-	-
Fuzing and S/A	5.0	18.0	90.0
Power Supply	7.5	18.0	135.0
Ablation Materials			
End flight	9.0	21.0	189.0
Launch	20.0	21.0	420.0
Control System			
Fuel tanks	3.7	52.4	193.9
Pressurizing assembly	2.9	51.0	147.9
Combustion chambers	2.4	50.4	121.0
Control nozzles	1.0	50.4	50.4
Servos and valves	3.0	49.8	149.4
Plumbing	1.0	50.0	50.0
Control Propellant	34.5	52.4	1807.8
Rocket Propellant	280.0	34.5	9660.0
Launch Conditions	581.0	32.63	18,959.0
Final Conditions	255.5	27.18	69,452.0

The above component design study deals with the mechanical feasibility of a 60-inch diameter, 14 percent thick configuration. The performance of this configuration will now be investigated and compared with the thicker 21

SECRET

3.10.19

percent configuration. Performance curves similar to those shown in subsection 3.9 are shown in which the maneuver capability, yawing moment capability, and roll angular acceleration are plotted as functions of reaction jet thrust. The range variation with altitude is also shown for an 800 foot per second launch condition.

Figure 3.10.12 presents the maneuverability as a function of reaction jet thrust for the empty weight and corresponding center of gravity determined from Table 3.10.4. Figure 3.10.12 shows that a reaction thrust per jet of 500 pounds at Mach 2 and 3 will yield 40 g's and 98 g's, respectively. In order to obtain 50 aerodynamic g's a reaction thrust per jet of 625 pounds at Mach 2 and 250 pounds at Mach 3 would be required. Comparison of Figure 3.10.8 for the 21 percent thick configuration and Figure 3.10.12 for the 14 percent thick configuration reveals that the latter is more maneuverable than the thicker configuration. The reasons for the increased maneuverability is the lower disk loading and the more favorable center of gravity position.

The variation of range with altitude for the 14 percent configuration is shown in Figure 3.10.13. Comparison with Figure 3.10.9 reveals that the range is somewhat greater for the 14 percent thick configuration at the lower altitude where the lower drag is important.

Figure 3.10.14 presents the estimated yawing moment variation with yaw angle for launch conditions of Mach 2.5 at 60,000 feet altitude. This launch condition was again chosen as it is the most severe condition anticipated. The full weight and corresponding center of gravity position as determined in Table 3.10.4 were used in this plot. Figure 3.10.14 shows that the 14 percent thick model is slightly more difficult to launch omnidirectionally. About 425 pounds per jet of reaction thrust could be required to control the aerodynamic yawing moment at launch. It should be noted that thrust vector control of the main propulsion system is available during the boost phase of flight and may be used to supplement reaction controls if needed. More control force is required because the center of gravity position is less favorable in yaw. However, since the reaction force required to produce acceptable normal acceleration (Figure 3.10.12) is approximately the same as that required to stabilize the missile in yaw in the omni-launch phase of flight (Figure 3.10.14), the center of gravity variation for the 14 percent missile is acceptable.

As shown in Figure 3.10.7, the 14 percent thick configuration is highly maneuverable in the roll plane. A reaction thrust per jet of 400 pounds will result in a roll angular acceleration of 86 radians per second per second.

The estimated weights and other data determined as a result of these feasibility designs and layouts will be employed as the bases of design scaling which is discussed below.

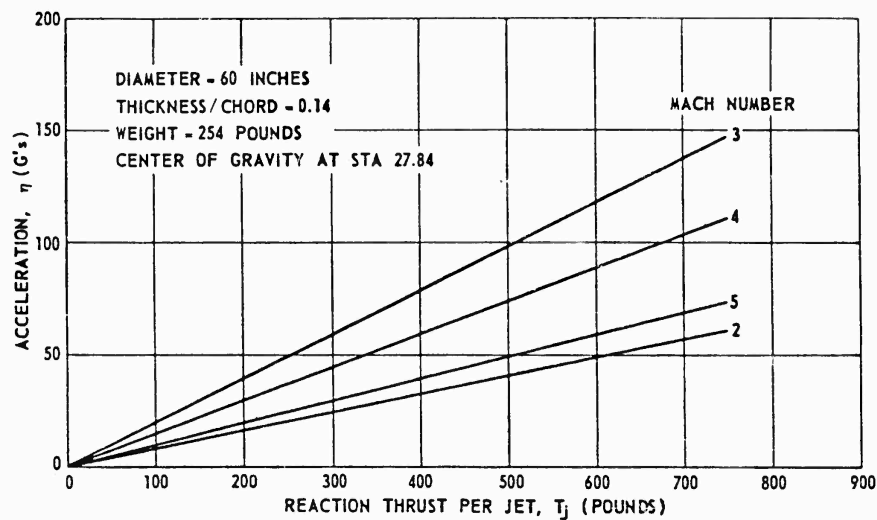


Figure 3.10.12. Variation of Maneuverability With Reaction Jet Thrust.

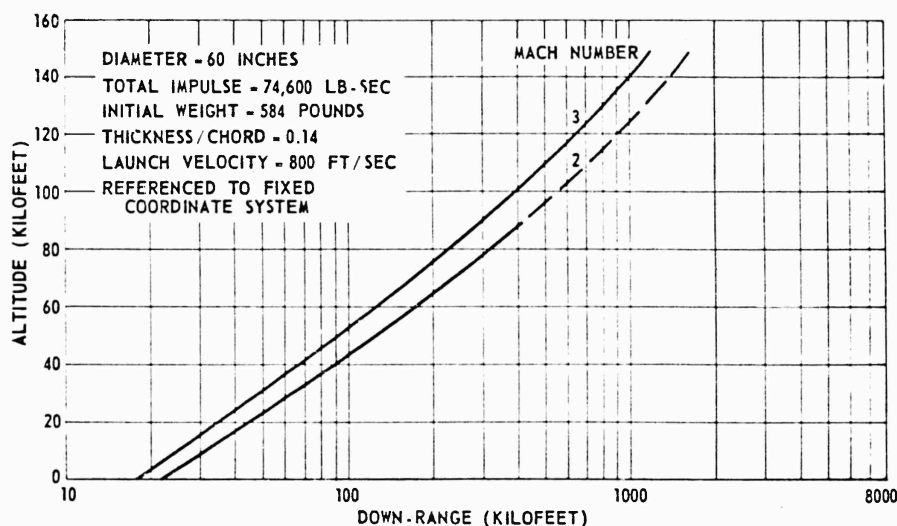


Figure 3.10.13. Effect of Altitude on Downrange.

3.10.2 DESIGN SCALING

Having established nominal designs for 60-inch diameter configurations of 14 percent and 21 percent thickness-to-chord ratios, it is necessary to develop means of estimating the effects of changing missile size on the weights of the various components and on the performance of the resulting missiles. The

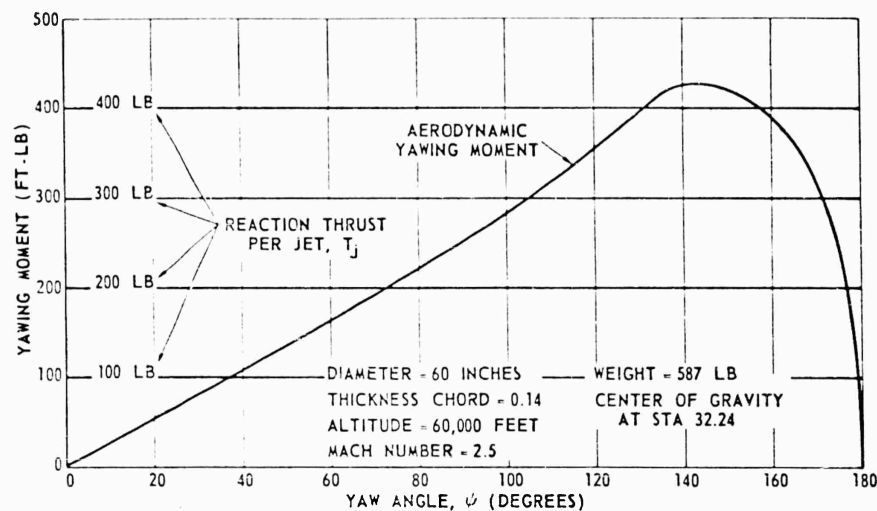


Figure 3.10.14. Required and Available Yawing Moment at Launch.

purpose of this section is to develop these techniques and, utilizing the nominal 60-inch diameter missile designs as bases, to apply the techniques to scaled missiles having diameters ranging from 30 inches to 120 inches.

The results of the design scaling of the PYE WACKET missile are not intended to yield detailed design information but rather to indicate general trends and first order estimates of weights and performance capabilities for use in making general weapon system evaluations based on missile size. More accurate design information can only be provided by performing actual designs with careful attention to mission constraints and requirements. Each major munition component was therefore analyzed to determine the effect of changing the missile diameter on its weight and size.

All design scaling was based upon the nominal 60-inch diameter missiles of 14 percent and 21 percent thickness-to-chord ratios. The design scaling techniques and method of presentation utilized in this report were developed specifically for the blunted lenticular PYE WACKET missile configuration.

One of the prime considerations in design scaling is the investigation of the effect of varying missile diameter on launch weight. The overall missile density is considered to be nominally independent of missile diameter over the range of scaling from 30 inches diameter to 120 inches diameter. From actual tabulation of conventional missile densities and from the investigation of the PYE WACKET configuration this is found to be a reasonable assumption for the accuracy to be expected in this scaling procedure. The overall missile density is a function of design and packaging efficiency and available state-of-the-art materials and techniques. Figure 3.10.15 presents the scaled missile total volume as a function of the missile body diameter for the 14

SECRET

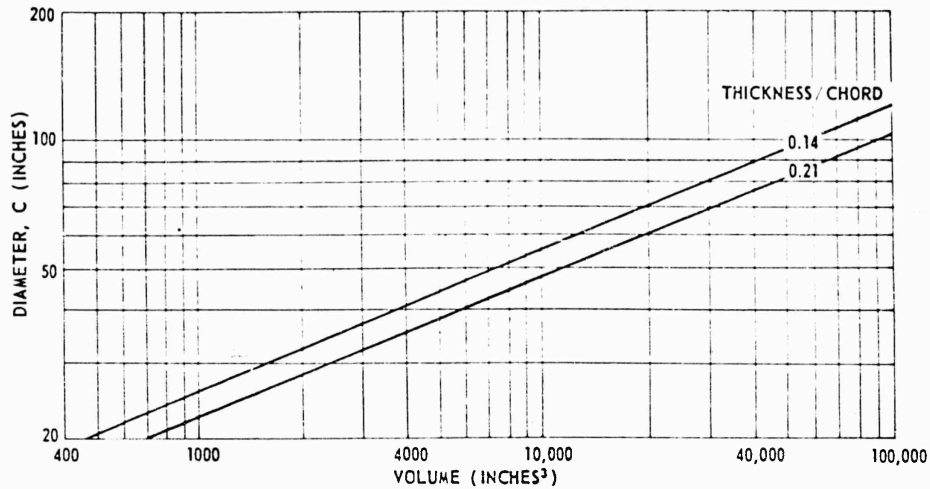


Figure 3.10.15. Scaled Total Volume.

percent and 21 percent thickness-to-chord ratios. This volume is proportional to the cube of the missile diameter.

Throughout the design scaling every effort has been made to determine the scaling relationships on a dimensional analysis or quasi-analytical basis. However, for some portions such as the payload items an analytical approach was not possible. For purposes of this scaling investigation the payload is defined as the high explosive warhead or the combined nuclear warhead and adaption kit. For the payload components, design scaling information was obtained from other missile programs; using this information empirical relationships were established.

In the following text, the scaling relationships are developed for each major subsystem or munitions component.

STRUCTURE GROUP. Though the rocket motor case is assumed to be an integral portion of the missile structure it will be discussed with the Rocket Motor Group as a matter of convenience. For purposes of this scaling analysis the structure group will be defined as including all those portions of the missile having as their primary function the maintenance of missile structural integrity excluding the rocket motor case. The structure therefore consists of the following major groups.

1. Leading edge
2. Missile skin
3. Joints and mounting structure

Leading Edge. The leading edge is that portion of the structure which extends over the forward 180 degrees of the periphery of the missile.

SECRET

3.10.23

The leading edge is constructed of a quasi-laminated section as shown in Figures 3.10.1 and 3.10.2. The section thickness of each material in this edge is controlled primarily by considerations of manufacturability and thermal environments and is considered to be relatively independent of missile size over the scaling range.

The weight of the leading edge is given by

$$W_E = \frac{\pi}{2} C \bar{\rho}_E \quad (3.10.1)$$

Assuming that the leading edge blunting radius remains constant and independent of missile size, the scaled weight, W_i , for a leading edge having an average weight-per-unit length of ρ_e and extending around equal portions of the periphery of a missile of diameter is given by

$$W_i = W_o \frac{\bar{\rho}_{E_i}}{\bar{\rho}_{E_o}} \frac{C_i}{C_o} \quad (3.10.2)$$

By the assumption $\bar{\rho}_{E_i} \approx \bar{\rho}_{E_o}$ over the scaling range

$$W_i = W_o \frac{C_i}{C_o} \quad (3.10.3)$$

assuming the weight curve passes through the origin, or is zero for $C_o = 0$.

Within the accuracy of scaling the leading edge weight can therefore be considered to vary as a linear function of the missile diameter over the scaling range of diameters, assuming utilization of the same material, construction and leading edge radius.

Missile Skins. The design of the skin was assumed to be controlled by the allowable bending stress. Other factors such as buckling were not considered. The skin is considered to be made up of honeycomb construction with thin gage metal brazed to a honeycomb core. For purposes of this scaling the skin was considered to be continuously variable in thickness with the core depth varying linearly with the brazed cover skins.

In order to develop scaling techniques for the skins, the missile was treated as a simple beam. The forces acting on this beam consist of air loads, control loads, and inertia loads as illustrated in Figure 3.10.16.

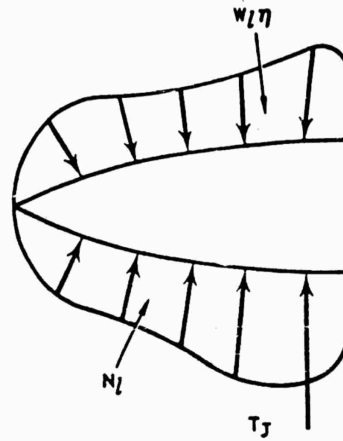


Figure 3.10.16. Beam Loading.

where:

W_e = weight per unit area

N_e = lift per unit

T_j = reaction jet thrust (treated as a concentrated load)

A simplification was achieved by considering the inertia loads and the air loads as concentrated loads as illustrated in Figure 3.10.17

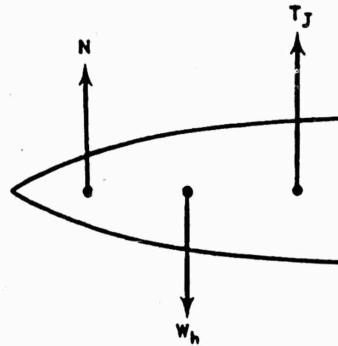


Figure 3.10.17. Resultant Forces Diagram.

Considering a simple case, in a steady state maneuver an equilibrium condition exists such that the net moment about a section is proportional to a resultant force N' and a length (proportional to C), 1

$$N' \ell = M \tag{3.10.4}$$

The elementary stress relation for bending load is

$$s = \frac{Mh}{I} \quad (3.10.5)$$

The area moment of inertia, I , of any spanwise section is

$$I = (t_s k) h^2$$

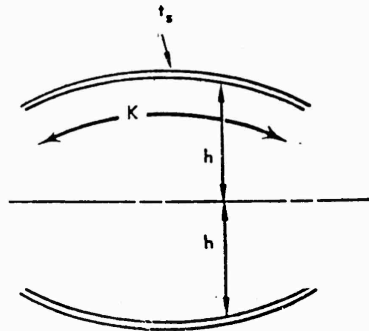


Figure 3.10.18. Spanwise Section.

Substituting the expressions for M and I into the elementary stress relationship yields

$$s = \frac{Mh}{I} = \frac{N'lh}{t_s kh^2} = \frac{N'l}{t_s kh} \quad (3.10.6)$$

since $N' = \frac{\eta W'}{g}$ and W' : Volume: C^3

where W is the weight ahead of the section considered. (Assuming that the average density is constant and that the maximum acceleration, η , is constant.)

For any maneuver η ,

$$N' : C^3$$

Also:

$$l : k : h : C$$

therefore

$$s : \frac{C^4}{t_s C^2} : \frac{C^2}{t_s} \quad (3.10.7)$$

SECRET

In order to maintain constant stress in the skin t_s must be proportional to C^2 . Since the weight of the skin is

$$W = A t_s \quad (3.10.8)$$

where A is the area of the skin and is proportional to C^2 .

$$W = A t_s : C^2 C^2 : C^4 \quad (3.10.9)$$

The relationship for determining the scaled weights of the skin elements is therefore

$$W_i = W_o \left(\frac{C_i}{C_o} \right)^4 \quad (3.10.10)$$

This scaling relationship was established by varying the allowable bending stress of the skin as the criterion. Applying other criteria, such as buckling, will lead to a similar scaling equation.

Joints. The weight of the joints is assumed to be proportional to the missile diameter while the mounting structure weight is seen to be proportional to the product of missile diameter and thickness. Under the original assumption of constant missile thickness-to-diameter ratio the mounting structure is therefore proportional to the square of missile diameter.

In algebraic form this may be expressed by

$$W_i = \alpha \frac{C_i}{C_o} + \beta \left(\frac{C_i}{C_o} \right)^2 \quad (3.10.11)$$

where α represents the weight of joints and β represents the weight of mounting structure.

Combination of the appropriate equations developed above yields a scaling equation of the form

$$W_i = \delta \frac{C_i}{C_o} + \beta \left(\frac{C_i}{C_o} \right)^2 + \gamma \left(\frac{C_i}{C_o} \right)^4 \quad (3.10.12)$$

for the entire basic structural group (again assuming the weight curve passes through the origin).

The weight of the structural group or any of its components for a scaled missile of diameter C, can be obtained by substitution of the weight values W_o for a reference missile of diameter C_o of known weights which meets the scaling assumptions.

SECRET

3.10.27

where:

δ	=	weight of leading edge + weight of missile joints
β	=	weight of mounting structure
γ	=	weight of missile skins
C_1	=	diameter of scaled missile in question
C_0	=	60 inches
W_1	=	scaled group weight

Such an analysis is simplified; however, detailed designs can be expected to approximate this relation.

Figure 3.10.19 was prepared by calculation of the above equation for initial values from the feasibility designs of the nominal 60-inch missiles.

ROCKET MOTOR GROUP. The rocket motor group is arbitrarily defined in this study as consisting of the rocket motor case, (for solid propellant), main nozzle, and main nozzle controls.

The purpose of the following portion is to again arrive at an analytical expression for estimating the weight of the scaled rocket motor group for PYE WACKET missiles from 30 to 120 inches diameter. This is accomplished by applying scaling techniques similar to those developed for the structures group above. This scaling is limited to the same basic design as employed for the feasibility designs of the nominal 60-inch diameter missiles.

Rocket Motor Case. For the purposes of this scaling the rocket motor case will be assumed to be designed by its stress requirements as a pressure vessel with all other loads considered negligible. Since the internal pressure is of the order of 250 LB/IN.² and the maximum airload pressure is of the order of 5 LB./IN.², this assumption is permissible for the accuracy expected from this study.

The technique for scaling the rocket motor case is very similar to that used for the missile skins. Again the elementary stress relationship for bending load is used

$$s = \frac{Mh}{I} \quad (3.10.13)$$

where M is defined as some force times moment arm, h is some reference length, and

$$I = \left(\frac{t}{s} K\right) h^2 \quad (3.10.14)$$

As in the case of the missile skins

$$s = \frac{FLh}{t_s K h^2} \quad (3.10.15)$$

SECRET

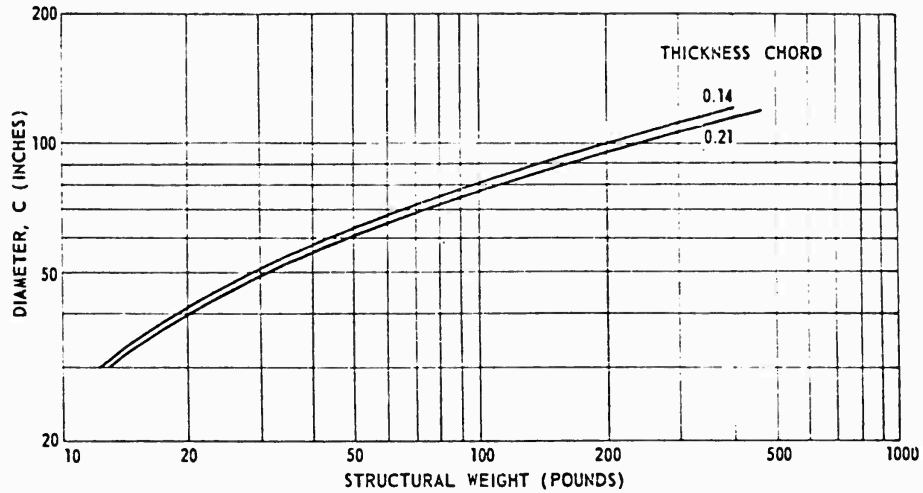


Figure 3.10.19. Scaled Structural Weights.

however, where $F : C^3$ for the missile skins, for the pressure vessel.

$$F : P_c A \tag{3.10.16}$$

and since P_c is assumed constant.

$$F : C^2 \tag{3.10.17}$$

Therefore $s : \frac{C}{t_s}$ for the rocket motor case instead of $\frac{C^2}{t_s}$ as in the case of the

missile skins.

Following a development similar to that used for the missile skins where a constant stress is maintained

$$t_s : C \tag{3.10.18}$$

and

$$W = A t_s : C^2 C : C^3 \tag{3.10.19}$$

The scaled rocket motor case weight can be determined for the relationship

$$W_i = W_o \left(\frac{C_i}{C_o} \right)^3 \tag{3.10.20}$$

SECRET

This equation is valid as long as the rocket motor case is designed by its stress requirements and the same materials are used for all sizes of missiles.

Restrictor. The restrictor or inhibitor is the material required between the solid propellant grain and the rocket motor case. The thickness of this material is determined by its manufacturability and flame inhibiting characteristics. Assuming the thickness and density of this material to be constant for all the scaled missiles, the total weight allotment necessary for this is proportional to the area to be covered and hence as shown in the above paragraphs is given by

$$W_r = W_o \left(\frac{C_i}{C_o} \right)^2 \quad (3.10.21)$$

Main Nozzle. One of the primary considerations in determining the scaling relationships for the main nozzle is the determination of the thrust which the nozzle is expected to deliver.

From the scaled performance studies to follow it was found that by assuming constant boost acceleration at burnout a good performance comparison could be made for the various scaled missiles. No attempt was made to make the assumed thrust levels completely compatible with nozzle limitations discussed in the propulsion section.

For the scaled performance calculations the thrust levels were arbitrarily chosen to provide 50 g's of boost acceleration at rocket motor burnout. All components used with the missile will be capable of withstanding 50 g's. For calculation this thrust was maintained at a constant value throughout the boost phase of flight.

The effects of missile payload on the thrust (T) was determined in the performance scaling study, presented later, to be dependent upon the missile diameter by the following relationships

$$T: \left(\frac{C_i}{C_o} \right)^{2.64} \quad (3.10.22)$$

for missiles within the scaling limits with warheads which were arbitrarily chosen to satisfy the relation

$$\frac{W_w/H_o}{W_{L_o}} = \frac{W_w/H_1}{W_{L_1}} \quad (3.10.23)$$

On the basis of constant mechanical loads all of the nozzle dimensions would be expected to vary proportionally; however, the thermal characteristics of the nozzle are non-linear for changes of nozzle wall thickness. For the same boost thrust durations the nozzle wall thickness would be expected to remain constant due to thermal requirements on the nozzle.

SECRET

The boost duration was shown from the scaled performance calculations (presented later) to be almost constant with changes of missile size, and the assumption was therefore made that the nozzle is of constant thickness and is linearly scaleable in all other dimensions as a function of the thrust level.

It can be shown that the surface area of the nozzle may be expressed by

$$A : D_{th}^3 \quad (3.10.24)$$

For constant nozzle wall thickness the amount of material in the nozzle is shown to be proportional to D_{th}^3 .

The thrust T is given by the expression

$$T = k P_c D_{th}^2 \quad (3.10.25)$$

From the scaled trajectory calculations the thrust was shown to actually vary by the relation

$$T : \left(\frac{C_i}{C_o} \right)^{2.64} \quad (3.10.26)$$

when based on a constant boost acceleration of 50 g's at rocket motor burnout. By utilization of the basic scaling assumption that chamber pressure P_c is constant for all missiles, the previous equations can be combined to show that

$$k P_c D_{th}^2 = \left(\frac{C_i}{C_o} \right)^{2.64} \quad (3.10.27)$$

and therefore the obvious conclusion that

$$D_{th} : \left(\frac{C_i}{C_o} \right)^{1.32} \quad (3.10.28)$$

On the basis of utilization of the same material for all nozzles the variation of the weight of the nozzle is given by

$$W : \left(\frac{C_i}{C_o} \right)^{3.96} \quad (3.10.29)$$

SECRET

3.10.31

The weight required for nozzle attachments and controls is considered to be approximately proportional to the weight of the nozzle itself. Comparison with actual designs showed this to be a reasonably accurate assumption. The scaled weight of the nozzle together with its attachments and controls is therefore given by

$$W_i = W_o \left(\frac{C_i}{C_o} \right)^{3.96} \quad (3.10.30)$$

By combination of the above expression for the weight variation of each component of the rocket motor group the scaled weight of the entire rocket motor group less propellant can be expressed by the generalized relationship

$$W_1 = \alpha \left(\frac{C_i}{C_o} \right)^2 + \beta \left(\frac{C_i}{C_o} \right)^3 + \gamma \left(\frac{C_i}{C_o} \right)^{3.96} \quad (3.10.31)$$

where W_1 is assumed to pass through the origin and

W_1	=	scaled weight of rocket motor group
C_1	=	scaled diameter of missile in question
C_o	=	nominal missile diameter = 60 inches
α	=	inhibitor weight from nominal missile
β	=	rocket motor case weight from nominal missile
γ	=	weight of main nozzle, attachments and controls from nominal missile

Utilizing this equation with the initial conditions from the nominal 60-inch diameter missiles the curves of Figure 3.10.20 were developed.

CONTROLS GROUP. The controls group is made up of the four thrust chamber fixed nozzle assemblies, control servos and valves, control propellant, pressurization unit, and tankage. All electronic portions of the control system are arbitrarily associated with the autopilot for purposes of convenience in analyzing the scaling functions though they are functionally a part of the control system.

The moment generated by the aerodynamic forces can be approximated by

$$M : A P_a x \text{ where } P_a = \frac{\text{Aerodynamic lift}}{A} \quad (3.10.32)$$

where x is the distance between the center of gravity and aerodynamic center of pressure. Similarly, the moment produced by the reaction controls can be approximated by

SECRET

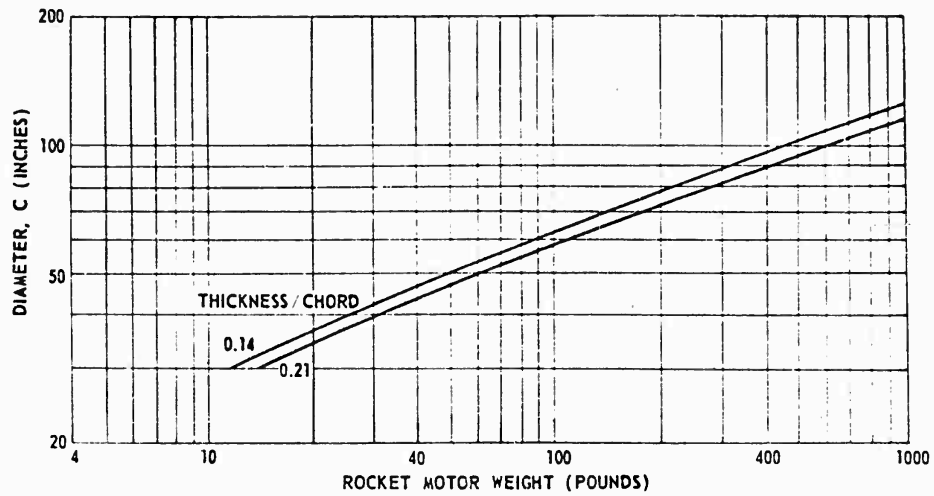


Figure 3.10.20. Scaled Rocket Weights.

$$M_y : Tl \quad (3.10.33)$$

where T is the differential reaction thrust and l is the distance between the reaction nozzle and the missile c.g. If the reaction moment is made to balance the aerodynamic moment,

$$M = M_y \quad (3.10.34)$$

$$A P_a X : Tl$$

Utilizing the previously developed relationships,

$$P_a : C$$

$$A : C^2 \quad (3.10.35)$$

$$l : C$$

the scaling derivations were greatly simplified and the comparisons are still valid by assuming that the stability margin is constant for all missiles.

$$X : C$$

SECRET

3.10.33

Therefore, the thrust (T) is scaleable by the relation

$$T = \frac{AP_0 X}{\ell} \quad (3.10.36)$$

and hence

$$T : C^3 \quad (3.10.37)$$

Assuming a constant control propellant specific impulse, the control propellant weight is scaleable by the relationship

$$W_i = W_o \left(\frac{C_i}{C_o} \right)^3 \left(\frac{\gamma}{\gamma_o} \right) \quad (3.10.38)$$

where τ is the required equivalent duration of reaction control. In order to estimate the effect of this duration of control it was necessary to assume that control "duty cycle" (proportionate time the controls are operating at each level) is the same for all scaled missiles. From trajectories which were calculated for performance scaling and with a missile payload equivalent to 10 percent of the missile launch weight, it was found that the required duration of flight and hence duration of control varies by the relation

$$\gamma : C^{.8/5} \quad (3.10.39)$$

for the missiles of 14 percent thickness and by the relation

$$\gamma = C^{.581} \quad (3.10.40)$$

for the missiles of 21 percent thickness.

The weight of the pressurization unit is approximately proportional to the control propellant volume or weight.

The scaled weight of control propellant and pressurization unit by combination of the above results is given by

$$W_i = W_o \left(\frac{C_i}{C_o} \right)^3 \left(\frac{C_i}{C_o} \right)^{.8/5} = W_o \left(\frac{C_i}{C_o} \right)^{3.8/5} \quad (3.10.41)$$

for the missiles of 14 percent thickness and by the expression

$$W_i = W_o \left(\frac{C_i}{C_o} \right)^3 \left(\frac{C_i}{C_o} \right)^{.581} = W_o \left(\frac{C_i}{C_o} \right)^{3.581} \quad (3.10.42)$$

for the missiles of 21 percent thickness.

SECRET

W_0 represents the nominal weight of the control propellant and pressurization system from the feasibility designs.

For a tankage system based on a constant level of pressurization and similar tankage configurations, the stress in the tank and the volume of control propellant determines the tank weights required. The tankage weight can therefore be considered to be proportional to the control propellant weight.

Within the accuracy and range of scaling the valves and servos are considered to be unchanged with variations in missile diameter. The designs of the combustion chambers and nozzles are dependent upon the required thrust level.

Since:

$T : C^3$ as seen above, and $T : D_{th}^2$ as seen for the main nozzle, it is apparent that $D_{th} : C^{1.5}$

The weight of the control nozzles is a function of D_{th}^3 as shown for the main nozzle. They are, therefore, scaleable by the relationship

$$W_1 = W_0 \left(\frac{C_1}{C_0} \right)^{4.5} \quad (3.10.43)$$

By combinations of the above equations the generalized scaling equation for estimating the weight of the entire control system of the missiles of 21 percent thickness becomes

$$W_1 = \alpha_0 + \gamma_0 \left(\frac{C_1}{C_0} \right)^{3.581} + \delta_0 \left(\frac{C_1}{C_0} \right)^{4.5} \quad (3.10.44)$$

and for the missiles of 14 percent thickness becomes

$$W_1 = \alpha_0 + \gamma_0 \left(\frac{C_1}{C_0} \right)^{3.815} + \delta_0 \left(\frac{C_1}{C_0} \right)^{4.5} \quad (3.10.45)$$

where W_1 is assumed to pass through the origin and

- α_0 = weight of valves, servos, and plumbing
- γ_0 = control propellant weight, pressurizing assembly, and tankage
- δ_0 = nozzle and thrust chamber weight

These equations are depicted graphically in the curves of Figures 3.10.21.

ELECTRONICS SECTION. The major portion of the electronics section is composed of electronic guidance and autopilot assemblies. The weights and volumes required for the electronics section are highly dependent upon type of

SECRET

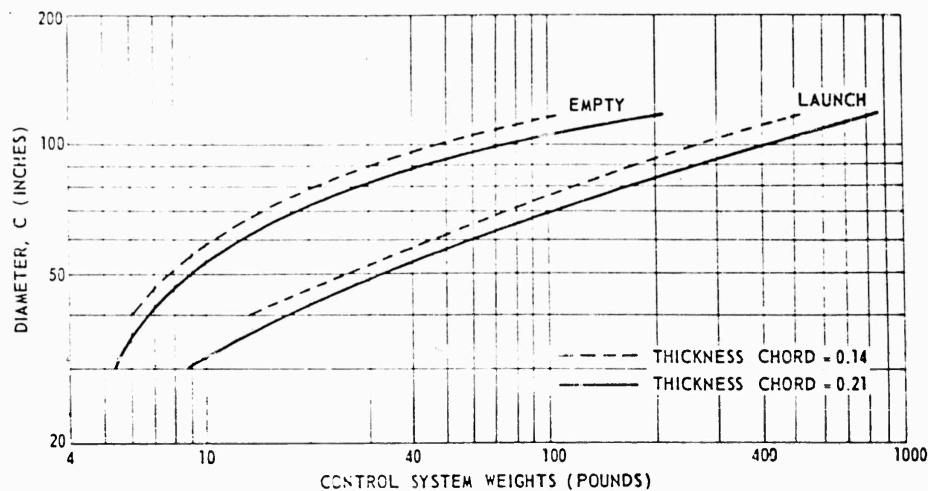


Figure 3.10.21. Scaled Control System Weights.

guidance and control employed, degree of sophistication, and type of packaging utilized. Each of these factors is in turn highly influenced by such factors as state-of-the-art, cost, and mission. Despite this seeming matrix of possibilities it is possible by making several assumptions to estimate the weight of the electronics section.

It should be noted that a preliminary examination of the guidance problem is presented in subsection 3.8. However, since no definite mission has been established for PYE WACKET the following guidance assumptions were made for purposes of convenience in design scaling.

1. There is no discrete range or missile size for transition from one guidance system to another.
2. For short range missiles a passive or semiactive system will be used which will acquire the target before launch and will home throughout its entire flight.
3. For the medium size missiles a two stage guidance will be employed which will consist of a terminal homing phase similar to that used in the the small missiles. The midcourse (and launching phase) will be either a command system or a quasi-inertial programmed system.
4. The larger missiles will require a more sophisticated midcourse guidance of the command or inertial type in addition to a longer range homing guidance phase.

The number of components required to implement a typical IR system is shown in Figure 3.10.22. A typical semiactive CW doppler system can be implemented by approximately the number of components shown in Figure 3.10.23.

SECRET

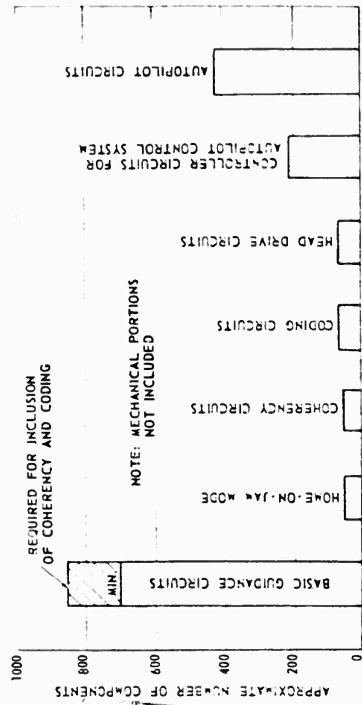


Figure 3.10.23. Typical Semiactive CW Doppler Guidance System.

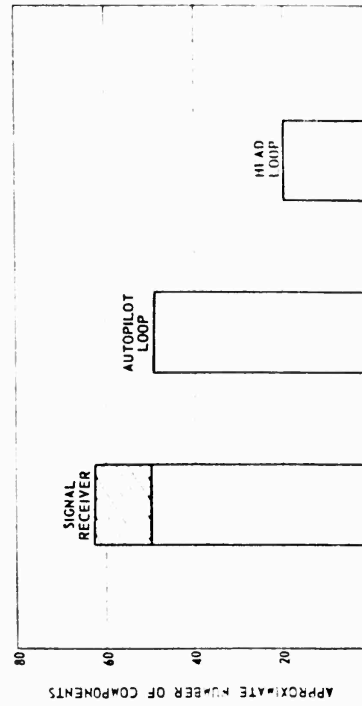


Figure 3.10.22. Typical IR Homing System.

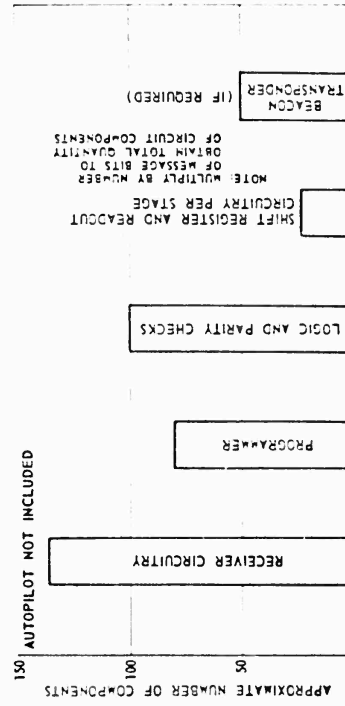


Figure 3.10.24. Typical Command Guidance.

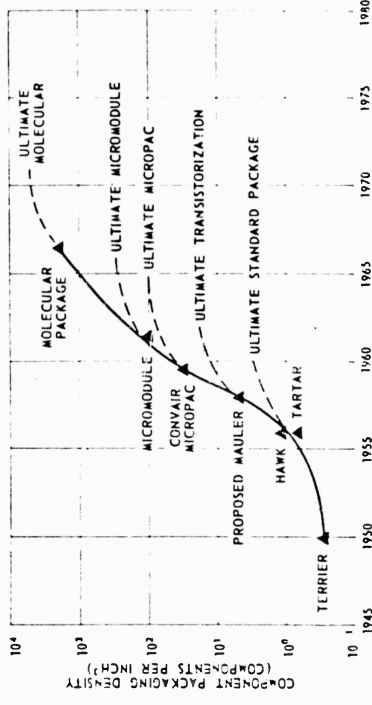


Figure 3.10.25. Evolution of Electronic Packaging.

SECRET

The actual number of components, of course, depends on the degree of sophistication and number of supplementary circuits employed.

A typical command guidance system requires approximately the number of components shown in Figure 3.10.24. The type of components employed in a command system are normally packageable with a very high density of components per cubic inch even with the employment of standard components.

The number of components packageable per cubic inch by various packaging techniques is shown in Figure 3.10.25. The points shown in this curve indicate values actually achieved as noted. The effective space utilization factors have been considered for each type packaging. The ultimate achievable values are based upon actual experience and research or upon projected estimates for future systems.

In compilation of the data for this curve all special components such as klystrons, magnetrons, etc., were excluded from the tabulation. The curve reflects the values to be expected from electronic assemblies with the normal ratio of electronic component types. Computer circuits as employed in command guidance systems are capable of higher component densities than normal circuitry due to the low power requirements and different ratio of component types.

With the standard or transistorized circuits, standard components are used and are joined together by mounting the components on a suitable structure and interconnecting the appropriate leads as shown in Figure 3.10.26 (A) and (B), Figures 3.10.27, and 3.10.28. The Convair micropac employs welded lead interconnections of standard parts which are then encapsulated to provide mechanical support. This type packaging is shown by Figure 3.10.26 (C) and the proposed package in Figure 3.10.29.

Several methods of electronic packaging were investigated for use in the PYE WACKET design. These were the micromodule, modular circuitry, and the welded module technique.

The micromodule, and microcircuitry in general, consists of miniature wafers upon which are deposited (etched or fabricated) the individual components. One or more components are placed on each wafer. The wafers can then be stacked together and the components connected together on the edges of the wafers. The advantage offered by this type packaging are higher component densities and standardized package dimensions. Difficulty is experienced in actual use from the electrical cross-coupling of electronic signals due to the type of construction. However, this type circuitry is not yet commercially available with wide component selections and the present cost is somewhat excessive for the minor improvement over packaging techniques utilizing standard components. Therefore this method was not considered for use on PYE WACKET in the immediate time period.

Molecular circuitry offers the greatest component packaging density known today. A molecular or solid-state circuit is produced by "growing" a single

SECRET

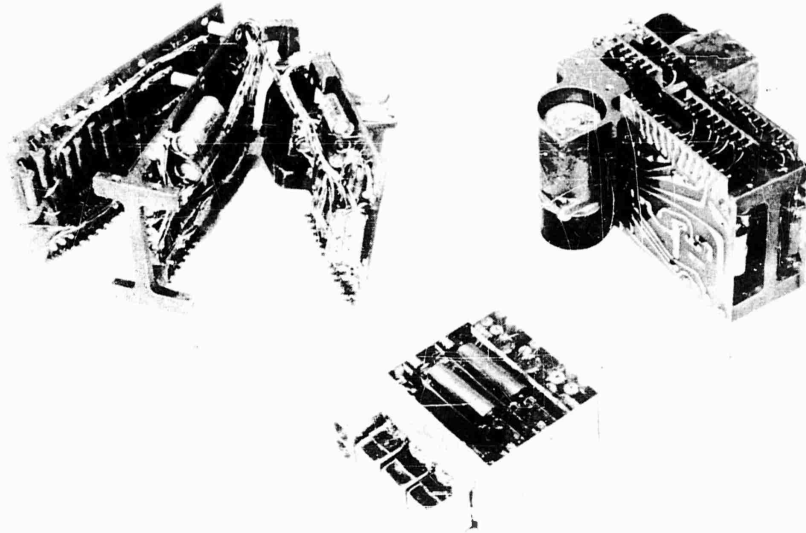


Figure 3.10.26. Standard and Improved Standard Packaging.

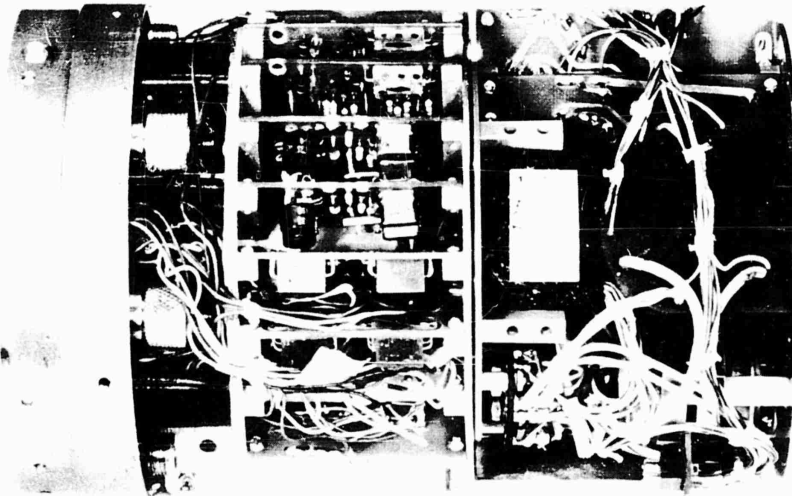


Figure 3.10.27. Transistorized Guidance Package.

SECRET



Figure 3.10.28. Transistorized Video Amplifier.

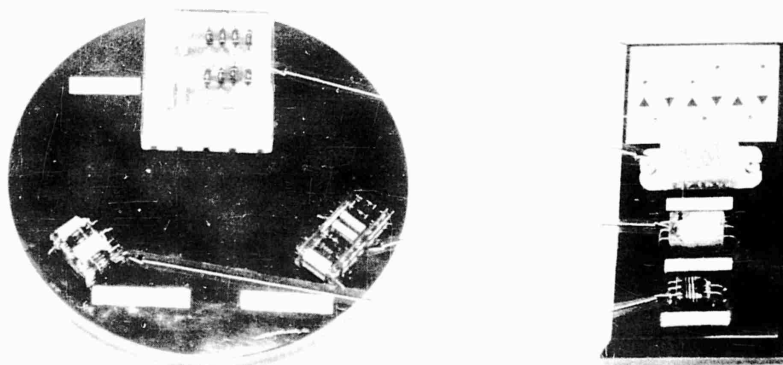


Figure 3.10.29. Evolution in Packaging Diode Assembly.

SECRET

solid state element which contains an entire circuit. This molecular circuit is "grown" by much the same process as is currently used to produce crystal diodes, transistors, etc. Though this offers the ultimate in miniaturization of electronic packages, each circuit must be individually designed and "grown" within specifications. This type of circuitry is not likely to be available for production design within the initial time period for the development of PYE WACKET. Therefore it was also dropped from consideration for the immediate time period.

For the initial PYE WACKET time period a type of packaging was chosen which is similar to the Convair micropac and utilizes welded construction of commercially available subminiature components. This appears to be the best compromise of cost, miniaturization, reliability, and availability.

The welded module technique has been developed as an immediate solution to the problem of subminiaturization in transistorized missile-borne electronics. This method of electronic packaging consists of placing standard circuit elements side by side and forming the circuit connections on a three-dimensional basis, as opposed to the two-dimensional printed circuit board. The wires are joined by electrical resistance spot welding, which is similar to vacuum tube construction. A metallic ribbon may be used as the common lead joining medium to give a uniform weld to the wide range of component lead sizes and materials. After assembly and electrical check-out the unit is encapsulated to form a module. The resulting subminiature package is a maximum density assembly with standard components utilizing all practical space within the package.

Figure 3.10.30 is an actual photo of the electronic package mockup for the PYE WACKET configuration.

Since the same control functions are required for any PYE WACKET missile and inert weight minimization is important for all missiles, the autopilot weight is considered to be constant throughout the range of scaling. A curve of the expected electronics section weight is given in Figure 3.10.31. This curve was prepared by utilizing the above information to indicate trends and by drawing upon experience from other guidance and autopilot programs of a similar nature to indicate the actual weights to be encountered.

FUZE SYSTEM. The fuze group consists of (1) the safe-and-arm mechanism for a high explosive warhead, (2) the target detection device (including antennas), and (3) the warhead detonation circuitry. Items 1 and 3 are independent of missile size and hence are considered to be of constant weight and non-scalable. The weight of the target detection device is a relatively discrete function of its performance requirements. The smallest practical fuze for missile application is a simple VT type fuze. Such a fuze offers the obvious advantage of minimum size and weight but has little counter-countermeasure (CCM) capability. If range rate is available from the guidance, the

SECRET

3. 10. 41

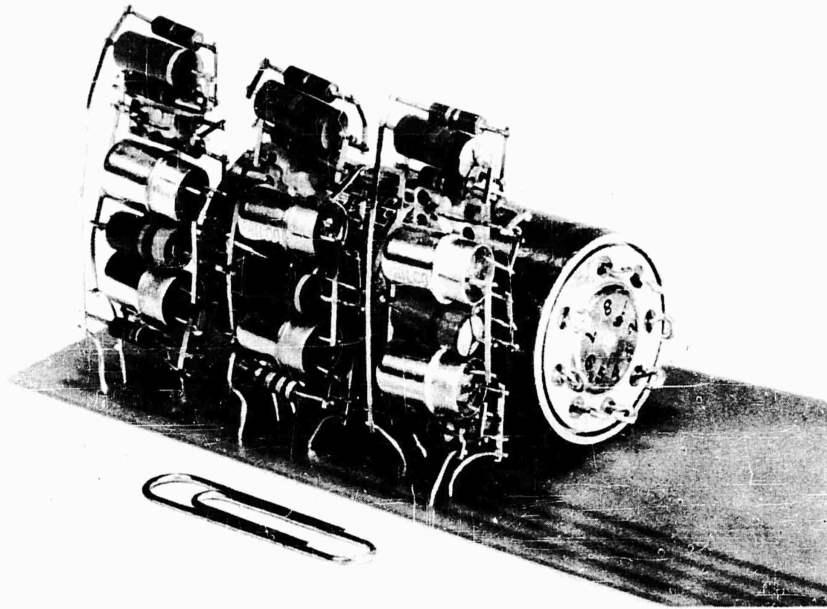


Figure 3.10.30. PYE WACKET Electronic Package Mockup.

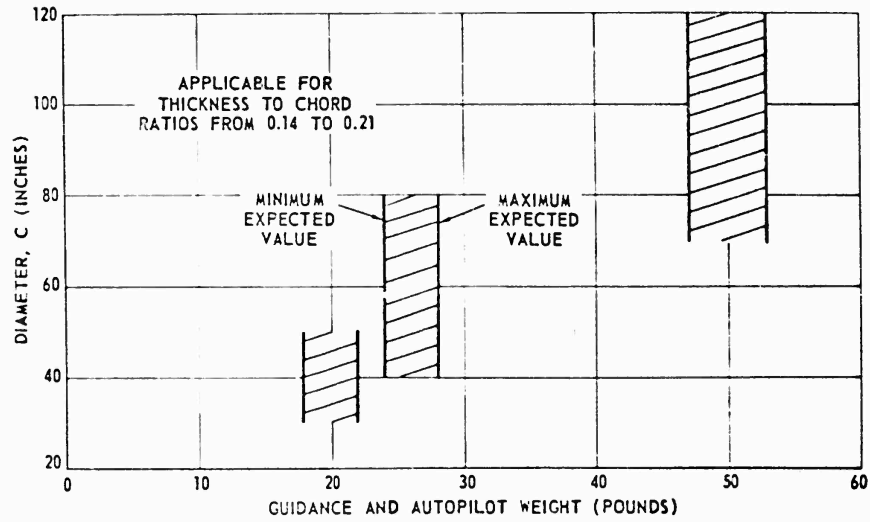


Figure 3.10.31. Scaled Electronic Section Weights.

SECRET

performance can be improved on this type of fuze with a variable delay-time from detection to detonation. However, this type of fuze produces an RF lobe pattern which is very broad and poorly defined since it operates at relatively low RF frequencies and is, therefore, highly sensitive to changes in spatial loading or power supply fluctuations. A VT fuze of this type sets up a static oscillation so that any change in spatial loading such as the sudden presence of another object within the lobe causes a detonation signal to be initiated.

Additional improvements over the VT fuze performance necessitate an incremental weight increase to a fixed-angle-fuze of approximately 5 pounds. This allows utilization of a narrow fixed angle lobe pattern with its improved sensitivity and better CCM performance. Slightly more sophisticated circuitry can then be utilized for more accurate fuzing. This results in a reduction of effective missile miss-distance. In addition, the fixed angle lobe gives good directivity in target detection. By utilizing the proper angle the warhead fragments can be dispersed more effectively.

An improvement over the fixed angle fuze can be obtained by an increase in weight to approximately 15 pounds. A coherent type RF fuze can be designed at this weight. Such a coherent type RF fuze offers excellent CCM performance. In the larger missiles which will accommodate this increased weight, the excellent CCM performance and detonation time optimization are very attractive features as means of improving the missile effectiveness.

An adaption kit weighing 15 pounds was estimated as that which is achievable and is acceptable for use with nuclear warheads for airborne use. This unit would only be employed when a nuclear warhead is used.

The expected fuze weights for the scaled PYE WACKET missiles are shown in Figure 3.10.32. These curves were drawn by recourse to experience since analytical expressions for fuze weight variations are impossible. Where the exact weight will lie within the shaded region is highly dependent upon the quality of the design used.

For purposes of performance scaling the 5 pound fuze was used for all missiles up to 70 inches diameter and the 15 pound fuze was used for missile diameter from 70 to 120 inches. The adaption kit was considered a part of the nuclear warhead and was therefore treated parametrically as part of the warhead weight.

BATTERY POWER SUPPLY. The feasibility designs of the nominal missiles employ a thermal battery for electrical power. A thermal battery was chosen because it meets the safety and storage requirements and is ready for immediate service without prelaunching attention. Electronic circuits are provided for voltage regulation and for DC to AC conversion.

Thermal batteries have a known achievable output up to approximately 4.0 watt-hours per pound depending upon the size of the battery and its application. Other known missile systems utilize batteries delivering 0.5 to 2.0 watt hours per pound. The actual battery size for the feasibility designs was

SECRET

3.10.43

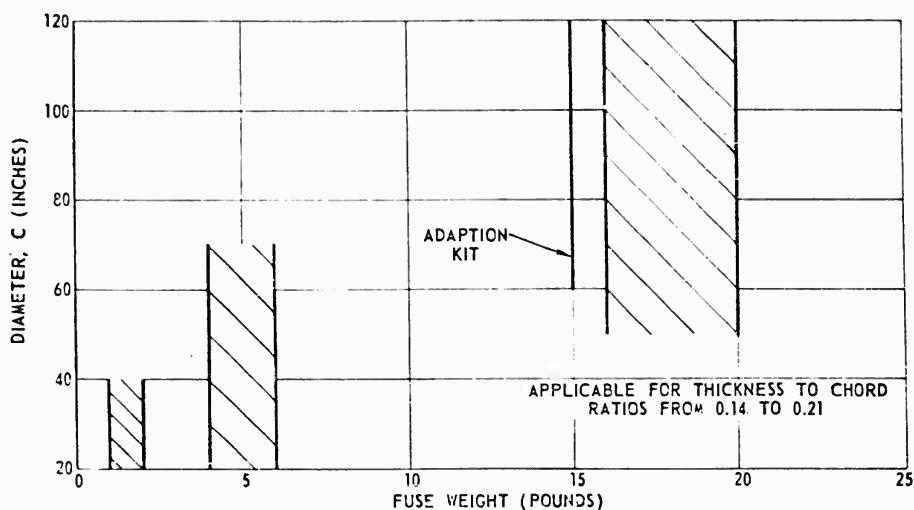


Figure 3.10.32. Scaled Fuze Weights.

based upon an output of 1.7 watt-hours per pound and a requirement of 20 watts per pound of electronics for the duration of missile flight.

The weights for the battery system may be approximated by the relation

$$W_i = k W_{EL} \gamma_m \tag{3.10.46}$$

where W_{EL} = weight of electronics

As determined in the performance scaling study (presented later), the flight duration is approximated for the missiles of 14 percent thickness by the relation

$$\gamma_m : C^{.815} \tag{3.10.47}$$

and for missiles of 21 percent thickness by the relation

$$\gamma_m : C^{.581} \tag{3.10.48}$$

Utilizing a constant battery output per pound for all missiles the sealed weights can be approximated by

$$W_i = W_o \frac{W_{EL1}}{W_{ELo}} \left(\frac{C_1}{C_o} \right)^{.815} \tag{3.10.49}$$

SECRET

for the missiles of 14 percent thickness and by the relation

$$W_1 = W_0 \frac{W_{EL1}}{W_{EL0}} \left(\frac{C_1}{C_0} \right)^{.581} \quad (3.10.50)$$

for the missiles of 21 percent thickness.

The curves of Figures 3.10.33 and 3.10.34 show plots of this equation for the scaled PYE WACKET missiles based upon the values for the nominal 60-inch diameter missiles and the electronics weights from Figure 3.10.31.

ABLATIVE SURFACE. The high rate of aerodynamic heating of the PYE WACKET missiles requires that protective techniques be employed to maintain the temperature within acceptable limits for the structural skin. After completing preliminary aerodynamic heating calculations, a thin teflon ablative surface coating was selected as the means of controlling skin temperature. This covering is designed to keep the skin temperature below approximately 800°F.

The determination of the required weight of ablation material for the nominal 60-inch diameter missile necessitates lengthy calculations and computer solutions. Determination of the actual weights for any size missile will, of course, require similar detailed solutions utilizing actual missile parameters and trajectories.

By employing the general equations for ablative surfaces and making sufficient simplifying assumptions for the purposes of scaling it was possible to obtain an analytical expression for first order estimates of the weight of ablative material. On the basis of equal conditions such as altitude, ambient temperature, materials, etc., the weight of ablation material required can be approximately scaled by the relation

$$W_1 = W_0 \left(\frac{A_1}{A_0} \right) \left(\frac{\gamma_1}{\gamma_0} \right) \left(\frac{V_1^{3.8}}{V_0^{3.8}} \right) \quad (3.10.51)$$

The linear duration approximation neglects the time required for the surface to reach the ablation temperature.

The area of surface to be covered, A, is, as shown previously, approximated by

$$A = \frac{\pi}{4} C^2 \quad (3.10.52)$$

SECRET

3.10.45

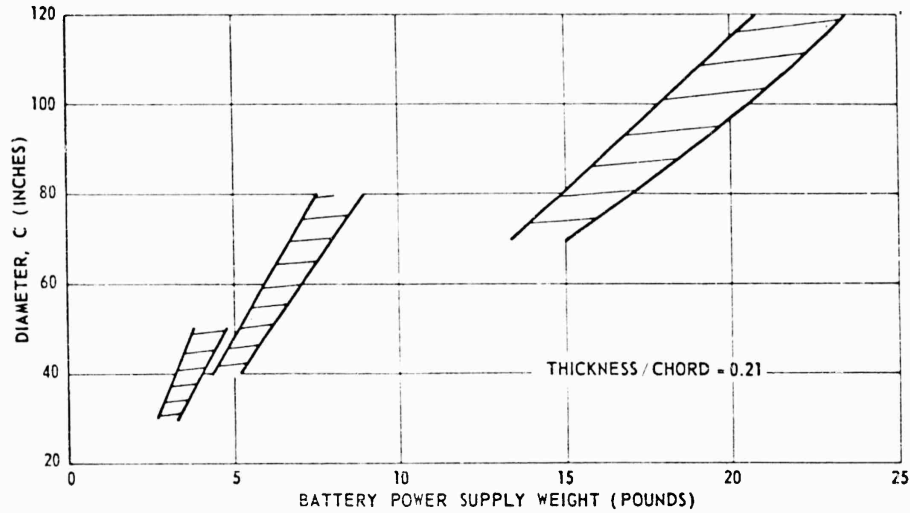


Figure 3.10.33. Scaled Battery Power Supply Weights.

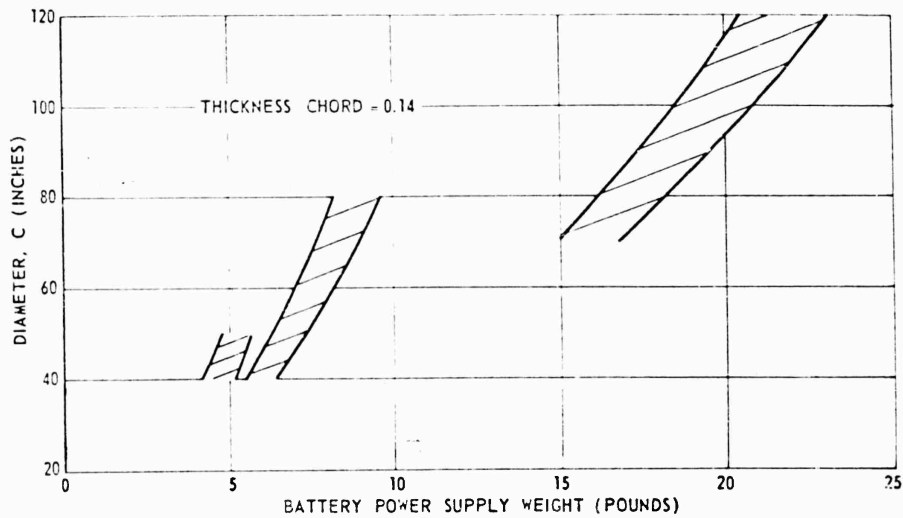


Figure 3.10.34. Scaled Battery Power Supply Weights.

The flight duration, τ , to 1500 FT/SEC, and velocity as determined in the performance scaling section (Figure 3.10.35) is seen to vary approximately by the relation

$$\tau : C^{.581} \tag{3.10.53}$$

for the 21 percent thickness missiles having diameters between approximately 40 and 120 inches but drops off more rapidly for missile diameters less than 40 inches.

SECRET

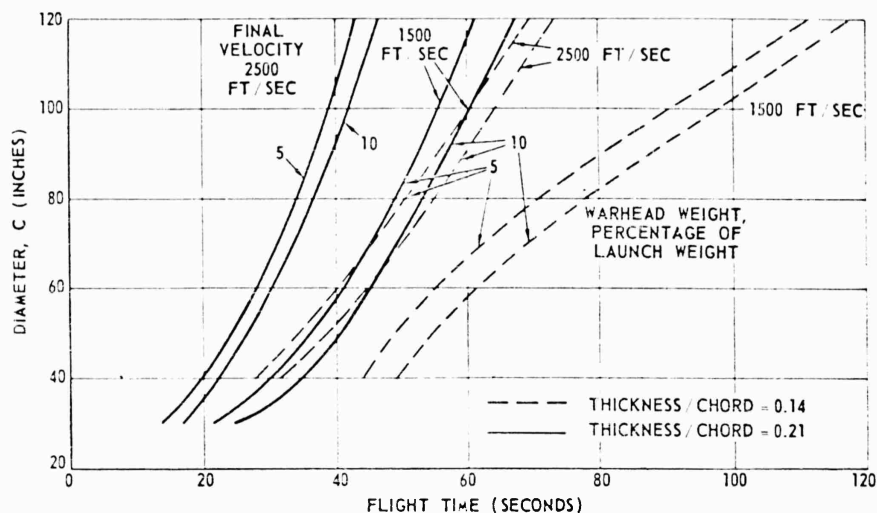


Figure 3.10.35. Scaled Flight Times.

Likewise for the 14 percent thickness missiles the flight time, τ , is seen to approximate very closely the proportionality

$$\tau: C^{.8/5} \tag{3.10.54}$$

for missiles from 40 to 120 inches.

Using the scaled relations determined in previous sections, maximum burnout velocity is found to increase for diameters up to approximately 70 inches and thereafter decrease somewhat. Since a detailed study of specific designs would probably show improved mass ratios with corresponding increased burnout velocities, burnout velocity was assumed constant for purposes of determining weights of ablation material. This assumption is compatible with the first order approach necessarily employed throughout the scaling section. Utilizing the assumption of constant burnout velocity and the foregoing relations, the ablation weights were determined as follows:

For missiles of 14 percent thickness ratio

$$W_i = W_o \left(\frac{C_i}{C_o}\right)^2 \left(\frac{C_i}{C_o}\right)^{0.58} = W_o \left(\frac{C_i}{C_o}\right)^{2.58} \tag{3.10.55}$$

This relation will tend to overestimate ablation material weights for missile diameters less than 40 inches.

For 14 percent t/C vehicles

$$W_i = W_o \left(\frac{C_i}{C_o}\right)^2 \left(\frac{C_i}{C_o}\right)^{0.8/5} = W_o \left(\frac{C_i}{C_o}\right)^{2.8/5} \tag{3.10.56}$$

SECRET

where W_0 = ablation material for the 60-inch diameter vehicle and $C_0 = 60$ inches (again assuming W_1 passes through the origin of the weight-diameter curve).

These foregoing equations for determining the scaled weight of the ablation material will give reasonably accurate first approximations of actual weights and are graphically shown in Figure 3.10.36.

MISCELLANEOUS WEIGHTS. The miscellaneous weights such as minor attachment and mounting hardware, interconnections, etc., have been considered to be a part of the subsystem with which they are associated. The weights of the missile harnessing, umbilical connector, and encapsulation however, are treated as separate weights in this scaling. Harnesses are routed along the inside of the periphery of the missile and assuming the same number of wires to be required for all missiles these harness weights are therefore considered to be proportional to missile diameter. The electronic packages are best fabricated by encapsulating the complete circuits in a suitable material as noted in the previous discussion of packaging techniques. The weight of this material is arbitrarily treated as a miscellaneous weight since it adds nothing to the function of the electronic packages but only acts as isolation from shock, vibration, and environments.

The weight of this encapsulation is proportional to the volume occupied and hence may be very nearly approximated as being proportional to the weight of the electronic assemblies to be encapsulated.

Miscellaneous weights of the scaled PYE WACKET missiles of diameter, C , can now be scaled by the generalized relation

$$W_1 = \alpha \frac{C_1}{C_0} + \beta \frac{W_{EL1}}{W_{EL0}} \quad (3.10.57)$$

where α represents the weight of harnessing and β represents the weight of encapsulation material used in the nominal ($C_0 = 60$ inches) diameter missiles, (again assuming W_1 passes through origin). The curve of Figure 3.10.37 depicts graphically this variation with missile diameter as plotted from this scaling equation.

Since the weight of the electronic section is independent of the ratio of thickness to diameter (t/C), the miscellaneous weights are also independent of t/C .

3.10.3 PERFORMANCE SCALING

Performance comparisons of the scaled PYE WACKET missiles were made on the basis of 2500 FT/SEC initial launch velocity. Trajectories were calculated for non-maneuvering flight at a constant altitude of 60,000 feet and alignment of missile flight vector along the initial velocity vector. All trajectories were computed for the same maximum range with the same final velocity. The thrust

SECRET

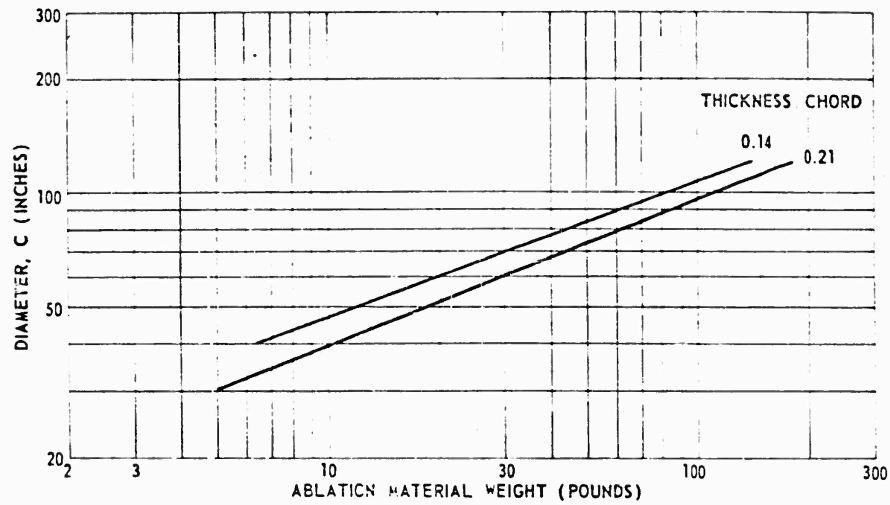


Figure 3.10.36. Scaled Ablation Material Weights.

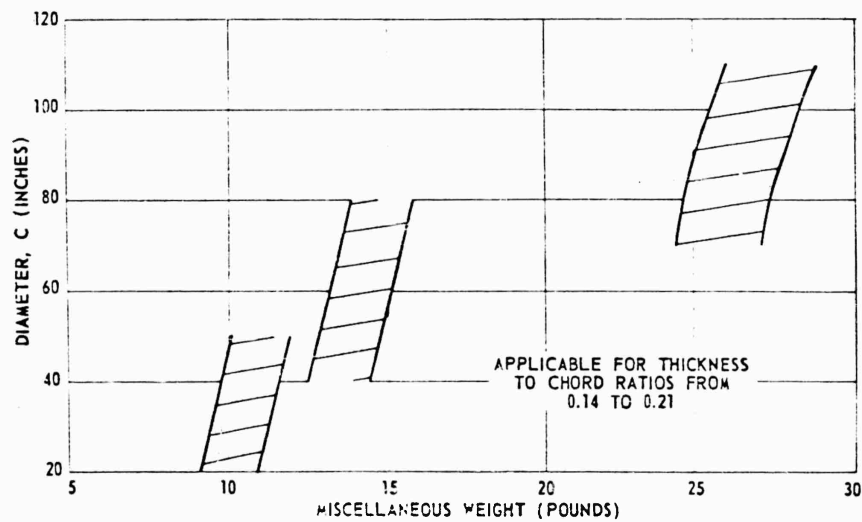


Figure 3.10.37. Scaled Miscellaneous Weights.

level of each size missile was selected to give the same boost acceleration to each missile and was considered to be a constant thrust during the entire boost phase of flight. Aerodynamic analyses have shown that the zero-lift-drag coefficient (C_{D_0}) is relatively independent of missile diameter over the range of scaling for constant thickness-to-chord ratios.

The minimum empty weight associated with each diameter missile was chosen for performance comparison purposes.

SECRET

3.10.49

The actual scaled launch weight based upon the scaled volumes of Figure 3.10.15 and a constant overall density of .0445 LB/IN³ is plotted in Figure 3.10.31 for the nominal thickness-to-chord ratios of 14 percent and 21 percent over the range of scaled diameters. This curve is used for obtaining the launch weights used for scaled performance comparisons.

Some of the subsystems weights cannot be presented by single value functions of missile diameter but are of one or more discrete values. Some missile sizes may accommodate either of these discrete values. The continuous scaling curves are considered to be average values of what may be encountered in actual detail designs. The relation of actual weights to the scaled values will depend a great deal on the quality of design and the emphasis placed on weight savings and cost during the early stages of missile design and development. Costs, material availability, and quality control practices may also influence any final design weights.

The difference between the inert weight and the actual launch weight is the portion available for the payload (warhead) and propellant. The division between propellant and warhead was not shown because of the lack of sufficient target, guidance and mission data to define adequate warhead weights. Assumption of a value for warhead weight however, will define the amount of propellant available for any diameter missile chosen.

Typical designs usually result in a warhead weight which is between 5 percent and 20 percent of the missile launch weight for interceptor missiles.

The actual weight of warhead chosen can be converted to a percentage of launch weight by means of the curves of Figure 3.10.38. This allows for a parametric comparison of scaled performance.

From the scaled trajectories the range performance comparison (based on fixed coordinates) shown in Figure 3.10.4, was prepared to show the performance trends associated with changes of missile diameter and payload weights. These curves show the range performance variations to be expected by changes of missile diameter from 30 inches to 120 inches. Figure 3.10.4 is arbitrarily based upon effective terminal velocities of 1500 FT/SEC and 2500 FT/SEC.

Flight time-to-target shown in Figure 3.10.35 and maximum standoff distances which are actually range performance based on moving coordinates are shown in Figure 3.10.39 and are important parameters in performance comparisons. The scaled standoff distance based on a 2500 FT/SEC constant velocity launching aircraft flying the direction of missile flight is shown in Figure 3.10.39.

These foregoing curves may be used as a means of estimating weights, performance and diameters for various possible PYE WACKET missiles.

All performance scaling was based upon design values for the nominal 60-inch diameter missiles of 14 percent and 21 percent thickness-to-chord ratios.

SECRET

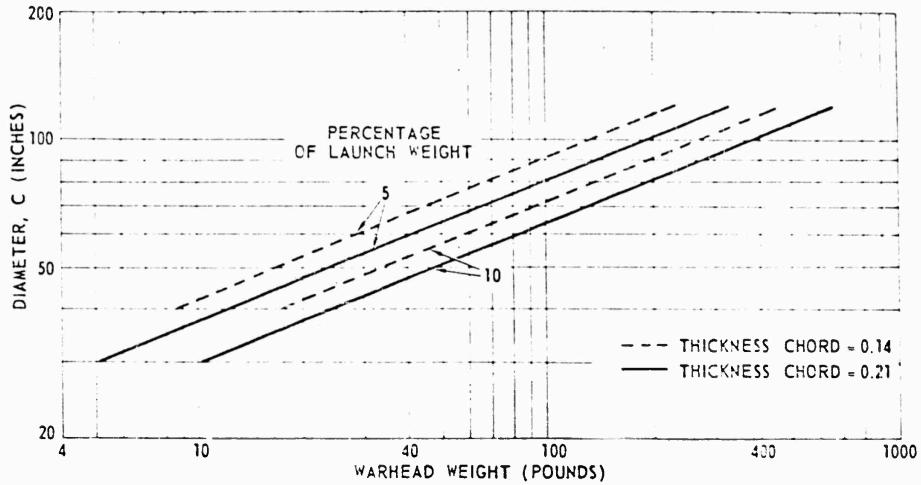


Figure 3.10.38. Scaled Warhead Weights.

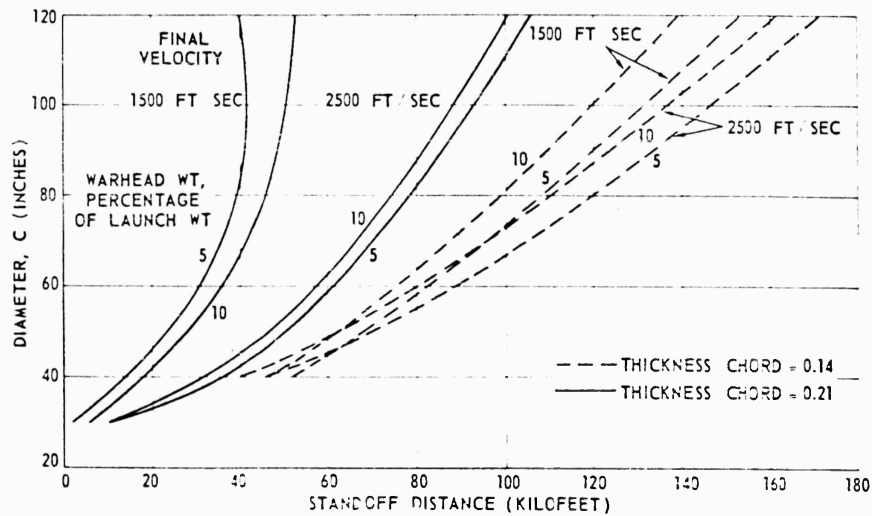


Figure 3.10.39. Scaled Standoff Distances.

The scaling curves presented in this sub section are applicable to scaled PYE WACKET missiles within the initial PYE WACKET development time period and within the first order approximations necessarily employed. Some improvements can be expected during subsequent time periods due to improved materials and techniques. The foreseeable improvement that may be expected in the area of electronic packaging is presented in Figure 3.10.25.

SECRET

3.10.4 SMALL MISSILE DESIGN

In addition to the feasibility designs of the nominal 60-inch diameter missile, a similar feasibility design was conducted on a smaller PYE WACKET missile. This smaller missile has the same basic configuration as the larger nominal missile and a diameter of 36 inches. A 21 percent thickness-to-diameter ratio was chosen for the smaller missile to facilitate component packaging while affording the greatest reduction of diameter. This small PYE WACKET missile is based upon the utilization of more advanced techniques.

The principal advantages of the advanced missile are its reduced weight and size. This reduced size increases the number which can be carried by any particular aircraft and greatly reduces the problem of handling, shipment and launching.

The layout of the 36-inch diameter missile is shown in Figure 3.10.40. Several layouts were made to ascertain the best arrangement. It was found that the layout presented in Figure 3.10.40 gave the best space utilization and best center of gravity location, during flight. An infrared guidance system is packaged in the front of the missile. This guidance system is discussed in subsection 3.8 of this report.

The fuze is an active fixed angle type which can best optimize the fuzing problem for maximum kill probability. The fuze, electronic package and safe and arm mechanism are packaged as shown in Figure 3.10.40. The entire fuze package would be encapsulated similar to the guidance package and may be electrically shielded by means of direct deposition of metallic film.

The safe and arm mechanism is a serial inertial, electrical mechanism which gives positive safing under all conditions of shipment and handling. The high boost thrust for a finite period of the time insures positive and reliable arming at a safe distance by utilization of a mechanical integrating mechanism which completes the detonation train to the warhead. Arming cannot occur until the missile has experienced the proper boost acceleration in the proper direction for a specified finite length of time.

The warhead is centrally located between the forward rocket motor bulkhead and the guidance package. Warhead support is furnished by attachment to the forward mounting beams. With the 36-inch PYE WACKET configuration only a limited diameter of a standard cylindrically constructed warhead could be accommodated due to the compound curvature of the surface and the thin section available for packaging in the forward section of the missile. To overcome these packaging difficulties and obtain a more efficient warhead space utilization a controlled fragmentation contoured type warhead which fits the missile contour and employs flat aft and front surfaces was chosen. The feasibility of a continuous-rod type warhead for this PYE WACKET missile was not completely investigated during this study. The feasibility design of the 36-inch missile employs a 20-pound controlled fragmentation contoured type warhead.

SECRET

A pancake type solid propellant rocket motor and a reaction control system similar to those discussed for the 60-inch diameter missiles were also assumed. The weight and balance statement for the 36-inch missile is shown in Table 3.10.5 and the thickness chart is shown in Table 3.10.6.

To better illustrate the packaging arrangement of the 36-inch diameter missile a conceptual mockup was constructed. Figures, 3.10.6, 3.10.41, 3.10.42, and 3.10.43 are photographs of this mockup. Figure 3.10.6 is a top view of the vehicle; on either side of the aft end the jet control nozzles may be seen. Figure 3.10.39 shows the interior arrangement. The rocket motor and elliptical nozzle are visible as are the thrust chambers, propellant tanks, and pressurizing tanks for the reaction control assembly. The forward-area components are best seen in Figure 3.10.40. Locations and relative sizes of the electronic section, power supply, warhead, and fuse can be seen.

In order to complete the feasibility study for the smaller missile configuration, its performance was examined. First consideration was given to the examination of maneuver capability as a function of reaction jet thrust. The center of pressure variation with Mach number was assumed to be identical to the wind tunnel results for a 14 percent thick configuration. It was also assumed that the center of pressure did not vary with angle of attack, which the wind tunnel results substantially verify over the limited test range. The empty weight and corresponding center of gravity as determined in Table 3.10.5 were used in the computation of maneuver capabilities.

Table 3.10.5
WEIGHT AND BALANCE STATEMENT FOR 36-INCH DIAMETER
21 PERCENT PYE WACKET MISSILE

Item	Weight (LB)	Arm (IN.)	Moment (IN/LB)
Structure Group			
Skins	2.4	29.0	69.6
Leading edge	6.0	5.3	31.8
Mounting structure	.6	11.0	6.6
Joints	3.5	22.0	77.0
Rocket Motor			
Motor case	11.2	23.1	258.7
Restrictor	3.1	22.1	68.5
Igniter	.5	18.0	9.0
Nozzle (main)	4.7	31.2	146.6
Nozzle controls	1.3	31.1	40.4

SECRET

SECRET

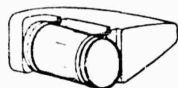
Item	Weight (LB)	Arm (IN)	Moment (IN/LB)
Guidance	5.7	5.8	33.1
Auto Pilot	7.0	5.8	40.6
Harnessing	2.8	6.4	17.9
Warhead	20.	11.5	230.0
Adaption Kit	None	-	-
Fuzing and S/A	4.0	11.9	47.6
Power Supply	2.0	11.9	23.8
Ablation Materials			
End flight	1.9	10.5	20.0
Launch	8.5	10.5	89.2
Control System			
Fuel tanks	1.75	32.30	56.5
Pressurizing assembly	1.30	31.65	41.2
Combustion chambers	1.60	31.30	50.1
Control nozzles	.75	31.20	23.4
Servos and valves	2.10	30.70	64.5
Plumbing	.70	31.25	21.9
Control Propellant	8.5	32.30	274.5
Rocket Propellant	100.0	21.30	2130.0
Launch Conditions	200.00	19.26	3852.5
Final Conditions	84.90	16.24	1379.2

The smaller, 36-inch diameter, configuration is highly maneuverable. The center of gravity is located close to the center of pressure allowing small control forces in pitch. However, the small center of pressure variation with Mach number results in a large variation of maneuverability with Mach number. At Mach 2, about 100 pounds thrust per jet is required to achieve 50 g's as shown in Figure 3.10.41. At Mach 3, only about 7 pounds per jet is required.

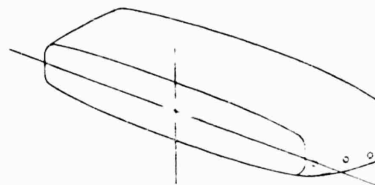
Figure 3.10.45 presents the variation of range with altitude assuming a launch velocity of 800 FT/SEC. A thrust value of 5000 pounds and a burning time of 5.2 seconds was assumed. Assuming an end velocity of 2000 FT/SEC, the 36-inch diameter configuration has a range of 22,000 feet at 30,000 feet altitude and 300,000 feet at 90,000 feet altitude.

Figure 3.10.46 presents the estimated yawing moment variation with yaw angle for the 36-inch diameter, 21 percent thickness configuration for launch conditions of Mach 2.5 at 60,000 feet altitude. This launch condition is shown because it is the most severe condition anticipated for this configuration. The yaw moment capability of reaction jets is also shown on the plot for various

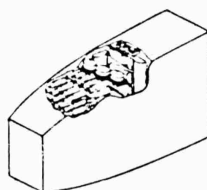
SECRET



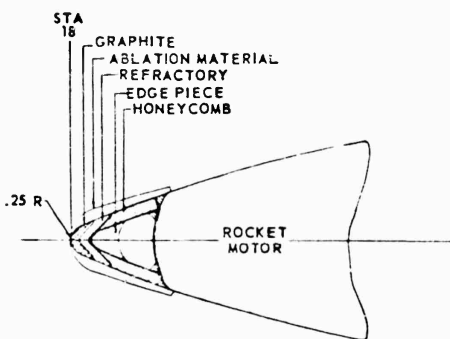
BATTERY
PERSPECTIVE VIEW



WARHEAD
PERSPECTIVE VIEW



TYP. PACKAGE INSERT
PERSPECTIVE VIEW



LEADING EDGE
AT STA. 18 - ROTATED 45°

STRUCT
SUPPORT

STA
GUIDE

STA
ROCKET

1

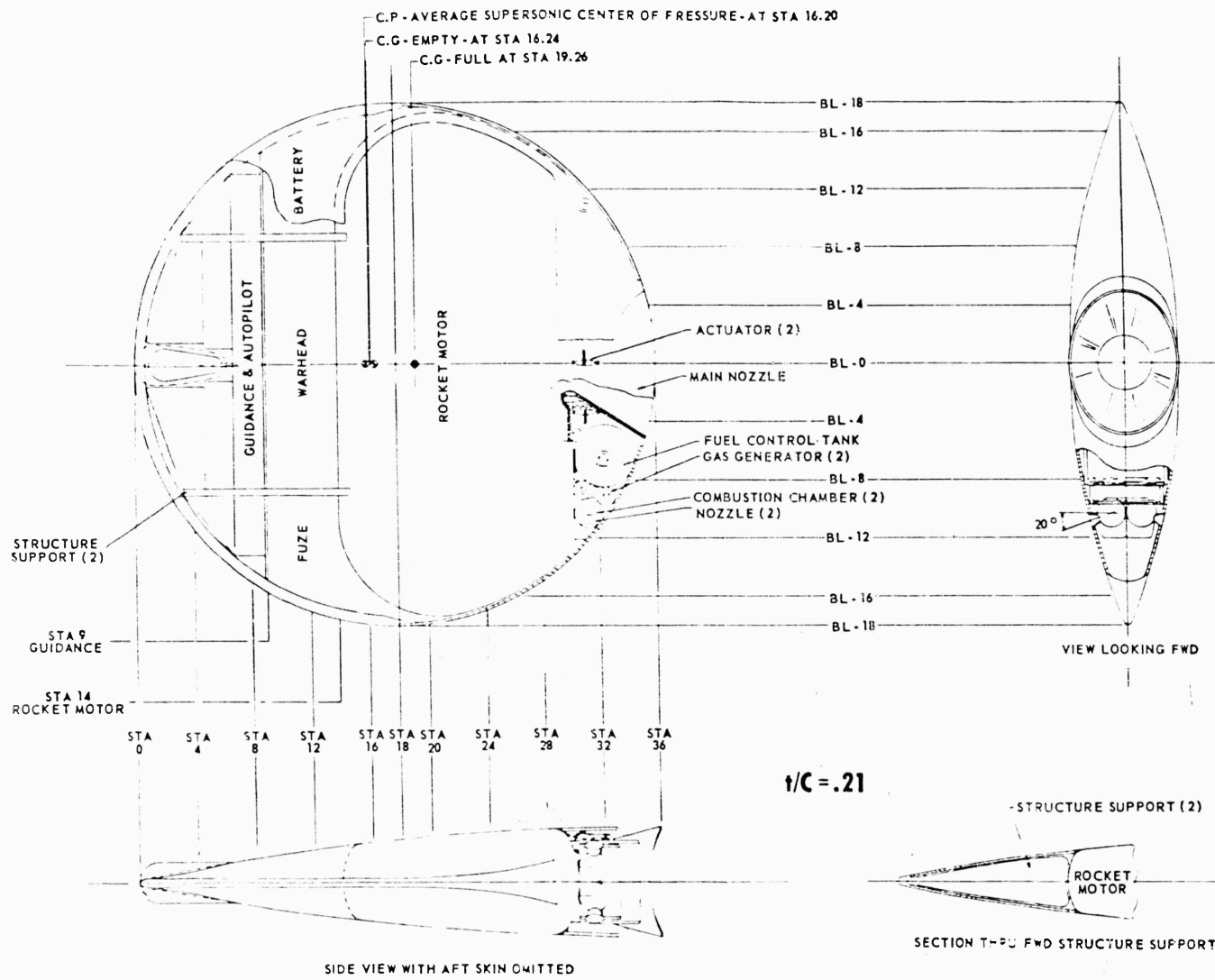


Figure 3.10.40. Feasibility Layout of 36-Inch Diameter 21

2

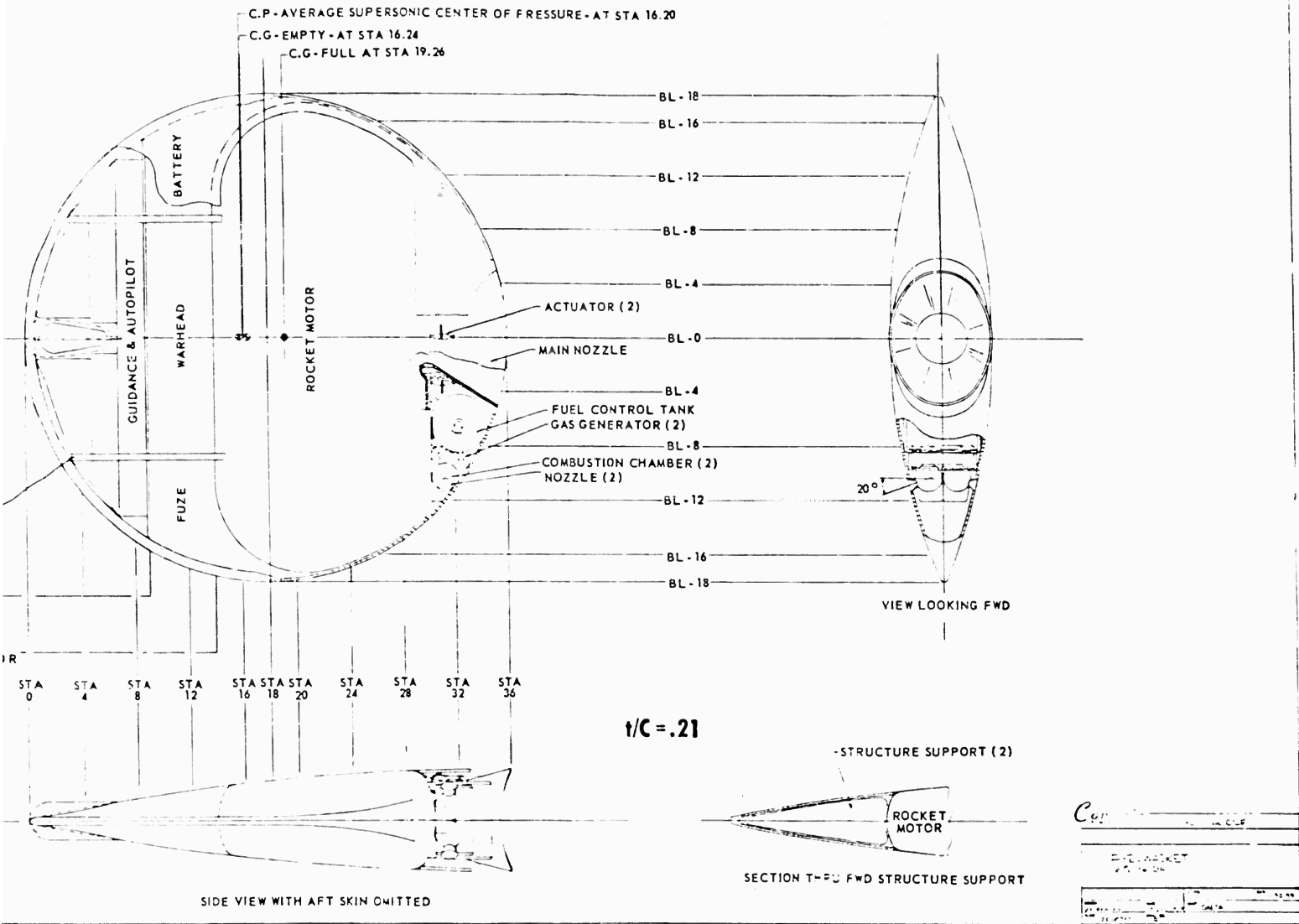


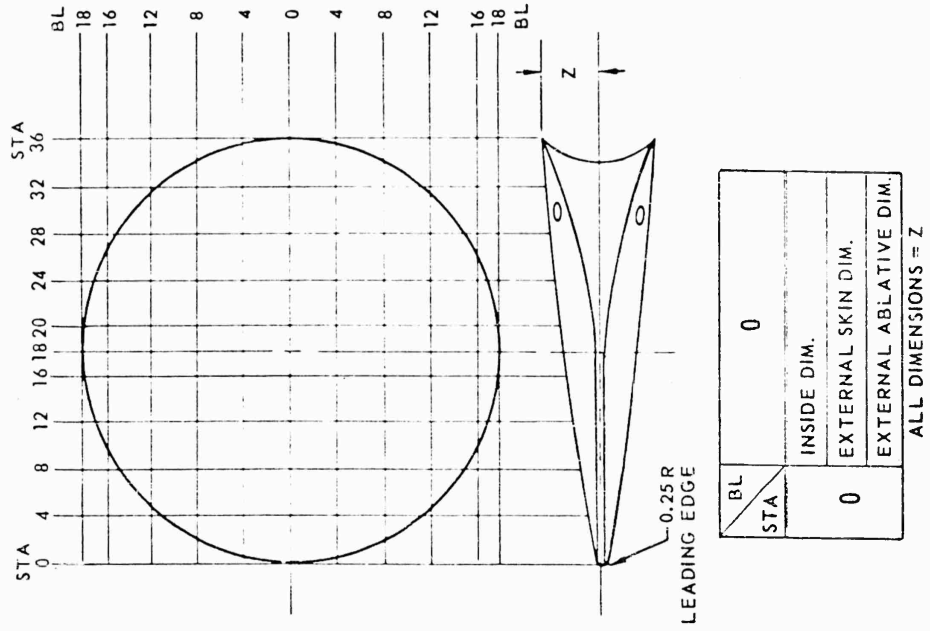
Figure 3.10.40. Feasibility Layout of 36 - Inch Diameter 21% PYE WACKET Missile.

3

SECRET

Table 3.10.6
 PYE WACKET 21 PERCENT 36-INCH DIAMETER

		PYE-WACKET 21% 36" DIA						
BL STA	0	4	8	12	16	18		
0	.201							
4	.772	.683	.405					
8	1.439	1.345	1.068	.565				
12	2.014	1.922	1.639	1.115	.280			
16	2.497	2.407	2.115	1.560	.629			
18	2.887	2.802	2.303	1.747	.816			
20	2.992	2.802	2.320	1.737	.734	.014		
24	3.079	2.989	2.507	1.924	.921	.201		
30	3.387	3.293	2.684	2.063	.959			
32	3.419	3.319	2.770	2.014	.772			
36	3.606	3.506	2.957	2.201	.959			
	2.549	3.419	2.892	2.014				
	3.736	3.606	3.079	2.201				
	3.593							
	3.780							



SECRET

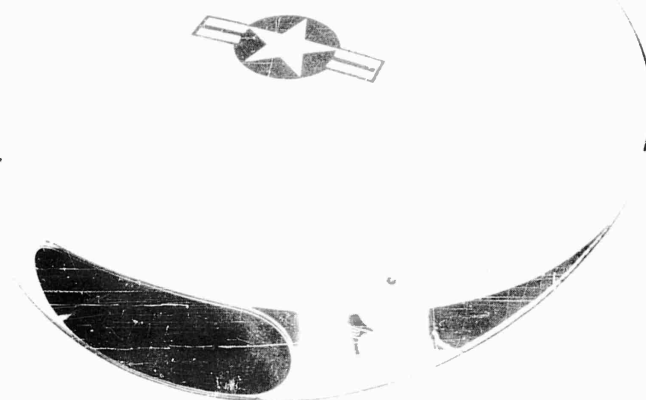


Figure 3.10.41. PYE WACKET 36-Inch Mockup.

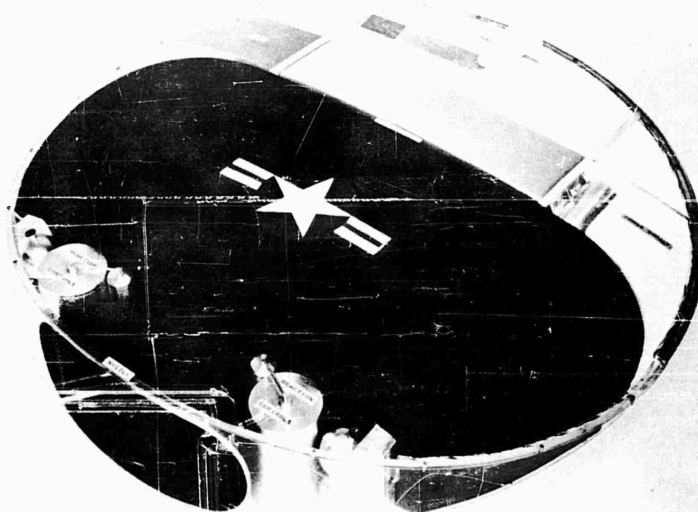


Figure 3.10.42. PYE WACKET 36-Inch Mockup.

SECRET

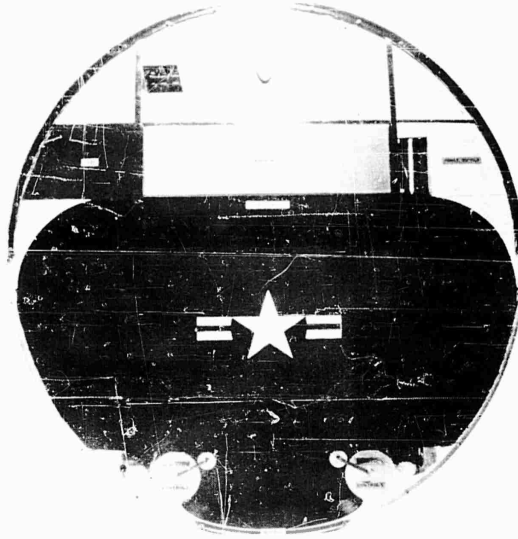


Figure 3.10.43. PYE WACKET 36-Inch Mockup.

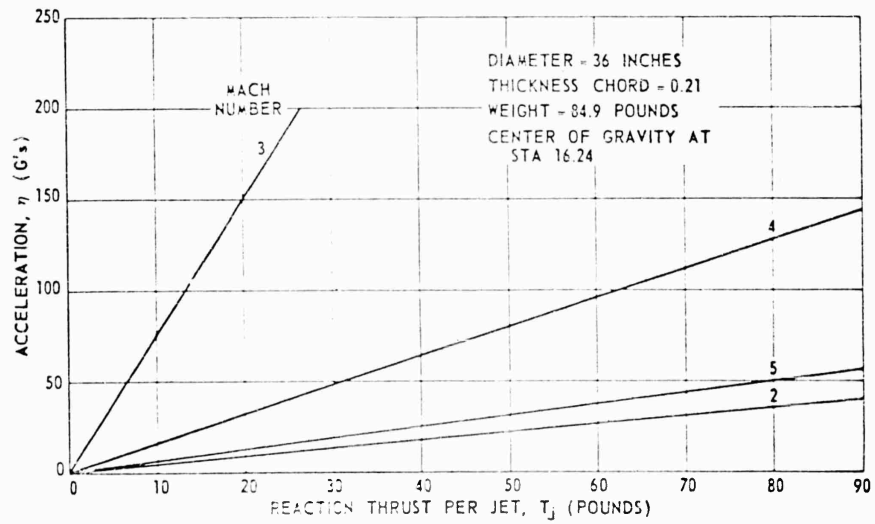


Figure 3.10.44. Variation of Maneuverability With Reaction Jet Thrust.

SECRET

3.10.59

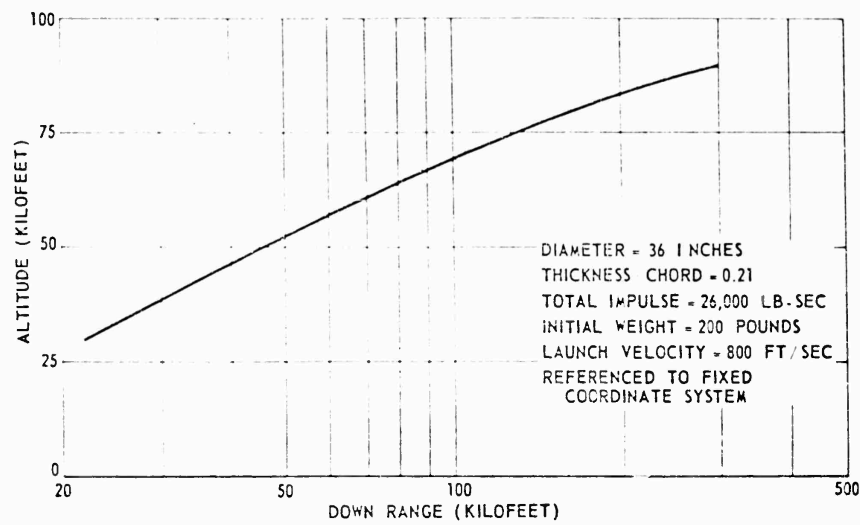


Figure 3.10.45. Effect of Altitude on Downrange.

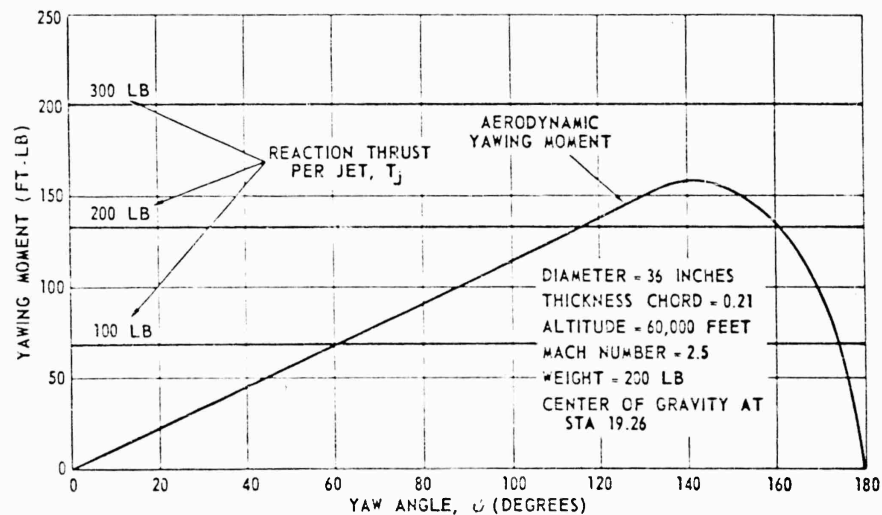


Figure 3.10.46. Required and Available Yawing Moment at Launch.

thrust levels. The launch weight and corresponding center of gravity position as determined from Table 3.10.5 were used in the computations.

The roll angular acceleration is shown in Figure 3.10.47 as a function of reaction jet thrust. Because of the low weight and corresponding low roll moment of inertia, the roll acceleration is extremely high. A roll acceleration of 1100 radians per second per second is possible with a reaction thrust per jet of 100 pounds.

SECRET

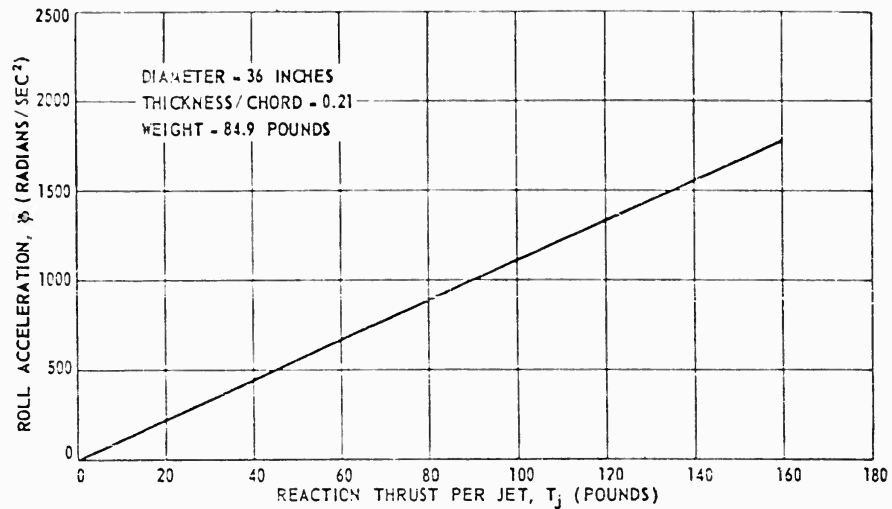


Figure 3.10.47. Variation of Roll Acceleration With Reaction Jet Thrust.

Comparison of Figures 3.10.44 and 3.10.46 indicate that yaw control during boost presents the critical design condition for the 36-inch diameter reaction controls. However, it should be remembered that yaw control by thrust vector deflection is available during boost. Therefore, the reaction controls need not be overdesigned for the limited flight time when the missile is yawed at large angles with respect to the relative wind.

It should also be noted that a more advantageous center of gravity variation is possible by alterations in packaging. These alterations would result in a balance of reaction force required for glide phase maneuver and omni-launch stabilization in yaw. Such an alteration could result in the negation of the thrust vector deflection required in the yaw plane.

3.10.5 SUMMARY

The above paragraphs included feasible designs for missiles of 60 and 36 inches diameter. Thickness ratios of 14 percent and 21 percent were considered for the 60-inch diameter missile since studies of subsection 3.4 indicated that the performance capabilities were maximized for missiles with this range of thickness ratios. Considering maximum range capability, minimum time to target intercept, and packaging limits, the feasibility designs of the 60-inch diameter missiles were based on material and techniques which are sufficiently developed to allow production design to commence in the immediate time period.

The 36-inch diameter missile design was based on a 21 percent thickness ratio only since the small diameter of the missile necessitated sufficient thickness to allow adequate packaging space for propulsion, guidance, and control

SECRET

3.10.61

components. The feasibility design of the 36-inch diameter missile was based on advanced materials and techniques that would be available in the near future.

In addition to the feasible designs discussed above, scaling techniques were developed for estimating the effects of changing missile size on the weights of the various components and on the performance of the resulting missiles. These scaling techniques are based on the 60-inch diameter missiles of the immediate time period and apply to scaled missiles having diameters ranging from 30 inches to 120 inches.

It is emphasized that the results of the design scaling of the PYE WACKET missile are not intended to yield detailed or specific information but rather to indicate trends and first order estimates of weights and performance capabilities.

The results of this study indicate that both the 60-inch and 36-inch diameter PYE WACKET missiles are feasible from a design and performance standpoint. In particular, the advanced 36-inch diameter missile appears to offer adequate range performance with a significant reduction in size and weight.

3.10.6 SYMBOLS AND DEFINITIONS

W	Weight of general item without regard to specific missile
ρ	Density
C	Generalized missile diameter
s	Stress
M	Moment
h	Reference dimension for stress analysis
I	Moment of inertia
A	Area of surface
r	Radius
t	Thickness
T	Thrust
a	Crosssectional area
Δ	Incremental value
P	Pressure
k	Undefined constant of porportionality
η	Lateral dynamic load
d	Peripheral distance
D	Diameter
$\alpha, \beta, \gamma, \delta$	Generalized weight constants
v	Velocity
V	Volume
X	Distance between aerodynamic center of pressure and missile center of gravity
L	Length
:	Porportional to
τ	Flight duration

SECRET

Subscripts

M Missile
o Reference value from basic nominal 60 inch diameter missile
l Scaled value for scaled diameter missile
E Leading edge
s Skin
a Aerodynamic
W/H Warhead
L Launch
c Chamber
r Reaction controls
EL Electronics
i Incremental value
Th Throat
— Average value
Ex Exit
R Reference

SECRET

3.10.63

SECRET

**Section 4
RECOMMENDATIONS**

4.1 REVIEW OF RESULTS

This Phase I study has shown that the circular planform, blunted lenticular cross section configuration is feasible for the design of airborne weapons. Because of limitations on time and resources, emphasis was given to the evaluation of a vehicle suitable for manned aircraft defense. It is believed that other missions, including the several types discussed earlier in the text, might effectively use the PYE WACKET configuration. However, adhering to the basic philosophy employed in this study most of the discussion of recommendations will be directed toward airborne defense. In the concluding paragraphs of this section of the report a few brief recommendations concerning other applications will be made.

As developed in the previous text the PYE WACKET vehicle has the advantages of aerodynamic efficiency, high maneuverability, and cross-wind launch capability. It does have possible shortcomings in structural efficiency, particularly in packaging an integral propulsion system, as well as in longitudinal stability. The latter might be only a minor problem after rocket motor burn-out if the feasibility design layouts are a fair indicator.

The above are the general results of the study. Much work remains to be done in specific engineering studies and the establishment of detailed designs. The areas requiring additional information and, in many instances much work, are discussed in the paragraphs that follow. Subsequent to that discussion recommendations are made for an early test vehicle program based on "off-the-shelf" type components to demonstrate controllable missile flight and omnidirectional launch capability. Further, recommendations are made for an early start on a prototype missile based on the PYE WACKET concept.

4.2 WORK TO BE DONE

To make possible the preparation of drawings for actual vehicle fabrication, a large quantity of "design detail" data must be determined. The types of information obtained during this study have been primarily of the "go, no-go" type, which is satisfactory for a decision on the feasibility of the configuration. The next logical step is to obtain the detailed data required for the aerodynamic, propulsion, controls, and the other technical areas discussed in Section 3.

Aerodynamically, the acquisition of experimental data for design purposes has barely begun. Lift, drag and stability information must be obtained in all

SECRET

SECRET

flow regimes from the low speed incompressible region and extending well into the hypersonic range. Yaw data, in particular, should be acquired in the entire range from 0 to 180 degrees with a simulated jet-on condition. Aerodynamic data should be obtained on models that provide protuberances, joints, and other aerodynamic "dirt" sources as present on an actual vehicle. It will be necessary to provide methods of simulating the transients and flow field interferences that develop between parent vehicle and missile in the launch sequence.

Much work is yet to be done on the development of a stable launching system that provides sufficient ejection velocity without creating intolerable acceleration levels for missile components or instruments.

There are multi-coupled interactions among the propulsion system, basic structure, and the thermal protection which require thorough investigation to establish a compatible group of solutions. Technical and non-technical criteria including development time, cost, reliability, logistic considerations, and tactical convenience, must be considered prior to determining whether the propulsion system should use solid or packaged liquid propellants. Testing of structural models will be necessary to establish the dynamic and static characteristics. These results in turn might affect the rocket motor operating pressure and in this fashion influence motor performance.

Ablative materials and methods of bending these materials to the basic structure must be analyzed and verified by experimentation. Quantities of refractory materials and techniques for forming them into the leading edge of the vehicle present additional problems requiring solutions. Aeroelastic investigations are necessary to enable the establishment of dynamic structural performance limits.

The development of a workable control system that will provide artificial stability is fundamental to the success of the PYE WACKET concept. In addition, work must be done to establish acceptable reaction jet time constants. Wind tunnel studies are necessary to determine the effects of external air flow on creating "effective forces," as well as to establish the best reaction jet orientation. Autopilot design studies are a major necessity in establishing the gains and other characteristics to properly match the vehicle structure and the reaction motor characteristics.

These are the primary areas to be considered in establishing the design for a flyable vehicle.

4.3 TEST VEHICLE PROGRAM

Analyses, experimentation, and laboratory simulations are useful to the determination of concepts, and necessary to the establishment of a design that can be fabricated into a vehicle. However, they cannot furnish the final evidence of the practicality of a concept. This can only be established by the flight of hardware.

4.2

SECRET

SECRET

Flight testing is mandatory to the practical demonstration of:

1. Stabilized, controllable flight by means of a reaction jet control system
2. Omnidirectional launch capability

It is recommended that a program, resulting in the flight of a series of test vehicles, be initiated as early as possible. This program should consist essentially of the following:

1. Engineering analysis and design
2. Test vehicle fabrication and laboratory checkout
3. Flight tests and analysis

Starting with the premise of utilizing off-the-shelf components that can be used "as is" or with a minimum of modifications, much of the engineering work described above would be performed. Both vehicle performance and configuration dimensions will be directly dependent on available rocket engines that might be suitable for the test vehicles; peak velocity will probably be in the mid-supersonic range. Many of the tasks outlined in the previous section will take less effort than would be required, for, say a prototype missile that meets the requirements for a high performance mission. For example, aerodynamic heating and the design of thermal protection for the structure become nominal problems.

Thrust chambers and valving for the reaction jets and instruments for the autopilot appear to be straightforward adaptations of existing equipment. It is expected that considerable wind tunnel evaluation of the test vehicle configuration will be necessary in the subsonic, transonic, and supersonic ranges. Experimental data will be acquired, also, with simulated main propulsion and reaction jets.

The hardware required should be obtained early in the program to facilitate breadboard experimentation as well as to minimize fabrication delays. The entire task, including engineering, design, fabrication, checkout and flight test, should be programmed on a parallel (more correctly overlap) basis rather than pursuing each portion individually and doing the job in "series."

It is further recommended that a sufficient number of vehicles be fabricated so that allocations for the various flight test objectives are possible, for example:

1. Lot 1 - ground launched vehicles to checkout vehicle performance and stabilization characteristics.
2. Lot 2 - sled launched directly forward to check out launching equipment and response of control system in high speed interference flow.
3. Lot 3 - cross-wind launch from a moving sled to determine omnidirectional launch capabilities and check out control system response to programmed inputs.
4. Lot 4 - spare vehicles for contingencies, and special limited objective flights other than the above.

SECRET

It should be noted that in most missile flight test programs the first lot of vehicles is usually flown for propulsion and airframe checkout. A control system might be installed in the vehicle but would not be active. Though the control system is inactive, a telemeter monitor might be used to check the function of the control system under flight atmospheric, mechanical, and thermal environments. Prove-out of the PYE WACKET concept, on the other hand, will require flight test vehicles having actively functioning control systems to provide stabilization.

Later flight vehicles should have programmed inputs to the autopilot for the purpose of checking vehicle response and maneuverability as well as to simulate the "black box" input of guidance.

4.4 PROTOTYPE MISSILE

Indications are that bomber aircraft will retain some degree of strategic importance for at least 10 more years. These aircraft will require an active defense against enemy aircraft, attacking with conventional armament and missiles, as well as against surface-to-air missiles. Attack and interceptor aircraft could conceivably develop completely new and much more flexible tactics based on an omnidirectional launched missile. Furthermore, in the time period that follows, manned semiatmospheric and atmospheric-entry vehicles, performing military functions, will require some form of armament for active defense against enemy missiles.

To date, no modern general purpose armament has been developed to replace the traditional machine gun and cannon as manned aircraft defenses. PYE WACKET could fill this very serious need. However, prior to any development of PYE WACKET as an air launched missile, it is recommended that an intensive system engineering evaluation be made of current aircraft of long operational life expectancy and manned vehicles now under development, to determine the degree of compatibility among the search, track, and fire control systems, space allocation for stores and missile stowage, etc. to allow for the possibility of general purpose armament of PYE WACKET design that would be a "fit" to all. If this should be impossible, then the missile design should be accommodated to an advanced manned vehicle now under development with the possibilities of retrofit to at least one kind of long-operational life expectancy aircraft.

It is recommended that the usage survey be performed simultaneously with the test vehicle program discussed above. It is further recommended that engineering study efforts be initiated on long lead-time subsystems, e.g., the propulsion system, concurrent with the survey of aircraft applications. It is highly desirable that prototype engineering be initiated during the vehicle flight test phase, rather than at the conclusion of that phase, in order to shorten the

SECRET

total development period. A short development period is particularly important in view of the serious need for an effective defense system for manned aircraft.

4.5 OTHER APPLICATIONS

Other applications of the PYE WACKET configuration have been briefly discussed in this report. Because of the limitations on this study these received only a cursory review. Several of these possibilities, it is believed, should be examined for design feasibility. The off-set capability for air-to-surface missions is particularly attractive. The potential of the configuration for use in a compact, manned, satellite-station-to-earth-return vehicle also deserves technical consideration. Many other application possibilities have been suggested, but because of their peripheral nature, emphasis here is probably not warranted at this time.

SECRET

SECRET

Appendix A
RESEARCH AND DEVELOPMENT EXHIBIT

AIR PROVING GROUND CENTER
Eglin Air Force Base, Florida

R&D EXHIBIT NO. PGEM 58-162
DATE: 26 November 1958

(U) LENTICULAR ROCKET

1. SCOPE

1.1 This exhibit establishes the applied research requirements for the study and design of a guidable lenticular circular planform munitions concept as an airborne weapon.

1.2 Objective. - The objective of this program is to scientifically establish and demonstrate the feasibility and applicability of a new munitions concept.

2. APPLICABLE DOCUMENTS¹

2.1 The following documents, of the issue in effect on the date of the invitation for bids, shall form a part of this exhibit to the extent specified herein:

EXHIBITS

APGC 57-2

Contractor Prepared Technical
Publications

APGC 58-1

Manufacturer's Engineering Data
for Experimental Items

(Copies of documents required by contractors in connection with specific procurement functions should be obtained as directed by the Contracting Officer.)

¹ Unless otherwise described, all titles and documents referenced in this exhibit are UNCLASSIFIED.

SECRET

3. REQUIREMENTS

3.1 General Requirements. - The applied research efforts conducted under this exhibit shall consist of:

a. Investigative study and design of a lenticular circular planform rocket configuration as an airborne weapon.

b. Analysis and evaluation of design parameters and the determination of technical feasibility of the lenticular munitions concept as a significant advance in weaponry.

3.1.1 Approach. - Design study and analysis shall be undertaken to establish the technical feasibility of the lenticular circular planform configuration as (first) possessing superior aerodynamic launch, stability, and maneuver capabilities, and (secondly) as a potential airborne weapon with distinct advantages over the present weaponry state-of-the-art.

3.2 Military Requirements. - Studies and designs conducted under this exhibit shall be directed to a lenticular circular planform weapon designed to optimunly meet the performance capabilities delineated in the following military requirements:

a. Omnidirectional, guidable, weapon possessing a subsonic, transonic, and supersonic rocket launch capability in all directions, e.g., crosswind.

b. Weapon gross weight of approximately 350 pounds with a 2,000 to 7,000 foot minimum separation distance (stand-off) at 60,000 feet altitude and an approximate 800 pounds gross weight weapon for a desired long stand-off distance of 15 to 25 nautical miles.

c. Weapon external dimensions shall approximate 7.5 inches and 10 inches lenticular cross section thickness with a 60 inch circular planform diameter.

d. Weapon operational altitude shall be initially from sea level to 100,000 feet and within a temperature range of from -65°F to -165°F.

e. Weapon shall be structurally rigid to withstand extremely high launch accelerations, rapid change of thrust direction for quick maneuver, and terminal velocities in the order of M10.0.

SECRET

3.3 General Design Requirements

3.3.1 Aerodynamic Shape.- Design studies, analysis, and wind tunnel trials shall be conducted of aerodynamic shapes basically circular in planform, lenticular in cross section, that are determined to be most suitable for programmed and guidable weapon applications.

3.4 Metallurgical and Parts Design Features.- The lenticular rocket design shall incorporate the most modern metallurgical advances that can contribute peculiar advantages to the overall weapon design, and the miniaturization and optimization of weapon components. Particular attention is directed to the need for parts design of light weight, miniaturized construction with high strength characteristics to withstand forced ejection, launch, and the extremely rapid and severe maneuvers required of this weapon.

3.5 Accuracy.- Design effort shall be directed to a lenticular rocket accuracy goal of delivering the weapon within 5 to 10 milliradians of a pre-established point, within 5 milliseconds or less of a pre-determined time, and within 5 degrees and 500 feet per second of a pre-determinable velocity vector at that point. The spatial "point" is to be selectable at will on a 2,000 to 10,000 feet radius sphere centered on an aircraft coordinate system. The velocity vector requirement can be waived at less than 5,000 feet radius.

3.6 Drawings.- Drawings required by the contract shall be prepared in accordance with Exhibit APGC 58-1, Class I.

3.7 Reports.- Progress reports shall consist of:

- a. Letter Progress Reports
- b. Technical Notes
- c. Technical Report

3.7.1 Letter Progress Reports.- This report shall be in letter form and shall describe progress of the work accomplished, future plans, manpower, and time expended; other pertinent information.

3.7.2 Technical Notes - This report shall be prepared in the format and scope required by Exhibit APGC 57-2 unless otherwise specified in the contract.

3.7.3 Technical Report.- The final report shall be prepared in accordance with Exhibit APGC 57-2 upon completion of all items of work.

SECRET

SECRET

4. INSPECTION AND TEST PROCEDURES

4.1 Presubmission Testing.- No item, part, or complete equipment shall be submitted by the contractor until it has been previously tested and inspected by the contractor and found to comply to the best of his knowledge and belief with the requirements of this exhibit. With the consent of the contractor and at the discretion of the procuring activity, this prior test and inspection may be participated in or witnessed by the procuring activity with the object of eliminating the necessity of repeating such test and inspection after the equipment has been formally submitted to the contracting activity.

4.2 Inspection Tests.- Acceptance or approval of material during the course of manufacture shall in no case be construed as a guaranty of the acceptance of the finished product.

4.3 Test Facilities.- The contractor shall furnish testing facilities and shall be responsible for accomplishing all tests necessary to determine compliance with this exhibit.

NOTICE: When Government drawings, specifications, or other data are used for any purpose other than in connection with a definitely related Government procurement operation, the United States Government thereby incurs no responsibility nor any obligation whatsoever, and the fact that the Government may have formulated, furnished, or in any way supplied the said drawings, specifications, or other data is not to be regarded by implication or otherwise as in any manner licensing the holder or any other person or corporation or conveying any rights or permission to manufacture, use, or sell any patented invention that may be in any way related thereto.

SECRET

INITIAL DISTRIBUTION

1	Hq USAF (WSEG)	1	NY ARDC Regional Ofc
1	Hq USAF (AFDAP-W/SA)	1	AF Ofc of Scientific Rsch
1	Hq USAF (AFDAP/W-AD)	3	ARDC (RDLR)
1	Hq USAF (AFOOP-ST)	1	ARDC (RDRWM)
1	Hq USAF (AFOAT)	1	ARDC (RDRCE)
1	Hq USAF (AFPTR-D)	2	WADD (WCORC)
1	Hq USAF (AFDRD-ER-4)	5	WADD (WCLGDPL)
1	USAF Dep IG for Insp (AFCDI-B)	1	WADD (WCLFSH)
1	DOD Dep Dir Rsch & Engi- neering, Ofc of Asst Dir of Fuels Mtal & Ord	1	WADD (WCLCM)
2	Ofc Asst Secy of AF (Rsch & Dev)	2	WADD (RDZSB)
3	Hq USAF (AFDRD-CV)	2	WADD (RDZST)
3	Hq USAF (AFDAP-TA)	2	WADD (RDZSD)
1	Hq USAF (AFDRD-DS)	2	WADD (RDZSX)
1	Hq USAF (AFDDP)	1	WADD (RDZSXD)
1	Hq USAF (AFDAP-SA)	2	WADD (RDZSS)
1	Hq USAF (AFDAP-AD)	3	WADD (V/STOL WSPO)
1	Hq USAF (AFOOP-TA)	2	WADD (WCLGST)
1	Hq USAF (AFOOP-SA)	1	AMC (MCMSRM)
1	Hq USAF (AFORO-SA)	2	Western GEEIA Rgn
1	Hq USAF (AFORO-TA)	5	SAC (OA)
1	Hq USAF (AFORO-AD)	1	SAC Dep D/Ops
2	Hq USAF (AFGOA)	1	SAC (DORQ)
1	ATIC (AFGIN-4B1a)	1	SAC (DORQP)
1	ARDC (RDRWM)	1	SAC (DORQO)
1	ARDC (RDRWA)	1	SAC (DORQA)
1	ARDC (RDMTT)	1	SAC (DM6B)
1	ARDC (RDMTI-1)	1	SAC (OAPT)
1	ARDC (RDMTI-2)	1	SAC (OAWS)
1	ARDC (RDRCE)	1	SAC (OAOC)
2	WADD (WWAT)	1	SAC (DORQM)
1	ARDC Ofc, Redstone Arsenal	1	SAC (OA, Scientific Advisor)
1	ARDC Ofc, Pac Msl Rg	1	TAC (TOD)
1	ARDC Ofc, NEODTC, Nav Propellant Plant	1	TAC (TORQ-T)
3	AU(AUL-9764)	1	TAC (TMD)
		1	ADC (ADOCE-DL)
		1	ADC (ADOOA)
		1	ADC (ADOTS)
		1	AAC (DCS/O, Ops Anal)
		1	USAFE (ADVON)(OA)
		2	USAFE (ADVON)(OTREQ)
		2	PACAF (PFOOP-RQ)

INITIAL DISTRIBUTION (Cont'd)

4	Federal Avn Agcy, Bureau of R&D, Records Officer	1	Convair Div, Gen Dynamics Corp
2	Federal Avn Agcy, Bureau of R&D, Nat Avn Fac Exper Cen	1	NASA Space Task Group
		1	NOTS, Code 556
1	Inst of Air Wpns Res (Lib)	1	AFBMD (WFTV)
2	USAF Proj RAND	1	AFBMD (WDEA)
1	DASA (Doc Lib Br)	1	AFBMD (WDZ)
1	Fld Comd DASA (FCDV)	1	NASA, Ames Aeronautical Lab
3	NASA (Ames Rsch Cen, Lib)		
1	Army Ballistic Msl Agcy, ORDAB-HT		
2	Ofc of Ord Rsch, Internal Rsch Div		
2	USA Electronic PG, Tech Lib		
2	Army Ord, ORDTU		
1	Army Rocket & Guided Msl Agcy, ORDXR-RED		
2	Ch of Nav Ops, Op03EG		
1	Nav Air Rsch & Dev Act Comd, Tech Lib		
1	NATC (Armt Test Div)		
1	Nav PG, Tech Lib		
1	Nav Ord Lab, Lib		
1	Nav Ord Lab, Tech Lib		
1	Bureau of Nav Wpns, Capt Ruckner(R)		
1	Bureau of Nav Wpns, (RU)		
1	Bureau of Nav Wpns, (RUAW)		
1	Bureau of Nav Wpns (RUAW4)		
2	Bureau of Nav Wpns Convl Air Wpns Sys Ofc, Code RM 377		
2	Ch of Nav Ops, OP-07		
1	US Marine Corps, AO4E		
1	US Marine Corps, AAP		
1	Marine Corps, Landing Force Dev Cen		
15	ASTIA (TIPCR)		